Radar Cross Section

Second Edition

Eugene F. Knott
John F. Shaeffer
Michael T. Tuley

Raleigh, NC
www.scitechpub.com

Printed in the United States of America

10 9 8 7 6 5 4 3 2 1

ISBN: 1-891121-25-1

SciTech books may be purchased at quantity discounts for educational, business, or sales promotional use. For information contact the publisher:

SciTech Publishing, Inc.
Raleigh, NC 27613
(919) 866-1501
www.scitechpub.com

Library of Congress Cataloging-in-Publication Data

Knott, Eugene F.
Radar cross section / Eugene Knott, John Shaeffer, Michael Tuley—2nd ed.
ISBN 1-891121-25-1
1. Radar. I. Shaeffer, John F. II. Tuley, Michael T.

TK6580.K56 2004 92-37802
621.3848—dc20 CIP

Preface to the Second Edition

We noted in our preface to the first edition of this book that advances in both prediction and measurement technology had moved steadily forward over the years, and would continue to do so. The accuracy of the latter forecast, and the fact that the book continues to be an essential part of Georgia Tech's short course on radar cross section reduction, impelled us to undertake a revision. The revision reflects what we learned about readers' needs and interests in the presentation of the short course.

Readers familiar with the first edition will discover that material of marginal interest has been purged to make room for more useful information and that a significant amount of new material has been added, some of which is published here for the first time. The result is that the second edition is some 20% fatter than the first.

Some of the revisionary work amounted to a mere shifting of information from one place in the book to another, with no net change in content. The improvement of existing illustrations throughout the book and the exploitation of modern printing technology similarly brought about little net change in content, but the reader will see that the book is now much easier to read. Nevertheless, new illustrations and a great deal of new information have been added.

In response to reader demand, we shifted the discussion of basic relationships from other chapters to Chapter 1. Although the information in Chapters 2 and 3 is essentially the same as that in the first edition, we have given the material somewhat different emphasis. We present in Chapter 4 new (and more) examples of field distributions and RCS predictions as obtained by means of the method of moments. We include in Chapter 5 an analysis of traveling wave lobes that shows how the errors in two separate approximations tend to cancel each other for a nearly perfect result. Chapter 6 has been completely rewritten, including a novel chart comparing the creeping wave echoes of metal spheres, cylinders, and circular disks.

Chapter 7 now includes some of the practical considerations (*do*s and *don't*s) of planform shaping to reduce target echoes. By deleting marginally useful material on absorbers, we were able to compress the former Chapters 8 and 9 into a single Chapter 8 and at the same time provide significantly more material on nonspecular absorbers. The revised Chapter 9 is essentially the former Chapter 10, with a bit more analysis of transmission line measurements of absorber samples. Chapter 10 is completely new, treating the problem of reducing the echoes from antennas, for which the frequency-selective surface is but one approach.

We have expanded Chapter 11 to include a section on the calibration of RCS measurements. In the revised Chapter 12 we explain why the antennas of an outdoor ground-plane test range may almost always be aimed along a local horizontal, and not upward toward the test object. Chapter 13 now contains a discussion of the compact range, an indoor RCS test facility that emulates a free-space (plane wave) test environment in very short distance. Chapter 14 has been expanded to include examples of radar imagery derived from coherent measurements of test objects.

Eugene F. Knott
John F. Shaeffer
Michael T. Tuley
September 1992

Preface to the First Edition

The term *radar cross section,* and its acronym RCS, is familiar to most scientists and engineers involved in radar systems, but to others it may seem to be an obscure characteristic of a body or target scanned by a radar beam. They have somehow learned or heard that this strange area is not necessarily the geometrical cross section of the body; if not, then what is it? The name *radar* itself may even evoke memories of difficult electromagnetic courses taken in college and therefore, for some, the concept of radar cross section is mysterious and elusive.

In order to acquaint scientists and engineers who may be competent in their own disciplines with a seemingly new and unfamiliar technology, Georgia Tech introduced a short course on radar cross section reduction in January 1983. The course focused not only on what radar cross section is, but how to reduce it as well. Accompanying the formal lectures was a set of course notes numbering over 700 pages. This book is an outgrowth of those notes.

As the reader will perceive, the book is not intended as an exhaustive survey or treatise. Such would defeat our purpose of exposing the novice to what can quickly become a very complicated subject. For those who wish to pursue the subject in more detail, several books are available that delve into the intricacies of prediction and measurement techniques. In addition, many of these books are classics, giving far more information than is included here. The reader will find many of these books and papers listed in the references at the end of each chapter.

In addressing our purpose of presenting the flavor of RCS, if not its intricacies, we have organized the book into five groups of chapters. Chapters 1 and 2 contain background information; Chapters 3 through 5 introduce the concept of scattering and present useful RCS prediction techniques; Chapter 6 displays examples of RCS behavior for simple and complex bodies; Chapters 7 through 9 address radar cross section reduction methods; Chapters 10 through 13 discuss techniques for measuring absorber properties and the scattering characteristics of test targets; and

Chapter 14 examines practical ways to identify scattering mechanisms on complex targets.

The reader should appreciate that technological advances have been steady in this field, and will continue to be so, and that even during publication of this book measurement and prediction techniques are being improved and modified. Moreover, in the interest of national security, some aspects of radar cross section measurement, prediction, and reduction cannot be presented here. Therefore, the book is not as detailed nor as complete as the authors would have preferred. Nevertheless, we think that it fills a need in the engineering community. We hope the reader agrees.

Eugene F. Knott
John F. Shaeffer
Michael T. Tuley
June 1985

Contents

Chapter 1
Introduction

Eugene F. Knott

1.1 OVERVIEW

This book is an introduction to the rather broad field of the echo characteristics of radar targets. It is intended to acquaint engineers, scientists, and program managers with what may be a new and unfamiliar discipline, even though a great body of knowledge has existed since the widespread use of radar in World War II. Modern weapons systems often carry RCS performance specifications in addition to other, more conventional requirements, such as speed, weight, and payload. Integrating these specifications into a new or existing system requires that engineers of several disciplines interact with each other. Our intention is to improve that interaction by showing why certain electromagnetic design procedures or features are important in the overall system design.

An integrated design approach is obviously a vital one, especially for complex systems or weapons. Aircraft designers and manufacturers have used it for decades, relying on the interaction between specialists to reconcile differences in individual approaches to mission objectives. Experts in propulsion, aerodynamics, structures, and avionics are only a few examples of the specialists called on to participate in the overall design effort. For many years, however, smaller, less astute airframe manufacturers included the RCS specialist only in the final stages of design, not in the early stages of concept definition. This specialist's role was confined essentially to the application of electromagnetic band-aids to the prototype airframe.

The result was that although a new missile or aircraft might have the required range, speed, and payload, its radar echo could be so strong that the craft stood a high probability of being shot down before completing its mission. Because

shaping is one of the most important ways of controlling that echo and because the RCS expert was seldom consulted early enough to influence the configuration of the vehicle, little could be done to improve its echo characteristics. The development of the SR-71 spy plane was a remarkable exception to this general exclusion.

Lockheed was awarded the contract for the A-12 (Lockheed's designation for the closely related SR-71) on August 29, 1959, but the existence of the effort was not made public until President Johnson's announcement of it in 1964 [1]. The aircraft was designed at Lockheed's famed Skunk Works under the guidance of the late Kelly Johnson, who knew full well that RCS experts *had* to be included on the design team at the inception of the project. The physical shape of the SR-71 is evidence of their influence and a testimonial to Johnson's foresight.

To the disappointment of many SR-71 pilots—and the consternation of a few avid admirers of the airplane—the U.S. Air Force officially retired the SR-71 in 1990. This led to the speculation that a top-secret replacement was in the Skunk Works, if not already in the sky. Indeed, *Time* magazine reported that this replacement (allegedly code-named *Senior Citizen,* perhaps with tongue in cheek) was a hypersonic craft capable of speeds of 4,000 mph [2]. The Air Force neither confirmed nor denied the existence of *Senior Citizen* at the time, a position often taken on advanced programs in the early stages of their development.

There comes a time, however, when the existence of the weapon can no longer be denied; this usually happens after it is pressed into operational readiness and has been observed. Sometimes the sheer size and political impact of the program leads to premature exposure, which seems to have been the case of the B-2 stealth bomber. In other cases, an official admission of the existence of the program is never made, as with the fabled F-19 stealth fighter. The F-19 was never built, nor its prototype ever displayed, yet its planform was widely circulated by a hobby-model manufacturer. Although the true source of the mythical F-19 planform may never be known, the planform was markedly different from that of the real stealth fighter, the F-117A. Therefore, it is altogether possible that the F-19 was an aberration, whether deliberate or inadvertent, of the true direction being pursued in U.S. technology at the time.

It can be shown that the rounded planform of the mythical F-19 is not quite as stealthy as the straight-edged planform of the real F-117A. Indeed, the simple formulas found in later chapters of this book make it possible to make first-order estimates of the echoes from many planforms, from which one may rank relative "stealthiness." Such estimates depend on a knowledge of basic target echoing characteristics, and if they lack the precision we might demand, we can always resort to measurements to validate them. Therefore, one of the primary objectives of this book is to acquaint the reader with basic echoing properties, whether measured or predicted, for targets that may be real or imagined.

To accomplish this, we have grouped the material into the following five categories:

- Background information;
- Electromagnetics;
- RCS phenomenology;
- Shaping and absorbing materials;
- Measurements.

The background information is contained in this chapter and in Chapter 2. Because the radar echo mechanism is strictly an electromagnetic phenomenon, we devote three chapters (Chapters 3 through 5) to the development of electromagnetic theory and RCS prediction techniques; examples of the echoes from simple and complex objects are presented in Chapter 6.

The control—actually, the suppression—of the echo properties of constructed targets is of great practical and tactical importance, and the two primary ways of reducing echoes are by shaping and by using absorbing materials. Shaping is discussed in Chapter 7; the analysis and design of radar absorbers is discussed in Chapter 8; and Chapter 10 is devoted to the characterization and suppression of the returns from antenna structures in particular. The measurement and evaluation of absorbers is treated in Chapter 9; and RCS measurement techniques are described in Chapters 11 through 13. The analysis and interpretation of RCS measurements is given in Chapter 14.

1.2 RADAR SYSTEMS

The acronym *radar* was coined during World War II and was so new that many 1945 dictionaries did not list the word. It stands for "radio detection and ranging," and since its introduction in the 1940s, it has become a common household word. Radar was initially developed to replace visual target detection for several reasons. Radio waves suffer much less attenuation through the atmosphere than light waves, and signals in the lower frequency ranges actually propagate over the visible horizon. This makes it possible to detect targets long before they are visible optically. Radars also work well at night when there is little or no ambient light to illuminate the target.

A radar emits its own energy and does not rely on the illumination of the target by other sources. As such, it is an active device, rather than a passive sensor. In fact, a major advantage of radar is that it is an active system which can clock the time it takes for energy to travel to the target and back again.

The radar uses the known velocity of propagation of an electromagnetic wave to determine the distance to the target. The velocity of light is 186,282 miles per second, but a more convenient number to remember is 11.8 inches per nanosecond.

Within a margin for error of only 1.6%, this is 1 foot per nanosecond. Accounting for the two-way propagation (out to the target and back again), the distance R to the target is simply

$$R = c\Delta t/2$$

where c is the speed of light and Δt is the time interval between the transmission of an energy pulse and the reception of the radar echo. Thus, the radar is a timing device.

However, distance alone does not reveal the target location. Two direction angles must be measured, and there are a variety of ways to do so. Fortunately, because of the nature of most radar antennas, it can be done simply by measuring the direction in which the antenna is pointed. If the antenna is mounted on a pedestal having two axes of rotation (azimuth and elevation, for example), the two angles can be measured by devices mounted on the rotation shafts. The distance and the two angular directions then serve to locate the target.

In many instances the target is low enough on the horizon that an elevation angle measurement is unnecessary. Morever, there are other cases when the waves propagating between the target and the radar curve gently downward with increasing distance, hence the elevation angle of the antenna does not indicate the true elevation angle to the target. This curving or bending is due to a gradual reduction in the atmospheric index of refraction with increasing height; the bending itself is called *refraction.*

Like the eye and other optical systems, the radar antenna is deliberately designed to be more sensitive in a given direction than in other directions. This serves to concentrate more energy on the target upon transmission and to increase the receiver sensitivity upon reception. The directivity increases as the antenna becomes physically larger, and energy concentrations of 1000 to 100,000 times the omnidirectional value are not uncommon.

Phased arrays are another common form of antenna. They consist of a large collection of elementary antennas, such as dipoles or waveguide slots, each of which is excited or fed from a distribution network. Depending on the spacing between elements and the relative phase of their excitation, the net radiation from this collection can be swept from one direction to another without any physical motion of the array itself. Since this scanning can be done electronically, very high scan rates can be achieved.

Whether or not a radar is caused to scan depends on its mission and deployment. Low-frequency radars are typically long-range systems used for surveillance and detection well beyond the horizon. Lowfrequency antennas are usually fixed, permanent installations because of their large size. Shorter range surveillance systems operate at higher frequencies and are typically scanned in azimuth; some scan in elevation as well as azimuth with an up and down nodding

motion, superposed on a slower azimuth scan. Scanning radars can be found in land-based systems, on ships, and in aircraft.

Fire control radars track their targets in space. The tracking systems, therefore, must include angle tracking as well as range tracking. A computer is often an integral part of the radar, extracting trajectory information from the track history and feeding pointing information to the gun or other firing system. Terminal homing radars are small and light, because they must fit inside a relatively confined area in a missile. There has been a tendency to exploit shorter wavelength instrumentation for these systems because of weight and space constraints.

The great variety of radars and their missions make it impossible to list and discuss the many kinds. Consequently, the systems discussed in Chapter 2 are generic, and only a few examples are given. The simplest system is the *moving target indicator* (MTI) radar, whose output indicates only targets that move; an example is a police radar. The radar emits a continuous stream of energy, and a sample of the transmitted signal is used as a local oscillator signal, to be mixed with the received target signal. This "mixing" action generates a signal whose frequency is the difference between the transmitted frequency and the target reflected frequency. The only way the two frequencies can be different is if the target is in motion, in which case the difference frequency is proportional to the component of the target velocity toward or away from the radar.

Except for *continuous wave* (CW) radar systems, radars are pulsed because of the need to emit a burst of energy and then remain quiet while "listening" for the echo. In addition, pulsed operation allows high-power transmission for short intervals of time. Typically, a conventional pulsed radar is "on" for only 0.1% to 0.5% of the time, and consequently it spends most of its time listening for the echo.

1.3 ELECTROMAGNETICS

We live in an environment of *electromagnetic* (EM) waves, and the microwave frequencies of radar systems occupy only a small region of the EM spectrum. Nevertheless, these waves, whether light, radio, or microwaves, all obey the same physical laws. The laws governing the behavior of EM waves were established by the year 1900, thanks to the pioneering efforts of researchers like Hertz, Faraday, Ampere, Coulomb, and Maxwell.

Early experimenters were downright curious, and inventors like Bell and Edison exploited known phenomena, as well as undertaking their own profit-oriented research. Each made his own contribution, but it was James Clerk Maxwell who assembled the results of the experimenters and formulated the basis of modern electromagnetic theory. His famous four equations, augmented by a handful of others, are the foundations of the theory, much as the Navier-Stokes equations are the foundations of fluid mechanics.

The EM waves of concern to us are harmonic in both time and space, for which Maxwell's equations take on a specific form. Remote from any source of radiation and reflection, the electric and magnetic fields remain at right angles to each other as well as to the direction of propagation. The electric and magnetic fields both attain their maximum values at the same time and place, and in the course of their harmonic variation they also go to zero at the same time and place.

When an EM wave impinges on a body, it induces oscillating charges and currents inside that body and on its surface. For the special case of a perfectly conducting body, the induced charges and currents are confined to the surface, and at microwave frequencies, even a poorly conducting metal like steel approximates the behavior of a perfect conductor. Therefore, even if the body is a thin steel shell, there are no induced fields or charges inside, provided the shell is a closed surface.

Even if the body is a dielectric material capable of supporting induced charge and currents in its interior, attention can be confined to the charges and currents induced on its surface. As shown in Chapter 3, the electric and magnetic fields at any point in space can be expressed in terms of a surface integral of the charges and currents induced on the surface of a body. Although this is a well-known result for source-free regions, it is rather remarkable that we do not need to know the interior distributions of charge and current in order to calculate the scattered fields.

The total field at an observation point due to radiation by induced fields over the surface of the target obstacle is composed of the incident and scattered fields. Presumably, the incident field is known, and all that need be done is to subtract it from the total field in order to obtain the field scattered by the body. This is trivial.

What is not so trivial is estimating the induced charges and currents. Indeed, this is the crux of the problem, for if the charge and current distributions are known, the integral can be evaluated, numerically if not analytically. Finding the induced fields is the problem, but in some cases the integral equation can be broken into a collection of homogeneous linear equations that are then amenable to solution.

However, such a solution is restricted by computer memory to bodies not much more than a wavelength in size. If some particular feature of the target can be exploited, such as roll symmetry or the two-dimensional nature of infinite bodies, the size that can be treated approaches about 10 wavelengths. This form of solution for the induced currents and charges is called the *method of moments,* and the fields on the body must be sampled at intervals of around $\lambda/10$. The interaction of each segment with every other segment creates a square matrix that, when inverted, yields the solution.

Another approach to finding the fields scattered by the body is to restrict our attention to the far field and to make what is known as the tangent plane approximation. It results in a prescription known as physical optics, which yields a great

deal of useful information. In applying the tangent plane approximation, we first identify the local patch of integration over the body surface. An infinite plane must be tangent to the body there, and the local tangential fields are assigned the identical values that they would have had, if the body had been truly flat and infinite in extent at the tangent point.

These local tangential fields are available from the theory of geometric optics, which simply invokes the known boundary conditions for an infinite plane separating two different media. Usually the body is taken to be metallic, but the approach also works for dielectric materials. It has even been applied successfully to thin membranes, such as found in soap bubbles and the leaves of trees.

Having invoked the tangent plane approximation, we can evaluate the surface integral. Note that the problem of solving for the induced surface fields has been completely bypassed; in essence, the local radius of curvature has been assumed to be large enough that the induced fields are negligibly different than those of an infinite sheet viewed from the same angle.

There are only a few cases in which the surface integral can be evaluated exactly, and even then we must bear in mind that the integral itself is now only approximate. The integral is almost trivial if the body is a flat plate, and rapidly becomes complicated even for a cylinder, as shown in Chapter 5. Generally, there is no exact evaluation for doubly curved surfaces except for very symmetrical bodies, and the method of steepest descents must be used.

1.4 RCS PHENOMENOLOGY

Whatever the case, evaluation of the physical optics integral yields important and useful results. In the case of a flat plate, it yields the correct result when the plate is viewed at broadside incidence, and the answer is reasonably accurate several degrees away from the specular (broadside) orientation. In fact, the angular sector over which the theory gives acceptable results depends on the electrical size of the plate.

However, another analytical procedure can be used: the *geometrical theory of diffraction* (GTD). In formulating his GTD, J. B. Keller extended the notion of geometric optics for the single ray reflected by a surface to a cone of rays diffracted by an edge. The cone of diffraction still contains the geometric optics feature whereby diffracted rays leave the edge at the same angle made by the incident ray. However, the theory can be exploited to postulate induced edge currents, which expand the angular (nonspecular) coverage of the diffracted fields. More importantly, GTD has a built-in polarization dependence that is absent in physical optics and geometric optics.

Examination of the results for a flat plate gives some insight into a hierarchy of scattering types. The broadside return from the plate is proportional to the

square of the area of the plate and the square of the frequency. For this particular orientation, the plate behaves like a dihedral or trihedral corner reflector, whose returns also increase with the square of the area and the square of the frequency. Thus, the trihedral corner, the dihedral corner viewed in a direction perpendicular to its axis, and the flat plate viewed at normal incidence all constitute one class of scatterer.

If the plate is oriented off the specular angle, but in such a way as to maintain a pair of edges perpendicular to the radar line of sight, the radar return is no longer proportional to the square of its area, but to the square of the edge length. The return is also independent of frequency, a characteristic shared by the doubly curved surfaces, of which the sphere is an example. Thus, spheroids and edges presented normal to the line of sight have frequency-independent echo strengths.

If the plate is angled so that no edge is perpendicular to the radar line of sight, the radar simply senses the returns from the four corners. The echo of a corner has no dependence on length because a corner or vertex has no physical dimension: it is a point. Therefore, the returns from vertices vary inversely with the square of the frequency.

Consequently, a rather simple structure like a flat plate exhibits at least three kinds of scattering behavior, depending on its orientation. A cylinder also has more than one kind of scattering behavior: at broadside incidence, the return from a cylinder varies as the cube of some body dimension and directly with the frequency. When the cylinder is tilted with respect to the line of sight, its return degenerates to the contributions from a pair of curved edges, one at either end. The echo from a curved edge varies inversely with the frequency, and therefore lies somewhere between the characteristic of a straight edge and the characteristic of a vertex.

These characteristics do not include the creeping wave mechanism, which is a phenomenon generally associated with smooth bodies that are not large with respect to the wavelength. The creeping wave is launched at a shadow boundary and traverses the shadowed side of a smooth body, eventually emerging at the shadow boundary on the other side of the body. It loses energy as it propagates around the rear curved surface, and the longer the electrical path length, the more energy it loses. The creeping wave phenomenon becomes negligible for most bodies that are larger than a dozen or so wavelengths.

A wave often confused with the creeping wave is the surface traveling wave launched along surfaces at small grazing angles. The phenomenon occurs only when a component of the electric polarization is parallel to the surface along the direction of incidence, when the angle of incidence is within a few degrees of grazing, and when a discontinuity at the far end of the body reflects the wave back toward the radar. The difference between this mechanism and the creeping wave mechanism is that the wave travels along an illuminated surface in the one case and over a shadowed surface in the other. The surface wave contribution can be reduced by smoothing out the discontinuity at the rear of the body, which urges the wave forward into the shadow region where it becomes a creeping wave.

1.5 ABSORBING MATERIALS

One way of reducing the radar echo from a body is to soak up the incident electromagnetic energy, thereby reducing the net energy available for reflection back to the target. In order to absorb energy, materials must be found in which the induced currents are in phase with the incident fields, as are the currents in a resistor. In fact, many absorbing materials are manufactured with carbon providing the loss mechanism, and the dissipation of energy takes place by the conversion of electromagnetic energy into heat.

Energy absorption, however, does not necessarily require carbon. There are dielectric materials whose indices of refraction are complex numbers, and it is the imaginary part that gives rise to the loss. The molecules in the material are essentially small dipoles that try to orient themselves along the incident field. If the field changes too fast or if the dipoles lag the impressed field variations, torque is exerted and energy is deposited in the material. The dipoles experience a kind of molecular friction as they try to follow the oscillations in the fields.

Conduction losses are lumped together with the imaginary part of the index of refraction for engineering convenience. Moreover, magnetic losses can occur as well as electric losses, because the index of refraction contains the product of the magnetic permeability and the electric permittivity. Thus, lossy materials may also include ferrites or carbonyl iron in addition to, or in the place of, carbon.

The earliest form of radar absorber, the Salisbury screen, was a sheet of porous material impregnated with graphite and spaced a quarter-wavelength off a metallic backing plate. We know from transmission line theory that a short circuit (the metal plate) placed a quarter-wavelength behind a load effectively creates an open circuit at the load itself. Thus, the incident wave "sees" free space and there is no reflection. In fact, all of the power in the incident wave is delivered to the resistive sheet and none is reflected.

If the spacing between the sheet and the metal backing plate is not a quarter-wavelength, the wave sees a finite impedance in parallel with the impedance of the resistive sheet, producing a net complex impedance different from that of free space. Consequently, part of the incident power in the wave is reflected, with the reflection being greater the more the frequency of the incident wave moves away from the ideal spacing. Therefore, the Salisbury screen is a narrowband device.

The bandwidth can be increased by cascading several sheets, one behind the other and separated by spacers. The resistance should decrease from sheet to sheet, with the lower values being used for the sheets closer to the metal backing plate. This collection of sheets is called a *Jaumann absorber,* and the bandwidth rises with each additional sheet used in the design. However, additional sheets require additional spacers, and the thickness of the absorber increases.

The resistive sheet is only one form of absorber; there are bulk materials that are loaded with carbon as well. Although the conductivity of carbon is much

lower than metals such as aluminum and steel, it is still too high to be used as a solid material. The bulk conductivity must be reduced, typically by spreading a thin coating on the fibers of a fibrous mat or by infusing carbon in a matrix of spongy urethane foam.

Graded dielectric materials are manufactured by bonding together two or more layers of these spongy sheets. The carbon loading density must increase from layer to layer, with the highest loading (highest conductivity) being in the layer closest to the metal backing whose reflectivity is to be reduced. Unfortunately, these materials are bulky and fragile, and they are not suitable for applications involving exposure to weather and wind blast.

Much thinner absorbers can be fabricated by the use of materials having magnetic losses. Magnetic substances of value are iron oxides (ferrites) and carbonyl iron. The ferrites can be sintered in solid form, and the carbonyl dust can be mixed with an organic binder to form a matrix of the appropriate loss density. Although for a given level of performance the magnetic materials are typically thinner than ordinary dielectric absorbers, they are heavy because of their high concentrations of iron.

Another kind of material, called *circuit analog RAM,* utilizes lossy material deposited in geometric patterns on a thin lossless film. The thickness of the deposit, which is like aquadag, controls the effective resistance of the layer; and the geometry of the pattern controls the effective inductance and capacitance. Thus, the layer can be tailored to specific values of inductance, capacitance, and resistance, and its performance can be analyzed in terms of lumped elements. Typically, an absorber panel is composed of more than one layer and the layers are separated by light, low-density spacers. Absorber panels can be made that are much more durable than the foam materials mentioned previously.

Finally, hybrid absorbers can be designed and fabricated using combinations of the materials mentioned earlier. The design requires a knowledge or tabulation of the electromagnetic properties of the materials, including those of the spacers and the bonding agents used to hold the layers together. Typically, we seek a broadband design, and consequently, these electromagnetic properties should be available over the intended range of frequencies.

In addition to absorber materials, only one other method has been found practical for radar cross section control: shaping. Shaping is a more useful tool for systems in the design stage, but only if RCS threat sectors can be identified. The technique is virtually useless for retrofitting to existing vehicles because of the cost and probable impairment of the vehicle's mission. For example, moving the jet intakes of an aircraft from below the wings to above the fuselage is out of the question for operational aircraft.

If all viewing angles are equally likely, shaping offers no advantage, due to a rule of thumb that states that a reduction in the RCS at one aspect angle is always accompanied by an enhancement at another. For most airborne systems, however,

RCS control is of more importance in the angular forward cone than in the broadside sectors. Therefore, shaping can be used to shift large returns from the nose-on region to the broadside sectors. Highly swept wings are an example, but we should appreciate that shaping is best performed in the system design stages.

Antennas present special echo reduction problems that neither shaping nor absorbing materials, either alone or combined, can treat. The application of absorbers threatens to reduce the very signals the antenna is intended to radiate or capture, thereby degrading performance of the system it services. Shaping the antenna to produce a low echo counters the very shape or configuration needed for adequate sensitivity. As shown in Chapter 10, useful antenna designs exploit other concepts that may or may not involve shaping or absorbers, depending on the frequency spectra of the intended antenna operating signals and the threat waveform.

One concept is the frequency-selective surface, which can be manufactured to attenuate or transmit desired signal frequencies. When used to pass narrowband signals, it can be shaped to shield or conceal an antenna from all signals except those at the antenna operating frequencies. At all other frequencies it behaves like a good deflector when shaped to reflect the incident threat signal in directions away from the source. Another concept exploits cancellation, in which the two recognized components of the antenna echo are balanced against each other. One component is due to the physical structure of the antenna exposed to the incident wave. The other is due to unavoidable mismatches between the inherent impedance of the antenna, which is governed by its physical and electrical properties, and the impedance of the load "seen" by the antenna at its terminals. The very nature of such cancellation schemes precludes any hope of broadband antenna echo suppression, however.

A third option is to design a retractable antenna that is deployed only when needed, such as the one allegedly used for the F-117A instrument landing system [3]. Because this very practical solution circumvents all the complexities of other options and because it is so simple in concept, we omit it in our discussion of Chapter 10.

1.6 MEASUREMENTS

As in any other design requirement, RCS measurements are necessary to verify anticipated performance as well as to evaluate design approaches. In addition, measurements are required for the evaluation of absorber designs. Consequently, several chapters are devoted to the discussion of measurement tools and facilities. Chapter 9 focuses on material measurements, and Chapters 11 through 13 describe RCS measurement techniques and facilities.

Absorber materials can be tested in several ways, one of which is with a coaxial or waveguide transmission line. This technique is advantageous in that the

equipment can be set up on a laboratory bench and the fields to be measured are totally confined within the transmission line itself. Basic measurement techniques require that the voltage reflection coefficient of a material sample be measured, and this requires either multiple measurements with different terminations or a slotted section (a length of transmission line with a small probe inserted into the line to sample the field). The amplitude of the internal standing wave pattern gives the magnitude of the reflection, and the shift of the pattern one way or the other (when the sample is inserted in the line) gives the phase angle.

In the days when equipment was not as advanced as it is now, the measurements had to be performed manually at each frequency of interest. The introduction of time domain reflectometry and swept signal sources has made the task much easier and much faster to perform. In either event, the magnitude and phase of the reflection coefficient can be used, along with the sample thickness, to calculate the electromagnetic properties of the sample.

Transmission line techniques also have disadvantages: samples must be very carefully machined to fit inside the waveguide or coaxial line, and there is a risk of creating higher order field modes within the sample. Improperly fitting samples and higher order modes lead to erroneous results. Moreover, if the material is not homogenous, there is the risk of characterizing a sheet or panel of material on the basis of inhomogeneities existing in the small sample.

These errors can be reduced by testing or measuring large panels of absorbing materials, but it cannot be done in a transmission line. In one technique, the famous NRL arch method, the absorber panel is illuminated by a small horn. The system is calibrated by replacing the absorber panel with a metallic plate. Two horns, one for transmission and one for reception, are mounted on an arch centered over the test panel, and measurements can be conducted for a variety of angles of incidence and reflection.

It is difficult to measure the relative phase of the reflected signal, and consequently, the arch technique is typically used only for characterizing the amplitude of the reflection. However, the natural isolation between the transmitting and receiving horns makes it easy to use swept frequency sources, and consequently, the measurements can be made rapidly and the results displayed as a function of frequency minutes after the measurements.

However, the NRL arch technique may place the test panel in the near field, yielding reflectivity values that are lower than might be measured under farfield conditions. An alternative is to utilize an RCS measurements range where farfield conditions can usually be met. The material sample is mounted on a flat plate, which is in turn installed on a target support column in a vertical position. The plate is rotated through 360° in azimuth, and the broadside flash from the back side of the metal plate serves to calibrate the broadside flash from the absorber-covered side. Unless special instrumentation is available, the measurements must be repeated for each frequency of interest.

An RCS range serves a much more valuable purpose than merely evaluating absorber samples. The RCS range is a tool for engineering and scientific studies, as well as testing the performances of various design approaches or simply constructing a database for a collection of targets or target conditions. Such measurements are useful in characterizing the actual radar signatures of operational systems in dynamic flight scenarios.

As with any other engineering tool, RCS ranges have their particular virtues and shortcomings, and they come in all sizes, shapes, and geometries. Early RCS measurement facilities were indoor anechoic chambers, although some measurements were made by training a radar on an outdoor target. Currently, a large number of indoor and outdoor ranges are in operation throughout the United States and some of them are described in Chapters 12 and 13.

Indoor ranges suffer limitations in the sizes of the targets that can be measured, whereas outdoor ranges suffer as much as 35% downtime due to unfavorable weather conditions. Although the indoor ranges offer protection against the weather and unauthorized exposure of the target, outdoor ranges can often measure full-scale targets under farfield conditions. Most, but not all, outdoor ranges take advantage of the ground-plane effect, which actually enhances system sensitivity.

A problem common to both indoor and outdoor ranges is how to expose the target to the incident radar beam on an "invisible" target support. As shown in Chapter 11, no target support mechanism is actually invisible, although some are acceptably so. Plastic foam has been a traditional material for target supports, but a recent improvement is the absorber-covered metal pylon. Nonetheless, the pylon is not without its limitations, one of which is the necessity to machine a hole in the target for mounting attachments. The hole itself can introduce undesired target reflections.

Outdoor ranges invariably use pulsed radar instrumentation, whereas indoor ranges use CW and FM/CM systems. The measured patterns are essentially the same in either case, provided that the pulse width of the outdoor system is long enough to comfortably bracket the target. In each case it is possible with stepped frequency synthesizers to collect coherent signature data that can be processed to create radar imagery. As we shall see, radar imagery is of great diagnostic value and is another tool for use in RCS control.

1.7 BASIC DEFINITIONS

As we shall see in Chapter 2, a radar is device designed to emit an electromagnetic signal and "listen" for an echo, the purpose usually being to determine the location, if not the characteristics, of a target in the beam of the radar. To maximize system sensitivity and reduce interference due to unwanted signals or echoes, we typically emit relatively short bursts or pulses of *radio-frequency* (RF) energy. Although in

a few special cases we rely on exceptionally short pulses of energy, most of the time the pulse contains at least several cycles of RF and often several thousands of cycles. Over the duration of the pulse, therefore, the signal varies sinusoidally in time, usually at a single frequency.

This simple harmonic variation can be described in two convenient ways, one the complement of the other: the exponential functions $\exp(j\omega t)$ and $\exp(-i\omega t)$, where $\omega = 2\pi f$ is the *radian frequency* of the signal whose frequency is f, and $i = j = \sqrt{-1}$. Although both i and j are pure imaginary numbers, we carefully distinguish one from the other for reasons to be explained in a moment.

The signals we emit, and the echo signals we capture, vary with distance as well as over time. They decay in amplitude as they spread away from a source of excitation, whether that source be an active emitter or a passive echoing object, becoming weaker with increasing distance. In addition to this decay in strength, the signal undergoes a change in phase that we describe as the product kr, where $k = 2\pi/\lambda$ is the *wavenumber* and r is the distance traveled. Therefore, like the product ωt, the product kr is an angle. The wavelength of the signal is $\lambda = c/f$, where c is the speed of light in the medium in which the signal propagates. In unbounded free space, the speed of light is about 0.29979 meter (0.98357 ft) per nanosecond.

If we agree that r is a positive distance measured away from the source, the spatial and temporal variation of the signal must be written as

$$A(r)\exp[j(\omega t - kr)] \tag{1.1}$$

$$A(r)\exp[-i(\omega t - kr)] \tag{1.2}$$

where $A(r)$ is a function, possibly complex, that describes the decay in signal intensity with increasing distance. The first of these (with the j) represents the time convention preferred by engineers, and the second is the one preferred by physicists. The two are equally useful descriptions of the variation of electromagnetic fields in time and space, as only the real part of the signal can be measured and the real parts of the two forms are identical.

We use the second form exclusively in this book, primarily because we prefer that phase increase with increasing distance instead of increasing time. According to expressions (1.1) and (1.2), we cannot choose both, and readers who prefer that phase increase with increasing time instead of increasing distance need only replace i with $-j$ wherever it appears in the book.

The wavenumber k is the rate of change of phase with increasing distance and depends on the electromagnetic characteristics of the medium in which the signal propagates. Most of the time that medium is the air in the earth's atmosphere, whose properties, at least for our purposes here, are very close to those of free space. The free-space wavenumber is

$$k = \omega\sqrt{\mu_0\epsilon_0} \tag{1.3}$$

where μ_0 and ϵ_0 are the *permeability* and *permittivity* of free space, which are 0.4π microhenry per meter and 8.854 picofarad per meter, respectively. In most of our text we use the symbol k to denote the free-space wavenumber, but in come cases when other values are also used, we append the subscript 0 to distinguish the free-space value from others, as k_0. The propagation in other media, such as dielectric materials and radar absorbers, is given by

$$k = k_0\sqrt{\mu_r\epsilon_r} \tag{1.4}$$

where μ_r and ϵ_r are the *relative* permeability and permittivity of the medium, usually signified by the subscript r. As we shall see in Chapter 8, these quantities may be complex, and the imaginary part of their product describes the loss of energy in the material as waves progress through it. The complex root $\sqrt{\mu_r\epsilon_r}$ is known as the *index of refraction*.

The propagation of electromagnetic fields can be described with remarkable accuracy by a set of mathematical expressions known as *Maxwell's equations*. Aided by a small handful of auxiliary relationships, we can use Maxwell's equations to examine the behavior of electric and magnetic fields at almost any point in space, given a source of excitation. Among the salient features of these fields are the facts that they are vector quantities (characterized by direction as well as amplitude) and that the electric and magnetic fields of a wave spawned by a distant source are oriented at right angles both to each other and to the direction of propagation. The latter fact leads to the notion of polarization that, by convention and unless explicitly stated otherwise, always refers to the orientation of the electric field vector.

In some cases the polarization is referenced to the local horizontal of the radar site itself. This description is unambiguous when the emitted electric field is parallel to the ground (horizontal polarization), but is less than perfect when the emitted magnetic field is parallel to the ground. The latter case is known as *vertical polarization*, even if the radiated electric field must have a horizontal component, in addition to a vertical component, to be at right angles to both the magnetic field and the direction of propagation.

In other cases the polarization may be referenced to a characteristic dimension of the target exposed to the incident wave. When the object is an infinite cylindrical (two-dimensional) structure, for example, the incident field may be described as *parallel, E-polarized*, or *TM* (transverse magnetic) when the electric field is parallel to, or not perpendicular to, the axis (infinite dimension) of the structure. The corresponding descriptors for the other polarization is *perpendicular, H-polarized*, or *TE* (transverse electric).

These are examples of *linear* polarization, in which the spatial orientation of the electric field does not change with increasing distance. Some radars, on the other hand, radiate and capture *circularly polarized* waves, whose electric and magnetic field directions rotate about the direction of propagation with increasing distance. In this case the emitted and received polarizations are characterized by

the rotation sense (right or left). Circular polarization is typically generated by helical antennas and crossed-dipole feeds of reflector antennas, and they can be synthesized analytically by forming the coherent sum of a pair of linearly polarized waves, one shifted in phase from the other by 90°. Because the complete *polarization scattering matrix* (described in Chapter 3) can be defined and measured with either polarization set and transformed to the other by means of a simple manipulation of complex numbers, however, we consider linear polarization exclusively in this book.

When we place an object in the beam of a radar, we will find that it disperses some of the incident energy in all directions. This dispersal is called *scattering*, a term borrowed from physics, and the resulting field distribution in space depends on the size, shape, and composition of the object and on the waveform and direction of arrival of the incident wave. The spatial distribution of the scattered energy can be described in terms of a *scattering cross section* (another term borrowed from physics), and the object itself—and even parts of it—are often called *scatterers*.

This general distribution of the scattered field, to the exclusion of the incident field, is called *bistatic scattering*, implying all scattering directions where a finite angle is subtended by the direction of incidence and the direction of interest. In the case of most radar, the two directions are the same because the source (transmitter) and detector (receiver) are very near each other, if not coincident. In this case the echo detected by the receiver is called *monostatic scattering* or *backscattering*, the first implying a single direction, and the second explicitly denoting the direction back to the radar. The two terms are synonymous.

Although *scattering* might imply a nebulous, perhaps even random, field distribution due to the immersion of an object in a simple electromagnetic field, the notion of an area, albeit fictitious, seems to be more easily understood. Antenna engineers have long ascribed the signal capturing capability of antennas to a fictitious "effective area" that is often not even remotely related to the physical area of the antenna. The effective area of a half-wave dipole antenna, for example, is not much smaller than one square wavelength even though the physical area of the dipole can be much smaller. It is probably natural and convenient to describe the echo characteristics of targets in the beam of a radar in terms of an area. For arbitrary directions, that area is known as the *bistatic scattering cross section*, and when the direction of interest is back to the radar, it is called the *backscattering cross section* or the *radar cross section*. Whatever we choose to call it, we may develop a quite formal definition for it.

This definition assumes that the radar is far enough from the scatterer for the wave impinging on it to be a spherical wave whose field intensity decays inversely as the distance increases between the two. It also assumes that the target is small enough, and the distance again large enough, that the wave scattered by the target and received by a radar is also spherical. In the end, the definition of radar cross section hinges on a comparison of two power densities, one measured at the target and the other at the radar receiver.

To see why, consider the power density of the incident wave, which is the product

$$W_i = E_i H_i/2 = Y_0|E_i|^2/2 \tag{1.5}$$

where E_i and H_i are the strengths of the incident electric and magnetic fields and Y_o is the admittance of free space (0.00165 S). If E_i and H_i are measured in volts per meter and amperes per meter, the power density is gauged in watts per square meter of area erected perpendicular to the direction of power flow. We assume that a scatterer exposed to this wave behaves like an antenna, extracting power from it by virtue of some effective "capture" area σ. As antenna engineers have always done, we calculate this extracted power by forming the product of the power density and the capture area,

$$P = \sigma W_i = \sigma Y_0|E_i|^2/2 \tag{1.6}$$

We now assume that our target scatters the captured power equally in all directions. If the target is small compared to the distance R at which this scattering is observed, the scattered power density will decay with R according to

$$W_s = \frac{P}{4\pi R^2} = \frac{\sigma Y_0|E_i|^2}{8\pi R^2} \tag{1.7}$$

Note that, although R is measured away from the target, no specific direction is assumed. As in (1.5) we may express the scattered power density in terms of the scattered electric field strength,

$$W_s = E_s H_s/2 = Y_0|E_s|^2/2 \tag{1.8}$$

We may equate eqs. (1.7) and (1.8) and solve for the capture area σ:

$$\sigma = 4\pi R^2 \frac{|E_s|^2}{|E_i|^2} \tag{1.9}$$

An equally valid development of this expression relies on the incident and scattered magnetic field strengths, in which event the electric fields, in (1.9) may be simply replaced by the corresponding magnetic fields.

The "capture" area σ is the radar cross section (or scattering cross section) of the target or scatterer, and (1.9) affords us a way of measuring it. We need measure only the distance R, the incident electric field strength or power density at the target, and the scattered field strength or power density at the distance R, and then form the ratio indicated in the expression. As we will see in later chapters, however, these three quantities need not be measured directly.

We have assumed the scatterer to be small enough to radiate energy uniformly in all directions, which might imply that the scatterer is a point target with no dimension. This restriction is not essential, however. Indeed, except near the forward shadow zone, the fields scattered by a large, perfectly conducting sphere are also distributed uniformly in all directions. Since this uniform power distribution is proportional to the projected area of the sphere, the optically large sphere is a useful mental concept. *The radar cross section of a target is the projected area of a metal sphere that would scatter the same power in the same direction that the target does.*

Although a useful mental aid, the equivalent sphere concept demands some mental agility. We know, for example, that the radar cross section of almost all scatterers, even elementary ones, depends on the angle of arrival of the incident wave and the scattering direction. Because the scattering cross section varies with angle, we must be mentally prepared to allow the size of this fictitious equivalent sphere to expand or contract as the angles of incidence and scattering change. Therefore, the notion of an equivalent sphere replacing the target is probably not as appropriate as one might have thought. The difficulty, of course, is that in defining radar cross section we have defied known fact by assuming the target to scatter energy uniformly in all directions.

Moreover, the fact that (1.9) depends on the distance R is disturbing. This dependence on distance implies that the target characteristic we hope to determine, either by measurement or calculation, is a function of the measurement environment, clearly an undesirable qualification. In an attempt to eliminate this undesirable influence, we "standardize" the definition of RCS by forcing R to approach infinity:

$$\sigma = \lim_{R\to\infty} 4\pi R^2 \frac{|E_s|^2}{|E_i|^2} \tag{1.10}$$

Equation (1.10) is the formal definition of radar cross section.

The limiting process is more an academic refinement than a necessity, however. Whether we seek to measure the RCS of a target on the test range or calculate it analytically, we will discover that the scattered field strength decays inversely with R, resulting in an implicit R^2 term in the denominator that cancels the explicit R^2 term in the numerator. And although targets are measured on most test ranges at distances considerably less than infinity, the distances actually used—typically from a few dozen to a few thousand meters—are usually great enough to be acceptably close to "infinity."

As formal as it is, the definition given in (1.10) does not account for the polarization of the receiver. A more precise form of the expression is

$$\sigma = \lim_{R\to\infty} 4\pi R^2 \frac{|\hat{e}_r \cdot \bar{E}_s|^2}{|E_i|^2} \tag{1.11}$$

where $\hat{e}_r$ is a unit vector aligned along the electric polarization of the receiver and $\bar{E}_s$ is the vector scattered field. An equivalent expression accounting for the magnetic polarization of the receiver may be used when the incident and scattered magnetic fields are the basis of the development of the expression. As we will see in later chapters, the polarizations of both the receiver and the source of illumination may be arbitrary, but we can characterize all possible combinations with the measurement of just four specific quantities known as the *polarization scattering matrix*.

Because the radar cross section is a real number formed by squaring the amplitude of a complex number representing the scattered electric field, all phase information is destroyed or ignored. To preserve phase information, it is often convenient to deal with the complex scattered fields themselves. We can accommodate this by assuming that even if σ may be a pure real number, we may regard its root, $\sqrt{\sigma}$, as a complex number in which phase information is implicitly retained. When that is the case, we may extract the square root of (1.11):

$$\sqrt{\sigma} = \lim_{R\to\infty} 2\sqrt{\pi}R\frac{\hat{e}_r \cdot \bar{E}_s}{E_i} \tag{1.12}$$

We will have occasion to use this expression in later chapters.

Although there are no known two-dimensional objects—infinite cylindrical structures—in the physical world, the scattering by such bodies is often analytically tractable when the scattering by truncated, three-dimensional versions of them is not. In the two-dimensional case the scattering cross section becomes a *scattering width*, in units of length, not area. The reduction to two dimensions from three results in a slightly different form for the radar cross section, this time *per unit length*:

$$\sigma_{2D} = \lim_{\rho\to\infty} 2\pi\rho\frac{|V_s|^2}{|V_i|^2} \tag{1.13}$$

where the V_s represents the electric or magnetic incident and scattered fields, depending on the incident polarization, and ρ is the distance from the axis of the structure to the observation point, as measured in a plane transverse to the axis.

The solutions of two-dimensional scattering problems are invariably carried out for two primary polarizations, one for the incident electric field parallel to the cylinder axis (E-polarization or TM incidence) and the other for the incident magnetic field parallel to the axis (H-polarization or TE incidence). We may investigate three-dimensional scattering behavior in a few simple cases by assuming that the corresponding two-dimensional solution holds for small, incremental lengths of a truncated, three-dimensional version of the structure. This being the case, we permit the incident wave to illuminate the body from an oblique direction, not necessarily perpendicular to the axis of the truncated body. Assuming this

modification of the phase of the incident wave at each point along the body axis, we integrate the two-dimensional result along the body length. If the incident wave arrives in a plane inclined at an angle θ from a transverse plane through the body, we find the two- and three-dimensional results to be related by

$$\sigma_{3D} = (2\sigma_{2D}/\lambda)\left|\frac{l \sin(kl \sin \theta)}{kl \sin \theta}\right|^2 \tag{1.14}$$

where l is the length of the truncated body.

This very useful relationship must be applied with due appreciation for its limitations, however. First, it ignores any field perturbations due to the end effects created by truncating the infinite structure; therefore, it cannot be expected to hold for short, thick bodies. Second, it does not include the effects of fields or waves that may propagate along the length of the body. This is because the reflections of those fields from the finite ends of the truncated body are not included in the two-dimensional solution. Third, the accuracy of the prescription deteriorates as θ swings further from incidence normal to the cylindrical axis. The approximation may hold for angles as high as 30° or 40° or so, but should be considered unreliable for angles greater than this. Fourth, the truncation of the infinite structure will create some edges on the truncated body that, even if shielded from the incident wave in the two-dimensional solution, will be exposed to the incident wave in the three-dimensional version. Because these edges are not present in the two-dimensional solution, their effects are not included in the conversion to the three-dimensional world.

1.8 SUMMARY

Although the notion of radar "stealth" is relatively recent application of the word to advanced U.S. Department of Defense weapon-development programs, the design of radar-stealthy aircraft began in earnest well before 1960. Although we may advance technology every year, the principles of radar stealth have been well known, if not well practiced, for several decades. The world's first major stealth project appears to have been the development of the SR-71 spyplane, followed by the F-117A fighter and the B-2 bomber. Others are on the drawing boards at this moment, and unidentifiable prototypes may even be airborne.

Although no classified information can be published here, we suffer no constraint in the publication of principles. We continue in the following chapters to explain how generic radars work and why the echo of the target is so fundamental to determining its apparent location in space. The determination of that echo, for both developmental and academic purposes, is eventually governed by Maxwell's equations, whether we accomplish it experimentally or theoretically. We may re-

duce the probability of successful detection, lock-on, or tracking by reducing the echo; there are several ways of doing so, some more effective than others. As we shall see, all carry a penalty.

Shaping is intended to deflect target reflections away from the threat radar, but we must first know the direction to the radar. Absorbers bring about a different reduction in the echo signal by converting some of the incident radar energy into thermal energy, like a toaster, even if the temperature rise may be unmeasurable. Absorbers alone contribute neither lift nor thrust, however, and they always reduce our payload or compound our maintenance problems. Cancellation schemes balance the echo of deliberately introduced reflectors against the natural echo of the target. Because good cancellation at one frequency eventually brings about good enhancement at another, cancellation schemes have not been particularly attractive in the past.

However, if we are successful in bringing about a significant reduction in our apparent echo, by whatever means, we must demonstrate it to our customer. We may do so with models, whose echoes may be measured in relatively modest indoor test chambers, and, if we are employed by a large airframe manufacturer, we will likely do it on an outdoor test range with full-scale components, if not the entire airframe. We cannot stop with the mere collection of data, however, as the task remains of deciding how valid it is, what it means, and how we will apply it in the next phase of development. That decision is the subject of our final chapter.

REFERENCES

[1] O'Leary, Michael, and Eric Schulzinger, *SR-71*, Motorbooks International, Osceola, WI, 1991, pp. 13, 17.

[2] "R.A.F. to U.S.A.F.: Gotcha!" *Time*, May 25, 1992, p. 15.

[3] Sweetman, Bill, and James Goodall, *Lockheed F-117A*, Motorbooks International, Osceola, WI, 1990, p. 42.

Chapter 2
Radar Fundamentals

M. T. Tuley

2.1 INTRODUCTION

Although the study of radar cross section and its reduction are interesting from a purely academic point of view, we assume that the reader has a practical application in mind. That application is typically the prediction of a radar's performance against a given target, and then modification of the target RCS to reduce the performance of the radar.

The purpose of this chapter is to provide a brief survey of radar fundamentals that can be used to put the RCS and *RCS reduction* (RCSR) problems in context. Obviously, only some of the most basic points concerning radar can be covered in a single chapter, and the reader who seeks more detail can find it in any one of a number of books on the general topic of radar [1–5]. Here, after a brief history, radar system fundamentals are covered, with a focus on how radars discriminate in their measurement space of range, angle, and doppler. The radar range equation is developed, and its implication for RCSR is examined. Detection theory is then briefly discussed, and, finally, *electronic countermeasure* (ECM) techniques are outlined, with an emphasis on the effects of RCS control on ECM effectiveness.

2.2 HISTORY OF RADAR DEVELOPMENT

Radar did not come to the forefront as a useful sensor until World War II, when tremendous strides were made in both the theory and practice of radar technology. The earliest account of the reflection of radio frequency waves from metallic and

dielectric bodies was given by Hertz, who in 1886 used a 450 MHz spark-gap transmitter and receiver to test Maxwell's theories. The first detection of what might be called a military target by radar was achieved by Christian Hulsmeyer, a German engineer, who demonstrated a ship detection device to the German Navy in 1903. However, the range of the device was so limited that little interest was generated.

The earliest U.S. radar detection work was carried out by Taylor and Young of the Naval Research Laboratory (NRL). In late 1922 they used a continuous wave interference radar operating at 60 MHz to detect a wooden ship. The first radar detection of aircraft in the United States, also accomplished using a CW interference radar, was made in 1930 by Hyland of NRL.

Early radar work, both in the United States and abroad, often used a CW transmitter. These radars detected targets by sensing the modulation of the received signal caused by the doppler shifted reflection from the target beating with the direct signal from the transmitter. Low transmitting frequencies were used because high-power transmitters were not available at the higher frequencies. These CW radars detected the presence of a target, but no range information could be extracted (making it doubtful if they should even be included in the class of objects whose name stands for "radio detection and ranging"). Also, at the low frequencies used, only coarse angular information was available. To allow range measurement, modulation of the signal waveform was required, and so pulsed systems were developed.

A pulsed radar operating at 28 MHz and using 5μs pulses was developed at NRL and tested in early 1935. The tests were unsuccessful, but the radar was subsequently modified, and it detected its first target echo in 1936. Shortly after that, in late 1936, the U.S. Army Signal Corps tested its first pulsed radar. The Army also developed the first operational antiaircraft fire control radar in the United States, the SCR-268, which was fielded in 1938. It was an SCR-270, the long-range surveillance companion to the SCR-268, that detected Japanese aircraft at a range of over 130 mi as they approached Oahu, Hawaii, on the morning of December 7, 1941 [6].

The British successfully demonstrated a pulsed radar at 12 MHz in 1935, obtaining detection ranges of more than 40 mi against a bomber aircraft. Both the United States and Britain were aware of the reduction of the physical size of equipment and angular resolution advantages available at higher frequencies, and groups in both countries were working at 200 MHz by the late 1930s.

The pivotal event allowing the practical development of microwave radar was the invention of the cavity magnetron by Randall and Boot in Britain. The magnetron is a self-excited crossed-field (i.e., the magnetic and electric fields are perpendicular) oscillator whose frequency of operation is determined by the dimensions of a regular series of holes and slots cut into a cylindrical anode structure surrounding a cylindrical cathode. The first cavity magnetron produced a peak

pulse power of 100 kW at 3 GHz, a power level much greater than had previously been achieved at those frequencies. In late 1940, Britain and the United States began cooperative efforts in the radar area. The focal point for U.S. radar development efforts during World War II was the Radiation Laboratory, established at MIT in November 1940. The initial staff of 40 had grown to about 4,000 by mid-1945, and their activities are documented in a 28 volume set of books (commonly known as the Rad Lab Series [7]), which even now, almost 50 years later, provides a valuable reference on radar fundamentals.

Improvements in radar technology have been enormous since World War II. In the transmitter area, the development of the high-power *traveling wave tube* (TWT), millimeter-wave power tubes, solid-state microwave sources, and stable computer controlled oscillators have been important. In the receiver area, solid-state technology has improved mixers and allowed development of low-noise amplifiers. In the antenna area, large-scale phased arrays have become practical. In signal processing, as in every other area of radar, the advent of the small, fast digital computer has made practical radar techniques that could not otherwise have been considered.

It is interesting to note that the advent of "stealth" technology has somewhat reversed the historic trend in radar development toward the use of higher frequencies. Low cross section vehicles will generally show an RCS behavior proportional to the radar wavelength squared. This functional dependence, which is driven by the shaping that must be employed if very low RCS values are to be obtained, has understandably renewed interest in lower frequency radars.

2.3 RADAR FREQUENCY BANDS

A radar may be defined as a device that transmits an electromagnetic wave and detects objects by virtue of the energy scattered from them in the direction of the receiver. In that regard, a radar could operate at any frequency. Practically speaking, the devices we normally designate as radars are limited to a relatively narrow slice of the electromagnetic spectrum for reasons of availability of components, propagation effects, angular resolution requirements, target scattering characteristics, international regulations, and a host of other concerns. Generally, radars fall within the frequency limits given by the standard radar bands in Table 2.1, adapted from [8]. These bands cover a frequency range from 3 MHz to 300 GHz, but the greatest number of operational radars fall within what are commonly called the *microwave frequency bands*, designated in the table as L, S, C, X, and K_u. A significant number of UHF and VHF radars are also deployed as long-range surveillance systems and, as noted previously, have a potential for countering traditional RCSR techniques.

The radar band designations began in World War II as a security measure, but they have since come into standard usage. In general, the bands are divided

Table 2.1
Radar and ECM Bands

*Standard Radar Bands**		*Electronic Countermeasures Bands***	
Band Designation (1)	*Frequency Range (MHz)*	*Band Designation*	*Frequency Range (MHz)*
HF	3–30	A	0–250
VHF (2)	30–300	B	250–500
		C	500–1000
UHF (2)	300–1000	D	1000–2000
		E	2000–3000
L	1000–2000	F	3000–4000
S	2000–4000	G	4000–6000
		H	6000–8000
C	4000–8000	I	8000–10,000
X	8000–12,000	J	10,000–20,000
K_u	12,000–18,000	K	20,000–40,000
		L	40,000–60,000
K	18,000–27,000	M	60,000–100,000
K_a	27,000–40,000		
Millimeter (3)	40,000–300,000		

Notes: (1) British usage in the past has corresponded generally, but not exactly, with the letter-designated bands.
(2) The following *approximate* lower frequency ranges are sometimes given letter designations: P band (225–390 MHz); G band (150–225 MHz); and I band (100–150 MHz).
(3) The following *approximate* higher frequency ranges are sometimes given letter designations: Q band (36–46 GHz); V band (46–56 GHz); and W band (56–100 GHz).

*From IEEE Standard 521-1976, 30 November 1976.
**From AFR-55-44(AR105-86, OPNAVINST 3430.9B, MEO 3430.1), 27 October 1964.

so that the power sources, propagation effects, and target reflectivity are similar for frequencies within a band, but may be very different from one band to another. Table 2.2 provides typical uses for the most commonly employed bands. VHF and UHF radars are generally used for very long-range surveillance, because of the ability to obtain very large power-aperture products at the lower frequencies and their favorable clutter and propagation characteristics. However, fine angular resolution at these frequencies requires very large antennas (getting even a 5° azimuth beamwidth at 150 MHz would require a 28 m wide antenna), so precise target localization is difficult to obtain. Search radars and tracking radars are most often found in one of the higher radar bands, with S, C, and X bands the most prevalent. K_u, K_a, and higher frequencies are finding increasing use in mapping, fire control, and missile guidance applications, because small beamwidths can be obtained using

Table 2.2
Radar Frequency Bands and General Usages

Band Designation	*Frequency Range*	*General Usage*
VHF	50–300 MHz	Very Long-Range Surveillance
UHF	300–1000 MHz	Very Long-Range Surveillance
L	1–2 GHz	Long-Range Surveillance, Enroute Traffic Control
S	2–4 GHz	Moderate Range Surveillance, Terminal Traffic Control, Long-Range Weather
C	4–8 GHz	Long-Range Tracking, Airborne Weather Detection
X	8–12 GHz	Short Range Tracking, Missile Guidance, Mapping, Marine Radar, Airborne Intercept
K_u	12–18 GHz	High Resolution Mapping, Satellite Altimetry
K	18–27 GHz	Little Used (Water Vapor Absorption)
K_a	27–40 GHz	Very High Resolution Mapping, Airport Surveillance
Millimeter	40–100+ GHz	Experimental

reasonably sized antennas and small fractional bandwidths can provide excellent range resolution.

Table 2.1 also provides the electronic countermeasure band designations listed in Department of Defense instructions. Whereas IEEE Standard 521-1976 specifically notes that the ECM band designations are not consistent with radar practice, use of the ECM band descriptors in radar work has become pervasive. Therefore, the designer of a radar absorber would be well advised, when asked about performance of the product at C band, to be sure the questioner means 4–8 GHz and not 500–1000 MHz.

2.4 RADAR SYSTEM FUNDAMENTALS

Radars are built in a wide variety of types and for a large number of different applications. In the early years, civilian use of radar was limited to navigation and traffic control (air and marine). However, as radar became more widespread and technology improved, weather detection and tracking, automobile speed detection, collision avoidance, and buried object detection also became important civilian radar applications.

Most of the civilian applications also apply in the military arena. In addition, military radars are used for surveillance, early warning, weapons control, and intelligence functions. The military has been a strong driver in the advance of radar technology. In fact, of the more than 100 United States and foreign radars listed in [9], fewer than 20 have purely civilian designations. Obviously, it is impossible in the space available here to describe all the different types of radars that have been developed and deployed. Instead, a different approach has been taken. First, the basic elements that make up all radar systems are described. Then, the two fundamental divisions of radar are discussed: CW and pulsed systems. Next, systems are discussed based on methods used to provide discrimination in the radar measurement space of range, angle, and doppler. Finally, a modern instrumentation radar is examined to illustrate how maximum accuracy can be achieved in the range, cross-range, and doppler dimensions.

2.4.1 Basic Radar System Elements

All functional radars must contain at least four basic subsystems: a transmitter, an antenna or antennas, a receiver, and an indicator. More typically, the block diagram of a pulsed radar might be divided into the seven subsystems shown in Figure 2.1, with each block encompassing one of the design subspecialties of radar engineering [2,3].

Timing control within the radar is the function of the synchronizer, which provides signals to the exciter, modulator, receiver, and display. Because radars basically measure time delay, accurate timing and synchronization are crucial to radar operation.

The transmitter subsystem, which typically consists of a power supply, modulator, and *radio-frequency* (RF) amplifier, creates the waveform to be transmitted. The exciter provides an RF drive signal to the RF amplifier which also receives a pulse from the modulator. The modulated pulse is amplified, passed through a duplexer, which directs outgoing signals to the antenna and incoming signals to the receiver, and is sent via waveguide (typically) to the antenna for transmission.

The transmitter type and the source selected for a radar depend on the power required, the allowable cost, and the details of the application. The required output power is often derived directly from a power oscillator, and the magnetron is a prime example of such a device. Pulsed magnetrons can be built with output powers in excess of 10 MW. They require no exciter, fairly simple modulators, are efficient, and are relatively inexpensive. Magnetron disadvantages include a low duty cycle, narrow bandwidth, and a difficulty in coherent operation.

Coherent radars are more often implemented using a *master-oscillator-power-amplifier* (MOPA) chain. The master oscillator may be crystal controlled to provide maximum frequency stability. *Traveling-wave-tube* (TWT) amplifiers are typically

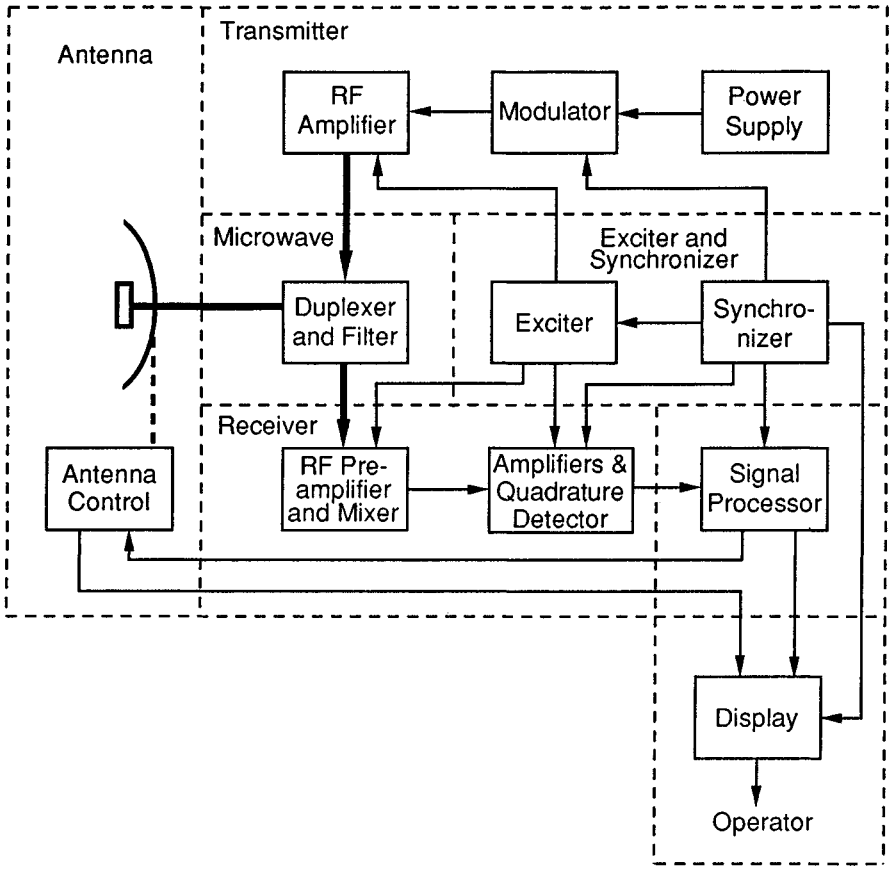

Figure 2.1. Block diagram of typical pulsed radar (adapted from [2]).

used as the low and medium power amplifiers in a MOPA chain, with either a high-power TWT, *crossed-field amplifier* (CFA), or klystron used in the final amplifier stage. The major advantages of a MOPA transmitter are coherent signal generation and extreme flexibility in signal design and coding. Disadvantages compared to the magnetron include size, weight, cost, and transmitter complexity. Ewell [10] provides an excellent treatment on the design of radar transmitters.

The antenna is the device used to couple energy between free space and the transmission lines inside the radar. The transmitting antenna must take the RF energy from the transmitter and convert it into a beam of the desired shape illuminating the desired volume of space. The receiving antenna must receive electromagnetic energy from specific directions and guide that energy into the

receiver. In most radars, the same antenna is used for both transmission and reception. When that is the case, a duplexer must be used to switch the antenna between the transmitter and receiver and protect the receiver from the transmitted pulse.

Radar antennas have taken many forms over the years. A number of excellent general antenna texts also cover antennas suitable for radar [11,12], and [13,14] provide detailed treatments of radar antenna design and analysis. For this brief overview of radar fundamentals, the important points to be covered regarding antennas are the relationships between antenna size and beamwidth and between beamwidth and antenna gain.

Antenna beamwidths are normally measured between the half-power points of the one-way antenna pattern. For antennas with asymmetrical patterns, separate azimuth and elevation beamwidths will be specified. There is an inverse relationship between the beamwidth and the antenna aperture size in the plane of the measurement. The exact equation that relates beamwidth and aperture dimension is dependent on the aperture illumination function, which controls mainlobe width and sidelobe levels. However, a practical rule-of-thumb for typical illumination functions expresses the beamwidth θ in terms of the aperture length L and wavelength λ as

$$\theta \cong 1.2\lambda/L \text{ (rad)} \cong 70\lambda/L \text{ (deg)} \tag{2.1}$$

Although (2.1) is only approximately correct, it is a useful expression for calculating required antenna dimensions. For example, according to (2.1), achieving a 1° azimuth beamwidth at X band (10 GHz), where the wavelength is about 3 cm, would require just over a 2 m wide antenna. Contrast that with L band (1.25 GHz), where a 17 m wide antenna would be required for the same beamwidth, or VHF (150 MHz), where a 140 m wide antenna would be needed.

Antenna gain is a measure of the radiation intensity produced by the antenna in a given direction compared to that of perfectly efficient isotropic antenna with the same input power [8]. There is a relationship between antenna aperture area A and peak antenna gain G, given by [4]

$$G = \eta\,(4\pi A/\lambda^2) \tag{2.2}$$

where η, the aperture efficiency, is a factor less than 1, which accounts for such things as ohmic losses, illumination taper, feed spillover, and aperture blockage. The relationship between antenna beamwidth and dimensions and eq. (2.2) can be combined to provide rules-of-thumb for antenna gain in terms of antenna beamwidth. If $\eta = 1$ and a uniformly illuminated aperture is assumed ($\theta = \lambda/L$ rad), then $G = 41{,}259/\theta_a\theta_e$ for a rectangular antenna, where θ_a and θ_e are the azimuth and elevation beamwidths in degrees. However, aperture efficiencies are typically

less than 0.9, and Barton [2] claims for an array antenna that $G = 37{,}100/\theta_a\theta_e$ for all practical illuminations. For a reflector antenna, the value of the constant is lower, with 27,000 a typical number, because of feed spillover and aperture blockage—losses not faced in an array antenna. Therefore, for an array antenna with 1° beamwidths in both the azimuth and elevation planes, we might expect to achieve about a 45 dB gain, whereas for a reflector antenna with the same beamwidths, the gain would be about 44 dB.

Signals captured by the antenna are routed into a receiver for detection and signal processing. In almost all modern pulsed radars, a superheterodyne receiver is employed, where the RF signal is mixed down to a lower *intermediate frequency* (IF) for further processing. Typical IF frequencies range from 30 MHz for simple narrowband systems to as high as 3 GHz for some wideband radars and instrumentation systems. After amplification, filtering, and possible additional downconversion to lower frequencies, the IF signal is detected. In noncoherent systems, the detection process rectifies the envelope of the IF signal. Coherent systems generally employ quadrature detection. *In-phase* (I) signals are produced by mixing the received signal and a local oscillator signal that is phase coherent with the transmitted waveform. *Quadrature-phase* (Q) signals are produced by mixing a 90° phase shifted version of the received signal with the local oscillator. The I and Q signals then contain phase and amplitude information about the received waveform. Many of the desired processing schemes (e.g., pulse doppler and synthetic aperture) require phase information, and so those techniques must employ coherent processing.

Modern radars are generally computer controlled and do their signal processing digitally. *Analog-to-digital* (A/D) convertors are used to provide the digital signal required for further processing. Some details about typical processing schemes employed are covered in discussing examples of radar systems.

The final components of the radar are the indicator and operator. Although simple *plan position indicator* (PPI) scopes depicting signals that have been subjected to little other than amplification and detection are still in use, modern radars typically present the operator a highly processed display. In many systems, the declaration of detection and the institution of tracking has been taken out of the hands of the operator and made the responsibility of the computer.

2.4.2 Continuous Wave Radars

The simplest type of radar, and the type first demonstrated by Hulsmeyer in 1903, is the CW radar. As noted earlier, an unmodulated CW radar has the significant limitation of providing no range information. Nevertheless CW radars are of historical importance, and they probably still represent the most widely used type of system in their application as speed measuring devices. Police radars are normally

CW homodyne systems that use a portion of the transmitted signal as the local oscillator. Thus, objects whose radial velocity is zero relative to the radar will mix down to dc. For moving objects, a doppler shift will result whose frequency f_d is given by

$$f_d = 2v_r/\lambda \tag{2.3}$$

where v_r is the radial velocity of the target relative to the radar. Therefore, at X band, a target moving toward a stationary radar at 60 mph will give a doppler shift of about 1800 Hz. A simple frequency counter constitutes the indicator for such a radar.

One advantage of the CW radar is that the unity duty cycle provides the highest average power possible for a given peak source power. This makes CW particularly attractive for seeker applications, where size and power limitations place substantial constraints on system implementation. The lack of range information can be overcome by modulating the CW waveform, so that a "timing mark" is available. Frequency and phase coding are the two techniques normally employed in modulating CW radars.

Frequency modulated continuous wave (FM-CW) radars vary the frequency of the transmitted signal and measure the range based on the frequency difference between the instantaneous transmitted and received signals. Typical modulations include triangular, sawtooth, and sinusoidal. Current applications of FM-CW include altimeters, tracking radars, and high-resolution instrumentation systems.

Another method of providing a timing mark is by phase coding the CW signal. Either a binary or a polyphase code can be used. In binary coding the signal is divided into segments, with a +1 represented by 0° phase and a zero represented by a 180° phase shift with respect to the carrier. The return signal can then be correlated with a delayed version of the transmitted code to produce range discrimination approximately equal to half the bit length.

2.4.3 Pulsed Radar

As indicated earlier, obtaining range information requires that the transmitted signal be coded to allow an elapsed time measurement to be made between some reference time and the time that the signal is received back from the target. Frequency and phase coding in CW systems have been discussed, but by far the most common coding technique is the amplitude modulation employed in the pulsed radar, the time line for which is indicated in Figure 2.2. Referring to Figure 2.1, timing for the pulses is provided by the synchronizer, which triggers the transmitter and simultaneously begins a range strobe on the indicator. From Figure 2.2, the transmitted pulse leaves the antenna at time 0 and travels toward the target at the

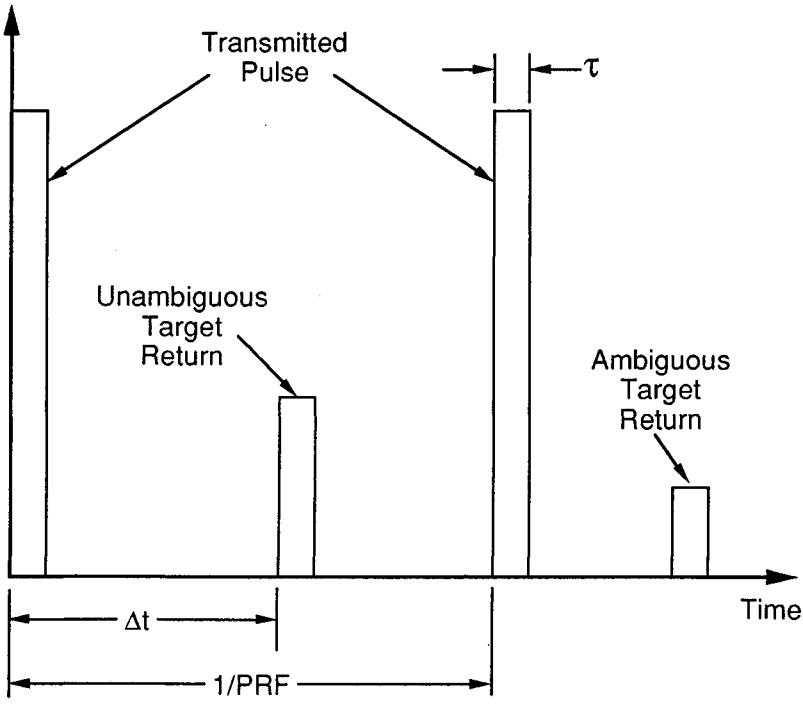

Figure 2.2. Simple pulsed radar time line.

speed of light. When the pulse reaches the target, it is reflected, and a portion of the energy returns to the radar, where it is detected and displayed. The range to the target is given by the two-way transit time Δt and the speed of light c as

$$R = c\Delta t/2 \tag{2.4}$$

A handy rule-of-thumb for calculating range is that the velocity of light is about 30 cm per ns (or about 1 ft per ns). Thus, a Δt of 1 μs (1000 ns) represents a radar range to the target of 150 m.

A radar typically transmits a continuous train of pulses at some *pulse repetition frequency* (PRF), as shown in Figure 2.2. A return from an earlier pulse received after a subsequent pulse was transmitted would be interpreted to be coming from a target at a much shorter range, producing a range ambiguity. Because the primary task of a search radar is to provide the range and angular coordinates of a target, ambiguities in range are undesirable. In addition, a range ambiguous target will

be displayed at a shorter range and may thereby be masked by close-in clutter return. The maximum unambiguous range a radar can measure with a single PRF is given by

$$R_{\text{unamb}} = c/(2f_r) \tag{2.5}$$

where f_r is the PRF in Hz. Thus, a radar with a 2 kHz PRF would have a maximum unambiguous range of about 75 km. A range ambiguity can be sensed and decoded through the use of multiple PRFs. However, use of such methods entails additional radar complexity, so many search radars are designed to be range unambiguous to their maximum desired operating range.

In addition to their wide operational employment, pulsed radars are often used as instrumentation radars, both in field situations and on outdoor ranges. One major advantage of the pulsed radar is that range discrimination is available based on the time of arrival of the return. However, simple pulsed radars are more difficult to use indoors because the short ranges involved require very short receiver recovery times.

2.4.4 Range Discrimination

In a sense, a simple pulsed radar impresses an amplitude code on a CW signal that allows range discrimination. For an uncoded pulse, the range resolution achieved is a function of the width of the pulse and is given by

$$\Delta R = c\tau/2 \tag{2.6}$$

where τ is the pulsewidth. Thus, a 1 ns pulse provides a 15 cm range resolution.

If a given range resolution is desired, the pulsewidth can be designed, based on (2.6), to achieve that resolution. However, the energy on target is the parameter that is important for detection in noise, and for a given peak power and unambiguous range, shorter pulses mean less energy per unit time (less average power) delivered to the target. Further coding can be impressed on a pulse, or a series of pulses, to provide additional range discrimination while keeping the pulsewidth long enough to provide a high average power.

Fundamentally, range resolution in a radar system is not defined by the pulsewidth. Instead, the total bandwidth of the transmitted waveform sets the range resolution. The relationship between range resolution and bandwidth becomes clear when we recognize that the temporal response and complex frequency spectrum of the radar waveform constitute a Fourier transform pair. The spectrum of a rectangular pulse is a $\sin(x)/x$ function with a bandwidth at the -4 dB points given by $1/\tau$. Recognizing that the bandwidth and pulsewidth for an uncoded pulse are related by $B = 1/\tau$, and substituting into (2.6) gives

$$\Delta R = c/(2B) \tag{2.7}$$

In fact, (2.7) is the more fundamental equation from which (2.6) should be derived, although we have chosen to proceed in the other direction. Note that in a coherent system that maintains a phase reference from pulse-to-pulse, it is immaterial whether the bandwidth is achieved within a single pulse or over a series of pulses processed together. The important parameter is the total frequency interval processed.

One way to provide a wider bandwidth than would be given by an unmodulated pulse is to linearly sweep or "chirp" the frequency of the signal within each pulse. In the receiver, a dispersive filter (i.e., a delay line with variable delay versus frequency) having a delay characteristic that is the inverse of the chirp compresses the output pulse, giving rise to the name of the technique as pulse compression.

Figure 2.3 illustrates the waveforms present in a linear FM pulse compression system. The achievable resolution is related to the swept bandwidth by (2.7). In most practical implementations, some amplitude weighting is applied in the pulse compression filter to reduce the range sidelobes in the compressed waveform of Figure 2.3(d) below the levels given by the $\sin(x)/x$ pattern shown. As in CW radars, phase coding may also be used in a pulsed system to provide additional resolution through pulse compression. In effect, the phase coding increases the bandwidth of the waveform by the factor of the number of chips of code used within the pulse.

As noted earlier, if the system is phase coherent on a pulse-to-pulse basis, the waveform bandwidth does not have to be achieved on a single pulse. The advent of highly stable computer controlled frequency synthesizers has allowed the implementation of "step chirp" radars that step the frequency from one pulse to the next to achieve the total desired bandwidth. One major advantage of such a technique is that it does not require large instantaneous bandwidth radar components, and so much wider total bandwidths can be achieved than are typical of conventional pulse compression systems.

By *fast Fourier transforming* (FFT) the complex frequency samples of a wideband step chirp system, the time response of a short pulse system can be obtained, where the equivalent pulsewidth is equal to $1/B$, with B the total bandwidth over which frequencies have been stepped. Obviously, a stable phase reference and coherent operation on a pulse-to-pulse basis are required in implementing such a system, but that technique is now routinely used on indoor and outdoor ranges [15]. On indoor ranges, stepped CW or gated stepped CW systems are often used because of the simplicity of implementation and because a standard vector network analyzer can be used as the receiver-processor.

A separate question from range resolution is tracking the target in range. Most radar systems that provide automatic range tracking of targets do so with a split-gate tracker. In such a tracker, two identical contiguous gates are formed that sample the radar return over a small range increment. The video voltage into each gate is integrated over the time period corresponding to the length of the gate. The outputs from the two gates are subtracted, and the difference voltage provides

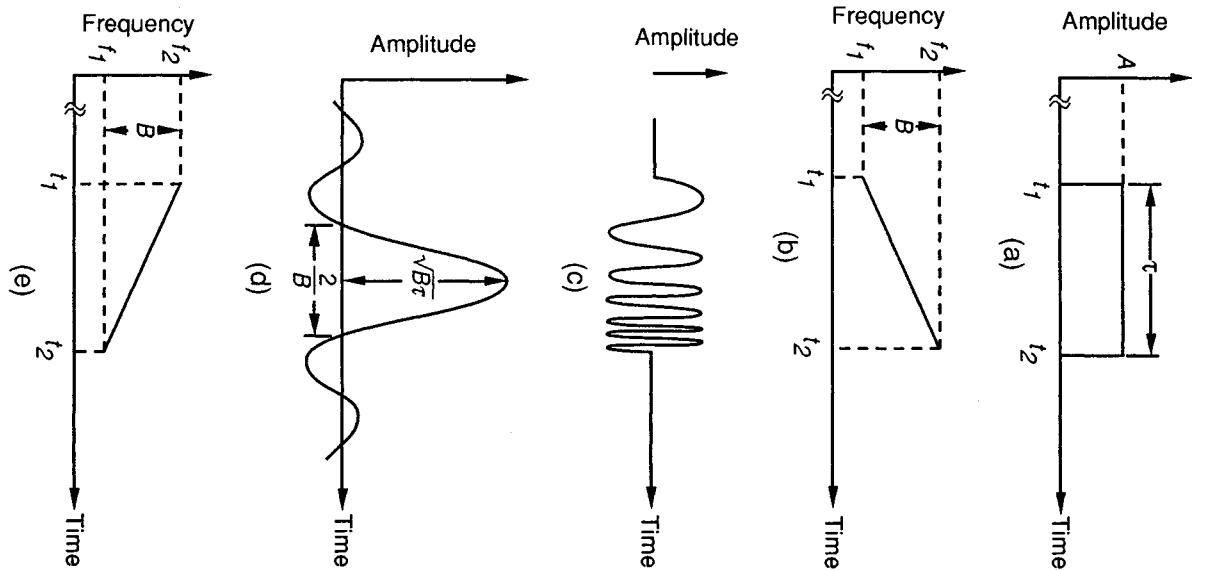

Figure 2.3. Frequency-modulation pulse compression waveforms: (a) amplitude of the transmitted waveform; (b) frequency of the transmitted waveform; (c) time waveform; (d) compressed pulse; (e) output characteristics of the pulse compression filter (from [1]).

an error signal used to drive the range position of the tracker. If the tracker is centered on the target, the voltages in the early and late gates will be equal, and there will be a zero difference signal. However, if the tracker moves off center, the early and late gate voltages will no longer cancel, and the resulting error signal will drive the tracker back toward the center of the target.

2.4.5 Angle Discrimination

Providing angle discrimination in a radar is generally the function of the antenna subsystem. In addition to the angular resolution provided by the antenna, doppler information about the target can be used in postprocessing to provide cross-range information, which is related to angle. For a simple radar, the angular discrimination is approximated by the half-power (3 dB) beamwidth of the antenna. The cross-range resolution ΔR_c for that case is given by

$$\Delta R_c = R\theta \tag{2.8}$$

where θ is the 3 dB beamwidth of the antenna in the plane of the cross-range measurement. One obvious implication of (2.8) is that the precision with which the radar can locate a target in three-dimensional space degrades as the range to the target increases.

For tracking applications, the inherent angular resolution of the radar beam is often not sufficient to provide the tracking accuracies required by a system. In addition, a tracking error signal is often desired for input into tracking control loops. A simple method of obtaining the direction of a target in one dimension, relative to some reference, is to switch the beam position symmetrically to either side of the reference and to measure the amplitude of the target return in each position. Such a technique is called *sequential lobing,* and the target is centered when the outputs at the two positions are equal. The technique can be extended to two dimensions by using two sets of beam positions orthogonal to one another.

A logical extension to sequential lobing, called *conical scan*, rotates the radar beam in a circle about the reference direction and continuously measures the target return. The low-frequency portion of the detected output of such system will be a sinusoid at the rotation frequency. The amplitude of the sine wave is proportional to the total angular error. The phase, relative to the scan position, indicates the direction of the error. Conical scan systems are relatively easy to implement, but they suffer several disadvantages. The first is that pulses over the complete conical scan period must be processed to determine the track error, and changes in target RCS over the scan period will induce track errors. A second disadvantage, related to the first, is that a jammer modulated at the conical scan frequency will also

induce error signals into the receiver and can cause loss of track. One technique to counter jamming is to deny knowledge of the scan frequency. This is accomplished with *conical-scan-on-receive-only* (COSRO) systems, for which the illuminating beam does not scan and only the receiving pattern rotates.

A technique to reduce tracking sensitivity to target amplitude fluctuations and jamming is to provide an error signal based on a single pulse, and such a technique is called *monopulse* [16]. In monopulse systems, simultaneous lobes are created, and a comparison is made, either in amplitude or phase, between them. Figure 2.4 illustrates how the beams are formed for amplitude monopulse and

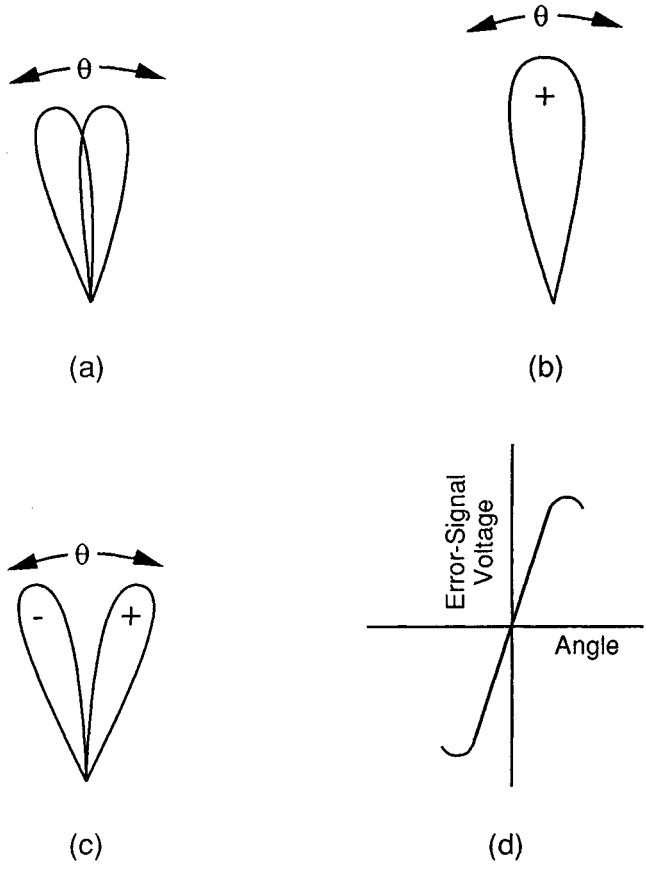

Figure 2.4. Amplitude monopulse antenna patterns and error signal: (a) squinted antenna patterns; (b) sum pattern; (c) difference pattern; (d) error signal (from [1]).

shows the resulting error voltage as a function of angle off boresight. As can be noted, the individual beams are squinted relative to each other. A sum beam consisting of the in-phase sum of the two squinted beams is transmitted, and sum and difference beams are formed in the receiver by summing the two beams in phase and out of phase, respectively. When normalized by the sum signal (Σ), which takes out the effects of variations in target RCS, the amplitude and phase of the difference signal (Δ) give the magnitude and direction of the error. Thus, the monopulse error voltage ϵ is given by

$$\epsilon = k \, \mathrm{Re}[\Delta/\Sigma] \tag{2.9}$$

Where k, called the error slope, is simply a proportionality constant, and Re[ ] indicates the real part of the ratio.

Phase comparison monopulse is used less often than amplitude monopulse, because it is less efficient for a given aperture size. It is basically an interferometric technique that compares the phase of the signals at the two antenna feeds to calculate target direction. Beam squint is not required for phase monopulse, so it is often used in planar antenna configurations to reduce the complexity of the antenna design. In any event, monopulse requires either a coherent multichannel receiver or multiplexing of the sum and difference signals, and thus is more expensive to implement than a conical scan. However, the relative immunity of monopulse to simple jamming has made it the preferred modern tracking technique.

2.4.6 Doppler Discrimination

The doppler shift caused by the radial motion of a target can be used as an additional discriminant for moving targets in a fixed target and clutter background. *Moving target indication* (MTI) and *pulse doppler* (PD) radars make use of doppler to separate targets from clutter. The designation of a radar as an MTI system rather than a PD system is rather arbitrary, but historically, doppler processing radars that are unambiguous in range and ambiguous in doppler are designated as *MTI systems*. Radars that are ambiguous in range but unambiguous in velocity ("high prf") or ambiguous in both range and doppler ("medium prf") have generally been called *pulse doppler radars*.

Although noncoherent methods of achieving MTI have been developed, coherent systems are normally employed. Coherency implies that the local oscillator can maintain phase coherence with the transmitted pulse over the period of the expected return, so that the phase shift associated with doppler can be detected.

A simple method of implementing MTI is by use of a delay line canceller. The simplest version of the delay line canceller utilizes a single delay line and a

single loop, as shown in Figure 2.5. The coherent video signal is split, and one-half the signal is delayed by one pulse repetition interval then subtracted from the undelayed signal. Targets at a constant range will experience no phase shift pulse to pulse, and therefore will cancel in the subtractor. The returns from moving targets, on the other hand, will experience a phase shift due to changing range and will not cancel. In fact, for targets that move radially a quarter-wavelength between pulses, the two-way phase shift will be 180°, and the delayed and undelayed signals will coherently reinforce in the subtractor, giving a peak response. However, targets moving any multiple of a half-wavelength radially between pulses will experience the equivalent of a 360° phase shift, and their delayed and undelayed returns will cancel. So at radial velocities (called *blind speeds*) given by

$$V_n = n\lambda f_r/2 \qquad n = \ldots -2, -1, 0, 1, 2, \ldots \tag{2.10}$$

no output will occur. In addition, signal losses will occur for velocities near the blind speeds, as is also illustrated in Figure 2.5. Multiple loop cancellers may be used to give a sharper notch at the blind speeds, and PRF jitter can be used to eliminate all blind speeds except the one at zero velocity.

Modern pulse doppler systems typically employ digital processors rather than delay line cancellers. Usually a pulse burst (generally at least eight pulses) is transmitted, and the return is Fourier transformed in the receiver signal processor. The FFT output provides signal levels as a function of doppler frequency and allows discrimination between targets and clutter. In airborne radars one advantage of the digital approach is that computer processing allows much more effective

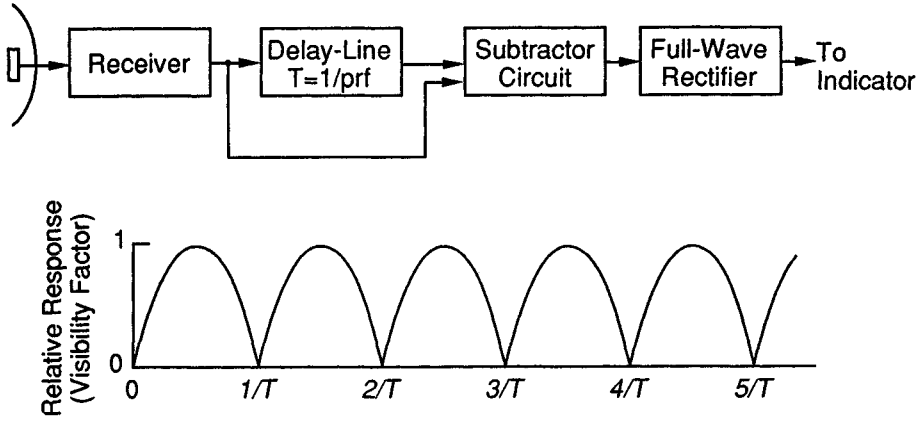

Figure 2.5. Single-pulse delay line canceller (from [1]).

suppression of the nonzero doppler clutter caused by radar motion than can be achieved in analog systems.

The ability to do doppler discrimination in a coherent system also allows doppler to be employed in certain situations for improved cross-range resolution. *Synthetic aperture radars* (SAR) make use of the fact that, for an antenna squinted away from the direction of motion of the radar (normal to the direction of flight is generally used), every point on the ground within a given range resolution cell will have a unique doppler history. The doppler or phase history gathered over a series of pulses can be used, via either a correlator or FFT, to provide cross-range discrimination. If focused processing is employed (i.e., a phase history correction is applied for each range), cross-range resolution can theoretically approach the limit

$$\Delta R_c = D/2 \quad \text{(focused SAR)} \tag{2.11}$$

where D is the length of the aperture in the cross-range direction.

In SAR, motion of the radar is used to create a doppler history for the target (generally the terrain to be imaged). However, if the target has angular rotation motion relative to the radar, doppler can be used to give cross-range discrimination in a method called *inverse SAR* (ISAR). For simplicity, assume a target rotating on a turntable. A fixed measurement radar located some distance from the turntable is boresighted on the target. The target scatterers at the center of rotation will have zero doppler, but scatterers away from the center of rotation will have a doppler that is dependent on the rotation rate and their distance from the center of rotation projected into the plane of the incident radar wave. If a series of pulses is collected as the target is rotating and an FFT is applied to the group of pulses, the result will be a cross-range map of the return from the target. The cross-range resolution limit for the map is given by

$$\Delta R_c = \lambda/2\Delta\theta \quad \text{(ISAR)} \tag{2.12}$$

where $\Delta\theta$ is the total rotation angle over which the data are collected.

A very popular method for gathering high-range and cross-range resolution image data on instrumentation ranges is to employ a wideband step chirp for high-range resolution and ISAR processing for high cross-range resolution. A complete set of frequency samples is gathered at each angle position to be processed. At that point the raw data are a two-dimensional array of complex numbers whose columns (for example) represent frequency samples over the radar bandwidth at a given angle, and whose rows represent samples at single frequency over the angular window ($\Delta\theta$). A two-dimensional (2-D) FFT can then be applied to the data to produce a high-resolution image in both range and cross-range. In selecting the frequency and angle step sizes, care must be taken to ensure that samples are

close enough together in both domains so that range and doppler ambiguities are not created. Range ambiguities will cause aliasing in range, whereas doppler ambiguities will produce cross-range aliasing.

2.4.7 An Instrumentation Radar Example

In Section 2.7, detection performance predictions are provided for three nominal operational radars designed to detect and engage airborne targets. However, after discussing how a radar discriminates in its measurement space, it is instructive to consider how instrumentation systems designed for highly accurate and sensitive RCS measurements achieve their goals.

An excellent example of the technology applied in modern instrumentation radars is provided by the System Planning Corporation Mark IV system. That radar, whose block diagram is shown in Figure 2.6, is a wideband, coherent, step chirp system that uses doppler processing to provide ISAR images. The system has been designed to operate over a 0.1–40 GHz frequency range and at 94 GHz. The wide total system bandwidth is achieved by using individual RF subsystems in each frequency band (up to 12, total) that accept S band local oscillator and exciter signals and provide an IF signal in S band back to the receiver, regardless of the transmitting frequency. This allows a common receiver, A/D convertor, and signal processor to be utilized for all the frequency bands.

Pulses are transmitted in bursts at a single frequency so that coherent integration can be employed to increase the system sensitivity. For example, 1024 pulses may be transmitted at each frequency giving a coherent integration gain of 30 dB. After transmitting a burst of pulses at one frequency, the frequency is stepped, and another burst of pulses is transmitted. Because of the large number of pulses that may be desired at each frequency and the large number of frequency steps required to prevent aliasing if a wide total bandwidth is desired, high PRFs are used (for example, at X band 256 frequency steps over a 2 GHz total frequency range would not be unusual, with, perhaps, 512 pulses integrated at each frequency).

Because most instrumentation radars are employed at short ranges (when compared to operational systems), relatively high PRFs can generally be used without range ambiguity. However, the maximum PRF on the MK IV is 4 MHz, which translates to an ambiguous range of 37.5 m. For cases where a PRF must be used that folds ambiguous clutter into the target range cell, a pseudo-random binary phase code can be applied to each block of pulses. Processing is set up so that the code correlates only for return delays in the vicinity of the target, eliminating integration gain on ambiguous clutter while maintaining the gain on signals from the target range cell. By using large amounts of coherent integration, the MK IV is capable of dynamic ranges in excess of 90 dB.

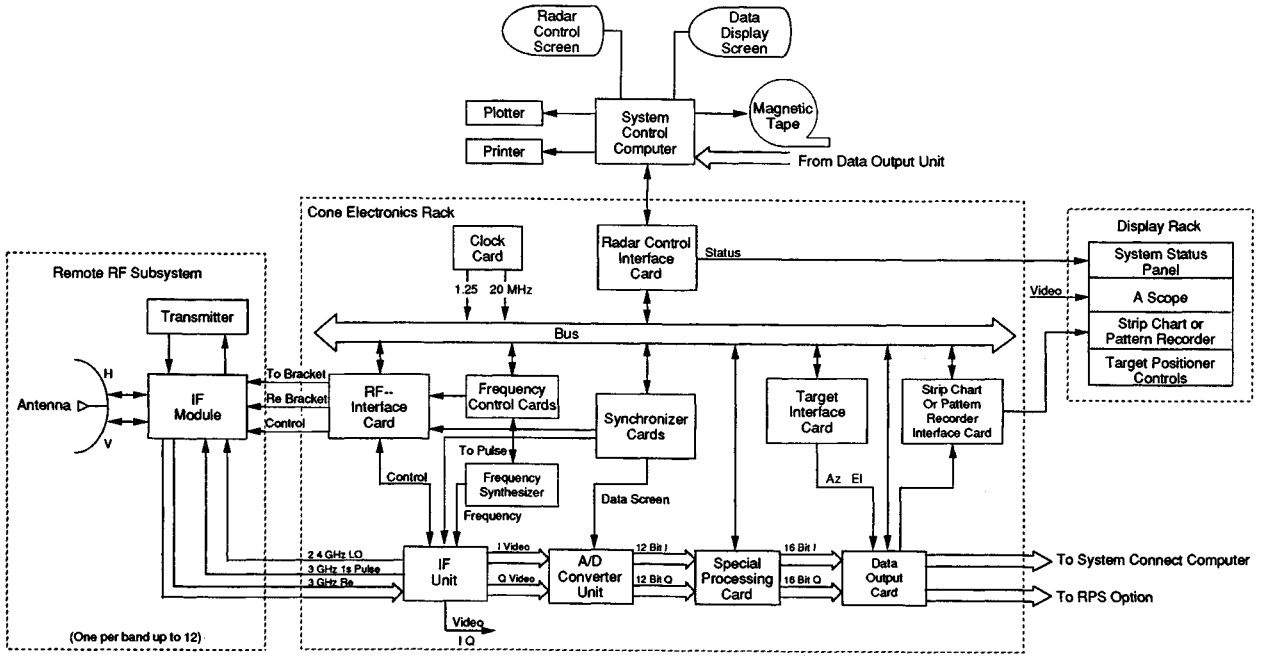

Figure 2.6. Block diagram of the System Planning Corporation MK IV instrumentation radar (Courtesy of System Planning Corporation).

The system is also pulse-to-pulse polarization agile and provides both parallel and orthogonal polarization channels, so full polarization scattering matrix data can be collected. ISAR images are produced by performing a 2-D FFT on the data arriving from a rotating target, as described earlier. Various weightings can be applied to the data to control range and cross-range sidelobes. The output is available in near-real time on a color display, which color codes RCS amplitudes. Hard copy output is available from a color printer.

Because carefully calibrated RCS data are required from the system, a large amount of effort has been put forth to ensure that the system is very stable, that I and Q channels are orthogonal and balanced, that A/D convertors are well characterized, and that stray signals in the radar do not contaminate the target data. In addition, calibration procedures have been devised that define the system transfer function at each frequency to allow precise single frequency and chirp measurements.

The class of systems that the MK IV represents typify the technology that over the past decade has provided orders of magnitude improvements in system sensitivity and capability for RCS diagnostics. The advent of very stable computer controlled frequency synthesizers, wideband high-speed A/D convertors, and improved digital signal processing have allowed widespread implementation of systems like the MK IV whose capabilities would simply not have been achievable only a few years ago.

2.5 THE RADAR RANGE EQUATION

The *radar range equation* (RRE) provides the most useful mathematical relationship available to the engineer in assessing both the need for and the resulting effectiveness of efforts to reduce radar target cross section. In its complete form [17], the radar equation accounts for

- Radar system parameters;
- Target parameters;
- Background effects (clutter, noise, interference, and jamming);
- Propagation effects (reflection, refraction, and diffraction);
- Propagation medium (absorption and scatter).

When fully implemented, the radar equation can be used to estimate radar system performance, and the bottom line for any RCS control task is its effect on radar performance. Therefore, a thorough knowledge of the radar equation and its implications are vitally necessary in the area of RCSR. Luckily, the fundamental form of the equation is based on very simple geometric principles, as is shown.

2.5.1 Derivation of the Radar Range Equation

Assume that a radar transmitter has a power output of P_t watts, which is delivered to an antenna with an isotropic pattern. At a distance R from the antenna, the

power density is simply the power transmitted divided by the area of the sphere over which it has evenly spread:

$$\text{Power density at range } R = P_t/4\pi R^2 \quad (\text{W/m}^2) \tag{2.13}$$

If a directional antenna is used instead of an isotropic one, then the power density at a point in space is modified by the power gain of the antenna in that direction, $G_t(\theta, \phi)$, where θ and ϕ define the principal plane angles from the main beam of the antenna. We will consider only the simplest case, that for the target in the main beam of the radar, so the power density at the target, located at a distance R, is simply

$$\text{Power density} = P_t G_t/4\pi R^2 \quad (\text{W/m}^2) \tag{2.14}$$

where G_t is the peak gain of the antenna.

The concept of RCS was discussed briefly in Chapter 1 and in more detail throughout the book, so it will suffice here to simply define the RCS, σ, as the projected area that would be required to intercept and radiate isotropically the same power as the target radiates toward the radar receiving antenna. Therefore, we can treat the problem as though the target intercepts the power:

$$\text{Power intercepted} = P_t G_t \sigma/4\pi R^2 \quad (\text{W}) \tag{2.15}$$

and radiates it isotropically. Then the power density at the radar receiving antenna (which for simplicity is assumed to be collocated with the transmitting antenna) is

$$\text{Power density} = P_t G_t \sigma/(4\pi)^2 R^4 \quad (\text{W/m}^2) \tag{2.16}$$

The power received by the radar antenna is simply the power density at the antenna, multiplied by the effective capture area of the antenna. However, it is usually more convenient to work with antenna gain, where the gain and capture area are related by

$$A_c = G_r \lambda^2/4\pi \quad (\text{m}^2) \tag{2.17}$$

Also, if we assume that the same antenna is used for transmission and reception, so that $G_t = G_r = G$, then the received power is

$$P_r = P_t G^2 \lambda^2 \sigma/(4\pi)^3 R^4 \quad (\text{W}) \tag{2.18}$$

This is the simplest form of the radar range equation and ignores a number of effects that can be critical in detailed radar performance analysis. Nevertheless, it is invaluable for rough performance calculations, and it is particularly handy for assessing expected changes in radar performance for a given change in RCS.

For detection range estimates it is convenient to cast the radar equation in a slightly different form. In the simple case of detection of a target in receiver noise, a required minimum signal-to-noise ratio can be defined, based on the required detection probability, target statistics, and radar characteristics. Because receiver noise can be considered to have a constant average power, the minimum signal-to-noise ratio defines the minimum level of received signal, P_{min}, that can be tolerated. Therefore, the maximum detection range is given by

$$R_{max} = [P_t G^2 \lambda^2 \sigma / (4\pi)^3 P_{min}]^{1/4} \quad \text{(m)} \tag{2.19}$$

The sobering fact gleaned from (2.19) is that the maximum detection range (in free space) varies only as the fourth root of the RCS. Therefore, a factor of 16 reduction in RCS will be required to halve the maximum detection range, and a factor of 10,000 reduction in RCS will be required to cut the detection range by a factor of 10. For detection in clutter or multipath, the relationship between RCS and maximum detection range becomes more complicated, and those cases will not be treated here.

2.5.2 The Decibel Scale

In working with the RRE, the variables involved will often cover many orders of magnitude. For example, transmitted powers may be measured in megawatts, although received powers are in the picowatt range. Likewise, radars may deal with targets whose RCS values range from millions of square meters (ships) to a small fraction of a square meter (birds and insects).

Because of the wide range of variability involved, radar engineers typically convert parameter values to a logarithmic scale for RRE calculations (although computers and hand calculators have made this conversion less necessary than it was in the days of slide rules). In addition, the wide dynamic range of most RCS plots requires that some method be used to allow visualization of data covering many orders of magnitude, and logarithmic scales provide that feature. Therefore, RCS is almost always plotted using logarithmic scales, either through the use of logarithmic graph paper or by plotting the logarithm of the RCS on a linear scale.

The logarithmic unit commonly used in radar is the decibel, denoted dB, which is defined as

$$P(\text{dB}) = 10 \log_{10}(P/P_0) \tag{2.20}$$

where P_0 is a reference level. Decibels must always be expressed in terms of a ratio and therefore require a reference unit. For power, the reference unit is typically either 1 W or 1 mW, and the notation dBW of dBm is normally used so

that the reference unit is provided. For RCS, the most common reference is 1 m^2, and dB referenced to a square meter are denoted dBsm or dBm^2. RCS values are sometimes normalized by the wavelength at which they were measured or calculated, in which case the units are denoted $dB\lambda^2$.

When converted to decibels, (2.18) will typically be written

$$P_r\,(\text{dBm}) = P_t\,(\text{dBm}) + 2G\,(\text{dB}) + 20\log(\lambda) + \sigma\,(\text{dBsm}) - 33 - 40\log(R) \tag{2.21}$$

Transmitted power, antenna gain, and RCS values are often provided to the user in dB, so no conversion is shown for them. Wavelength and range are normally expressed in linear units and must be converted to dB to be used in (2.21). Equation (2.21) represents a set of simple sum and difference operations, compared to the products and quotients required in (2.18), hence its attractiveness for back-of-the-envelope calculations.

2.6 RADAR DETECTION

The entire premise that RCSR can be used to delay or prevent radar detection is predicated on the fact that a radar must detect a target in a background of other signals. If no signals were competing with the target return, additional amplification could be added in the radar receiver to provide a detectable output, no matter how small the input. However, there are always other background signals in which the target must be detected. These include cosmic and atmospheric noise (which may usually be neglected at L band and above), terrain backscatter (land and sea clutter), atmospheric clutter (backscatter from dust, refractive changes, and hydrometeors), unintentional radio frequency interference from other emitters, and electronic countermeasures (chaff, jammers, etc.). Models exist that describe the effects of all of the above types of background interference [3,17–19]. However, those effects obviously complicate the detection process, and it is beyond the scope of this book to delve into the subtleties of radar detection in jamming and cluttered environments. Therefore, this section concentrates on the simplest case, that of detection of a target in receiver noise. Note, however, that the assumption of detection in noise may not be too farfetched, as many of the discrimination techniques described earlier (e.g., MTI, pulse compression, imaging) are specifically intended to reduce clutter and, ideally, produce system noise limited detection.

2.6.1 The Decision Process

The radar detection problem is normally approached through the concepts of statistical decision theory, because it involves the detection of a random time-

varying signal in a randomly varying background. There are a number of excellent texts on detection theory, both general [20,21] and dealing specifically with radar detection [22,23]. The radar detection decision is typically posed as a hypothesis test, where the two hypotheses are

- H_0: no target is present (noise only)
- H_1: a target is present (target return plus noise)

and the goal is to formulate a test that maximizes the probability of choice of the correct hypothesis, based on constraints concerning errors in the decision.

The error constraint normally used in radar is to limit the number of times H_1 is chosen when in fact no target is present (i.e., a false alarm) to a certain level. This essentially involves correct placement of a threshold (see Fig. 2.7) so that noise alone will cross the threshold at an acceptable rate. Threshold placement obviously requires a knowledge of the statistics of the receiver noise.

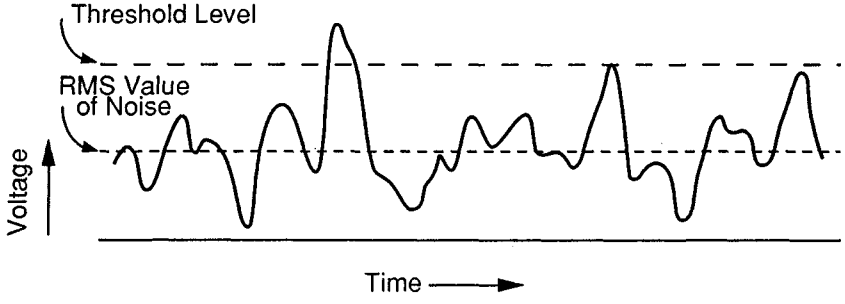

Figure 2.7. Typical radar receiver output envelope as a function of time (from [1]).

2.6.2 Noise Statistics

For a typical radar receiver, thermal noise power generated by the random motion of conduction electrons in the input stages limits the signal that can be detected. The available thermal noise power is a function of the temperature T and the noise bandwidth B_n of the receiver and is given by

$$P_n = kTB_n \quad \text{(W)} \tag{2.22}$$

where k is Boltzmann's constant $= 1.38 \times 10^{-23}$ J/K. At room temperature (290 K), $P_n = -114$ dBm for a lossless receiver with a 1 MHz bandwidth. The noise

bandwidth of the receiver is a function of the IF filter response shape, but the 3 dB IF bandwidth is normally used without appreciable error [1].

The ideal receiver would add no noise to the signal to be amplified, and the input and output signal-to-noise ratios would be the same. Actual receivers add some noise of their own, and the noise figure F, defined for a linear system as

$$F = (S_{in}/N_{in})/(S_{out}/N_{out}) \tag{2.23}$$

is the measure of how much the receiver degrades the input signal-to-noise ratio.

Additional losses (scanning, beamshape, collapsing, integration, etc.) in the radar system can be defined that further degrade the received signal power. If those losses are lumped and are designated by L, then the radar equation can be expressed in terms of the *signal-to-noise ratio* (SNR) as

$$\text{SNR} = P_t G^2 \lambda^2 \sigma / (4\pi)^3 R^4 k T B_n F L \tag{2.24}$$

The thermal noise voltage in the IF stages before the detector can be described statistically as a bivariate Gaussian process (I and Q signals), with each component having a zero mean and a variance equal to half of the noise power, as shown in Figure 2.8. The envelope of the noise process after passage through a linear detector is Rayleigh distributed (also Fig. 2.8), and it is this detected noise signal to which a threshold is normally applied.

2.6.3 Single-Pulse Probability of Detection for a Nonfluctuating Target

The Neyman-Pearson criterion, one often applied in radar, maximizes the probability of detection for a fixed false alarm probability. Therefore, the calculation of detection probability first requires that the value of the threshold be determined and then, based on that threshold, the probability of detection can be calculated from the target-plus-noise density function.

The threshold level for a given false alarm rate can be set based on the noise distribution, where the probability of false alarm is given by

$$\begin{aligned} P_f &= \int_{V_t}^{\infty} p_n(v)\, dv = \int_{V_t}^{\infty} \frac{v}{N} \exp\left(\frac{-v^2}{2N}\right) dv \\ P_f &= \exp\left(-V_t^2/2N\right) \end{aligned} \tag{2.25}$$

where V_t is the threshold voltage and N is the noise power.

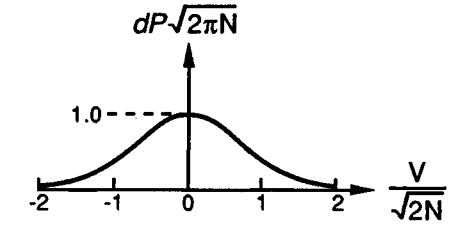

Gaussian IF Noise

$$dP_v = \frac{1}{\sqrt{2\pi N}} \exp\left(\frac{-V^2}{2N}\right) dV$$

(a)

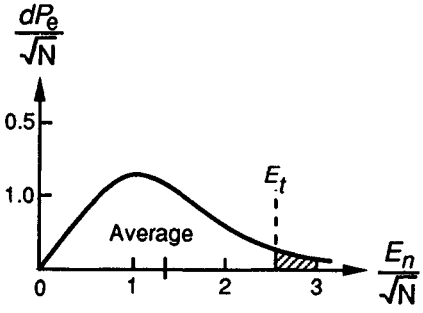

Rayleigh Distributed Envelope

$$E_n = \sqrt{I^2 + Q^2}:$$

$$dP_e = \frac{E_n}{N} \exp\left(\frac{-E_n^2}{2N}\right) dE_n$$

(b)

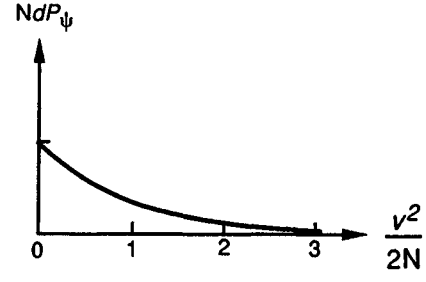

Exponentially Distributed Noise Power

$$dP_\psi = \frac{1}{N} \exp\left(\frac{-\psi}{N}\right) d_\psi$$

(c)

Figure 2.8. Thermal noise distributions in the radar receiver: (a) Gaussian IF noise; (b) Rayleigh distributed envelope; (c) exponentially distributed noise power (from [25]).

For a nonfluctuating target with a voltage amplitude A, Rice [24] gives the combined target-plus-noise probability density function at the output of the detector as

$$p(v)dv = \frac{v}{N} \exp\left(\frac{-v^2 + A^2}{2N}\right) I_0\left(\frac{vA}{N}\right) dv \tag{2.26}$$

where $I_0(\ )$ is the modified Bessel function of order zero. The probability of detection is given by

$$P_d = \int_{V_t}^{\infty} p(v)dv = \int_{V_t}^{\infty} \frac{V}{N} \exp\left(\frac{-v^2 + A^2}{2N}\right) I_0\left(\frac{vA}{N}\right) dv \tag{2.27}$$

which has not been evaluated in closed form. However, when evaluated numerically and expressed in terms of signal-to-noise ratio, the curves of Figure 2.9 result. These curves represent detection based on processing a single pulse. Note that for reasonable false alarm rates (10^{-6} or lower) large values of signal-to-noise ratio are required for a significant detection probability. For example, with a 1 MHz

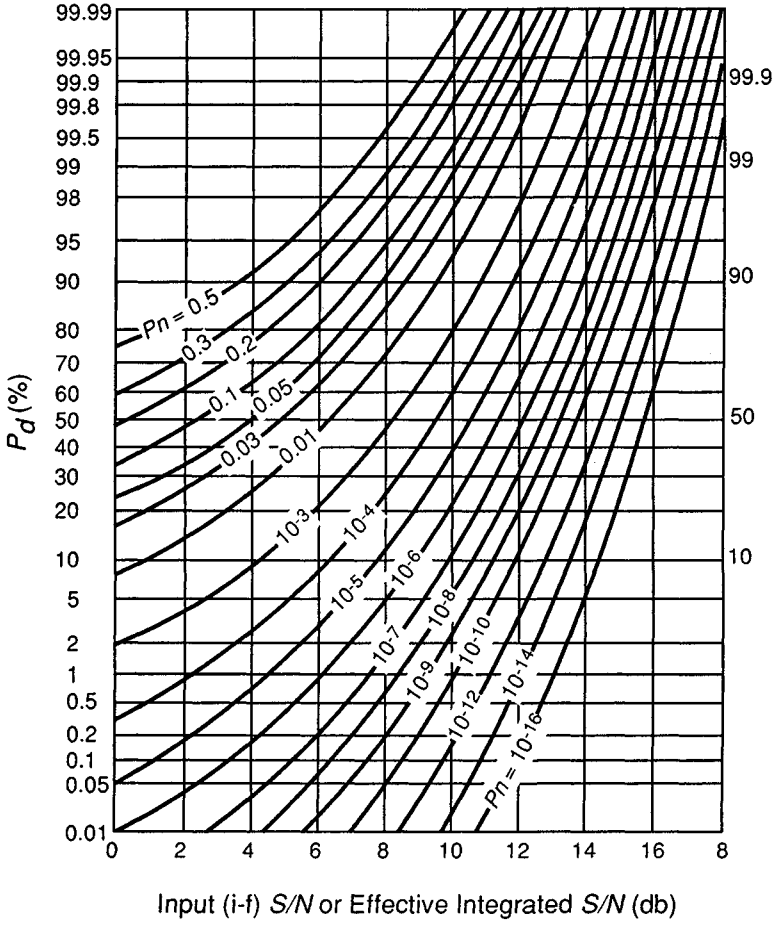

Figure 2.9. Probability of detection as a function of the signal-to-noise ratio (from [25]).

bandwidth, a false alarm rate of less than 1×10^{-6} is required if an average of at least 1 s between false alarms is desired. Even at that rate, a signal-to-noise ratio of almost 12 dB is required for a $P_d = 0.5$.

2.6.4 Pulse Integration

In general, many pulses are received from a target on a single scan by the search radar antenna. Therefore, the single-pulse probability of detection calculated in (2.27) is not realistic because the sum of the returns from multiple pulses is used in the detection decision. The process of summing the available pulses to enhance detection is called *integration*, and it relies on the fact that the noise signal decorrelates from pulse to pulse to allow the signal return to be enhanced relative to the noise.

Integration can be accomplished at IF or video in the receiver. If the integration is carried out with the phase preserved (coherent integration), an increase in single-pulse signal-to-noise ratio by a maximum factor of the number of pulses integrated can be achieved. Thus for 20 pulses integrated, the required single-pulse signal-to-noise ratio for a given detection probability might be reduced by 13 dB because of the integration gain. If post detection integration is used, the phase information is discarded, and a less efficient integrator is obtained. One common method of post detection integration is on the CRT screen using phosphor persistence and the integration ability of the operator's eye.

2.6.5 Detection of Fluctuating Targets

The basic work on detection of fluctuating targets was done by Peter Swerling [26], who defined four cases of fluctuating targets based on two RCS distributions and two fluctuation rates. They are

Amplitude Distribution	*Slow Fluctuation*	*Fast Fluctuation*
$dP = \frac{1}{<\sigma>} \exp\left[\frac{-\sigma}{<\sigma>}\right] d\sigma$	*Case 1*	*Case 2*
$dP = \frac{4\sigma}{<\sigma>^2} \exp[-2\sigma/<\sigma>] d\sigma$	*Case 3*	*Case 4*

where $<\sigma>$ is the average RCS.

The first amplitude distribution can be recognized as Rayleigh, whereas the second is the square root of a chi-squared distribution with four degrees of freedom. Physically, a Rayleigh distribution is given by a large number of nearly equal

amplitude scatterers adding together with random phases. The chi-squared distribution represents a body with one dominant plus many small scatterers. The slow fluctuation case assumes constant RCS during a scan, with scan-to-scan variations. The fast fluctuation cases represents targets whose return is independent pulse-to-pulse.

Figure 2.10 illustrates the additional loss due to target fluctuation for the slowly varying Swerling cases 1 and 3. Note that the loss is greatest at the higher probabilities of detection and that the curve is not particularly sensitive to false alarm rate. For rapidly varying targets the fluctuation loss is related to that for the slowly varying target and to the number of pulses integrated, n, by

$$\begin{aligned} L_{f2} &\cong [L_{f1}]^{1/n} \quad \text{(Case 2 target)} \\ L_{f4} &\cong [L_{f3}]^{1/n} \quad \text{(Case 4 target)} \end{aligned} \tag{2.28}$$

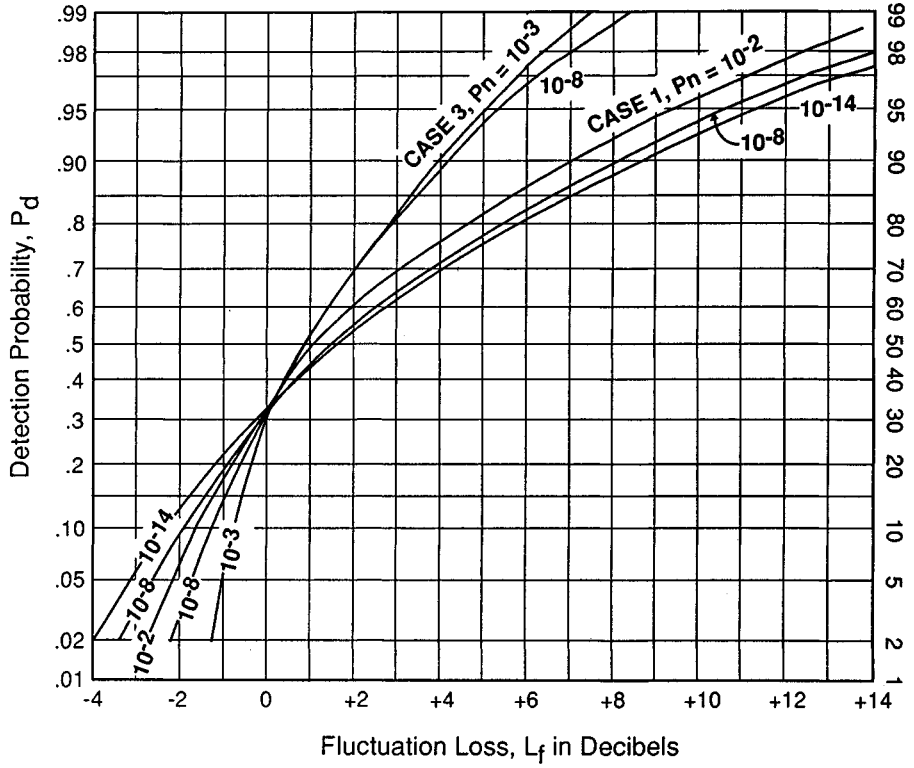

Figure 2.10. Target fluctuation loss for Swerling case 1 and 3 targets as a function of probability of detection, with false alarm rate as a parameter (from [25]).

2.7 RADAR SYSTEM PERFORMANCE EXAMPLES

Sections 2.5 and 2.6 provide the basic information necessary to calculate the performance of example radar systems. Figure 2.11 indicates a scenario that might be typical for an aircraft attacking a ground target complex. In the worst of situations (from the point of view of the aircraft), threat radars might include long-range surveillance radars from VHF through S band, missile system related acquisition and tracking radars in C band or X band, and *airborne interceptor* (AI) radars in X band or K_u band.

It is instructive to choose several types of systems and examine detection performance for representative system parameter sets. In predicting detection range, a requirement for a 13 dB integrated signal-to-noise ratio will be imposed, which represents a single dwell probability of detection of just under 90% on a nonfluctuating target for a false alarm probability of 1×10^{-6}. Although any particular choice of signal-to-noise ratio is arbitrary, numbers close to 13 dB are often used in system performance calculations.

2.7.1 L Band Surveillance Radar

Frequencies around 1 GHz are typical for surveillance radars intended to detect airborne targets at ranges up to several hundred nautical miles. FAA *air route surveillance radars* (ARSR) are civilian examples of such radars, and they are generally implemented at L band. High powers are easy to obtain at 1 GHz, and a reasonably sized antenna can have good gain and relatively narrow beamwidths: a 10 m antenna will provide approximately a 2° beamwidth.

As noted in Section 2.6.4, coherent integration raises the signal-to-noise ratio by a factor equal to the number of pulses integrated. For a circularly scanning radar, which is typical of surveillance systems, the number of *pulses-per-scan* (PPS) on a target is given by

$$\text{PPS} = \Theta f_r/\omega \tag{2.29}$$

where Θ is the azimuth 3 dB beamwidth of the antenna, ω is the antenna scan rate, and f_r is the radar pulse repetition frequency.

When implemented in (2.24) and solved for range, the result is

$$R = [P_t G^2 \lambda^2 \sigma \Theta f_r/(4\pi)^3(\text{SNR})kTB_n FL\omega]^{1/4} \tag{2.30}$$

where SNR is the signal-to-noise ratio for the minimum desired probability of detection and associated false alarm rate (in our example cases, 13 dB). A representative L band air search radar might have the following parameters:

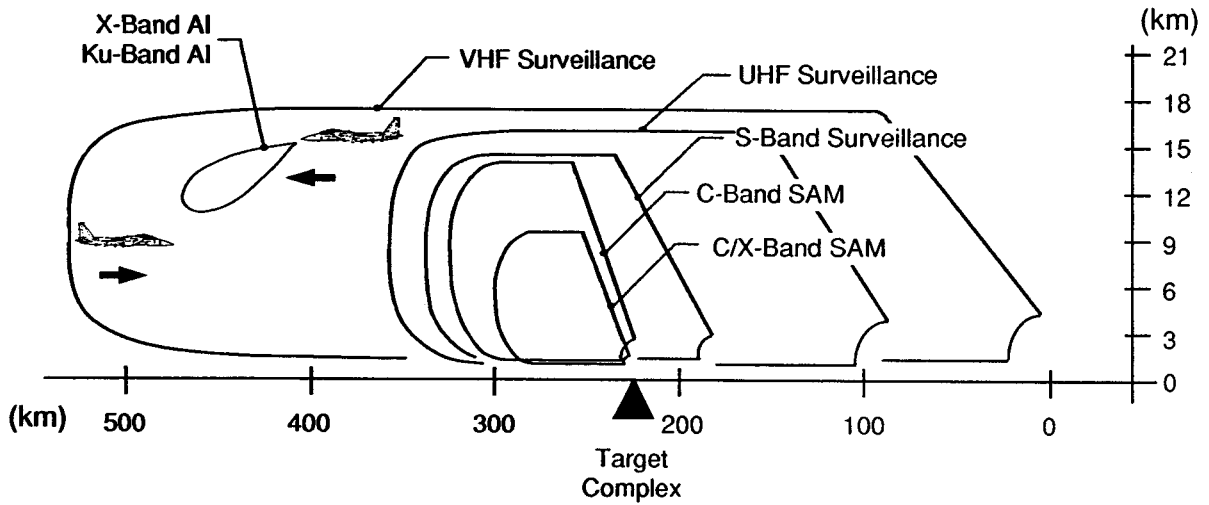

Figure 2.11. Examples of search radar placement and coverage.

P_t = 1 MW L = 6 dB
G = 35 dB Θ = 2 deg
f = 1.25 GHz (λ = 0.24 m) ω = 36 deg/s (10 s scan)
B_n = 500 kHz (2 μs pulse) f_r = 250 Hz (R_{unamb} = 600 km)
F = 4 dB

Solving (2.30) for these parameters provides a predicted detection range of 317 km, or 171 nmi, against a 1 m^2 RCS target. Note that reducing the RCS from 0 dBsm to −40 dBsm will reduce the detection range in noise from 317 km to 32 km. However, if a −40 dBsm aircraft target can be detected at that range, so can birds, insect swarms, and any other targets with RCS levels above −40 dBsm. Although MTI may remove some of these undesired targets, it does so with the attendant potential loss of desired targets, because of the doppler ambiguity inherent in such a low PRF radar (the first ambiguous velocity is at 30 knots, so any target with a radial velocity over 30 knots will alias in doppler). The loss of targets in the nulls of the MTI filter can be offset by staggering the PRF to move around the "blind speeds." This solution, however, increases the complexity of the radar and results in additional signal processing losses and, hence, poorer sensitivity.

2.7.2 Airborne Interceptor Radar

Because of the limited available aperture and the requirement for good angular resolution, modern *airborne interceptor* (AI) radars are typically implemented at X band or K_u band. In "lookdown" operation where targets are at lower altitudes than the radar, clutter return from the terrain will normally be orders of magnitude larger than the target signal. To provide operation in heavy clutter environments, pulse doppler radars are often employed so that targets can be separated from the background using doppler as a discriminant.

Both high PRF (unambiguous in doppler, but ambiguous in range) and medium PRF (ambiguous in range and doppler) systems are used. The high PRF systems have the advantages of unambiguous target doppler and higher average power due to higher duty cycles. For those systems, PRF values of 100 kHz to 300 kHz are typical, so the maximum unambiguous range is well less than one nautical mile. Therefore, only one or two range gates are generally implemented. In a tail-chase situation, targets will generally occupy doppler bins containing close-in sidelobe clutter and are likely to be masked. With only one or two range gates, range cannot be used as a discriminant against clutter. Medium PRF systems have the disadvantage of being ambiguous in both range and doppler. However, the lower PRF (typically 10–20 kHz) allows a number of range gates to be implemented within the ambiguous range swath, with each range gate followed by a doppler filter bank. The ability to separate the return in multiple range bins and doppler

filters provides an additional means to suppress clutter, thus improving detection of tail-chase targets. If necessary, by judicious choice of PRF, the target can be placed in a portion of a range gate that has the least clutter, thereby additionally improving the probability of detection. AI radars will often employ both medium and high PRF modes, with the mode of choice depending on the target situation. A typical medium PRF pulsed doppler AI radar might have the following parameters:

P_t = 5 kW	L = 16 dB
G = 36 dB	Θ = 2.5 deg
f = 10 GHz (λ = 0.03 m)	ω = 80 deg/s (sector scan)
B_n = 1 MHz (1 μs pulse)	f_r = 12,500 Hz (R_{unamb} = 12 km)
F = 4 dB	

Note that the antenna gain is about the same as for the L band system, because the increase by a factor of 8 in frequency offsets the much smaller antenna size. The large value of loss is seen because of such things as range and doppler filter straddle, and beamshape losses in two dimensions.

Applying (2.30) to these parameters, a detection range of 36 km, or 20 nmi is obtained. Note that for the PRF and pulsewidth shown, the duty cycle for the transmitter is only 1.25% (pulsewidth of 1×10^{-6} times PRF of 12,500). AI radar sources are typically designed to operate at much higher duty cycles. In this case, a 20 μs phase coded pulse might be generated, and then compressed to 1 μs on reception, providing a 13 dB enhancement in signal-to-noise ratio and just over a factor of 2 improvement in detection range to 76 km.

2.7.3 Active Missile Seeker Radar

The AI discussed previously might employ an active or semiactive missile as a weapon (it might also employ a passive IR system, but that is a topic for a different book). For the semiactive seeker, the launch aircraft will typically continue to illuminate the target for the duration of the missile flight, which may severely constrain aircraft maneuverability during that period. Because of the inherent problems and disadvantages of requiring continuous illumination of the target by the AI radar, active radar seekers have many advantages for air-to-air missiles, in spite of their increased cost and complexity compared to semiactive systems.

As might be expected, the power and antenna gain achieved with an active seeker are limited. Because operation in severe clutter is required, high PRF pulsed doppler systems are often employed. Because of the combination of pulse burst processing in an FFT and integration of multiple bursts, the definition of pulses

integrated is modified to correspond to an effective number of integrated pulses. Radar parameters for a typical seeker are as follows:

P_t = 2 kW	F = 4 dB
G = 24 dB	L = 13 dB
f = 10 GHz (λ = 0.03 m)	$(\Theta f_r/\omega)_{\text{eff}}$ = 32
B = 125 Hz (doppler filter)	

The calculated detection range for the seeker is 35 km or about 19 nmi. This is only about half the detection range of the AI radar with pulse compression, and if the missile range at firing is significantly in excess of the detection range, the missile would be required to acquire the target sometime in the mid-course phase.

2.7.4 Performance Summary

The point predictions for the three radars are informative. A better view of performance is provided in Figure 2.12, which plots predicted detection range as a function of target RCS for the three systems. The significant detection range advantage of the surveillance radar for large RCS targets is clearly seen on the plot.

However, the inherent assumption underlying the plot is that RCS is independent of frequency. As is demonstrated in Chapter 7, low-RCS shapes have an

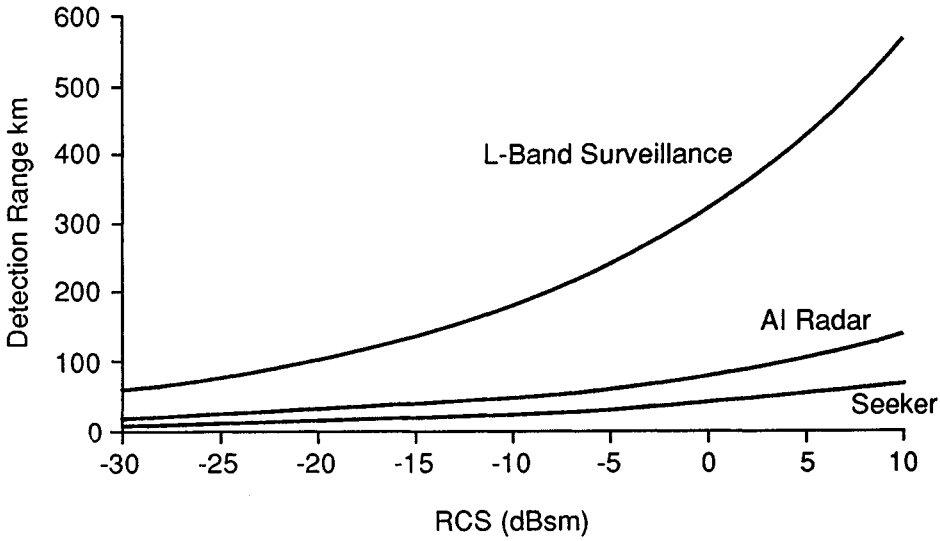

Figure 2.12. Detection performance predictions for three example systems.

RCS functional dependency of λ^2. Therefore, the RCS of a vehicle designed for minimum RCS in the threat sector would be expected to have an 18 dB lower RCS at 10 GHz than at 1.25 GHz.

Assume, for example, a target shaped for low RCS having a -20 dBsm cross section at 10 GHz. The RCS at 1.25 GHz, using a λ^2 dependency, would be -2 dBsm. For that case, the surveillance radar would have a 283 km (153 nmi) detection range. On the other hand, the AI radar with pulse compression would be reduced to a 24 km (13 nmi) detection range, and the missile to 11 km (6 nmi). The disparity becomes even more apparent for wider spreads in radar frequency. For instance, if a UHF surveillance radar is postulated, instead of the L band system, the detection range should equal or exceed the preceding 283 km figure, depending on exact system parameters assumed. However, it would be unlikely in that case that the surveillance radar would have sufficient resolution to vector an interceptor sufficiently accurately so that hand-off to the AI radar could be accomplished.

2.8 ELECTRONIC COUNTERMEASURES

This final topic in radar fundamentals is included because of its importance to the engineer concerned with RCS prediction and control. RCSR constitutes a passive countermeasure, and sometimes sufficiently low RCS can be obtained to allow the treated vehicle to be hidden in clutter and to escape detection altogether. However, if detection occurs, then a reduced RCS is beneficial, because ECM techniques rely on distraction of the radar from the target by a larger signal.

ECM may utilize any one of a number of techniques for its performance. Examples include saturating the radar screen to hide the desired target by using a stand-off jammer, creating false targets with chaff, or using a deception jammer to break radar track on the target. In the case of chaff, the idea is to force the tracking radar off the target (and preferably onto the chaff cloud). However, when deployed from an aircraft, the rate at which the chaff slows and moves out of the doppler filter passband of MTI or PD systems is extremely rapid. Therefore, chaff is typically employed in the terminal phase of a missile engagement, and it is required only to break the track for a sufficient period that the missile is unable to recover. Obviously, a significant amplitude advantage in chaff RCS over target RCS is desired, both to pull the track centroid as far off the target as possible and to maintain the chaff RCS advantage in the doppler passband as long as possible.

Deception jammers are generally carried on the jamming vehicle. Thus, spatial separation of the jammer and target cannot be used to break track, as can be done with chaff. In addition, most modern missiles have a *home-on-jam* (HOJ) mode, and thus simple barrage jamming by the target platform will also be unsuccessful. For that reason, deception jammers must produce a signal that appears to be a legitimate target signal coming from somewhere other than the target. One

successful deception technique, mentioned previously in connection with conical scan radars, is to produce a jamming signal amplitude modulated at the conical scan frequency. If sufficiently strong, such a signal will mask the signal from the target and produce a false error signal likely to cause a loss of track.

Monopulse systems are immune to amplitude modulation jamming because they produce an error signal based on each pulse. Therefore, other techniques such as *range gate pull off* (RGPO) or *velocity gate pull off* (VGPO), must be used to break track. In RGPO, the jamming pulses are given increasing delays with time so that the range gate of the tracking radar will walk off the target with the jamming pulse. VGPO performs a similar function by slowly ramping the frequency to move a velocity gate off the target.

All of these jamming methods require that the jamming signal overcome the skin return from the target. The basic measure of the return from the jammer versus the normal radar return is called the *J-to-S* (*J/S*) ratio. For a jammer with an output power P_j (the spectrum of which is assumed to fall completely within the radar receiver bandwidth) and an antenna gain G_j, the power received by a radar with antenna gain G is

$$J = P_j G_j G \lambda^2 / (4\pi)^2 R^2 \quad \text{(W)} \tag{2.31}$$

The skin return is simply given by the radar range equation, (2.18), and so

$$J/S = 4\pi P_j G_j R^2 / P_t G \sigma \tag{2.32}$$

For situations where the bandwidth of the jamming signal is greater than the receiver bandwidth, only the portion of the power that falls within the receiver bandwidth should be used in (2.32).

Several things are noteworthy about (2.32). First, J/S is proportional to R^2. Therefore, J/S decreases as the range closes, and at some range the minimum value of J/S for successful jamming will be reached. This range is normally called the *burn-through range*. Second, J/S varies inversely with σ, as expected, so that the lower the RCS, the more effective is the jamming. In addition, because J/S varies only as R^2, a 6 dB reduction in RCS will halve the burn-through range, rather than the 12 dB required in the nonjamming situation to halve the detection range. In the same vein, note that for passive ECM, such as chaff or towed decoys, any RCS advantage gained from signature reduction is range independent, as long as both the false and real target remain in the same radar resolution cell.

RCSR is only one method in a "bag of tricks" for reducing vulnerability. Intelligence, tactics, and countermeasures can also play a large part in increasing mission effectiveness. Therefore, the requirements for and cost of RCSR should be evaluated for the integrated system and not separated for the total engagement problem.

2.9 SUMMARY

The purpose of this chapter has been to provide a brief overview of radar fundamentals. It has purposely been long on explanation and short on complicated equations, and the interested reader is encouraged to consult the references for details on the areas discussed. The intent has been to give a flavor for some of the concerns and techniques of the "other side" — the radar engineer charged with detecting your stealthy vehicle. To do that, the radar coordinates in which a target can be discriminated — range, angle, and doppler — were discussed, and the limits on discrimination explored. The radar range equation was presented, received power was tied to detection considerations, and the results were applied to three representative radar systems. Finally, ECM was discussed, and its ability to alter the character of the radar-target engagement was pointed out.

One key point to to remember from this chapter is that RCSR rarely provides a one-to-one trade-off on detection range. In free space, 12 dB of RCSR is required to halve the detection range. The situation may be better in other environments than receiver noise, but clutter is typically not homogeneous, and the RCSR designer should not rely too heavily on the belief that clutter will hide his vehicle. In an environment where ECM is called for, on-board jamming effectiveness varies with the square of the range, rather than the inverse fourth power dependence seen in the radar equation, so the situation is more favorable than for detection.

RCSR always exists as a systems trade-off. An adequate evaluation of RCSR needs and effectiveness requires knowledge of the threat radars, the environment, available countermeasures, and measures of mission effectiveness. For practical systems development, RCS design cannot exist in a vacuum. It must be considered as an integrated part of a platform's defensive weapons suite.

REFERENCES

[1] Skolnik, M. I., *Introduction to Radar Systems,* 2nd ed., McGraw-Hill, New York, 1980.

[2] Barton, D. K., *Modern Radar System Analysis,* Artech House, Norwood, MA, 1988.

[3] Nathanson, F. E., *Radar Design Principles,* 2nd ed., McGraw-Hill, New York, 1991.

[4] Eaves, J. L., and E. K. Reedy, *Principles of Modern Radar,* Van Nostrand Reinhold, New York, 1987.

[5] Skolnik, M. I., *Radar Handbook,* 2nd ed., McGraw-Hill, New York, 1990.

[6] Lockhard, J., "The SCR-270-B on Oahu, Hawaii—Reminiscences," *IEEE-AESS Magazine,* December 1991, pp. 8–9.

[7] MIT Radiation Laboratory Series, McGraw-Hill, New York, 1947.

[8] *IEEE Standard Dictionary of Electrical and Electronics Terms,* 3rd ed., ANSI/IEEE Standard 100-1984.

[9] Brookner, E., *Radar Technology,* Artech House, Norwood, MA, 1978.

[10] Ewell, G. W., *Radar Transmitters,* McGraw-Hill, New York, 1981.

[11] Stutzman, W. L., and G. A. Thiele, *Antenna Theory and Design,* John Wiley & Sons, New York, 1981.

[12] Balanis, C. A., *Antenna Theory,* Harper and Row, New York, 1982.
[13] Hansen, R. C., ed., *Microwave Scanning Antennas,* Academic Press, New York, 1964.
[14] Johnson, R. C., and H. Jasik, *Antenna Engineering Handbook,* McGraw-Hill, New York, 1984.
[15] Kurtz, J. L., and J. A. Scheer, "High Resolution RCS Measurements," in *Radar Reflectivity Measurement: Techniques and Applications,* N. C. Currie, ed., Artech House, Norwood, MA. 1989.
[16] Sherman, S. M., *Monopulse Principles and Techniques,* Artech House, Norwood MA, 1984.
[17] Blake, L. V., *Radar Range Performance Analysis,* Artech House, Norwood, MA, 1986.
[18] Long, M. W., *Radar Reflectivity of Land and Sea,* Artech House, Norwood, MA, 1983.
[19] Boyd, J. A., et al., *Electronic Countermeasures,* Peninsula Publishing, Los Altos, Ca, 1978.
[20] Wozencraft, J. M., and I. M. Jacobs, *Principles of Communication Engineering,* John Wiley & Sons, New York, 1968.
[21] Van Trees, H. L., *Detection, Estimation, and Modulation Theory,* John Wiley & Sons, New York, 1965.
[22] DiFranco, J. V., and W. L. Rubin, *Radar Detection,* Artech House, Norwood, MA, 1980.
[23] Meyer, D. P., and H. A. Mayer, *Radar Target Detection,* Academic Press, New York, 1973.
[24] Rice, S. O., "Mathematical Analysis of Random Noise," *B.S.T.J.,* Vol. 23, No. 3, July 1944, and *B.S.T.J.,* Vol. 24, No. 1, January 1945.
[25] Barton, D. K., "Detection and Measurement," Chapter 2 in [9].
[26] P. Swerling, "Probability of Detection for Fluctuating Targets," *IRE Trans. on Information Theory,* Vol IT-6, No. 2, April 1960.

Chapter 3
Physics and Overview of Electromagnetic Scattering

J. F. Shaeffer

3.1 INTRODUCTION

The objective of this chapter is to introduce the concept of radar cross section and the fundamentals of electromagnetic scattering in an overview fashion so that the reader may then delve into the remainder of the book. The topics to be presented are

- *Terms:* The definition of radar cross section from IEEE, an intuitive derivation, the polarization scattering matrix for linear polarization and its conversion to circular polarization, and the definition of total cross section and extinction cross section and the forward scattering theorem;
- *Fundamental physical processes of electromagnetic scattering:* Electromagnetic wave fundamentals, induced charges and currents, field lines attached to charges, near, intermediate and far fields, solenoidal and conservative fields, and the concepts for scattered, incident, and total field;
- *Scattering regimes:* The low-frequency Rayleigh region with induced-dipole-like scattering, the resonant region with attached surface wave scattering; and the high-frequency optics region with the concepts of individual scattering centers; opticslike specular, end-region, and diffraction scattering mechanisms; phasor addition as how various scattering mechanisms sum to form a total scattered field; and the concepts for coherent and incoherent sums of individual scattering centers;
- *Electromagnetic theory:* Field quantities and their sources; Maxwell's equations in differential and integral form; vector and scalar potentials as sources for solenoidal and conservative field components; wave equation and char-

acteristic solutions; waves at boundaries; reflection, transmission, and absorption coefficients; Fresnel reflection coefficients; EM wave formalism compared to transmission line theory; surface current point of view; and the Stratton-Chu integral equation formulation of Maxwell's equations with currents and charges as field sources.

3.2 RADAR CROSS SECTION DEFINITION

Radar cross section is a measure of power scattered in a given direction when a target is illuminated by an incident wave. RCS is normalized to the power density of the incident wave at the target so that it does not depend on the distance of the target from the illumination source. This removes the effects of the transmitter power level and distance to target when the illuminating wave decreases in intensity due to inverse square spherical spreading. RCS is also normalized so that inverse square fall-off of scattered intensity due to spherical spreading is not a factor so that we do not need to know the position of the receiver. RCS has been defined to characterize the target characteristics and not the effects of transmitter power, receiver sensitivity, and the position of the transmitter or receiver distance. Another term for RCS is *echo area.*

3.2.1 IEEE RCS Definition

The IEEE dictionary of electrical and electronics terms [1] defines RCS as a measure of reflective strength of a target defined as 4π times the ratio of the power per unit solid angle scattered in a specified direction to the power per unit area in a plane wave incident on the scatterer from a specified direction. More precisely, it is the limit of that ratio as the distance from the scatterer to the point where the scattered power is measured approaches infinity:

$$\sigma = \lim_{r \to \infty} 4\pi r^2 \frac{|\mathbf{E}^{\text{scat}}|^2}{|\mathbf{E}^{\text{inc}}|^2} \tag{3.1}$$

where $\mathbf{E}^{\text{scat}}$ is the scattered electric field and $\mathbf{E}^{\text{inc}}$ is the field incident at the target. Three cases are distinguished: monostatic or backscatter, forward scattering, and bistatic scattering.

3.2.2 Intuitive Derivation for Scattering Cross Section

A formal cross section may be defined for the energy that is scattered, absorbed, removed from the incident wave, and the total cross section. The scattered energy is of greatest practical interest because it represents the energy available for detection.

The formal IEEE definition for RCS can be made more intuitive from the following derivation, Figure 3.1. Let the incident power density at scattering target from a distant radar be P_i W/m^2 (which automatically removes from the definition transmitter power and inverse square intensity fall-off). The amount of power intercepted by the target is then related to its cross section σ, with units of area, so that the intercepted power is (σP_i) W. This intercepted power is then either reradiated as the scattered power or absorbed as heat. Assume for now that it is reradiated as scattered power *uniformly* in all 4π sr of space so that the scattered power density, watts/meter^2, is given by

$$P_s = \frac{\sigma P_i}{4\pi R^2}, \quad \text{W/m}^2 \tag{3.2}$$

We then solve (3.2) for σ and consider that the distance R is far from the target to avoid nearfield effects:

$$\sigma = 4\pi R^2 \frac{P_s}{P_i} \tag{3.3}$$

RCS is therefore fundamentally a ratio of scattered power density to incident power density. The power or intensity of an EM wave is proportional to the square of the electric or magnetic field, so RCS can be expressed as

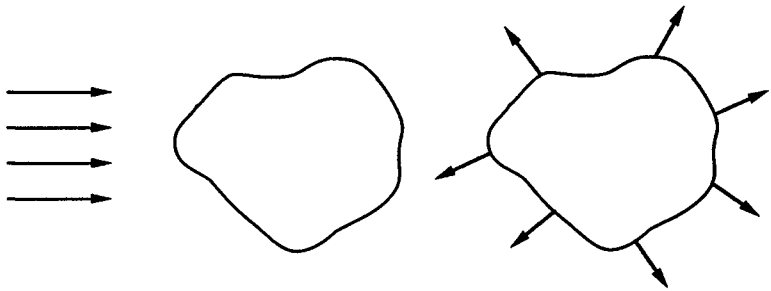

$$\text{Hence RCS, } \sigma = 4\pi r^2 \frac{P_s}{P_i}$$

Figure 3.1. Intuitive definition for radar cross section.

$$\sigma = 4\pi R^2 \frac{|\mathbf{E}^{\text{scat}}|^2}{|\mathbf{E}^{\text{inc}}|^2} = 4\pi R^2 \frac{|\mathbf{H}^{\text{scat}}|^2}{|\mathbf{H}^{\text{inc}}|^2} \tag{3.4}$$

because in the far field either **E** or **H** is sufficient to describe the EM wave.

The unit for cross section σ is area, usually in square meters, or may be nondimensional by dividing by wavelength squared, σ/λ^2.

This definition is made more recognizable by examination of the basic radar range equation for power received by the radar, P_r, in terms of transmitted, scattered, and received power:

$$P_r = \frac{\left(\dfrac{P_t G_t}{4\pi R^2}\right)\sigma}{4\pi R^2}(A_r) \tag{3.5}$$

The first term in the numerator is the power density at the target from the transmitter. This term has units of watts per meter^2. This incident power flux is multiplied by the cross section (area) and represents the power reflected back toward the receiver. When this is divided by the return path spherical spreading, we obtain the power density at the receiver for capture by the receiving antenna effective area A_r.

Radar cross section is a function of

- Position of transmitter relative to target;
- Position of receiver relative to target;
- Target geometry and material composition;
- Angular orientation of target relative to transmitter and receiver;
- Frequency or wavelength;
- Transmitter polarization;
- Receiver polarization.

The general notation for indicating polarization and angle functionality is

$$\sigma^{tr}(\theta^t, \phi^t, \theta^r, \phi^r) \tag{3.6}$$

where t and r refer to transmitter and receiver polarization, typically horizontal or vertical, and angular coordinates.

Bistatic cross section is for the case when the transmitter and receiver are at different locations, Figure 3.2, so that (3.6) applies; that is, angular location of target relative to transmitter and receiver must be specified.

Forward cross section is the measure of scattered power in the forward direction; that is, in the same direction as the incident field. This forward scattered power is usually 180° out of phase with the incident field so that when added to the incident field a shadow region is formed behind the scattering object.

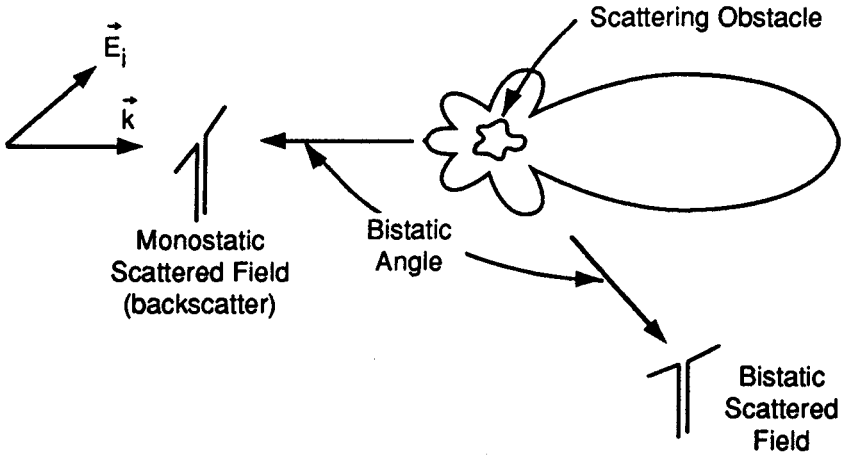

Figure 3.2. Monostatic and bistatic scattering.

Monostatic or backscatter cross section is the usual case of interest for most radar systems where the receiver and transmitter are collocated, oftentimes using the same antenna for transmitting and receiving, Figure 3.2. In this case only one set of angular coordinates is needed. Most experimental measurements are of backscatter cross section. Analytical RCS predictions, however, are much easier to do for bistatic cross section, with the illumination source fixed and the receiver position moved. One must be careful about analytical RCS predictions as to just which quantity is being presented.

Radar cross section of a target may also be a function of the pulse width τ of the incident radiation. When τ is large enough, $\tau > 2\ L/c$, where L is the body size and c the speed of light, the entire target is illuminated at once. This is the usual case for microsecond pulsewidths that have a spatial extent of 1000 ft or more. This is loosely equivalent to the target being illuminated by a continuous wave at a specific frequency, CW illumination. This is known as *long-pulse illumination* and is the usual measurement case. When very short transmitter pulses are used, such as nanosecond pulses with a spatial extent of only several feet, $\tau < 2\ L/c$, then each scatterer on the target contributes independently to the return. In this case the RCS is a collection of individual scattering returns separated in time. Short-pulse radars (or their wide bandwidth equivalent) are often used to identify these scattering centers on complex targets.

RCS Customary Notation

The units for radar cross section are square meters. This *does not* necessarily relate to the physical size of a target. Although it is generally true that larger physical

targets have larger cross sections (e.g., the optical front face reflection for a sphere is proportional to its projected area, $\sigma_{\text{sphere}} = \pi a^2$), not all RCS scattering mechanisms are related to size as is shown in the hierarchy of scattering table. Typical values of RCS can span 10^{-5} m^2 for insects to 10^{+6} m^2 for large ships. Due to the large dynamic range of RCS, a logarithmic power scale is most often used with the reference value of $\sigma_{\text{ref}} = 1$ m^2:

$$\sigma_{\text{dBsm}} = \sigma_{\text{dBm}^2} = 10 \log_{10}\left(\frac{\sigma_{m^2}}{\sigma_{\text{ref}}}\right) = 10 \log_{10}\left(\frac{\sigma_{m^2}}{1}\right) \tag{3.7}$$

Two notations are used. The dBsm notation is customary within the academic, government, and industrial communities. The dBm^2 notation is less used, typically in radar system design literature. A comparison of the square meter and dBsm scales is shown in Figure 3.3. It is noted that 1 m^2 corresponds to 0 dBsm with fractional values having negative dBsm values; for example, 0.01 m^2 = −20 dBsm.

3.2.3 Other Cross-Section Concepts

The cross-section concept defined above is for the power density scattered by a target in a given direction. As such it is our working definition because it represents or defines the power that may eventually be radiated back to a radar receiving antenna for possible detection. Often this cross section is referred to as the *differential scattering cross section,* as it gives the angular distribution of scattered power.

Several other scattering definitions may also be given. They are for power that is absorbed by a target, for the total power removed from the incident field, for the total power scattered by a target, and the forward scatter theorem. These additional concepts not often used in practice.

Absorption Cross Section

A scattering target may also absorb some of the incident EM wave power in addition to scattering. The absorption cross section is a measure of the absorbed incident power. Perfectly conducting targets do not absorb power as the resistivity is identically zero. They can only scatter. However, nonperfect conductor targets, such as those with absorbing materials, can turn some of the incident energy into heat. This energy of course is then not available for reradiation. The absorption cross section is defined as the amount of power absorbed by the target, in watts, normalized to the incident power density, in watts/meter^2:

$$\sigma_a = \frac{\text{power absorbed (W)}}{\text{incident power density (W/m}^2\text{)}} = \text{m}^2 \tag{3.8}$$

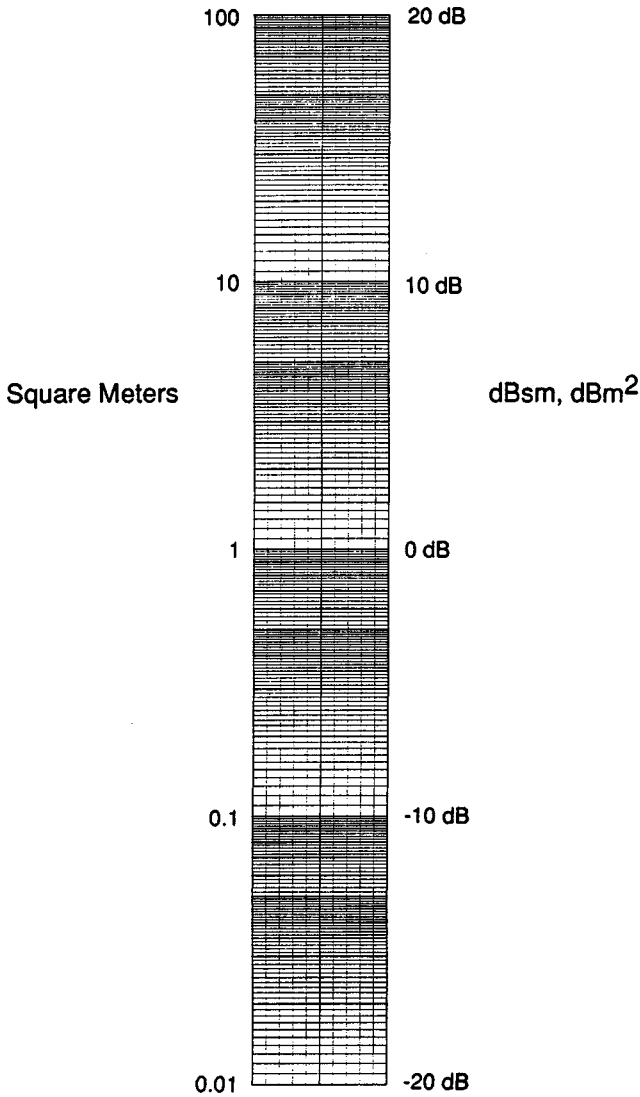

Figure 3.3. RCS linear square meter and logarithmic decibel scales compared.

which depends on only transmitter location angular coordinates. The amount of power absorbed by a target may be specified in terms of currents and resistivities of the target and may be computed from analytical models, but otherwise it is difficult to determine.

Extinction Cross Section

Power scattered and/or absorbed by a target is removed from the incident EM wave. Total power removed by virtue of scattering and absorption, in watts, normalized to the incident power density, in watts/meter^2, is defined as the extinction cross section:

$$\begin{aligned}\sigma_e &= \frac{\text{power removed by scattering and absorption (W)}}{\text{incident power density (W/m}^2\text{)}} \\ &= \sigma_T + \sigma_a\end{aligned} \tag{3.9}$$

The extinction cross section is equal to the sum of the total scattering cross section, defined below, and the absorption cross section.

Total Cross Section

The total scattering cross section σ_T is a measure of the total power scattered by a target in all 4π sr spatial directions:

$$\sigma_T = \frac{\text{total scattered power (W)}}{\text{incident power density (W/m}^2\text{)}}, \qquad \text{m}^2 \tag{3.10}$$

It is formally defined by integrating the scattering (differential) cross section σ over all spatial directions:

$$\sigma_T = \frac{1}{4\pi}\int \sigma \, d\Omega = \frac{1}{4\pi}\int_0^{\pi}\int_0^{2\pi} \sigma(\theta^s, \phi^s) \sin\theta \, d\theta \, d\phi \tag{3.11}$$

This is also the 4π steradian spatial average cross section. If $\sigma(\theta, \phi)$ were constant over all spatial directions (a physical impossibility), then $\sigma_T = \sigma$. The total cross section has the physical interpretation of an area normal to the incident EM wave that intercepts an amount of incident power equal to the scattered power.

The usual scattering cross section (differential) then may also be defined in terms of the total cross section σ_T:

$$\sigma = 4\pi \frac{d\sigma_T}{d\Omega} \tag{3.12}$$

where we see why the term *differential* is applied; that is, it gives the amount of scattered power as a function of spatial coordinates.

Forward-Scattering Theorem

The electric field scattered in the forward direction, when added to the incident field forms a shadow behind the target. (The forward-scattered field is 180° out of phase with the incident field, so addition actually means subtraction.) The darkness of this shadow is a measure of how much power was removed from the incident EM wave; that is, the greater the scattering the greater is the forward scatter and the darker is the shadow. The forward-scatter theorem relates the total cross section, which is the power removed from the incident wave by scattering, to the forward-scattered field. The explicit form is proportional to the imaginary part of the scattering amplitude F evaluated in the forward direction, written as [2,3]

$$\begin{aligned} \sigma_T = \int(\sigma_s + \sigma_a)\, d\Omega &= -\frac{4\pi}{k^2}\Im\{F(\theta_f, \phi_f)\} \\ &= -\frac{\sqrt{4\pi}}{k}\Im\{\sqrt{\sigma(\theta_f, \phi_f)}\} \qquad \text{m}^2 \end{aligned} \tag{3.13}$$

where we have used the standard expression for the differential cross section defined in terms of the scattering amplitude function $F(\theta, \varphi)$:

$$\sigma(\theta, \phi) = \frac{4\pi}{k^2}|F(\theta, \phi)|^2 \tag{3.14}$$

Therefore the total power removed from the incident wave is related to the field scattered in the forward direction.

Each of these concepts for EM scattering has equivalent analogs for acoustic and particle physics scattering.

3.2.4 Polarization Scattering Matrix

Radar cross section, as a scalar number, is a function of the polarization of the incident and received wave. A more complete description of the interaction of the incident wave and the target is given by the *polarization scattering matrix* (PSM), which relates the scattered electric field vector $\mathbf{E}^s$ to the incident field vector $\mathbf{E}^i$, component by component. In matrix notation, this is

$$\mathbf{E}^s = \bar{S} \cdot \mathbf{E}^i \tag{3.15}$$

As **E** can be decomposed into two independent directions or polarizations, because there is no component in the direction of propagation **k**, the polarization scattering matrix S is a 2×2 complex matrix:

$$\begin{bmatrix} \mathbf{E}_1^s \\ \mathbf{E}_2^s \end{bmatrix} = \begin{bmatrix} S_{11} & S_{12} \\ S_{21} & S_{22} \end{bmatrix} \begin{bmatrix} \mathbf{E}_1^i \\ \mathbf{E}_2^i \end{bmatrix} \tag{3.16}$$

where $\mathbf{E}^s$ and $\mathbf{E}^i$ are the scattered and incident fields, each with independent vector components $\mathbf{E}_1$ and $\mathbf{E}_2$. The components of S are related to the square root of cross section

$$S_{ij} = \frac{\sqrt{\sigma_{ij}}}{4\pi r^2} \tag{3.17}$$

where we recognize $\sqrt{\sigma}$ as a complex number that has amplitude as well as phase. The radar received voltage, V_r, depends on the polarization of the receiver, $\hat{n}_r$, by

$$V_r \propto \hat{n}_r \cdot \mathbf{E}^s = \hat{n}_r \cdot (\mathbf{E}_1^s + \mathbf{E}_2^s) \tag{3.18}$$

and on the polarization of the transmitted wave by

$$\mathbf{E}^i = \alpha \mathbf{E}_1^i + \beta \mathbf{E}_2^i \tag{3.19}$$

where α and β are the transmitted components of each polarization along the directions of $\mathbf{E}_1^i$ and $\mathbf{E}_2^i$, respectively.

The scattering matrix is specified by eight scalar quantities, four amplitudes, and four phases. One phase angle is arbitrary and used as a reference for the other three. If the radar system is monostatic (backscatter), then $S_{12} = S_{21}$ and **S** can then be specified by five quantities. If we had a coherent radar that transmitted and received two orthogonal polarizations, then the scattering matrix could be determined for a given aspect (θ, φ) at frequency f. For a given target, aspect angle and frequency, we can extract no more signal information than that contained in the scattering matrix. The PSM approach to scattering is discussed by Huynen [4] who considers the eigenvalues and eigenvectors of the scattering matrix functions of target size, orientation, symmetry, double bounce polarization, and characteristic angle. Such information can be useful for target identification.

The PSM matrix can be defined for linear or circular polarization. Typical linear polarization directions are horizontal and vertical for experimental work and θ and ϕ spherical directions for analytical work.

Scattering Matrix for Circular Polarization

In circular polarization, the electric field vector rotates in the plane perpendicular to propagation. The two independent directions then correspond to right- and

lefthand rotation defined as clockwise or counterclockwise when the wave is viewed by a person looking at the wave going away from the observer, Figure 3.4. This is the IEEE definition for circular polarization (i.e., righthand polarization), the electric field vector rotates counterclockwise in time for an approaching wave and clockwise for a receding wave; for a lefthand polarization, the electric field vector rotates clockwise for an approaching wave and counterclockwise for a receding wave, [5]. Linear polarization can be transformed into circular polarization by shifting the phase of a linear component by 90°. Transmitted circular polarization can be defined in terms of horizontal and vertical polarizations, where circular polarization circulation view is from an observer located at the transmitter [5]:

$$\begin{bmatrix} \mathbf{E}^t_{\mathrm{rc}} \\ \mathbf{E}^t_{\mathrm{lc}} \end{bmatrix} = \frac{1}{\sqrt{2}} \begin{bmatrix} 1 & +j \\ 1 & -j \end{bmatrix} \begin{bmatrix} \mathbf{E}^t_h \\ \mathbf{E}^t_v \end{bmatrix} \tag{3.20}$$

The inverse transform for transmitted linear in terms of transmitted circular is

$$\begin{bmatrix} \mathbf{E}^t_h \\ \mathbf{E}^t_v \end{bmatrix} = \frac{1}{\sqrt{2}} \begin{bmatrix} 1 & 1 \\ -j & +j \end{bmatrix} \begin{bmatrix} \mathbf{E}^t_{\mathrm{rc}} \\ \mathbf{E}^t_{\mathrm{lc}} \end{bmatrix} \tag{3.21}$$

as we may verify by taking the matrix inverse of (3.20).

Received polarization can also be defined in a similar manner, except now the lc and rc definitions change because the viewer is now looking in the direction of propagation, which is from the target toward the receiver, and the radar system has defined lc and rc as looking away. Therefore,

$$\begin{bmatrix} \mathbf{E}^r_{\mathrm{rc}} \\ \mathbf{E}^r_{\mathrm{lc}} \end{bmatrix} = \frac{1}{\sqrt{2}} \begin{bmatrix} 1 & -j \\ 1 & +j \end{bmatrix} \begin{bmatrix} \mathbf{E}^r_h \\ \mathbf{E}^r_v \end{bmatrix} \tag{3.22}$$

which is seen to be the complex conjugate of the transmitted case (3.20).

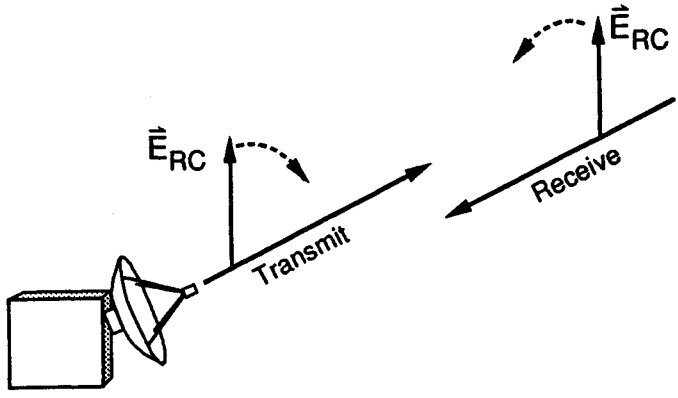

Figure 3.4. Right circular polarization for transmitting and receiving directions. RC is defined as clockwise rotation of E when viewed in direction of propagation.

The circular polarization PSM contains no more information than the linear PSM. If one has computed or measured a linear PSM, the corresponding circular PSM can be obtained by using (3.20)-(3.22) to obtain [5]

$$\begin{bmatrix} S_{lc,lc} & S_{lc,rc} \\ S_{rc,lc} & S_{rc,rc} \end{bmatrix} = \frac{1}{2}\begin{bmatrix} 1 & -j \\ 1 & +j \end{bmatrix}\begin{bmatrix} S_{h,h} & S_{h,v} \\ S_{v,h} & S_{v,v} \end{bmatrix}\begin{bmatrix} 1 & 1 \\ -j & +j \end{bmatrix} \tag{3.23}$$

A characteristic feature of circular polarization is that single-bounce scattering changes the polarization from lc to rc or rc to lc. For linear polarization single-bounce specular scattering, the scattered energy has the same polarization as the incident polarization. This occurs due to the scattered field having a 180° phase shift from the incident field; that is, in the opposite direction (reflection coefficient $R = -1$).

3.3 FUNDAMENTAL SCATTERING MECHANISMS

3.3.1 Electromagnetic Wave Fundamentals

An electromagnetic wave is vector in nature and composed of both electric E and magnetic H fields, which are able to propagate by themselves. As we shall see later, a time-changing E field is the source for H and a time-changing H is the source for E. Therefore once launched, an EM wave is able to propagate on its own. EM waves propagate in free space as well inside material media. All EM waves decay in magnitude as they propagate away from their launching source due to spherical spreading, unless anomalous propagation occurs, such as in ducted propagation.

The three most fundamental characteristics of an EM wave are related. The wavelength (spatial variation) times the frequency (temporal variation) is equal to the velocity of propagation:

$$\lambda f = v \tag{3.24}$$

Wavelength λ represents the spatial distance over which the field quantities make a complete cycle; that is, change in value from zero to a positive peak, back through zero to a negative peak, and back to zero, measured in distance, Figure 3.5. The direction of propagation of an EM wave is specified by the wave vector $\mathbf{k}$, which has a magnitude inversely related to wavelength, $k = 2\pi/\lambda$. Frequency f represents the number of cycles per second for the wave, measured in Hertz. Radian frequency ω is $2\pi f$. Alternately the reciprocal of frequency, $\tau = 1/f$, represents the time required for a wave to make a complete cycle. The maximum velocity of an EM wave occurs in a vacuum and is the speed of light, approximately 3×10^8 m/s. Wavelength scales can be very long, such as 5×10^6 m $\sim$ 3107 mi for 60 Hz

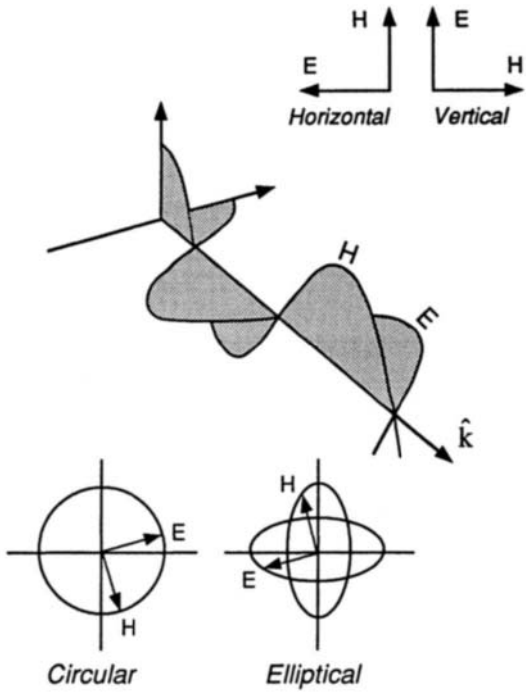

Figure 3.5. Wave nature of an electromagnetic field.

radiation, to very short such as 10^{-7} m for light. For typical radar applications Table 3.1 shows the range of wavelength and frequency values usually of interest. Although this is certainly only a small part of the EM spectrum, it is nevertheless a broad range of values.

Sources for E and H fields are charges and currents. Near sources, the field lines originate on local charges; that is, the field lines are conservative. As the fields propagate away from sources, they can no longer remain attached to the source charges. Now they must close back on themselves in a solenoidal fashion. This is the case for a free-space EM wave.

The direction of **E** and **H** must be perpendicular to **k**. Therefore E and H must reside in a plane perpendicular to **k**. The directions of E and H are still somewhat arbitrary. The specific direction of **E** is called the *polarization of the wave.* It may be linear or circular; that is, it rotates as the wave propagates. For linear polarization the usual directions are horizontal or vertical if we are doing experimental work, or for theoretical work, we refer to a spherical coordinate system, using the polar angle θ and azimuth angle ϕ vector directions, Figure 3.6.

Table 3.1
Frequency and Wavelength Bands of Interest for Radar Cross Section

Band	*Frequency*	*Wavelength*
HF	5–30 MHz	200–33 ft
VHF	50–300 MHz	18–3 ft
UHF	300–1000 MHz	3–1 ft
L	1–2 GHz	1–0.5 ft
S	2–4 GHz	6–3 in.
C	4–8 GHz	3–1.5 in.
X	8–12.5 GHz	1.5–0.9 in.
K_u	12.5–18 GHz	0.9–0.66 in.
K_a	26.5–40 GHz	0.45–0.3 in.

In free space, the **E** and **H** fields are perpendicular to each other and to the direction of propagation **k**, Figure 3.5. The electric field E has units of (volts / meter) whereas the magnetic field H has units of (amperes/meter). The propagation vector **k** points in the direction of travel of the wave and has a scalar magnitude related to the reciprocal of wavelength, $k = 2\pi/\lambda$, m^{-1}. In free space the **E** and **H** fields are in phase; that is, when **E** peaks so does **H**.

An EM wave represents the transport of energy. This is specified in terms of power flux density, watts/meter^2, and is vector in nature because a spatial direction is involved. This is the Poynting vector defined as

$$\mathbf{P} = \mathbf{E} \times \mathbf{H} \qquad W/m^2 \tag{3.25}$$

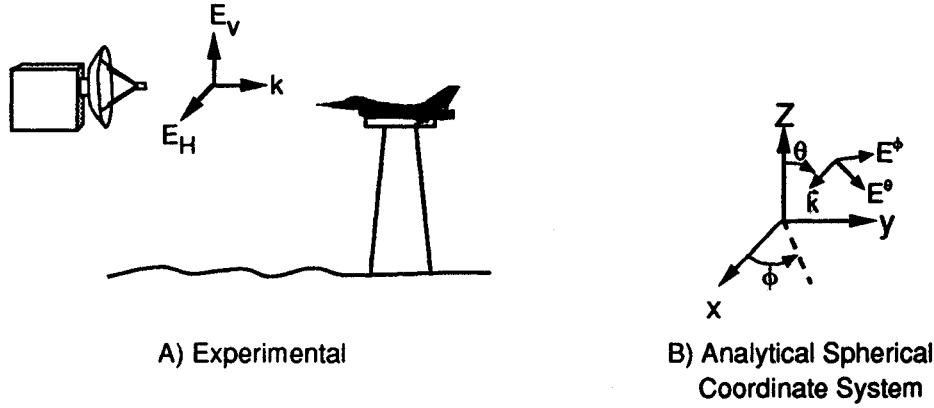

Figure 3.6. Typical linear polarizations for experimental and analytical work.

E and H fields also represent energy storage. Energy is split equally between the E and H fields. The energy density is given in terms of the E and H field quantities and parameters that characterize the material ability to store energy:

$$U = \frac{1}{2}\epsilon E^2 + \frac{1}{2}\mu H^2 \qquad \text{W/m}^3 \tag{3.26}$$

Permittivity, ϵ, characterizes a materials ability to store electrical energy. It is related to capacitance and has units of farads per meter. The free-space value, denoted by the subscript zero, is approximately 8.85×10^{-12} f/m. Permeability, μ, characterizes a materials ability to store magnetic energy. It is related to inductance and has units of henrys per meter. Its free space value is defined exactly as $4\pi \times 10^{-7}$ h/m.

The velocity of an EM wave is inversely related to energy storage,

$$v = \frac{1}{\sqrt{\epsilon\mu}} \qquad \text{m/s} \tag{3.27}$$

which for free space has the value

$$c = \frac{1}{\sqrt{\epsilon_0\mu_0}} \approx 3 \times 10^8 \qquad \text{m/s} \tag{3.28}$$

The speed of light in a vacuum represents the least storage of energy.

Actual values for E and H fields, although sometimes specified as microvolts or microamps per meter, are usually not of interest. They always decay with distance away from a source due to spherical spreading. However, the *ratio* of E to H is of interest, and it is called the *wave impedance.* In free space it is

$$\eta = \frac{E}{H} = \sqrt{\frac{\mu_0}{\epsilon_0}} \approx 120\pi \approx 377 \qquad \Omega \tag{3.29}$$

Although equal energy is contained in E and H, their numeric values differ by the value of the wave impedance. When a wave is near a conducting surface where the tangential E must become small or zero, the wave impedance becomes small.

In a material medium the character of an EM wave differs from free space due to varying amounts of energy storage in E and H fields. Because all materials store at least some electrical or magnetic energy, the wave velocity is always less than free space. Then, depending on specific values of ϵ and μ the wave impedance is no longer 377 (unless $\epsilon = \mu$), and there may be a phase difference between E and H; that is, they do not peak at the same time. A wave propagating in a

conducting medium (but not a perfect conductor) has $\eta << 377$, and E lags behind H typically by 45° due to storage of electrical energy.

3.3.2 The Scattering Process

The scattering process can be characterized in two ways. The first is to think of an EM wave as a billiard ball that reflects or bounces off surfaces often in a specular manner; that is, angle of incidence = angle of reflection. This view does not examine the details of the interaction of the wave with a surface. The second approach is to consider the details of the interaction, which involve induced charges and currents and the fields that they reradiate.

When an EM wave propagating in free space impinges on a material object characterized by ϵ and μ, not free-space values, energy is reflected, transmitted, or absorbed, Figure 3.7. Because radar cross section is concerned principally with scattering from conducting surfaces, let us specialize our scattering process arguments for this case. A *perfect electric conductor* (PEC) is characterized by $\epsilon_r = \epsilon' - j\sigma/\epsilon_0\omega = \infty$ as the conductivity σ, the reciprocal of resistivity, is infinite. This would suggest that a PEC could store an infinite amount electrical energy, a physical impossibility. Thus the electric field must be zero in a PEC. Another view of a conductor is that its electrons are free to move instantly in response to an electric field. However, because these electrons represent a charge density, they create their own electric field, which we call the *scattered field.* These electrons can move only so long as the total electric field is not zero. The field created by

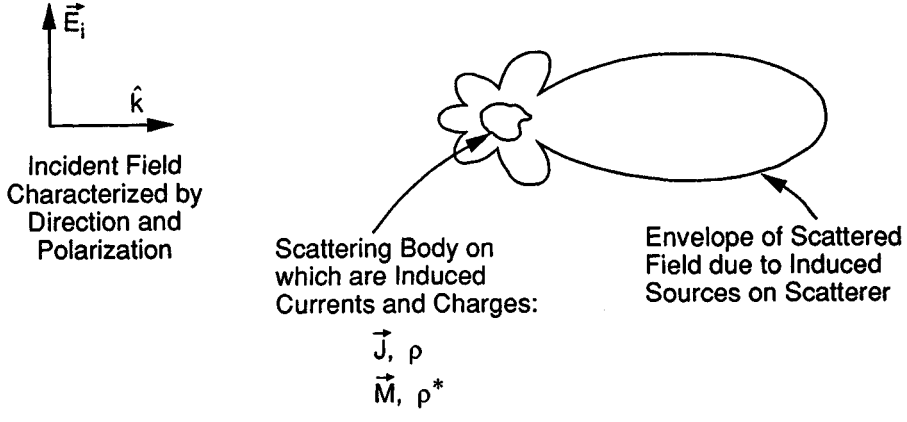

Figure 3.7. Basic electromagnetic scattering process.

these electrons is in the opposite direction to the applied field. Therefore, when the scattered field is equal and opposite to the incident field, the total field on the conductor is zero, and a force is no longer acting to move the electrons. This is the notion that a PEC surface has a boundary condition of zero tangential electric field.

This instantaneous equilibrium does not last. The incident wave is a time-changing field. The free electrons move in response to the changing incident field to always keep the total tangential surface field zero. With Figure 3.8 showing the background geometry and field computation, a time sequence is shown in Figure 3.9 for a 1λ square plate geometry illuminated perpendicular to the plate with E^{inc} along the x direction. Four time values are shown, 0°, 30°, 60°, and 90° phase. (The remainder of the time sequence from 90° to 360° is a repeat of the 0° to 90° quarter, but with differing signs.) At 0° time phase, the incident E field is a maximum at

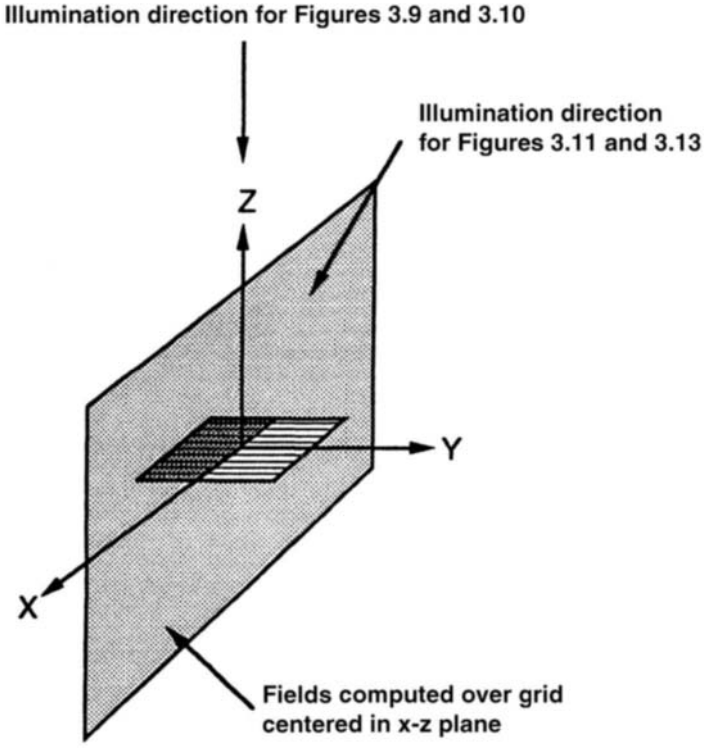

Figure 3.8. Geometry and field computation plane for Figures 3.9 to 3.13.

the plate, and the scattered field by the plate is the opposite direction to make the total tangential field zero. Later in time the incident wave peak passes beyond the plate and the plate-scattered field begins to propagate out and away from the plate, as seen in Figure 3.9(b) through 3.9(d). At time phase of 90°, the incident wave has a null at the plate.

The time-varying incident field causes a time-varying charge separation to occur on the conductor which represents a current flow. These charges and currents

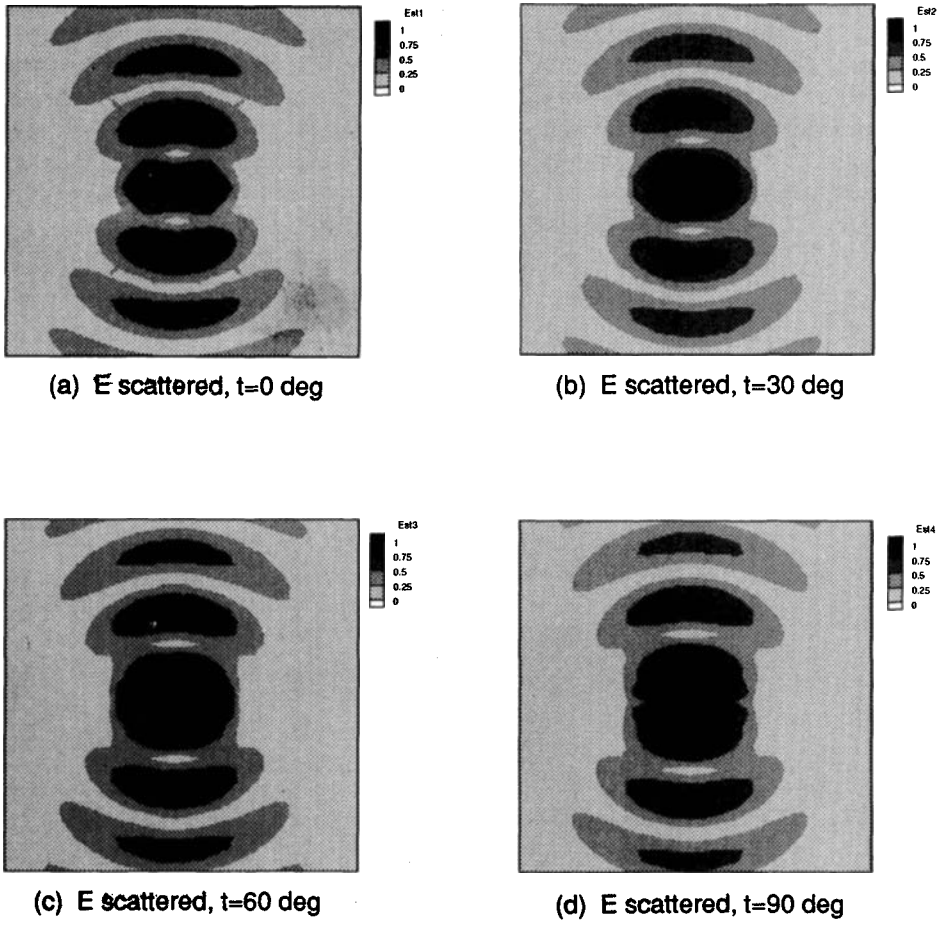

Figure 3.9. Time sequence for scattered field from a 1λ plate due to a plane wave incident normal to plate.

represent the sources for the scattered field. As the charges move, the attached field lines move with the charge. Field lines more than $\lambda/2$ away from the surface cannot keep up with the charge movement due to the finite speed of light. The more distant field lines begin to close back on themselves and propagate on their own away from the source charges; that is, an EM wave is launched and becomes a self-propagating entity.

In the Fresnel or near zone, the E field lines end on surface charges, and the fields are mostly conservative in nature. In the Fraunhofer or far field, the E fields completely close back on themselves, the field is solenoidal. An example of a near- to farfield transition for scattered field contour levels (but not vector direction) is shown in Figure 3.10 for a 2λ plate illuminated perpendicular to the plate as shown in the geometry illustration of Figure 3.8. The scattered field is symmetric about the plate; that is, the reflected and forward waves are the same as is required by symmetry. The forward-scattered wave is out of phase with the incident field so, when the two are added, a shadow is formed behind the plate. The two major lobes are the forward and reflected lobes in addition to four minor lobes at $\pm 45°$.

A very convenient description for E and H fields is to decompose the total field into an incident part due to sources that are far away and a scattered part due to the charges and currents induced on a scattering body.

$$\begin{aligned} \mathbf{E}^{\text{total}} &= \mathbf{E}^{\text{incident}} + \mathbf{E}^{\text{scattered}} \\ \mathbf{H}^{\text{total}} &= \mathbf{H}^{\text{incident}} + \mathbf{H}^{\text{scattered}} \end{aligned} \tag{3.30}$$

The incident field, which is spherical with its $1/R$ spatial decay, is often taken as a plane wave in the target vicinity; that is,

$$\mathbf{E}^{\text{incident}} = \hat{\mathbf{u}}^{\text{pol}}\mathbf{E}_0\, e^{-j(\mathbf{k}\cdot\mathbf{R}-\omega t)} \tag{3.31}$$

which represents an incident plane wave with polarization direction $\mathbf{u}$, direction of propagation $\mathbf{k}$, and frequency ω. Because $f\lambda = c$, the radian frequency $\omega = 2\pi f$ and wave number $k = 2\pi/\lambda$ are related, $\omega/k = c$. An example of an incident plane wave magnitude in the x-z plane (Fig. 3.8) is shown in Figure 3.11, for $\omega t = 0$, traveling toward the origin at 45° with respect to the x axis (not very exciting!).

The field scattered in the x,z plane (Fig. 3.8), that is, radiated by induced charges and currents, by a 2λ plate illuminated at 45° is shown in Figure 3.12, for $\omega t = 0$. We see two principal scattered-field directions, one reflected mostly in the specular direction (angle of incidence = angle of reflection) and one in the forward direction. This latter component is out of phase with the incident field so that it subtracts from the incident field to form a shadow behind the plate.

Next Page

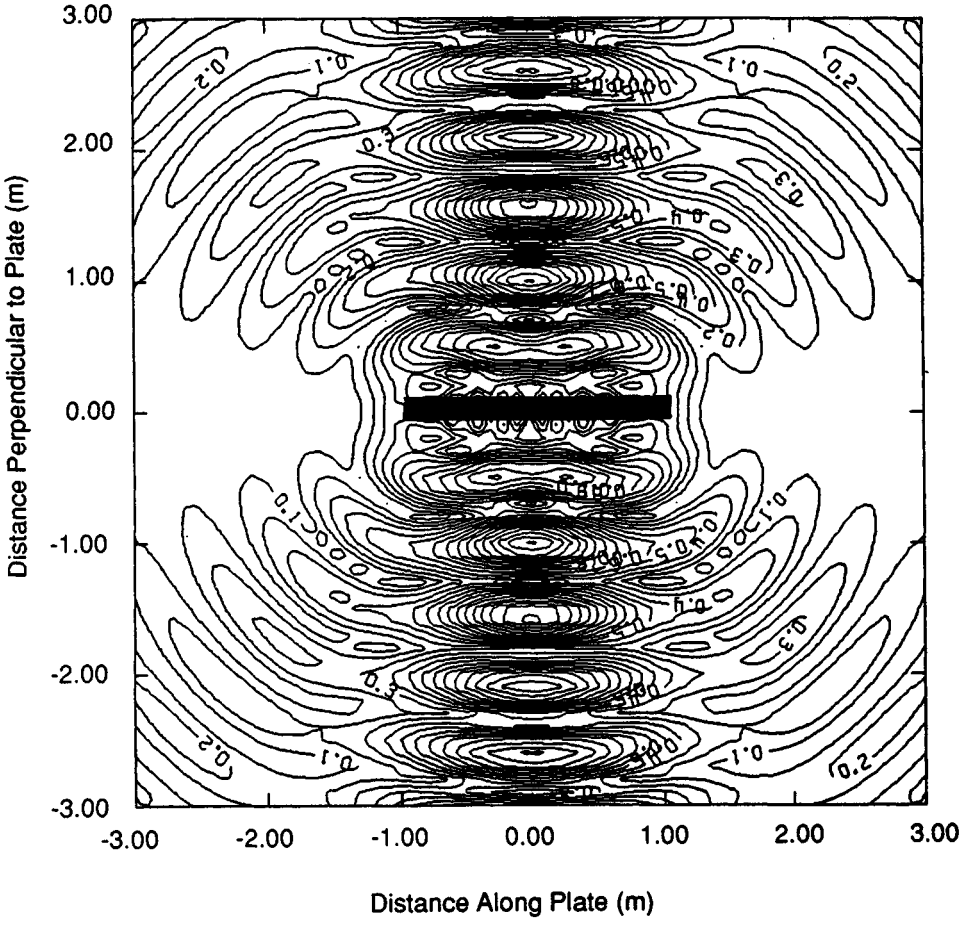

Figure 3.10. Scattered field from 2λ plate excited normal to plate.

The total field is the sum of the incident and scattered components. This is shown in Figure 3.13, for $\omega t = 0$, where we can clearly see the shadow behind the plate and the interference pattern of the specular scattered field with the incident wave.

3.4 SCATTERING REGIMES

Three regimes characterize RCS scattering, depending on the ratio of wavelength λ to body size L, λ/L or inversely, kL. The three regimes are the Rayleigh region, the resonant region, and the optics region corresponding to $\lambda \gg L$,

Chapter 4
Exact Prediction Techniques

J. F. Shaeffer

4.1 INTRODUCTION

The objective of this chapter is to review briefly the classical modal solutions for 2-D cylinders and spheres and then to examine the powerful numerical techniques used to solve Maxwell's equations as expressed by the Stratton-Chu integral formulations and the differential equation formulations.

Exact solutions for practical geometries for scattering are rarely found. This is because the wave equation is solvable by historical analytical methods when the scattering geometry coincides with one of the few separable coordinate systems for which exact series solutions are available. Unfortunately, few practical geometries match the solutions available.

Computer solutions started to gain momentum in the late 1960s after publication of Harrington's [1] classic book on using the method of moments to solve the integral formulation of Maxwell's equations. Until then this formulation was considered only of theoretical interest because we could obtain no practical solutions.

A principal objective of solving Maxwell's equations is to predict the RCS scattering behavior. Although this is certainly a valid objective, we also need to use our solutions to gain an appreciation of the scattering process. Therefore we should also ask our tools to show phenomenological results of how an electromagnetic wave interacts with a scattering body. Hence, surface currents and near fields are of interest. Imaging, using analytical and computer codes, should also be pursued to gain understanding of scattering mechanisms and spatial regions on the bodies that produce a scattered field.

Differential equation numerical techniques are now developing rapidly and for certain classes of problems, particularly those with variable material properties, is the method of choice.

Exact solutions are *always* needed when scattering phenomenon involve non-optical collective effects of surface traveling, creeping, and edge waves. This is the case for resonant region scattering, where the body size is approximately 1 to 10 wavelengths in size. In the optical scattering region, specular scattering and diffraction dominates, and the high frequency approximations discussed in the next chapter are usually satisfactory.

4.2 CLASSICAL MODAL SOLUTIONS

One might ask why we would still be interested in analytical solutions that have limited practical application. Although numerical techniques may provide answers for applications, analysis will always be a fundamental and essential tool for making advances in electromagnetic modeling phenomena. Analysis is required to provide insight into complex phenomena. Analysis is required for the development of robust problem formulations and numerical methods. Finally analytical solutions often provide the benchmark results from which to compare numerical solutions (after Collin [2]). The integral and differential equation numerical formulations, although they contain "all of the essential physics," do not yield physical insight into the scattering process.

Classical Separation of Variables

Maxwell's equations for time harmonic waves in a source-free region, which show that a time change **E** is the source for **H**, and that a time-changing **H** is the source for **E**, can be recast in terms of the wave equation for either the electric or magnetic field:

$$\nabla^2 \mathbf{F} + k^2 \mathbf{F} = 0 \tag{4.1}$$

where **F** represents either **E** or **H** and k is the wave number. This is the second-order partial differential equation whose solution can yield the fields scattered by simple bodies [3]. The solution is limited to simple bodies because a coordinate system must be found for which the body surface coincides with one of the coordinates. Examples are the infinite cylinder and sphere, whose surfaces coincide with radial coordinates $\rho = a$ (cylinder) or $r = a$ (sphere), where a is the radius. There are few coordinate systems for which this requirement can be satisfied.

Equation (4.1) must be satisfied by each of the three rectangular components of the vector field **F**. If we represent any one of those vector components by a function V, then V is a solution of the scalar wave equation:

$$\nabla^2 V + k^2 V = 0 \tag{4.2}$$

To solve this equation using separation of variables, we must represent the function V in terms of three other functions, each of which depends on only one coordinate:

$$V(u_1, u_2, u_3) = V_1(u_1)\, V_2(u_2)\, V_3(u_3) \tag{4.3}$$

where u_1, u_2, and u_3 represent the three coordinates. These could be the $x,y,$ and z of a rectangular system or the r, θ, and φ of a spherical system. In addition to rectangular, cylindrical, and spherical coordinate systems, there are a number of other specialized coordinated systems for which the wave equation is separable.

The separation of variable approach to solving the partial differential equation yields three ordinary differential equations, each involving a pair of separation constants that must be introduced. These constants may be discreet numbers or may represent a continuous spectrum, but they must be determined by invoking the boundary conditions for the fields at the surface of the body. These separation constants may be determined if the body is perfectly "soft" or perfectly "hard," terms that arise in acoustical scattering. *Soft boundary conditions* refer to the value of the surface quantity "whereas" *hard* refers to its rate of change normal to the surface:

$$V = 0 \qquad \text{(perfectly soft)} \tag{4.4}$$

$$\frac{\partial V}{\partial n} = 0 \qquad \text{(perfectly hard)} \tag{4.5}$$

where n is the coordinate normal to the surface. If the body is penetrable, or has surface impedance that is neither zero nor infinity, then the scalar wave equation is completely separable only for rectangular, spherical, and cylindrical coordinate systems.

The solutions of the vector wave equation always involve polynomials or infinite series that are not necessarily easy to generate. In much the same way that an infinite series of sine and cosine functions (the Fourier series) can be combined to describe any periodic wave form, an infinite collection of Bessel functions can be combined to duplicate the total fields around the surface of a circular cylinder illuminated by a single plane wave. For spherical coordinate systems, the associated Legendre polynomials are the class of functions used to generate the solution.

When evaluating the infinite series, we truncate the series at the term where additional terms would no longer change our desired solution precision. As the body becomes larger as measured in terms of wavelength, however, more terms are usually required. And for bodies larger than 10 to 20λ, exact solutions are no longer attractive because optical effects now usually dominate the scattering and these are much easier to predict using the high-frequency approximations discussed in the next chapter.

When separable, the wave equation yields the exact solution for the total field everywhere in space, and typically the incident field is expanded in terms of

elemental waves in the coordinate system being used. The scattering in any direction is obtainable this way, and it will be found that the scattered field decays with increasing distance from the obstacle. When the scattered field is normalized to the incident field, squared, and then multiplied by the area of a sphere whose radius is the distance to the observation point, we obtain the radar cross section. In two dimensions we use the circumference that then yields a scattering width, which may be interpreted as the radar cross section per unit length of the two-dimensional body.

Two-Dimensional Cylinder Example

In two dimensions we distinguish two cases depending on whether the incident electric or magnetic field is parallel to the infinite z axis. The results for a 2-D "infinite" cylinder for the two polarization cases are

$$E^s = -\sum_{n=0}^{\infty} \epsilon_n (\mathrm{j})^n \frac{J_n(ka)}{H_n^{(2)}(ka)} H_n^{(2)}(k\rho) \cos n\phi \tag{4.6}$$

$$H^s = -\sum_{n=0}^{\infty} \epsilon_n (\mathrm{j})^n \frac{J_n'(ka)}{H_n^{(2)\prime}(ka)} H_n^{(2)}(k\rho) \cos n\phi \tag{4.7}$$

where the primes indicate the derivative with respect to the argument, and

$$\epsilon_n = \begin{cases} 1, & n = 0 \\ 2, & n \neq 0 \end{cases} \tag{4.8}$$

The Hankel function is a linear combination of the Bessel functions of the first and second kinds,

$$H_n^{(2)}(ka) = J_n(ka) - \mathrm{j}Y_n(ka) \tag{4.9}$$

In these equations, a is the radius of the cylinder, ρ is the distance from the cylinder axis to the point of observation of the scattered field, and ϕ is the bistatic angle subtended at the cylinder axis between the directions of incidence and scattering. The Hankel function in the numerator represents an outward traveling wave, and for large arguments its intensity decays as $(k\rho)^{-1/2}$.

The scattering width of the cylinder (the radar cross section per unit length) for the two cases is

$$\sigma_e = \frac{2\lambda}{\pi} \left| \sum_{n=0}^{\infty} \epsilon_n (-1)^n \frac{J_n(ka)}{H_n^{(2)}(ka)} \cos n\phi \right|^2 \tag{4.10}$$

$$\sigma_h = \frac{2\lambda}{\pi} \left| \sum_{n=0}^{\infty} \epsilon_n (-1)^n \frac{J_n'(ka)}{H_n^{(2)\prime}(ka)} \cos n\phi \right|^2 \tag{4.11}$$

The backscattering width can be obtained from these formulas simply by allowing ϕ to be zero, and Figure 5.6 illustrates how the backscattering depends on the size of the cylinder.

Three-Dimensional Sphere Example

In the case of the sphere, the scattered field must be represented in terms of θ and ϕ components, where θ is the bistatic angle subtended in the directions of incidence and scattering at the center of the sphere, and ϕ is the angle between the plane of scattering (formed by the directions of incidence and scattering) and the plane containing the incident electric field and direction of incidence (see Fig. 4.1 for details of the scattering geometry). The components of the scattered field are

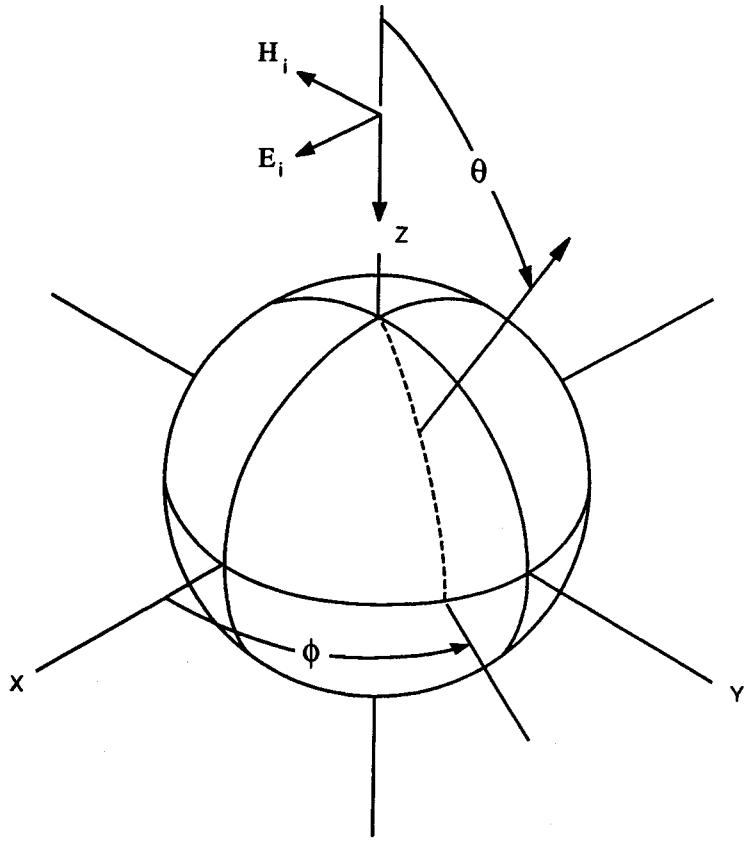

Figure 4.1. Spherical polar scattering geometry.

$$E_\theta^s = \frac{je^{-jka}\cos\phi}{kr}\sum_{n=1}^{\infty}(-1)^n\frac{2n+1}{n(n+1)}\left[b_n\frac{\partial P_n^1(\cos\theta)}{\partial\theta} - a_n\frac{P_n^1(\cos\theta)}{\sin\theta}\right] \tag{4.12}$$

$$E_\phi^s = \frac{-je^{-jka}\sin\phi}{kr}\sum_{n=1}^{\infty}(-1)^n\frac{2n+1}{n(n+1)}\left[b_n\frac{P_n^1(\cos\theta)}{\sin\theta} - a_n\frac{\partial P_n^1(\cos\theta)}{\partial\theta}\right] \tag{4.13}$$

where r is the distance to the point of observation, a is the radius of the sphere, and $P_n^1(\cos\theta)$ is the associated Legendre function of order n and degree 1. The general function is defined as

$$P_n^m(x) = \frac{(1-x^2)^{m/2}}{2^n n!}\cdot\frac{d^{n+m}(x^2-1)^n}{dx^{n+m}} \tag{4.14}$$

hence, the first three orders of $P_n^1(\cos\theta)$ have the values:

$$\begin{aligned} P_0^1(\cos\theta) &= 0 \\ P_1^1(\cos\theta) &= \sin\theta \\ P_2^1(\cos\theta) &= \frac{3}{2}\sin 2\theta \end{aligned} \tag{4.15}$$

The coefficients a_n and b_n are

$$a_n = \frac{j_n(ka)}{h_n^{(2)}(ka)} \tag{4.16}$$

$$b_n = \frac{ka\,j_{n-1}(ka) - nj_n(ka)}{ka\,h_{n-1}^{(2)}(ka) - nh_n^{(2)}(ka)} \tag{4.17}$$

where $h_n^{(2)}(x) = j_n(x) - jy_y(x)$, in which $j_n(x)$ and $y_n(x)$ are the spherical Bessel functions of the first and second kinds, respectively. These are ordinary Bessel functions of half-order, and the first pairs are

$$\begin{aligned} j_0(x) &= \frac{\sin x}{x} & y_0(x) &= -\frac{\cos x}{x} \\ j_1(x) &= \frac{1}{x}\left(\frac{\sin x}{x} - \cos x\right) & y_1(x) &= -\frac{1}{x}\left(\frac{\cos x}{x} + \sin x\right) \end{aligned} \tag{4.18}$$

In the backscattering direction, (4.13) becomes zero and the radar cross section is

$$\sigma = \frac{\lambda^2}{\pi}\left|\sum_{n=1}^{\infty}(-1)^n(n+1/2)(b_n - a_n)\right|^2 \tag{4.19}$$

This is the expression used to generate Figures 3.14 and 6.5.

As recently as 1960, the computation of these functions was often performed by groups of computers, people operating desk calculators, and working with published tables of functions, such as those found in the NBS *Handbook of Mathematical Functions* [4]. The desk calculators were mechanical and had little capability for internal storage of intermediate results, and the computers had to print column after column of numbers to be used in subsequent calculations. Anyone who has not had to generate literally reams of numbers cannot appreciate the value of even the simplest hand-held electronic calculator. Even the large, high-speed electronic computer, however, does not solve all our problems. For example, the ascending series representation of $J_n(x)$, the Bessel function of the first kind of order n, becomes unstable as the argument approaches 20 or 30, and we must generate the functions using a technique known as backward recursion. $Y_n(x)$, the Bessel function of the second kind of order n, can be computed using forward recursion. However, even these techniques also become troublesome for large orders because the recursion generates very large numbers before the numbers are normalized (i.e., arithmetic overflow).

For backscatter the series solution predicts the scattering due to induced dipole moment when the sphere size ka is less than unity, and the front face and creeping wave scattering mechanism when the sphere size is $1 < ka < 10$. In the optical region when $ka > 10$, the front face specular return dominates the scattering. Now many terms are needed to evaluate the series, and as with the cylinder, we no longer need the series solution because the front face reflection is simply given by the geometric optics backscatter result of $\sigma = \pi a^2$.

A FORTRAN computer code listing is shown in Listing 4.1 that computes backscatter, equation 4.19, from a perfectly conducting sphere, normalized to its projected area πa^2, over a range of ka values from .05 to 10. This algorithm produced the results shown in Figure 4.2.

4.3 INTEGRAL EQUATION SOLUTIONS

The integral equation formulation of Maxwell's equations is exact and valid for bodies very large or very small compared to a wavelength. The numerical solution to these equations then represents an "approximate solution to an exact formulation." The standard solution technique has been called the *method of moments* (MOM), which is very similar to the Rayleigh Ritz procedure for solving integral equations. The MOM approach became popular after Harrington's [1] publication. The method remains the method of choice today; however, the differential equation solution approach is developing rapidly. This section will outline the approach. The reader is directed to Harrington [1], Mitra [5], Miller [6], Miller, Medgyesi-Mitschang, and Newman [7], Hansen [8], and Wang [9] for greater detail.

Because the MOM represents the solution for an exact formulation, it is required whenever the high-frequency specular, end-region, and diffraction approximations are no longer adequate; that is, when surface traveling, creeping, and edge waves are also important, such as in the resonant region. The exact

```
C     EFK's Sphere RCS Program

      Complex Escat

C     Compute as function of ka, Rcs normalized to (pi a**2)

      Iout = 2
        Open( Iout, File='Sphere.prn' )
        kmax = 200
        Do 100 k = 1, kmax
          fka = 0.05 * Float(k)
          Call Sphere( Escat, fka )
          Rcs = 20. * Alog10 ( Cabs( Escat ) )
          Write( Iout, * ) fka, Rcs
100   Continue
        Close (Iout)
        End
C++++++++++++++++++++++++++++++++++++++++++++++++++++++++++++++++++++++++++++++
      Subroutine Sphere( Escat, fka )

C  RCS of conducting sphere using infinite series of spherical Bessel Functions
C   Each new term is formed from the previous term by recursion.  The
C   recursion variables are complex double precision.
C   Input ka, output Escat

      Complex Escat
      Complex*16 Sum, Del, F1, F2
      Data Eps/1.0E-6/

C       Initialize running sum, first term, and recursive indexes.

10          Sum = Cmplx(0.0,0.0)
            F1  = Cmplx(0.0,1.0)
            F2  = Cmplx(1.0,0.0)
            M   = 1
            N   = 0
            L   = -1
C        Advance indexes and compute next term

20          L = - L
            N = N + 1
            M = M + 2
            Del = ( 2 * N - 1 ) * F2  / fka - F1
            F1  = F2
            F2  = Del
            Del = L * M / ( F2 * ( fka * F1 - N * F2 ) )
            Sum = Sum + Del

C           Do it again is term not small enough
              If( CDABS( Del ) .GT. Eps ) Goto 20

            Escat = Sum

          Return
          End
```

Listing 4.1. FORTRAN algorithm to compute the backscatter from a perfectly conducting sphere as a function of *ka*.

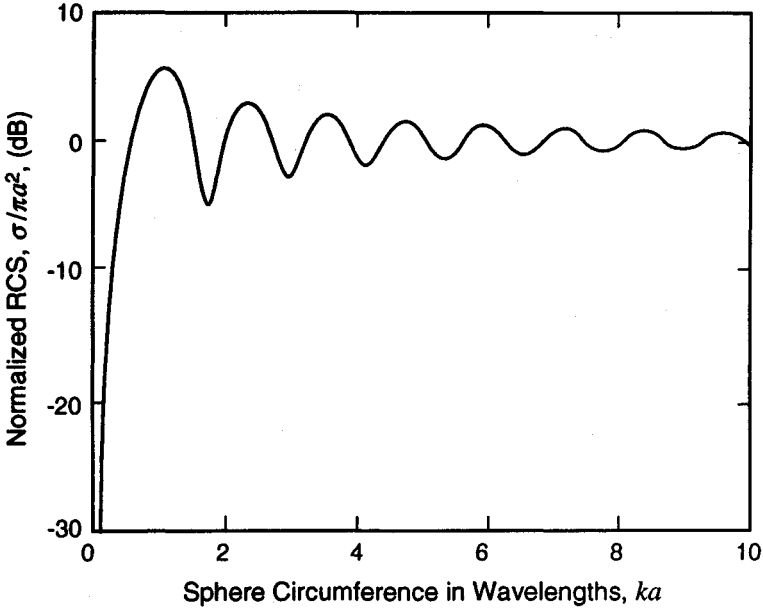

Figure 4.2. Sphere RCS backscatter as a function of *ka* as computed by the algorithm shown in Listing 4.1.

formulation computes the influence of every part of the body with every other part, thus all electromagnetic phenomena are included: specular, end region, diffraction, multiple bounce, traveling, creeping, and edge wave effects and shadowing.

The objective of this presentation of the integral equation formulation will not be to instruct the reader on how to work the equations, but rather to present an overview of the method. As a starting point, we will present the basic electric field and magnetic field integral equations. From these we will obtain the equations that must be solved after the EM boundary conditions have been applied to the surface of the scattering body. The procedure for solving for the unknown surface currents will then be presented, including a discussion of operator notation, the expansion of the induced currents in a finite series of basis functions, and the development of the interaction matrix. Finally, once the surface currents have been

found, the scattered field will be determined. Several examples of the scattering from simple bodies will be given, showing the solution for induced currents and the resultant scattered field. The physical meaning of the results will be interpreted in terms of the Green's function and its gradient (Huygen's wavelets), and the matrix elements will be related to the field at one point on a scattering body produced by the currents flowing on another part of the body.

Although the integral equation formulation is exact, some analysts may regard the solutions as numerical methods, which inherently have less than exact characteristics. However, the power and utility of these methods lie in their application to arbitrary geometries for arbitrary electromagnetic excitations. The integral equation methods are limited to the low frequency and resonant frequency ranges. Although the methods apply in principle to any frequency range, they suffer two practical limitations in the high-frequency region. First, the matrix for large body problems (relative to a wavelength) becomes very large, precluding solution even by today's large, high-speed, mainframe computers. Second, the need for matrix element interaction in the high-frequency region decreases significantly because the scattering becomes more a localized phenomenon than a collective phenomenon.

The term *method of moments*, and the associated acronym MOM or MM, has been applied to the matrix solution of the EM integral equations. The problems solved by MOM include wires, two-dimensional and three-dimensional surfaces using surface patches, *bodies of revolution* (BOR), and *bodies of translation* (BOT). The solution goal, whether viewed as the end itself or as a necessary step for obtaining the scattered fields, is to determine the currents induced on the scattering body. These currents are functions of the incident polarization, the direction of arrival of the incident wave, and of how various parts of the scattering body interact.

4.3.1 EM Integral Equations

The electromagnetic integral equations were obtained by Stratton and Chu using the vector Green's theorem in conjunction with Maxwell's equations. These equations give the prescription for scattered fields in terms of surface current sources. Surface **E** and **H** vectors are decomposed into tangential and perpendicular components.

The total electric and magnetic fields are written as the sum of the incident and scattered fields,

$$\begin{aligned} \mathbf{E}^T &= \mathbf{E}^i + \mathbf{E}^s \\ \mathbf{H}^T &= \mathbf{H}^i + \mathbf{H}^s \end{aligned} \tag{4.20}$$

The scattered **E** and **H** fields are given by the Stratton-Chu integrals [10]:

$$\mathbf{E}^s = \oint_s [-j\omega\mu(\hat{n} \times \mathbf{H})\psi + (\hat{n} \times \mathbf{E}) \times \nabla\psi + (\hat{n} \cdot \mathbf{E})\nabla\psi]dS$$
$$\mathbf{H}^s = -\oint_s [-j\omega\epsilon(\hat{n} \times \mathbf{E})\psi - (\hat{n} \times \mathbf{H}) \times \nabla\psi - (\hat{n} \cdot \mathbf{H})\nabla\psi]dS \tag{4.21}$$

where ψ is the free-space Green's function, ω is the radian frequency, μ and ϵ are the permeability and permittivity, and $\hat{n}$ is the outward unit normal on surface S. The scattered electric field has as its surface sources the tangential components of the total magnetic and electric fields (electric and magnetic currents) and the perpendicular component of magnetic field (magnetic charge).

The tangential and perpendicular components of the surface field are interpreted as currents and charges:

$$\begin{aligned} \mathbf{J} &= \hat{n} \times \mathbf{H}^T && \text{electric current} \\ \mathbf{M} &= -\hat{n} \times \mathbf{E}^T && \text{magnetic current} \\ \rho &= \epsilon\hat{n} \cdot \mathbf{E}^T && \text{electric charge} \\ \rho^* &= \mu\hat{n} \cdot \mathbf{H}^T && \text{magnetic charge} \end{aligned} \tag{4.22}$$

where $\hat{n}$ is the unit normal to the surface.

The Green's function ψ and its gradient $\nabla\psi$ are the mathematical equivalents of Huygen's wavelets. That is, each elemental surface current or charge is related to the scattered field by means of the Huygen wavelet and the total field is simply the sum (integral) over all such surface current elements. Huygen's wavelets are graphically shown in Figure 4.3, in which the scattering from a flat surface due to an incident plane wave is shown by the heavy arrow. Each wavelet has a radius corresponding to the time history of excitations by the incident wave. The scattered waves generated by the summation of wavelets have two components, the first being the specularly reflected wave whose angle of reflection is equal to the angle of incidence. The second is a forward scattered wave propagating in the same direction as the incident wave, but with the opposite phase. As a result, when the forward scattered wave is added to the incident wave, it creates a shadow or null total field on the back side of the flat surface.

Mathematically, the Green's function relates an elemental source current or charge to the field at the observation point. The three-dimensional Green's function is an outward scalar spherical wave whose intensity falls off as inverse to distance:

$$\psi = \frac{e^{-jkr}}{4\pi R} \tag{4.23}$$

where an $e^{j\omega t}$ time dependence has been assumed and where R is the distance from the elemental source (prime coordinates) to the observer:

$$R = [(x - x')^2 + (y - y')^2 + (z - z')^2]^{1/2} \tag{4.24}$$

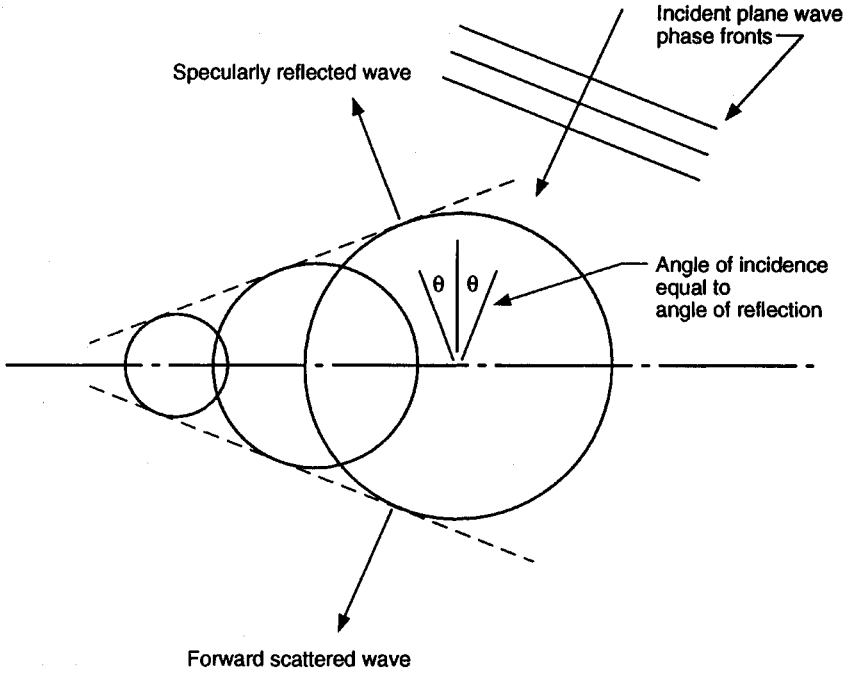

Figure 4.3. Huygen's wavelet wavefront construction analogy for the free-space Green's function.

Recalling that the gradient points in the direction of the maximum rate of change of the function, the gradient of the Green's function is an outward vector spherical wave:

$$\begin{aligned} \nabla\psi &= (1 - jkR)\frac{e^{-jkR}}{4\pi R^2}\hat{R} \\ &= (1 - jkR)\psi\hat{R}/R \end{aligned} \tag{4.25}$$

whose vector direction $\hat{R}$ is radially outward from each elemental source. The far zone E and H fields must be perpendicular to the radial vector $\nabla\psi$, and this requirement is contained inherently within the integral formulation, as we shall shortly see. The decay of this wave in the near field, $kR \ll 1$, is inversely as the square of the distance, whereas in the far field, $kR \gg 1$, it is inversely as the first power of the distance. Figure 4.4 further illustrates the physical nature of the Green's function and its gradient.

This definition of the Green's function is not valid when the sources and field points coincide, since $R = 0$ and ψ and $\nabla\psi$ are infinite. In these cases, we must recognize that a Green's function can still be defined in the sense that it represents

a "self" term. Self terms for currents and charge sheets are derivable from Maxwell's equations using the integral form of the curl and divergence equations with elemental loops (lines) and pillboxes (volumes). The results are

$$(\hat{n} \times \mathbf{H})_{\text{self}} = \frac{\mathbf{J}}{2}, \qquad (\hat{n} \times \mathbf{E})_{\text{self}} = \frac{\mathbf{M}}{2}$$
$$(\hat{n} \cdot \mathbf{E})_{\text{self}} = \frac{\rho}{2\epsilon}, \qquad (\hat{n} \cdot \mathbf{H})_{\text{self}} = \frac{\rho^*}{2\mu} \tag{4.26}$$

where E and H are the total fields on the surface due to currents $\mathbf{J}$ and $\mathbf{M}$ and charge densities ρ and ρ^*. When the Stratton-Chu equations include spatial locations where source and field points coincide, we must write out the self term explicitly and specify that the surface integrals exclude the troublesome self region. The symbol for such an integral is the integral sign with a bar through it and is called the principal value integral.

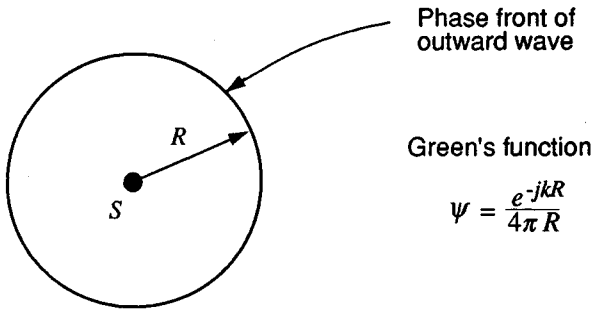

Spherical scalar wave "radiating" from Source S

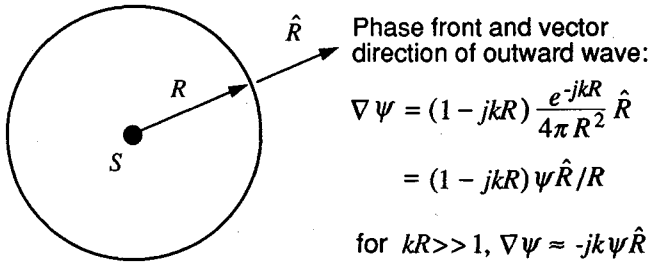

Spherical vector wave "radiating" from Source S

Figure 4.4. Interpretation of the Green's function and its gradient as a Huygen wavelet.

When we consider scattering from imperfect conductors, such as dielectric and magnetic bodies, we must include magnetic as well as electric currents and charges. For the discussions that follow, we will specialize the scattering formulation to that from a perfect conductor, so that the total tangential electric field is 0 at the surface. Then we need not consider magnetic currents or charges as sources of the scattered E and H fields. Our specialization still enables us to examine the nature of the solutions for a practical case without undue complication. For perfect conductors, with the magnetic sources set to 0 the integral forms for the E and H fields become

$$\begin{aligned} \mathbf{E}^s &= \int_s [-j\omega\mu(\hat{n} \times \mathbf{H})\psi + (\hat{n} \cdot \mathbf{E})\nabla\psi]dS = \int_s [-j\omega\mu\mathbf{J}\psi + \frac{1}{\epsilon}\rho\nabla\psi]dS \\ \mathbf{H}^s &= \int_s (\hat{n} \times \mathbf{H}) \times \nabla\psi \, dS = \int_s \mathbf{J} \times \nabla\psi \, dS \end{aligned} \tag{4.27}$$

These equations are known as the *electric* and *magnetic field integral equations* (EFIE and MFIE), respectively. These forms show that the scattered E field is caused only by electric currents and charges, whereas the scattered H field is caused only by electric currents. The next step is to apply the boundary conditions.

4.3.2 Boundary Conditions

The EFIE and MFIE are not yet in the form required to effect a solution. To do so, we must apply (4.27) to the surface of a perfectly conducting scattering body, for which we know that the tangential components of the fields are zero.

First, the surface charge density is rewritten invoking the conservation of charge using the continuity equation:

$$(\hat{n} \cdot \mathbf{E}) = \frac{\rho}{\epsilon} = \frac{-j}{\omega\epsilon}(\nabla \cdot \mathbf{J}) \tag{4.28}$$

This states that charge can be neither created nor destroyed, hence the charge density must change as current flows into or out of a given location.

When the observation point is on the surface, where the field values are known from the boundary conditions, the resulting forms for the EFIE and MFIE may be obtained as follows [5]:

$$\begin{aligned} \hat{n} \times \mathbf{E}^T &= n \times (\mathbf{E}^i + \mathbf{E}^s) = 0 \\ \hat{n} \times \mathbf{H}^T &= \hat{n} \times (\mathbf{H}^i + \mathbf{H}^s) = \mathbf{J} \end{aligned} \tag{4.29}$$

which leads to

$$\hat{n} \times \mathbf{E}^i = -\hat{n} \times \mathbf{E}^s = \hat{n} \times \int [-j\omega\mu\mathbf{J}\psi + \frac{-j}{\omega\epsilon}\nabla \cdot \mathbf{J}\nabla\psi] \, dS \tag{4.30}$$

$$\hat{n} \times \mathbf{H}^i = \frac{\mathbf{J}}{2} - \hat{n} \times \int \mathbf{J} \times \nabla\psi \, ds \tag{4.31}$$

Equations (4.30) and (4.31) are thus the starting points for obtaining the unknown surface current density. Except for frequencies corresponding to interior body resonances, either form may be used. When the surface becomes very thin, such as for wires and thin cylinders, the EFIE must be used because of the difficulty in adequately representing $\nabla\psi$ in the MFIE for these cases. For closed smooth conductors, the MFIE is often applied.

The EFIE is an integral equation of the first kind because the unknowns occur only within the integral. The MFIE is an integral equation of the second kind because the unknown current J occurs by itself and within the integral. The MFIE is particularly noteworthy because the integral contribution to the current density can be of secondary importance compared to the incident field. In fact, as will be shown in the next chapter, the physical optics assumption for the high-frequency region explicitly ignores the field expressed by the integral, so that the current density is given by twice the tangential component of the incident magnetic field without the need to solve an integral equation.

The next step is to solve for the unknown current density.

4.3.3 Solution Procedures

The procedures required to find the unknown current density involve

- Expressing the unknown in terms of a set of basis functions with unknown coefficients;
- Defining weighting or testing functions;
- Explicitly defining interaction matrix elements;
- Inverting the matrix;
- Specifying the polarization and direction of the incident field and computing the resultant current density;
- Computing the scattered field radiated by these induced currents.

Monostatic scattering patterns require more computation than bistatic patterns because the induced currents must be computed for each angle of incidence. However, scattering needs to be computed in only one direction, back toward the source of illumination.

Because our goal is an overall appreciation of the technique, we will specialize our solution to the slightly simpler MFIE for a two-dimentional closed surface. The solution of integral equations is mathematically associated with the theory of linear vector spaces.*

The unknown current density is a surface vector function. Therefore, the series expansion must have unknown coefficients for two orthogonal directions on any surface patch. For wires, however, current is usually assumed to flow axially along the wire so that only one vector direction is needed for each segment. The

*At internal resonances, a combination of the EFIE and MFIE is used. This is called the combined field integral equation, CFIE.

key assumption in breaking up the surface into patches is that the phase of the current is constant over each patch or segment. Because the actual phase angle varies spatially with distance, the constant phase requirement over each surface patch requires 7 to 10 samples per wavelength to adequately sample the actual variation. This requirement, in turn, dictates the matrix size for a given problem. Because the number of unknowns increases as the square of the number of surface patches MOM is typically used only for resonant region scattering.

The unknown surface currents are typically expanded as

$$\begin{aligned} \mathbf{J} &= \sum_{i=1}^{N} b_{x,i} f(t)\hat{u}_x + b_{y,i} f(t)\hat{u}_y \qquad \text{(for 3-D surfaces)} \\ &= \sum_{i=1}^{N} b_i \mathbf{f}_i(t) \qquad \text{(for wires or 2-D surfaces)} \end{aligned} \tag{4.32}$$

where $\hat{u}_x$ and $\hat{u}_y$ are the orthogonal unit surface vectors, $f(t)$ is an expansion function, and b is the complex (magnitude and phase) unknown current coefficient.

Before going further, we shall introduce the vector operator formalism used to considerably shorten the mathematical notation. It is traditional to compactly write the EFIE and MFIE integrals with linear operators, which are "shorthand" mathematical notations and in no way does the notation change the physics or numerical procedures. The electric field operator is defined as

$$L_E(\mathbf{J}) = \hat{n} \times \int [-j\omega\mu \mathbf{J}\psi + \frac{1}{-j\omega\epsilon}(\nabla \cdot \mathbf{J})\nabla\psi] \, dS \tag{4.33}$$

and the magnetic field operator is defined as

$$L_H(\mathbf{J}) = \frac{\mathbf{J}}{2} - \hat{n} \times \int \mathbf{J} \times \nabla\psi \, dS \tag{4.34}$$

The physical interpretation of these operators is that they give the tangential scattered field on the surface due to a surface current J.

With the aid of this operator notation, the solution is obtained by inserting the series expansion of the unknown currents into the MFIE and remembering that the unknown coefficients are constants that may be brought out from under the integral operators:

$$L_H(\mathbf{J}) = \sum_{i=1}^{N} b_i L_H(\mathbf{f}_i) = \hat{n} \times \mathbf{H}^i \tag{4.35}$$

The next step is to multiply each side of (4.35) by a vector weighting function $\mathbf{W}_j$ and integrate the result over each surface patch. The mathematical notation for this step is that of a generalized inner product and is given the following symbols:

$$<\mathbf{W}, L_H(\mathbf{J})> = \int \mathbf{W} \cdot L_H(\mathbf{J})\, dS \tag{4.36}$$

This step can be physically interpreted as the way in which continuous boundary conditions over a surface region are expressed as single-average values at one localized point on the surface. The inner product is applied to each of the N surface current patch samples to arrive at a set of N equations in N unknowns:

$$\sum_{i=1}^{N} b_i <\mathbf{W}_j, L_H(\mathbf{f}_i)> = <\mathbf{W}_j, \hat{n} \times \mathbf{H}^i> \tag{4.37}$$

for $j = 1$ to N.

This set of linear equations for the unknown current coefficients b_i can be compactly expressed in matrix notation as

$$\bar{\bar{Z}}\mathbf{b} = \mathbf{H}^i \tag{4.38}$$

where the matrix elements are given by

$$Z_{ij} = <\mathbf{W}_j, L_H(\mathbf{f}_i)> \tag{4.39}$$

and the unknown current coefficients are expressed as a generalized column vector,

$$\mathbf{b} = \begin{bmatrix} b_1 \\ \cdot \\ \cdot \\ \cdot \\ b_N \end{bmatrix} \tag{4.40}$$

The known incident fields, which represent the forcing function for the solution, are also expressed as a generalized column vector:

$$\mathbf{H}_j^i = <\mathbf{W}_j, \hat{n} \times \mathbf{H}^i> \tag{4.41}$$

The physical meaning of each term is clear. The matrix elements express the electrical interaction of each part of the scattering surface with every other part. The ijth matrix element is a measure of the fields produced at the ith surface patch

created by a unit current located at the jth surface patch. For general 3-D problems, each matrix element is a fourfold integral that results when the surface effect of a source segment (twofold integral) on the sample surface (another twofold integral) is computed. Because the matrix elements are for unit currents, the matrix and its elements are independent of the actual electrical excitation of the body. The matrix is simply a measure of the electrical interaction of the body with itself and as such is a function of body geometry and frequency.

The unknown current coefficients are constants for each small surface patch and may be removed from within the integrals to form the unknown surface current column vector. The excitation vector on the righthand side is the forcing function for the solution. Its elements are the integral of the weighting function W with the incident field. Physically, this integral is again a finite measure of how the incident field varies over each surface patch. The excitation vector is sometimes called the *voltage vector*, particularly when the EFIE is used, in which case the applied excitation is an incident electric field.

The physical meaning of the matrix equation can be made clearer if we examine the jth row of (4.37), which represents the fields on the jth segment from the incident field plus that from all the other surface segments. The term on the righthand side represents the excitation field, whereas the terms on the lefthand side represent the field at the jth segment from each of the other segments, each with current b_i. The jth term is the self term and represents the fields at the jth location due to jth location currents.

The solution for the surface currents is formally given by

$$[b] = [Z]^{-1}[H] \tag{4.42}$$

The solution procedure is to compute the matrix elements, specify the polarization and incident direction of the illuminating field, compute the excitation vector, invert the impedance matrix, and then solve for the currents.

4.3.4 Scattered Fields

Once the currents are known for a given excitation, the scattered fields due to these currents may be computed from the EFIE or MFIE expressions (4.27). Usually, only the farfield values are of interest, and therefore, the farfield Green's function gradient is used in the EFIE and MFIE to obtain [10]

$$\bar{E}^s = \frac{-j\omega\mu}{4\pi R} e^{-jkR} \int_s [\mathbf{J} - (\mathbf{J}\cdot \hat{R})] e^{+j\mathbf{k}\cdot\mathbf{r}} \, dS \tag{4.43}$$

$$\bar{H}^s = \frac{+j\omega\epsilon}{4\pi R} e^{-jkR} \int_s \sqrt{\frac{\mu}{\epsilon}} (\mathbf{J} \times \mathbf{R}) e^{+j\mathbf{k}\cdot\mathbf{r}} \, dS \tag{4.44}$$

where R is the distance from a local origin to the observation point and r is a local surface coordinate.

The choice between the farfield EFIE or MFIE is not significant, because in the farfield E and H are related by Maxwell's equations. For bistatic computation, either (4.43) or (4.44) is evaluated for the angles of interest. For monostatic computations, only the backscattered field is computed, and then the entire process must be repeated to determine a new set of surface currents for the next illumination angle. Once the scattered fields are known, the RCS may be computed using (3.1).

Further insight into the far zone fields as a function of current sources can be gained from examining the preceding expressions. As we have already seen, elemental sources are related to observed fields via a Green's function that is spherical in nature. However, the farfield patterns produced by elemental current sources are shaped like doughnuts with nulls along the vector direction of the current element (see Fig. 4.5). From the far zone expression for magnetic field, we see the $\mathbf{H}^s$ is a cross product of the current element $\mathbf{J}$ and the radial vector of $\nabla\psi$. This creates a doughnut shape with an $\mathbf{H}$ vector transverse to the radial

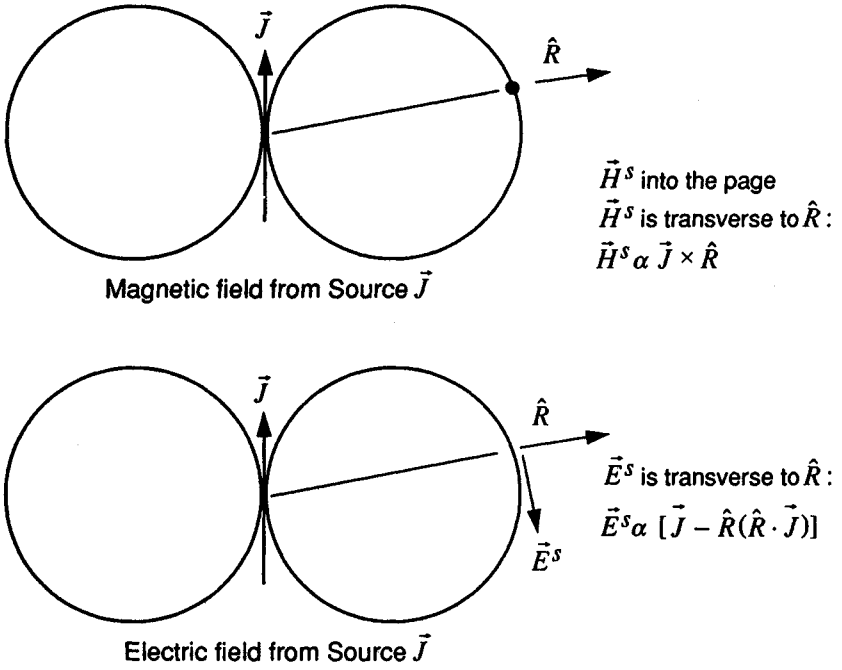

Figure 4.5. Far zone fields from elemental electric and magnetic currents.

direction, as is required for an outward wave. From the expression for the far zone electric field, we see that $\mathbf{E}^s$ is the product of the scalar Green's function and the transverse components of the current element $\mathbf{J}$, that is, the radial component of $\mathbf{J}$ is vectorially subtracted and does not contribute to $\mathbf{E}^s$ in the far field. When the farfield point lies along the $\mathbf{J}$ direction, $\mathbf{J}$ is entirely radial, hence there is no contribution to the far field in this direction. This again creates the doughnut pattern. The vector direction of $\mathbf{E}^s$ is, of course, transverse to the radial direction because only the transverse components of $\mathbf{J}$ contribute to the far field. The integration process forms the phasor and vector sum of all such current elements to arrive at the net field due to all elemental sources $\mathbf{J}$.

When we actually compute the far zone $\mathbf{E}^s$ field from (4.43) the radial component of $\mathbf{J}$ is subtracted prior to integration, as indicated; however, a computational simpler approach is often used. Namely, we compute the two polarization components of E by using a dot product of the current $\mathbf{J}$ with the unit polarization vector $\mathbf{n}^\alpha$ where $\alpha = \theta$ or φ so that $\mathbf{n}$ is perpendicular to the radial direction of $\mathbf{k}$:

$$E^{s,\alpha} = -j\omega\mu \frac{e^{-jkR_0}}{4\pi R_0} \int (\hat{\mathbf{n}}^\alpha \cdot \mathbf{J})\, e^{jk\cdot r}\, dS \tag{4.45}$$

4.3.5 Example Solutions

The scattering process can be understood by examining the solution for the induced currents and resultant scattered field for a collection of simple body geometries. For this purpose, we have chosen some rather elementary shapes: a wire, the infinite circular cylinder, a rectangular cylinder, and a body of revolution with attached wires. Each configuration reveals something different about the induced currents and the far field that results from those currents.

The first example of scattering predictions is for a wire 2λ in length illuminated by a wave whose incident E field has a component along the wire. The results presented here are from Harrington [1], who used a MOM wire code to compute the induced currents from which the bistatic scattering patterns were computed. The results for six angles of illumination are presented in Figure 4.6. The most interesting characteristic is that, for even a short wire, the specular reflectivity nature of high-frequency scattering is obvious. We can see that the angle of the major scattering lobe is equal to the incident angle. This behavior becomes more pronounced as the wire becomes longer, for which the major lobes become narrower in width and more intense. The wire is not an effective scatterer when viewed near end-on incidence because the component of the incident E field along the wire direction is small.

Note the presence of the traveling wave lobe, which appears in the case of an incident angle of 30°. This lobe is aligned back in the general direction of the

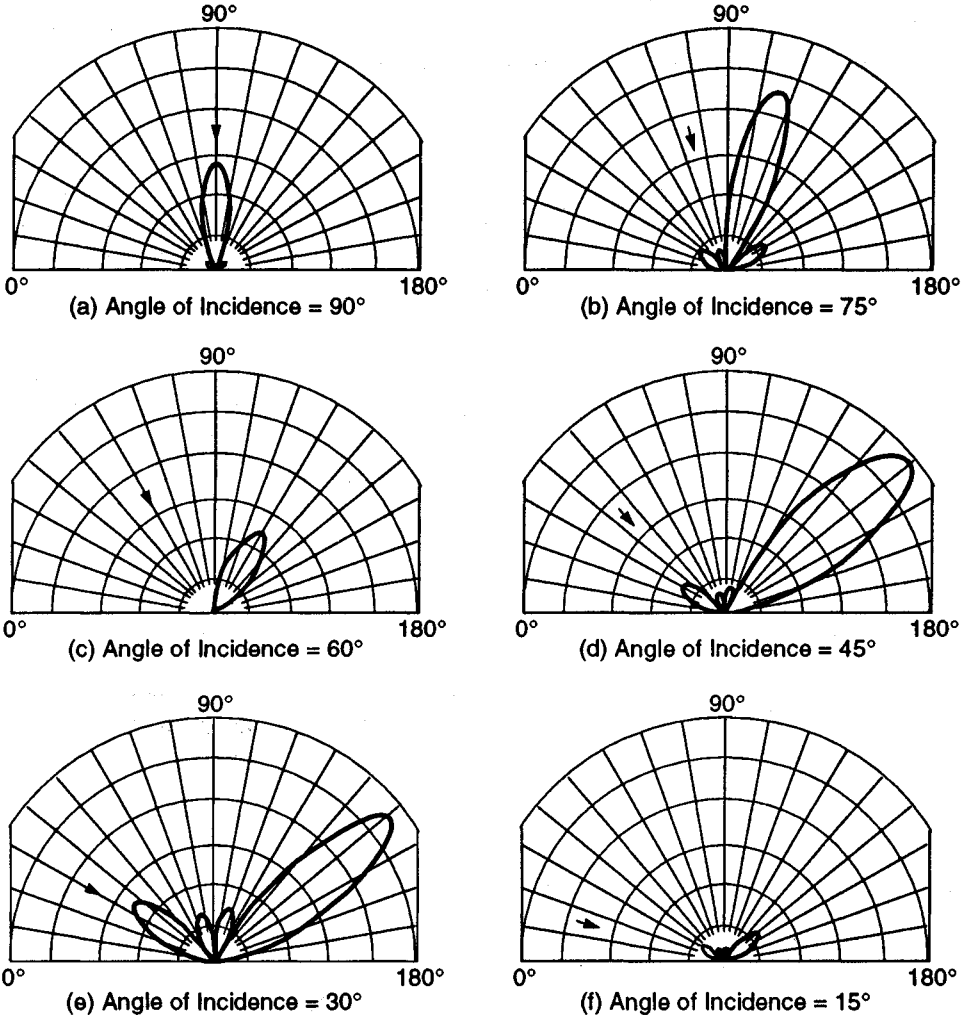

Figure 4.6. Bistatic RCS patterns of a straight wire 2λ in length (from [1]).

illumination and peaks near 35°. It is caused by a reflection of the induced forward current on the wire, giving rise to a backward current that radiates the traveling wave lobe. The angular location of this lobe is discussed in Chapter 5. The formula given there predicts a location of 34.6°, which agrees quite well with the numerical results.

Before we examine the scattered patterns for two-dimensional structures, the reader should bear in mind that only the scattered field is presented. The total field is the sum of the incident and scattered fields.

$$\mathbf{H}^T = \mathbf{H}^i + \mathbf{H}^s$$

and in the shadow region behind the scatterer the total field is small. To create the shadow, the forward-scattered field must cancel the incident field. Therefore, it must have nearly the same magnitude, but the opposite phase, as the illuminating field, so that phasor addition (subtraction in this case) of the two creates a shadow. In the scattering patterns that follow, the shadow-creating forward-scatter lobe is the strongest lobe.

The next examples are for two-dimensional scattering results for the case where there is a component of the incident E field along the surface (H field transverse to plane of Fig. 4.7). The numerical method used is that given by Harrington [1] for two-dimensional MFIE MOM computations. The reader is urged

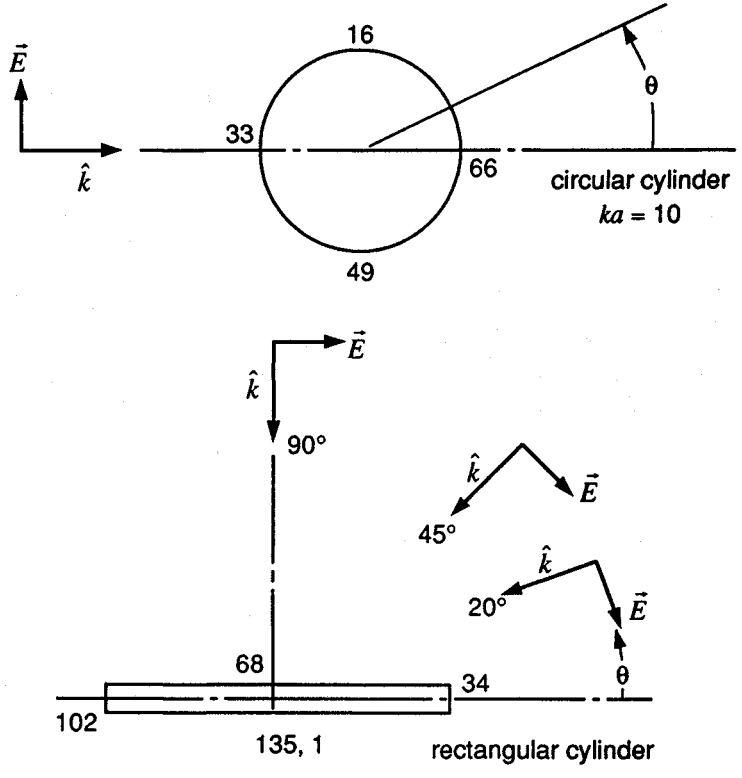

Figure 4.7. Two-dimensional MOM geometries. Numerical values signify segment numbers.

to examine the computed current distributions of the following examples. Because these were obtained using numerical solution techniques for the exact EM formulation, we may take these results as "exact" currents. It is instructive to compare them with the assumed physical optics currents, as discussed in Chapter 5, in which currents on the illuminated surfaces are taken as twice the tangential magnetic field strength, whereas the currents on the shadow surfaces are taken as 0.

The currents induced on a circular cylinder and the resultant bistatic scattering patterns are shown in Figure 4.8 for $ka = 10$. The amplitude of the computed current density is normalized to the tangential component of the incident magnetic field and is plotted as a function of the circle segment number defined in Figure 4.7. The angle of illumination was 180°. We see that the illuminated side currents have peak values of twice the incident magnetic field, whereas those on the shadow side decrease toward zero. The RCS in the backward direction (at 180°) is fairly constant, agreeing very well with the high frequency 2-D geometric optics result of $\sigma = \pi a = 5\text{m} = 7$ dBm.

The results for a rectangular cylinder with a transverse cross section $1\lambda \times 10\lambda$ are shown for an illumination angle of 90°, Figure 4.9. Again the currents are plotted versus the segment index number defined in Figure 4.7. The bistatic scattering pattern shows the specular nature of the scattering process; the major scattering lobe is aligned along the direction where the angle of reflection is equal to the angle of incidence.

The current distribution on the rectangular cylinder for incidence normal to the broadside agrees well with the PO approximation. Near the corners, however, we see decaying ripples, which suggest the presence of the surface current wave due to edge diffraction. These ripples indicate that the corners are secondary scattering centers.

A final example of an exact MOM solution involves a solution for wire elements attached to a body of revolution. MOM solutions of BORs have been obtained by Mautz and Harrington [11] using current expansion functions that take into account azimuthal symmetry, resulting in azimuthal modal expansion for the currents. The result is that the BOR impedance matrix can be reduced to a set of independent submatrices for each circumferential mode. The MOM solutions for wires in the presence of BORs [12] involve not only the wire solutions, but also the electrical interaction between the wires and the BOR.

The attachment of the wires to the BOR requires the introduction of a special current basis function, which mathematically represents the physical nature of the currents in the vicinity of the junction [13,14]. The scattering geometry illustrated is for a hemispherical capped cylinder (the BOR) with wire loops attached (Fig. 4.11). The system matrix (Fig. 4.10) illustrates six types of component electrical interaction elements:

- BOR-BOR in block diagonal modal form;
- Wire-wire;
- Junction-junction;

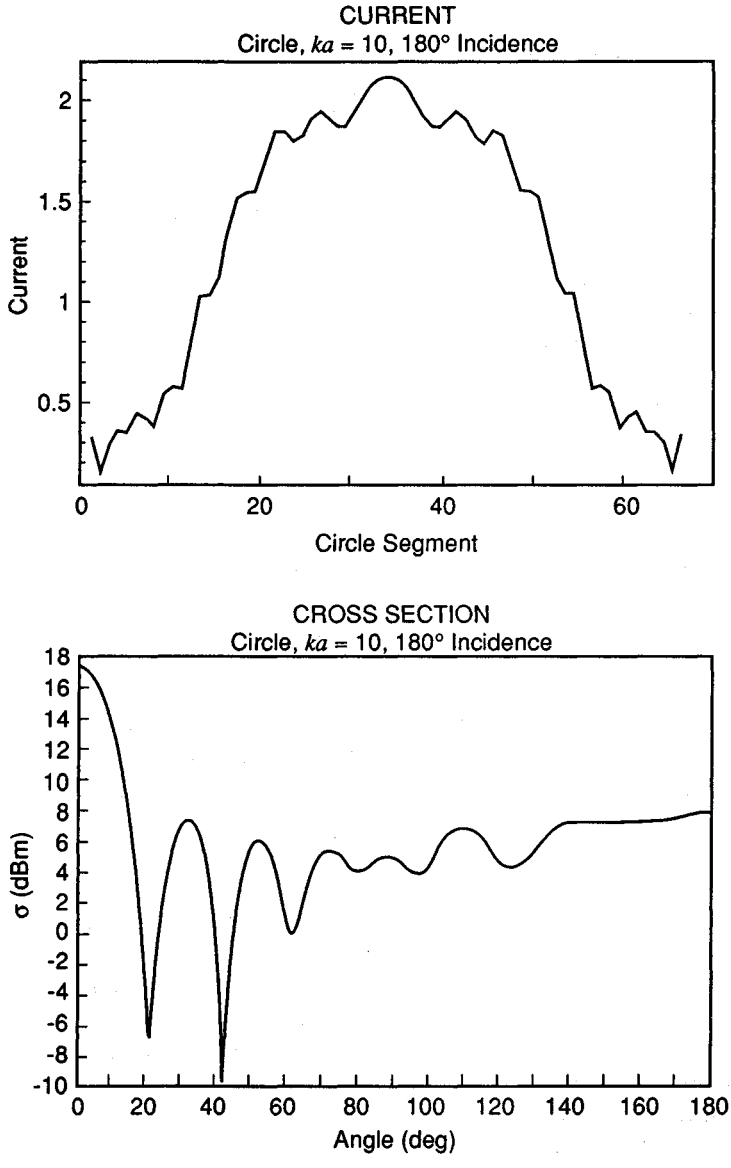

Figure 4.8. 2-D circular cylinder current distribution and bistatic scattering pattern. Illumination is from $\theta = 180°$.

- BOR-wire;
- BOR-junction;
- Wire-junction.

(a)

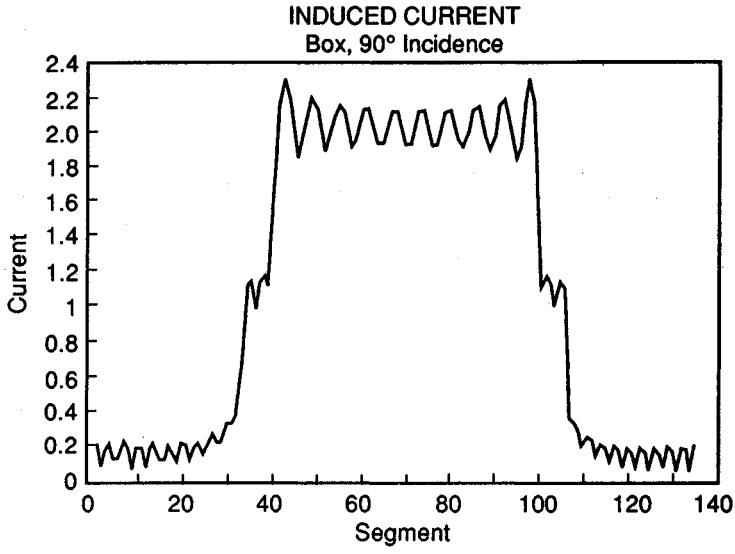

(b)

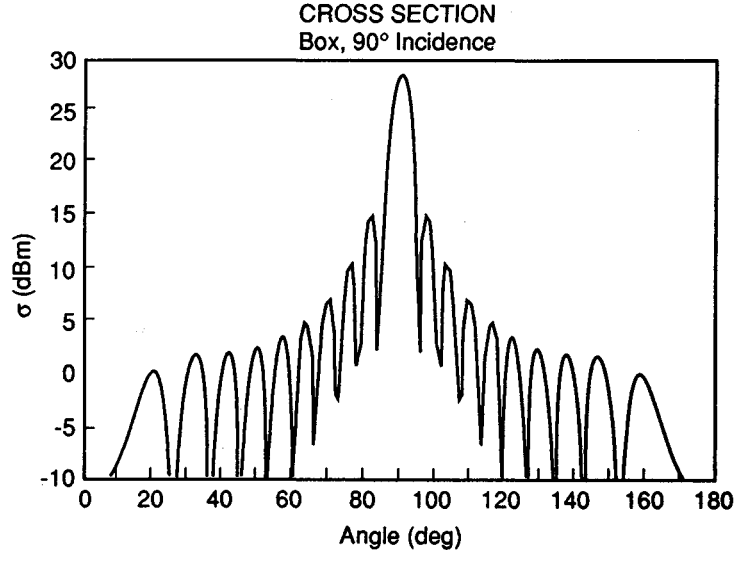

Figure 4.9. 2-D rectangular 1 × 10 λ cylinder illuminated at θ = 90°: (a) current, (b) Bistatic RCS.

These submatrices express the electrical interaction of each part of the body with itself and with the other parts of the body. The current expansion coefficients form the unknown current vector and the righthand side is the known voltage vector, which is different for each excitation (incident wave). An example of the measured and computed scattering for a BOR with attached wire is shown in Figure 4.11.

Next Page

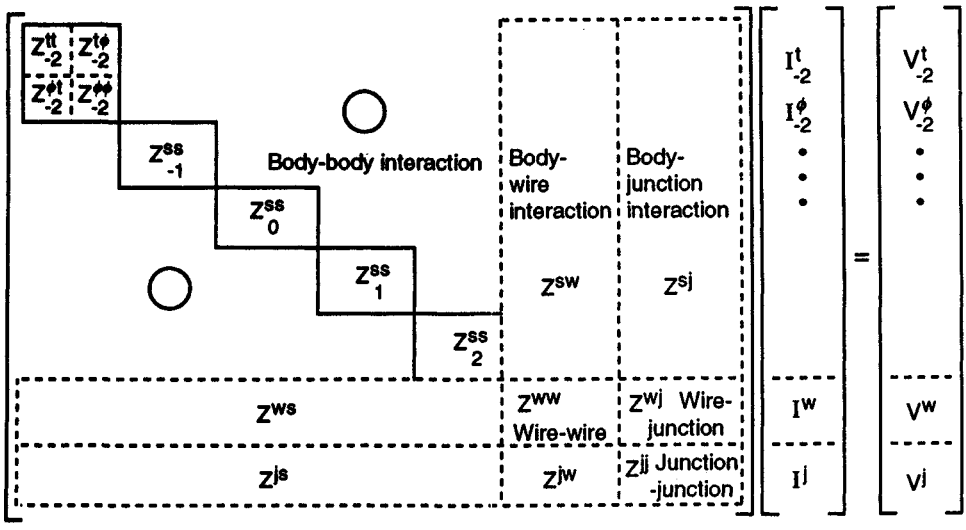

Figure 4.10. Composite BOR-wire junction system matrix.

4.4 PHENOMENOLOGY: SURFACE CURRENTS, NEAR FIELDS, AND IMAGING

The mathematics of the numerical solution approach sheds absolutely no insight into the physical mechanisms responsible for scattering even though all electromagnetic interactions are accounted for. Therefore it becomes important for the analyst who desires more information than just the scattered fields to also compute quantities such as induced surface currents, near fields, and images of currents producing the scattered radiation.

4.4.1 Time-Varying Vectors

Currents and fields are time-varying quantities. We may desire to examine either the time variation or the time average *root mean square* (rms) values. Vector quantities have components that are complex numbers. Each spatial vector component has its own magnitude and phase. Each vector is understood to be multiplied by the time dependence factor $e^{j\omega t}$.

Real-world physical quantities, however, are not complex. Complex notation is the formal process by which the time delay due to the finite speed of propagation is expressed by phase (delay). The physical quantity is always understood to be the Re part of the complex number. For an arbitrary complex vector **E** with $e^{j\omega t}$ time dependence, the physical value is the Re part:

Chapter 5
High-Frequency RCS Prediction Techniques

E.F. Knott

5.1 OVERVIEW

We have seen in Chapters 3 and 4 how scattering solutions may be affected in the Rayleigh and resonant regions, and in this chapter we will discuss high-frequency RCS prediction techniques. It must be emphasized at the outset that the term *high frequency* refers not so much to the actual frequency of the incident wave as to the size of the target when compared to the incident wavelength. In the high-frequency range, the scattering obstacle should be at least five wavelengths in size, although reasonably accurate results may be obtained for some bodies even smaller than this.

The high-frequency region is of great practical importance, as may be seen from a consideration of typical threat radars and targets. Threat radars range from low-frequency systems used for surveillance to the higher frequencies used for fire control and command-guided surface-to-air missile systems. Long-range surveillance radars use frequencies down to the VHF region or lower because the signals propagate well beyond the visible horizon. The wavelengths can be as long as about 10m, hence airborne targets are not likely to be more than two or three wavelengths in size. This is the edge of the high-frequency RCS region, and high-frequency prediction techniques may not be useful for such targets. However, the wavelengths of radars operating in the UHF bands are on the order of a meter or shorter, hence most airborne target will be at least 10 wavelengths long. At fire control radar wavelengths, the targets may be hundreds of wavelengths long, and high-frequency prediction methods are very useful. Therefore, although the methods may not be applicable to the very low, over-the-horizon radars, most targets

of practical interest are assuredly electrically large for radar frequencies of 1 GHz and above.

The simplicity of high-frequency prediction methods is due to the fact that each part of the body essentially scatters energy independent of all other parts. Therefore, the fields induced on a portion of the target are due to only the incident wave and not the energy scattered by other parts. This makes it relatively simple to estimate the induced fields and to integrate them over the body surface to obtain the far scattered field and, therefore, the RCS. There are a few exceptions to this general assumption, however, such as reentrant structures for which some internal features may be illuminated by specular reflections from other internal features. Examples are engine intakes and corner reflectors for which other procedures must be used [1].

The electrical size requirement actually applies to individual scattering features and not the overall target length. In practice, high-frequency methods can be applied only to relatively simple shapes that are easily described in mathematical terms. Examples are elementary surfaces and simple curves representing edges. If surfaces or edges cannot be described by simple mathematical expressions, they must be approximated or replaced by those that can. Therefore, we are ultimately forced to approximate the actual target by a collection of simple shapes. As such, the high-frequency size requirement (that the body be at least several wavelengths in size) applies to these simple shapes and not necessarily to the overall target. Even so, most target features are still within the high-frequency scattering region, and the methods described later can be used.

Probably the oldest and simplest is the method of geometric optics, developed many years ago in early studies of light. The radar cross section, even in bistatic directions, is given by a very simple formula that involves only the local radii of curvature at the specular point. However, this simple prescription fails when one or both radii of curvature becomes infinite, as in the case of a cylinder or flat plate, and we might then turn to the method of physical optics. The local radii of curvature of the surface may be infinite, yet physical optics gives the correct result if the surface is not too small and if the scattering direction does not swing too far from the specular direction. However, physical optics fails at wide angles from the specular direction.

The reason for the failure of physical optics is that the contributions from edges are ignored, and at this point we can invoke Keller's geometrical theory of edge diffraction [2]. Noted for its "cookbook" simplicty, GTD is based on the canonical solution for diffraction by a wedge and gives remarkably good answers for a wide variety of scattering problems. However, it is a wide-angle theory, and it fails in the transition regions of the shadow and reflection boundaries, which will be explained later. Uniform asymptotic solutions have been devised that overcome these difficulties [3], but GTD suffers yet another shortcoming, giving infinite results at caustics, among which is the important case of scattering along the axis of a ring discontinuity.

The *method of equivalent currents* (MEC) was developed to overcome the caustic difficulties of GTD [4–6], but the method does not address the singularities in the diffraction coefficients. In an effort parallel to that of Keller, Ufimtsev developed his *physical theory of diffraction* (PTD) for treating edges [7]. Like Keller, he turned to the solution of the canonical wedges problem, but he sought to approximate the edge contribution by subtracting the incident field and the physical optics fields from the exact solution for the total field. As a result, his diffraction coefficients can be expressed as the difference between Keller's diffraction coefficients and a set of physical optics coefficients. It turns out that each set is singular along the reflection or shadow boundaries, but the difference remains finite. Despite this serendipity, both GTD and PTD apply only to scattering directions lying on the Keller cone, which will be explained later.

In an attempt to overcome this restriction, Mitzner [8] devised his *incremental length diffraction coefficient* (ILDC), thus extending Ufimtsev's theory to arbitrary directions, but this is precisely what the method of equivalent currents did for Keller's theory. Thus, there is an exact parallel between Mitzner's extension of PTD and Michaeli's extension of GTD. Unfortunately, none of the four theories adequately treats the surface traveling wave contributions from long structures illuminated at grazing incidence.

Surface traveling waves are induced on long surfaces, even wires, when there is a component of the incident electric field is tangent to the surface and in the direction of propagation of the surface wave. This kind of current wave is responsible for the familiar end-fire radiation characteristics of long-wire antennas. The forward traveling wave does not contribute significantly to the backscattered energy, but if the far end of the surface is bounded by a discontinuity, as is usually the case, the current wave is reflected. The backward traveling current wave also radiates in an end-fire mode, but this time in the direction of the radar. Thus, the surface traveling wave can give rise to large contributions to the radar cross section of long, smooth structures. None of the high-frequency theories predicts the effect in and of itself, although the repeated application of GTD to account for multiply diffracted rays seems to work for relatively simple structures [9].

5.2 GEOMETRIC OPTICS

The theory of geometric optics was used for many years by astronomers and lens makers in designing and building optical systems. It accounts not only for the way light rays are reflected from smooth surfaces, but for the change in the angle of the transmitted ray when light passes from one medium to another. This was of considerable importance in the design of lenses, because the bending of the transmitted ray depends not only on the wavelength of the light, but on the refractive index of the lens materials, which itself varies with the wavelength. When used to predict the scattering of radar waves from objects of practical interest, the body

surfaces are usually assumed to be perfectly conducting, although this is not necessarily a restriction.

Geometric optics is a ray-tracing procedure in which the wavelength is allowed to become infinitesimally small. This being the case, energy propagates along slender tubes according to the formula.

$$u = Pe^{ikS} \tag{5.1}$$

where the amplitude P represents the intensity of either the magnetic or electric field transverse to the direction of propagation. The amplitude P and the phase factor S are both functions of position in space and may be complex numbers. Propagation is in the direction given by ΔS, hence surfaces of constant S are surfaces of constant phase. Equation (5.1) is a solution of the wave equation in the limit of vanishing wavelength, and because the field components are transverse to the direction of propagation, the solution is not valid near discontinuities such as edges. (The actual fields near edges have radial as well as transverse components.)

When a ray strikes a smooth flat surface separating two media of different refractive index, part of the energy is reflected and part is transmitted across the boundary into the second medium. When the electromagnetic boundary conditions are invoked, we find that the transmitted ray propagates in a direction different from that of the incident ray (refraction), and the angle of the reflected ray, as measured from the surface normal, is equal to the angle of the incident ray. The effect is known as Snell's law, and the amplitude and phase of both the reflected and transmitted rays can be calculated. When normalized with respect to the amplitude of the incident ray, the complex amplitudes of the reflected and transmitted rays are none other than the classic Fresnel reflection and transmission coefficients discussed in Chapter 3.

The reflection coefficient for a perfectly conducting surface is -1, implying a 180° phase shift and no reduction of the intensity of the reflected wave. This is true only at the point of reflection (the specular point), and if the ray is due to a point source of energy some finite distance from the surface, the reflected ray decays in intensity as it travels away from the specular point. The decay in intensity is due, of course, to the spreading of energy, and the effect can be accentuated if the reflecting surface is curved. It is also possible for the energy in a ray bundle to increase, which is precisely the effect desired of focused mirrors. In this case, a caustic may be formed when an infinity of rays converge at a point or a line.

The decay or increase in energy can be calculated by invoking the principle of conservation of energy along a ray tube, such as shown in Figure 5.1. By demanding that all the energy entering the tube at one end be transmitted to the other, we will find that the ratio of the power density at the output to that at the input is

$$\frac{|A(s)|^2}{|A(o)|^2} = \frac{\rho_1\rho_2}{(s + \rho_1)(s + \rho_2)} \tag{5.2}$$

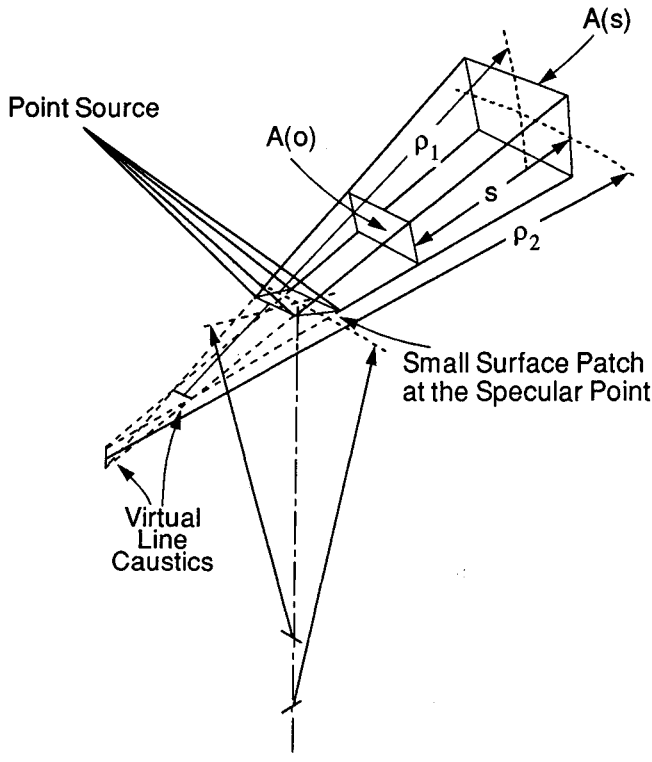

Figure 5.1. Geometrical optics reflection from a doubly curved surface. The curvature of the reflected wavefront is given by ρ_1 and ρ_2 and that of the reflecting surface is a_1 and a_2. In general, the planes containing a_1 and a_2 are neither parallel nor perpendicular to the plane of incidence. The radii ρ_1 and ρ_2 are measured at the caustics (here below the actual surface) formed by extending the reflected ray tube backward until the rays meet.

where $A(o)$ and $A(s)$ are the field intensities at the input and output, respectively, s is the distance along the tube between the two ends, and ρ_1 and ρ_2 are the principal radii of curvature of the wavefront at the output of the tube.

If the body is illuminated by a spherical wave due to a point source located a finite distance away, as in Figure 5.1, we can find the image of the source in the surface by extending the reflected ray tube backward until the sides of the tube intersect. Because of the differences in the surface radii of curvature, the two sides of the tube will intersect along a line that does not necessarily coincide with the intersection of the top and bottom of the tube, hence the image of a point source in a curved surface does not generally yield another point. The effect is called *astigmatism,* and the result is a blurred image.

The radii of curvature of the reflected wavefront at the specular point can be related to the radii of curvature of the incident wavefront and the radii of curvature of the body there. The relationship is not a simple one, and it involves not only the angle of arrival of the incident ray, but also the angle by which the principal planes of the body curvature are rotated out of the plane of incidence. (The reader may find the complete formula in [3].) This relationship may be inserted in (5.2) and the distance s may be measured from the specular point to the point of observation. If the direction of observation is now taken to be back toward the source, s becomes the distance R in (1.11). If R is forced to infinity, as required by the formula, the angular dependence on the local angle of arrival of the incident ray disappears. In addition, the angular rotation of the principal planes of the body radii of curvature out of the plane of incidence also drops out of the expression. The results of the calculation are simply

$$\sigma = \pi a_1 a_2 \tag{5.3}$$

where a_1 and a_2 are the principal radii of curvature of the body at the specular point.

Note that this very simple expression exhibits absolutely no dependence on the frequency of the incident wave. Moreover, even though we have not demonstrated it, this is also the result for bistatic directions. Therefore, when applied to the very simple case of scattering by a sphere, the radar cross section is simply the projected area of the sphere, no matter what the bistatic angle. For general spheroids, because the specular point shifts over the surface of the body as the scattering direction moves, and the body curvature changes over the surface, the bistatic scattering will change with the bistatic angle. The formula can be used as it stands for perfectly conducting bodies, but other terms must be included for nonconducting penetrable bodies such as raindrops. The radii of curvature of the body should be large compared to the wavelength, but reasonably accurate results can be obtained for bodies as small as two or three wavelengths in diameter. The theory of geometric optics can even be applied to the scattering of soap bubbles by estimating the reflection coefficient of a thin membrane [10].

Note that the radii of curvature used in (5.3) must be those at the specular point. Therefore, one of the problems that must be addressed in practical computation schemes is the identification of the specular point. For arbitrary bodies, this is not always an easy task, and even for simple structures such as spheroids, the analyst may generate more solutions than needed. Unless care is taken in the solution, the analyst may generate a fourth-order (quartic) equation to be solved, for which there are four solutions (roots), only one of which is the desired one. Nevertheless, all four must be found before the proper one is selected. The multiplicity of roots usually stems from an all too casual definition of the problem, such as the failure to distinguish negative angles from positive ones. In any event, identification of the specular point is a necessary step in the application of the theory of geometric optics.

A serious shortcoming of the theory can be noted immediately from the form of the result. Since the RCS depends on the radii of curvature of the body at the specular point, the formula predicts infinite results for flat or singly curved surfaces, for which one or both radii of curvature are infinite. Fortunately, there is a way around the dilemma.

5.3 PHYSICAL OPTICS

The theory of physical optics overcomes the catastrophe of the infinities of flat and singly curved surfaces by approximating the induced surface fields and integrating them to obtain the scattered field. Because the induced fields remain finite, the scattered fields are finite as well. The beginning point is the Stratton-Chu integral equations presented in Chapter 3. These expressions hold for a closed scattering surface, and Stratton has demonstrated [11] that, if the surface is not closed, additional terms must be added (line integrals around the edge bounding the open surface) to account for the edge discontinuity. Two simplifications can be made immediately in the integrals. One is the farfield approximation, in which the distance R from an origin in or near the obstacle to the farfield observation point is much larger than any obstacle dimension. This allows the gradient of the Green's function to be well approximated by

$$\nabla\psi \simeq ik\hat{s}\psi \tag{5.4}$$

where $\hat{s}$ is a unit vector aligned along the scattering direction. Under farfield conditions, the line integrals can be represented as surface integrals, and when combined with the other terms, another simplification results. It will be found that there can be no component of the surface field distribution along the scattering direction [12], whence the Stratton-Chu integrals can be written as

$$\bar{E}_s = ik\psi_0 \int_s \hat{s} \times [\hat{n} \times \bar{E} - Z_0\hat{s} \times (\hat{n} \times \bar{H})]\, e^{ik\bar{r}\cdot(\hat{i}-\hat{s})}\, dS \tag{5.5}$$

$$\bar{H}_s = ik\psi_0 \int_s \hat{s} \times [\hat{n} \times \bar{H} + Y_0\hat{s} \times (\hat{n} \times \bar{E})]\, e^{ik\bar{r}\cdot(\hat{i}-\hat{s})}\, dS \tag{5.6}$$

where $\hat{i}$ is a unit vector along the direction of incidence, $\bar{r}$ is now the position vector from the local origin to the surface patch dS, $Y_0 = 1/Z_0$ is the admittance of free space, and $\psi_0 = \exp(ikR)/4\pi R$ is the farfield Green's function. Note that the scattered fields are represented in terms of the tangential components of the total fields on the surface, hence the desired scattered fields appear on both sides of the equation. Either of the two equations can be used to calculate the far scattered field because of the relationship

$$\bar{H}_s = Y_0\hat{s} \times \bar{E}_s \tag{5.7}$$

We will use (5.5) by way of illustration.

We can approximate the total fields within the integrals by making the *tangent plane approximation*. That is, we assign the surface fields the values they would have had if the body had been perfectly smooth and flat at the surface patch of integration dS. This approximation can be made for any body material, but we shall assume the body to be perfectly conducting. In this case, the tangential components of the total fields are

$$\hat{n} \times \bar{E} = 0 \tag{5.8}$$

$$\hat{n} \times \bar{H} = 2\hat{n} \times \bar{H}_i \tag{5.9}$$

where $\bar{H}_i$ is the incident magnetic field strength at the surface path. If the incident wave propagates in a direction given by the unit vector $\hat{i}$, with a magnetic intensity H_0 and a magnetic polarization along the unit vector $\hat{h}_i$, (5.5) becomes the physical optics integral:

$$\bar{E}_s = -i2kZ_0H_0\psi_0 \int_s \hat{s} \times [\hat{s} \times (\hat{n} \times \bar{h}_i)]e^{ik\hat{r}\cdot(\hat{i}-\hat{s})}dS \tag{5.10}$$

where the surface S is now the illuminated portion of the body. In other words, the tangential fields on shaded portions of the body are assumed to be precisely zero.

In the computation of the scattering from complex objects in the high-frequency region, the fields scattered by the many different components must be calculated and then added together before squaring to obtain the scattered power. This preserves the phase relationship between the various scatterers on the target so that interference effects may be faithfully represented, but it requires that we calculate quantities proportional to the square root of eq. (1.11), namely (1.12). Despite the fact that (1.12) implicitly contains phase information, we would like to eliminate the range dependence in the phase factor as well as in the amplitude. We find it convenient, therefore, to multiply (1.12) by $\exp(-ikR)$:

$$\sqrt{\sigma} = \lim_{R\to\infty} 2\sqrt{\pi}\, R\frac{\bar{E}_s \cdot \hat{e}_r}{E_0} e^{ikR} \tag{5.11}$$

When (5.10) is substituted into (5.11), we have the physical optics expression for the square root of the RCS:

$$\sqrt{\sigma} = -i\frac{k}{\sqrt{\pi}} \int_s \hat{n} \cdot \hat{e}_r \times \hat{h}_i\, e^{ik\hat{r}\cdot(\hat{i}-\hat{s})}\, dS \tag{5.12}$$

The integral can be evaluated exactly for only a handful of cases that include flat plates, cylinders, and spherical caps viewed at axial incidence. In the case of

flat plates, a coordinate system can be established in terms of two variables over the surface of the plate plus the position vector $\bar{r}_0$ of the orgin of the coordinate system:

$$\bar{r} = \bar{r}_0 + x\hat{x} + y\hat{y} \tag{5.13}$$

Therefore, the only term in (5.12) that varies over the surface is the phase term, all other terms being constant. The evaluation of the integral is particularly simple for a flat rectangular plate, the result being

$$\begin{aligned}\sqrt{\sigma} = & -\mathrm{i}\frac{kLW}{\sqrt{\pi}}\,\hat{n}\cdot\hat{e}_r\times\hat{h}_i\,\mathrm{e}^{\mathrm{i}k\bar{r}_0\cdot(\hat{i}-\hat{s})} \\ & \times\frac{\sin\left[(1/2)k\bar{L}\cdot(\hat{i}-\hat{s})\right]}{(1/2)\,k\bar{L}\cdot(\hat{i}-\hat{s})}\cdot\frac{\sin\left[(1/2)k\bar{W}\cdot(\hat{i}-\hat{s})\right]}{(1/2)k\bar{W}\cdot(\hat{i}-\hat{s})}\end{aligned} \tag{5.14}$$

where $\bar{W}$ and $\bar{L}$ are vectors aligned along the width and length of the plate and have the attributes of length as well as direction. Note that this is a bistatic result because no restrictions have been placed on the directions of incidence and scattering.

By way of illustration, Figure 5.2 shows the bistatic scattering pattern for a plate illuminated at an oblique angle. Note that there are two prominent lobes, one precisely in the forward direction and one in the specular direction. The lobes are equal in amplitude, which occurs only for flat structures like the plate. The strength of the forward scattered lobe for any obstacle is proportional to the projected area of the obstacle, and for the plate, the strength of the specular lobe is also proportional to the projected area. For scattering obstacles of other shapes, however, the specular lobe, if there is one, is less intense. The strong forward scattering combines with the incident field to create a shadow behind the obstacle.

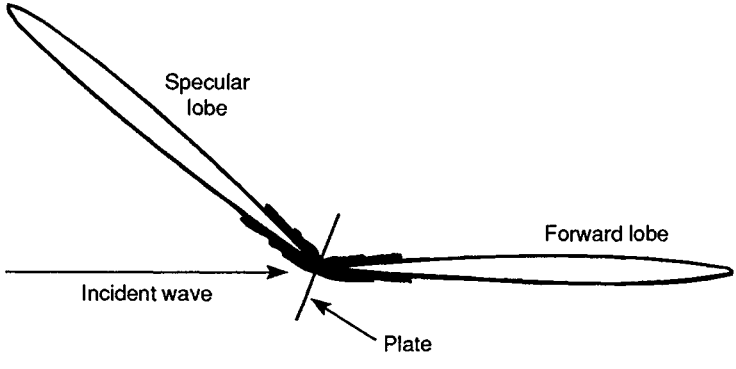

Figure 5.2. Bistatic scattering pattern of a flat plate.

Figure 5.3 illustrates the bistatic scattering for a collection of incident angles in which the forward lobe has been omitted for clarity. Note that the main lobe is always centered on the specular direction. Although it may be difficult to detect differences in the amplitudes of the lobes from the small-scale patterns in this figure, the strength of the specular lobe decreases with the projection of the area of the plate in the specular direction, as suggested by the first two patterns at the upper left.

The quadrilateral plate is an inconvenient surface element for modeling some surfaces. A more basic element is the triangular plate: any large, smooth surface can be approximated by a collection of small triangles placed edge to edge over the surface. Moreover, as shown by Gordon [13], the surface integral in (5.12) can be easily converted to a contour integral. When evaluated for polygonal plates, we obtain the expression

$$\sqrt{\sigma} = -\frac{\hat{n} \cdot \hat{e}_r \times \hat{h}_i}{\sqrt{\pi}\, T} e^{ik\bar{r}_0 \cdot \bar{w}} \sum_{m=1}^{M} (\hat{p} \cdot \bar{a}_m)\, e^{ik\bar{r}_m \cdot \bar{w}} \frac{\sin(k\bar{a}_m \cdot \bar{w}/2)}{k\bar{a}_m \cdot \bar{w}/2} \tag{5.15}$$

where

σ = bistatic RCS of the plate
$\hat{n}$ = the unit normal of the illuminated plate surface
$\hat{e}_r$ = a unit vector along the electric polarization of a farfield receiver

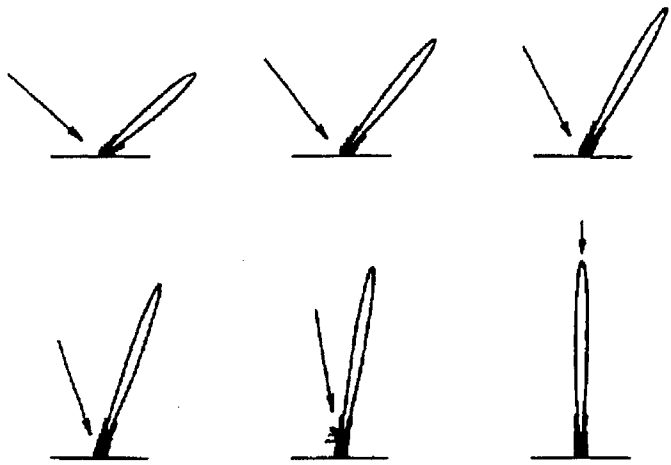

Figure 5.3. The main scattering lobe is always centered on the specular direction.

$\hat{h}_i$ = a unit vector along the incident magnetic field
$\bar{r}_0$ = the position vector of an origin on or near the plate
$\bar{w} = \hat{\imath} - \hat{s}$
$\bar{a}_m$ = a vector describing the length and orientation of the mth edge of the plate, arranged tip to tail around the perimeter
$\bar{r}_m$ = the position vector of the midpoint of the mth edge
T = the length of the projection of $\bar{w}$ onto the plane of the plate
$\hat{p} = \hat{n} \times \bar{w} / |\hat{n} \times \bar{w}|$ = a unit vector in the plane of the plate perpendicular to $\bar{w}$
M = the number of plate edges

Note that the total return is composed of a collection of $\sin(x)/x$ patterns, one for each edge, and that the expression appears to become singular when the factor $T = 0$. This implies that there is no component of $(\hat{\imath} - \hat{s})$ in the plane of the plate, and consequently, the surface coincides with the surface of equal phase delay from the source to the farfield point of observation. In other words, not even the phase varies over the surface, hence, the integral (5.10) reduces simply to the area of the plate, A. Thus, in the event $T = 0$, (5.15) becomes

$$\sqrt{\sigma} = -\frac{ikA}{\sqrt{\pi}} \hat{n} \cdot \hat{e}_r \cdot \hat{h}_i \, e^{ik\bar{r}_0 \cdot \bar{w}} \tag{5.16}$$

For monostatic scattering, this becomes the familiar broadside return:

$$\sigma = 4\pi A^2/\lambda^2 \tag{5.17}$$

The physical optics integral is a bit more difficult to evaluate when applied to a right circular cylinder. The integration is best performed in cylindrical coordinates, for which the surface patch of integration is

$$dS = a \, d\phi \, dz \tag{5.18}$$

and in which the surface position vector $\bar{r}$ can be expressed in terms of axial and circumferential components:

$$\bar{r} = \bar{r}_0 + z\hat{z} + a\hat{n} \tag{5.19}$$

where a is the radius of the cylinder, $\hat{z}$ is a unit vector along the cylinder axis, $\hat{n}$ is an outward surface normal on the curved surface, and $\bar{r}_0$ is, as with the flat plate, the position vector to the origin of the coordinate system from some main origin associated with the mother target of which the cylinder is a component. It is assumed that the cylinder has end caps whose returns can be calculated from the

flat plate expression, hence, only the contribution from the curved surface is to be calculated here.

When (5.18) and (5.19) are inserted in (5.12), the result is expressed in terms of two integrals, one with a variable of integration along the axial direction and the other with a variable in the circumferential direction. The expression is

$$\sqrt{\sigma} = -\mathrm{i}\frac{ka}{\sqrt{\pi}} I_z I_\phi \, \mathrm{e}^{\mathrm{i}k\hat{r}_0\cdot(\hat{i}-\hat{s})} \tag{5.20}$$

where the axial and circumferential integrals are

$$I_z = \int_{-l/2}^{l/2} \mathrm{e}^{\mathrm{i}kz\hat{z}\cdot(\hat{i}-\hat{s})}\,\mathrm{d}z \tag{5.21}$$

$$I_\phi = \int_{-\pi/2}^{\pi/2} \hat{n}\cdot\hat{e}_r \times \hat{h}_i \, \mathrm{e}^{\mathrm{i}ka\hat{n}\cdot(\hat{i}-\hat{s})}\,\mathrm{d}\phi \tag{5.22}$$

where ϕ is the circumferential angle of the surface position vector from the plane containing the incident direction and the cylinder axis. The axial integral is easily evaluated, and the result for a cylinder of length l is

$$I_z = l\frac{\sin\left[(1/2)\,kl\hat{z}\cdot(\hat{i}-\hat{s})\right]}{(1/2)\,kl\hat{z}\cdot(\hat{i}-\hat{s})} \tag{5.23}$$

Note that this result is the $\sin(x)/x$ function characteristic of uniformly illuminated rectangular apertures, and we can perform the integration exactly, even for bistatic directions. However, the circumferential integral is not so easily evaluated.

The reason is, at least for bistatic scattering, that the limits of integration of the ϕ integral are not symmetrically disposed with respect to the specular line along the side of the cylinder. This specular line is located in such a way that a surface normal erected anywhere along the line bisects the projections of the angles of incidence and scattering onto a plane perpendicular to the cylinder axis, and the limits of integration are the shadow boundaries due to the incident wave. An exact evaluation of the ϕ integral is available only when the limits of integration are from $-\pi/2$ to $\pi/2$, and this occurs only when the scattering direction lies in the plane of incidence (i.e., the plane containing the incident direction and the cylinder axis). Nevertheless, the integral can be evaluated approximately by means of the method of stationary phase and, for all except cylinders with small diameters, it yields quite acceptable results.

It is common in physical optics problems to encounter integrals in which the phase of the integrand varies rapidly over the surface. The real and imaginary components vary more or less as sinusoids, and as such, the negative cycles of the

variation tend to cancel the positive cycles. Over curved surfaces, however, there is usually a point at which the phase variation slows down and actually stops, and then begins varying in the opposite sense. This point of phase reversal is the dominant contribution to the integral, and it can be evaluated by the method of stationary phase.

We can expand the phase function in a Taylor series, and if all terms beyond the second derivative of that series are ignored, we obtain the approximation

$$\int g(\phi)\, e^{if(\phi)}\, d\phi \simeq \left[\frac{2\pi}{-if''(\phi_0)}\right]^{1/2} g(\phi_0)\, e^{if(\phi_0)} \tag{5.24}$$

where the double prime indicates the second derivative. In this expression, ϕ_0 is the value of the coordinate that forces the first derivative $f'(\phi)$ to zero. In the case at hand, it is none other than the circumferential location of the specular line, at which point the phase is indeed stationary.

Therefore, let us express the outward surface normal $\hat{n}$ in terms of the angle ϕ:

$$\hat{n} = \hat{x} \cos \phi + \hat{y} \sin \phi \tag{5.25}$$

where ϕ is measured from the plane containing the cylinder axis and the incident direction. The angle $\phi = 0$ is the stationary phase point, and the ϕ-integral of (5.22) becomes

$$I_\phi = \hat{n}_0 \cdot \hat{e}_r \times \hat{h}_i\, e^{ika\hat{n}_0 \cdot (\hat{i} - \hat{s})}\, e^{-i\pi/4} \left[\frac{a}{\lambda}\, \hat{n}_0 \cdot (\hat{i} - \hat{s})\right]^{1/2} \tag{5.26}$$

where $\hat{n}_0$ is the outward surface normal erected anywhere along the specular line. When this result is substituted for the ϕ integral of (5.20) and (5.23) substituted for the z-integral, we obtain the bistatic scattering formula for the cylinder:

$$\sqrt{\sigma} = -il \left[\frac{2ka}{\hat{n}_0 \cdot (\hat{i} - \hat{s})}\right]^{1/2} \frac{\sin[(1/2)kl\hat{z} \cdot (\hat{i} - \hat{s})]}{(1/2)kl\hat{z} \cdot (\hat{i} - \hat{s})}$$
$$\times (\hat{n}_0 \cdot \hat{e}_r \times \hat{h}_i)\, e^{ik\bar{r}_0 \cdot (\hat{i} - \hat{s})}\, e^{ika\hat{n} \cdot (\hat{i} - \hat{s})}\, e^{-i\pi/4} \tag{5.27}$$

Note that the stationary phase integration yields a phase factor $\exp(-i\pi/4)$ because of the minus sign in the denominator of the radical of (5.24). If the quantity $\hat{n}_0 \cdot (\hat{i} - \hat{s})$ in (5.27) is negative, the extraction of the root will generate an additional phase factor $\exp(i\pi/2)$, which advances the phase to $\exp(i\pi/4)$. Therefore, the sign of the exponent of the trailing phase term will always be opposite of that of the exponential $\exp[ika\hat{n}_0 \cdot (\hat{i} - \hat{s})]$.

For the case of backscattering, the scattering direction points back in the direction of incidence, and (5.27) reduces to

$$\sqrt{\sigma} = -il\sqrt{ka\hat{n}_0 \cdot \hat{i}}\,\frac{\sin(kl\hat{z}\cdot\hat{i})}{kl\hat{z}\cdot\hat{i}}\,e^{i2k\bar{r}_0\cdot\hat{i}}\,e^{i2ka\hat{n}_0\cdot\hat{i}}e^{-i\pi/4} \tag{5.28}$$

If we take the amplitude of this expression and square it, we obtain the familiar equation for the monostatic radar cross section of the right circular cylinder:

$$\sigma = kal^2\left|\cos\theta_i\,\frac{\sin(kl\sin\theta_i)}{kl\sin\theta_i}\right|^2 \tag{5.29}$$

where θ_i is the angle from broadside incidence (see Fig. 5.4). Note that the RCS rises linearly with the electrical circumference of the cylinder and with the square of its length.

When the cylinder axis and the directions of incidence and scattering all lie in the same plane, as suggested in Figure 5.4, the physical optics integral can be evaluated exactly, even if the integral itself is an approximation. In this event, the limits of integration (i.e., the shadow boundaries along the side of the cylinder) in (5.22) are symmetrically placed on either side of the specular line. In this event, the ϕ integral can be evaluated exactly, and for the case of backscattering, (5.22) becomes

$$I_\phi = \{\pi\,[S_1(2ka\cos\theta) + iJ_1(2ka\cos\theta)] - 2\}\cos\theta \tag{5.30}$$

where S_1 and J_1 are the Struve function and the Bessel function of the first kind, respectively. It turns out, however, that this exact evaluation of the ϕ integral does not necessarily yield more accurate results than the stationary phase approximation.

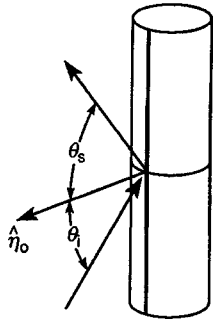

Figure 5.4. Cylinder bistatic scattering geometry for scattering in the plane of incidence. The specular scattering arises from a line down the side of the cylinder and the vector n_0 is a unit surface normal erected on that line.

A comparison of the result from the two ways of evaluating the integral in the case of backscattering is shown in Figure 5.5. The two traces represent the broadside RCS of the cylinder normalized with respect to the square of the length, with the solid trace representing the results of the stationary phase evaluation. As suggested by (5.29), the RCS is a straight line that varies linearly with the electrical circumference of the cylinder. The dashed line represents the solution in which the ϕ integral is given by (5.30), and it oscillates about the line representing the stationary phase approximation. The reason for the undulation is that the discontinuity in the assumed induced surface fields gives rise to a contribution from the shadow boundary that goes in and out of phase with the specular return from the near side of the cylinder as the cylinder grows electrically larger. Indeed, the periodicity of the undulation is appropriate to the returns from two scattering centers separated by the cylinder radius. It should be noted from (5.28) that the backscattering depends on the angle of incidence, but not on the polarization. Therefore, physical optics gives the same results for any incident polarization, whether we use the exact evaluation of the physical optics integral or the stationary phase approximation.

By contrast, the exact solution of the wave equation for the circular cylinder depends on the incident polarization, as is shown in Figure 5.6. The solid and dashed traces represent the solution when the incident electric and magnetic fields

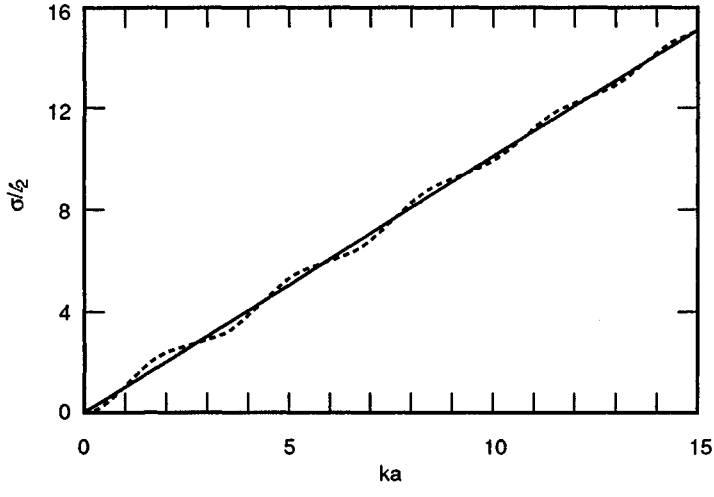

Figure 5.5. RCS of the cylinder as obtained from the physical optics approximation. The dashed trace is obtained from an exact evaluation of the PO integral, and the solid trace is obtained from a stationary phase evaluation.

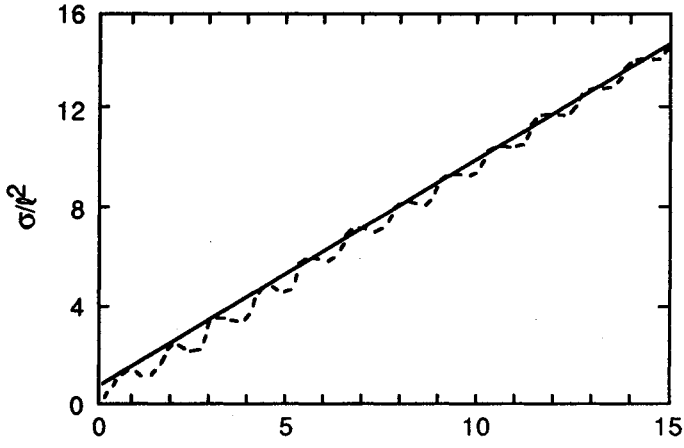

Figure 5.6. RCS of the cylinder as obtained from the exact (two-dimensional) solution. The solid trace is for *E*-polarization and the dashed for *H*-polarization.

are parallel to the cylinder axis, called *E*- and *H*-polarization, respectively. The exact *H*-polarization solution exhibits undulations not unlike those of the dashed trace of Figure 5.5, but the periodicity is quite different. The source of the undulations in the exact solution is a creeping wave that circles the rear of the cylinder boundary. However, because it actually traverses the rear of the cylinder, the phase of the creeping wave is delayed significantly more than that of the fictitious shadow boundary contribution, hence, the period of the undulations is much shorter than those of the Struve function solution represented by the dashed trace of Figure 5.5. The undulations in the dashed trace of Figure 5.6 are due to precisely the same mechanism that creates the undulations for the sphere shown in Figure 3.14.

The errors in the physical optics approximation are worse for small cylinders than for large ones, as shown in Table 5.1. Neither form of the PO approximation works as well for *H*-polarization as it does for *E*-polarization, the error being on the order of 2.5 to 3.5 dB for $ka = 1.4$ (for *E*-polarization, it is on the order of 0.5 dB or less). The error in the PO approximation decreases to 0.15 dB or less for $ka = 9.7$ and diminishes even further with increasing size. Therefore, the approximation is well within a decibel of the exact solution for cylinders as small as 1.5 wavelengths in diameter. Moreover, the stationary phase approximation yields slightly better accuracy than does the exact evaluation of the PO integral. Because the exact evaluation requires the generation of Struve functions, a significant undertaking, the stationary phase result is far more appealing.

As with the right circular cylinder, the physical optics integral cannot be evaluated in a closed form solution for even a sphere for bistatic directions. Again,

Table 5.1
Errors of the Physical Optics Approximation

	Decibel Errors			
	Stat. phase	Stat. phase	Struve	Struve
ka	exact *H*	exact *E*	exact *H*	exact *E*
1.4	2.50	−0.61	3.35	0.25
4.9	0.44	−0.09	0.66	0.13
9.7	0.15	−0.03	0.08	−0.10

this is because the limits of integration are not symmetrically disposed about the specular direction. For the same reason, we cannot even compute the RCS of a spherical cap in other than the backscattering and forward scattering directions. Nevertheless, it is of interest to examine the results for the special case of backscattering.

Upon evaluating the physical optics integral for the sphere, we obtain the result [14]

$$\sqrt{\sigma} = \sqrt{\pi}\, a \left[\left(1 + \frac{1}{i2ka} \right) e^{-i2ka} - \frac{1}{i2ka} \right] \tag{5.31}$$

where a is the radius of the sphere and the phase of the echo has been referenced to the center of the sphere. Note that this expression contains three terms, the first of which is identical to the geometric optics result obtained earlier. The second term is a correction to the first and agrees with the next term in the exact solution, also call the *Mie series*. The phase of these two terms is retarded by twice the radius of the sphere and is therefore consistent with the location of the specular point at the front of the sphere (nearest the radar). The third term is due to the discontinuity of the assumed induced currents across the shadow boundary, and the phase of this term is consistent with the location of the shadow boundary. However, we must regard the term as fictitious because the induced currents do not drop suddenly to zero at the shadow boundary as assumed. Indeed, the result of (5.31) is more appropriate to the scattering from a hemispherical shell than to a complete sphere because, in that case, the induced fields change rapidly at the edge, which is also the shadow boundary.

For all the backscattering cases just considered, the polarization term $\hat{e}_r \times \hat{h}_i$ always yields a maximum when the receiver polarization is aligned along the incident polarization and yields precisely zero when aligned 90° from that polarization. Hence, physical optics can yield no estimate of the cross-polarized return. Also, because the theory includes an erroneous contribution due to the shadow boundaries on otherwise smooth objects, we might be better off using the theory of geometric optics for smooth, doubly curved bodies. In addition to these failures,

physical optics also gives increasingly erroneous results as the scattering direction moves further away from the specular direction, as will be shown in Chapter 6. The reason for this last failure is that the role of the edges bounding the surface has been ignored. These failures were recognized by Keller and Ufimtsev, and their pioneering efforts considerably advanced the ease with which RCS calculations can be performed.

5.4 GEOMETRICAL THEORY OF DIFFRACTION

Keller was well aware of the wide-angle failure of physical optics and introduced his classic geometrical theory of diffraction as a way of computing scattered fields well away from the specular directions. It was shown earlier that when a ray or electromagnetic wave impinges on a flat infinite surface, part of the wave or ray is reflected and part is transmitted through the surface. Whether the surface is dielectric or perfectly conducting, the reflected ray can propagate in only one direction in space; that direction is in the plane of incidence containing the incident ray and the surface normal, and it subtends the same angle with respect to the surface normal as does the incident ray. This unique specular direction of the reflected ray is a consequence of the doubly infinite size of the surface.

If the doubly infinite surface is now halved, thereby generating an edge, we may think of the reflected (or scattered) fields as arising from two sources, one being a surface contribution, as before, plus an edge contribution. Ignoring for the moment the surface contribution, let us consider the edge and the components of an incident ray parallel and perpendicular to it. We would expect reflected ray components along the edge to be constrained to a unique direction because that dimension of the edge is infinite. However, we would expect the transverse components of reflected rays to propagate in all directions perpendicular to the edge because the transverse dimension of the edge is zero. Thus, in contrast to the single, unique direction taken by the ray reflected by a surface, an edge-reflected ray can lie anywhere along a forward cone whose half-angle is precisely that subtended by the edge and the incident ray. This is the well-known Keller cone sketched in Figure 5.7. It represents the extension of Fermat's principle to diffraction by an edge, and the rays are understood to be *diffracted* rays.

If the edge singularity were somehow divorced from the surface it bounds, it would be a filament. If it were a conducting filament (i.e., a wire), we would expect the diffracted rays to have the same amplitude no matter where on the diffraction cone they might be. Indeed, this is the case. But how do we account for the presence of the surface that ends at the edge? Certainly, the diffracted rays on one side must be weaker than those on the other, especially for directions shaded from the incident ray by the surface itself. In other words, we expect the intensities of the diffracted rays to vary from one direction to another around the diffraction cone. What is that variation?

To get an answer, Keller turned to the exact solution of a two-dimensional canonical problem, the diffraction from an infinite wedge or half-plane, such as

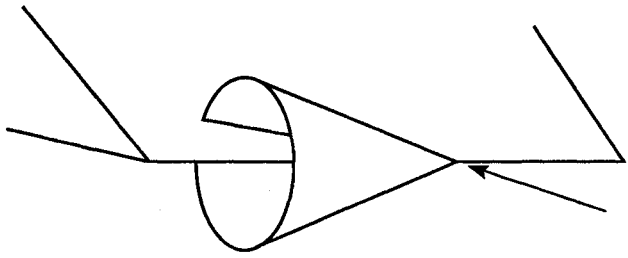

Figure 5.7. The Keller cone of diffracted rays.

obtained by Sommerfeld [15, 16]. In Sommerfeld's two-dimensional problem, the incident ray impinges on the edge at right angles, and Sommerfeld represented the diffracted rays as a spectrum of plane waves. His solution amounts to finding the coefficients of each of the elementary plane waves diffracted by the edge. Hence, for any scattering direction, the strength of the diffracted ray can be calculated. The Sommerfeld two-dimensional solution for diffracted rays can be applied to Keller's three-dimensional problem by adjusting Sommerfeld's propagation constants to match the transverse propagation components of Keller's problem. The direction-dependent amplitudes of Sommerfeld's solution then make it possible to estimate the amplitude and phase of a diffracted ray anywhere on the Keller cone. This yielded the key ingredient of the theory: the *diffraction coefficients,* which depend on the polarization of the incident ray.

The other ingredients of Keller's GTD include the decay in field intensity away from the diffracting edge and the phase of the ray along its propagation path. The intensity of the diffracted ray thus has the form

$$u = \frac{De^{iks}}{[s(1 + s/\rho_1)]^{1/2}} Ae^{ik\psi} \tag{5.32}$$

where D is a diffraction coefficient depending on the polarization and angle of arrival of the incident ray and the direction of the scattered ray, s is the distance along the ray from the edge element to a farfield observation point, A and ψ are the amplitude and phase of the incident ray, respectively, and ρ_1 is the distance from the edge element to a caustic of the diffracted ray.

When (5.32) is applied to the components of the far diffracted electric field, the diffracted field can be expressed as

$$\begin{aligned} \bar{E}_d = & -\frac{\Gamma e^{iks}}{\sin^3 \beta} [(\hat{t} \cdot \bar{E}_i)(X - Y)\hat{s} \times (\hat{s} \times \hat{t}) \\ & + Z_0 (\hat{t} \cdot \bar{H}_i)(X + Y)\hat{s} \times \hat{t}] \end{aligned} \tag{5.33}$$

where Γ is a divergence factor accounting for the nature of the edge excitation (plane wave, spherical wave, et cetera) and the spreading of energy away from the edge, and β is the angle subtended by the edge and the incident ray. In this expression, $\hat{t}$ is a unit vector aligned along the edge, and the diffraction coefficients are given by

$$X = \frac{(1/n)\sin(\pi/n)}{\cos(\pi/n) - \cos[(\psi_s - \psi_i)/n]} \tag{5.34}$$

$$Y = \frac{(1/n)\sin(\pi/n)}{\cos(\pi/n) - \cos[(\psi_s + \psi_i)/n]} \tag{5.35}$$

where n is the exterior wedge angle normalized with respect to π, and ψ_i and ψ_s are the angles of the transverse components of the incident and diffracted directions with respect to one of the surfaces meeting at the edge, as shown in Figure 5.8. It should be noted that (5.34) and (5.35) are the form of the diffraction coefficients as suggested by Ufimtsev, although Ufimtsev did not specifically label them X and Y. The notation is not due to Keller either, but to Senior and Ushlenghi [17]. We

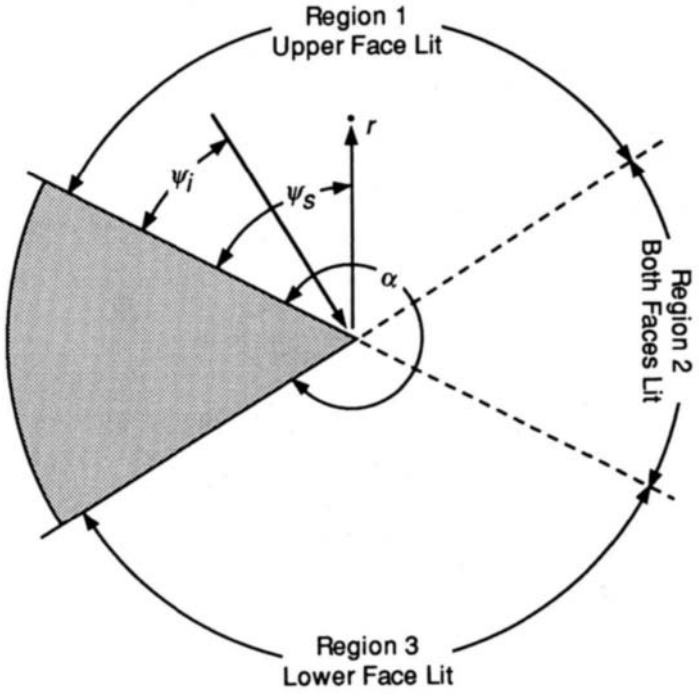

Figure 5.8. Geometry for wedge diffraction.

use the difference in the coefficients for those components of the incident magnetic polarizations along the edge. To obtain the RCS due to an edge, we need only substitute the field of (5.33) into (1.12) or (5.11).

In applying (5.33) to a scattering obstacle with edges, we must first find those edge elements for which a generator on the local Keller cone pierces the farfield observation point. We can imagine hundreds, and perhaps thousands, of little Keller cones erected on edges all over the target and dozens distributed along all curved edges. Only the contributions from those edges having Keller-cone directions toward the farfield point are included in the calculation, and all others are ignored. Thus, GTD is a kind of specular theory in precisely the way geometric optics is specular and, like geometric optics, GTD has certain failures.

For one, the diffraction coefficients are actually the result of a wide angle evaluation of an integral, and if the scattering direction approaches too close to a shadow boundary or reflection boundary, one or the other of the coefficients becomes singular. The results are obviously wrong because the far diffracted fields must remain finite in the real world. The difficulty can be traced to the wide angle approximation of the integral mentioned previously, which is not valid in the transition regions of the reflection and shadow boundaries. The coefficients should be replaced by more accurate expressions than those of (5.34) and (5.35), which shall be addressed later. In addition to the failure of the diffraction coefficients in the transition regions, there may be curved edges on the scattering obstacle for which the Keller cones erected at every point along the contour contain the scattering direction. In this case, an infinity of points contribute to the far diffracted field, and we obtain an infinite result. It is serious enough to cause concern because it occurs, for example, whenever a ring, such as the open end of a tube, is presented normal to the incident wave. Such features are common on bodies of revolution of great practical and tactical importance.

5.5 A UNIFORM ASYMPTOTIC THEORY

Kouyoumjian and Pathak are generally credited with the development of the *uniform theory of diffraction* (UTD) [3], and Lee and Deschamps for developing the *uniform asymptotic theory* (UAT) [18, 19]. Each strives to accurately represent the diffracted field, but by using different approaches. Although Deschamps, Boersma, and Lee [19] contend that their UAT recovers the exact solution for the diffraction of a three-dimensional half-plane, here we shall summarize the procedure used in the UTD of Kouyoumjian and Pathak.

The singularities in the diffraction coefficients are overcome in the UTD essentially by the multiplication of the diffraction coefficients by a Fresnel integral. At the shadow boundary or the reflection boundary, the modifying Fresnel integral is zero whereas the diffraction coefficient is infinite, but the product of the two remains finite. The prescription given by Kouyoumjian and Pathak is

$$X = \frac{1}{2}\left[\cot\frac{\pi + (\psi_s - \psi_i)}{2n} F[kLa^+(\psi_s - \psi_i)] + \cot\frac{\pi - (\psi_s - \psi_i)}{2n} F[kLa^-(\psi_s - \psi_i)]\right] \tag{5.36}$$

$$Y = \frac{1}{2}\left[\cot\frac{\pi + (\psi_s + \psi_i)}{2n} F[kLa^+(\psi_s + \psi_i)] + \cot\frac{\pi - (\psi_s + \psi_i)}{2n} F[kLa^-(\psi_s + \psi_i)]\right] \tag{5.37}$$

where L is a function that depends on the nature of the source of the incident wave (i.e., plane wave, spherical wave, et cetera) and is given explicitly in [3]. The function F is the Fresnel integral:

$$F(Q) = -i\,2\sqrt{Q}\,e^{-iQ}\int_{\sqrt{Q}}^{\infty} e^{iz^2}\,dz \tag{5.38}$$

and it can be verified that, when the argument Q is large, (5.36) and (5.37) reduce exactly to the wide-angle coefficients given in (5.34) and (5.35).

The function

$$a^{\pm}(\eta) = 2\cos^2\left[\frac{1}{2}(2n\pi N^{\pm} - \eta)\right] \tag{5.39}$$

where the integers N are those that most nearly satisfy

$$2n\pi N^+ - \eta = \pi,\ 2n\pi N^- - \eta = -\pi$$

In the transition regions, the cotangent functions rise to infinity whereas the Fresnel integrals drop to 0 in such a way that the product remains finite:

$$\cot\frac{\pi \pm \epsilon}{2n} F[kLa^{\pm}(\epsilon)] \simeq n\{\sqrt{2\pi kL}\,\operatorname{sgn}\epsilon - 2kL\epsilon\,e^{-i\pi/4}\}\,e^{-i\pi/4} \tag{5.40}$$

where ϵ is a small angle measured from the optical shadow or reflection boundary, as the case may be. The amplitude of this function is the same on either side of that boundary, but its sign changes; hence the diffraction coefficients are discontinuous across the boundary. The discontinuity is necessary to compensate for the abrupt change of the geometrical optics field from the illuminated region to the shadowed region or from one side of the reflection boundary to the other side.

The Fresnel integral approaches unity for large arguments, hence its value can be taken as one for wide angles. Therefore, for angles well away from either

transition region, we may use the simpler expressions, (5.34) and (5.35). When the scattering direction approaches one of the transition regions, only the affected diffraction coefficient needs to be calculated more carefully with the aid of either (5.36) or (5.37). This is because X becomes singular at the shadow boundary, but Y becomes singular at the reflection boundary, hence they never become singular simultaneously. For this reason, it is necessary to use the more complicated expression involving the Fresnel integral only for the affected diffraction coefficient. Figure 5.9 compares the behavior of the diffraction coefficients of (5.34) through (5.37) in the transition regions. It can be seen that the UTD indeed removes the singularities.

However, the uniform theory of diffraction does not eliminate the difficulties of the caustics of GTD, where an infinity of rays may converge. This is a particularly serious flaw, because many bodies of great practical interest are bodies of revolution. As such, many have ring discontinuities where different surfaces join each other, such as the junction between a cylinder and a cone, a very common feature of reentrant bodies. The caustics due to such rings coincide with the body axis in the far field, and we obtain the wrong answer for important aspect angles such as nose-on incidence. However, there is a way to fix the difficulty: the method of equivalent currents.

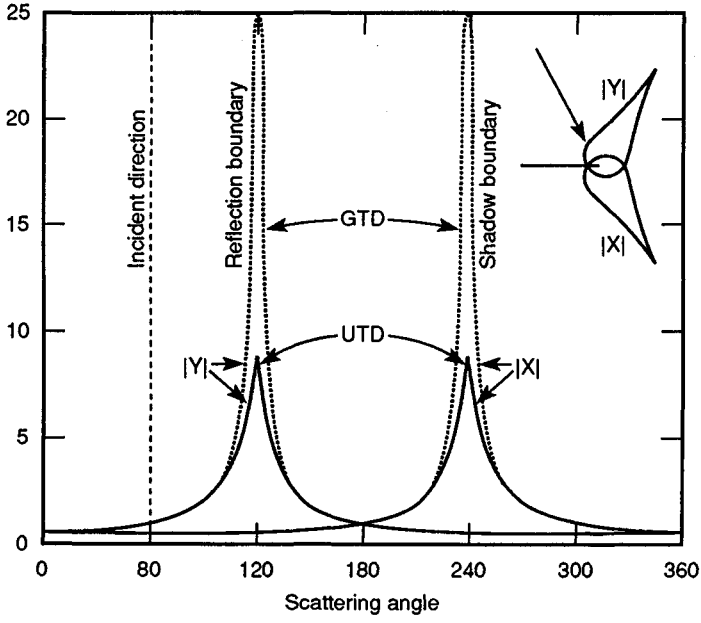

Figure 5.9. Comparison of the diffraction coefficients of GTD and UTD for an incident angle of 60° on the edge of a half-plane. Inset shows a polar diagram of the cofficients.

5.6 THE METHOD OF EQUIVALENT CURRENTS

The method of equivalent currents stems from the fact that any finite current distribution yields a finite result for the far diffracted field when that distribution is summed in a radiation integral. If the proper distribution can be found, then the axial caustics of the GTD can be avoided. Moreover, the method of equivalent currents extends the promise that the diffracted fields can be computed for scattering directions not on the Keller cone, a significant extension of Keller's theory. Thus, there are two important motivations for devising equivalent currents.

The notion of equivalent currents was employed by Millar in his studies of the diffraction by apertures [20], and Ryan and Peters used them to compute the fields along the axial caustics of bodies of revolution [4]. The basic approach is to postulate the existence of filamentary electric and magnetic currents I_e and I_m at each point around the singularity (the edge contour) and to sum them in the farfield radiation integral:

$$\bar{E}_d = -ik\psi_0 \int [Z_0 I_e \hat{s} \times (\hat{s} \times \hat{t}) + I_m (\hat{s} \times \hat{t})] \, e^{-ik\hat{r}\cdot\hat{s}} \, dt \tag{5.41}$$

where ψ_0 is the farfield Green's function defined earlier and $\hat{t}$ is a unit vector aligned along the contour. As we shall see, the equivalent currents are fictitious because they depend on the scattering direction as well as the direction of incidence, but they overcome the caustic difficulties. Perhaps the strongest defense of them is that they yield what appears to be the correct result in directions where GTD does not.

The equivalent currents proposed by Ryan and Peters are

$$I_e = i2 \, (X - Y) \, (\hat{t} \cdot \bar{E}_i)/kZ_0 \tag{5.42}$$

$$I_m = i2 \, (X + Y) \, (\hat{t} \cdot \bar{H}_i)/kY_0 \tag{5.43}$$

When these currents are used in (5.41), we can obtain the scattered fields anywhere, not just on the Keller cone. Later, Knott and Senior improved the equivalent current prescription by requiring that a stationary phase evaluation of the integral (5.41) yield the exact GTD result for directions on the Keller cone [5]. This had the effect of dividing the currents in (5.42) and (5.43) by $\sin^2\beta$, where β is the angle subtended by the incident ray and the local edge tangent where the currents are postulated. The two prescriptions become identical when $\beta = 90°$, of course, such as for backscattering along the axis of a ring discontinuity.

In an attempt to extend the equivalent current notion to general bistatic cases, in which the scattering direction need not lie on the Keller cone, Knott and Senior interpreted the product

$$\sin^2 \beta = \sin \beta_i \sin \beta_s \tag{5.44}$$

where the subscripts i and s denote the angle subtended by the incident and scattering directions. For the cases they studied, however, β_i and β_s remained close enough to each other that the distinction between the two interpretations was small. When the equivalent currents are inserted in (5.41), the result is the contour integral:

$$\begin{aligned}\bar{E}_d = & -2E_0\psi_0 \int_c \frac{e^{ik\bar{r}\cdot(\hat{i}-\hat{s})}}{\sin\beta_i \sin\beta_s} \\ & \times [(\hat{t}\cdot\hat{e}_i)(X-Y)\hat{s}\times(\hat{s}\times\hat{t}) + (\hat{t}\cdot\hat{h}_i)(X+Y)\hat{s}\times\hat{t}]dt\end{aligned} \tag{5.45}$$

where $\hat{e}_i$ and $\hat{h}_i$ are unit vectors aligned along the incident electric and magnetic fields and the contour c includes only the illuminated portions of the edge.

We have already seen that the diffraction coefficients X and Y depend on the projections of the directions of incidence and scattering onto the plane perpendicular to the edge. These coefficients vary around the edge singularity with the result that the integral cannot be evaluated in closed form for the general case. This need not deter us, of course, because there are ways to perform the integration, even if approximate. For one, the integral can always be evaluated numerically with a computer, although this is not a very effective method. Another option is to expand the diffraction coefficients in a Fourier series, which is usually effective for circular discontinuities. The method of stationary phase is particularly useful, and as expected, the result is that the scattering is due primarily to the "flash points" around the contour where incident and scattering directions subtend identically the same angle. In this case, the scattering direction lies on the Keller cones erected at the flash points. For special cases in which the phase is constant around the contour, the flash points spread out over the entire edge, and instead of a pair of bright flash points (one each at the near and far edges of a ring, for example), the entire ring lights up.

In examining these equivalent current postulates, Michaeli proposed a more rigorous development [6]. He considered the farfield contribution due to two narrow surface strips (one on each face of a wedge) meeting at an edge element and integrated the induced currents along the strips. In the direction along the surfaces perpendicular to the edge, only the asymptotic contribution of the end-point of integration (the edge) is retained, and upon comparing the result with the form of the surface integral (5.41), Michaeli deduced the form of the equivalent currents. He then related the surface integrals to the canonical solution for the wedge and arrived at the equivalent current prescription:

$$I_e = \frac{i2\,(\hat{t}\cdot\bar{E}_i)\,D_e}{kZ_0 \sin^2\beta_i} + \frac{i2\,(\hat{t}\cdot\bar{H}_i)\,D_{em}}{k\sin\beta_i} \tag{5.46}$$

$$I_m = -\frac{i2\,(\hat{t}\cdot\bar{H}_i)\,D_m}{kY_0 \sin\beta_i \sin\beta_s} \tag{5.47}$$

where the diffraction coefficients D_e, D_m, and D_{em} are

$$D_e = \frac{\frac{1}{n}\sin\frac{\phi_i}{n}}{\cos\frac{\pi-\alpha_1}{n} - \cos\frac{\phi_i}{n}} + \frac{\frac{1}{n}\sin\frac{\phi_i}{n}}{\cos\frac{\pi-\alpha_2}{n} + \cos\frac{\phi_i}{n}} \tag{5.48}$$

$$D_m = \frac{\sin\phi_s}{\sin\alpha_1}\cdot\frac{\frac{1}{n}\sin\frac{\pi-\alpha_1}{n}}{\cos\frac{\pi-\alpha_1}{n} - \cos\frac{\phi_i}{n}} + \frac{\sin(n\pi-\phi_s)}{\sin\alpha_2}\cdot\frac{\frac{1}{n}\sin\frac{\pi-\alpha_2}{n}}{\cos\frac{\pi-\alpha_2}{n} + \cos\frac{\phi_i}{n}} \tag{5.49}$$

$$D_{em} = \frac{Q}{\sin\beta_i}\left[\frac{\cos\phi_s}{\sin\alpha_1}\cdot\frac{\frac{1}{n}\sin\frac{\pi-\alpha_1}{n}}{\cos\frac{\pi-\alpha_1}{n} - \cos\frac{\phi_i}{n}} - \frac{\cos(n\pi-\phi_s)}{\sin\alpha_2}\cdot\frac{\frac{1}{n}\sin\frac{\pi-\alpha_2}{n}}{\cos\frac{\pi-\alpha_2}{n} + \cos\frac{\phi_i}{n}}\right] \tag{5.50}$$

with

$$Q = \sin\beta_s\cot\beta_i - \sin\beta_i\cot\beta_s \tag{5.51}$$

$$\sin\alpha_1 = [\sin^2\beta_i - \sin^2\beta_s\cos^2\phi_s]^{1/2}/\sin\beta_i \tag{5.52}$$

$$\sin\alpha_2 = [\sin^2\beta_i - \sin^2\beta_s\cos^2(n\pi-\phi_s)]^{1/2}/\sin\beta_i \tag{5.53}$$

The diffraction coefficients in (5.48) through (5.50) reduce exactly to the Keller coefficients X and Y when the scattering direction lies on the Keller cone, as indeed they must. For arbitrary directions, they are very complicated, and there is no more hope of evaluating a contour integral containing them (via the equivalent currents) than there is with the simpler expressions devised by Ryan and Peters or Knott and Senior. Nevertheless, Michaeli's equivalent currents are more complete and were derived more rigorously. Note from (5.46), for example, that the equivalent electric current is due to the excitation of the edge element by the incident magnetic field as well as the incident electric field, a feature missing from the previous equivalent current theories. In addition, it would appear that Michaeli

devised a new set of diffraction coefficients because those in (5.48) through (5.50) are the generalized versions of the Keller coefficients X and Y. We will have more to say about this in a moment.

Whatever the case, the equivalent currents extend Keller's GTD in two important aspects. First, edge-diffracted fields remain finite in caustic directions. Although the caustics may be corrected in other ways, the equivalent currents represent a unified approach. Second, the scattering direction is no longer confined to a generator of the Keller cone, a significant extension. These two improvements are sufficient motivation to use the equivalent currents in any serious computation of the scattering by simple bodies, although the complexity of the diffraction coefficients may prohibit the implementation of the method for complex bodies composed of hundreds or thousands of facets.

Despite Michaeli's extension of Keller's theory to arbitrary directions not on the Keller cone, the diffraction coefficients become singular in the transition regions of the shadow and reflection boundaries. That defect could be remedied by the development of a uniform theory like the UTD discussed previously, but at the time of this writing, such a theory has not yet been put forth. An alternative is the *incremental length diffraction coefficient* (ILDC) developed by Mitzner [8], which remains finite in the transition regions (as discussed in Section 5.8). However, because Mitzner's theory is based on Ufimtsev's PTD, we discuss the latter first.

5.7 THE PHYSICAL THEORY OF DIFFRACTION

Like Keller, Ufimtsev sought a more accurate representation of the scattered fields than yielded by physical optics and he relied on the canonical solution of the scattering by a wedge for his diffraction coefficients, but, unlike Keller, he retained in his solution the approximate physical optics result and sought instead a correction by which to improve the physical optics approximation. He therefore represented the scattered field as the sum of the physical optics contribution and an edge contribution, using the exact solution of the two-dimensional wedge problem to extract the latter. That is, if we have in hand the exact solution and subtract from it the physical optics (surface) contribution, what remains must be the contribution from the edge itself, there being no other scattering features present except the surface and the edge.

In developing his PTD, Ufimtsev claims to have considered the "nonuniform" induced edge currents in addition to the "uniform" induced surface currents of physical optics, but nowhere in his work will the reader find an explicit representation of the edge currents. He considered instead the scattered fields, not the surface currents, of the exact solution for a wedge. Nevertheless, we are seldom interested in the surface field, except as a means by which to compute the scattered field, hence his approach is defensible.

As in most two-dimensional problems, Ufimtsev recognized two distinct cases depending on whether the incident field is polarized parallel or perpendicular to the edge. Arbitrary polarizations, of course, can be handled as linear combinations of the two cases. He represented the total fields (incident plus scattered fields) as

$$E_z = E_{oz}[u(r, \psi_s - \psi_i) - u(r, \psi_s + \psi_i)] \tag{5.54}$$

$$H_z = H_{oz}[u(r, \psi_s - \psi_i) + u(r, \psi_s + \psi_i)] \tag{5.55}$$

where

$$u(r, \psi) = \frac{1}{2\alpha} \int_C \frac{e^{-ikr\cos\beta}}{1 - \exp[i\pi(\beta + \psi)/\alpha]} \, d\beta \tag{5.56}$$

where r is the distance from the edge to the point of observation, ψ_s is the angular coordinate of that point above one face of the wedge, ψ_i is the direction of arrival of the incident wave, similarly measured, α is the external wedge angle, and C is the Sommerfeld contour in the complex plane. Equations (5.54) through (5.56) represent Sommerfeld's classic solution of the wedge problem.

To obtain the edge-diffracted field, Ufimtsev subtracted the incident field and the physical optics approximation of the scattered field. We have seen that the physical optics field is a surface integral, and in the case of the wedge, the surface is infinite in extent. How, then, did Ufimtsev obtain a finite result? He did so by ignoring the contribution at infinity, but not without justification. We have seen that the result of evaluating the physical optics integral yields the contributions of the stationary phase points or the end-points of integration or both. In the case of the wedge, one of the end-points is the edge itself, but there is no "other" end-point. Even if there were, we could force it to be so far away that the resultant scattered fields would be insignificant. This is exactly the procedure used by Michaeli in developing his equivalent currents. Thus, the physical optics contribution to be subtracted from the exact solution arises from the edge itself. As we shall see, its contribution will be in the form of a diffraction coefficient.

Depending on the direction of arrival of the incident wave, there are three possible physical optics contributions to subtract from the exact solution. One occurs if the upper face is illuminated, but not the lower face, another occurs if the lower face is illuminated, but not the upper, and the third occurs if both faces are illuminated. Thus, Ufimtsev's results have different forms in each of the three different regions shown in Figure 5.8. It is a small annoyance to keep track of these three regions in implementing the PTD in practical computations, but it is a small price to pay for the other advantages of the theory.

Integral (5.56) in the exact solution must be evaluated and substituted in (5.54) and (5.55), and this can be done by means of the familiar method of sta-

tionary phase. The result is none other than the Keller diffraction coefficients of (5.34) and (5.35), at least for angles not too close to the shadow or reflection boundaries. A more exact evaluation of the integral in the transition regions is not necessary, however, because the physical optics contributions effectively eliminate the singularities. Ufimtsev's results can be summarized as follows:

$$E_z^s = E_{oz} f \frac{e^{i(kr+\pi/4)}}{\sqrt{2\pi kr}} \tag{5.57}$$

$$H_z^s = H_{oz} g \frac{e^{i(kr+\pi/4)}}{\sqrt{2\pi kr}} \tag{5.58}$$

where the diffraction coefficients are

$$f = \begin{cases} (X - Y) - (X_1 - Y_1) & 0 \le \psi_i \le \alpha - \pi, \\ (X - Y) - (X_1 - Y_1) - (X_2 - Y_2) & \alpha - \pi \le \psi_i \le \pi, \\ (X - Y) - (X_2 - Y_2) & \pi \le \psi_i \le \alpha. \end{cases} \tag{5.59}$$

$$g = \begin{cases} (X + Y) - (X_1 + Y_1) & 0 \le \psi_i \le \alpha - \pi, \\ (X + Y) - (X_1 + Y_1) - (X_2 + Y_2) & \alpha - \pi \le \psi_i \le \pi, \\ (X + Y) - (X_2 + Y_2) & \pi \le \psi_i \le \alpha. \end{cases} \tag{5.60}$$

where the unsubscripted coefficients are the Keller coefficients of (5.34) and (5.35). The subscripted coefficients are due to the uniform physical optics contributions:

$$X_1 = -\frac{1}{2} \tan [(\psi_s - \psi_i)/2] \tag{5.61}$$

$$Y_1 = -\frac{1}{2} \tan [(\psi_s + \psi_i)/2] \tag{5.62}$$

$$X_2 = \frac{1}{2} \tan [(\psi_s - \psi_i)/2] \tag{5.63}$$

$$Y_2 = -\frac{1}{2} \tan [\alpha - (\psi_s + \psi_i)/2] \tag{5.64}$$

Thus, as evidenced by (5.59) and (5.60), Ufimtsev's diffraction coefficients are none other than Keller's, but modified by the presence of the physical optics "diffraction coefficients." These expressions are well worth considering in more detail.

First, the Keller coefficients should be expected to be singular along the reflection and shadow boundaries. Keller's prescription is obtained from the exact

solution for an infinite wedge, and if we believe that solution, then the fields must be infinite along the reflection boundary. All the incident rays striking the surface must be reflected in the specular direction, and because there is an infinity of such rays, they will produce an infinite field. The same is true at the shadow boundary, marked by no incident field just inside the shadow zone to the full incident field just outside it. The diffraction coefficient must completely cancel the incident field over the entire half-space screened from the incident wave by the wedge surfaces. Hence, it is not unexpected that the diffraction coefficient rises to infinity at the shadow boundary as well as at the reflection boundary.

However, the physical optics contribution from an infinite half-space must also rise to infinity because of the infinite size of the surfaces. Indeed, (5.61) and (5.63) become infinite along the shadow boundaries, whereas (5.62) and (5.64) become infinite along the reflection boundaries. Thus, it would appear that the infinities of the exact solution could be handled adequately by the physical optics diffraction coefficients. This is, in fact, the case, and because the physical optics components have been subtracted by Ufimtsev from the exact solution, what remains is the diffraction from the edge alone. The distinction between the diffraction coefficients of Keller and Ufimtsev, therefore, is that Keller's coefficients inherently contain both surface and edge contributions, whereas Ufimtsev's coefficients contain only the edge contributions. Keller's become infinite in the transition regions but Ufimtsev's remain finite. In fact, it can be shown that in the transition regions Ufimtsev's diffraction coefficients approach the value

$$X - X_1 \text{ or } X - X_2 \to -\frac{1}{2n}\cot\frac{\pi}{n} \tag{5.65}$$

$$Y - Y_1 \text{ or } Y - Y_2 \to -\frac{1}{2n}\cot\frac{\pi}{n} \tag{5.66}$$

Figures 5.10 and 5.11 are graphical comparisons of the diffraction coefficients of Keller and Ufimtsev for the simple case of a half-plane illuminated at an angle of 60° from the surface. In contrast to Figure 5.9 in which the magnitude of the coefficients are displayed, we have retained the sign of the terms in these illustrations. Figure 5.10 compares Keller's X coefficient with Ufimtsev's $X - X'$; Keller's X becomes singular, as noted earlier, along the shadow boundary (240°), and the coefficient changes sign from one side of the shadow boundary to the other. Ufimtsev's coefficient also changes sign at the shadow boundary, but is zero there. It is zero only because the internal wedge angle is zero, and takes on nonzero values at the shadow boundary in accordance with (5.65) for nonzero wedge angles. Keller's Y is compared with Ufimtsev's $Y - Y'$ in Figure 5.11, and it can be seen that the behavior in the diffraction coefficients at the reflection boundary is similar to that at the shadow boundary.

Either the PTD or the GTD can be used to estimate the fields scattered by finite bodies, of course, but the diffraction coefficients come from the solution for

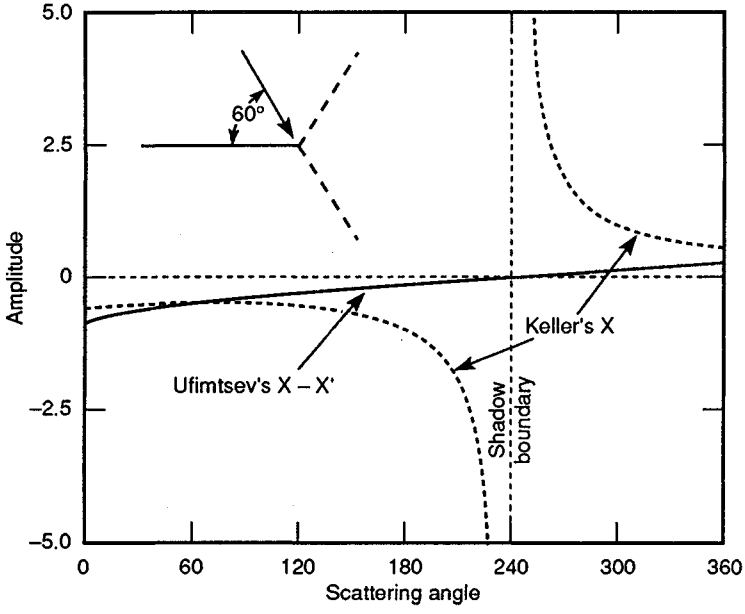

Figure 5.10. Comparison of Keller's X coefficient with Ufimtsev's $X - X'$.

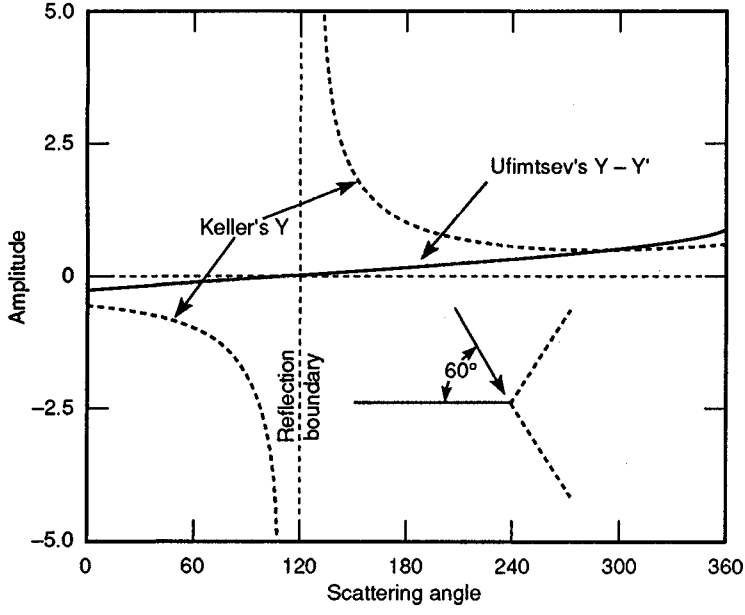

Figure 5.11. Comparison of Keller's Y coefficient with Ufimtsev's $Y - Y'$.

a semiinfinite structure. As such, difficulties will be experienced in problems solved by use of the GTD due to the singularities, although the estimates based on PTD will remain well behaved. However, because the PTD yields only the contributions due to edges, some other method, such as physical optics, must be used to obtain the surface contributions. It seems paradoxical to substract the physical optics contribution to obtain well-behaved diffraction coefficients, only to add them back in treating finite structures, yet the technique works out quite well. However, because both the GTD and the PTD rely on the exact solution of the two-dimensional wedge problem, they are applicable only to scattering directions on the Keller cone. We have seen how the equivalent currents of Michaeli extended the GTD to arbitrary directions. Let us now examine how Mitzner extended the PTD with his incremental diffraction coefficient.

5.8 THE INCREMENTAL LENGTH DIFFRACTION COEFFICIENT

Mitzner's original work was published in a government report of limited distribution [8], thereby denying access to the scattering community at large. However, distribution of the report is now unlimited, making it more available to researchers than previously.

Mitzner focuses immediately on an incremental form for his results with the understanding that the scattering from an edge of any contour can be obtained by integrating over the illuminated portions of the contour. He expresses the far diffracted field in terms of a dyadic diffraction coefficient $\overline{\overline{d}}$,

$$\bar{E}_d = E_i \frac{e^{i(kR-\pi/4)}}{\sqrt{2\pi R}} \overline{\overline{d}} \cdot \hat{p}\, dt \tag{5.67}$$

where $\hat{p}$ is a unit vector aligned along the incident electric polarization. In developing his ILDC, he establishes two pairs of unit vectors, one pair perpendicular and parallel to the plane of incidence, and one pair perpendicular and parallel to the plane of scattering. The plane of incidence is that plane containing the edge element dt and the incident direction, and the plane of scattering contains the edge element and the direction of scattering. These unit vectors are

$$\hat{e}^i_\perp = \hat{t} \times \hat{i}/|\hat{t} \times \hat{i}| \tag{5.68}$$

$$\hat{e}^i_\parallel = \hat{i} \times \hat{e}^i_\perp \tag{5.69}$$

$$\hat{e}^s_\perp = \hat{t} \times \hat{s}/|\hat{t} \times \hat{s}| \tag{5.70}$$

$$\hat{e}^s_\parallel = \hat{s} \times \hat{e}^s_\perp \tag{5.71}$$

where $\hat{t}$ is a unit vector along the edge. (Mitzner chooses his $\hat{t}$ in the opposite direction of that used by Michaeli [21]. He also used the symbol α to denote the

interior wedge half-angle, whereas we have used that symbol to denote the complete external wedge angle. The notational difference has been accounted for in the diffraction coefficients that follow.)

Mitzner expresses the diffraction dyad in terms of components along these directions,

$$\overline{\overline{d}} = d_{\perp\perp}\,\hat{e}^s_\perp\hat{e}^i_\perp + d_{\perp\parallel}\,\hat{e}^s_\perp\,\hat{e}^i_\parallel + d_{\parallel\perp}\,\hat{e}^s_\parallel\,\hat{e}^i_\perp + d_{\parallel\parallel}\,\hat{e}^s_\parallel\,\hat{e}^i_\parallel \tag{5.72}$$

Similarly, we may express the incident field polarization as

$$\hat{p} = \hat{e}^i_\perp \cos\gamma + \hat{e}^i_\parallel \sin\gamma \tag{5.73}$$

where γ is the angle subtended by the incident polarization and the normal to the plane of incidence. We may therefore express the produce $\overline{\overline{d}} \cdot \hat{p}$ as

$$\overline{\overline{d}} \cdot \hat{p} = d_{\perp\perp}\,\hat{e}^s_\perp \cos\gamma + d_{\perp\parallel}\,\hat{e}^s_\perp \sin\gamma + d_{\parallel}d_{\perp}\,\hat{e}^s_\parallel \cos\gamma + d_{\parallel\parallel}\,\hat{e}^s_\parallel \sin\gamma \tag{5.74}$$

To evaluate the components of (5.74), and thereby obtain expressions for the ILDC that can be compared to Michaeli's diffraction coefficients, we must apply eqs. (3.46A) through (3.67) of Mitzner's report. There is an error in the last term of Mitzner's eq. (3.46A), and the function $\sin[(\beta_s + \beta_i)/2]$ appearing therein must be replaced by $\sin[(\beta_s - \beta_i)/2]$. When this is done and the diffraction coefficients are expressed in Michaeli's form, we obtain

$$D_\perp = D_m - D'_\perp \tag{5.75}$$

$$D_\parallel = D_e - D'_\parallel \tag{5.76}$$

$$D_{\parallel\perp} = D_{em} \sin\beta_i - D'_{\parallel\perp} \tag{5.77}$$

where the primed diffraction coefficients are the physical optics terms,

$$D'_\perp = -U^+ \frac{\sin\phi_s}{\cos\alpha_1 + \cos\phi_i} - U^- \frac{\sin(n\pi - \phi_s)}{\cos\alpha_2 + \cos(n\pi - \phi_i)} \tag{5.78}$$

$$D'_\parallel = -U^+ \frac{\sin\phi_i}{\cos\alpha_1 + \cos\phi_i} - U^- \frac{\sin(n\pi - \phi_i)}{\cos\alpha_2 + \cos(n\pi - \phi_i)} \tag{5.79}$$

$$\begin{aligned} D'_{\parallel\perp} = {} & -U^+ \left[\frac{Q\cos\phi_s}{\cos\alpha_1 + \cos\phi_i} - \cos\beta_i\right] \\ & + U^- \left[\frac{Q\cos(n\pi - \phi_s)}{\cos\alpha_2 + \cos(n\pi - \phi_i)} - \cos\beta_i\right] \end{aligned} \tag{5.80}$$

In (5.78) through (5.80), the quantities Q, α_1, and α_2 are defined in (5.51) through (5.53), and the step functions are

$$U^+ = \begin{cases} 1, \text{ for "plus" face illumination} \\ 0, \text{ otherwise} \end{cases} \tag{5.81}$$

$$U^- = \begin{cases} 1, \text{ for "minus" face illumination} \\ 0, \text{ otherwise} \end{cases} \tag{5.82}$$

These step functions toggle on or off the appropriate physical optics coefficients, depending on whether a given wedge face is illuminated. Note that the components of Mitzner's ILDC are identical to those of Michaeli, modified by the removal of the physical optics coefficients. It can be shown that Mitzner's diffraction coefficients reduce exactly to those of Ufimtsev when the scattering direction lies on the Keller cone. Although the physical optics terms become singular along the reflection and shadow boundaries, Mitzner's ILDC remains finite in the transition regions because the singularities in the physical optics coefficients precisely cancel those in Michaeli's diffraction coefficients.

It should be clear that Mitzner's ILDC extends Ufimtsev's PTD to arbitrary directions in precisely the same way Michaeli's equivalent current approach extends Keller's theory. The singularities in Michaeli's coefficients can be attributed to a surface term that is cancelled in Mitzner's coefficients by the singularity in the physical optics term. The price we pay for this highly desirable result is that two separate computations are required for any finite edged body. One is the edge contribution as given in (5.75) through (5.80), and the other is a physical optics integral over the illuminated portions of the body. Despite the very practical extension to arbitrary directions both these theories represent, the edge elements are assumed to scatter independently. Consequently, in and of themselves, they cannot handle a case of great practical importance: surface traveling waves.

5.9 THE SURFACE TRAVELING WAVE

Like long-wire antennas, long, smooth surfaces can support traveling waves of current, not unlike one-conductor transmission lines do. Surface waves are launched only when the incident electric field has components perpendicular and parallel to the surface in the plane of incidence defined by the surface normal and the direction of incidence, as shown in the upper sketch of Figure 5.12. If there is no electric field component in the plane of incidence, as in the lower diagram, the surface traveling wave is not excited.

It is convenient for analytical purposes to assume the surface current to be of uniform intensity along the surface, no matter how it was launched, and that it

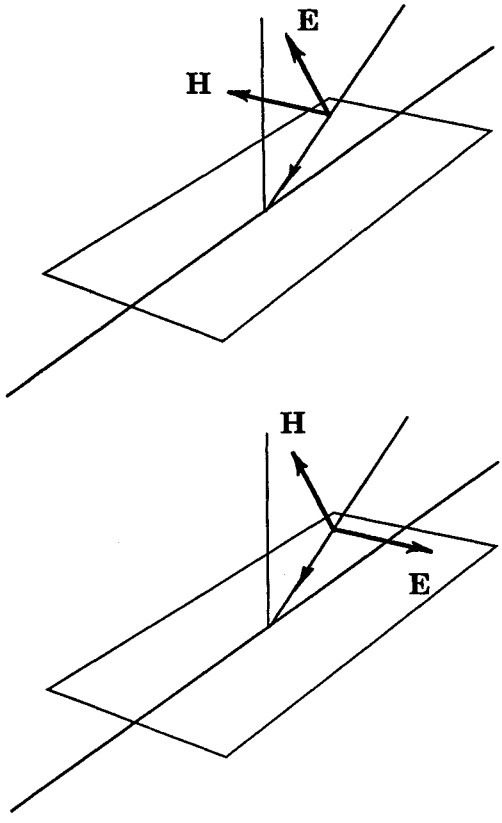

Figure 5.12. The surface traveling wave is excited when the incident electric field has components perpendicular and parallel to the surface in the plane containing the surface normal and the direction of incidence. Therefore, a surface wave can be launched in the case illustrated in the upper sketch, but not in the case illustrated in the lower one.

propagates with a velocity $v = pc$, where c is the speed of light and $p \leq 1$. When we insert the assumed uniform current into the radiation integral (5.41), set the magnetic current to zero, and then integrate over the length l of the surface, we find that the radiated far field has the form

$$E = Q\,(kl/2)\,\sin\theta\,(\sin f)/f \tag{5.83}$$

where

$$f = (kl/2)\,(1/p - \cos\theta) \tag{5.84}$$

and Q is a constant of proportionality. Here θ is the angle to a farfield observation point as measured from the direction of current flow. The $(\sin f)/f$ term in (5.83)

is the direct result of our assumption that the current intensity does not vary from one end of the surface to the other. As we shall see in Chapter 6, the RCS patterns of simple, straight-sided structures support the constant-amplitude assumption.

In most cases of practical interest, the current wave propagates at the speed of light, for which $p = 1$. Illustrative plots of (5.83) are shown for this case in the polar diagrams of Figure 5.13 for $l = 3$, 10, and 20λ. Note that the peaks of the sidelobes of all three patterns lie on a common locus independent of the length l, and that the field is zero along the direction of current flow ($\theta = 0$). The first peak of the pattern moves closer to $\theta = 0$ and becomes stronger as l increases. The locus of the sidelobe peaks is given by the expression

$$E = Q \cot(\theta/2) \tag{5.85}$$

which becomes singular at $\theta = 0$. Note that the peak sidelobe amplitudes do not depend on the length l of the assumed uniform current distribution.

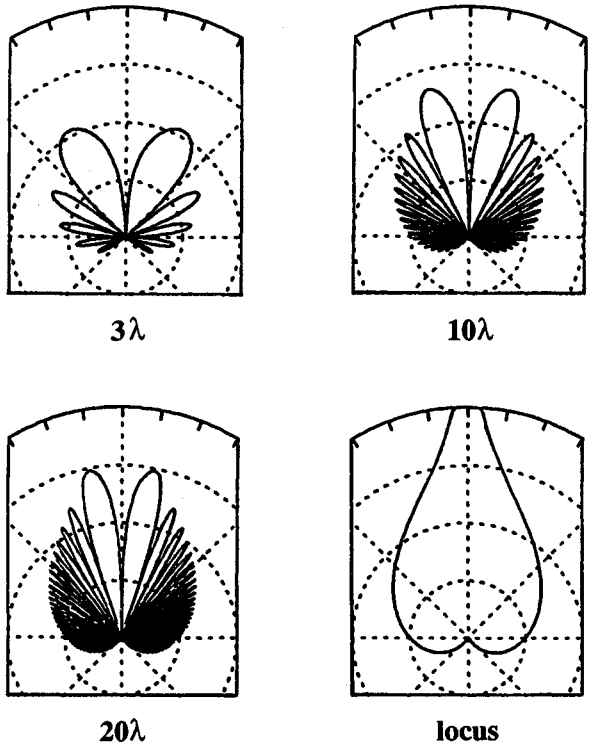

Figure 5.13. Patterns of (5.83) for $l = 3$, 10, and 20λ with the constant Q set to unity. The pattern in the lower right is the locus of the sidelobe peaks. (Radial scale is 10 dB per division.)

The patterns in Figure 5.13 are for a surface wave traveling toward the top of the page, and we see that the radiation is more intense in that general direction than toward the bottom (in a backward cone of directions). The traveling current wave is reflected when it reaches the end of the scattering body, generating a current wave propagating in the reverse direction. The radiation pattern of the reflected current wave has the same kind of pattern as the forward current wave, but because the currents propagate in the backward direction, the radiation patterns are inverted from those shown in the figure. Therefore, the backward-traveling wave concerns us in the backscattering case, not the forward-traveling wave.

The first lobe off the axis of either one is clearly the most intense of any, and it is useful for diagnostic purposes to be able to estimate where this strongest lobe occurs. To find that angular location, we may differentiate (5.83) with respect to θ and determine the angle that forces the derivative to zero. This results in the transcendental equation [22]

$$pf(1 - \cos^2\theta)\cos f - (p - \cos\theta)\sin f = 0 \tag{5.86}$$

When $p = 1$, which is usually the case of interest, (5.86) reduces to

$$f(1 + \cos\theta)\cos f - \sin f = 0 \tag{5.87}$$

Because this expression holds for each lobe in the pattern, there are a host of solutions, one for each lobe. Each solution depends, in turn, on the length of the surface by virtue of (5.84), but, as shown in Figure 5.14 for the first lobe in the pattern, that dependence is a weak one. Note that the solution f changes by only a few percent for surfaces longer than a few wavelengths. Once we find f, we may determine the angle of the lobe from

$$\theta = \cos^{-1}[1 - (2f/kl)] \tag{5.88}$$

In light of the persistence of the solution for very long lengths down to surface lengths of only a wavelength or two, it is useful to pursue the asymptotic solution as the surface becomes infinitely long. In this event θ approaches zero, yet the solution f remains finite. Thus, the asymptotic form of (5.87) is

$$2f\cos f - \sin f = 0 \tag{5.89}$$

The solution of (5.89) for the first four lobes of the pattern are $f = \pm 1.165561$, ± 4.604217, ± 7.789884, and ± 10.949944.

Although these solutions are strictly valid only for very long surfaces, we may find the lobe location with surprising accuracy for surfaces barely a wavelength long by invoking the small-argument approximation for $\cos\theta$,

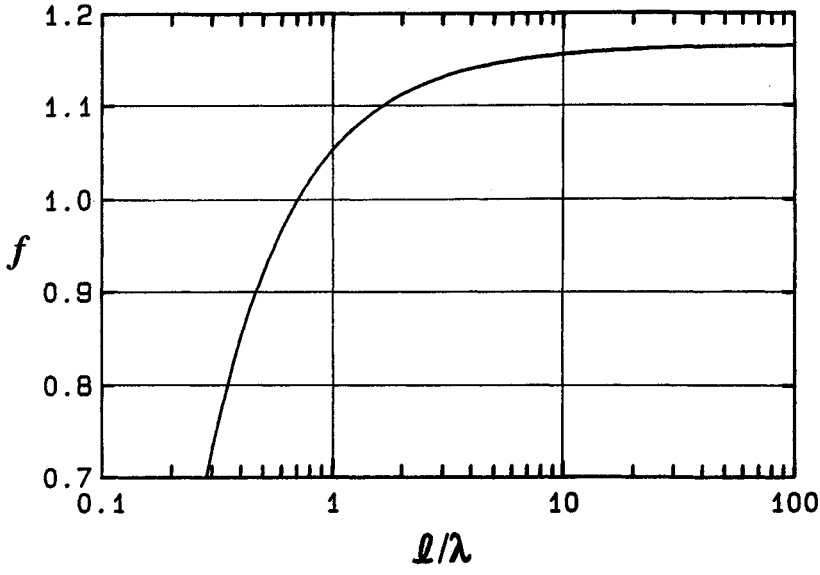

Figure 5.14. The solution of (5.87) for the first lobe depends only weakly on the length of the surface.

$$\cos\theta \approx 1 - \theta^2/2 \tag{5.90}$$

When we set $p = 1$ in (5.84), insert the asymptotic solution f and the value from (5.90), solve for θ and convert the result to degrees from radians, we emerge with the lobe-location prediction:

$$\theta_n = C_n(\lambda/l)^{1/2} \tag{5.91}$$

where $C_n = 49.35, 98.09, 127.59$, and 151.28 for the first four lobes. This estimate for the first lobe position ($C_1 = 49.35$) is in error by only 2.5° for $l = \lambda/2$, which can hardly be considered a long surface. The fact that the approximation of holds for such short lengths (and such high angles) can be traced to the rapid turn-down in the solution f as the surface becomes shorter than 3λ. The error in the $\cos\theta$ approximation is offset, in essence, by the error of our assumption that the solution f is a straight line across the chart in Figure 5.14. Our simple prediction of the traveling wave lobe location is therefore an example of two slight wrongs making a nearly perfect right.

Despite our success in predicting the angular behavior of the traveling current wave contribution to the far scattered field for abruptly terminated surfaces, how-

ever, our ability to estimate its amplitude for arbitrary surface configurations is not nearly as well developed. It is sometimes possible to account for multiple reflections of surface waves from the ends of simple bodies using diffraction concepts, from which all forward- and backward-traveling wave contributions may be summed coherently to form what appears to be a single forward-traveling wave contribution and a single backward-traveling wave contribution to the far field. Although Ross accomplished this for flat plates by including diffraction effects up to the third order [9], and Shamansky, Dominek, and Peters did it for wires [23], the general traveling-wave prescription for arbitrary surfaces, even flat ones, for arbitrary incidence will probably remain elusive for a long time.

5.10 SUMMARY

In this chapter we have discussed the more important of the high frequency methods for predicting the RCS of simple structures. The great utility of these theories is that in the high frequency region, the target elements scatter the incident wave independently of one another. This makes its possible to assemble a collection of relatively simple shapes, such as flat plates, cylinders, and spheroids to model a complicated target. The analytical high-frequency formulas are relatively easy to derive for specific geometries, and we only need to sum the individual contributions coherently to obtain the total RCS of the target.

The simplest of those theories is geometric optics, which is best used for doubly curved surfaces. The formula is deceptively simple, and the same formula holds for bistatic directions, as well as in the backward direction, as long as the forward direction is avoided. The implementation of geometric optics requires only that there exist a specular point on the body and that the principal radii of curvature be specified there. We have shown that geometric optics fails when one or both radii of curvature is infinite, as is the case for flat and singly curved surfaces, and in this event the theory of physical optics proves most helpful.

The theory of physical optics uses the tangent plane approximation of the induced surface currents, and thus relies on estimates of the surface fields from geometric optics. The induced currents are integrated over the illuminated portions of the body to obtain the far scattered fields, and the integral, although itself an approximation of the actual scattered fields, can sometimes be evaluated exactly. For those cases when an exact closed-form evaluation cannot be obtained, the method of stationary phase often yields quite acceptable results. On the other hand, when applied to smooth bodies such as spheroids, physical optics yields an erroneous contribution due to the abrupt discontinuity in the assumed surface fields at shadow boundaries. Thus, for smooth objects of any appreciable size, we might be better off using the simpler theory of geometric optics.

However, the physical optics prediction fails by progressively wider margins as the scattering direction moves further from the specular direction. This is because

the surface effects decay to the levels of edge effects, and the edge contributions are not well modeled in physical optics. The edge returns can be more accurately predicted in the non-specular regions with Keller's geometrical theory of diffraction, and the theory is attractively couched in terms of a pair of simple diffraction coefficients. Nonetheless, the GTD has its own set of difficulties, among them the singularities in the diffraction coefficients, the existence of caustics, and the restriction of the scattering direction to the Keller cone.

The first of these can be overcome with a uniform theory of diffraction and the UTD developed by Koumyoujian and Pathak was described. The singularities in the diffraction coefficients are multiplied by a Fresnel integral that drops to zero as the diffraction coefficients rise to infinity. The product remains finite and exhibits the proper change in sign from one side of the shadow or reflection boundary to the other. The caustic difficulties can be overcome by the method of equivalent currents, which postulates the existence of filamentary electric and magnetic currents along an edge singularity. When summed in the radiation integral, the equivalent currents guarantee finite fields at the observation point, provided we have well-behaved diffraction coefficients available. The equivalent currents also make it possible to compute the scattered field for arbitrary directions as well as those on the Keller cone.

We have shown that the diffraction coefficients of Ufimtsev's PTD are not singular, like those of Keller's GTD, and thus may be more attractive for RCS predictions. This is because Ufimtsev has, in essence, deleted the singularity in the Keller coefficients by subtracting a physical optics coefficient. As a result, the PTD contains only the edge contribution, while the GTD contains that contribution plus a surface contribution. Nevertheless, Ufimtsev's PTD is restricted, as in Keller's GTD, to directions lying on the Keller cone. Mitzner, with his incremental length diffraction coefficient, extented Ufimtsev's theory to arbitrary directions in much the same way Michaeli extended Keller's theory. Thus, the high frequency diffraction theories seem to have reached the stage where edge scattering can be accurately predicted.

Alas, this is not yet the case. The surface traveling wave, although a high frequency phenomenon, involves the entire surface as well as the edges bounding that surface, and the diffraction theories can account for only the localized edge diffraction. However, repeated application of the diffraction theories to account for multiple interactions between edges offers some promise of modeling the surface traveling wave effect. The incremental prescriptions of Mitzner and Michaeli hold well enough over edge sections whose contours change slowly, but those theories cannot be expected to work in the vicinity of corners whose edge takes an abrupt turn. Because the corner is a discontinuity where we would expect a strong reflection of a surface wave launched along the edge, a corner diffraction coefficient is badly needed. If one were available, then theories similar to those of Mitzner and Michaeli might be applied to account for multiple corner diffraction.

REFERENCES

[1] Knott, E. F., "A Tool for Predicting the Radar Cross Section of an Arbitrary Trihedral Corner," presented at the IEEE SOUTHEASTCON'81 Conference, Huntsville, Alabama, 6–8 April 1981, IEEE Publication 81CH1650-1, pp. 17–20.

[2] Keller, J.B., "Diffraction by an Aperture," *J. App. Phys.*, Vol. 28, No. 4, April 1957, pp. 426–444.

[3] Kouyoumjian, R. G., and P. H. Pathak, "A Uniform Theory of Diffraction for an Edge in a Perfectly Conducting Surface," *Proc. IEEE*, Vol. 62, No. 11, November 1974, pp. 1448–1461.

[4] Ryan, C. E., Jr., and L. Peters, Jr., "Evaluation of Edge-Diffracted Fields Including Equivalent Currents for Caustic Regions," *IEEE Trans. on Antennas and Propag.*, Vol. AP-17, No. 3, May 1969, pp. 292–299. See also Correction in Vol. AP-18, March 1970, p. 275.

[5] Knott, E. F., and T. B. A. Senior, "Equivalent Currents for a Ring Discontinuity," *IEEE Trans. on Antennas and Propag.*, Vol. AP-21, September 1973, pp. 693–695.

[6] Michaeli, A., "Equivalent Edge Currents for Arbitrary Aspects of Observation," *IEEE Trans. on Antennas and Propag.*, Vol. AP-32, No. 3, March 1984, pp. 252–258. See also correction in Vol. AP-33, February 1985, p. 227.

[7] Ufimtsev, P. Ia., "Approximate Computation of the Diffraction of Plane Electromagnetic Waves at Certain Metal Bodies: Pt. I. Diffraction Patterns at a Wedge and a Ribbon," *Zh. Tekhn. Fiz.* (USSR), Vol. 27, No. 8, 1957, pp. 1708–1718.

[8] Mitzner, K.M., "Incremental Length Diffraction Coefficients," Technical Rep. No. AFAL-TR-73-296, Northrop Corporation, Aircraft Division, April 1974.

[9] Ross, R. A., "Radar Cross Section of Rectangular Plates as a Function of Aspect Angle," *IEEE Trans. on Antennas and Propag.*, Vol. AP-14, No. 3, May 1966, pp. 329–335.

[10] Plummer, D. K., L. E. Hinton, E. F. Knott, and C. J. Ray, "Non-Metallic Chaff Study," Report NADC-79200-30, prepared for the Department of the Navy, Naval Air Development Center by the Georgia Institute of Technology, Engineering Experiment Station, June 1980.

[11] Stratton, J. A., *Electromagnetic Theory*, McGraw-Hill, New York, 1941, pp. 464–470.

[12] Ruck, G. T., D. E. Barrick, W. D. Stuart, and C. K. Krichbaum, *Radar Cross Section Handbook*, Vol. 1, Plenum Press, New York, 1970, pp. 50–59.

[13] Gordon, W. B., "Far Field Approximation of the Kirchhoff-Helmholtz Representation of Scattered Fields," *IEEE Trans. on Antennas and Propag.*, Vol. AP-23, No. 5, July 1975, pp. 590–592.

[14] Senior, T. B. A., "A Survey of Analytical Techniques for Cross-Section Estimation," *Proc. IEEE*, Vol. 53, No. 8, August 1965, pp. 822–833.

[15] Sommerfeld, A., "Mathematische Theorie der Diffraction," *Math Ann.*, Vol. 47, 1896, pp. 317–374.

[16] Sommerfeld, A., "Lectures on Theorectical Physics," *Optics*, Vol. 4, Academic Press, New York, 1964.

[17] Senior, T. B. A., and P. L. E. Uslenghi, "High-Frequency Backscattering from a Finite Cone," *Radio Science*, Vol. 6, No. 3, March 1971, pp. 393–406.

[18] Lee, S. W., and G. A. Deschamps, "A Uniform Asymptotic Theory of Electromagnetic Diffraction by a Curved Wedge," *IEEE Trans. on Antennas and Propag.*, Vol. AP-24, No. 1, January 1976, pp. 25–34.

[19] Deschamps, G. A., J. Boersma, and S. W. Lee, "Three-Dimensional Half-Plane Diffraction: Exact Solution and Testing of Uniform Theories," *IEEE Trans. on Antennas and Propag.*, Vol. AP-32, No. 3, March 1984, pp. 264-271.

[20] Millar, R. F., "An Approximate Theory of the Diffraction of an Electromagnetic Wave by an Aperture in a Plane Screen," *Proc. IEE*, Vol. 103, Part C, March 1956, pp. 177–185.

[21] Knott, E. F., "The Relationship between Mitzner's ILDC and Michaeli's Equivalent Currents," *IEEE Trans. on Antennas and Propag.*, Vol. AP-33, No. 1, January 1985, pp. 112–114.

[22] Knott, E. F., "Traveling Wave Lobe Locations," *IEEE Trans. on Antennas and Propag.*, Vol. 38, November 1990, pp. 1859–1862.

[23] Shamansky, H. T., A. K. Dominek, and L. Peters, Jr., "Electromagnetic Scattering by a Straight Thin Wire," *IEEE Trans. on Antennas and Propag.*, Vol. 37, August 1989, pp. 1019–1025.

Chapter 6
Phenomenological Examples of Radar Cross Section

Eugene F. Knott

6.1 INTRODUCTION

In Chapter 3 the reader was acquainted with the electromagnetic basis of radar echoes and in Chapters 4 and 5 with ways the echo may be predicted. As sound as those prescriptions may be, however, they are merely collections of formulas and equations that may not help us understand the echoing properties of targets of interest. In this chapter we present examples of the characteristics of both simple and complex targets.

By *simple* we mean metallic objects having elementary shapes, such as a sphere, a circular cylinder, or a flat plate. Simple targets may be arranged in a hierarchy according to the strength and frequency dependence of the echo, and this ordering gives us some insight into their relative importance. The hierarchy of scattering mechanisms is particularly useful when we approach the task of reducing the echo from complex targets. By *complex* we mean objects whose surfaces are not good conductors, whose composition is not uniform or homogeneous, whose profiles defy mathematical description, or combinations of all of these.

All targets of tactical, strategic, or civilian importance are complex targets; for example, missiles, fighters, bombers, jet liners, ships, sailboats, automobiles, trucks, birds, insects, brush, and trees. We attempt to detect and track military targets in the interest of national defense, civilian targets in the enforcement of drug and traffic laws, and sometimes we track natural targets, like birds and bugs, because clouds or swarms of them happen to be in the scene at the time. The echoes from vegetation and the terrain itself are clues to environmental and geo-

logical conditions when observed by satellite radars, but we hope to avoid or exclude them when we use tactical or police radars to sense intruders or speeders. We exclude them in our discussion of echo phenomenology as well and focus instead on those from hard (manufactured) targets.

Although all targets are complex (save those we use in calibration and testing), we can best understand them as collections of simple shapes. This is largely due to the fact that our minds and analytical tools are capable of conceiving and handling simple shapes at best. As such, we approximate the actual surface contours of complex shapes by fictitious, mathematically tractable contours, at least in a local sense. This approach is reasonably effective for both the understanding and the prediction of echo characteristics. Indeed, the decomposition of a complicated profile into simple curves is the assumption on which most of our high-frequency echo-estimation computer codes are based. Therefore, even though all practical targets are complex, the simple shape or simple surface feature is the key to understanding and predicting combined effects.

We use the hypothetical missile depicted in Figure 6.1 to illustrate the kinds of radar echoes we may expect to receive from hard targets. Although this target is an airborne weapon, many of the basic scattering mechanisms noted in the figure are typical of other kinds of targets as well. We list the scattering mechanisms more or less in descending order of importance. (The discussion is taken nearly verbatim from [1], with permission.)

Reentrant Structures

Jet intakes and exhausts and rocket motor exhausts are reentrant structures that tend to reflect significant incident radar energy back in the direction from which it came. To a lesser degree, but still of considerable importance, are echoes due to waves that pass through antenna radomes and infrared sensor windows, bounce off the sensor inside, and return to the radar system. Structures like these are good reflectors because their internal features are mostly metallic, hence most of the energy entering them must come back out again, especially when seen from directions not too far from the surface normal of the duct or radome aperture.

When seen in the nose-on region, for example, the compressor stage of the jet engine, although convoluted by the doubly curved surfaces of the turbine blades, efficiently blocks waves from passing through to successive stages of the engine and tends to reflect the energy back to the source. When seen from the rear, as suggested in Figure 6.1, the final stages of the turbine present much the same kind of blockage. Similarly, many antenna and electrooptic sensors have flat faces under their protective covers, and the ensemble forms a reflective cavity at radar frequencies. These cavities and reentrant structures are strong scatterers, and their electromagnetic behavior is not unlike that of the corner reflector discussed in Section 6.2.

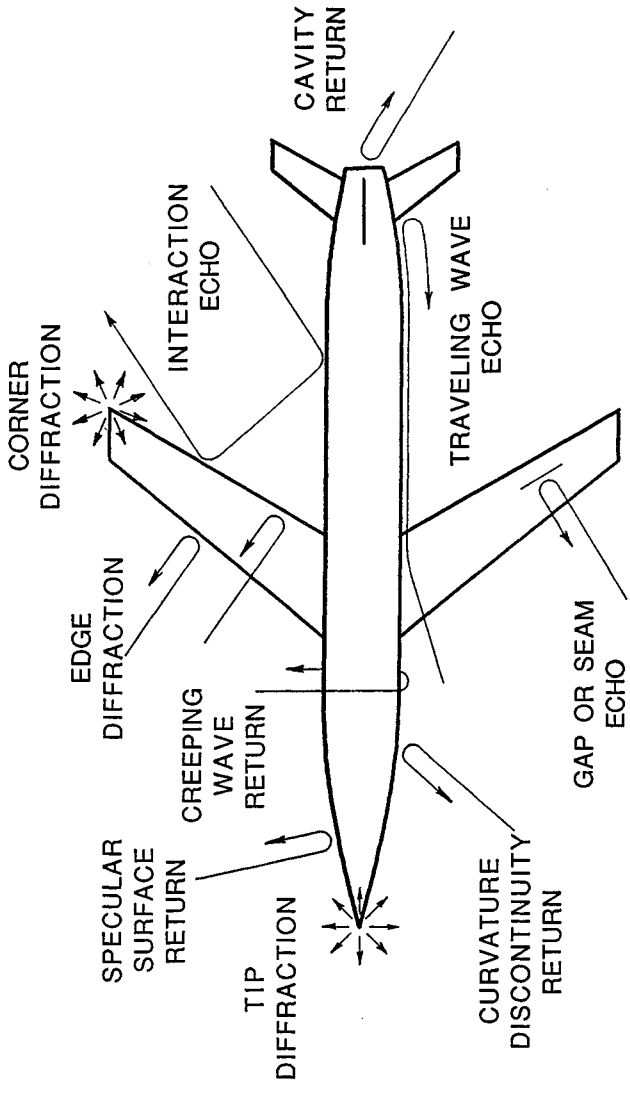

Figure 6.1. Hypothetical airframe illustrating several scattering mechanisms ([1], Fig. 2, p. 116.) (Copyright 1992 AIAA; reprinted with permission.)

Specular Scattering

A specular scatterer is any part of the target whose surface is perpendicular to the line of sight. This includes flat, singly curved and doubly curved surfaces, and the curvature of the surface governs the magnitude of the echo and the persistence of

the return in aspect angle. Flat surfaces are very strong scatterers at normal incidence, for which the entire surface "lights up," but the echo falls off rapidly as the angle of incidence moves away from the surface normal. The specular surface degenerates to a bright line along a generator of the surface when it is singly curved, examples of which are the cone and the right circular cylinder. It becomes a bright point when the surface is doubly curved, like that of a spheroid.

As we saw in Section 5.2, the magnitude of the specular scattering from these surfaces varies inversely with the Gaussian curvature, hence the echo from a flat plate can be orders of magnitude larger than that from a spheroid of comparable size. The angle over which that echo remains large varies inversely with the curvature, however, with the result that the echo from a spheroidal surface will not change much with viewing angle, whereas that of a plate will. This persistence in the echo is a factor in the dichotomy of using surface shaping as an echo reduction tool. RCS suppression experts prefer flat or straight surfaces angled well away from the specular direction as an echo reduction technique over the reduced amplitudes offered by singly or doubly curved surfaces. This is simply because the angular persistence of the echoes from curved surfaces fails to offset the amplitude reduction they offer.

Traveling Wave Echoes

An incident radar wave can launch *traveling current waves* that propagate down a surface along a geodesic path to a surface boundary, such as an edge or vertex, which then may reflect the current wave, generating a *backward*-traveling wave. The forward- and backward-traveling (reflected) current waves are not unlike those deliberately excited on *end-fire antennas*, and although they radiate energy in all directions, the intensity of the radiation toward the radar can be significant. Even though it was once thought that traveling wave echoes were characteristic of long, straight surfaces illuminated at low grazing angles of incidence, the phenomenon also exists for bodies considerably shorter and thus occurs at significant surface grazing angles (as high as 25° or more).

Traveling waves are significant only when a component of the incident electric field is parallel to the surface and in the plane containing the surface normal and the direction of incidence. This being the case, they excite the trailing edges of wings and horizontal stabilizers seen from slightly above or below the yaw plane near nose-on aspects for vertically polarized incident waves, and they excite the trailing edges of vertical fins seen slightly from the left or right of nose-on for horizontally polarized incident waves. The leading and trailing edges of horizontal airfoils also support surface traveling waves for horizontally polarized waves if the angle of incidence to the edge is within 20° or 30° of grazing the edge. Therefore, traveling waves are significant to the radar observables analyst.

Edge and Vertex Diffraction

Edges, tips, and vertexes of any kind are discontinuities that will scatter radar energy. The angular distribution of the scattered energy depends on the angle of arrival of the incident wave, the scattering direction of interest (usually back to the radar), and the nature of the discontinuity. This is true whether the discontinuity is illuminated directly by the incident wave or excited indirectly via a creeping wave or traveling wave, for which the excitation is a surface wave that seldom arrives at the discontinuity along the same direction as the direct radar wave. Traveling wave excitation usually generates a stronger echo than the discontinuity excited directly by the incident wave, especially if it is at the far end of a long metallic surface. Traveling wave echoes tend to be more significant than the diffraction of energy from directly illuminated edges.

Creeping Waves

A creeping wave is a form of traveling wave launched along surfaces shadowed from the incident wave. Like the traveling wave, the creeping wave follows surface geodesics and can be reflected by obstacles or discontinuities, even if the discontinuities happen to be in or on shadowed surfaces. It is launched into the shadow region at a shadow boundary separating the lit side of a smooth surface from the shaded side. If no discontinuity is encountered along the geodesic path, the creeping wave will eventually emerge from the shaded side of the body at a shadow boundary, where a portion of it is launched back toward the radar. Unlike the traveling wave, however, whose amplitude generally increases with the distance traveled, the intensity of the creeping wave decreases with increasing distance. This is because the traveling wave "feeds" on energy supplied by the incident wave over illuminated surfaces, whereas the creeping wave sheds energy incrementally as it traverses curved, shaded surfaces.

Although the perfectly conducting sphere is the body classically used to illustrate the creeping wave phenomenon, creeping waves can spin around the back side of any smooth, curved object, whether singly or doubly curved. In Figure 6.1, for example, a creeping wave is shown skirting the presumably smooth singly curved fuselage of a missile body. Notwithstanding the academic interest in creeping waves, however, they are of little practical significance on bodies like that shown in the figure. We find few creeping wave echo sources of any significance on a missile, and the specular echo from the side of the fuselage will be far stronger than any creeping wave return.

Interactions

Although all parts of a target interact to some degree with all other parts, the interactions are significant only when the parts are within a few wavelengths of

each other or when energy is focused on one part by another. Even though the profiles of most missiles are such that strong interactions hardly ever occur, the analyst is well advised to be aware that they do constitute potential scattering mechanisms.

Surface Discontinuities

Any discontinuity in an otherwise continuous surface constitutes an echo source. Gaps, ridges, and seams are inevitable discontinuities found on every airframe, and each one increases the target echo. Even a discontinuity in surface curvature is an echo source, albeit a minor one, and will be present even if the junction between two surfaces of different curvature is perfectly smooth. Discontinuities in curvature are not usually echo mechanisms that must be dealt with, for their effects will be masked by the echo mechanisms just discussed. If the observables suppression expert has done the job well, the target echo will be below acceptable levels by the time we must consider suppressing those due to discontinuities in curvature.

6.2 SPECULAR SCATTERING

We have already seen that specular scattering is an opticslike reflection, as from a mirror or polished surface. The specular direction $\hat{s}$ (not necessarily the general scattering direction used in Chap. 5) may be defined as

$$\hat{s} = \hat{i} - 2\hat{n}\,(\hat{n} \cdot \hat{i}) \tag{6.1}$$

where $\hat{n}$ is the outward normal erected on a surface patch exposed to the incident wave propagating in the direction given by the unit vector $\hat{i}$. This expression declares that, to find the specular direction, we need only reverse the normal component of the direction of incidence. A consequence is that $\hat{n}$, $\hat{s}$, and $\hat{i}$ are coplanar and the surface normal bisects the angle between the directions of incidence and scattering, as shown in Figure 3.11.

When the scattering surface is a flat plate, and when the source and receiver are both in the far field of the plate, all rays from source to plate to receiver arrive in phase in the specular direction, even though the phase of the incident wave may vary over the surface. Therefore, as suggested in Figure 5.2, there is only one specular direction when the illuminated surface is a flat one. There is an infinity of specular directions, on the other hand, for singly and doubly curved surfaces, because there is an infinity of points on such surfaces where the total path length can be minimized by moving either the source, the receiver, or both. We can identify a *specular point* on the surface where this occurs, as in Figure 3.9, and we

can show that most of the energy scattered from the surface in the vicinity of specular point arrives in phase at the receiver. This minimum-path phenomenon is the basis for the stationary-phase evaluation of the physical optics integral employed in Section 5.3.

The specular point therefore moves over the surface in such a way that $\hat{n}$ has no component along the difference vector $(\hat{i} - \hat{s})$. When the specular point slides off the physical surface, the specular scattering mechanism disappears and other mechanisms become more significant. One specular direction vitally concerns us: when the direction of scattering is back in the direction of incidence, which is the case for most tactical radars. In this event $\hat{s} = -\hat{i}$, which (6.1) admits can occur only when the direction of incidence is along the surface normal. Specular backscattering is characterized by echoes so intense and so costly to reduce with absorbers that we usually resort to shaping to suppress them. Moreover, the infinity of specular directions associated with curved surfaces sometimes induces us to build weapons with as few curved surfaces as possible. A radical, but successful, example is the F-117A stealth fighter unveiled by the U.S. Air Force in 1990.

We may classify specular scattering according to the Gaussian curvature of the surface responsible for the reflection, as listed in Table 6.1. Simple examples are the flat plate, the circular cylinder, and the spheroid; and the formulas for the echo strength (the RCS) are valid only when the direction of incidence is along the surface normal. Other expressions must be used when that is not the case. Note that the plate, cylinder and sphere are preceded in the table by the corner reflector. Although none of the corner reflector surfaces may be normal to the direction of incidence, an incident wave suffers multiple reflections that are specular in the bistatic sense, and the last of them is a reflection back in the direction of the incident wave. However, we first discuss the plate, cylinder, and sphere as examples of specular scatterers before considering the corner reflector.

Table 6.1
Intensity and Frequency Dependence of Specular Echoes
(in all cases the radar line of sight is perpendicular to the surface)

Surface Type	*Example*	*Radii of curvature*	*Frequency dependence*	*Specular RCS*
Corner reflector	Dihedral, Trihedral		f^2	$\sigma = 4\pi A_{\text{eff}}^2/\lambda^2$
Flat	Plate	∞, ∞	f^2	$\sigma = 4\pi A^2/\lambda^2$
Singly curved	Cylinder	a, ∞	f^1	$\sigma = kal^2$
Doubly curved	Spheroid	a_1, a_2	f^0	$\sigma = \pi a_1 a_2$

A_{eff} = effective area of corner
A = area of plate
a = radius of sphere or cylinder
l = cylinder length

An example of the intensity of the specular scattering from a flat plate is shown in Figure 6.2, containing one pair of several pairs of patterns designed by Ross to compare predictions with measurements [2]. The measured data were collected by rotating a plate about a vertical axis, as suggested in Figure 9.21, for vertical and horizontal incident polarizations. The specular return from the surface of the plate lies at the extreme left side of the charts, and edge-on incidence is at the extreme right. The pattern between the two extremes exhibits the undulating $(\sin x)/x$ characteristics of a uniformly illuminated aperture as obtained from the theory of physical optics. Beyond aspect angles of 40° or so, that pattern gives way to other scattering mechanisms. One is edge diffraction, a dominant effect in the edge-on region when the incident electric vector is parallel to the edge (vertical

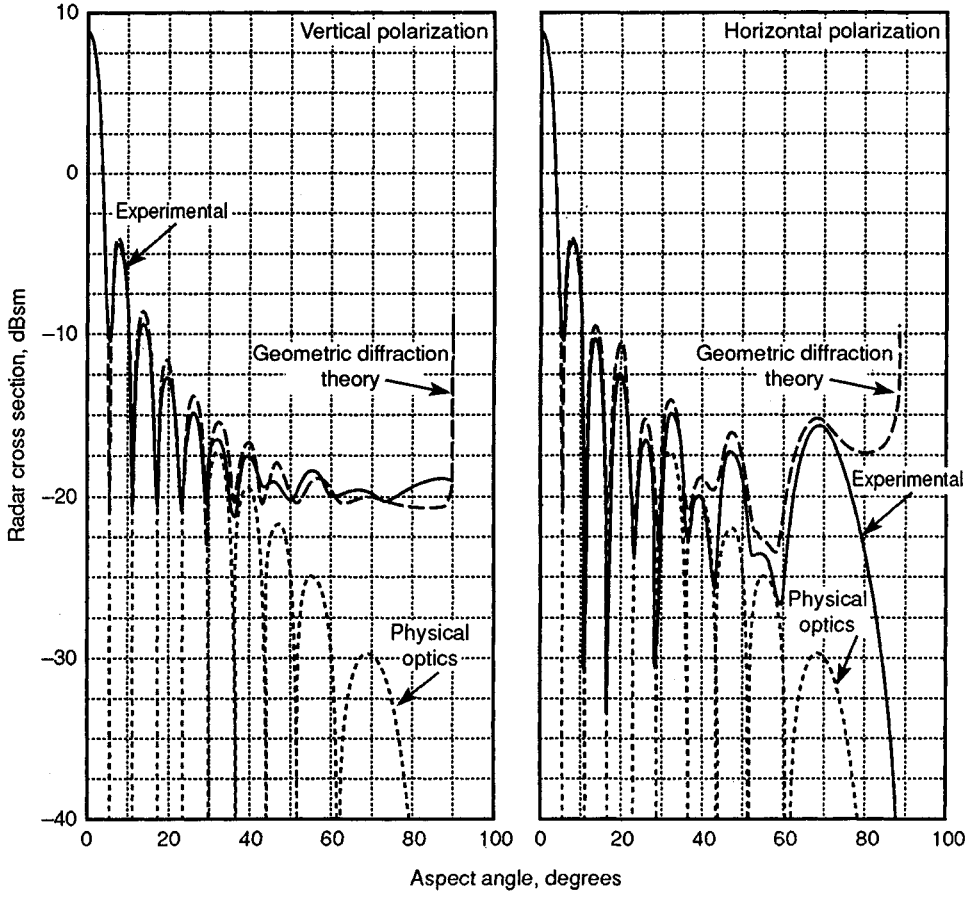

Figure 6.2. RCS patterns of a 6.5-in. square plate at a wavelength of 1.28 inches (from [2], Fig. 5, pp. 333. Copyright 1966 IEEE; reprinted with permission).

polarization), and the other is the surface traveling wave echo, a dominant mechanism for horizontal polarization. The flat plate therefore exhibits three different scattering mechanisms, of which the specular lobe at left is only one.

Its intensity matches the value listed in Table 6.1 within a fraction of a decibel, one reason why the flat plate is often used as a calibration device for RCS measurements. The angular width of the specular lobe narrows as the plate dimension in the plane of measurement becomes longer, one reason for choosing the flat surfaces of a faceted target as long as possible. The specular lobe of a very flat, very smooth surface 100λ long is only 0.01 rad (0.6°) wide, as measured from null to null. Thus, even if we cannot arrange to direct the specular lobe out of the threat sector, its narrowness helps reduce the probability of detection.

The pattern of an end-capped right circular cylinder exhibits many of the same characteristics, as suggested in Figure 6.3. Indeed, this pattern has four specular lobes: the one at the center of the pattern and the one split at the two sides of this 360° chart being those of the flat, circular ends of the cylinder and the ones at $\pm 90°$ being the specular echoes from its curved sides. Using the dimensions listed in the figure caption and the third formula listed in Table 6.1, we calculate a broadside echo of 4 m^2 (6 dBsm), the very value attained at broadside incidence in the pattern.

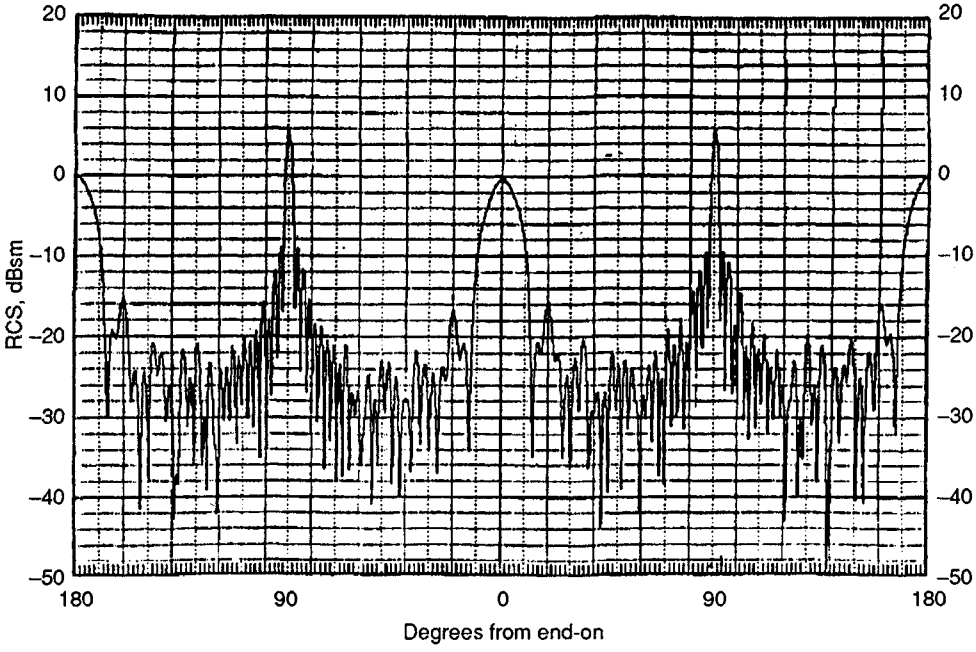

Figure 6.3. RCS pattern of a right circular cylinder 5.5 in. in diameter and 28 in. long measured at a frequency of 5.4 GHz for vertical incident polarization.

We are not surprised by this close agreement between measurement and prediction, however. Unknown to the reader, but certainly known to us, is the fact that the broadside echoes from this cylinder were used to calibrate a set of measurements of other targets. As such, the specular echoes registered at $\pm 90°$ in Figure 6.3 can be none other than the values manually inserted into the data processing system by the system operators. If we install the calibration cylinder as an "unknown" target to be measured, if the calibration levels are derived from the very target being measured, and if system calibration has not "drifted" over time, we can expect to register on our chart precisely the values we specified at the outset.

Let us therefore check the pattern by calculating the theoretical echo from the flat ends of the cylinder using the flat-plate formula in Table 6.1. For a circular plate 5.5 in. in diameter and a test frequency of 5.4 GHz, we obtain a value of 0.96 m^2 (-0.2 dBsm), which is very close to the level reached by the specular lobe at the center of the pattern. Because the broadside RCS varies directly with frequency whereas the end-on RCS varies with the square of the frequency, we conclude that the pattern is consistent and probably an accurate one. Although not discussed here, diffraction from the curved edges of the ends of the cylinder becomes important in the intermediate regions between the end-on and broadside specular responses. Therefore, the echo pattern of the cylinder, like that of the flat plate, is due to more than one scattering mechanism.

The simplest conceivable body with a doubly curved surface is the metal sphere, whose frequency-dependent scattering characteristics were used to illustrate the three scattering regimes discussed in Section 3.3. Because the sphere is a body of radial symmetry, its backscattering pattern is monotonously dreary, exhibiting no change at all with changing aspect angle. Indeed, instead of this nonvarying pattern, we chose to display in Figure 3.14 the variation of its echo as a function of its electrical circumference. As shown in Figure 6.4, that variation

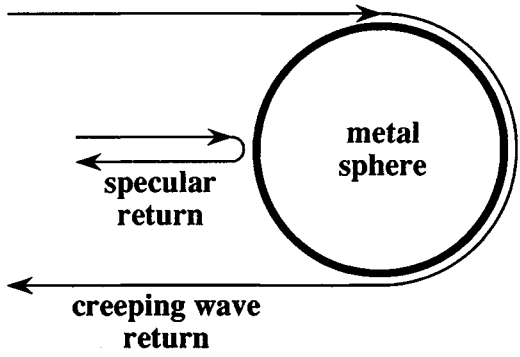

Figure 6.4. The echo from a metal sphere includes a creeping wave contribution as well as a specular component.

is due to two mechanisms, one a specular reflection from the near side of the sphere and the other a creeping wave—actually, an infinity of creeping waves—skirting the shadowed rear side. We defer for the moment a discussion of the creeping wave, noting only that the specular echo given by the fourth formula in Table 6.1 (in this instance for $a_1 = a_2$ is the sphere radius) becomes progressively more accurate as the sphere grows electrically larger.

Therefore, the radar echo from even the simplest of conceivable three-dimensional bodies is due to no fewer than two scattering mechanisms. Figure 6.5 charts the RCS of the metal sphere as a function of its electrical circumference in linear coordinates, which should be compared with the log-log chart of the same behavior in Figure 3.14. The error of the optics formula for the RCS of the sphere is less than 5% (0.2 dB) for a sphere whose circumference is 20λ (diameter about 6.4λ).

Reentrant structures may also be regarded as specular scatterers, even though the normal of no single internal surface may be parallel to the line of sight. The simplest example is the right-angled dihedral corner reflector shown in Figure 6.6. The perpendicularity of its faces ensures that, if a ray enters the aperture of the reflector perpendicular to the dihedral axis, a pair of specular bistatic reflections sends the ray back out the aperture in the direction from which it came. The intensity of the corner reflector echo is given by the formula

$$\sigma = 4\pi A_{\text{eff}}^2/\lambda^2 \tag{6.2}$$

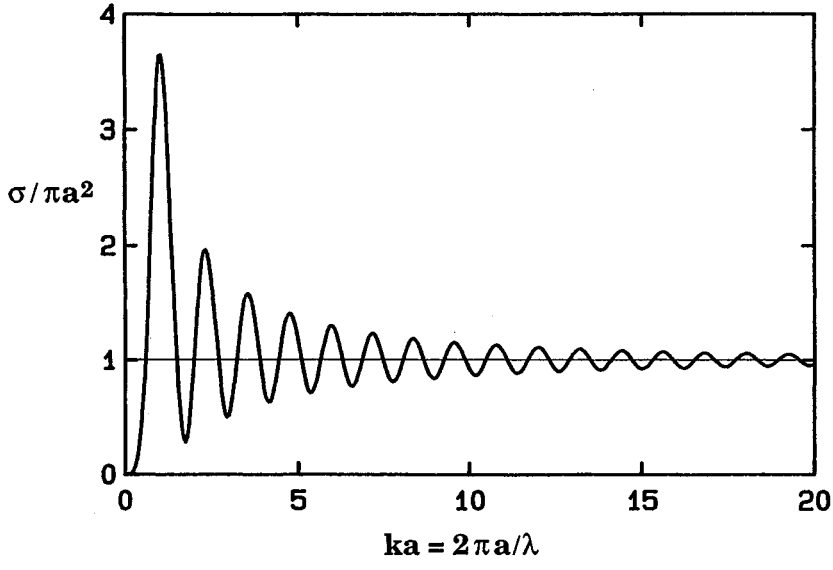

Figure 6.5. Theoretical RCS of a perfectly conducting sphere as charted in linear coordinates. A log-log version appears in Figure 3.14.

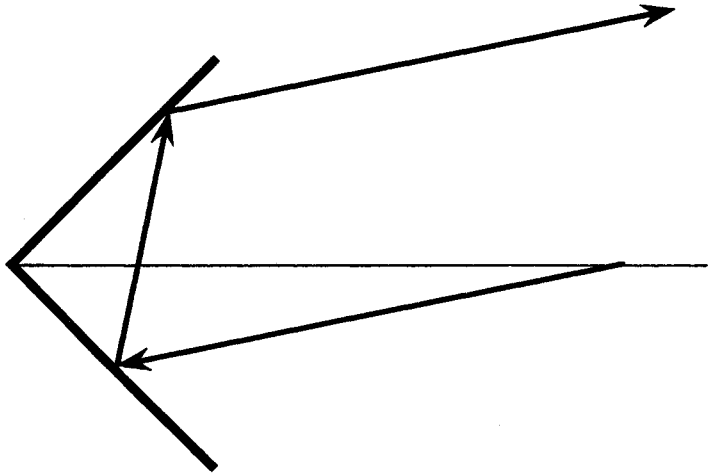

Figure 6.6. Rays entering a right-angled corner are reflected back in the direction from which they came.

where A_{eff} is the *effective* projected area of the dihedral perpendicular to the line of sight. Because some rays reflected by one face are not completely intercepted by the opposite face, the effective double-bounce area is generally less than the actual area. Note that (6.2) has the same form as the flat-plate formula listed in Table 6.1, except that we must use the effective area instead of the actual area.

The pattern of a right-angled dihedral corner reflector is shown by way of example in Figure 6.7, the broad central region of which is dominated by the double-bounce mechanism illustrated in Figure 6.6, while the two "ears" at $\pm 45°$ are single-bounce specular returns from the flat faces. The sidelobes of the single-bounce returns produce the undulations in the central part of the pattern. Because those sidelobes are much weaker than the double-bounce mechanism, their effect amounts to only ripples in the pattern. The peak return at the center of the pattern is about 11 dBsm, very nearly that calculated from (6.2) at the test frequency of 9.4 GHz.

The double-bounce echo can be reduced if the faces are angled further apart, as suggested in Figure 6.8. Here the faces are the same size as those of the reflector of Figure 6.7, except that the interior angle is 100° instead of 90°. (Indeed, the reflector was the same sheet of folded metal, with its faces pried apart an additional 10°.) Note that this simple reconfiguration spoils the double-bounce mechanism and results in a reduction of more than 20 dB at the center of the pattern. The angle needed to achieve such reductions becomes less the larger are the reflector faces, a fact that influences the fabrication tolerances of reflectors used as echo calibration devices on RCS test ranges.

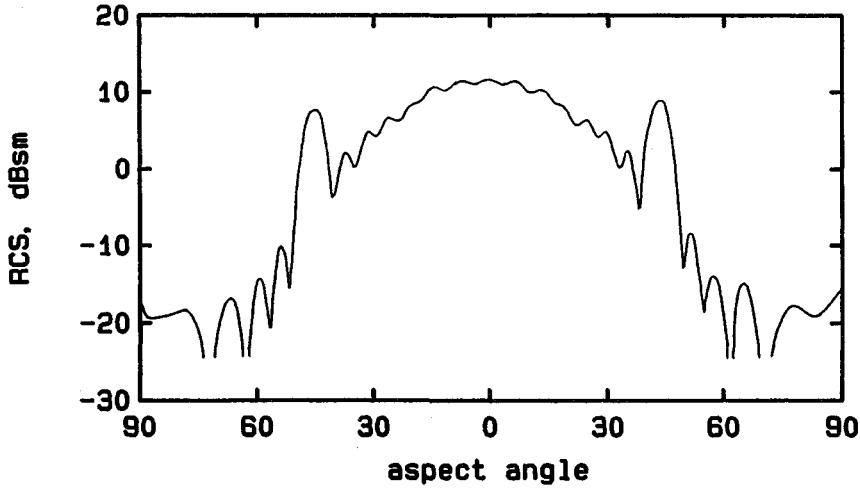

Figure 6.7. RCS pattern of a 90° dihedral corner reflector with square faces 17.9 cm along a side measured at 9.4 GHz.

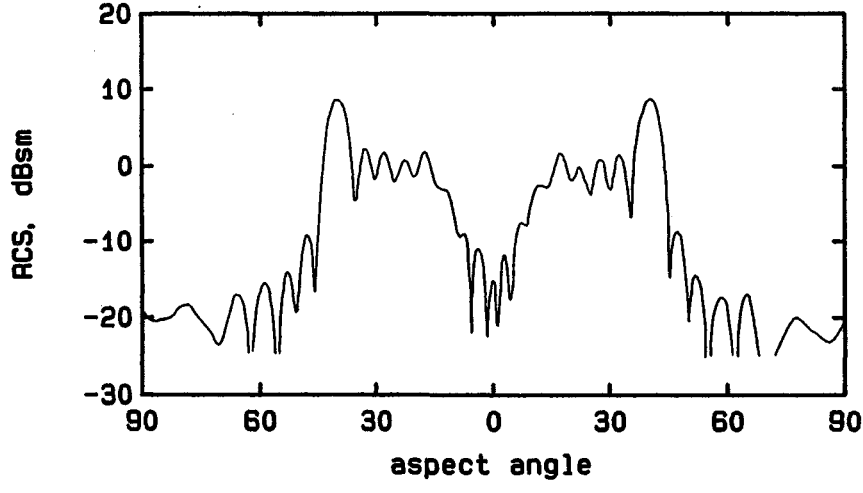

Figure 6.8. RCS pattern of a 100° dihedral corner reflector with square faces 17.9 cm along a side measured at 9.4 GHz.

In addition to the single- and double-bounce mechanisms, edge diffraction also contributes to the total echo from the dihedral corner. Although this complexity has been explored by several researchers, analyses have been restricted to incidence perpendicular to the dihedral axis [4–7]. The addition of a third face perpendicular to the first two creates the trihedral corner, thereby generating a triple-bounce mechanism responsible for a broad pattern in two orthogonal planes, as shown in Figure 6.9. The breadth and intensity of the pattern is one reason the

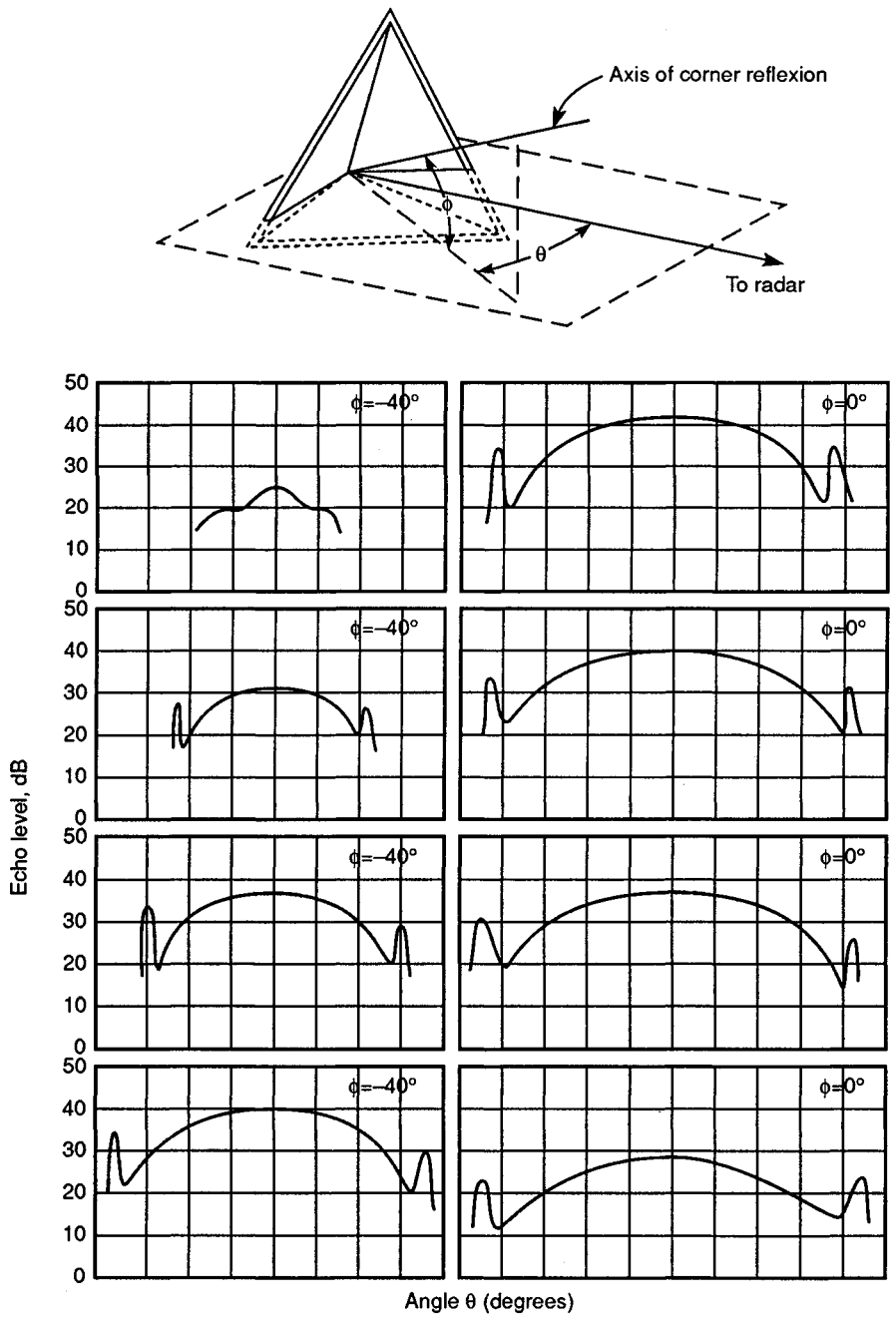

Figure 6.9. RCS pattern of the triangular-faced trihedral corner reflector (from [3]). (Copyright 1947 AT&T; reprinted with permission.)

trihedral corner is used as an echo enhancement device on sailboats and other targets to improve their detectability to navigation radars. It is also used as a calibration device on RCS test ranges because of the intensity of the echo and the accuracy and simplicity with which it may be calculated.

In calculating the echo from the triangular-faced trihedral, as with the rectangular-faced dihedral, we must find the effective area, which includes only those portions of its surfaces that participate in the triple-bounce mechanism. When viewed along the axis of symmetry perpendicular to the trihedral aperture, the effective area is the central hexagon shown in Figure 6.10. When we insert the value for this area in (6.2), we find the on-axis echo to be

$$\sigma = \pi l^4/3\lambda^2 \tag{6.3}$$

where l is the length of one edge of the triangular aperture.

Corner reflectors are therefore reentrant structures whose echoes are relatively easy to predict for cardinal angles of incidence for simple geometries. Of more interest, and considerably more difficult to predict, are the echoes from engine intakes and exhausts. Although an incremental form of (6.2) is the one to use in that case, the task of finding the field distribution of the departing waves over the exit aperture, and then integrating that distribution to determine the RCS,

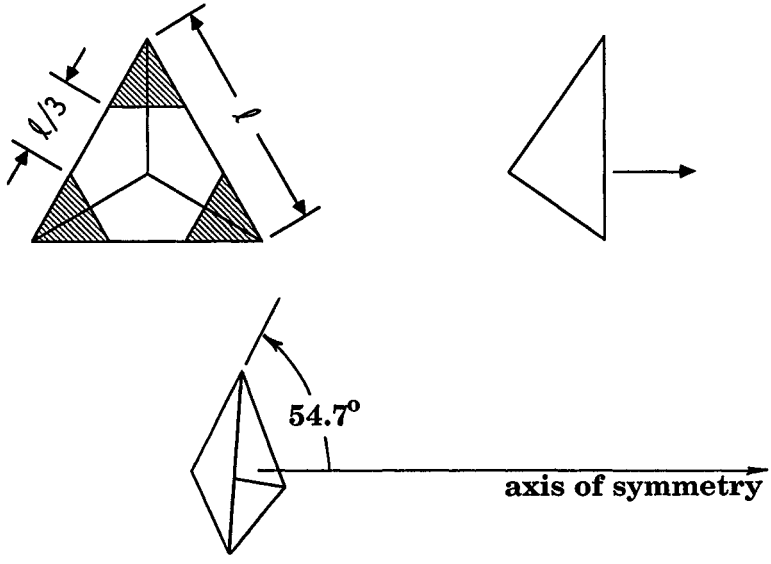

Figure 6.10. In calculating the effective area of the triangular-faced trihedral corner reflector when seen along the axis of symmetry, we must ignore the shaded regions near the tips (from [8]). (Copyright 1993 Van Nostrand Reinhold Publishing Co.; reprinted with permission.)

is not simple; we typically rely on measurements instead. Unfortunately, measurements of jet intake and exhaust ducts are highly classified, and we can offer no measured examples. However, we can cite some calculations of simple duct models that have appeared in the open literature.

We have already noted that the compressor state of a jet turbine forms the rear face of what can be a deep cavity when seen in a forward sector, and it reflects almost all of the energy reaching it back out the engine intake. The same mechanism is involved in the echoes from the exhaust duct seen from the rear. Although not all the energy entering the duct is directed back toward the radar when it emerges, that which does is significant. And although we cannot compute the echo using simple back-of-the-envelope formulas like (6.2), we may put the digital computer to use. Indeed, the patterns in Figures 6.11 and 6.12 were computed by a Cray X-MP computer.

The duct in this case was a circular one 10λ in diameter and 20λ long, and it does not necessarily simulate the geometry used for any operational jet engine. The echoes from two versions were computed, one a straight cylindrical geometry and the other a serpentine geometry formed by displacing the rear of the duct precisely one diameter off the centerline of the intake aperture. The theory of geometric optics was used in a ray-tracing scheme to account for the distribution of the fields over the intake aperture due to rays entering the duct, suffering internal reflections in accordance with Snell's law (angle of reflection equals angle of incidence at all internal surfaces), and passing back out the aperture. The aperture

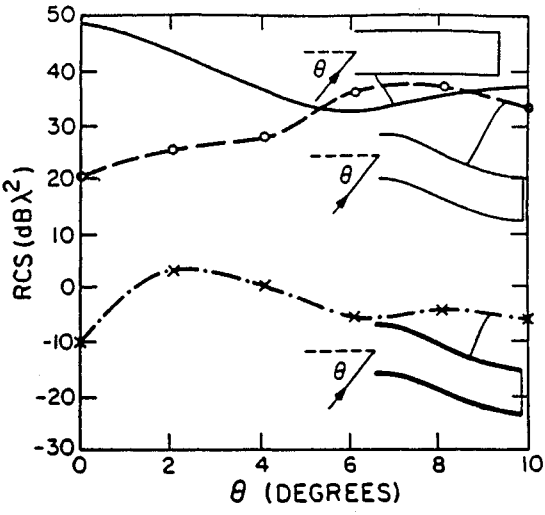

Figure 6.11. Calculated RCS for straight and serpentine circular ducts with and without an internal absorber lining for incident electric field parallel to the duct aperture. The ducts in all cases were 10λ in diameter, 20λ long, and sealed at the rear with a bare metal plate (from [9], Fig. 16, p. 204). (Copyright 1989 IEEE; reprinted with permission.)

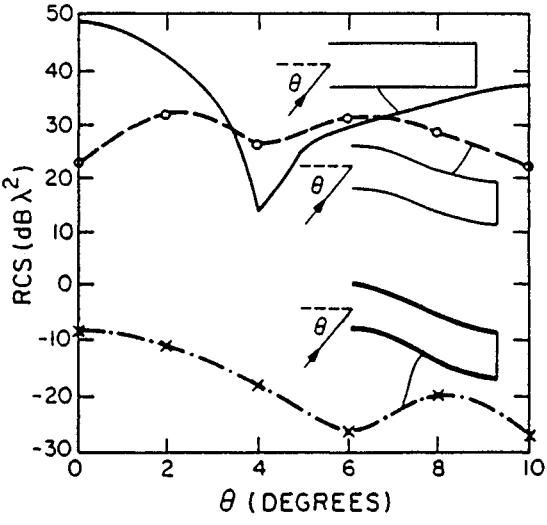

Figure 6.12. Calculated RCS for straight and serpentine circular ducts with and without an internal absorber lining for incident magnetic field parallel to the duct aperture. The ducts in all cases were 10λ in diameter, 20λ long, and sealed at the rear with a bare metal plate (from [9], Fig. 16, p. 204). (Copyright 1989 IEEE; reprinted with permission.)

distribution was summed coherently to determine the far scattered fields, from which the RCS was computed.

Figures 6.11 and 6.12 show the predictions when the incident electric and incident magnetic fields are parallel to the aperture, respectively. The solid trace at the top of each chart is for the straight duct without any absorber lining, and at $\theta = 0$ (which we henceforth consider nose-on incidence), the echo is 48.9 dBλ^2, as may be calculated for a circular disk 10λ in diameter. The echo decreases away from this angle and drops into a null, the null in Figure 6.12 being deeper and occurring at a smaller angle than the one in Figure 6.11. When the duct is twisted into a serpentine shape, the echo drops by more than 25 dB at nose-on incidence because much of the energy reflected back out the aperture is directed away from the direction of incidence.

Away from nose-on incidence, the echo from the unlined serpentine duct climbs to the intensity of the echo from the straight duct and for some angles exceeds it. Therefore, the serpentine duct offers no practical echo suppression except very close to nose-on incidence. When the duct is lined with absorber, however, we note a dramatic reduction in the echo for all the angles of incidence covered in the chart. In Figure 6.11, the reduction is of the order of 35 dB over most of the pattern and amounts to a whopping 60 dB at nose-on incidence. Except for a 1° sector near 4°, the reduction displayed in Figure 6.12 is even better, amounting to about 50 dB over most of the pattern.

These dramatic reductions are due to a multitude of internal reflections offered by the serpentine duct to and the lateral displacement of the rear of the duct so that it is seldom seen directly from the direction of the radar. The dielectric constant of the absorber lining the duct was a relatively modest $\epsilon_r = 1.5 + i\,2.0$ and was $\lambda/4$ thick. Although the bistatic echo reduction of such a layer ranges from -15 dB to -5 dB, depending on the polarization and bistatic angle, the cumulative effect of the absorption on multiple internal reflections becomes significant. Therefore, the echoes from reentrant structures like jet intakes are high, but can be reduced by convoluting the duct and lining it with absorbing material.

6.3 SURFACE WAVES

We have already noted in Section 6.1 that traveling surface waves may be launched along metal surfaces, and we recognize two kinds, depending on whether the surface is illuminated by the incident wave or shaded from it by other parts of the body. We distinguish between the two by simply calling the former a traveling wave and the latter a creeping wave, although both "travel." The traveling wave is excited by the incident wave when the incident electric field has components perpendicular and parallel to the surface in the plane of incidence defined by the surface normal and the direction of incidence, as shown in the upper sketch of Figure 5.12. If there is no electric field component in the plane of incidence, as in the lower diagram, the surface traveling wave is not excited.

As we saw in Chapter 5, the surface currents supporting the traveling wave propagate over metal surfaces close to the speed of light. The far electric field radiated by a current wave of constant amplitude has the form given by (5.83) and (5.84), rewritten here as

$$E = Q\,(kl/2)\sin\theta\,\frac{\sin\left[(kl/2)\,(1-\cos\theta)\right]}{(kl/2)\,(1-\cos\theta)} \tag{6.4}$$

where we have set $p = 1$. The expression is fairly accurate for straight surface features, and we can accommodate slightly curved surfaces by retaining $p = 1$ and devising an effective value for it that accounts for a slightly longer propagation path over the curved surface as compared to a straight one.

If we accept (6.4) as the pattern generated by a backward-traveling wave on a body, that wave being due to the reflection of a forward-traveling current wave, it is generally the first lobe of (6.4) that concerns us. This is because the first lobe is the strongest one in the pattern, and the one most likely to reveal our presence if we have angled our surface normal well away from a forward threat sector. As such, we would like to have some idea of its intensity.

Although we are not likely to employ square plates in the design of a stealth aircraft nor to present their edges perpendicular to the line of sight at low angles of incidence, Ross's flat-plate patterns illustrate the surface traveling wave. The

lobe at $\theta = 69°$ in the right-hand pattern of Figure 6.2, for example, is the first peak of the backward-traveling wave echo contribution from the plate, and it lies within 1° of the first value listed in eq. (5.91), bearing in mind that the angle in (5.91) is measured from grazing, not broadside, incidence. Indeed, if we examine the remaining flat-plate patterns in Ross's paper [2] (but not presented here), we find that the first peaks of the traveling wave response also lie within 1° of the predicted angle. Therefore, the mechanism seems to be well understood.

Because the first lobe in the traveling wave radiation pattern is the strongest one, it is of interest to relate its amplitude to the surface at hand. The strength of the pattern is governed by the constant Q in (6.4), which in turn depends on the nature of the surface and the angle of arrival of the incident wave. We should therefore allow Q to be a function instead of a mere constant; and even if we can seldom develop theoretical prescriptions for that function, we can at least determine useful empirical relationships for the amplitude of the first lobe in the pattern. We therefore return to the asymptotic solution of (5.87).

If we admit $f = 1.165561$ as the asymptotic solution for $p = 1$, we may insert that value in (5.84), solve the expression for $\cos \theta$ and use the result to calculate $(kl/2) \sin \theta$. When we insert this value in (6.4) and use the resulting scattered field to calculate the radar cross section, we obtain

$$\sigma/\lambda^2 = P\,[(l/\lambda)^2 - (f/\pi)^2]\,[(\sin f)/f]^2 \tag{6.5}$$

where P is an empirical function to be determined. Note that the dependence on surface length appears in a single variable in the expression, and aside from P, all quantities are constants. In the case at hand, P also appears to be a constant; within 0.3 dB, the value $P = 1.75$ predicts the RCS of the first traveling-wave lobes of Ross's square plates, whose edges were 3.1, 3.9, and 5.1λ along a side.

For plates of this size, the second term within the first brackets of (6.5) is negligible in comparison to the first, and the expression becomes simply $\sigma = 1.09\ l^2$, independent of frequency. This yields a value of -15.3 dBsm for the first traveling wave peak in the right-hand pattern of Figure 6.2, barely 0.4 dB above the value registered there. The applicability of the empirical result is limited, however, because the range in the size of Ross's plates is limited, the plates were square, and one edge was presented perpendicular to the line of sight.

Although we have emphasized that a reflection of a forward-traveling wave by a discontinuity at the far end of a surface produces a backward-traveling wave, the two waves actually constitute an infinity of forward- and backward-traveling waves. Just as the far end of the body reflects a forward-traveling wave in the backward direction, the near end of the body reflects a backward-traveling wave in the forward direction. Because neither reflection is perfect, the intensity of higher-order traveling waves are less intense than their progenitors, and they eventually decay to unmeasurable levels. Although each reflected wave is weaker than the wave that spawned it, all propagate along the surface with the same speed, and the patterns radiated by all are sensibly identical in form, if not in amplitude.

Under steady-state conditions in the frequency domain, we cannot separate any single forward-traveling wave from any other, nor any single backward-traveling wave from any other. All travel at the same speed, and we can discern only the coherent sum of all forward-traveling waves from the coherent sum of all backward-traveling waves. As best we can perceive with narrowband equipment, therefore, there seem to be only two traveling waves, one going forward and one going backward, both radiating patterns essentially as described by (6.4), with the angle θ measured from the direction of current flow.

Although the surface traveling wave mechanism may dominate the scattering from straight target features illuminated at low grazing angles, the mechanism is present, if not apparent, even at normal incidence. Indeed, Einarsson notes that the currents induced on straight wires have, in general, three components for any angle of incidence [10]. One is a backward-traveling wave, one is a forward-traveling wave, and one is a kind of physical optics component whose phase angle tracks that of the incident wave along the wire. Although all three are present, the backward-traveling wave mechanism dominates the backscattering pattern near end-on incidence and physical-optics-like mechanism dominates it in the specular region. The forward-traveling wave mechanism and the physical-optics-like mechanism have comparable contributions in the bistatic pattern near the specular direction for low grazing angles.

An example of the backscattering of a wire is shown in the theoretical pattern of Figure 6.13. The wire was about 16.5λ long, for which eq. (5.86) predicts the first backward-traveling wave lobe will peak at 12.1°, very close to the actual location displayed in the figure. If no traveling waves had been induced along the wire, the specular region at the right side of the pattern would have exhibited the sin x/x pattern characteristic of a uniformly illuminated aperture. However, the pattern due to traveling current waves fills the even-numbered nulls in the specular region and alternately modulates the amplitudes of the near-specular sidelobes. Therefore, the traveling wave mechanism exists even at broadside incidence.

Figure 6.14 charts the amplitude of the first peak of the traveling wave echo from a thin wire as a function of the wire length. The solid line in the figure was sketched by the original researchers through data extracted from 81 measured backscattering patterns, each recorded for a different wire length. The echo undulates with a period of $\lambda/2$, and we have added to the original chart a dashed line through the peaks of the variation as obtained with the empirical prescription

$$\sigma/\lambda^2 = 2.6\ (\lambda/l)\ [(l/\lambda)^2 - (f/\pi)^2]\ [(\sin f)/f]^2 - (2/\pi) \tag{6.6}$$

This prediction is meaningless for very short wires because it becomes singular for zero length, and the trailing constant becomes insignificant for wires longer than a few wavelengths. The locus of the peaks in Figure 6.14 suggests that the traveling-wave echo of the wire rises linearly with electrical wire length, and we have merely attempted to preserve the form of (6.5) in devising the empirical description.

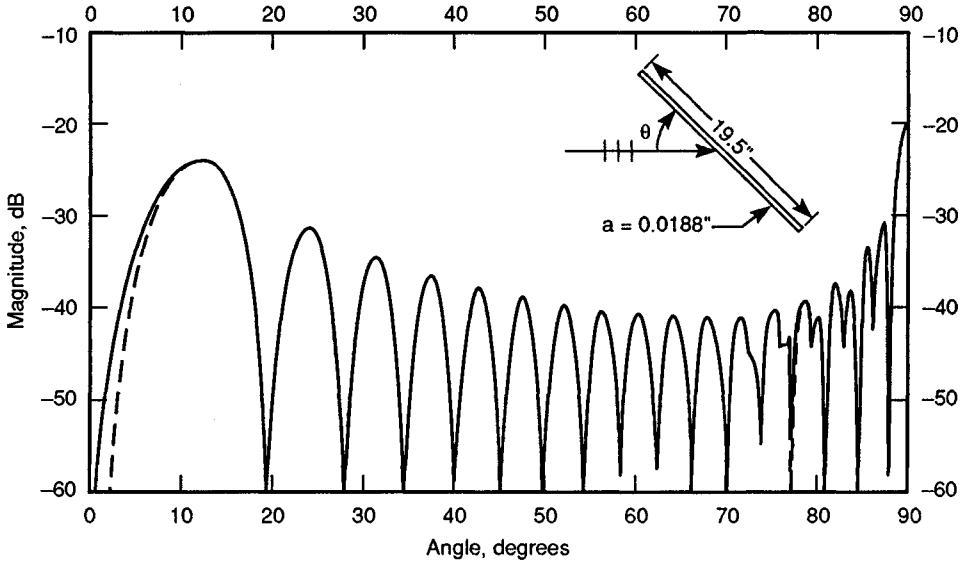

Figure 6.13. Computed backscattering pattern of a wire 19.5 in. long and 0.0376 in. in diameter at 10 GHz (from [11], Fig. 3, p. 1021). (Copyright 1989 IEEE; reprinted with permission.)

The far edge of a plate or the far end of a wire defines an abrupt discontinuity that generates backward-traveling current waves with significant echo contributions, but any discontinuity on the surface can reflect the traveling wave. Examples are the gap, slot, and step discontinuities shown in Figure 6.15. The magnitude of the reflection of the surface traveling wave depends on the size and shape of the discontinuity and on the angle of arrival of the surface wave with respect to the axis of the discontinuity. In some cases it is possible to angle the axis out of the threat sector, a version of which is the sawtoothed edges of the weapon bay doors and landing-gear bay doors of some advanced aircraft. In other cases, a gap may be temporarily covered with metal tape or sealed with radar-absorbing putty. Because the tape or putty is destroyed when the door is opened, it must be reapplied at the beginning of each mission.

Whether the target is a wire or a flat facet, and aside from what happens in the specular region, it is clear that when we shape our target to swing specular surface echoes well out of the threat sector, we risk the hazard of swinging traveling lobe echoes into it. Unlike the specular echo, however, traveling wave echoes are relatively easy to suppress with materials with only modest loss. The most common method of suppression is to apply surface-wave absorbers like those described in Chapter 8. Because the surfaces that may support the traveling wave mechanism are usually dozens or hundreds of wavelengths long for frequencies above 1 GHz

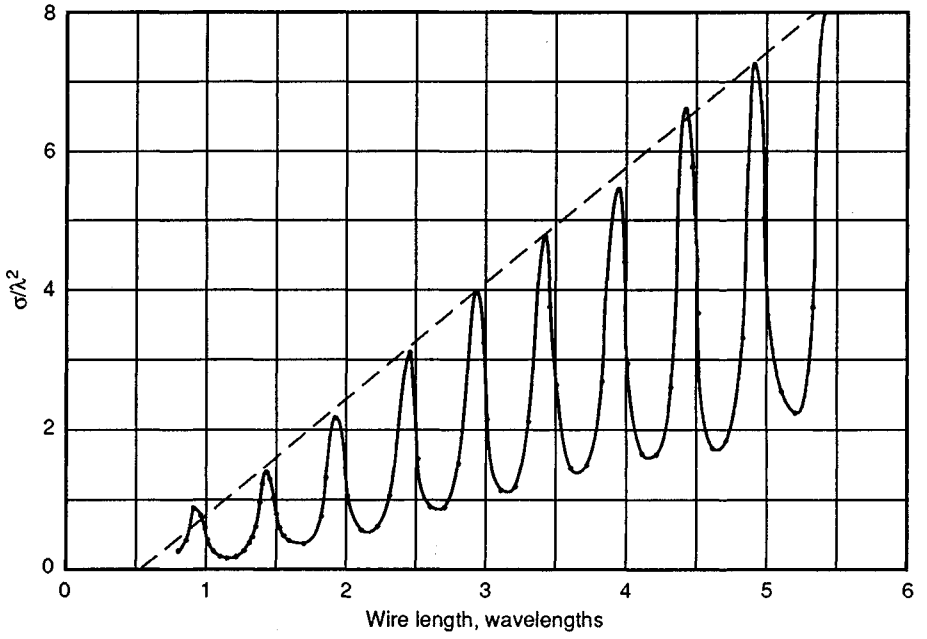

Figure 6.14. The first peak of the traveling wave echo from a thin wire of length l as measured at the University of Michigan (from [12], Fig. 3-3a). Dashed line is an empirical fit, and the wire was $\lambda/80$ in diameter.

or so, the material does not have to be a particularly lossy one. Although the attenuation of the surface wave, in, say, dB per wavelength, may be modest, the total end-to-end attenuation may be substantial by virtue of the sheer length of the surface. Moreover, the surface wave must traverse the surface twice (once in the forward direction and once in the backward direction), effectively doubling the loss afforded by a surface wave absorber. Therefore, the absorber used to attenuate traveling waves does not need to be as thick or as lossy as that used to suppress specular echoes.

Like the traveling wave launched along lit surfaces, the creeping wave launched along shaded surfaces also requires a normal component of electric field. Once launched at a shadow boundary, it follows a geodesic path along the surface and sheds energy continuously, as suggested in Figure 6.16. Therefore, unlike the traveling wave on lit surfaces, which appears to suffer little attenuation as it propagates along the surface, at least in the absence of any absorptive mechanism, the creeping wave decays in amplitude with increasing distance. A generic form for the rate of decay is

$$\sigma_{cw}/\sigma_{op} = \alpha\,(ka)^{\beta} \exp\,[-\gamma(ka/2)^{1/3}] \tag{6.7}$$

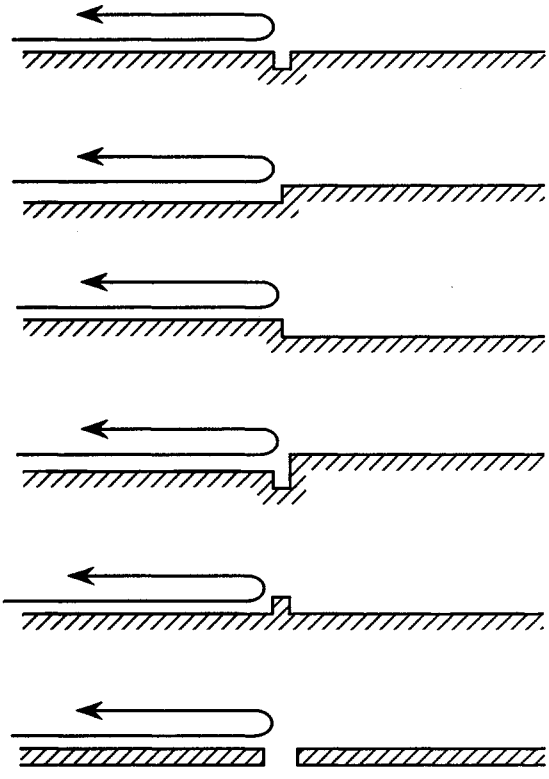

Figure 6.15. Surface discontinuities like gaps, slots, steps, and seams can reflect the surface wave in the backward direction.

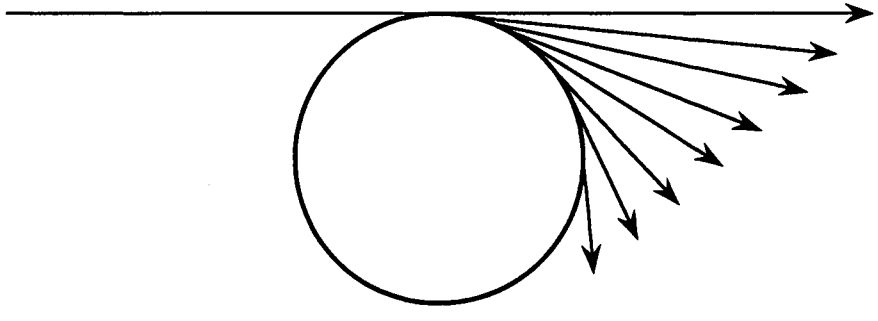

Figure 6.16. The creeping wave sheds energy incrementally as it travels around a curved surface.

where we have normalized the creeping wave contribution with respect to the optics return, and the constants α, β, and γ depend on the surface profile over which the wave creeps. We will return to this generic description in a moment.

Creeping waves can skirt the rear of thin objects as well as fat ones, and the circular metal disk is an example [13]. There is probably a creeping wave for most angles of incidence, but the mechanism is enhanced when the disk is seen edge-on with the incident polarization in the plane of the disk. As with the sphere, there are two contributions, one a specular diffraction from the near edge of the disk and the other a creeping wave that goes around the back side. The two alternately combine in and out of phase with increasing disk size, just as they do for a sphere.

A comparison of measured and predicted edge-on scattering from thin metal disks is shown in Figure 6.17. Charted here is the magnitude of a quantity S that is proportional to the scattered electric field and related to the RCS by the formula

$$\sigma/\lambda^2 = |S|^2/\pi \tag{6.8}$$

Note that the amplitude of the excursion near the center of the chart ranges from about 0.25 at the minima to about 1.4 at the maxima, a ratio of 5.6 to 1. The peak-to-peak excursion therefore amounts to about 15 dB, a far greater swing than we saw for a sphere of this electrical size. In contrast to the sphere, for which the

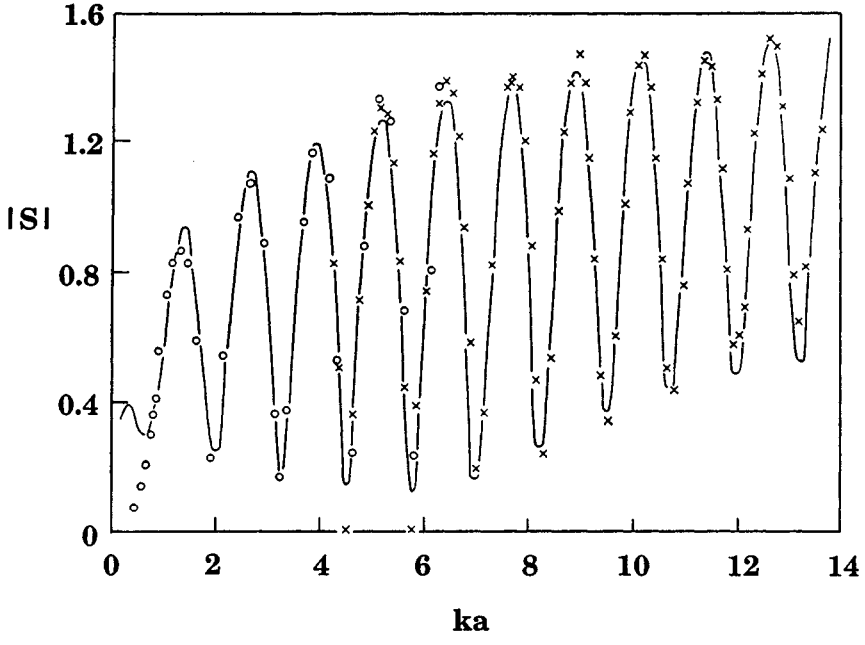

Figure 6.17. Measured and predicted edge-on scattering from thin circular disks. Solid trace is the prediction and the crosses and open circles are measured values (from [13], Fig. 5, p. 756). (Copyright 1969 IEEE; reprinted with permission.)

creeping wave is much smaller than the specular sphere echo, at least for spheres greater than a few wavelengths in diameter, the echo contribution from creeping wave on the disk is comparable to the return from the edge.

Indeed, the relative strengths of creeping waves are illustrated in Figure 6.18 for the sphere, the infinite circular cylinder, and the disk just discussed. The traces for the metal sphere and circular cylinder were deduced from the exact solutions for the scattering from those bodies, and the charted echo strength for the disk is that given by Senior [13]. The plotted curves are relative to the optics return, as suggested by (6.7), and the constants appropriate to the three bodies are listed in Table 6.2. The creeping wave for the disk is the strongest of the three and that from the infinite circular cylinder the weakest; note that the normalized echoes are separated from each other by more than an order of magnitude.

No known military or civilian targets are built of spheres, cylinders, or disks, but rounded surfaces or edges may be found on many targets and creeping waves may certainly propagate along such features when shaded from the incident wave. The echo contributions of creeping waves are small enough, however, to be neg-

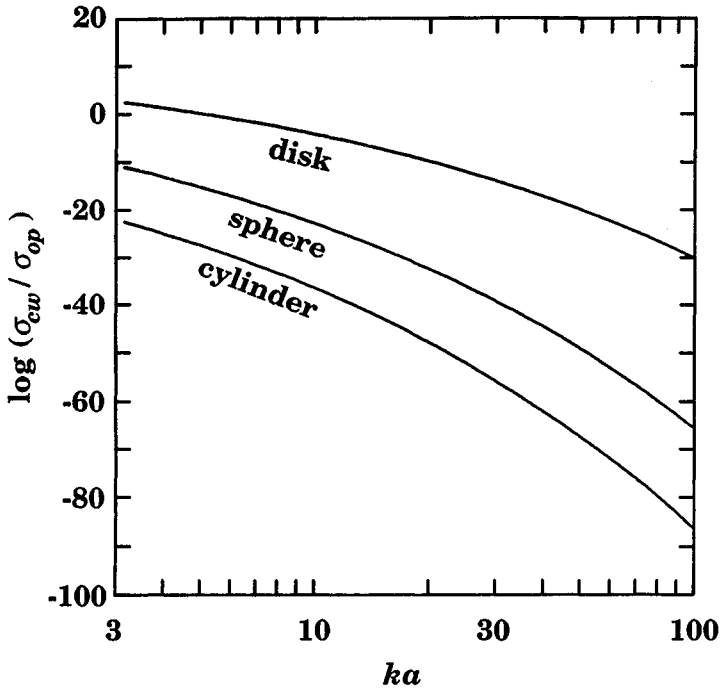

Figure 6.18. The creeping wave echo from the metal sphere, the infinite circular cylinder, and the circular disk as a function of *ka*. This behavior is well approximated by (6.7) with the constants listed in Table 6.2.

Next Page

Table 6.2.
Surface Wave Echo Characteristics

Type	*Surface feature*	*Examples*	*Echo characteristic*			
Traveling wave	Straight or slightly curved, lit	Flat plate; thin edge; wire; long, thin bodies	peak near $\theta = 49.35\sqrt{\lambda/l}$			
			Eq. (6.7) constants			optics return
			α	β	γ	
Creeping wave	Curved, shaded	Disk, sphere, cylinder	62.8	0.333	3.43	$a\lambda/2\pi$
			26.4	−0.0058	4.98	πa^2
			4.77	−0.124	5.67	πa

l = length of straight surface feature
a = radius of surface curvature

ligible in almost all cases of practical interest. Indeed, the diffraction from edges is a far more significant scattering mechanism.

6.4 DIFFRACTION

As we shall see in Chapter 7, the design of a faceted airframe drastically reduces the number of specular directions from which large echoes will be observed, but this faceting will create a multitude of edges. The notion of a specular direction is still preserved, as in the Keller cone of scattered rays in Figure 5.7, but the scattering in that event is spread over a cone. The cone collapses to a disk when we see the edge at normal incidence, and although the intensity of the backscattered echo may be less than that from a flat plate, it can still be strong. An example of edge diffraction might be the scattering from the leading edge of a wing, indicated in Figure 6.1 for the right wing of the missile.

Even if we manage to angle a surface so that the surface is never seen from a direction anywhere near the direction of its surface normal, we may still have an edge with a large number of "specular" directions spread over a plane perpendicular to the edge. So, even though we may rely on shaping to direct a specular surface reflection away from the radar, we must also rely on shaping to direct edge scattering away from the radar. This means we must choose the sweep angle of the wing to direct the edge diffraction out of the threat cone, which is usually centered on the direction of flight.

If the edge is a curved one, an infinity of nonparallel planes are perpendicular to the edge containing a specular direction, each erected at a different place along the edge. Because curved edges are generated by the intersections of curved sur-

Chapter 7
Radar Cross Section Reduction

J. F. Shaeffer, M. T. Tuley, and E. F. Knott

7.1 BACKGROUND

It has been apparent for some time that the development of increasingly sophisticated detection systems threatens to reduce the mission effectiveness of many types of weapons platforms. Strong attention is now being given to methods of increasing survivability by reducing detectability. Because the specific configuration of any platform is determined by many factors involved in its mission, the final design represents a compromise between conflicting requirements. The purpose of this chapter is to survey some of the *radar cross section reduction* (RCSR) options available. Although we focus on the radar signature, remember that other signatures must also be considered (e.g., infrared, acoustic, magnetic, optical), and design for signature control must carefully balance all signatures and threats.

This chapter is intentionally tutorial, with emphasis on concepts rather than application to specific systems. There are several reasons for this approach. For one, access to many research and development efforts is limited in the interest of national security. Also, there are other media for the exchange of technical information on specific application efforts.

Complex targets like ships and aircraft can be represented as collections of basic geometric elements, such as flat plates, cone frusta, spheroids, edges, vertices, or blended surfaces. As such, we typically isolate the dominant sources of target echo and fix our attention on a limited number of individual elements instead of the composite target. The widespread use of *high-range resolution* (HRR) and inverse synthetic aperture radar images as diagnostic tools has firmly entrenched the scattering center concept as the most useful method of analyzing the return

from complex bodies. At high frequencies, such an approach can certainly be justified, as it is the underlying assumption in the optics theories we use to calculate RCS. At lower frequencies, extended portions of the target may interact to provide a return that is more difficult to separate into individual scattering centers, but even there the theories that apply to simple scatterers provide insight into the behavior of complicated bodies.

We emphasize that radar cross section reduction is a study of compromises in which advantages are balanced against disadvantages, and this fact should become apparent. When target surfaces are reshaped or reoriented to achieve the reduction, RCSR at one viewing angle is usually accompanied by an enhancement at another. If *radar absorbing materials* (RAM) are used, the reduction is obtained by the dissipation of energy within the material, thus leaving the RCS levels relatively unchanged in other directions. On the other hand, the use of RAM is paid for with added weight, volume, and surface maintenance problems. Thus, each approach involves its own form of trade-off. This is another reason why we cannot deal with specific systems: the trade-offs cannot be made without information that is not currently available.

No matter the technique employed, each decrement in RCS is obtained at successively higher cost. The first 50% reduction is usually quite inexpensive, but the next 10% is a little more expensive, the next more costly still, until a 99% reduction may be prohibitively costly, in terms of dollars as well as trade-offs in weight, size, and configuration. The cutoff point for deciding how much RCS reduction to incorporate depends on a host of variables, such as relative effectiveness, incremental cost, and the platform's mission. Because each particular platform poses its own particular problems, we cannot establish the optimum RCS design approach for the general case. However, the concepts and principles illustrated here should make it easier to arrive at such a decision when specific systems are considered.

7.2 THE FOUR BASIC METHODS OF RCSR

There are only four basic techniques for reducing radar cross section:

1. Shaping;
2. Radar absorbing materials;
3. Passive cancellation;
4. Active cancellation.

Each method has advantages and disadvantages. The remainder of this section provides a brief overview of the four techniques. The two most practical and most often applied RCSR techniques are listed first, shaping and radar absorbing materials. In current RCS designs, shaping techniques are first employed to create a planform design with inherently low RCS in the primary threat sectors. Radar absorbing materials are then used to treat areas whose shape could not be optimized or to reduce the effects of creeping waves or traveling waves on the signature.

Radar absorbing materials are covered in detail in Chapter 8, and so are discussed only briefly here. The focus of this chapter, after a consideration of the "RCSR numbers game," is on shaping for radar signature control.

7.2.1 Shaping

The objective of shaping is to orient the target surfaces and edges to deflect the scattered energy in directions away from the radar. This cannot be done for all viewing angles within the entire sphere of solid angles because there will always be viewing angles at which surfaces are seen at normal incidence, and there the echoes will be high. The success of shaping depends on the existence of angular sectors over which low radar cross section is less important than over others. Note that in design for reduced RCS, emphasis has been focused almost exclusively on monostatic radars. The shaping guidelines presented in this chapter would have to be significantly modified if bistatic radars were the threat. Nevertheless, most current radar systems are monostatic, so the assumption that the threat is monostatic is a good one.

Typically, a forward cone of angles is of primary interest for RCSR, hence, we normally want to "shift" large cross sections out of the forward sector and toward broadside. This can be accomplished by sweeping airfoils back at sharper angles, for example. The forward sector includes the elevation plane as well as the azimuth plane, and if a target is hardly ever seen from above, echo sources, such as engine intakes, can be placed on the top side of the target where they may be hidden by the forward portion of the body when viewed from below. Similarly, for a low flyer whose major threats might be look-down radars, engine inlets might instead be placed on the underside of the fuselage.

For more "boxy" structures, such as ships and ground vehicles, internal dihedral and trihedral corner and "top hat" (right circular cylinder with its axis perpendicular to a flat plate) returns are the major RCS contributors, and those can be avoided by bringing intersecting surfaces together at acute or obtuse angles. Because of the presence of the sea surface, vertical bulkheads and masts on ships, in particular, form efficient corners, and the effect can be reduced by tilting the bulkheads away from the vertical. However, this is virtually impossible to do with existing vessels and therefore is a real consideration only in new designs. Even in the case of a new design, the amount of bulkhead tilt is a trade-off between RCSR performance and cost.

7.2.2 Radar Absorbing Materials

As the name implies, radar absorbing materials reduce the energy reflected back to the radar by means of absorption. Radar energy is absorbed through one or more of several loss mechanisms, which may involve the dielectric or magnetic properties of the material. The loss is actually the conversion of radio frequency

energy into heat, and although most absorbers do not dissipate enough energy to become even detectably warm when illuminated by a radar, this is nevertheless the mechanism by which they operate.

Underlying the operation of RAM is the fact that substances either exist or can be fabricated whose indices of refraction are complex numbers. In the index of refraction, which includes magnetic as well as electrical effects, the imaginary part accounts for the loss. At microwave frequencies, the loss is due to the finite conductivity of the material, as well as a kind of molecular friction experienced by molecules in attempting to follow the alternating fields of an impressed wave. It is customary to lump the effects of all loss mechanisms into the permittivity and permeability of the material because the engineer is usually interested in only the cumulative effect.

Carbon was the basic material used in the fabrication of early absorbers because of its imperfect conductivity, and it continues to be important today. In fact, many commercial carbon-based materials now being marketed have designs that have not changed substantially for more than 20 years. Most are intended for experimental and diagnostic work, including the construction of indoor microwave anechoic chambers, but these materials are not easily applied to operational weapons platforms. They are usually too bulky and fragile in operational environments.

Instead, magnetic absorbers are used more widely for operational systems. The loss mechanism is primarily due to a magnetic dipole moment, and compounds of iron are the basic ingredients. Carbonyl iron has been used extensively, as have oxides of iron (ferrites). Magnetic materials offer the advantage of compactness because they are typically a fraction of the thickness of dielectric absorbers. However, magnetic absorbers are heavy because of their iron content and are inherently more narrowband than their dielectric counterparts. The basic lossy material is usually embedded in a matrix or binder such that the composite structure has the electromagnetic characteristics appropriate to a given range of frequencies.

7.2.3 Passive Cancellation

Passive cancellation, one form of which is known as impedance loading, received a great deal of attention in the 1960s, but the method is severely limited. The basic concept is to introduce an echo source whose amplitude and phase can be adjusted to cancel another echo source. This can be accomplished for relatively simple objects, provided that a loading point can be identified on the body. A port can be machined in the body, and the size and shape of the interior cavity can be designed to present an optimum impedance at the aperture. Unfortunately, even for simple bodies, it is extremely difficult to generate the required frequency dependence for this built-in impedance, and the reduction obtained for one frequency in the spectrum rapidly disappears as the frequency changes.

Furthermore, typical weapons platforms are hundreds of wavelengths in size and have dozens, if not hundreds, of echo sources. Clearly, it is not practical to devise a passive cancellation treatment for each of these sources. In addition, the

cancellation can revert to a reinforcement with a small change in frequency or viewing angle. Consequently, passive cancellation has for the most part been discarded as a useful RCS reduction technique.

7.2.4 Active Cancellation

Also known as *active loading,* active cancellation is even more ambitious than passive loading. In essence, the target must emit radiation in time coincidence with the incoming pulse whose amplitude and phase cancel the reflected energy. This implies that the target must be "smart" enough to sense the angle of arrival, intensity, frequency, and waveform of the incident wave. It must also be smart enough to know its own echo characteristics for that particular wave length and angle of arrival rapidly enough to generate the proper waveform and frequency. Such a system must also be versatile enough to adjust and radiate a pulse of the proper amplitude and phase at the proper time. Clearly, the relative difficulty of active cancellation increases with increasing frequency, as scattering centers go in and out of phase with smaller aspect changes and where scattering patterns become more complex.

Thus, if it has a place at all, active cancellation appears most suitable for low-frequency RCSR, where use of absorber and shaping become very difficult and scattering patterns exhibit broader lobes. Research on the technique is likely to continue because other practical means of RCSR are also difficult to apply for low frequencies. Nevertheless, it is worthwhile to remember that an active canceler that is not working correctly has another name—it is called a beacon!

7.2.5 The Penalties of RCSR

Most of the time, the requirement for reduced radar echo conflicts with conventional or traditional requirements for structures. As a result, the final system design is a compromise that inevitably increases the cost of the overall system, from initial engineering through production. Cost is only one penalty of RCSR; others are

1. Reduced payload;
2. Reduced range;
3. Added weight;
4. Increased maintenance.

The relative importance of each factor depends on the mission of the particular platform involved, of course, and these factors change from one system to another. Not surprisingly, radar cross section reduction cannot always be justified, at least in terms of improved detection ranges. In one study, for example, Georgia Tech calculated the detection range for a hypothetical sea target ingressing against shore-based radars. The detection range was decreased less than 10% despite drastic changes in the target to reduce its radar echo. One reason for this was that

the assumed threats were very sensitive and the target was detected as it came over the horizon, treated or not. On the other hand, although unsupportable on the basis of detection, RCSR for that platform may well have been justified when considered in concert with electronic countermeasures.

In any event, the radar signature is simply one part of a platform specification. Trade-offs will always have to be made with respect to a large number of operational characteristics. Only when all of the characteristics are jointly considered in light of the platform mission can a truly optimum solution to maximize survivability and mission effectiveness be devised.

7.3 THE RCSR NUMBERS GAME

Before discussing some practical ways to reduce the RCS of a given target, it is instructive to consider a few illustrative numerical exercises. If a target can be resolved into a collection of N discrete scatterers or scattering centers, then the net radar return at a given frequency is

$$\sigma = \left| \sum_{n=1}^{N} \sqrt{\sigma_n}\, e^{j\phi_n} \right|^2 \tag{7.1}$$

where σ_n is the RCS of the nth scatterer and ϕ_n is the relative phase of that particular contribution due to its physical location in space. Equation (7.1) will be recognized as a coherent sum because the phase contribution of each scatterer is included in the summation.

The coherent sum is for a particular aspect angle, because not all of the scattering elements on a target are visible at the same time. Some are shielded from the radar, for example, by other parts of the target itself. Consequently, the number of contributing scatterers N will change from one aspect angle to another as certain features come into, or disappear from, view.

Moreover, the amplitudes of the individual returns (σ_n) are aspect-angle sensitive, changing with the viewing angle. Therefore, the radar cross section is a function, not merely a fixed number. Some of the individual contributions are quite broad in their aspect angle dependence, whereas others are quite narrow.

Similarly, each individual phase angle ϕ_n depends on the distance between the scatterer and the radar. The phase angle is a function of the radar frequency as well as the distance, and consequently the coherent sum changes from one radar frequency to another. Also, because the distance of each scatterer depends on the target aspect angle, the relative phase of each contributor changes with aspect.

For large targets, such as those that are at least a few tens of wavelengths in size, the phase angle variations produce rapid fluctuations in the total return. However, because the returns from individual contributors vary relatively slowly

with aspect angle, the mean return can be surprisingly steady over aspect intervals of a few degrees. These mean values are more useful in characterizing the gross target returns than the detailed structure of a given target echo measured at a certain frequency.

This gives rise to the notion of forming the noncoherent sum. In many cases it can be safely argued that all phase angles are equally likely. Those cases are when the target is large, the wavelength is short, or both. If all phase angles are equally likely, then a good statistical characterization of the target is the noncoherent sum:

$$\sigma = \sum_{n=1}^{N} \sigma_n \tag{7.2}$$

The RCS pattern predicted by (7.2) does not have the rapid fluctuations characteristic of the more accurate (7.1); therefore, scintillation in the pattern is largely lost.

A caution is in order, however. Many RCS codes break a target into a large number of discrete scatterers, and the total RCS is assumed to be the coherent superposition of the individual returns, per (7.1). If each scattering element represents a complete coherent scattering area on the target, then (7.2) can be applied with some confidence that the result will match the mean RCS. However, if coherent scattering areas are subdivided into small elements in an RCS code, then (7.2) cannot generally be applied. A simple example is a square flat plate. Assume that such a plate is modeled in a physical optics code using four smaller square plates, rather than one large one. At specular incidence, the RCS calculated from (7.2) will be one-fourth the correct answer given by (7.1). Off normal incidence, the RCS calculated by (7.2) may be as much as 6 dB lower or many decibels higher than that given by (7.1). In particular, for plates much larger than a wavelength viewed near grazing and along the diagonal (a desirable situation for low RCS, as will be shown later), the noncoherent RCS calculated by using (7.2) will be much larger than will the average of the coherent RCS taken over moderate angles. The situation becomes worse as the plate is subdivided further, as might be the case where a RCS code attempts to match a blended surface with many small flat facets. Thus, caution is in order.

Nevertheless, when dealing with distinct scattering centers, as might be derived from ISAR measurements, the noncoherent sum is particularly useful in illustrating the need to first reduce the returns of the dominant scatterers before considering the less dominant ones. Assume, for example, that a very simple target has but three contributors and that the return from one of them is 10 times stronger than the returns from the other two. For the sake of numerical comparison, assume its return is 200 m^2, whereas the returns from the remaining two are only 20 m^2

each. Using the noncoherent sum to evaluate the effect of reducing the returns of the three, we can construct Table 7.1, showing the effect of reducing the returns of one or all of the contributors.

Note that a 10 dB reduction in the return of the dominant scatterer amounts to only a 6 dB reduction in the total return. Therefore, although a dominant scatterer is present, the reduction in the total return of the target will always be less than the amount by which that individual return is reduced. We see from the table, for example, that a net reduction of 10 dB was accomplished only by reducing the returns of all three scatterers by 10 dB.

Can we do better by working harder on the dominant scatterer? The answer is yes. Suppose we can reduce the dominant scatterer by 15 dB, but the others by only 10 dB (due to the nature of the particular echo sources, for example), then our efforts have the results shown in Table 7.2. This table shows that even though we considerably improved the treatment of the dominant scatterer (from 10 dB reduction to 15 dB), the reduction in the total return improved by only 1.1 dB (from a 6 dB reduction to a 7.1 dB reduction). Clearly, the task is more difficult than might have been assumed at the outset. If one of the less important scatterers is given a 10 dB reduction in addition to a 15 dB reduction of the dominant scatterer,

Table 7.1
Effect of a Dominant Scatterer

	Untreated	Reduce σ_1 by 10 dB	Reduce σ_1, σ_2 by 10 dB	Reduce σ_1, σ_2, σ_3 by 10 dB
σ_1	200	20	20	20
σ_2	20	20	2	2
σ_3	20	20	20	2
Total	240	60	42	24
dB reduction	0	6	7.6	10

Table 7.2
Effect of Working Harder on the Dominant Scatterer

	Untreated	Reduce σ_1 by 15 dB	Reduce σ_1 by 15 dB, σ_2 by 10 dB	Reduce σ_1 by 15 dB, σ_2 by 10 dB σ_3 by 10 dB
σ_1	200	6.3	6.3	6.3
σ_2	20	20.0	2.0	2.0
σ_3	20	20.0	20.0	2.0
Total	240	46.3	28.3	10.3
dB reduction	0	7.1	9.3	13.7

the net reduction is 9.3 dB. Treatment of the third scatterer brings about a 13.7 dB total reduction.

Going a step further, we perform some total eliminations to examine the very best that could be done if only either the dominant or lesser contributors were absent. The results are shown in Table 7.3. Clearly, the total elimination of one or the other cannot produce a 10 dB reduction. Eliminating σ_1 results in a 7.8 dB reduction, but the elimination of σ_2 and σ_3 produces barely 1 dB of reduction.

What if all three scatterers had been of the same amplitude? Table 7.4, like Table 7.1, shows that *all* the scatterers must be reduced by 10 dB to effect a 10 dB reduction in the total. Consequently, as we might have guessed, it is important to concentrate first on the dominant scatterers on a target because a reduction there yields the greatest payoff. However, we must always be aware that the job is much more difficult when there are many echo sources, all of about the same magnitude. In that event, treatments must be devised for many scatterers instead of just a few.

Table 7.3
Effects of Selective Elimination of Scatterers

	Untreated	Eliminate σ_1	Eliminate σ_2 and σ_3
σ_1	200	0	200
σ_2	20	20	0
σ_3	20	20	0
Total	240	40	200
dB reduction	0	7.6	0.8

Table 7.4
Effect of Reduction When All Have the Same Amplitude

	Untreated	Reduce σ_1 by 10 dB	Reduce σ_1, σ_2 by 10 dB	Reduce σ_1, σ_2, σ_3 by 10 dB
σ_1	20	2	2	2
σ_2	20	20	2	2
σ_3	20	20	20	2
Total	60	42	24	6
dB reduction	0	1.6	4	10

7.4 SHAPING

Shaping is the first approach for radar cross section reduction if serious RCSR is desired. Shaping does not reduce cross section as measured over 4π sr sphere, but

rather reduces cross section over limited angular viewing regions. The goal of shaping is to bounce or redirect incident radar energy away from the threat receiver into nonthreat spatial regions. Most radar systems are monostatic with the receiver and transmitter collocated, so shaping is concerned with minimizing reflection in the backscatter direction. An alternative view of shaping is that we maximize scattering into directions of space for which threat receivers are not present. Therefore the goal of shaping is to reduce backscatter cross section while increasing forward (bistatic) cross section.

The reason shaping is so important to achieve significant detection range reduction is illustrated by the radar range equation. Detection range varies as the fourth root of cross section, $\sigma^{1/4}$. Based on an arbitrary 100 mile detection range, Table 7.5 shows how the detection range becomes smaller as the cross section is reduced. A 90% reduction of RCS (10 dB) reduces the detection range to 56 miles, 99% reduction (20 dB) to 32 miles, and a 99.9% reduction (30 dB) to 18 miles. Significant detection range reduction requires even more significant RCS reduction. The application of RAM alone will not suffice. Because several orders of magnitude reduction in RCS is required, shaping must be utilized as the main design approach.

Detection range reduction reduces the reaction time allowed to a defensive radar site. RCSR is not the only approach to reduce reaction time. Halving the reaction time may be achieved by reducing RCS by a factor of 16 (12 dB) or by doubling the vehicle velocity.

The RCS of most targets is related to their physical size. That is, larger targets generally have larger cross sections. However, by carefully following the shaping rules we can design targets whose RCS does not depend on size, at least within the threat sector.

The RCS of a system depends on all of its components. Although the historical emphasis has been to obtain a low RCS planform, this alone is not sufficient. The net system RCS is due not only to its geometric configuration (hard body) but is also due to its inlet and exhaust cavities, crew station, avionics sensors and antennas, and construction details (gaps, cracks, door openings, etc.). Even though this section concentrates on vehicle geometric shaping considerations, these other issues must also be considered.

Table 7.5
Arbitrary Detection Range versus RCS Reduction

Cross section reduction	Detection range
0%, 0 dB	100 (arbitrary)
90%, 10 dB	56
99%, 20 dB	32
99.9%, 30 dB	18
99.99%, 40 dB	10

Shaping as a tool for RCS reduction applies only to bodies much greater in size than the wavelength; that is, in cases in which optical scattering applies. In this region the zeroth order view is of ray path billiard-ball-bounce scattering where the angle of reflection is equal to the angle of incidence. For backscatter this means only those surfaces and edges whose normals point back toward the threat sector will have significant scattering.

7.4.1 Shaping Roadmap and Threat Sectors

Shaping of a target to reduce backscatter RCS cannot be done without consideration of mission requirements. The first design step is to define the threats expected for a specific mission: the types of radars, frequencies, polarizations, spatial locations, and detection ranges expected. Some missions may be covert so that very reduced RCS is desired, but other missions require only increased survivability. Some systems may be tactical and concerned with short-range fire control radar systems. Other systems might have strategic missions whose threat radar systems would be low-frequency search radars. Figure 7.1 shows conceptually how mission definition must precede vehicle shaping considerations.

Mission planning also plays a significant role in shaping considerations. One must know how a target will be viewed by a threat radar. Usually not all aspect viewing angles of a target are equally likely. (If they were, then shaping for RCS reduction would not be viable.) For air vehicles, the most critical region for low RCS is the front angular sector, typically $\pm 45°$ in azimuth and $\pm 15°$ in elevation, as shown in Figure 7.2. The side sector and rear sector are also of importance but less so. Air vehicle threat sectors are typically in the azimuth plane, $\pm 15°$ in elevation, but usually do not exist from directly above or below. Ship and ground target threat sectors are usually 360° in azimuth, but limited to 10° to 20° in elevation. Before shaping principles can be applied, we must know the spatial regions where low signatures are desired.

7.4.2 Shaping Goals

Simply stated, the goals of shaping are to have no specular returns in the threat sectors, that is, have no surface or edge normals pointing toward the threat sector; to have a very low sidelobes and "fuzz ball" levels; to have as few spikes as possible, with each unavoidable spike as narrow as possible; to have a low cross section over a large angular spatial region and over as wide a bandwidth of frequencies as possible. If one is successful in creating a low RCS target by shaping, the material treatment goals are then to reduce nonspecular returns from tips and edges and to reduce surface traveling, edge, and creeping waves. Specular RAM is reserved for those regions where shaping alone is not sufficient, such as cavities and edges viewed in a specular direction. The discussion of shaping must follow the high-

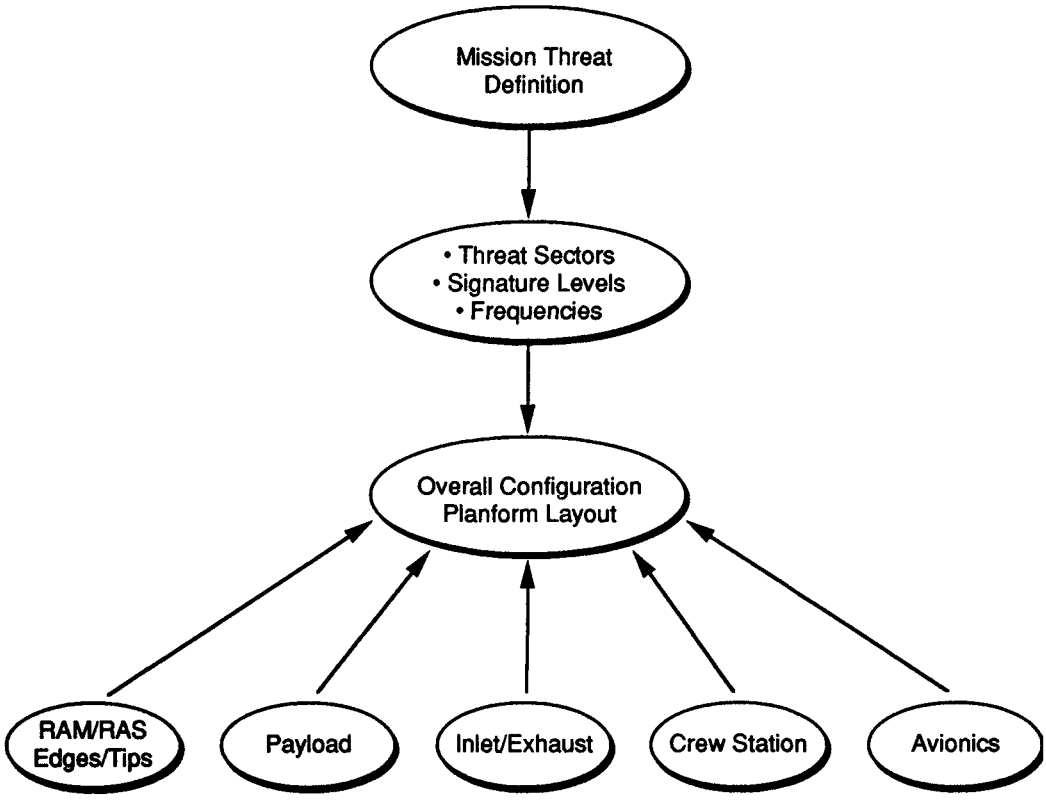

Figure 7.1. Shaping roadmap for the low-observable design process.

frequency scattering mechanisms. In rough order of magnitude (and hence importance for reduction), they are as follows.

Specular Scattering

This is the classical ray trace scattering where angle of reflection is equal to angle of incidence (billiard-ball-like scattering). The specular return is a very bright, high-level return is to be avoided entirely within the threat sector. For backscatter this means having no surface normals pointing into the threat region. Specular surfaces may be planar, singly curved, or doubly curved. Doubly and singly curved surfaces, because their surface normals point over wide regions of space, are to be avoided. Only when these surface normals point toward nonthreat sector regions

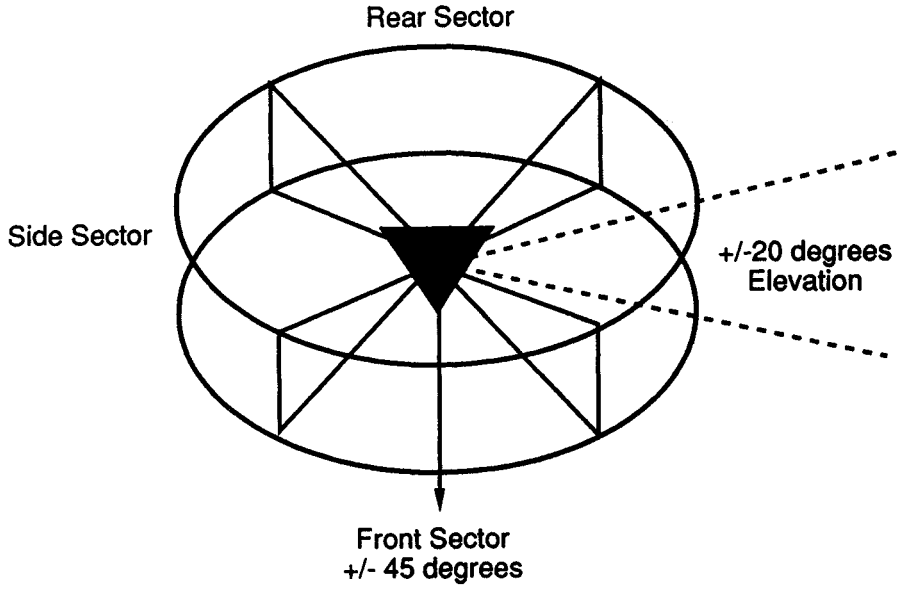

Figure 7.2. Example air vehicle threat sector definition.

are they acceptable. Curved or blended surfaces are desirable for lowering sidelobe levels and often for non-RCSR-related design issues. Planar surfaces have only one direction in space for which a specular return is obtained. These normals must also point well away from the threat regions.

Early shaping attempts replaced planar surfaces with singly or doubly curved surfaces. This was because the specular flash from plates is brighter than that from cylinders, which in turn is brighter than that from spheres. However, this was soon abandoned as an approach for two main reasons: (1) the specular flash from curved surfaces was still bright; and, worse, (2) the specular return from curved surfaces extended over significant angular regions. Design philosophy has moved to avoiding specular returns entirely. Figure 7.3 compares the physical optics returns for a flat plate, a cylinder, and a sphere.

Multiple-Bounce Structures

These scattering mechanisms are specular in nature, in that energy is reflected from one surface to another before "billiard ball bouncing" back toward the receiver. Multiple bounce structures range from trihedrals, which have a bright return over a significant angular region via a double or triple bounce, or from dihedrals,

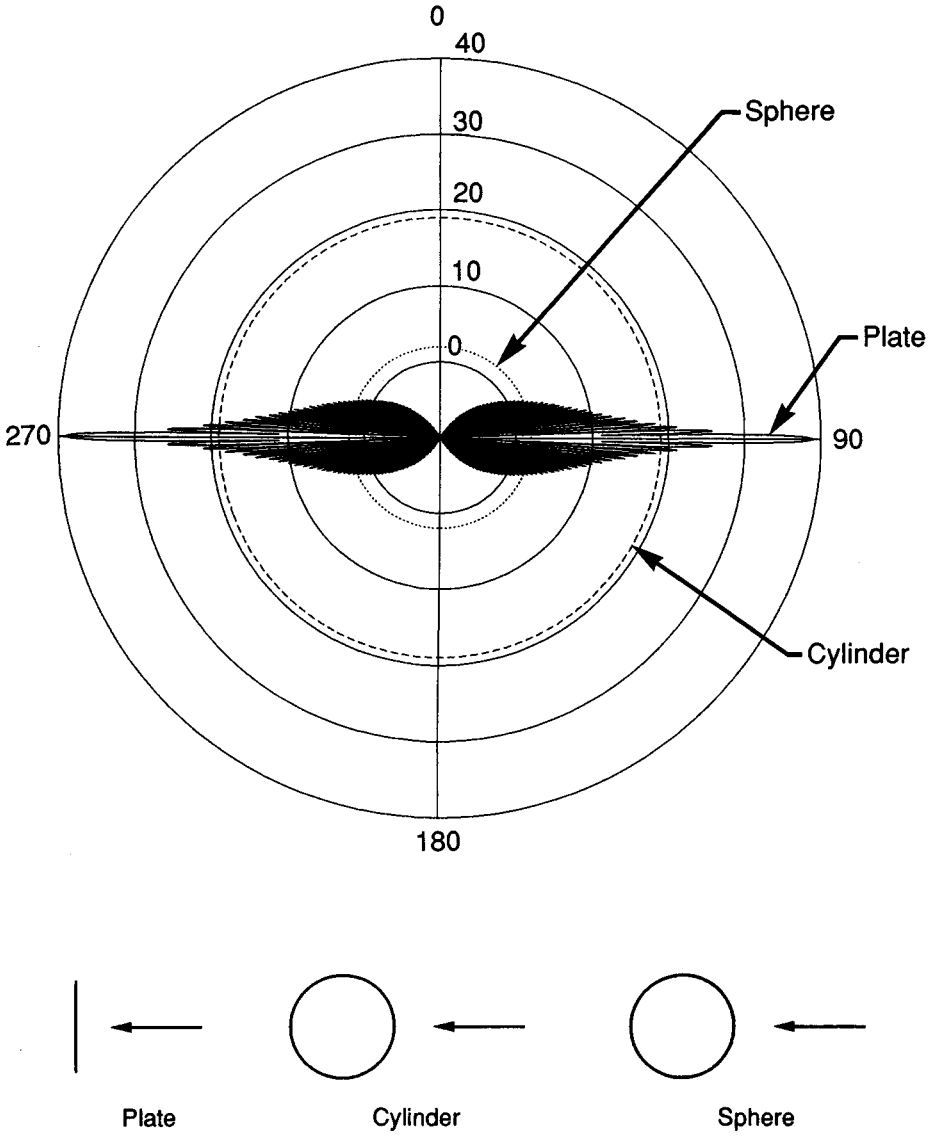

Figure 7.3. RCS backscatter from a plate, a cylinder, and a sphere.

which have a bright return in a plane perpendicular to the axis, or from cavities, where multiple bounces occur before the energy is directed back toward the radar. Distinct corner reflectors are to be absolutely avoided in low RCS design. However, the reader is cautioned that, although some corner reflectors are obvious, others

are not. The following are potential two-bounce corners: the intersection at right angles of a tail and fuselage, and the intersection of a trailing edge at right angles with a fuselage. Doubly curved surfaces must always be carefully examined to make sure no other structure is illuminating the surface. Often doubly curved surfaces provide second surface bounce from what initially looks like a rather benign geometry. Cavity inlets and exhausts, which cannot be avoided, must be designed either with covering screens or by serpentine shaping, Figure 7.4, to force multiple bounces of energy on the walls, where specular absorbers are then used to attenuate the multiple reflections.

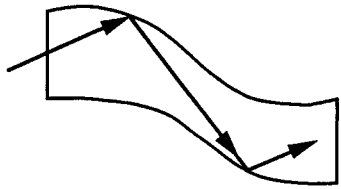

Figure 7.4. Duct cavity design for multiple bounce.

Sidelobe Scattering

Sidelobe scattering is an end-region discontinuity return caused by the fact that currents change abruptly from a finite value (on the conductor) to 0 (off the conductor). This abrupt transition is a scattering center. For flat plates it dominates the RCS pattern away from the specular direction. This return is *in addition to* edge diffraction effects. The physical optics return (no edge diffraction included) for a flat plate, Figure 14.3a, shows how the two end region scattering centers beat in and out of phase to form the sidelobe envelope. These end regions contribute to the plate RCS over most of the 0–180° viewing angles, falling off near grazing. The magnitude of the end-region scattering centers depends on the end-region area (size of the current discontinuity). For a plate viewed in a principal plane, the end-region area is as shown in Figure 7.5. One dimension is set by plate width and the other by the wavelength. When a plate is viewed along the diagonal, four end regions occur at the four corners of the plate as shown in Figure 7.5 and as seen in the k space image shown in Figure 14.5. In this case the area of the discontinuities is set by wavelength and the included angle of the corner. The four end-region discontinuity scattering center magnitudes are much smaller in magnitude (net area) than when the plate is viewed in a principal plane, hence the RCS sidelobe level of a plate viewed along a diagonal is much less, Figure 14.5.

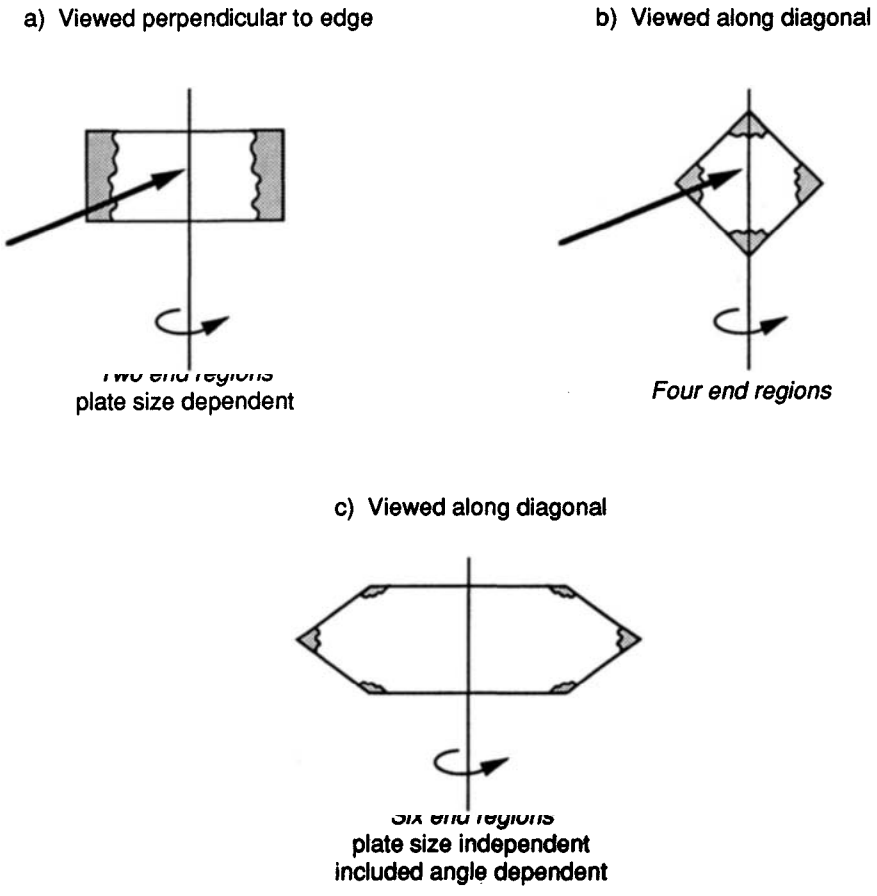

Figure 7.5. End-region discontinuities are scattering centers creating sidelobes for plate scattering.

Reduction of sidelobe scattering may take several forms:

1. View surfaces as close to grazing as possible. Sidelobe scattering centers diminish in magnitude as the end regions are viewed closer to grazing.
2. View planar facet end regions along the diagonal to minimizing the end-region area and hence scattering center magnitude.
3. When viewing planar facets into corners, make the corner included angle smaller.
4. Avoid abrupt end regions altogether. This may be accomplished by utilizing blended (curved) surfaces viewed near grazing incidence. The physical optics currents for this case taper smoothly to zero into the shadow region thus

avoiding an abrupt transition. This has the effect of avoiding the sharp discontinuity of currents and eliminating the end-region discontinuity return. By eliminating end regions, blended bodies have the potential for lower signatures than planar faceted bodies.

5. Eliminate the sharp discontinuity of currents by using tapered radar absorbing materials designed to smoothly taper surface currents to zero at the edge of a surface.

Edge Diffraction

Edge returns are diffraction scattering mechanisms that principally scatter in a specular direction. For backscatter, edges are bright specular scattering centers any time they are viewed perpendicular to the edge. The normal to an edge is not a single direction in space, but lies on a plane perpendicular to the edge, Figure 7.6. Edge return depends on polarization. Returns occur when the incident E field is polarized parallel to a leading edge or for E polarized perpendicular to a trailing edge.

Edge returns, being bright specularlike scattering centers, are treated for RCSR just like specular surface returns. They are to be avoided entirely in the threat sector. For air vehicle configurations where the threat sectors are near the horizontal azimuth plane this means avoiding vertical lines and sweeping horizontal wing and tail leading and trailing edges so that their normals point well away from the forward and rear threat sectors. If a trailing edge has a normal in the forward threat sector, it must be sawtoothed to move the angle out of the threat sector.

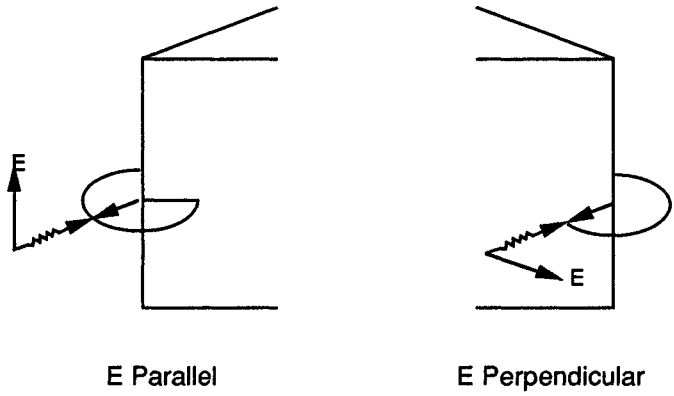

Figure 7.6. Edge normals for specular backscatter.

Surface Traveling, Edge, and Creeping Waves

Surface wave scattering mechanisms are nonspecular mechanisms that may dominate the RCS in the resonant region. Surface wave scattering is generally not of concern in the optics region because scattering magnitudes vary as λ^2. Shaping is not generally used to control these scattering mechanisms, rather radar absorbing material is typically used.

Tip Diffraction

Tip diffraction is a very small magnitude scattering center in the optics region. Its magnitude is proportional to λ^2 and the included angle of the tip. Tips at optics frequencies are not generally significant, and they can be made smaller by reducing the included angle. Hence ogival tips have higher scattering than *S* curvature tips, Figure 7.7. Reducing the included angle also reduces the end-region contribution because the ends are then viewed at a more shallow angle.

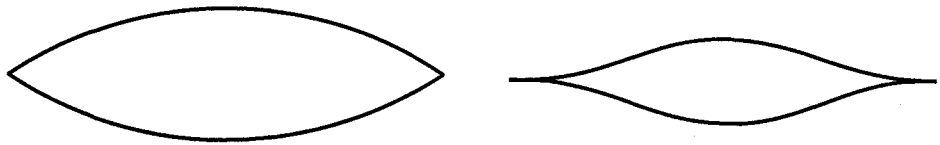

Figure 7.7. Tip scattering is proportional to included angle.

Planform Shaping

Planform shaping is the most fundamental choice in the "clean sheet of paper" design of any system with reduced RCS. Although the system RCS is composed of several sources, the body configuration *sets* the ultimate lowest level achievable for the system. The planform shape is driven entirely by the nature of the threat sector. The design rule is simple: the clean sheet of paper configuration must not have surface or edge specular returns within the primary threat sector. For air vehicles, with the primary threat sector being the front and the secondary threat sectors the side and rear, this means no specular spikes forward and a configuration with a minimum number of specular spikes in an azimuth cut. The following planform choices might be considered as starting concepts for air vehicles.

As a first trial planform, we might consider a saucer (flying UFO?) configuration. In this case we have a curved edge specular flash from every direction in azimuth which may be attenuated by utilizing bulk edge RAM. Except for the

curved edge specular, there would be no surface specular returns, and the end-region sidelobes would be minimal because the upper and lower surfaces are blended curved surfaces viewed near grazing. This is a clean simple body with minimum discontinuities. The curved edge flash, however, may not be sufficiently low to meet desired detection range reduction.

The next configuration one might consider is triangular, Figure 7.8. On first glance this could be considered a three spike design, and this would be true for only two special cases of linear polarization, H and V. The location of the edge spikes shift by 60° (for the equilateral triangle) when going from horizontal to vertical linear polarization, Figure 7.8. This occurs because for horizontal polarization, the specular spikes result when the E field is parallel to the edges, that is, leading edge polarization, but for vertical polarization, the specular spike results when the E field is perpendicular to the rear edges, that is, trailing edge polarization. For circular polarization, which is a linear combination of H and V, a six-spike pattern results, also shown in Figure 7.8. A similar six-spike pattern would result from a slant linear polarization 45° between horizontal and vertical. Therefore, an equilateral triangle is potentially a six-spike planform configuration.

The next ideal configuration would be a diamond shaped planform, sometimes called the *hopeless flying diamond,* which has good RCSR qualities, but is a poor practical choice. Nevertheless, the diamond has a four-spike azimuth pattern for V, H, and circular polarizations because the leading and trailing edges have been made parallel, Figure 7.8.

7.4.3 Other Issues

The goal of shaping is to eliminate specular returns in the threat sector. However, when the threats are in the horizontal azimuth plane, such as for air vehicles, we cannot avoid being perpendicular to certain features. Unavoidable spike flashes will occur. This reality then suggests the following: point the spikes well away from the primary threat sector; make the spikes as narrow as possible by making the spike-producing edge or surface as long as possible (RCS beamwidth is inversely proportional to base dimension length); make all other specular lines and surfaces on the body parallel to the major body lines to place all specular reflections in the same direction of space (i.e., stack lines).

In general, all body discontinuities are potential scattering centers. Low-RCS bodies are characterized as clean, simple shapes. This means that external carriage of stores or other equipment is detrimental to low RCS and therefore interior carriage is required.

The role of radar absorbing material on low-RCS targets that have been shaped is typically to further reduce residual scattering in the threat sector. If shaping has been applied successfully, then the remaining fuzz ball signature is due to second-order mechanisms such as edge waves, physical optics sidelobe energy, cavity returns, surface discontinuities, edge returns, or avionics sensors

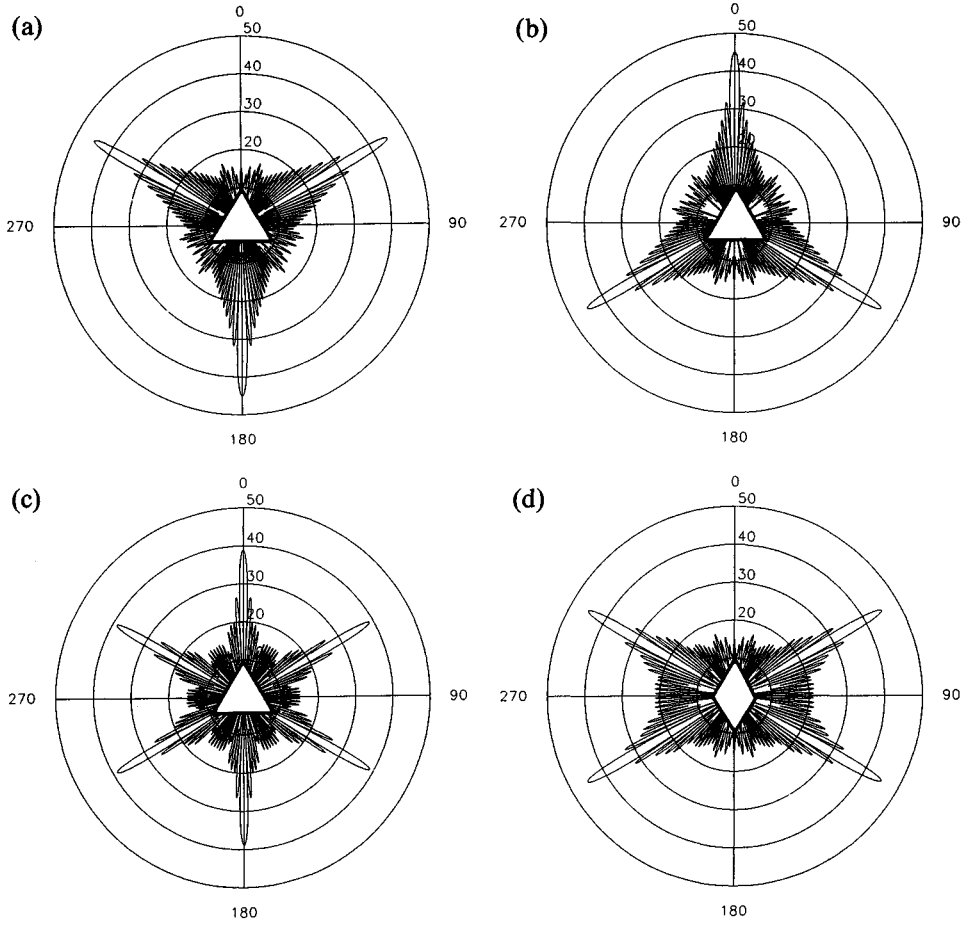

Figure 7.8. Planform RCS backscatter spikes for equilateral triangle (three or six spikes) and for diamond: a) parallel pol, b) perpendicular pol, c) circular pol, d) diamond, parallel pol.

and antennas. Radar absorbing materials are then used to further reduce these residual scattering mechanisms. For air vehicles, RAM edges are utilized, Figure 7.9. The most critical location for RAM is at the tips and along edges.

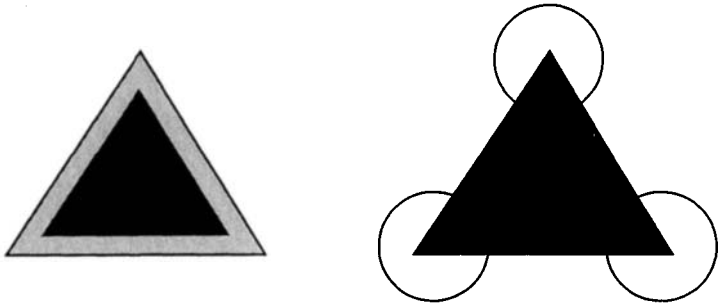

* Planform perimeter edges and tips:
reduction for
1) Edge waves (tips)
2) Edge specular flash
3) PO sidelobe envelope

Figure 7.9. Radar absorbing material locations for bodies where shaping has been used to reduce RCS.

7.4.4 Some Shaping Examples

We present two examples. The first illustrates the necessity to avoid being perpendicular to body lines in the threat sector. Consider a frontal threat sector in the horizontal azimuth plane for the two arrow targets shown in Figure 7.10. In the azimuth plane cut, no portion of these body surfaces is viewed in the specular direction. Let us make a physical optics RCS prediction without including edge diffraction or surface wave effects. This means we compute only the RCS due to specular and end-region returns. For these two bodies in the azimuth plane, we are not specular to any surface, therefore the PO prediction is entirely due to end-region sidelobe mechanisms. In body (b) we have a design in which two body lines have normals pointing at 0° toward the nose of the body, and in body (a) we have avoided this by moving the top body point forward. An examination of the two predicted PO RCS plots, Figure 7.10, shows that an RCS spike occurs every time

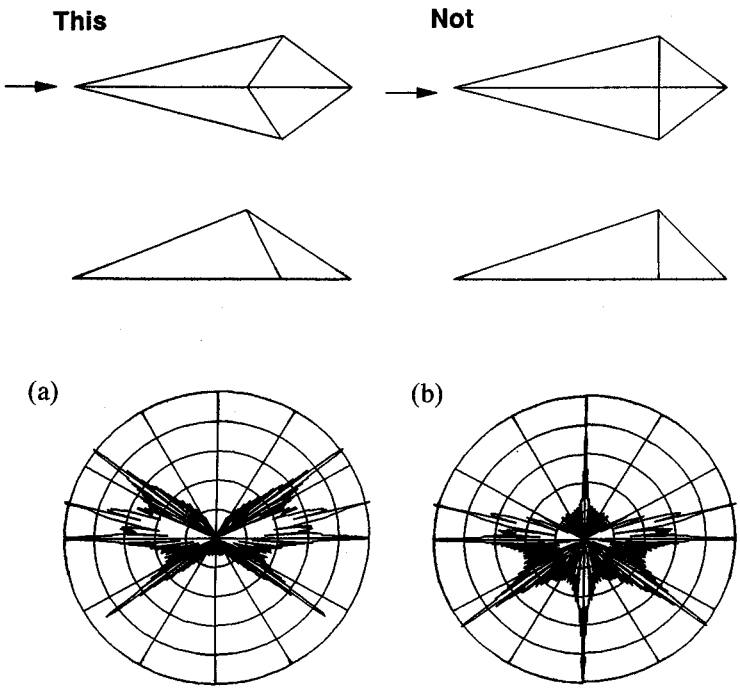

Figure 7.10. RCS backscatter spikes occur when body lines are viewed at normal incidence.

we are perpendicular to a body line in the azimuth plane cut. Therefore for body (b) we have a spike pointed down the front sector, not a very good situation for a low front-sector RCS target.

The second example compares a traditional, doubly curved aircraftlike body modeled with ellipsoids and a vehicle shaped for low RCS, Figure 7.11. The RCS polar plots at X band are shown in Figure 7.12, and the detection signal-to-noise ratio contours for a hypothetical radar system are shown in Figure 7.13. Consider the simple-shaped air vehicle-like structure for which we have applied some shaping principles. For this body the wing spikes have been moved away from the front sector and the tail lines in planform have been made parallel to the wing lines. In the azimuth plane, we are not specular to any surface, however, we do become specular to the wing and tail edges. Figure 7.12 shows the PO and edge diffraction computed RCS. The effects of reduced RCS on the signal-to-noise detection contours is shown in Figure 7.13, where it is clear that the reduced RCS target has a much smaller detection envelope.

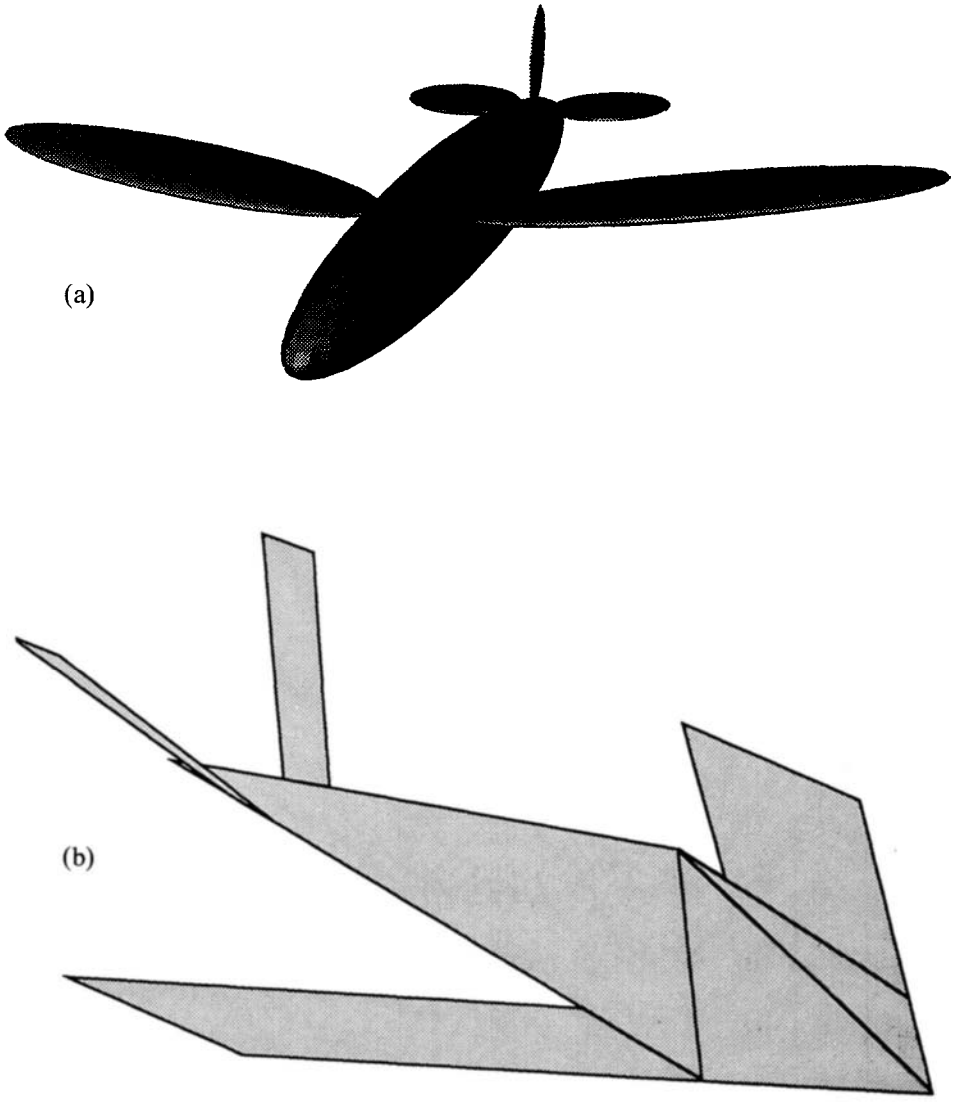

Figure 7.11. (a) Ellipse and (b) shaped air vehicle models.

7.4.5 Shaping Rule Summary

The following list is a summary of the shaping design rule guidelines. Although the bias is toward air vehicles, the reader may easily adapt these principles to other types of targets with different types of threat sectors:

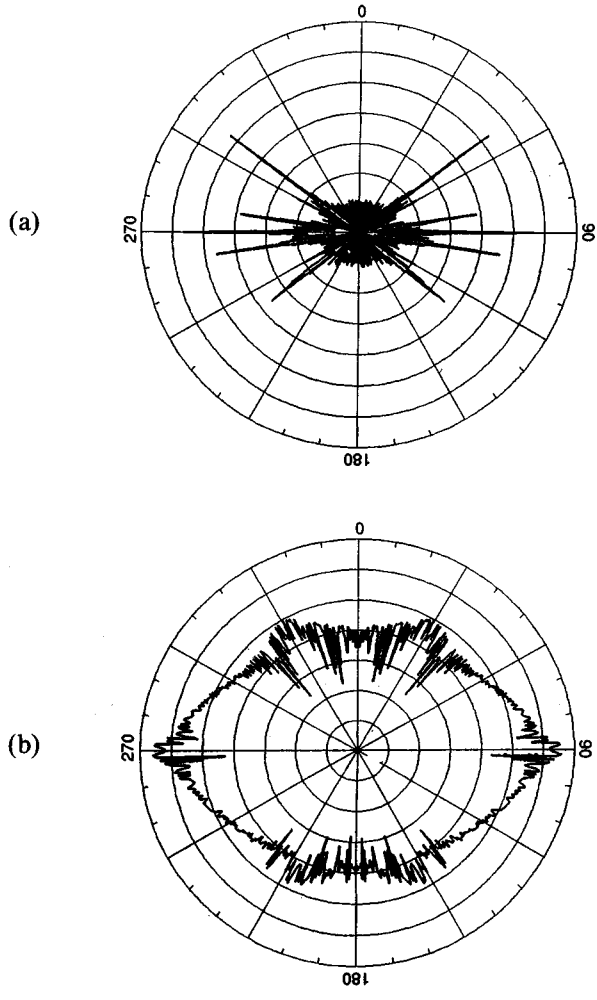

Figure 7.12. (a) Ellipse and (b) shaped air vehicle backscatter RCS.

1. Define mission and threat sectors.
2. Choose a planform shape with a minimum of specular spikes, place specular surface and edge returns well away from threat sectors.
3. Use long swept lines for narrow beamwidth spikes.
4. Use sloped, shallow surfaces viewed toward grazing.
5. Never view planform body lines perpendicularly in the threat sector.

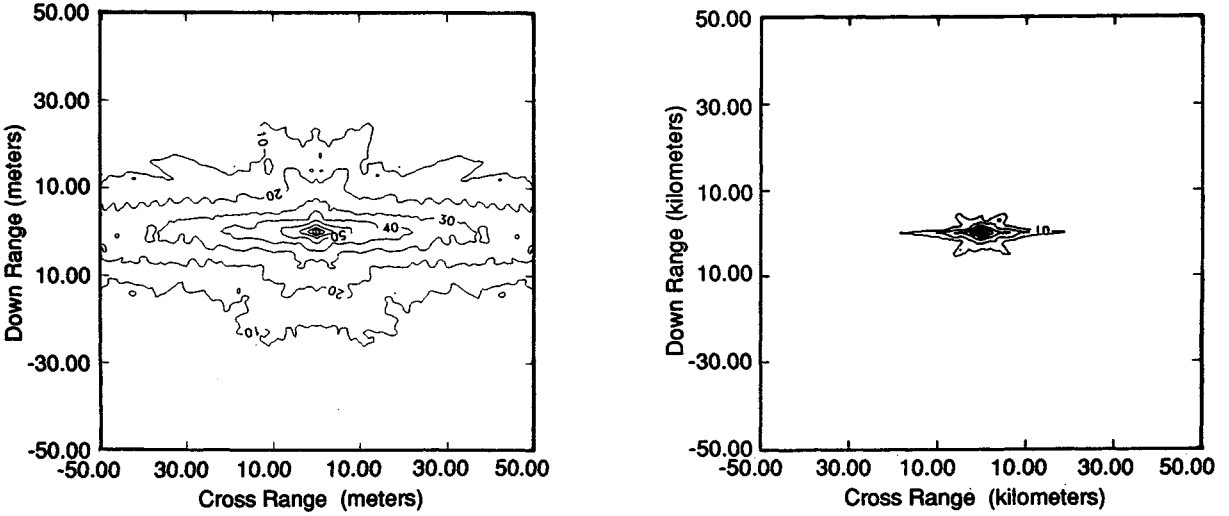

Figure 7.13. (a) Ellipse and (b) shaped air vehicle signal-to-noise ratio contours.

6. Stack all unavoidable body lines to place their specular spikes into a common direction.
7. Use smooth surfaces, not necessarily flat ones.
8. Minimize or eliminate surface discontinuities; for example, blended surfaces.
9. Use internal storage.
10. Blend crew station, air inlets and exhausts, antennas and sensors.
11. Minimize surface roughness.
12. Integrate your knowledge with that of other disciplines (this is the really hard part!).

7.5 SUMMARY

In this chapter we presented the four basic techniques for RCS reduction. Of the four, the use of shaping and radar absorbers are by far the most effective. As the design and use of RAM is covered in detail in Chapter 8, this chapter focuses on the fundamentals of shaping for RCSR. Shaping typically is available only for systems still in the design stage, because it can seldom be exploited for vehicles already in production. But, in those cases where shaping can be applied, it is the most effective method available for RCSR.

When shaping is considered in the initial design stages, there are some simple fundamental rules, which if intelligently applied, will result in a low-RCS design. The rules evolve from our desire to have vehicles that are large in size but low in radar cross section, and they presume that the most worrisome threats are at the higher microwave frequencies. Shapes that meet our needs are found to have RCS formulas with a size-to-the-zero-power dependence. Thus, the radar cross section of those shapes is not dependent on their size, and large versions of such shapes have the same RCS as small ones (it would be nice if there were objects whose cross section varied as size to a negative exponent, but we are not that lucky). Because RCS must ultimately have units of area, shapes whose radar cross section is size independent must have a λ^2 dependence. That implies that shape can be used to reduce the RCS at high frequencies, but that some other technique (typically RAM) must be employed at low frequencies.

The shaping rules discussed in Section 7.4 are simple. If these rules are followed, the basic planform shape will be commensurate with low RCS at high frequencies. However, at low frequencies, the effects of traveling waves (surface, edge, and creeping) will begin to dominate RCS. There, absorbing materials can be applied to reduce such effects. In addition, the simple rules stated previously ignore the need for sensors, inlets, exhausts, and so on. Those areas have their own RCS design guidelines, which generally begin with appropriate shaping rules (e.g., use of serpentine inlets, conformal antennas, or shaped frequency selective

surface radomes) and then use RAM to take care of problems where shaping alone will not do.

It is important to end this chapter on the note with which it started. That is, never forget that radar signature control is only one aspect of the total vehicle design problem. The final configuration of any platform is driven by a multitude of factors, which should ultimately be tied to mission effectiveness. Successful designs come from teams of engineers who understand the needs of all of the competing technologies and who work very hard to ensure that an intelligently integrated design results.

Chapter 8
Radar Absorbing Materials

M. T. Tuley

8.1 INTRODUCTION

Although shaping is the first line of RCSR and can provide dramatic reductions in signature over limited aspect angles, many situations require absorption of the incident electromagnetic energy, if design goals are to be achieved. Therefore, a knowledge of the design and application of radar absorbing materials is vital to the engineer whose task is to minimize the radar signature of a vehicle.

As discussed in Chapter 6, basic scattering phenomena may be broken down into specular and nonspecular mechanisms. As might be expected, RAM design must also be approached with consideration for the scattering mechanism of interest. Accordingly, in this chapter, RAM design and performance will first be discussed with reference to specular reflections. Then, the design performance of nonspecular RAM will be considered.

The electromagnetic aspects of RAM design focus principally on the synthesis of an arrangement of dielectric or magnetic materials that provide a specified impedance profile to an incident wave. A study of the evolution of RAM design is a study of the materials and techniques employed to achieve desirable impedance properties (and, hence, good absorptive qualities) over ever increasing bandwidths. In organizing the chapter, the basic theory underlying specular RAM design is first considered, and analytical design methods are presented. Then, the design methods are used to illustrate the types of structures typical of current RAM implementations and the performance that can be achieved in those implementations.

A study of the physics of electromagnetic wave absorption should begin with the microscopic or quantum theory of materials, but we will instead approach this

topic with a macroscopic view of electromagnetics. Although the loss mechanisms through which RAM operates are microscopic in nature (i.e., on the atomic and crystal lattice levels), the analysis of specular RAM is most easily handled by taking a classical transmission line approach to model the reflection and transmission properties of absorbers. Similarly, successful theoretical analyses of nonspecular RAM performance have often been based on dielectric waveguide theory. In effect, the design of RAM is simply the design of a lossy distributed network that matches the impedance of free space to that of a conducting body to be shielded.

Section 8.2 discusses loss mechanisms and relates them to the macroscopic electrical and magnetic properties of materials. The concept of terminating impedance is introduced and defined for semi-infinite slabs and for conductor-backed single layers of material. The formula for the reflection coefficient is provided, and its implication for the selection of desirable material properties is considered. Section 8.3 discusses specular reflection from flat dielectric multilayers for both the simple case of normal incidence and for the general case of off-normal incidence. An alternative approach to scattering calculations using a wave matrix formulation is then presented, and its application in light of current materials metrology techniques is discussed. Section 8.4 catalogs available types of dielectric absorber and discusses their design and level of performance. Section 8.5 provides information on circuit analog absorbers and frequency selective surfaces. Section 8.6 discusses magnetic RAM and its application to specular absorbers, and Section 8.7 briefly discusses hybrid RAM and radar absorbing structures. Section 8.8 considers the important topic of nonspecular RAM design and performance.

8.2 ELECTROMAGNETIC LOSS MECHANISMS

Radar absorbing materials are based on the fact that some substances absorb energy from electromagnetic fields passing through them. Such materials have indices of refraction that are complex numbers. In the index of refraction, which includes magnetic as well as electric effects, the imaginary component accounts for the loss in a material. The term *loss* refers to the dissipation of power or energy, quite analogous to the way energy is consumed by a resistor when electrical current passes through it. The loss is actually the conversion of electrical energy into heat, and although most absorbers do not dissipate enough energy to get detectably warm when illuminated by a radar, this is nevertheless the mechanism by which they operate. At microwave frequencies, the loss is due to a number of effects on the atomic and molecular level. However, for most practical electric absorbers a majority of the loss is due to the finite conductivity of the material, whereas for most magnetic absorbers at microwave frequencies, magnetization rotation within the domains is the principal loss mechanism. In any event, it is customary to group the effects of all loss mechanisms into the permittivity (ϵ) and permeability (μ) of the material because the engineer is usually interested only in the cumulative effect.

Several common usages exist for expressing the complex permittivity and permeability. Generally, we shall deal with the relative permittivity, ϵ_r, and relative permeability, μ_r, which are normalized by the free-space values, ϵ_0 and μ_0. The complex notation for ϵ_r and μ_r, is normally given as

$$\begin{aligned} \epsilon_r &= \epsilon_r' + \mathrm{i}\,\epsilon_r'' \\ \mu_r &= \mu_r' + \mathrm{i}\,\mu_r'' \end{aligned} \tag{8.1}$$

where the real (energy storage) part of each parameter is denoted by a prime and the imaginary (loss) part is denoted by a double prime. Because the conductivity σ of electric absorbers is often the major loss mechanism, it is convenient to express the effect of the conductivity in terms of ϵ_r''. For that case, ϵ_r'' and σ are related by

$$\epsilon_r'' = \sigma/\omega\epsilon_0 \tag{8.2}$$

where ω is the radian frequency. Equivalently, in polar notation,

$$\begin{aligned} \epsilon_r &= |\epsilon_r|\mathrm{e}^{\mathrm{i}\delta} \\ \mu_r &= |\mu_r|\mathrm{e}^{\mathrm{i}\delta_m} \end{aligned} \tag{8.3}$$

where δ and δ_m are the electric and magnetic loss tangents given by

$$\begin{aligned} \tan\delta &= \epsilon_r''/\epsilon_r' \\ \tan\delta_m &= \mu_r''/\mu_r' \end{aligned} \tag{8.4}$$

The index of refraction n is the ratio of the wavenumber describing wave propagation within the material to the free-space wavenumber and is to the geometric mean of the relative permittivity and permeability

$$n = k/k_0 = \sqrt{\mu_r\epsilon_r} \tag{8.5}$$

where k is the wavenumber in the material, and $k_0 = \omega\sqrt{\mu_0\epsilon_0}$ is the free-space wavenumber. Similarly, μ_r and ϵ_r also define the intrinsic impedance, Z, of the material:

$$Z = Z_0\sqrt{\mu_r/\epsilon_r} \tag{8.6}$$

where Z_0 is the impedance of free space, 120π, which is approximately 377Ω.

The intrinsic impedance is the impedance value seen by a normally incident wave on a semiinfinite slab of a material. In practical applications, a layer of dielectric will often be backed by a conducting surface. For that case a transmission

line analysis can be performed to find the effective input impedance at the front face of the layer.

For a flat metallic surface coated with a layer of dielectric material, the normalized input impedance η is given by

$$\eta = \sqrt{\mu_r/\epsilon_r} \tanh(-ik_0 d \sqrt{\mu_r \epsilon_r}) \tag{8.7}$$

where d is the thickness of the dielectric layer. This formula applies to a wave striking the surface at normal incidence, and it becomes more complicated when the wave arrives at oblique angles. The normalized impedance can be used to calculate the reflection coefficient R:

$$R = \frac{\eta - 1}{\eta + 1} \tag{8.8}$$

R, like η, is a complex number, but has a magnitude between 0 and 1.

In discussing reflection coefficients, it is customary to ignore the phase angle and to refer only to the "voltage" amplitude $|R|$, so that the power reflection in decibels is

$$|R| \text{ (dB)} = 20 \log_{10}|R| \tag{8.9}$$

In the discussion that follows, the terms *reflection coefficient* and *reflectivity* will be used essentially interchangeably.

The objective of RAM design is to produce a material for which $|R|$ remains as small as possible over as wide a frequency range as possible. It should be noted that unless the material has some loss, the amplitude of the reflection coefficient will be controlled entirely by the phase and amplitude relationship between the portion of the incident wave reflected at the front surface and the portion returning via reflections at the backing surface. In some cases, we may take advantage of the phase shift on reflection to provide resonant energy cancellation. This is inherently a narrowband RCSR technique. However, it is also often taken advantage of with lossy materials to provide improved performance at certain frequencies. The Dallenbach layer, which is discussed in detail in Section 8.4, is an example of an absorber that makes use of a combination of loss and resonant cancellation.

8.3 SPECULAR SCATTERING FROM DIELECTRIC MULTILAYERS

In RAM design, two questions concerning the electromagnetic properties of materials must be answered if absorption performance objectives are to be met (also, a host of other questions must be answered concerning physical and thermal prop-

erties of the RAM, but this discussion focuses on electromagnetic requirements). The first question to be answered is, "How do I get incident electromagnetic energy into the RAM?" As can be noted from (8.8), that question deals with the impedance mismatch seen by the wave as it enters the absorber. The second question to be answered is, "How do I absorb electromagnetic energy, once I have gotten the EM wave to enter the RAM?" That question deals with the mechanisms available for attenuating waves within materials. However, the two questions are coupled. Note that raising the value of ϵ_r'' or μ_r'' to increase loss also raises the value of the complex permittivity or permeability, thus affecting the reflection coefficient. For example, if we were able to design a nonmagnetic material with an ϵ_r' value of 1, and an ϵ_r'' of 10, the amplitude of the reflection for a wave normally incident on a semiinfinite slab would be $|R| = 0.63$, which is only 4 dB down from the reflection from a perfectly conducting surface. Even if ϵ_r'' were reduced to a value of 1, $|R| = 0.21$, just over 13 dB below the reflection from a perfect conductor. To reduce the front-face reflection to -20 dB would require $\epsilon_r'' < 0.41$ (even for the unlikely situation of $\epsilon_r' = 1$). For the $\epsilon_r'' = 10$ case, the attenuation of the EM energy within the material would be 116 dB per free-space wavelength traveled. For $\epsilon_r'' = 1$, the attenuation would drop to 25 dB/λ, and for $\epsilon_r'' = 0.41$, the attenuation is only 11 dB/λ. Therefore, adding loss to the material affects both the reflection coefficient and the achievable loss in a given material thickness, so that RAM design is always a trade-off between the requirements raised in the two questions discussed earlier.

In practice, the problem of getting energy into the RAM and then absorbing it is normally handled by changing the electrical properties of the absorber as a function of the distance the wave travels into the material. The theory required to analyze such behavior is relatively simple for the case of plane wave incidence on flat surfaces, where discrete layers of homogeneous (within the layer) isotropic material are used. The inclusion of very thin layers of resistive material (or impedance sheets) adds very little complication to the theory. Two equivalent forms of the general theory are provided in Sections 8.3.3 and 8.3.4.

8.3.1 Thin-Sheet Characterization Using Ohms per Square

A number of specular and nonspecular RAM designs employ thin resistive sheets to provide the loss mechanism. The characteristics of such sheets are usually described in terms of their resistance or impedance in "ohms per square" (often denoted Ω/sq. or $\Omega/\square$). Because that electrical unit is likely not familiar to many readers, it is worthwhile at this point to define it. If a block of material with a resistivity ρ in Ω-m, as shown in Figure 8.1(a), is used to make a resistor, the resistance between two opposite faces of the block is given by

$$R = \rho L/A = \rho L/WT \tag{8.10}$$

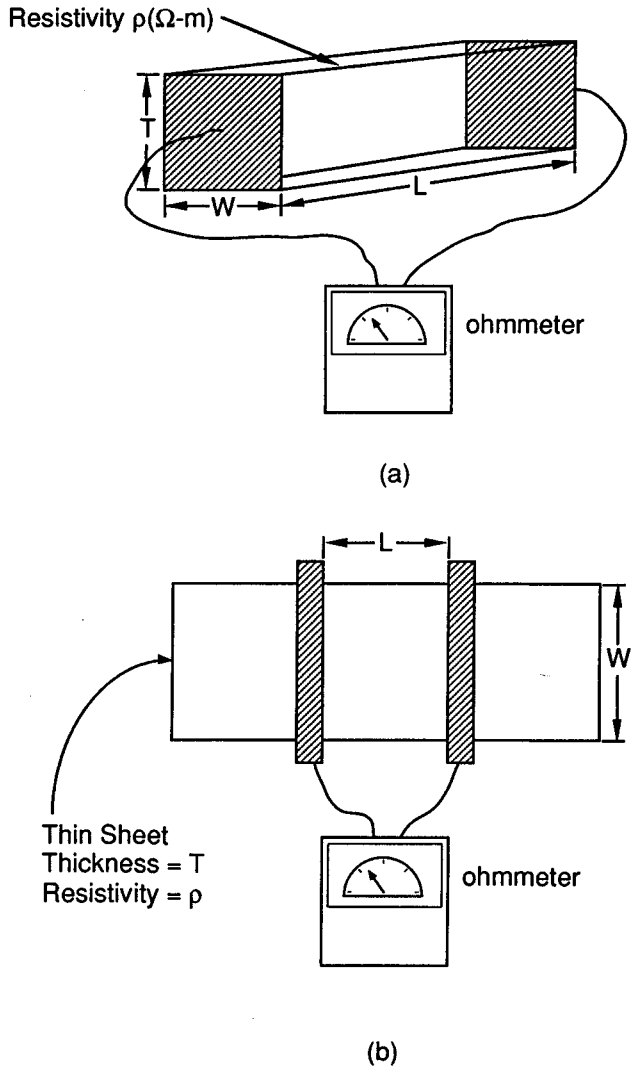

Figure 8.1. Origin of the ohms-per-square notation: (a) a block of resistive material, (b) ohms-per-square resistance measurement.

where L is the length of the block between the two faces, and the product of the width, W, and thickness, T, define the cross-sectional area, A, of the block of material.

If we take a sheet of material, place conductive bars across the width dimension, as shown in Figure 8.1(b), and measure the resistance between two bars

a distance W apart, (8.10) becomes $R = \rho/T = 1/\sigma T$ (the length and width, being equal, cancel). If we measure the resistance across any square piece of the material using the procedure just indicated, the result will be the same, regardless of the size of the square. Thus arises the nomenclature *ohms per square.*

In modeling electromagnetic performance, the concept of an infinitesimally thin impedance sheet is valid only if the sheet is much less than an electrical wavelength thick. For example, the theoretical Salisbury screen absorber (see Section 8.4.1) is made of an infinitesimally thin 377 Ω/sq. resistive sheet in front of a conducting plate. At frequencies where the sheet spacing from the plate is an odd number of quarter-wavelengths, a zero reflection coefficient is achieved at normal incidence. For a stand-off distance of 7.5 mm (λ/4 at 10 GHz), if a 0.1 mm thick resistive sheet with an $\epsilon_r' = 5$ is used, the maximum RCSR achieved is 31.6 dB at a frequency of 9.6 GHz, rather than infinite RCSR at 10 GHz. Use of a 1 mm thick, $\epsilon_r' = 5$ sheet would result in a maximum RCSR of 13.4 dB at 6.9 GHz. Note that both the real and imaginary parts of ϵ_r will affect the shift in the resonant frequency, and the maximum RCSR obtained. Thick resistive sheets (like those discussed as illustration) can be modeled as layers of finite thickness whose ϵ_r' is typically dominated by the base material, and whose lossy component is given by $\epsilon_r'' = \sigma/\omega\epsilon_0 = (\rho\omega\epsilon_0)^{-1}$.

In the next two subsections, the equations for normal incidence and then arbitrary incidence of an EM wave on a flat dielectric multilayer are developed. The problem is then approached from the wave matrix point of view, and the relationship between the scattering matrix and cascade matrix is provided. Finally, an approximate procedure for determining the reflection coefficient of complicated multilayers is discussed. This approximation is particularly helpful in providing a starting point for absorber codes that use optimizers to iterate a design.

8.3.2 Normal Incidence Scattering

Calculation of the reflection of a normally incident plane wave from an infinite flat multilayer structure is a straightforward problem involving application of boundary conditions derived from Maxwell's equations to the general solution for the electric and magnetic fields in each layer. The functional form of the fields, complex exponentials, and the stepping procedure required for multilayers make implementation of the equations on a computer (or programmable calculator) desirable. Note that existing transmission line design computer programs can often be used for absorber design, either as they are or with slight modifications.

The basic geometry to be considered is that of a finite number of dielectric layers stacked against a metallic backing plate, as shown in Figure 8.2. The layer properties may differ from one layer to the next, or they may be the same. It is assumed that impedance sheets of zero thickness may be sandwiched between layers, as suggested in Figure 8.3. The sheets can be characterized by a resistance value R in ohms per square, or by a conductance, G mhos per square, where

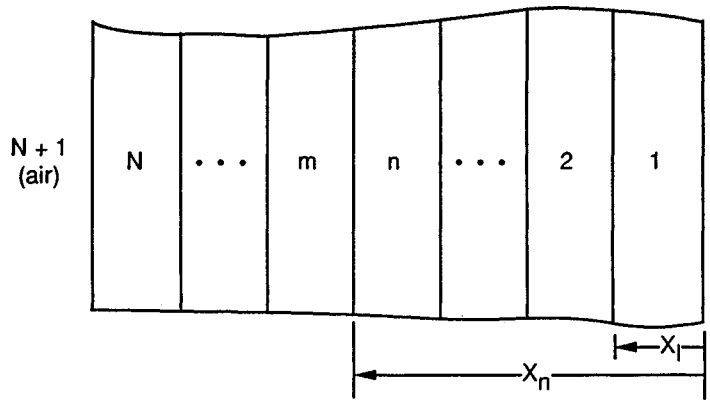

Figure 8.2. A sequence of N layers.

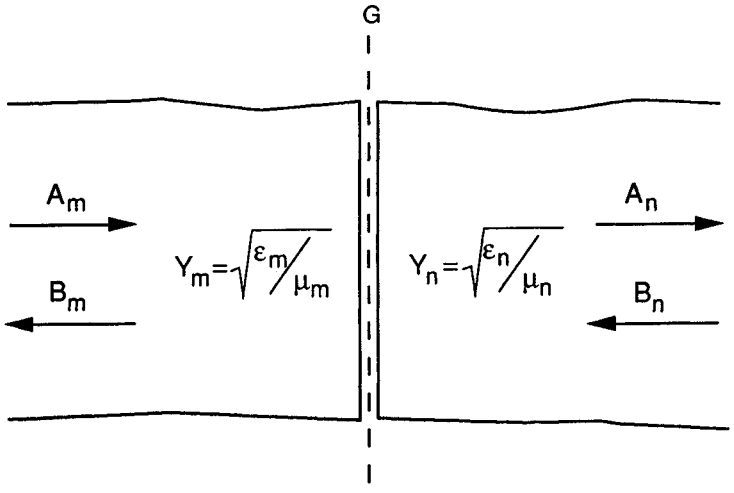

Figure 8.3. Resistive sheet sandwiched between two dielectric layers.

$G = R^{-1}$. For cases such as circuit analog absorbers, where the sheets can provide a complex impedance, the resistance R may be directly replaced by the impedance Z or the conductance G by the admittance Y. To minimize confusion in notation in the following analysis, G will be used for the sheet admittance to differentiate from the dielectric layer intrinsic admittance, which is denoted Y.

The approach used to analyze the scattering is to postulate the form of the electric and magnetic fields in the dielectric layers on either side of the resistive sheet and to specify the boundary conditions these fields must satisfy. This allows

the coefficients of the field representation on one side of the sheet to be related to those on the other side. Because the layers in Figure 8.2 are numbered outward from the backing plane, it is convenient to have x increasing to the left. Thus, the positive traveling wave will be associated with the B coefficients in Figure 8.3.

The electric and magnetic field structure in a given layer is taken to be

$$E = A\,e^{-ikx} + B\,e^{ikx} \tag{8.11}$$

$$H = Y(A\,e^{-ikx} - B\,e^{ikx}) \tag{8.12}$$

where A and B represent the amplitudes of forward and backward propagating waves, and Y is the layer intrinsic admittance. The boundary conditions to be satisfied at the interface are

$$\begin{aligned} GE^+ &= GE^- = J \\ H^+ &- H^- = J \end{aligned} \tag{8.13}$$

where the plus and minus superscripts denote the fields on opposite sides of the sheet, and J is the current flowing in the sheet.

If the resistive sheet location or the boundary between two layers is represented by x_n, and subscripts per Figure 8.2 are appended to the quantities in (8.11) and (8.12) to identify the two media, then the application of (8.13) yields two equations:

$$\begin{aligned} A_m\,e^{-ik_m x_n} + B_m\,e^{ik_m x_n} &= A_n\,e^{-ik_n x_n} + B_n\,e^{ik_n x_n} \\ Y_m(A_m\,e^{-ik_m x_n} - B_m\,e^{ik_m x_n}) &= (G + Y_n)A_n\,e^{-ik_n x_n} + (G - Y_n)B_n\,e^{ik_n x_n} \end{aligned} \tag{8.14}$$

These equations may be used to find A_m and B_m in terms of A_n and B_n:

$$\begin{aligned} A_m &= \frac{e^{ik_m x_n}}{2Y_m}[A_n(Y_m + Y_n + G)\,e^{-ik_n x_n} + B_n(Y_m - Y_n + G)\,e^{ik_n x_n}] \\ B_m &= \frac{e^{-ik_m x_n}}{2Y_m}[A_n(Y_m - Y_n - G)\,e^{-ik_n x_n} + B_n(Y_m + Y_n - G)\,e^{ik_n x_n}] \end{aligned} \tag{8.15}$$

The stepping procedure begins with the assignment of arbitrary values to A_1 and B_1, the coefficients of the fields in the first layer, which is adjacent to the metal sheet. For a metallic backing, the total electrical field must vanish on the sheet, therefore by (8.11), at $x = 0$, $B_1 = -A_1$. The arbitrary assignment $A_1 = 1$, $B_1 = -1$ satisfies this particular condition. If there is no metallic backing (i.e., if the backing is free space), no wave will be traveling to the left, hence $B_1 = 0$ at $x = 0$. Next, the transformer relations (8.15) are used at the first interface located at $x = x_1$, and A_2 and B_2 are calculated. (In a computer code, a pair of variables

may be replaced by updated values representing the change as a boundary is traversed.) The sequence is iterated until the $N + 1$ layer is reached, which is free space outside the structure.

Because the stepping is initiated by using arbitrary values for A_1 and B_1, the final results of A_{N+1} and B_{N+1} are in error by precisely the same amount as A_1 and B_1, because the transformations across the boundaries are linear operations. It can be assumed without loss of generality that outside the structure the incident wave has unit amplitude, and the reflected wave has an amplitude R (for the reflection coefficient). Therefore, all the coefficients could have been corrected by normalizing with respect to A_{N+1}, had it been known at the outset. Because the normalization constant is now known, the reflection coefficient R, associated with the structure, is simply

$$R = \frac{B_{N+1}}{A_{N+1}} \tag{8.16}$$

8.3.3 Oblique Incidence Scattering

The preceding discussion details the simplest case of scattering from planar multilayer structures, that of normal incidence. This section generalizes to the more complex case of oblique incidence. The geometry is similar to that defined in Figures 8.2 and 8.3, except that the directions of the propagating waves are not necessarily normal to the layer boundaries, an example of which is illustrated in Figure 8.4. For this case, the form of the wave will be

$$E = A\, e^{ik(-x\cos\theta + z\sin\theta)} + B\, e^{ik(x\cos\theta + z\sin\theta)} \tag{8.17}$$

where x is normal to the layer boundary and positive upward, and z is to the right in Figure 8.4. Note that (8.17) reduces exactly to (8.11) for $\theta = 0$.

Along with the previous boundary conditions on the z component of the fields, there is an additional requirement, given by Snell's law, that

$$k_m \sin\theta_m = k_n \sin\theta_n \tag{8.18}$$

Obviously, if k_m or k_n is complex, implying lossy media, the sine of the angles in general must also be complex for the equality to hold. The complex angle is a result of the fact that the planes of constant phase and planes of constant amplitude no longer coincide, and so a plane wave no longer exists [1]. Although the concept of a "complex angle" may be difficult to grasp, we may allow θ to be complex, so that

$$\theta = \theta' + i\theta'' \tag{8.19}$$

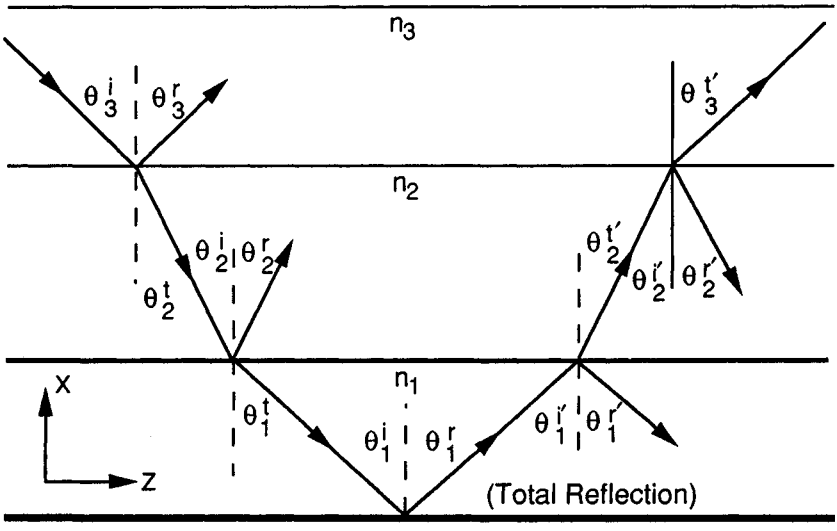

Figure 8.4. Wave propagation and reflection in a dielectric multilayer for oblique incidence.

Then

$$\sin \theta = \cosh \theta'' \sin \theta' + \mathrm{i} \sinh \theta'' \cos \theta' \tag{8.20}$$

The net result of having a complex angle is that the imaginary component introduces an attenuation factor in the propagation of the transmitted wave, in addition to the usual attenuation associated with the imaginary component of the complex wavenumber.

For the case of oblique incidence two cases must be considered. The first, for the electric field parallel to the interface, provides a formula for the coefficients of

$$\begin{aligned} A_m = {} & \frac{e^{ik_m x_n \cos\theta_m}}{2Y_m \cos \theta_m}[A_n(Y_m \cos \theta_m + Y_n \cos \theta_n + G)\, e^{-ik_n x_n \cos\theta_n} \\ & + B_n(Y_m \cos \theta_m - Y_n \cos \theta_n + G)\, e^{ik_n x_n \cos\theta_n}] \\ B_m = {} & \frac{e^{-ik_m x_n \cos\theta_m}}{2Y_m \cos \theta_m}[A_n(Y_m \cos \theta_m - Y_n \cos \theta_n - G)\, e^{-ik_n x_n \cos\theta_n} \\ & + B_n(Y_m \cos \theta_m + Y_n \cos \theta_n - G)\, e^{ik_n x_n \cos\theta_n}] \end{aligned} \tag{8.21}$$

The second case is for the magnetic field parallel to the interface, for which

$$A_m = \frac{e^{ik_m x_n \cos\theta_m}}{2Y_m \cos\theta_m}[A_n(Y_m \cos\theta_n + Y_n \cos\theta_m + G \cos\theta_n \cos\theta_m)\, e^{-ik_n x_n \cos\theta_n} + B_n(Y_m \cos\theta_n - Y_n \cos\theta_m + G \cos\theta_n \cos\theta_m)\, e^{ik_n x_n \cos\theta_n}] \quad (8.22)$$

$$B_m = \frac{e^{-ik_m x_n \cos\theta_m}}{2Y_m \cos\theta_m}[A_n(Y_m \cos\theta_n - Y_n \cos\theta_m - G \cos\theta_n \cos\theta_m)\, e^{-ik_n x_n \cos\theta_n} + B_n(Y_m \cos\theta_n + Y_n \cos\theta_m - G \cos\theta_n \cos\theta_m)\, e^{ik_n x_n \cos\theta_n}]$$

As in the case of normal incidence, a stepping procedure is used, where the boundary conditions at the innermost boundary are used to determine the relationship between A_1 and B_1. Each successive layer is then stepped through until free space is reached. However, for the case of oblique incidence, generally the incidence angle on the outermost layer is given, whereas the first angle required in the computation is that in the innermost layer. Therefore, a double stepping procedure is required, where we must begin at layer $N + 1$ (free space) and step inward, calculating the value of each θ by using Snell's law. These values can be stored and then recalled, as needed, when the program steps out from the inner layer outward to calculate the values of A and B. As before, the reflection coefficient is given by (8.16). Note from Figure 8.4 that this procedure calculates the specular reflection coefficient, not the backscatter reflection coefficient. Only in the case of normal incidence will the two coincide.

8.3.4 The Wave Matrix Approach to Scattering

An equivalent approach to calculation of scattering from flat multilayer dielectrics is the wave matrix approach. The basic analysis can be conducted in terms of either cascade matrices, relating the output side of a two-port to its input side, or in terms of scattering matrices, which relate the incident and reflected scattering coefficients. Collin [2] gives an excellent treatment of the cascade matrix approach in terms of reflection and transmission coefficients. The description given here utilizes the scattering matrix parameters because those are generally the most easily measured characteristics of a two-port network. This treatment follows Kerns and Beatty [3], and it should be noted that Collin's matrix notation and Kern's and Beatty's differ.

The shunt element circuit of Figure 8.5 might represent a circuit analog sheet or a resistive sheet in an absorber layup. The reflected waves (b_1, b_2) at each side of its two ports are related to the incident values (a_1, a_2) by the scattering matrix [S], where

$$\begin{bmatrix} b_1 \\ b_2 \end{bmatrix} = [S] \begin{bmatrix} a_1 \\ a_2 \end{bmatrix} = \begin{bmatrix} S_{11} S_{12} \\ S_{21} S_{22} \end{bmatrix} \begin{bmatrix} a_1 \\ a_2 \end{bmatrix} \quad (8.23)$$

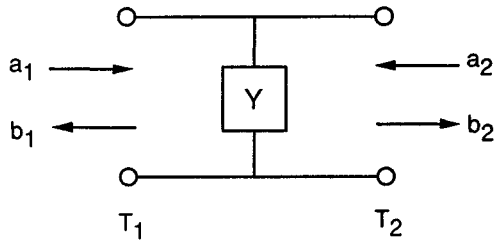

Figure 8.5. Shunt equivalent circuit element.

In terms of reflection and transmission coefficients, S_{11} is the reflection coefficient seen by a wave incident at port 1 with port 2 having a matched termination, similarly S_{22} is the reflection coefficient seen from port 2, and S_{12} and S_{21} are the transmission coefficients from ports 2 to 1 and 1 to 2, respectively. For a shunt circuit with admittance Y, the scattering matrix is

$$[S] = \frac{1}{2 + Y}\begin{bmatrix} -Y & 2 \\ 2 & -Y \end{bmatrix} \tag{8.24}$$

The scattering matrices necessary to define the other elements of a multilayer dielectric are the interface between dielectric layers and the phase shift due to a dielectric layer. A material interface is described in terms of the admittance on the "left" (Y^-) and "right" (Y^+) sides of the interface by

$$[S] = \frac{1}{Y^- + Y^+}\begin{bmatrix} Y^- - Y^+ & 2Y^+ \\ 2Y^- & Y^+ - Y^- \end{bmatrix} \tag{8.25}$$

where the admittances depend on the polarization and angle of incidence and are given by

$$Y_{TM}/Y_0 = \epsilon_r/\sqrt{\mu_r\epsilon_r - \sin^2\theta_0} \tag{8.26}$$

for the electric field parallel to the interface and

$$Y_{TE}/Y_0 = \sqrt{\mu_r\epsilon_r - \sin^2\theta_0}/\mu_r \tag{8.27}$$

for the magnetic field parallel to the interface, where θ_0 is the angle of incidence at the left side of the interface.

A slab of dielectric of thickness d potentially introduces a phase shift and a loss, and its scattering matrix is given by

$$[S] = \begin{bmatrix} 0 & \exp(-ikd) \\ \exp(ikd) & 0 \end{bmatrix} \tag{8.28}$$

where

$$k = k_0\sqrt{\mu_r\epsilon_r - \sin^2\theta_0} \tag{8.29}$$

An ability to directly use the scattering matrix components in absorber design is particularly useful in light of current materials metrology procedures. As described in Section 9.3.2, vector network analyzers can be configured to rapidly measure the scattering matrix parameters at closely spaced frequencies over a wide bandwidth. However, the definition of the scattering matrix, which relates the reflected signals on each side of a two-port device to the incident signals (i.e., from Figure 8.5, relates b_1 and b_2 and a_1 and a_2), is not suitable for calculation of the reflection and transmission properties of a multilayer configuration. What is required, instead, is a matrix formulation that relates the inputs and outputs on one side of the two-port to those on the other side (i.e., relates a_1 and b_1 to a_2 and b_2). For this purpose, the cascade matrix, $[R]$, is normally used, because the properties of a cascade connection of shunt elements and spacers is given by a total cascade matrix $[R_T]$, which is simply the product of the component matrices:

$$[R] = \begin{bmatrix} R_{11} & R_{12} \\ R_{21} & R_{22} \end{bmatrix} = \frac{1}{S_{21}}\begin{bmatrix} (S_{12}S_{21} - S_{11}S_{22}) & S_{11} \\ -S_{22} & 1 \end{bmatrix} \tag{8.30}$$

and

$$[S] = \frac{1}{R_{22}}\begin{bmatrix} R_{12} & (R_{11}R_{22} - R_{12}R_{21}) \\ 1 & -R_{21} \end{bmatrix} \tag{8.31}$$

The wave matrix approach is particularly useful in the analysis of *circuit analog* (CA) designs, for which it is often desirable to use the measured properties of fabricated CA sheets to predict performance.

8.3.5 An Approximate Scattering Analysis Procedure

The analyses of the proceeding sections provide excellent tools for the evaluation of RAM performance. For use in the design stage the formulations presented can be integrated with optimization routines to provide maximum performance within a given set of constraints. However, although current RAM design efforts are usually based on computer optimization techniques, it is desirable to begin the

optimization routine with a parameter set as close to optimum as practical. This generally implies that an analytical solution should be used to establish "first-cut" admittance parameters. Fortunately, RAM design practices are closely related to filter theory, and many of the tools developed for that arena can be utilized. This section briefly outlines the use of some of those tools in the design of broadband absorbers using resistive sheets or circuit analog sheets separated by low-loss dielectric spacers.

Figure 8.6 illustrates the typical model assumed for this analysis. As noted in Section 8.3.3, each resistive or circuit analog sheet can be represented as an admittance shunted across the transmission line. A multielement, broadband design implies that the reflection coefficient at each shunt admittance will be small. A small reflection coefficient implies a small admittance for each shunt element. The small individual reflection coefficients allow us to assume that the total reflection coefficient is simply the sum of the reflection coefficients for each shunt element, modified by the appropriate phase shift due to line length. With this simple assumption, the characteristics of the reflection coefficient of an absorber design can be tailored to standard functions, such as a maximally flat or minimum ripple (Chebyshev) behavior with frequency. The analysis shown here is very similar to that of Collin [4], who considered the design of multilayer transformers using small reflection theory. In fact, an absorber can be considered a transformer between free space and a very small impedance. The only modification of Collin's analysis is to use shunt elements instead of transmission lines with varying characteristic impedances.

The reflection coefficient R of the absorber circuit is approximately

$$R \simeq R_n + R_{n-1}\exp(\mathrm{i}2kd_n) + R_{n-2}\exp[\mathrm{i}2k(d_n + d_{n-1})] + \ldots + R_L\exp[\mathrm{i}2k(d_n + d_{n-1} + \ldots + d_1)] \tag{8.32}$$

where multiple reflections have been neglected. The power reflection is the square of the absolute value of (8.32); and for one shunt element and two shunt element circuits it is given by

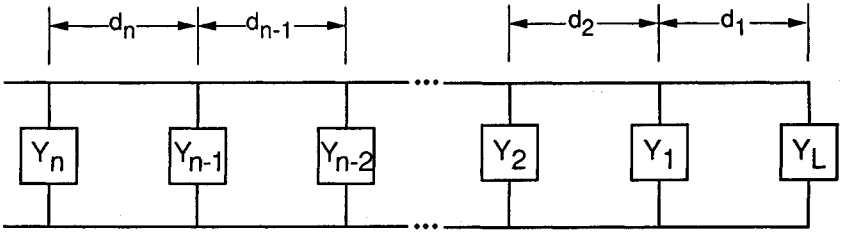

Figure 8.6. Circuit for approximate reflection analysis.

$$|R|^2 = \begin{cases} 1 - 2R_1 \cos 2\theta, & n = 1 \\ 1 - 2R_1 \cos 2\theta - 2R_2 \cos 4\theta, & n = 2 \end{cases} \tag{8.33}$$

where all lines are assumed to be of equal length ($\theta = kd$), the reflection coefficients are assumed to be real (to simplify the examples) and small, and the load reflection coefficient is -1 (i.e., a short circuit). The extension to $n > 2$ is straightforward. Equation (8.33) can be written as a polynomial in powers of cos θ by using standard identities, resulting in

$$\begin{aligned} |R|^2 &= (1 + 2R_1) - 4R_1 \cos^2 \theta, & n &= 1 \\ |R|^2 &= (1 + 2R_1 - 2R_2) + (-4R_1 + 16R_2) \cos^2 \theta - 16R_2 \cos^4 \theta, & n &= 2 \end{aligned} \tag{8.34}$$

A maximally flat design is achieved by setting the coefficients of all but the highest power terms to 0:

$$\begin{aligned} R_1 &= 1/2, & n &= 1 \\ R_1 &= 2/3, \quad R_2 = 1/6, & n &= 2 \end{aligned} \tag{8.35}$$

Similarly, a Chebyshev design is achieved by setting the coefficients equal to the Chebyshev polynomial coefficients:

$$\left.\begin{aligned} R_1 &= -1/(2 \sin \theta_1), \\ R_1 &= 4R_2 \sin^2 \theta_1 \\ R_2 &= 1/(2 - 8 \sin^2 \theta_1 - 2 \cos^4 \theta_1), \end{aligned}\right\} \quad \begin{aligned} n &= 1 \\ n &= 2 \end{aligned} \tag{8.36}$$

where θ_1 is evaluated at the edge of the frequency band.

Within the small reflection approximation, the reflection coefficient is related to the normalized shunt conductance via

$$R_n \simeq G_n/2 \tag{8.37}$$

It is interesting that this approximation provides the exact Salisbury screen result of a unity conductance for the single-layer maximally flat design. Similarly, the exact maximally flat result for the two-layer case is known to be

$$G_1 = \sqrt{2}, \qquad G_2 = 1 - 1/\sqrt{2} \tag{8.38}$$

which is very close to the approximate result of $G_1 = 4/3$, and $G_2 = 1/3$, found by using (8.35). The importance of this analysis is that it can easily be extended to complex admittances, additional layers, and other complications that render an exact analysis impossible. The approximate results can then be used as a starting

point for an optimization program. Figure 8.7 illustrates the exact solution for the two-layer design given in (8.38). Also shown is the approximate result given in (8.35).

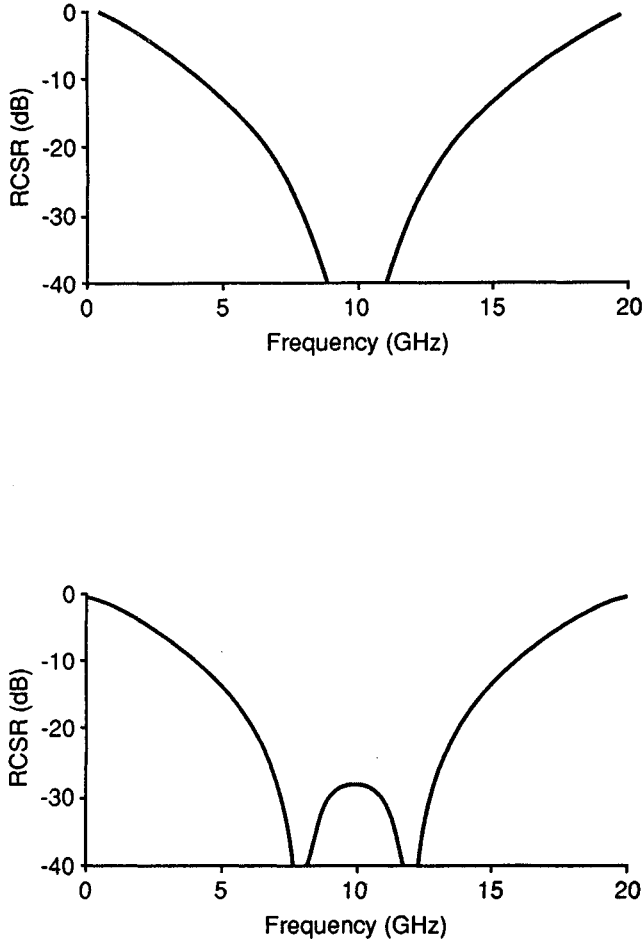

Figure 8.7. Two-layer maximally flat absorber for $d_1 = d_2 = \lambda_0/4$, $f_0 = 10$ GHz: (a) "exact" solution: $g_2 = 0.293$, $g_1 = 1.414$; (b) approximate solution: $g_2 = 0.333$, $g_1 = 1.333$.

8.4 DIELECTRIC MULTILAYER ABSORBER DESIGN AND PERFORMANCE

The ideal radar absorber would be thin, light, durable, easily applied, inexpensive, and have broadband frequency coverage. As an alternative, we might wish to have a structural RAM that is mechanically sound and has no size, weight, or cost

penalty over standard structural materials. As might be expected, neither of these ideal RAM types has yet been formulated. Nevertheless, since World War II (the Germans developed a magnetic RAM paint during the war and used it to reduce the RCS of submarine conning towers), a significant amount of effort has been invested in the development of absorbers that are practical for military applications.

To illustrate absorber design and performance, RAM types that are in widespread use are described and their properties are analyzed. Although the emphasis is on broadband absorbers, the descriptions start with simple, narrowband, single-layer absorbers, which form the components for multilayer broadband absorbers. An underlying assumption in the treatment provided is that RAM volume is a constraint. Therefore, little attention is given to the design of RAM for anechoic chambers and other similar applications, although those types of absorbers are briefly described as examples of geometric transition RAM and are described in more detail in Chapter 13.

8.4.1 Salisbury Screens and Dallenbach Layers

Two of the oldest and simplest types of absorbers are represented by Salisbury screens and Dallenbach layers. The Salisbury screen [5] is a resonant absorber created by placing a resistive sheet on a low dielectric constant spacer in front of a metal plate. The Dallenbach layer [6] consists of a homogeneous lossy layer backed by a metal plate. Each is analyzed in the following.

Figure 8.8 illustrates the geometry of the Salisbury screen. In the analysis of its performance, we assume that an infinitesimally thin resistive sheet of conduc-

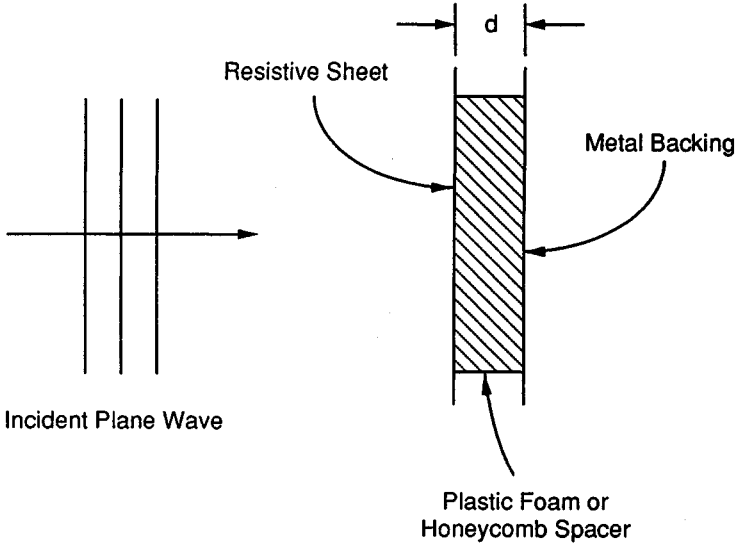

Figure 8.8. Salisbury screen.

tance G, normalized to free space, is placed a distance d from a metal plate. Typically, a foam or honeycomb spacer might be used, so spacer dielectric constants in the 1.03 to 1.1 range are normal. To simplify this analysis, the normalized permittivity of the spacer is assumed to be that of free space (i.e., $\epsilon_r = 1$).

From (8.16), the reflection coefficient for a dielectric multilayer will be 0 if B_{N+1} is forced to 0. For the simple case of the Salisbury screen, substituting in (8.15),

$$B_{N+1} = B_2 = \frac{e^{-ikd}}{2}[-G\, e^{-ikd} - (2 - G)\, e^{ikd}] \tag{8.39}$$

where $Y_1 = Y_2 = 1$ (free space), and $k_2 = k_0 = 2\pi/\lambda$ (the free-space wavenumber). $B_2 = 0$ only if the quantity in brackets is 0. This requires that the magnitudes of the two exponentials in the brackets be equal and that their phase angles be opposite. The equal amplitude requirement forces G to equal 1, or equivalently, the unnormalized resistance to be 377 Ω/sq. In that case, (8.39) becomes

$$B_2 = -e^{-ikd}\frac{e^{ikd} + e^{-ikd}}{2} = -e^{-ikd}\cos\frac{2\pi d}{\lambda} \tag{8.40}$$

The condition $B_2 = 0$ requires $\cos(2\pi d/\lambda) = 0$, which implies that

$$2\pi/\lambda = \frac{\pi}{2} + n\pi, \qquad n = 0, 1, 2, \ldots,$$

or

$$d = \frac{\lambda}{4} + \frac{n\lambda}{2} \tag{8.41}$$

Thus, for zero reflectivity, a Salisbury screen requires a 377 Ω/sq resistance sheet set at an odd multiple of an electrical quarter-wavelength in front of a perfectly reflective backing. Higher dielectric constant spacers may be used and still satisfy (8.40), but with a consequent reduction in bandwidth, because k for that case will be larger than k_0, and thus a given frequency change will cause a larger change in B_2 than for the $\epsilon_r = 1$ spacer.

Another way to think of the Salisbury screen is in transmission line terms. A quarter-wavelength transmission line transforms the short circuit at the metal plate into an open circuit ($G = 0$) at the resistive sheet. The sum of the sheet and open circuit admittances, which is the value seen by the impinging wave, is just that of the sheet, 1/377 mho, and thus a matched load is provided and no reflection occurs. By the same token, at multiple half-wavelength spacings, a short circuit is again seen and perfect reflection is obtained.

The screen performance for a 1.27 cm spacing is shown in Figure 8.9. Note that the reflection coefficient reaches its minimum value at a frequency of 5.9 GHz (λ = 5.08 cm). The best performance is obtained for a resistivity of 377 Ω/sq, but the performance is still a respectable −18 dB for a resistivity 20% lower (300Ω/sq). However, a resistivity of 200Ω/sq yields barely a −10 dB reflectivity level at the design spacing. The fractional bandwidth for the 377Ω/sq screen at a −20 dB reflectivity level is about 25%.

To achieve similar performance at a lower frequency, the spacing must be increased because the wavelength becomes longer. This effect is shown in Figure 8.10, and it will be observed that a pair of nulls now exist, one at three times the frequency of the other. The minimum reflectivity levels are the same as those in Figure 8.9. The nulls will occur at odd integral multiples of the lowest frequency due to the fact that the design spacing can be any odd multiple of a quarter-wavelength.

The Salisbury screen has been used in varying degrees in commercial absorbing materials. However, the rapid oscillations for large spacings would render it ineffective over a wide frequency range. For increased mechanical rigidity, plastics, honeycomb, or higher density foams may be used as spacers. To maintain the electrical spacing, the resistive sheet would be mounted over a dielectric layer trimmed to be an electrical quarter-wavelength in thickness. As noted before, the gains in mechanical rigidity and decreased thickness obtained by using a higher dielectric constant spacer are paid for in reduced absorber bandwidth.

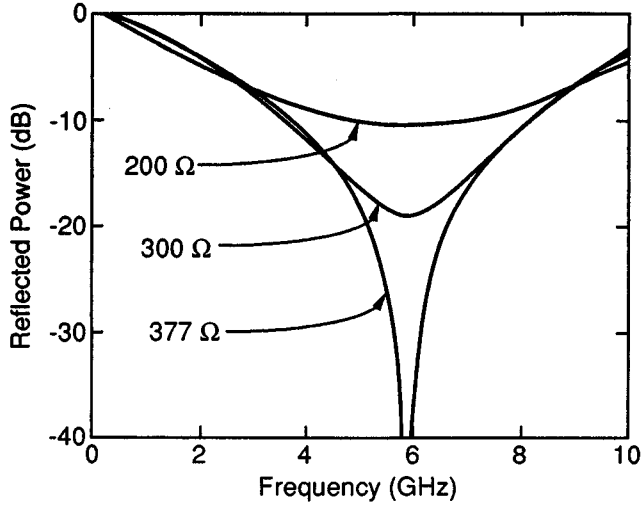

Figure 8.9. Theoretical performance of a Salisbury screen for a stand-off distance of 1.27 cm.

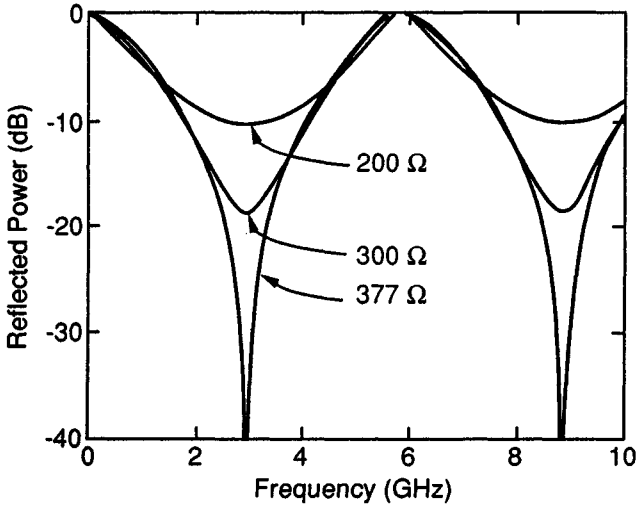

Figure 8.10. Theoretical performance of a Salisbury screen for a stand-off distance of 2.54 cm.

The preceding analysis assumed normal incidence of a plane wave on the absorber. It is interesting to explore the specular performance of the Salisbury screen at off-normal angles. It can be shown [6] that the magnitude of the reflection coefficients for both parallel and perpendicular polarizations are given approximately by

$$|R_\perp| = |R_\parallel| \simeq \frac{1 - \cos\theta}{1 + \cos\theta} \tag{8.42}$$

where θ is the angle off-normal. Equation (8.42) is plotted in Figure 8.11. Note that performance is better than 20 dB (i.e., $|R| < 0.1$) for angles up to 35°. A more exact analysis of general RAM performance as a function of incidence angle can be found in [7], but the error (8.42), is no worse than 5 dB, and therefore it is useful as a rough estimate of Salisbury screen behavior with angle.

Another simple resonant absorber, the Dallenbach layer, is constructed of a homogeneous lossy layer backed by a metallic plate. The reflection at the surface of a material is due to the impedance change seen by the wave at the interface between the two media. Therefore, if a material can be found whose impedance relative to free space equals 1 (i.e., $\mu_r = \epsilon_r$), there will be no reflection at the surface. In this case the attenuation will depend on the loss properties of the material (ϵ_r'', μ_r'') and the electrical thickness.

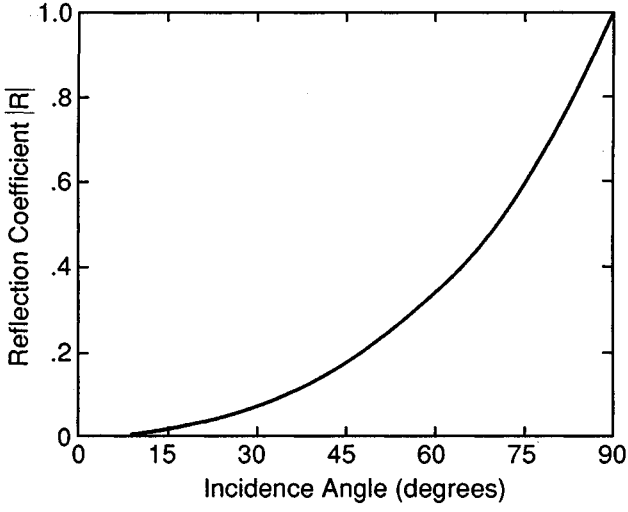

Figure 8.11. Reflection coefficient of a Salisbury screen as a function of the angle of incidence.

Unfortunately, materials with the appropriate dielectric and magnetic properties to act as a matched RAM over any appreciable frequency range are difficult to find, and so the question becomes one of optimizing the loss at a given frequency using available materials. For a single material layer backed by a conducting plate, the reflection coefficient is given by substituting (8.7) into (8.8) to provide

$$R = \frac{\sqrt{\mu_r/\epsilon_r}\tanh(-ikd) - 1}{\sqrt{\mu_r/\epsilon_r}\tanh(-ikd) + 1} \tag{8.43}$$

where d is the thickness of the layer. Figures 8.12 and 8.13 from [8] provide curves of reflection as a function of material thickness in wavelengths for several hypothetical materials. The permittivity and permeability are written in polar form per (8.3).

Several things should be noted from the plots. First, for nonmagnetic materials ($\mu_r = 1$), the best RCSR performance occurs when the material is near a quarter-wavelength thick electrically. The solid curve of Figure 8.12 illustrates this point. However, adding magnetic loss shifts the optimum electrical thickness to larger values because of the $+1$ reflection coefficient for the magnetic field at the conducting back plane. A pure magnetic absorber, if it were available, would have an optimum thickness near an electrical half-wavelength, as illustrated in Figure 8.13. Note on both figures that a hypothetical material with $\mu_r = \epsilon_r$, indicated by the diagonal traces, simply provides a linearly increasing loss in dB with increasing thickness in wavelengths.

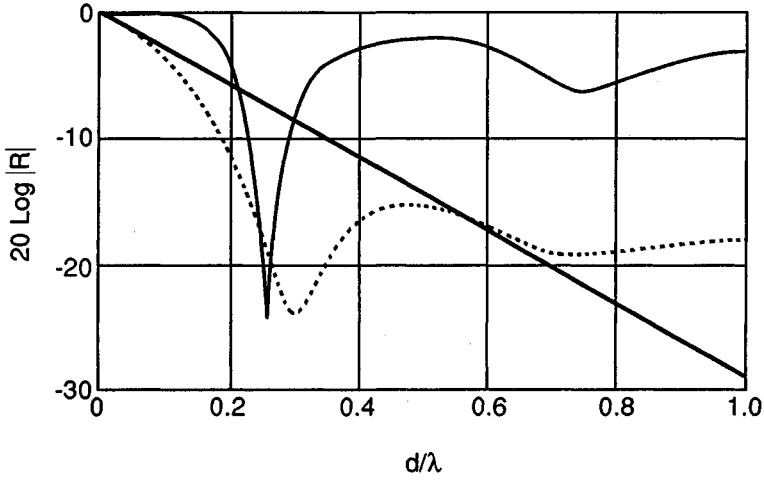

Figure 8.12. Reflectivity curves for dominantly electric materials. Solid trace is for $|\epsilon_r| = 16$, $|\mu_r| = 1$, $\delta_\epsilon = 20°$, and $\delta_\mu = 0°$. Dashed trace is for $|\epsilon_r| = 25$, $|\mu_r| = 16$, $\delta_\epsilon = 30°$, and $\delta_\mu = 20°$. Diagonal trace is for $|\epsilon_r| = |\mu_r| = 4$, $\delta_\epsilon = \delta_\mu = 15°$.

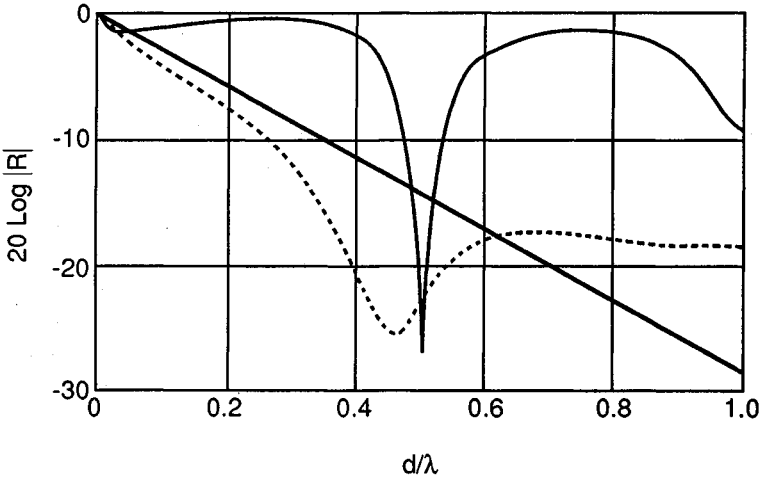

Figure 8.13. Reflectivity curves for dominantly magnetic materials. Solid trace is for $|\epsilon_r| = 1$, $|\mu_r| = 16$, $\delta_\epsilon = 0°$, and $\delta_\mu = 10°$. Dashed trace is for $|\epsilon_r| = 16$, $|\mu_r| = 25$, $\delta_\epsilon = 20°$, and $\delta_\mu = 30°$. Diagonal trace is for $|\epsilon_r| = |\mu_r| = 4$, $\delta_\epsilon = \delta_\mu = 15°$.

For off-normal incidence, the behavior of a homogeneous layer is similar to that for Salisbury screens [6]. For the case where the index of refraction of the layer is much greater than 1, (8.42) provides a much better approximation to the angular performance for the Dallenbach layer than it does for the Salisbury screen.

An additional question concerns the fractional bandwidth that can be achieved with the Dallenbach type absorber. Ruck [6] presents an analysis giving an approximate bandwidth for an ideal Dallenbach layer, assuming that the fractional bandwidth B is much less than 1, in terms of the material properties, the material thickness, and the wavelength at maximum RCSR performance, λ_0, for a given reflection level R as

$$B = 2\left[\frac{f - f_0}{f_0}\right] \simeq \frac{2|R|}{\pi|\mu_r - \epsilon_r|(d/\lambda_0)} \tag{8.44}$$

Figure 8.14 provides plots of bandwidth for 20 dB RCSR versus thickness for single layers with only electric or magnetic losses. Note that a material with purely dielectric loss has a fractional bandwidth around 20% for a material thickness close to $\lambda/4$, which is somewhat less bandwidth than for the Salisbury screen. For magnetic materials, the bandwidth increases as the material becomes thinner. The values plotted are not accurate for small electrical thicknesses because a large bandwidth violates an initial assumption. However, in the limit, the infinitesimally thin magnetic lossy layer is equivalent to a magnetic Salisbury screen that, in theory, has infinite bandwidth [6].

Another single layer absorber has been postulated and analyzed by Gauss at the Ballistic Research Laboratory [9]. It is based on mixing filaments of *radar absorbing chaff* (RAC) in a solid binder of near unity dielectric constant. Attenuation of the incident wave is provided by resistive dissipation in the filaments, which are metallic strands with length to diameter ratios of about 1000, and diameters of about 500 Å. Filament separations in the binder are one-half to one-third the filament length.

An analysis is provided in [9] for two cases; the first is a regular array of filaments in the matrix and the second is for filaments with random orientation. Calculated RCSR for a 2 cm thick application using a regular array of filaments exceeds 30 dB from 10 GHz through 100 GHz. For the random filament orientation, RCSR is 13 dB at 10 GHz, and greater than 30 dB from 30 GHz through 100 GHz. It should be noted that the RCSR values quoted are theoretical and are not based on measurements of fabricated samples.

8.4.2 Multilayer Dielectric Absorbers

As noted in Section 8.4.1, it is difficult to achieve the wide bandwidths generally desired of radar absorbers by using a thin single-layer absorber. Therefore, much work has been done in extending the bandwidth of absorbers through the use of multiple layers. The approach employed is the same as that for pyramidal and other geometric transition absorbers—slowly changing the effective impedance

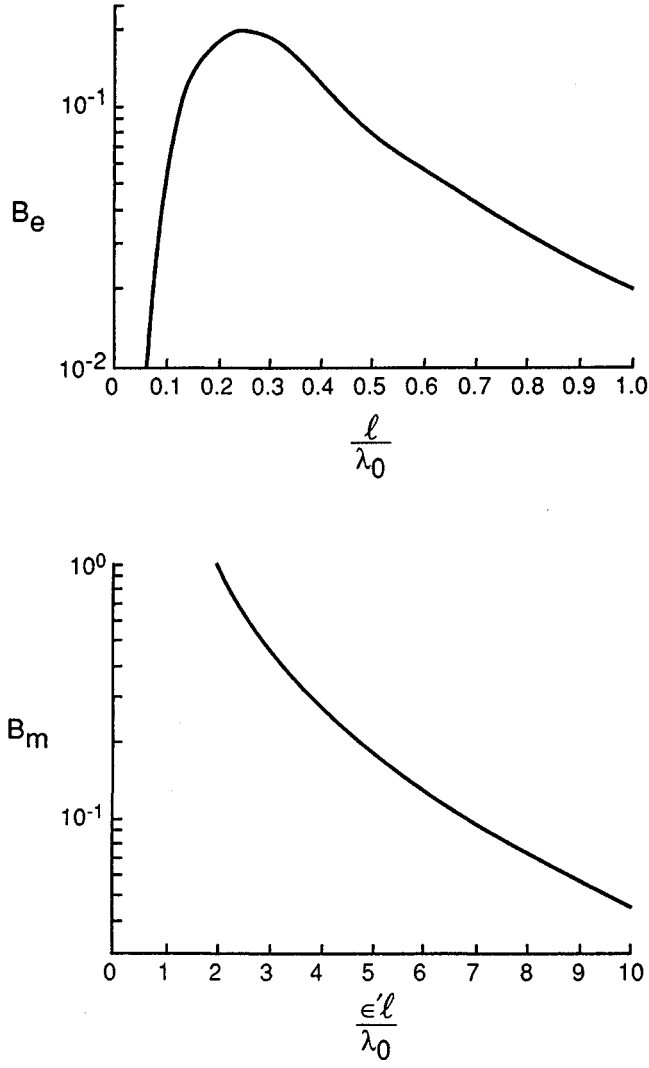

Figure 8.14. Bandwidths of thin homogeneous (a) electric or (b) magnetic layers as a function of layer thickness (from [6]).

with distance into the material to minimize reflections. Two important types of multilayer absorbers will be discussed, Jaumann absorbers and graded dielectric absorbers.

The bandwidth of a Salisbury screen can be improved by adding additional resistive sheets and spacers to form a Jaumann absorber. To provide maximum performance, the resistivity of the sheets should vary from a high value for the front sheet to a low value for the back. The bandwidth is dependent on the number of sheets used, as illustrated in Figure 8.15 and Table 8.1. For this illustration, the spacing between sheets was fixed at 7.5 mm (a quarter-wavelength at 10 GHz) and a quadratic resistance taper was used. The fractional bandwidth for slightly less than 20 dB performance is shown in the table. Note that a four-sheet structure has about four times the fractional bandwidth of a single layer, but is four times as thick (3 cm versus 7.5 mm).

Even better performance is available for Jaumann absorbers with more sheets, as illustrated by a six-layer RAM in [10]. A 3.56 mm spacing between

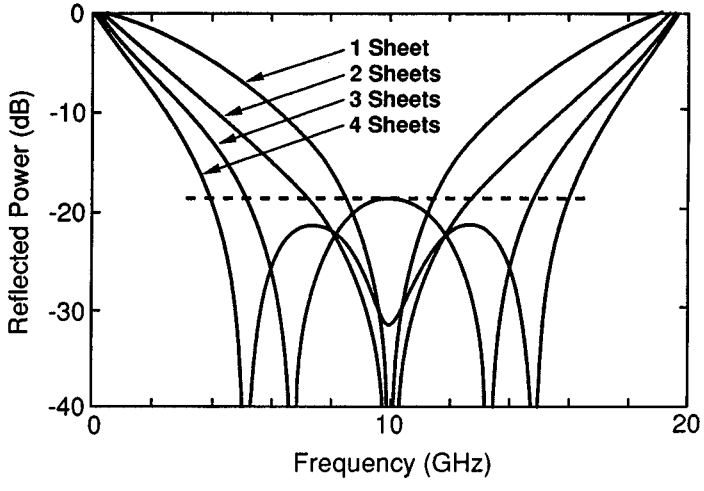

Figure 8.15. Predicted performance of multiple-sheet Jaumann absorbers.

Table 8.1
Bandwidth of Jaumann Absorbers

Number of sheets	*Fractional bandwidth*	*Total thickness (cm)*
1	0.27	0.75
2	0.55	1.50
3	0.95	2.25
4	1.16	3.00

layers with a spacer $\epsilon_r = 1.03$ (probably styrofoam) was used. Table 8.2 provides resistivity values for the lossy sheets, and Figure 8.16 provides a plot of the predicted RCSR performance. Note the large change in resistivity from front to back provided by the approximate quadratic taper used. An average RCSR of 30 dB was measured for this design over the range of 7 GHz through 15 GHz, with a minimum of 27 dB at 8 GHz (a 34 dB average RCSR is predicted). One extremely important point brought out in [10] is the requirement for homogeneous and isotropic lossy layers if high levels of reduction are to be achieved in practice.

As with the Jaumann absorber, where sheet resistance values are tapered to reduce reflection, a graded dielectric can be used to help match the impedance

Table 8.2
Resistive Sheet Values

Layer	*Resistivity (Ω/sq.)*
Front	9425
2	2513
3	1508
4	943
5	471
Back	236

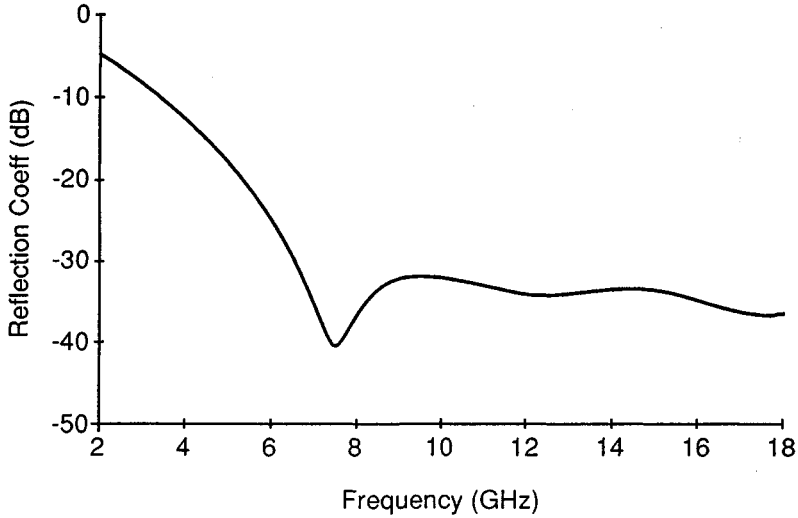

Figure 8.16. Predicted performance of a six-layer Jaumann absorber.

between free space and a perfect conductor. The optimum method for design of such an absorber would be to determine analytically the μ and ϵ required as a function of distance into the material to limit $|R|$ over a given frequency range, subject to incidence angle and thickness constraints. Unfortunately, this general form of the problem has not yet been solved [6].

A more successful and useful approach has been to assume a model for ϵ and μ as a function of the distance z into the absorber, and then to solve for the resulting reflection coefficient. A number of models have been used for the taper including linear, exponential, and one (Jacobs) making the fractional rate of change in ϵ_r per wavelength in the material a small constant. Table 8.3, extracted from [6], lists a half-dozen versions of tapers, along with the thickness required at the lowest frequency for 20 dB RCSR. Note that the minimum thickness is on the order of 0.3λ, implying that even in the ideal case, an absorber nearly 5 cm thick would be required for 20 dB performance down to 2 GHz.

Typically, practical graded dielectric RAMs are constructed of discrete layers, with properties changing from layer to layer. One commercial example is the AN series of graded dielectric absorbers made by Emerson and Cuming. AN-74, a three-layer foam absorber about 3 cm thick, is advertised to provide 20 dB RCSR down to 3.5 GHz. Dipped honeycombs, with successive dippings to lesser depths, have also been used to provide the conductivity gradient required for a graded dielectric absorber. Figure 8.17 provides measured reflectivity data for a commercial three-layer graded dielectric absorber about 1 cm thick.

Several other RAM types exist that are, in effect, graded dielectric absorbers. The first type appears to be a homogeneous single-layer absorber, but, due to its method of production, is actually a graded dielectric. The second type uses a geometric transition to provide an effective dielectric gradient.

A technique for reducing the reflection from the front face of a flat absorber is to produce a material whose intrinsic impedance is very close to unity. Two

Table 8.3
Several Graded Dielectric RAM Designs [6]

Type of variation	$\mu_r'(z)$	$\mu_r''(z)$	$\epsilon_r'(z)$	$\epsilon_r''(z)$	*Minimum* l/λ for $R \leq 0.1$
Ideal Jacobs	1	0	$(1 - z/l)^{-2}$	Small constant $\ll 1$	0.3
Finite Jacobs	1	0	$(1 - 0.95z/l)^{-2}$	1/2	0.42
Linear	1	0	1	$3z/l$	0.55
Exponential	1	0	1	$0.285 \exp(2.73z/l)$	0.35
Exponential	1	0	$2^{z/l}$	$5^{z/l} - 1$	0.56
Three-layer discrete approximation to exponential	1	0	1	0.58 for $0.344l$ 1.16 for $0.359l$ 3.48 for $0.297l$	0.33

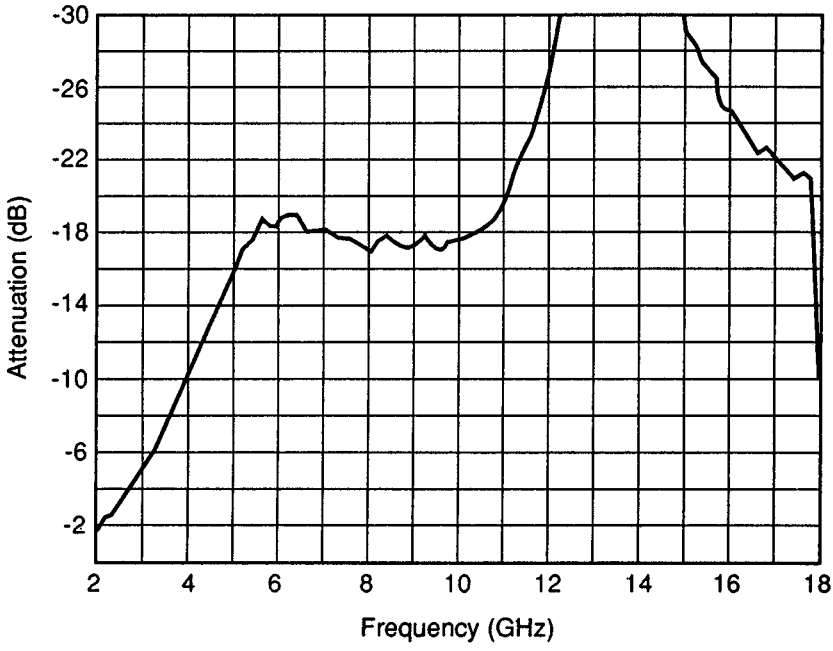

Figure 8.17. Measured reflectivity of a three-layer graded dielectric absorber.

common examples of absorbers employing such a technique are the hair-type and the carbon-loaded low-density foam absorbers. However, both types employ a conductivity gradient to some degree.

The original hair-type absorber was developed by NRL in the late 1940s for an anechoic chamber used to cover from 2.5 to 25 GHz [11]. The material is constructed by impregnating mats of curled animal hair with a mixture of conducting carbon black in neoprene. Because the mats normally are laid flat to dry after dipping, gravity tends to provide a dielectric gradient, as more of the conductive mixture ends up toward the back of the mat. Currently available commercial versions of hair-type absorbers require approximately a half-wavelength material thickness for 20 dB of RCSR [12]. Because of its poor structural properties and poor RCSR performance compared to pyramidal absorbers and graded dielectrics, hair-type absorbers tend to be used less than they once were.

A more recent version of the "hair mat" absorber is a netting absorber produced by the Plessey Corporation. A 1.2 cm thick plastic netting is provided with a conductive coating. Again, there is a variation in the amount of conductive material from front to rear, providing a dielectric gradient. Advertised RCSR

performance of the netting is better than 10 dB from 6 GHz through 100 GHz, with better than 15 dB performance over an 8 to 14 GHz band [13].

Another class of single-layer absorber (and the one most commonly used in anechoic chambers) depends upon carbon-loaded foam to provide loss, but also uses a geometric transition from free space to the highly lossy medium to provide a dielectric gradient and thereby reduce reflections. The most common form used in anechoic chambers is the pyramidal absorber illustrated in Figure 8.18. Other common shapes include an aggregate sine wave (convoluted) front, conical shapes, and off-normal angle wedges. These types of absorbers can provide reflectivity reductions in excess of 50 dB, but may require thicknesses in excess of 10λ to do so [14]. Figure 8.19 provides an indication of the RAM thickness needed for a given level of RCSR versus frequency, and of the performance of the RAM at angles far off-normal [15].

As requirements on sensitivity have increased for indoor ranges, significantly more effort has gone into the analysis of the performance of geometric transition absorbers [16,17]. Reference [17] provides an interesting comparison of the reflection coefficient for several shapes that might be used for anechoic chamber absorber. Compared are rectangular, sinusoidal, and triangular profiles. In all cases the analysis assumes that the basic material composing the absorber extends an infinite distance behind the front profile. The triangular profile is found to provide

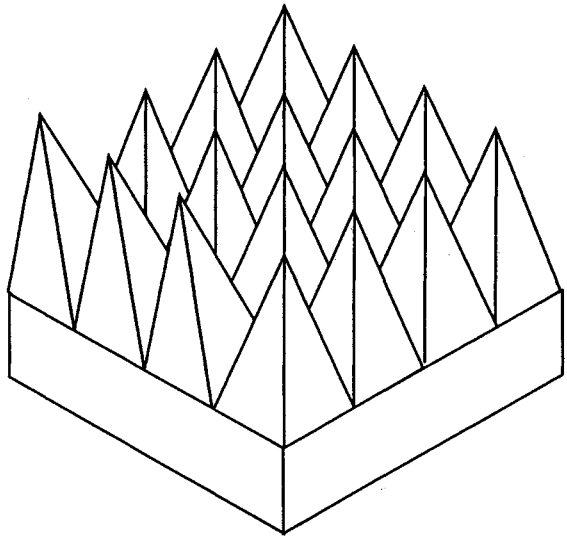

Figure 8.18. Geometric transition absorber.

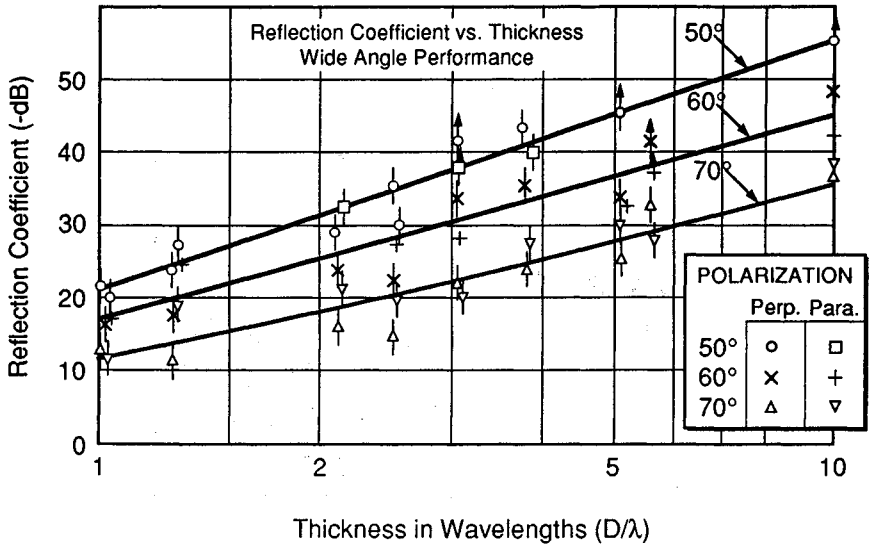

Figure 8.19. Reflection coefficient as a function of absorber thickness for pyramidal absorbers at various incidence angles (from [15]).

significantly better performance than the other two, because of the more gradual taper of the spatially averaged impedance seen by the incoming wave.

Figure 8.20, from [17], provides a plot of reflection coefficient for a 1λ deep version of a triangular profile and a variant of a triangular profile. Note that the variant provides almost 10 dB better performance at normal incidence than does the triangular profile, because of the better taper at the top and the inclusion of more absorptive material toward the bottom of the profile.

8.5 CIRCUIT ANALOG RAM AND FREQUENCY-SELECTIVE SURFACES

As pointed out previously, the design of specular RAM is equivalent to a transmission line matching problem, where the goal is to limit the reflection seen at the input caused by a short-circuit termination. The Salisbury screen and Jaumann absorbers use resistive sheets, which have only a real part to their admittance, as the matching elements. Significant flexibility can be gained in the design process if the sheets can have a susceptance as well as a conductance. This imaginary part of the admittance can be obtained by replacing the continuous resistive sheet with one whose conducting material has been deposited in appropriate geometrical patterns (e.g., dipoles, crosses, triangles), such as those shown in Figure 8.21. The

Chapter 9
Radar Absorber Measurement Techniques

Eugene F. Knott

9.1 OVERVIEW

Like any other product, the design of a radar absorber depends a great deal on its intended application. The application itself, along with the properties of the materials available to fabricate the product, lead to the evolution of one or more concepts or configurations. Once we evolve a design to suit the application, whether specified or perceived, we must verify the performance of the concept. If we are successful enough to develop a product line from it, we must assure our customer of our widely advertised performance by means of quality control. These three different requirements demand three different kinds of measurement and evaluation, as diagrammed in Figure 9.1.

The most basic information needed in the electrical design of the absorber is the electromagnetic properties of the materials we expect to use to manufacture it. Equally basic, although not listed in the diagram, are the physical properties of those materials, such as density, tensile strength, durability, chemical stability, and compatibility with bonding systems (adhesives). Bulk materials are characterized by their relative permeabilities and permittivities, whereas thin sheets are more conveniently characterized by complex impedances. Permeability and permittivity are recognized as complex quantities, and we typically normalize these values with respect to the corresponding free-space values. The impedance of a thin sheet is also a complex quantity (a resistance and a reactance). Although the unit of sheet impedance is ohms, measured results are typically labeled *ohms per square* to emphasize that a thin sheet, not a lumped element, was measured.

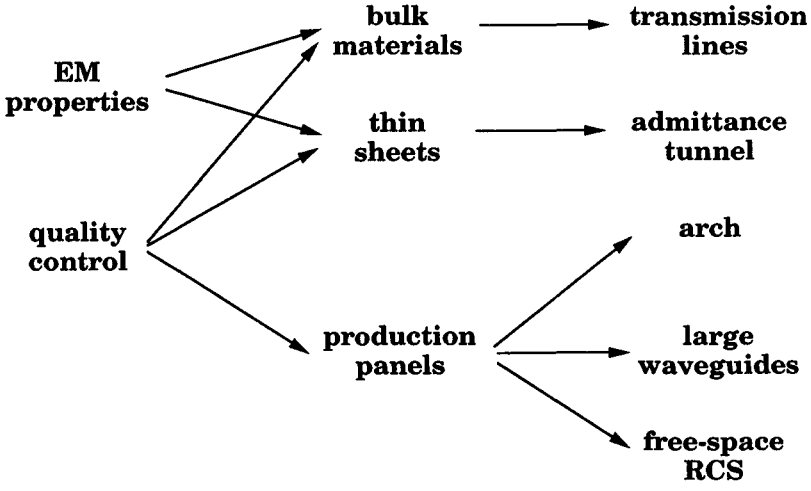

Figure 9.1. The objective of the measurement governs the equipment and test method used.

The relative permeability and permittivity of test samples are most accurately measured in small fixtures that are actually short sections of transmission lines. This minimizes the escape of energy from the system, thus reducing the risk that energy losses might be attributed to nonexistent losses within the test sample. It also allows an accurate evaluation of the material properties because of the well-documented soundness of the theory on which the measurements are based. Transmission-line measurement systems are also compact enough to fit on a laboratory bench, which makes them convenient to use and easy to operate. We present the basis of transmission-line theory in Section 9.2 and the extraction of the desired material properties from those measurements in Section 9.3.

The thin sheets used in the design of some absorbers are not easily measured in transmission lines, because it is difficult to install them in the sample holders ordinarily used to measure permeability and permittivity. A device called the *admittance tunnel* is used instead, and much larger samples are required. The admittance tunnel is an absorber-lined box typically fitted with a small transmitting horn at one end, a small receiving horn at the other, and the test sheet installed between the two. The sheet properties are calculated from a comparison of the signals received with and without the test sheet in place. In a less familiar version of the admittance tunnel, the receiving horn is replaced by a metal backing plate, and the reflection characteristics of the plate-backed sheet are measured instead. The admittance tunnel test fixture is discussed in Section 9.5.3.

Because transmission-line measurements demand exquisitely small samples at millimeter wavelengths, alternative methods must be used. One is the resonant cavity that, like the transmission line, is an enclosed system that prevents the escape of energy. The measured quantity in this case is a comparison of the Q (relative loss) and the resonant frequency of the cavity with and without a test sample packed inside. We discuss the interferometer in Section 9.5.2 as a special case of the cavity method.

We may estimate the electromagnetic performance of any absorber design by using the formulations given in Chapter 8 and the measured relative permeabilities and permittivities (or sheet impedances) described in Sections 9.3 and 9.5.3. Indeed, this estimate is one step that already should have been performed in the iterative design and optimization of the absorber. However, the estimate is subject to several sources of error, among them an inadequate knowledge of the electromagnetic properties of all the components in the absorber design, errors in the measurement of properties of individual components, and variations in manufacturing tolerances. It is therefore prudent, if not mandatory, that theoretical estimates of performance be verified by direct measurement of a test sample fabricated according to design specifications.

Because of inevitable variations in the electromagnetic properties from one point in the final product to another, and because the final product is much thicker than any of its component parts, this experimental verification of performance usually cannot be assessed in transmission-line measurements, as the individual components were. In addition, reflectivity of the fabricated test sample is of interest, not the electromagnetic parameters of the components used in its design. It is therefore more convenient, more realistic, and less costly to measure a large sample of the assembled absorber in a different kind of fixture. Figure 9.1 shows two options for such evaluations.

One is the classic NRL arch measurement and the other is a free-space RCS measurement of the absorber installed on a metal backing plate. We regard both as free-space methods because the test samples are not enclosed by the conductors of a transmission-line sample holder. Two differences distinguish them. In the arch setup, the bistatic reflectivity is measured, sometimes as a function of the bistatic angle, and the transmitting and receiving antennas are located within a few sample widths of the sample itself. In the free-space RCS method, the monostatic reflectivity is measured, usually as a function of the angle of arrival of the incident wave, with the sample located in the far field of the transmitting and receiving antennas. Both methods are discussed in Section 9.4.

We do not restrict our consideration of absorber measurement to stealth applications. Recognizing that pyramidal absorbers are used in test facilities and that they demand quality control as much as any other product, we cite an unusual test fixture designed for this particular need. It is the large waveguide described

in Section 9.5.1 and used primarily to evaluate chamber materials at low frequencies.

Few of the absorber evaluation techniques discussed in this chapter are new, as most of them rely on basic measurements of the reflection of energy from test samples, or the transmission of energy through them, or both. These kinds of measurements were once made at a relatively small number of test frequencies, due to limitations in equipment and the time required to set up and adjust the equipment. The development of reliable phase-locked, voltage-controlled signal sources in the 1960s and powerful microprocessors in the 1970s, and marriage of the two in the 1980s, has changed that. We now have sophisticated machines that can be programmed to collect coherent reflection and transmission data over octaves of bandwidth in a relatively short time, and the data can be stored digitally for any variety of subsequent processing. Nevertheless, we include in the chapter occasional discussions of how it used to be done.

9.2 TRANSMISSION LINE THEORY

9.2.1 Basic Relationships

The transmission line is a basic device used to measure the electromagnetic properties of materials because the theory of wave propagation within the line is well understood and RF energy is confined within the system. A sample holder—a short section of transmission line—is loaded with a test sample machined to fit the line, and the reflection of RF energy from it, or the transmission of RF energy through it, or both, are measured. Because the dependence of the two measured quantities on the electromagnetic properties of the material in the line is known, those properties may be extracted by appropriate manipulation of the test data.

The application of the theory demands that the transmission-line sample holder be uniform, which is to say neither the transverse dimensions of the line nor the properties of the material in it may vary along the length of the line. Although the uniformity in dimension is not an unreasonable restriction, the demanded uniformity in material properties does restrict the kinds of materials that may be accurately measured. The dielectric properties of honeycomb spacers used in the fabrication of some absorbing materials, for example, vary from point to point in the material. Unless the period of the variation is a small fraction of the wavelength or a small fraction of the transverse dimension of the line, the properties of the sample cannot be accurately deduced from the measurements.

With this uniformity understood, we may launch a signal down the line and observe (measure) the signal at the far end. The signal is assumed to be monochromatic and characterized by a propagation factor, γ, that is, in general, a complex number. When there are no ohmic losses in the line, γ is the imaginary number $ik = i2\pi/\lambda$, which describes the shift in the phase of the signal as it travels

along the line; in the absence of loss, there is no change in its amplitude. In the TEM (transverse electromagnetic) lines to be discussed in a moment, k is the wavenumber discussed in Chapter 8 and λ is the wavelength of the signal *as measured within the material in the line.* If there are energy losses in the line, due either to the finite conductivity of the conductors of the line or losses in the material filling it, γ and k are complex quantities. In the latter event, a complete characterization of propagation in the line demands that we account for the decay in amplitude, as well as the shift in phase, with increasing distance.

As agreed in Chapter 1, we allow our signal to vary harmonically with time as $\exp(-i\omega t)$, but we suppress that variation in any mathematical expressions for fields, voltages, or currents. To account for the possibility of reflections from the receiving end of the line, we must admit the existence of both forward- and backward-traveling waves. This being the case, the voltage at any point z along the transmission line may be represented as the sum of the voltages due to the forward and backward waves:

$$V(z) = V_i e^{-\gamma z} + V_r e^{\gamma z} \tag{9.1}$$

where V_i and V_r may be complex numbers, and the subscripts indicate the incident (forward) and reverse traveling voltage waves. The currents flowing in the conductors of the line may similarly be expressed as

$$I(z) = (V_i e^{\gamma z} - V_r e^{-\gamma z})/Z_0 \tag{9.2}$$

where Z_0 is the *characteristic impedance* of the line. The assumed (backward) direction of propagation in the second term in (9.1) and (9.2) is responsible for the reversal of the sign of the second term in (9.2) in comparison with that of the second term in (9.1).

We may form the ratio of (9.1) and (9.2) to determine the impedance at any point z along the line:

$$Z(z) = Z_0 \frac{V_i e^{\gamma z} + V_r e^{-\gamma z}}{V_i e^{\gamma z} - V_r e^{-\gamma z}} \tag{9.3}$$

In working with transmission lines we are almost always interested in the value of this impedance for two very specific positions along the line: at the load terminating the line and at some distance d *toward the source* from that load. If we denote the load impedance by Z_L, we may set $z = 0$ at the load and calculate the load *voltage reflection coefficient* V_r/V_i:

$$\Gamma_L = \frac{V_r}{V_i} = \frac{Z_L - Z_0}{Z_L + Z_0} \tag{9.4}$$

Now, by letting $z = -d$ and inserting the value of (9.4) for V_r/V_i back into (9.3), we have

$$Z_{\text{in}} = Z_0 \frac{Z_L \cosh \gamma d - Z_0 \sinh \gamma d}{Z_0 \cosh \gamma d - Z_L \sinh \gamma d} \tag{9.5}$$

where Z_{in} is understood to mean $Z(-d)$. The reader may note that the signs of the second terms in both the numerator and denominator of (9.5) are the reverse of the signs found in most texts on transmission lines. This is because those texts assume the $\exp(j\omega t)$ time dependence in contrast to our $\exp(-i\omega t)$. Whatever the time convention, (9.4) and (9.5) constitute the most useful relationships at our disposal for the measurement of test samples in transmission lines.

That utility is the theoretical basis relating the impedance at the input of a line of length d to the impedance terminating its output end. The "terminating" impedance might well be another transmission line of quite different characteristics and might well be followed by yet another transmission line. Thus, given the characteristic impedance, propagation constant and physical length of each section of any cascaded set of transmission lines, plus the value of the terminating impedance of the last one, we may calculate the impedance and effective reflection coefficient at the junction between any pair in addition to the impedance presented at the input of the first one. Equations (9.4) and (9.5) are therefore a pair of *transformer* equations that may be used to generate another pair of numbers (an impedance and a reflection coefficient) associated with the input end of the transmission line section, given the nature of the load at the output.

These two powerful expressions have yet another attraction: they demand no measurement of voltages or currents at the input or output ends of transmission lines, even though their development is based on a consideration of such quantities. Their transforming properties depend on only two comparisons: a comparison of the electrical length of the line with its physical length, and a comparison of the terminating impedance with the line's own characteristic impedance. Both comparisons can be deduced from measurements of amplitude and phase shift, and it does not matter whether we express them in terms of field strengths or voltages and currents. We will take advantage of this generality in a moment.

9.2.2 TEM Lines and Waveguides

Two kinds of transmission line are commonly used for the evaluation of bulk electromagnetic properties—the TEM line and the rectangular waveguide—but the propagation characteristics of the two are different. The electric and magnetic fields inside the TEM line are both transverse to the length of the line, as suggested in Figures 9.2 through 9.4, with the result that energy propagates within the line just as it would in an unbounded medium made of the same material filling the

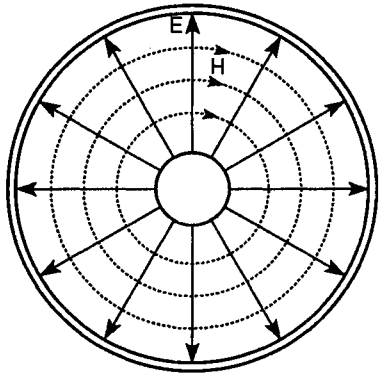

Figure 9.2. Electric field lines are radial and magnetic field lines are circumferential in the coaxial transmission line. Energy is constrained between the inner and outer conductors and does not escape the line.

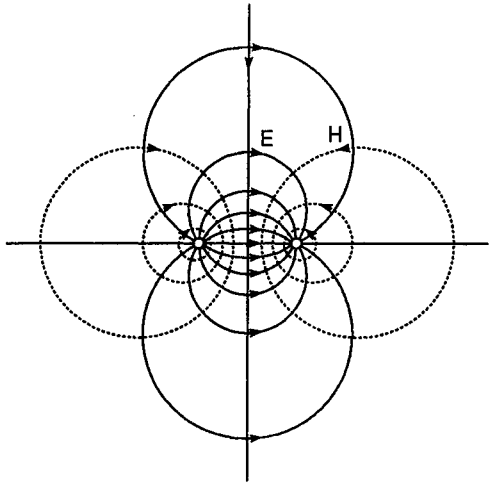

Figure 9.3. Electric and magnetic field lines lie on families of circles for the twin conductor line. Energy can be radiated from this line.

TEM line. The fields in waveguides (hollow conducting pipes), by contrast, must have components along the direction of propagation as well as transverse to it, a condition due to the lack of a second conductor within the pipe. The existence of these longitudinal field components is interpreted mathematically as a *pair* of waves that zigzag down the guide, one zigging while the other zags, as suggested in Figure 9.5.

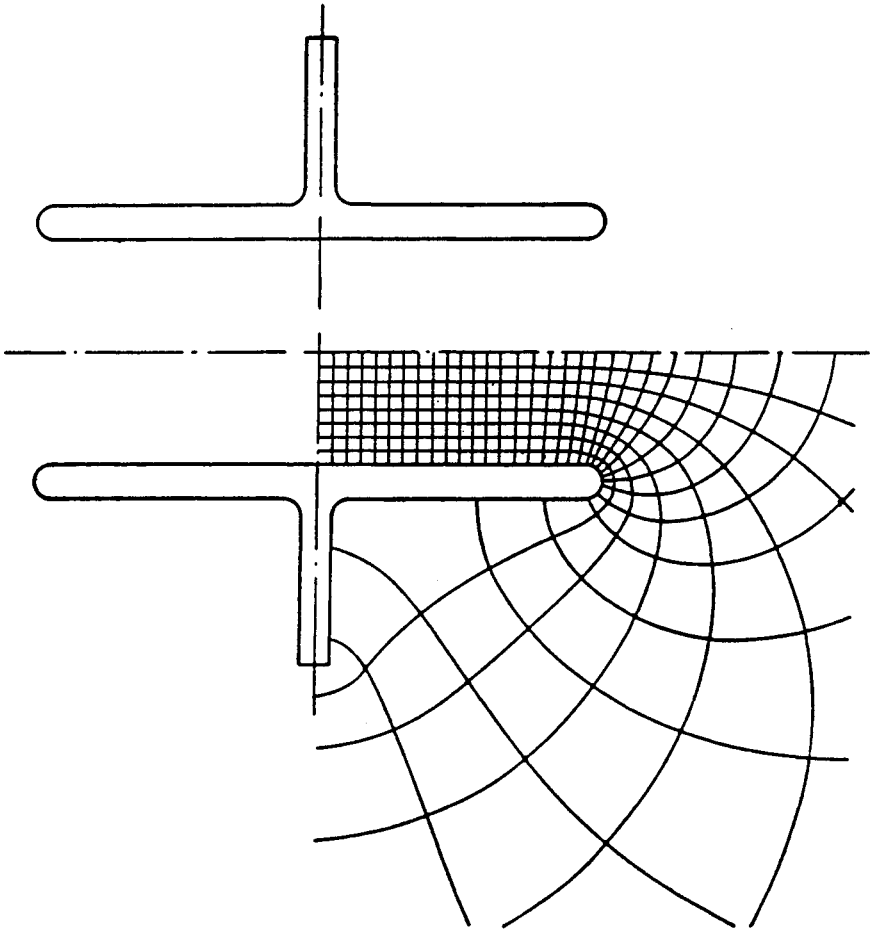

Figure 9.4. The field lines between the conductors of the parallel plate line are quite uniform, and the fields outside this region are relatively weak (from [1], Fig. 1.19d, p. 55. Copyright 1984, John Wiley & Sons; reprinted with permission).

This is due entirely to the fact that the waveguide has only one conducting boundary, with the result that no fewer than two waves must exist to enforce the boundary condition that the tangential electric field vanish at the conducting walls of the guide. A disconcerting consequence is that, when the frequency drops below well-defined *cutoff* values, the wave pair can no longer satisfy the electromagnetic boundary conditions and propagation virtually ceases. In essence, the waves rattle

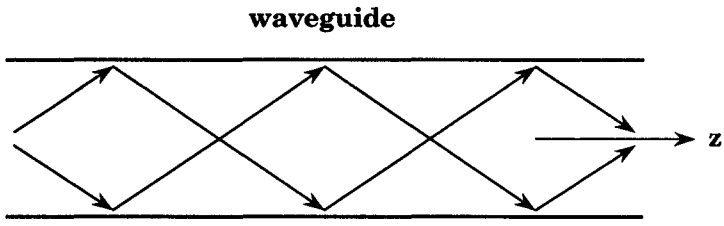

Figure 9.5. The increased wavelength of propagation down a waveguide is due to cross-guide propagation of a pair of zigzagging waves.

back and forth sideways between the walls of the guide instead of propagating along it, and no energy is conveyed from the input end to the output end. This restricts the bandwidth available for the measurement of the electromagnetic parameters of bulk materials in (hollow) waveguides.

A corollary of the cutoff phenomenon is that if the frequency is high enough, other zigzagging wave sets may also satisfy the boundary conditions, presenting the possibility that a waveguide may support more than one mode of propagation. Propagation modes that may exist are governed by the electrical height and width of rectangular waveguides and by the electrical circumference of circular waveguides, as measured in the material filling the guide. The method ordinarily used to prevent higher order mode propagation is to choose the transverse waveguide dimensions so that only the dominant (lowest order) mode can exist over the intended range of operating frequencies. For example, the frequency separation between the lowest and next-lowest mode of propagation in air-filled rectangular waveguides less than half a free-space wavelength in height is precisely an octave. This is why no single microwave band (i.e., L-band, S-band, C-band) covers more than an octave of bandwidth and why each band is instrumented with waveguides whose dimensions differ from one band to the next.

Waveguide propagation modes are grouped according to whether the electric or magnetic field is transverse to the direction of propagation, known as TE (transverse electric) and TM (transverse magnetic) modes, respectively. There is no component of electric field along the length of the waveguide in TE modes and no component of magnetic field along the length of the waveguide in TM modes. The two kinds of mode are further classed (by subscript) according to the number of half-cosine cycles that may exist along the width and height of the waveguide. Therefore, the electric field has no longitudinal component in the TE_{10} mode, no component along the wide dimension of the guide, and the intensity of the remaining field component (along the narrow dimension of the guide) varies cosinusoidally from zero at one side of the guide to a central maximum at the center to zero at the other side. This variation in field intensity is suggested in Figure 9.6.

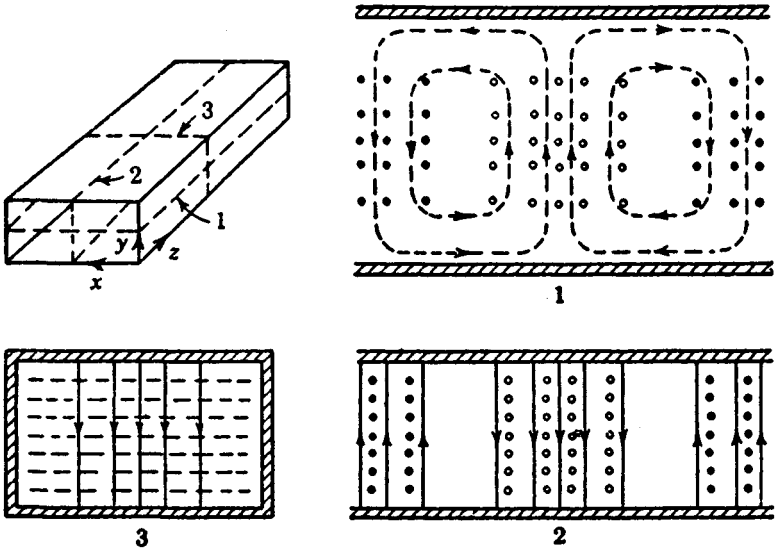

Figure 9.6. Field structure in rectangular waveguide for the TE_{10} mode of propagation (from [1], Table 8.7, p. 414. Copyright John Wiley & Sons, 1984; reprinted with permission).

The lateral components of the propagation directions of the zigzag waves in a waveguide results in a phase shift along the guide that is less than in free space. The wavelength, λ_g, used to reckon the propagation constant is therefore longer in the guide than in free space. The guide wavelength for an air-filled rectangular waveguide, for example, is

$$\lambda_g = \frac{\lambda_0}{\left[1 - \left(\frac{m\lambda_0}{2a}\right)^2 - \left(\frac{n\lambda_0}{2b}\right)^2\right]^{1/2}} \tag{9.6}$$

where m and n are the number of half-cosinusoidal field variations along the width a and height b of the guide, respectively, and λ_0 is the free-space wavelength of the signal. The normalized guide wavelength for the TE_{10} mode ($m = 1$, $n = 0$) is charted in Figure 9.7 by way of example for a standard X-band, air-filled rectangular waveguide (internal height and width of 0.4 × 0.9 in.). The guide wavelength rises to infinity at the cutoff frequency, which in this case is 6.56 GHz.

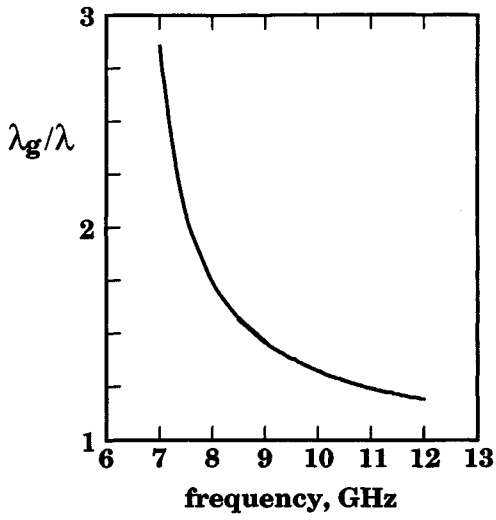

Figure 9.7. Normalized guide wavelength for a waveguide 0.9 in. wide and 0.4 in. high operated in the TE_{10} mode at X-band frequencies.

9.2.3 Sample Holders

The choice of whether to employ TEM or waveguide systems for the evaluation of material properties depends in no small measure on the equipment available, the frequencies for which such information is desired, and the physical size of any inhomogeneities that may be present in the test sample. The coaxial line (a TEM transmission line) is more convenient to use than the rectangular waveguide if the frequencies of interest cover more than an octave. This is because waves propagating in the coaxial line do not suffer the cutoff phenomenon; even direct current (zero frequency) can be transmitted down the line. A single, suitably designed coaxial sample holder, for example, can be used for material testing over the frequency decade between 1 and 10 GHz. It requires, by contrast, no fewer than four different waveguide sizes, and therefore four different sample holders and four different sets of tests, to service the same range of frequencies.

This is not to say that the TEM line cannot support higher order modes, however. When the mean circumference of the coaxial line exceeds a wavelength or so, for example, the line can support propagation modes having longitudinal field components. Because the mean circumference is governed by the size of the line, higher order modes in coaxial lines may be prevented by making the sample

holder small enough. This in turn demands smaller test samples, making the fabrication of the samples as well as the sample holder more costly. Smaller lines and samples also increase the possibility that small, undetected inhomogeneities in the sample can have a greater effect on the accuracy of the test data than they would in larger samples.

Just because the line is large enough to support higher order modes does not mean that such modes will, in fact, be present. Most of the time they may be prevented simply by minimizing discontinuities in the line that can excite them. In addition to careful design and fabrication of the sample holder, one of the simplest methods of accomplishing this is to avoid bends and turns in the lines connecting the sample holder to test signal generation and detection equipment. Because the insertion of the test sample in the sample holder increases the internal electrical dimensions of the line, these kinds of design considerations are as important for TE and TM waveguides as they are for TEM lines.

Because electromagnetic energy is confined between the conductors of the coaxial line of Figure 9.2, but can escape from the lines in Figure 9.3 and 9.4, the coaxial line is the most common TEM system used for measuring the properties of uniform test samples. The most common single-conductor line used for such tests is the rectangular waveguide. The coaxial line demands a washer-shaped test specimen whereas the test specimen needed for the rectangular waveguide is simply a slab, as illustrated in Figure 9.8. The samples may be as thick as can be conveniently handled and measured, but in many cases they are machined to a thickness of $\lambda/8$ or less, as measured in the material, to minimize the possibility of generating undesired (unaccountable) modes within the sample.

The samples should be fabricated to fit snugly within the sample holder, making good contact with all conducting surfaces, which sometimes complicates the design of the sample holder. Good contact is generally assured if the samples fit snugly in the holder without deformation, sometimes a difficult requirement to satisfy when the test material is soft or rubbery. Almost all sample holders are designed for easy removal from the test set-up so that the samples may be inserted

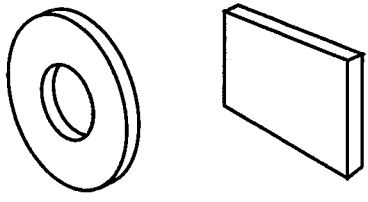

Figure 9.8. Test samples for coaxial lines and rectangular waveguides should be carefully machined to close tolerances.

into or tapped out of the holder with minimum disturbance to the rest of the system. Because the center conductor of the coaxial sample holder must be supported in place whether or not a sample is inside it (see Section 9.3), it is more complicated to design and handle than the rectangular waveguide sample holder. In either case it may be necessary to build a fixture for the sole purpose of inserting the sample and positioning it transverse to the guide dimensions.

9.3 TRANSMISSION LINE MEASUREMENTS

The measurement of test samples in transmission-line holders was once a laborious process because of the crudeness of the equipment available at the time. Although contemporary sample holders are no better than previous ones, we can now conduct tests at dozens of frequencies in the same time it used to take for a single frequency. Contemporary off-the-shelf instrumentation is designed for the rapid and convenient, if not accurate, measurement of the *scattering matrix* of any two-port device, whereas we were content then to measure only the reflections from the input end of the sample holder. To emphasize modern capabilities, we first consider how samples were typically measured before the eruption of push-button technology.

9.3.1 Open- and Short-Circuit Measurements

The elements of the typical, but archaic, test system are shown in Figure 9.9. Its five major elements were a signal source, a *slotted section* of waveguide or transmission line, the sample holder, a sliding short circuit, and a signal detector. Not shown in the diagram are other devices used to monitor the frequency and output power of the signal generator.

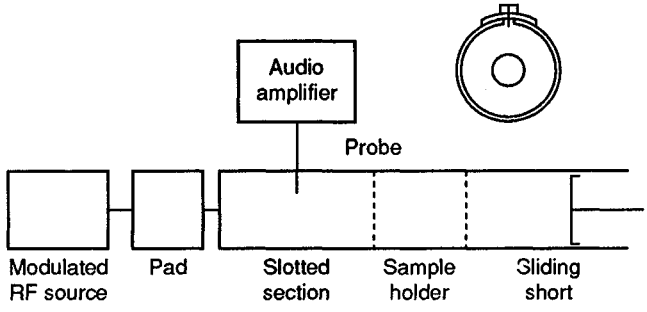

Figure 9.9. A simple bench setup uses a slotted section to sample the standing wave pattern inside the line due to reflections from the sample in the sample holder. The inset shows how a probe is inserted into the space between the conductors of the slotted section.

To protect the signal generator from the severe impedance mismatch presented by the sample and the short circuit behind it, the signal generator typically was separated from the rest of the system with a *pad*, a fixed attenuator. The signal itself was modulated at an audio rate so that a simple detector and audio amplifier could be used to measure the signal sensed by the probe of the slotted section. The amplifier output was simply an accurate panel meter calibrated in decibels. The sample was typically backed by a sliding short whose position relative to the rear face of the sample could be measured, either with a dial gauge or by counting screw turns.

The slotted section inserted between the sample holder and the signal generator allows us to sample a standing wave pattern inside the line. The slotted section is simply a short length of transmission line with a longitudinal slot machined in it. As shown in the inset, a small probe is inserted a short distance into the line through the slot to sample the electric field inside. This probe is mounted on a sliding carriage that may be moved along the line (toward or away from the generator), so that the standing wave pattern may be measured as a function of position from the front face of the test sample. The convenience and accuracy of the position measurement may be enhanced, particularly at higher frequencies, by a dial gauge mounted on or driven by the probe carriage. The slotted section shown in Figure 9.9 is a coaxial line, but waveguide slotted sections may also be used.

As we saw in Chapter 8, the reflection from a slab of material can be expressed in terms of the thickness and electromagnetic properties of the slab, the wavelength of the signal and the nature of the medium behind the slab. Because this is equally true of a material packed into transmission lines, we may deduce the properties of that material by measuring the reflection from it. The standing wave pattern in the slotted section was the yardstick by which the reflection from the sample was measured and interpreted.

The standing wave in the line is the sum of two waves traveling in opposite directions, as shown in Figure 9.10. A measurement of the *voltage standing wave ratio* (VSWR, pronounced *viswar*) is sufficient to determine the strength of the backward traveling wave compared to that of the incident wave:

$$\text{VSWR} = \frac{V_{\max}}{V_{\min}} = \frac{|V_i| + |V_r|}{|V_i| - |V_r|} \tag{9.7}$$

Under ideal conditions, this characterizes the amplitude of the reflection from the test sample, but for reasons that will become clear in a moment, the magnitude alone is not sufficient to completely characterize the sample material. We also need the phase of the reflection, which hinges on a knowledge of the relative location of peaks or nulls in the pattern as measured from the front face of the sample.

Although it might be thought that the pattern position could easily be established by the measurement of the physical dimensions of various parts of the system, it is easier and more accurate to measure the standing wave pattern in the absence of the sample. A precision short circuit (a carefully machined metal plug) is used

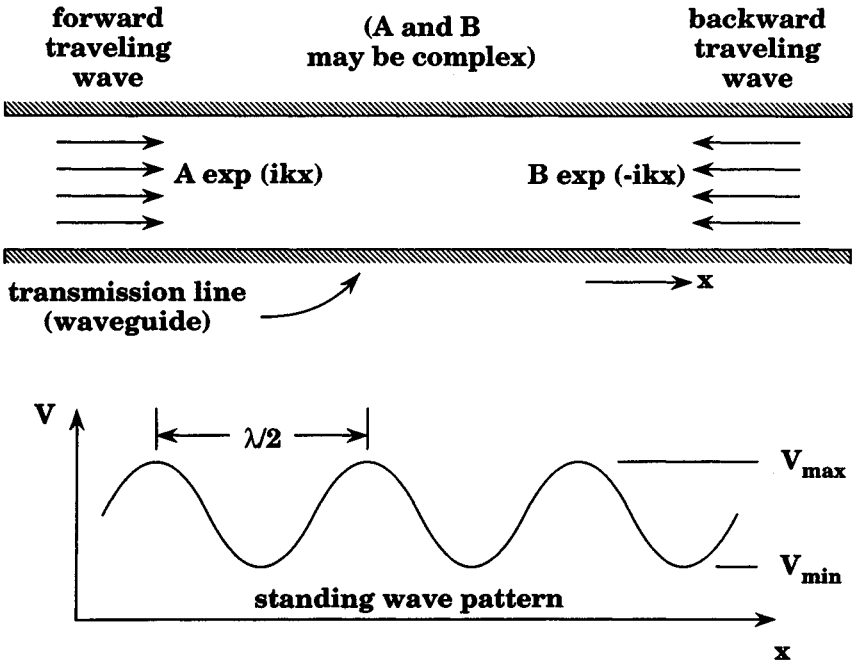

Figure 9.10. Two waves propagating in opposite directions create a standing wave with a period of precisely λ/2.

for this purpose. It is typically inserted in the sample holder so that the position of the front face of the plug matches that of the sample when the latter is installed. When displayed in the decibel format, the nulls are sharp and deep for this short-circuited condition, and their positions establish a *reference plane* (not at, but corresponding to, the location of the front face of the sample) for measurements of the test specimen. Residual losses in the system that might otherwise be assigned to losses in the sample may also be assessed in this calibration measurement and then accounted for when the complete set of test data is reduced and interpreted.

Therefore, it takes two sets of measurements to establish the phase and amplitude of the reflection from the test sample: one set with the sample installed and one set without it, the latter being essentially a calibration of the system. A comparison of the two VSWR readings gives us the amplitude, and the distance by which the nulls shift toward or away from the generator gives us the phase. In general, however, this is insufficient to uniquely determine the four intrinsic numbers—the real and imaginary parts of the relative permeability and permittivity—that characterize the material. The determination of four unknowns demands, in one way or another, the measurement of four quantities, and thus far we have measured only two.

We may wriggle out of the requirement to measure two additional quantities when there are no magnetic constituents in the sample, for then we can usually assume that the permeability of the sample is the same as that of free space. This being the case, the two quantities measured are sufficient to determine the permittivity. Even at that, however, we usually have to perform an additional system calibration, particularly if our sample is thin, has little loss, or both.

The reason for this is that the null shift for electrically thin samples is small, and an error in determining the shift in the nulls of the standing wave pattern becomes larger the thinner is the sample. Similarly, small sample losses become harder to separate from system losses the thinner is the sample. The accuracy of the measurement in these cases can be improved if we contrive to fabricate the test sample to be between $\lambda/8$ and $\lambda/4$ thick, as measured in the material. This seems to pose a dilemma: How do we estimate the optimum electrical thickness of a test sample whose electrical properties, by definition, are unknown? (If they were known, there would be no need to measure them in the first place.) Actually, we usually have some idea of what those properties are because we will have measured similar materials at comparable frequencies in the past.

If the sample is thin, we should probably back it with an open circuit to maximize the electric field at the sample. This has the effect of enhancing the apparent loss of the sample as it influences the VSWR to be measured, and this is one reason why we include the sliding short in the bench setup shown in Figure 9.9. We can create an open-circuit condition at the rear face of the sample by positioning the shorting plunger $\lambda_0/4$ behind the sample. We will have to establish that position, however, by other measurements with the empty sample holder in place, this time with no shorting plug in it, to determine the electrical position of the plunger to create that condition, as the physical position of the plunger is not necessarily an accurate indicator of the electrical position. In the few cases when we have precision open circuits on hand to install at the rear of the sample holder, the additional calibration is not needed, of course.

The sliding short is a useful device used to alternately install open or short circuits behind the test sample when we cannot assume that the permeability of the sample is the same as that of free space. In this event we have four quantities to measure instead of two (so that we have as many measured quantities on hand as we have unknowns to determine), and we must repeat our slotted-line standing-wave pattern measurements for two different conditions. Any two sets of measurements are theoretically useful, and one time-honored procedure was to measure the test sample when backed by a short circuit and again when backed by an open circuit. A more extensive set of data could be obtained and processed by measuring the standing wave pattern for several different short positions behind the sample, generating a locus of points on the complex plane whose analysis is likely to yield more accurate values of the four unknown quantities.

Although that may be the case, we will be content to illustrate the reduction of data collected with only short-circuit and open-circuit terminations backing the

rear face of the sample. For this purpose we assume the model shown in Figure 9.11, in which t is the physical sample thickness, Z_0 and k_0 are the characteristic impedance and propagation constants of the empty line, and Z_2 and k_2 are those of the sample-filled section of line. The latter depend on the relative permeability and relative permittivity of the material via

$$Z_2 = Z_0 \sqrt{\mu_r/\epsilon_r} \tag{9.8}$$

$$k_2 = k_0 \sqrt{\mu_r \epsilon_r} \tag{9.9}$$

If we contrive to measure the reflection coefficient at the front face of the sample for short- and open-circuit terminations at the rear of the sample, we may calculate the normalized impedances at the front face from (9.3). These will be found to be

$$z_{sc} = z_r \frac{(1 - w^2)}{(1 + w^2)} \tag{9.10}$$

$$z_{oc} = z_r \frac{(1 + w^2)}{(1 - w^2)} \tag{9.11}$$

where $w = \exp(ik_2 t)$ and $z_r = Z_2/Z_0$. The normalized impedances on the left sides of (9.10) and (9.11) are measured values, and z_r and w on the right sides are unknowns to be determined.

We now form the product and the ratio of (9.10) and (9.11), and inserting the values of (9.8) and (9.9), we have

$$\sqrt{\mu_r/\epsilon_r} = \sqrt{z_{sc}\, z_{oc}} \tag{9.12}$$

$$\sqrt{\mu_r \epsilon_r} = \frac{1}{i2k_0 t} \ln \frac{\sqrt{z_{oc}} - \sqrt{z_{sc}}}{\sqrt{z_{oc}} + \sqrt{z_{sc}}} \tag{9.13}$$

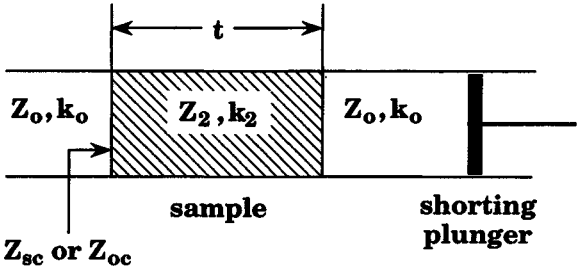

Figure 9.11. Electrical description of the measurement setup.

We then extract the desired values of μ_r and ϵ_r by forming the product and the ratio of (9.12) and (9.13):

$$\mu_r = \frac{\sqrt{z_{oc}z_{sc}}}{i2k_0t} \ln \frac{\sqrt{z_{oc}} - \sqrt{z_{sc}}}{\sqrt{z_{oc}} + \sqrt{z_{sc}}} \tag{9.14}$$

$$\epsilon_r = \frac{1}{i2k_0t\sqrt{z_{oc}z_{sc}}} \ln \frac{\sqrt{z_{oc}} - \sqrt{z_{sc}}}{\sqrt{z_{oc}} + \sqrt{z_{sc}}} \tag{9.15}$$

The solution represented by (9.14) and (9.15) is unique so long as the sample is less than $\lambda/2$ thick (as measured in the material), but is ambiguous otherwise. This is because the phase angle of w can be resolved no closer than an integral number of π rad and is the prime reason for fabricating thin test samples. Therefore we might deduce the wrong values for μ_r and ϵ_r if the sample happens to be too thick. However, there are two ways to resolve the ambiguity. One is to repeat the measurements with a different sample of the same batch of material cut to a slightly different thickness, and the other is to repeat the measurements at a slightly different frequency. The assumption in the latter case is that, even if the sample properties vary with frequency, the frequency difference is chosen small enough that that dependence does not materially influence the measured quantities. The disadvantage of the two methods of resolving the ambiguity is a doubling of the time and effort invested in testing.

If we can assume the material to be nonmagnetic (that its permeability is sensibly that of free space), the right sides of (9.10) and (9.11) contain only one complex unknown (the complex permittivity), and the left sides contain one complex measured value. In this event, only one complex measurement is required (either the short-circuit impedance or the open-circuit impedance at the front face of the sample). The resulting equation, either (9.10) or (9.11), then becomes a transcendental expression that may be solved graphically or by well-known mathematical techniques, such as the Newton-Raphson method. These methods of solution do not eliminate the ambiguity that results when the sample is more than $\lambda/2$ thick, however.

9.3.2 The Network Analyzer and the Scattering Matrix

The network analyzer has become a basic tool in the measurement of the properties of radar materials. It replaces the slotted section as a device for measuring the reflections from test samples, and it is capable of providing test data for literally dozens of frequencies at great convenience in relatively short time. Indeed, the Hewlett-Packard Company has even offered its Model 8510 series of network analyzers as basic instrumentation for RCS measurements as well as more mundane bench testing [2].

The network analyzer is a coherent instrument capable of a wide variety of measurements. The basic instrument compares an unknown signal with a reference signal of the same frequency, and its output is a signal or indication, either by panel meter deflections, real-time video displays, or streams of bits, of the amplitude and phase of the unknown signal. To preserve the coherence of this indication, the analyzer demands that the reference signal be derived from the same source used to excite the device under test, usually a two-port network. The purchaser of the instrument usually has the option of ordering a package complete with a self-contained, phase-locked, voltage-controlled signal source, a small but powerful internal microprocessor, a communication bus addressable by an external computer, and any of a variety of special-purpose interfaces (sometimes called *test sets*) designed for specific test requirements.

Because we are seldom interested in measurements made only at a single frequency, all contemporary network analyzers are designed to interface with controllable stepped-frequency signal sources, either internal or external. And because the general user is as interested in time-domain circuit properties as in the frequency response of a device, most display network analyzers are equipped with firmware that can transform test data back and forth between the two domains in real time (within one to six blinks of the eye). Any of several plug-in test sets are offered that expedite specific kinds of measurement, such as the reflection and transmission characteristics of two-port devices or their scattering matrices (S-parameters). Display options include Smith-chart representations and circuit gain or loss (amplitude) and phase, the latter in either rectangular or polar coordinates. Sets of precision devices (short circuits, open circuits, matched loads) are available in kits for calibration purposes.

The basic two-port representation now favored for materials testing is the S-parameter configuration shown in Figure 9.12. We encountered this configuration

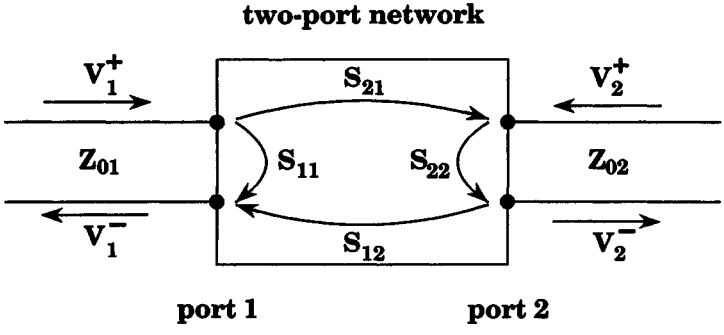

Figure 9.12. Four complex numbers characterize the scattering-matrix representation of two-port networks. It is not necessary to measure all four to determine the electromagnetic properties of passive absorbing materials.

in (8.24) and in Figure 8.4, in which the impedances of the input and output lines are both assumed matched. By "matched" we mean that the impedance Z_{01} of the input line has been carefully designed to "match" the impedance of the source, and that the impedance Z_{02} of the output line is similarly "matched" to the impedance of the load or detector terminating the output of the device. If these conditions can be maintained for all our test frequencies when the device (our test sample in its sample holder) is being measured, we may extract the desired electromagnetic parameters of our test material.

The complete characterization of the scattering matrix of an unknown device demands the measurement of no fewer than eight quantities: the amplitude and phase (or the real and imaginary parts) of the four scattering-matrix parameters. If the device is passive and reciprocal, however, as is the case for the materials we seek to measure, it can be shown that $S_{12} = S_{21}$ and $S_{11} = S_{22}$. Therefore, we need measure only two complex parameters (S_{11} and S_{21}) to characterize the material.

The basic measurement system is diagrammed in Figure 9.13. The slotted section described earlier is replaced in this system by a pair of directional couplers, one to sample the incident wave and one to sample the reflected wave, both of which may be routed to a detector and amplifiers (not shown) for measurement, amplification, and display. Although we may assemble these components on the test bench and perform the measurements manually, the manufacturers of some contemporary test equipment have developed systems in which most of the components are conveniently packaged into one or two units, as suggested in Figure 9.14.

In the more sophisticated designs, an internal signal source is controlled by a computer or microprocessor in the network analyzer itself, and a front-panel screen can display the measured data in any of several formats. The S-parameter test set contains the couplers and other devices needed to automate the process.

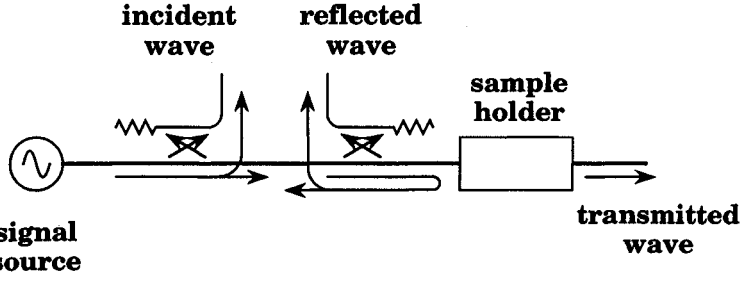

Figure 9.13. The three basic quantities measured in this generic test system are the incident, reflected, and transmitted waves.

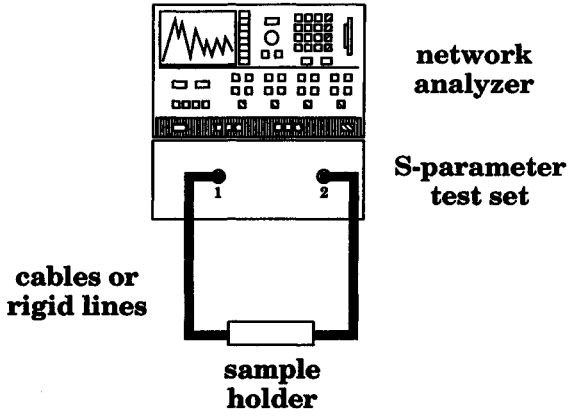

Figure 9.14. The S-parameter test set contains directional couplers and switching networks that simplify the operations required in the measurement of the scattering.

The test set has a pair of ports to which the test device is connected by means of cables or rigid coaxial lines, and some manufacturers even offer sets of "flexible arms" fitted with rotary joints to simplify making the connections. Precision calibration kits are also available to improve the accuracy of the measurements.

Indeed, calibration is essential in the measurement of the scattering matrix because of undesired, but unavoidable, contamination of the desired quantities by others. A complete calibration sequence demands a characterization of the characteristics of ports 1 and 2 of the test device by separately terminating the input and output lines to the two ports, respectively, with a short circuit, an open circuit and a matched load. This results in no fewer than six numbers (three per port) that are stored in internal memory for each frequency used in the measurements. A pair of "through" calibrations are also performed, the first with the ends of the two lines from the test set connected together (bypassing the sample holder), and the second with them connected to the input and output ports of the empty sample holder. The sample is then inserted in the sample holder for the final set of measurements.

The purpose of the calibration is to determine several undesired parameters that may be removed or suppressed from the test sample data by subsequent mathematical operations. When properly calibrated (measured) for each frequency in the data set, they include the effects of the directivity of and reflection from the couplers, reflections due to mismatches in the input and output test lines, and direct coupling of signals between the input and output ports of the device along external bypass routes. Although the microprocessor in the commercial network

analyzer is designed to account for these sources of error, it is seldom aware of what we actually need: a comparison of scattering matrices measured with and without a test sample inserted in the sample holder. Nevertheless, it can store the calibrated measurements for the two cases and fetch them from memory when instructed to do so by software we ourselves design to make that comparison.

To extract the relative permittivity and permeability of our sample from these two sets of measurements, we use the concept illustrated in Figure 9.15 and the coefficient-stepping procedure detailed in Chapter 8. We represent our sample holder as the central section of transmission line defined by the planes $z = 0$ and $z = t$ sandwiched between the input and output lines, whose characteristic impedance Z_0 and propagation constant k_0 also characterize the empty sample holder. We represent waves propagating in the forward direction (toward the sample) by A_1, A_2, and A_3, and those traveling back to the source by B_1, B_2, and B_3, all of which may be complex.

Invoking the definition of the scattering matrix in Chapter 8, we form the ratios B_3/A_3 and A_1/A_3 for the condition $B_1 = 0$ for the two cases (with and without the test sample in the sample holder). A comparison of the measured data for the two cases allows us to express the two scattering matrix elements as

$$S_{11} = \frac{u\,(1 - w^2)}{u^2 - w^2} \tag{9.16}$$

$$S_{21} = \frac{w\,(u^2 - 1)}{u^2 - w^2} \tag{9.17}$$

where

$$u = \frac{1 + y_r}{1 - y_r} \tag{9.18}$$

$$y_r = 1/z_r = \sqrt{\epsilon_r/\mu_r} \tag{9.19}$$

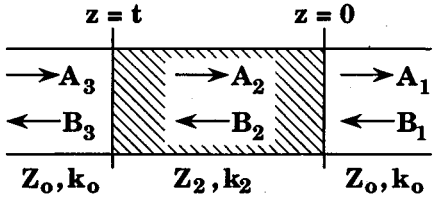

Figure 9.15. The sample holder is represented as a section of TEM transmission line of length t, characteristic impedance Z_2, and propagation constant k_2 sandwiched between a pair of lines whose characteristic impedances and propagation constants are Z_0 and k_0. Forward- and backward-traveling waves are characterized by coefficients A and B.

and where $w = \exp(ik_2t)$, as before. The unknowns to be determined in (9.16) and (9.17) are u and w, with S_{11} and S_{21} being the known (measured) quantities.

One solution is to solve (9.16) for w^2 and insert that value into (9.17), generating a quadratic equation for u in terms of known (measured) quantities. We therefore obtain the two equations

$$w^2 = \frac{u(1 - uS_{11})}{u - S_{11}} \tag{9.20}$$

$$u^2 + 2uQ + 1 = 0 \tag{9.21}$$

where

$$Q = [(S_{21})^2 - (S_{11})^2 - 1]/2S_{11} \tag{9.22}$$

Equation (9.20) admits to two principal solutions for u:

$$u = -Q \pm (Q^2 - 1)^{1/2} \tag{9.23}$$

which we must compute using complex arithmetic, as Q is complex. The negative option in (9.21) happens to be the one we need, from which we may calculate a number U:

$$U = \frac{u - 1}{u + 1} \tag{9.24}$$

Note that, by virtue of (9.18), U is none other than y_r expressed in terms of measured quantities:

$$\sqrt{\epsilon_r/\mu_r} = U \tag{9.25}$$

When we insert the now-known value of u into (9.20), and we generate another known number, call it W, also expressed in terms of measured quantities:

$$W = \frac{u(1 - uS_{11})}{u - S_{11}} \tag{9.26}$$

Therefore,

$$\sqrt{\mu_r\epsilon_r} = \frac{\ln W}{i2k_0t} \tag{9.27}$$

As in the short-circuit and open-circuit measurements discussed previously, we form the product and the ratio of (9.25) and (9.27) to extract the material properties:

$$\epsilon_r = \frac{U \ln W}{i2k_0 t} \tag{9.28}$$

$$\mu_r = \frac{\ln W}{i2k_0 tU} \tag{9.29}$$

This solution suffers the same ambiguity noted earlier, and if the sample is electrically thicker than $\lambda/2$, it may require additional measurements to resolve it.

It is not necessary to measure both S_{11} and S_{21} if the sample material is nonmagnetic, in which case only the unknown complex permittivity appears in the right sides of (9.16) and (9.17), and the left side of either contains a single, measured complex quantity. As in the open- and short-circuit measurements discussed earlier, this results in a transcendental equation that may be solved with easily applied mathematical procedures. If the attenuation through the material is not great, we usually rely on measurements of S_{21} to effect the solution because of the greater accuracy with which it can be measured in comparison to S_{11}.

9.3.3 Time-Domain Reflectometry

Although we may transform back and forth between the time and frequency domains when we use the ubiquitous network analyzer to collect our test data, the basic test signals are generated and detected in the frequency domain. We rely on the instrument's firmware to perform these forward and backward transformations digitally. It is also possible to make the basic measurements in the time domain, in which case the test instrument is called a *time-domain reflectometer*. Although time-domain reflectometry has fallen out of favor for materials testing, the instrument is of interest in its own right. One example is the test system described by Nicolson and Ross [3].

A diagram of the basic instrument is shown in Figure 9.16. It relies on a pulse generator for the signal source, whose ideal output is a unit step function,

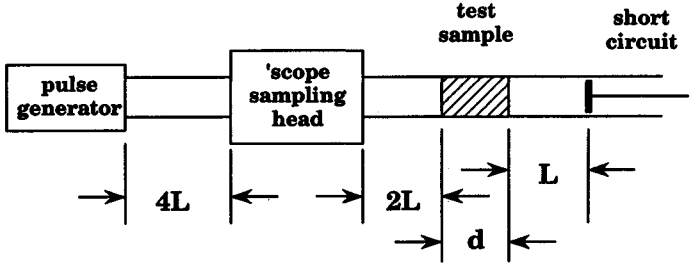

Figure 9.16. Basic elements of a time-domain reflectometer. The pulse generator emits pulses with fast rise times, and a sampling oscilloscope is used to collect and record the data. The specified separations between its components (not to scale in the diagram) help suppress the effects of undesired system reflections.

and on a sampling oscilloscope to detect and record the test data. To minimize the effects of undesired system reflections, the separations between the source and the oscilloscope, the oscilloscope and the sample, and the sample and the short circuit should be selected as shown in the figure. The ideal step function was approximated in this system by a relatively long, rectangular pulse that attained a steady voltage of 0.12 V in a rise time of 30 ps.

The measurement method hinges on the sampling of three different signals at three different times. The pulse emitted by the generator travels through the oscilloscope sampling head, constituting a sample of the incident waveform against which the remaining two signal samples must be compared. The second signal is a combination of reflections from the front and rear faces of the test sample, which is assumed electrically thin enough that the two reflected pulses cannot be distinguished from one another when sampled. Although they travel back toward the pulse generator in the opposite direction taken by the incident pulse, the oscilloscope sampling head neither knows nor cares which way they travel. The third signal sampled by the oscilloscope is the reflection of the pulse from the short circuit behind the test sample, which therefore passes through the sample twice, once each in opposite directions.

The second signal constitutes the sum of the front and rear face reflections, which is a signal proportional to S_{11}. Because the third signal traverses the sample twice, and because $S_{12} = S_{21}$ by reciprocity, it is proportional to S_{21}^2. The constant of proportionality in both cases is a system constant depending on many parameters, all of which can be accounted for when we normalize the second two signals with respect to the first (incident) signal in our processing. This processing is performed digitally after the waveforms are digitized and recorded by a computer not shown in Figure 9.16.

In principal, two sets of waveforms should be digitized and recorded. The first set should be a pair of calibration waveforms collected first with a short circuit installed at the position normally occupied by the front face of the sample, and then with the short circuit installed a distance behind the rear face of the sample. Because of the separation in the time of arrival of these two calibration waveforms at the sampling head, the second must be measured at a time delayed from the first. Except for this time delay, the two waveforms are sensibly identical, of course, and only the first need be measured in practice, because the time delay can be calculated from the known or measurable locations of the short circuit in the system. The sample may then be installed in the sample holder and the second set of waveforms collected.

These digitized, calibrated data may then be transformed from the time domain to the frequency domain, just as in the case of more familiar measurements made with the network analyzer. The first set of normalized data is the frequency-dependent scattering matrix element $S_{11}(\omega)$. The phase of each datum in the second normalized set must be shifted by $2k_0d$ (twice the electrical thickness of the sample in free-space wavelengths), thereby yielding the square of $S_{21}^2(\omega)$, from which $S_{21}(\omega)$ may be extracted by means of complex arithmetic. The measurements therefore

provide the left sides of (9.16) and (9.17), which may be solved for the complex relative permeability and permittivity for each of the discrete frequencies generated by the FFT in the transformation of the data to the frequency domain.

Figures 9.17 and 9.18 illustrate the results of measurements of a commercial magnetic absorbing material as obtained with a time-domain reflectometer. It is

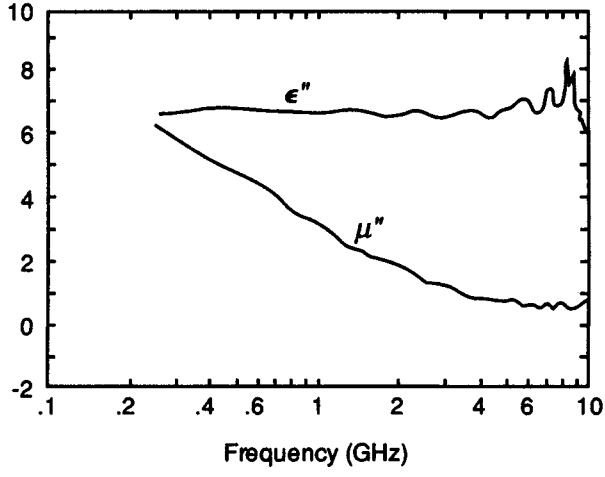

Figure 9.17. Real parts of the relative permeability and permittivity of a commercial absorbing material as obtained with a time-domain reflectometer.

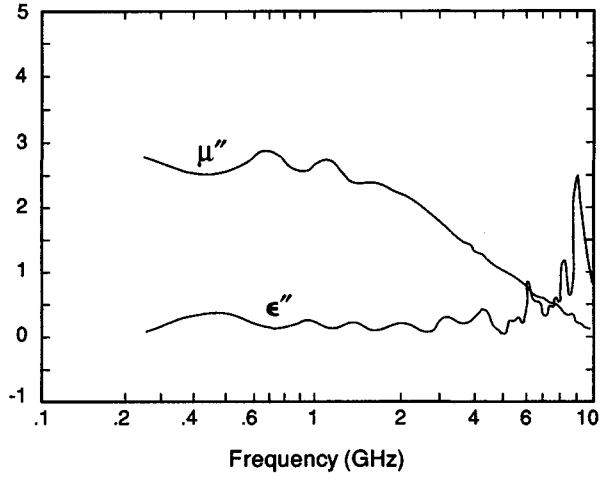

Figure 9.18. Imaginary parts of the relative permeability and permittivity of a commercial absorbing material as obtained with a time-domain reflectometer.

doubtful that the true characteristics of the material actually behave as measured, particularly for the upper range of the frequency plots. As suggested below, the small cyclic variations are probably due to the narrowness of the time window over which the signal pulses were sampled. In theory, the scattering matrix element $S_{11}(\omega)$ includes an infinity of multiple reflections between the front and rear faces of the test sample, and the sampling window should be wide enough to include the earliest (most significant) of them. If the sample losses are low and the sample is electrically long enough, we eliminate some of the reflections that are intrinsically part of the quantity defined as $S_{11}(\omega)$. The result of this exclusion is an interference "beat" between the reflections from the front and rear sample faces, producing the cyclic variations.

The period of the variation is about 425 MHz near a test frequency of 1 MHz, suggesting that the electrical thickness of the sample was about 13.9 in. This is the product of the physical sample thickness and the real part of the index of refraction, the latter of which may be estimated from the measured characteristics near 1 GHz. When we divide the deduced electrical thickness by the real part of the index of refraction, we obtain a physical thickness of 3.0 in., which we suspect is very close to the length of the sample actually used for these particular tests.

If we assume that we must include at least the first reflection from the rear face of the sample in our time window, the window width should be no less than twice the electrical sample thickness divided by the speed of light, which amounts to 2.4 ns. Because the test window was about 2.5 ns wide for these tests, all higher order reflections were excluded from the measurement or at least greatly attenuated, and the first reflection itself was probably not adequately represented in the sampled time-domain pulse. The result is a contamination of the true material properties, as derived from the measured pulses, by the slight modulation seen in Figures 9.17 and 9.18 in the region up to about 5 GHz.

The period of these cyclic variations gradually increases with increasing frequency, implying a reduction in the electrical thickness of the sample. As evidenced by the gradual decline of both the real and imaginary parts of the relative permeability with increasing frequency, this is indeed the case. Note that the amplitude of the modulation in the relative permittivity increases, particularly the imaginary part. Therefore, the accuracy of the test data above 5 GHz is suspect. It could probably be improved by expanding the width of the sampling window or reducing the thickness of the test sample or both.

9.4 FREE-SPACE METHODS

In contrast to the measurement of intrinsic material properties, the evaluation of absorbers for quality control or product development demands fewer measurements and less manipulation of test data and can often be accomplished with less sophisticated equipment. In the interest of economy, moreover, we would like the evaluation to be nondestructive so that we may retain the test panel in inventory for subsequent sale. And even if absorber samples can be sacrificed for the fab-

Chapter 10
Antenna RCS and RCSR

M. T. Tuley

10.1 INTRODUCTION

Designing a pilotless and sensorless vehicle with a low RCS might not be too difficult a task. However, useful platforms must always have sensors (and we could well include pilots in the category of sensors). Although the rules for shaping can often be applied to sensors, and RAM may sometimes be used to further reduce scattering into a threat region, designing low-RCS sensors is not an easy task. In this chapter we specifically focus on the scattering characteristics of antennas and on techniques for control of that scatter. More specifically, we concentrate on antennas that must operate in one or more of the threat radar bands, where simply covering the antenna with a RAM designed to provide attenuation out of the operating band is not an acceptable option.

For targets that have not been designed for low RCS and are dominated by specular scatter from large surfaces, the scattering from antennas is generally not felt to be of concern. Although that may often be true, antennas can also be the dominant scatterers for large RCS platforms. We show later that the RCS of an antenna due to its reradiation of an incident wave can be as large as that of a flat plate with an area equal to the antenna capture area. With that in mind, consider the fire control radar antennas aboard a platform such as a ship. Assuming a 2 m dish diameter, such antennas could have an RCS in K_u band (a likely operating frequency for antiship missiles) as large as 55 dBsm. To make matters worse, fire control radar systems are designed to accurately track a target, so the antenna in the tracking mode would present a very stable, nonfluctuating RCS on which an incoming missile could home. Although this example is the worst case (it assumes

no absorption of incident power in the antenna load), it does indicate the potential magnitude of the problem presented to the RCSR designer by antenna scatter.

This chapter covers three basic topics. Section 10.2 presents the fundamentals of antenna scattering theory. In this section the antenna gain and RCS are quantitatively related, antenna mode scatter and structural scatter are defined and explained, and the results are related to total antenna RCS. In Section 10.3 the scattering characteristics of a number of widely used antenna types are discussed. Among the types considered are reflector antennas, horn antennas, spiral antennas, microstrip patch antennas, and array antennas. Finally, in Section 10.4, techniques for RCSR are briefly discussed.

10.2 SCATTERING FUNDAMENTALS

Chapter 3 pointed out that objects scatter electromagnetic energy as a result of currents induced on them by an incident field. Therefore, any structure can be considered an antenna whose scattering pattern is controlled by the amplitude and phase of the currents induced. However, objects designed as antennas have two possible modes of scatter, rather than just the one described. The first is the scattering that occurs because the antenna is of a given shape, size, and material and is independent of the fact that the antenna was specifically designed to transmit or receive RF energy. The second scattering mode has to do directly with the fact that the antenna is designed to radiate or receive with a specific pattern. Those two components of antenna scatter have historically been called *structural mode* and *antenna mode* scattering. Although the concept of dividing antenna RCS into the two components is simple and easily grasped, there is no single definition of what constitutes each of the scattering modes. The remainder of Section 10.2 explores the connection between the radiation pattern of an antenna and the antenna RCS. After a relationship between gain and RCS has been established for a hypothetical antenna with no structure, the fundamental equation of antenna scattering, which includes the effect of the structure on antenna RCS, is developed. Finally, several of the common methods of defining structural mode versus antenna mode scattering are presented and discussed.

10.2.1 A Relationship Between Antenna Gain and Antenna RCS

It has long been recognized that there is a quantitative relationship between the gain of an antenna and the RCS of the antenna due solely to its reradiation properties [1,2]. Appel-Hansen [3] provides a derivation of that relationship for a simplified (but unrealizable) antenna for which all of the scattering arises from

energy collected by the aperture, travels through a lossless feed system, and is reradiated due to mismatch at the terminating load of the antenna.

Assume an antenna with an effective area A_e is illuminated by an incident plane wave with power density S_i. The power received by the antenna is simply given as

$$P_r = S_i A_e \tag{10.1}$$

If the antenna is terminated in a short circuit, there is perfect reflection of the received power and the total reradiated (scattered) power is equal to the received power. For an isotropic radiator the radiated power density at a range R would be the radiated power divided by the area of the sphere over which the power is distributed. However, antennas are not generally isotropic, and the definition of antenna gain is the factor by which the power density in a given direction exceeds the isotropic value. Therefore, the actual power density of the reradiated energy at a range R is

$$S_r = P_r G/(4\pi R^2) = S_i A_e G/(4\pi R^2) \tag{10.2}$$

The definition of RCS, when couched in terms of power densities rather than fields is

$$\sigma = \lim_{R\to\infty} (4\pi R^2)(|E_s|^2/|E_i|^2) = \lim_{R\to\infty} (4\pi R^2)(S_r/S_i) \tag{10.3}$$

Substituting (10.2) into (10.3) gives

$$\sigma = A_e G \tag{10.4}$$

but gain and effective area are related by

$$G = 4\pi A_e/\lambda^2 \tag{10.5}$$

so

$$\sigma = 4\pi A_e^2/\lambda^2 \tag{10.6}$$

which is the formula for flat plate normal incidence RCS. If only a portion of the collected energy is reflected from the termination (i.e., if some of the energy is

absorbed), the RCS will be multiplied by a factor equal to the squared magnitude of the reflection coefficient, Γ, giving

$$\sigma = 4\pi|\Gamma|^2 A_e^2/\lambda^2 \tag{10.7}$$

It must be reemphasized that this development represents only a portion of the scatter expected from real antennas. The preceding derivation considers only the scattered field due to the fact that the illuminated structure is an antenna; that is, that energy has been collected from free space, traveled down a transmission line to some termination, and been reradiated (the component often called the *antenna mode* scatter). It has ignored the *structural mode* scatter, which is the scatter that would have occurred from any body that is the same shape and made of the same material as the antenna. Section 10.2.2 provides more quantitative definitions of antenna mode and structural mode scatter.

It is easy to jump to the incorrect conclusion from (10.6) that an antenna will have an RCS equal to the flat plate formula applied to its physical aperture. This is rarely true for three reasons. First, the preceding derivation assumes that the antenna is terminated in a short circuit and all incident power is reradiated. In practice, an antenna will be terminated with a load that absorbs energy, and so only a portion of the captured energy will be reradiated, as indicated in (10.7). Second, note from (10.5) that the effective capture area is related to gain. The gain specified is that at the frequency of the incident radiation. If the incident frequency is far out of the normal operating band of the antenna, then the gain, and hence the effective capture area, may be much different than that which we might normally attribute to the antenna (e.g., the antenna's physical aperture). Finally, the correct treatment of the RCS must consider both antenna mode and structural mode scatter, as already noted and will be expanded on in Section 10.2.2.

10.2.2 Fundamental Antenna Scattering Equations

Although (10.7) establishes a connection between the antenna effective aperture and the antenna RCS, it was noted in the derivation that such an equation tells only part of the story. In this section the fundamental equations of scattering are developed for the case of an antenna fed from a single transmission line that supports only one propagating mode. The solution to this problem, as presented by Collin [4] and illustrated in Figure 10.1, is based on a scattering matrix representation of an antenna. The antenna scattering matrix **S** (in the following equations, matrices are indicated by bold symbols) relates incoming and outgoing spherical waves (b_i^+ and b_i^-) to each other and to the signals on the antenna transmission line (a^+ and a^-). The matrix relating these components is

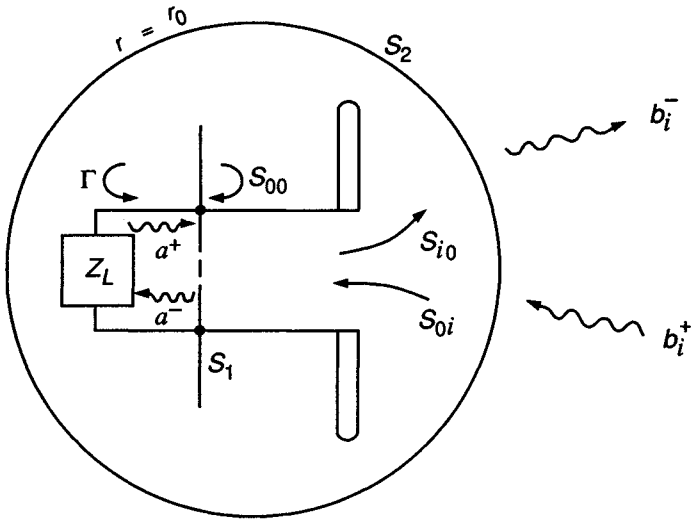

Figure 10.1. Scattering matrix representation of an antenna (from [4]).

$$\begin{bmatrix} a^- \\ b_1^- \\ b_2^- \\ \cdot \\ \cdot \\ \cdot \\ \cdot \\ \cdot \\ b_i^- \\ \cdot \\ \cdot \\ \cdot \end{bmatrix} = \begin{bmatrix} S_{00} & S_{01} & S_{02} \ldots \\ S_{10} & S_{11} & S_{12} \ldots \\ S_{20} & \cdot & \cdot \\ \cdot & \cdot & \cdot \\ \cdot & \cdot & \cdot \\ \cdot & & \\ \cdot & & \\ \cdot & & \\ S_{i0} & & \\ \cdot & & \\ \cdot & & \\ \cdot & & \end{bmatrix} \begin{bmatrix} a^+ \\ b_1^+ \\ b_2^+ \\ \cdot \\ \cdot \\ \cdot \\ \cdot \\ \cdot \\ b_i^+ \\ \cdot \\ \cdot \\ \cdot \end{bmatrix} \tag{10.8}$$

For the pure radiation case, all the $b_i^+ = 0$, so $a^- = S_{00}\, a^+$. Therefore, S_{00} is the reflection coefficient at the transmission line-antenna interface looking from the termination toward the antenna. Similarly, Γ is the reflection coefficient at the transmission line-load interface, looking from the antenna toward the load. The ith radiated mode amplitude is given by $b_i^- = S_{i0}\, a^+$, so the $\mathbf{S}_{i0}$ matrix (**S**, with all elements zero except the S_{i0} elements, where $i = 1, 2, 3, \ldots$) determines the

form of the radiation pattern of the antenna. Note also that the $\mathbf{S}_{ij}$ matrix (the $\mathbf{S}$ matrix with the first row and column replaced by all zeros) relates incoming and outgoing mode amplitudes without involving the transmission line or termination, so that submatrix is related to the structural scatter component.

If the antenna were not present, conservation of energy would require that the incoming and outgoing modes equal each other. The antenna absent case is indicated by the $\mathbf{S}$ matrix having a zero S_{00} element, all other diagonal elements equal 1, and zeros in all other positions, which is denoted $\mathbf{S}_0$. The scattered field is defined as the difference between the outgoing waves when the antenna is present and absent (a restatement of our earlier definition of the scattered field as the total field minus the incident field). Denoting the scattered field components by the vector $\mathbf{b}_s$,

$$\mathbf{b}_s = [\mathbf{S}_{i0}\mathbf{a}^+ + \mathbf{S}_{ij}\mathbf{b}_i{}^+] - \mathbf{S}_0\mathbf{b}_i{}^+ \tag{10.9}$$

where the $\mathbf{S}_{i0}$ matrix provides the relationship between signal reflected at the load and the outgoing spherical modes, and the terms have been grouped to show the total fields in the brackets and the incident field subtracted from it. With $a^+ = \Gamma a^-$, and using (10.8), (10.9) can be expanded as

$$\mathbf{b}_s = \left(\sum_{i=1}^{\infty} \frac{S_{0i}\Gamma}{1 - S_{00}\Gamma} b_i^+\right)\mathbf{S}_{i0} + (\mathbf{S}_{ij} - \mathbf{S}_0) \cdot \mathbf{b}^+ \tag{10.10}$$

For the special case of $Z_L = 0$, $\Gamma = -1$, and the scattered waves for a short-circuit termination, $\mathbf{b}_s{}^0$, are given by

$$\mathbf{b}_s{}^0 = -\left(\sum_{i=1}^{\infty} \frac{S_{0i}}{1 + S_{00}} b_i^+\right)\mathbf{S}_{i0} + (\mathbf{S}_{ij} - \mathbf{S}_0) \cdot \mathbf{b}^+ \tag{10.11}$$

Recognizing that for a unit current excitation $a^+ = Z_A/(1 + S_{00})$, the radiated field, $\mathbf{b}_r$, is given by

$$\mathbf{b}_r = \mathbf{S}_{i0} \cdot \mathbf{a}^+ = \left(\frac{Z_A}{1 + S_{00}}\right)\mathbf{S}_{i0} \tag{10.12}$$

Substituting from (10.11) and (10.12) into (10.10) gives

$$\mathbf{b}_s = \mathbf{b}_s{}^0 + \left[\sum_{i=1}^{\infty} \frac{S_{0i}}{Z_A}\left(1 + \Gamma\frac{1 + S_{00}}{1 - S_{00}\Gamma}\right) b_i^+\right]\mathbf{b}_r \tag{10.13}$$

The dependence on the scattering matrix parameters can be eliminated by recognizing that the short-circuit antenna current, $I(Z_L = 0) = I(0)$, is $a^+ - a^- = -2a^-$, and with $a^- = S_{00}a^+ + \Sigma S_{0i}b_i^+$, the factor multiplying $\mathbf{b}_r$ in (10.13) can be simplified to

$$-\frac{I(0)(1 + S_{00})}{2Z_A}\frac{1 + \Gamma}{1 - \Gamma S_{00}} = \frac{-Z_L I(0)}{Z_A + Z_L} \tag{10.14}$$

Finally, substituting (10.14) into (10.13), we obtain

$$\mathbf{b}_s = \mathbf{b}_s^0 - \left[\frac{I(0)Z_L}{Z_A + Z_L}\right]\mathbf{b}_r \tag{10.15}$$

which expresses the scattered field in terms of the modal components. The scattering matrix representation can be converted directly to field components, where $E_s(Z_L)$ is the scattered field for a given value of antenna load impedance and E_r is the radiated field for a unit current excitation, so that the scattered field is given by

$$E_s(Z_L) = E_s(Z_L = 0) - \left[\frac{I(0)Z_L}{Z_A + Z_L}\right]E_r \tag{10.16}$$

Thus, (10.16) has separated the scattered field from the antenna into two components. The first is the field scattered with the load replaced by a short circuit. From that term is subtracted a component proportional to the normalized radiated field (identical to the field the antenna would radiate if driven by a unit source current) and whose amplitude depends on the antenna and load impedances.

Note again that this derivation has assumed a monochromatic incident field, and so the radiated pattern (E_r) in the second term of (10.16) is the radiated pattern for a unit current excitation at the frequency of the incident field. That radiation pattern may or may not resemble the pattern in the operating band of the antenna. For example, if the transmission line from the termination to the antenna is a waveguide, and the frequency of interest is below waveguide cutoff, then the radiated pattern will be 0, and only the first term of (10.16) will contribute to the scattering.

The derivation just provided considers the incident and radiated fields as a collection of spherical wave modes, so any monochromatic far-field wave can be accurately modeled using that approach. However, the antenna feed structure is modeled as a single port having a single propagating mode. Obviously, such a model is limiting if multiple feed ports are present (e.g., phased arrays) or if more

than one mode can exist on the transmission line from the feed port to the antenna. The preceding equations have been generalized to account for multiple ports and multiple transmission line modes [5], although the results, as might be expected, are more complicated than for the simple case.

10.2.3 Structural Mode and Antenna Mode Scattering

Hansen [6] provides a development of the fundamental equation of scattering which parallels that of Collin, but he extends the form of (10.16) to consider reference conditions other than the short-circuit scattered field. If the antenna reflection coefficient Γ_A is defined as

$$\Gamma_A = (Z_A - Z_L)/(Z_A + Z_L) \tag{10.17}$$

then (10.16) becomes, with $E_s(Z_L = 0) = E_s(0)$,

$$E_s(Z_L) = E_s(0) - [I(0)(1 - \Gamma_A)/2]E_r \tag{10.18}$$

where, as in (10.16), E_r is the radiated field for a 1 amp antenna current excitation.

Equation (10.18) is couched in terms of scattered fields, but scattered fields are proportional to the square root of RCS, so (10.18) can easily be recast in the form

$$\sigma = |\sqrt{\sigma_s} - (1 - \Gamma_A)\sqrt{\sigma_r}\, e^{i\phi}|^2 \tag{10.19}$$

where σ_s and σ_r are the RCS values associated with each of the two terms in (10.18), and ϕ is the relative phase between the two components. As in (10.16), the RCS of the antenna is separated into two terms, one the RCS of the antenna terminated with a short circuit load. The second term, in effect, subtracts out the part of the antenna pattern component that is not reflected for the load, Z_L. Note that if the termination were actually a short circuit, $Z_L = 0$, $\Gamma_A = 1$, and the RCS is simply the short-circuit RCS, as it should be. For a matched load, $\Gamma_A = 0$, and the portion of the scatter due to antenna reradiation in the first term of (10.19) is simply subtracted out by the second term. Therefore, equation (10.19) satisfies our intuition, at least for the limiting cases.

Hansen [6] has chosen to call the first term in (10.19) the *structural* RCS and the second term the *antenna* RCS. However, he has also noted that (10.16) can be derived by using references other than the scattering measured for a short-circuit current. Use of other references leads to different (but equally valid) definitions of the "structural" and "antenna" components of the RCS. One case of interest is that for a matched antenna load. If $Z_L = Z_A$, (10.18) becomes

$$E_s(Z_L) = E_s(Z_A) + [I(0)\Gamma_A/2]E_r \tag{10.20}$$

where $E_s(Z_A)$ is the scattered field for the matched load condition. Recognizing that the matched load current $I_m = I(0)/2$, (10.20) becomes

$$E_s(Z_L) = E_s(Z_A) + I_m \Gamma_A E_r \tag{10.21}$$

For the matched load definition of the reference current, we might again call the RCS due to the first term the *structural component* and the RCS due to the second term the *antenna component.* However, the structural component is now that measured with a matched load termination, and so the second term must add in the correct portion of the radiated component of the scattered field, rather than subtract out some amount, as before.

The final reference condition widely used is from Green [7], who chose to define scattering in terms of a conjugate matched load and its associated current. For the case, the reflection coefficient is defined as

$$\Gamma_a^* = (Z_A^* - Z_L)/(Z_A + Z_L) \tag{10.22}$$

where the * indicates the complex conjugate of the impedance and the resulting values of other quantities (Γ_A and I_m) measured by using the definition of (10.22). Note that (10.17) and (10.22) are identical for real Z_A.

Following a similar procedure to that used to obtain (10.21), the scattered field can be written as

$$E_s(Z_L) = E_s(Z_A^*) + I_m^* \Gamma_A^* E_r \tag{10.23}$$

Green relates the first term in (10.23) to the structural RCS and the second to the antenna mode RCS. Due to the widespread influence of Green's thesis [7], which may have been the first widely distributed reference to analyze antenna RCSR fundamentals in detail, this is likely the most used definition of the terms antenna and structural scattering.

It is clear that the definitions of structural and antenna RCS are rather arbitrary and depend solely on how the reference scatter and its associated current are defined (those presented being the short-circuit, matched load, and conjugate matched load currents). Each of the three definitions discussed has merits. However, solely because of its intuitive appeal, the definition of the structural scattering component as that measured when the antenna is terminated in a matched load (i.e., (10.21)) is used in the remainder of this chapter. Real antenna impedances are generally assumed in our remaining examples, so (10.21) and (10.23) are identical for the cases considered.

In any event, for all of the definitions only the second term of (10.16), (10.19), (10.21), or (10.23) is related solely to the radiation pattern of the antenna, and that term's RCS value is also related to the flat plate equation, (10.6). The only difference between the definitions presented is whether the second term is subtracted from a quantity that implicitly contains the antenna pattern portion of the

scatter (i.e., (10.16)), or it is added to a quantity from which the antenna pattern portion of the scatter has been explicitly excluded (i.e., (10.21) and (10.23)).

10.2.4 The Minimum Scattering Antenna

The concept of the minimum scattering antenna, originally formulated by Montgomery, Dicke, and Purcell [8], and extended by Kahn and Kurss [9], appears often in the antenna RCS literature. In [4] a canonical *minimum scattering antenna* (MSA) is defined as a lossless antenna, fed from an N-port matched and uncoupled waveguide system (perhaps containing nonreciprocal elements) that is rendered invisible when all of the ports are terminated in open circuits. Such an antenna, when terminated in a matched load, will absorb exactly the same amount of power that it scatters. Carpenter and Anderson [5] extend the concept of the MSA developed for the single port case to the general N-port case.

As noted earlier, antennas generally do not scatter with the same pattern that they radiate. However, for the minimum scattering antenna, the character of the radiated and structurally scattered fields must be identical, if the antenna is to disappear. A short dipole is an example of an antenna for which the scattered and radiated fields are of the same nature (a short dipole both scatters and radiates the first electric dipole mode of the modal field expansion), and it is a minimum scattering antenna. Also, as required of an MSA, the short dipole terminated in a matched load scatters the same amount of power that it absorbs. The MSA definition would seen to imply that antennas with matched loads are large scatterers.

However, we have defined the scattered field as the total field minus the incident field. By that definition a sheet of perfect absorber scatters exactly the same amount of power it absorbs, as a forward scattered field that is the negative of the incident field is required to provide the shadow region behind the sheet. An aperture antenna with very small structural scatter and a matched load will behave very much like the absorber sheet [10]. It will exhibit very little backscatter, but will have the large forward scattered field component necessary to cancel the incident field in the shadow region. Therefore we must be careful to consider scattering only in the directions of interest.

One realization sparked by the concept of the minimum scattering antenna is the idea that the antenna and structural components can, in certain instances, be caused to cancel each other, so that zero scattering exists. Green [11] and Garbacz [12] provide an analysis based on a variation of (10.23) that indicates those cases where the antenna and structural RCS components of the scatter may cancel. If the numerator of (10.22) is negated so that Γ_A^* is defined as $(Z_L - Z_A^*)/(Z_L + Z_A)$, (10.23) becomes $E_s(Z_L) = E_s(Z_A^*) - I_m^* \Gamma_A^* E_r$, which can then be factored into the form

$$E_s(Z_L) = I_m^* E_r [E_s(Z_A^*)/I_m^* E_r - \Gamma_A^*] \tag{10.24}$$

When expressed in terms of RCS (and with the assumption of matched polarization), (10.24) becomes

$$\sigma(Z_L) = \sigma_a|A - \Gamma_A^*|^2 \tag{10.25}$$

where σ_a is the RCS of the antenna mode (using Green's conjugate match definition) and $A = E_s(Z_A^*)/I_m^* E_r$ is a complex number independent of the load impedance. Note that Γ_A^* has a magnitude less than or equal to 1 for passive loads, and a magnitude equal to 1 for purely reactive loads.

Three classes of antennas are derived from the analyses of Green and Garbacz. For antennas where $|A| > 1$, no passive load can reduce the total antenna RCS to 0, but reactive loads can be found that produce maximum and minimum RCS values. For $|A| = 1$, there is a reactive load that will reduce the RCS to 0. For $|A| < 1$, a dissipative load can be found that will reduce the RCS to 0, and there is a reactive load that gives maximum RCS. Note that, because σ_a is a function of the frequency and the angular position in the antenna pattern, as is A, the solution from (10.25) for the reflection coefficient and hence the load that gives minimum or zero scatter is likely to be a strong function of both aspect and frequency (and polarization, although we have ignored that effect here). In a real sense, application of (10.25) to reduce RCS is a form of passive cancellation, with all of the pitfalls and disadvantages of that technique noted earlier.

10.3 ANTENNA SCATTERING CHARACTERISTICS

The equations developed in Section 10.2 provide some appreciation of how antenna scattering arises, but they are not particularly useful for first principles characterization of antenna RCS, as the antenna scattering matrix has been developed for only a few simple cases. In fact, solving for antenna RCS by using a purely theoretical approach (and filling the associated scattering matrix) would require that Maxwell's equations be solved for the entire antenna system for every possible incident and outgoing spherical wave, a task that is, in most cases, clearly impractical.

However, for small antennas numerical methods such as the method of moments can be employed to explore antenna scattering for specific incident plane waves. In addition, the structural and antenna scattering components (regardless of which definition is chosen) can be measured on a combination antenna and RCS range, and those measurements can provide significant insight into the details of the mechanisms involved. Wideband RCS measurements processed to provide fine range resolution are particularly illustrative for diagnostic purposes, as path length differences can often be used to separate out antenna scattering components.

Because no general theory is adequate to determine antenna scattering characteristics for all antenna types of interest. the approach taken in this section is to provide a qualitative discussion of the important mechanisms in the scattering of

representative antenna types. Those qualitative discussions are bolstered by examples, where available and appropriate. The antenna types considered cover a number of types of particular interest for military systems and include reflector antennas, horns, spirals, microstrip patches, and arrays.

10.3.1 Horn Antennas

Flared horns often are used as feeds for reflector antennas, and their analysis also provides insight into the scattering from arrays with aperturelike radiators. For near-axial incidence there are two major components to the structural scattering term for horns. The first is diffraction from the edges of the mouth of the horn. The magnitude of the return from edges parallel to the incident polarization can be well approximated at L^2/π, where L is the edge length. The second component to the structural scatter is due to higher order modes induced in the horn that cannot propagate down the feed structure. Those modes are reflected at some point in the horn flare or throat structure [13]. At incidence angles far off the axial direction, reflections from the outer surface of the horn may also become important.

Williams [10] provides an analysis of the scatter from small horns, in which he models a horn as a collection of sectoral waveguide sections that alternatively have constant heights and widths. As an example, mode propagation and reflection are calculated to assess the scattering characteristics of the horn diagrammed in Figure 10.2. The results of the analysis are shown in Figure 10.3, where E- and H- plane plots of RCS are provided. Note that the vertical scales are in decibels normalized to a square wavelength. The horns are small enough that only a few higher order modes can propagate, so it is likely that the structural scatter is dominated by the horn edges. Using the L^2/π approximation given earlier, the coherent sum for the two edges parallel to the electric field vector is 1.03 λ^2 (just over 0 dBλ^2), which is very close to the value seen when the horn is terminated in a matched load. Two curves are shown for the horn terminated with a short circuit, one with the short circuit offset $\lambda/4$ from the other. For those two curves there will be a 180° phase relationship (because of the two-way travel) between the antenna components of the return. The antenna returns for the two cases will add to the structural return with opposite phases, giving an idea of the relative size of the antenna versus the structural component. The antenna mode RCS, calculated using (10.6) is 10.9 dBλ^2, which falls nicely between the two short-circuit curves at 0° incidence. Note that, off axis, the matched load RCS begins to rise. This is due to the creation of higher order modes in the throat of the horn that cannot propagate to the load to be absorbed. A major problem in predicting wide-angle horn RCS is that higher order modes with radiation patterns having peaks far off the horn boresight can be induced by either off-boresight illumination in the horn operating band or for any angle of illumination for frequencies well above the normal operating frequency of the horn.

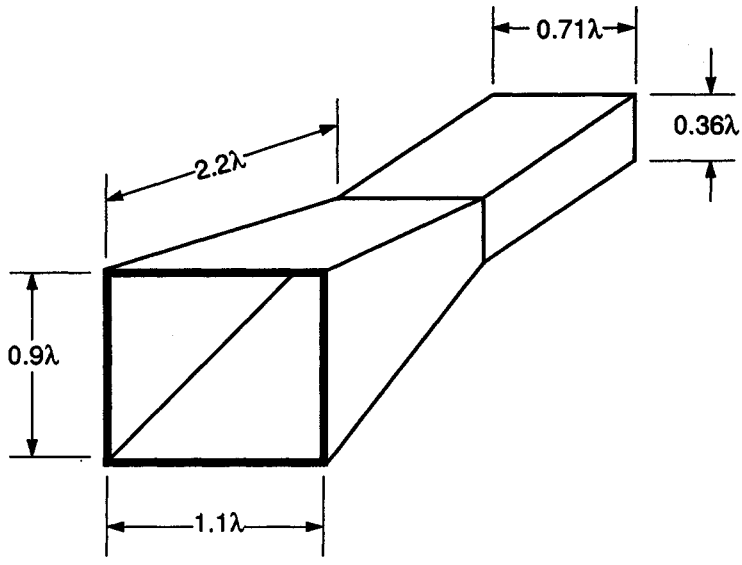

Figure 10.2. Pyramidal horn geometry (from [10]).

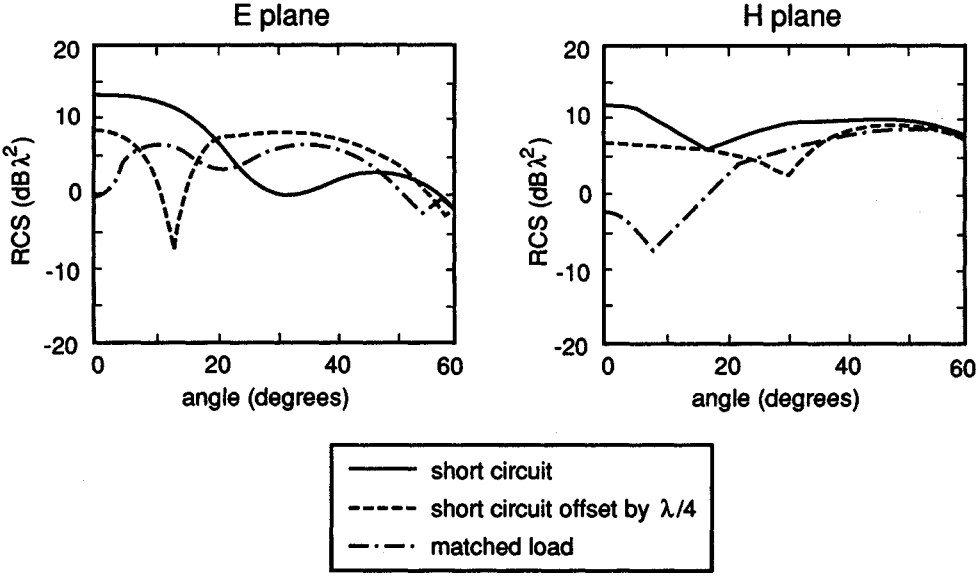

Figure 10.3. *E*- and *H*-plane RCS patterns for the horn of Figure 10.2 (from [10]).

An experimental demonstration of the scatter from horns is provided by Lindsey [14]. An X band standard gain horn with a 14.5 cm × 19.6 cm (5.7 × 7.7 in.) aperture was used as the scatterer. The horn was about 36 cm (14 in.) long. Coherent scattering measurements were taken over the frequency range 6.27–12.32 GHz in a swept-frequency mode, and an inverse FFT was applied to the frequency-domain data to provide high-range resolution RCS data. A bistatic setup was used, with separate transmitting and receiving horns, but the bistatic angle was not called out (we assume the angle was small). Note that if standard WR-90 waveguide was used in the waveguide-to-coaxial adapter used as the horn termination, the waveguide was below cutoff for the lowest propagating mode (TE10) at frequencies below 6.557 GHz [15]. That is likely the case, as [14] states that the horn was well matched over the entire band except for frequencies below waveguide cutoff.

Figure 10.4 provides measured data for two cases. In Figure 10.4(a) the horn is terminated with a 50 Ω matched load. The point labeled the *first structural mode* is caused by edge diffraction from the lips of the horn, and it has a best-fit RCS value of −19.7 dBsm. Edge diffraction returns from the two vertical lips of the horn, if exactly in phase, would be expected to provide an RCS of about −15.7 dBsm. As less than a 2° misalignment of the horn would cause the edge returns to cancel each other, the measured data fall within the range that might be expected from a standard experimental setup.

The second structural mode occurs very close to the termination, as can be seen in Figure 10.4(b), where the horn has been terminated by a short circuit. That return has two possible causes. The first is a severe mismatch near the feed (e.g., caused by misalignment of the waveguide flange). However, the return loss of the horn was measured over the band of the RCS data by using a vector network analyzer, and the mean loss was 13 dB (corresponding to a reflection coefficient of 0.22, or a voltage standing wave ratio of 1.58 : 1). Therefore, it is more likely that the return is due to higher order modes that were unable to propagate into the waveguide termination (the first higher order mode that propagates in WR-90 is at a frequency above 13 GHz, which is well above the highest frequency in the measurement).

The antenna mode return has a best-fit RCS of −3.6 dBsm. The flat plate formula of (10.6) is a function of wavelength, and so it is not clear what value for the short-circuit antenna mode RCS a wideband measurement should give. That is particularly true given that the waveguide phase velocity is a function of the frequency (i.e., the medium is dispersive). As the Fourier transform processing used to provide fine range resolution implicitly assumes that the phase change from a scatterer produced by a frequency change is a linear function of frequency, returns from a given point should be smeared in range. That effect is not evident in the measured data. However, the average RCS over the measurement band, calculated from (10.6), is about 10 dBsm, and the measured value is much lower than that.

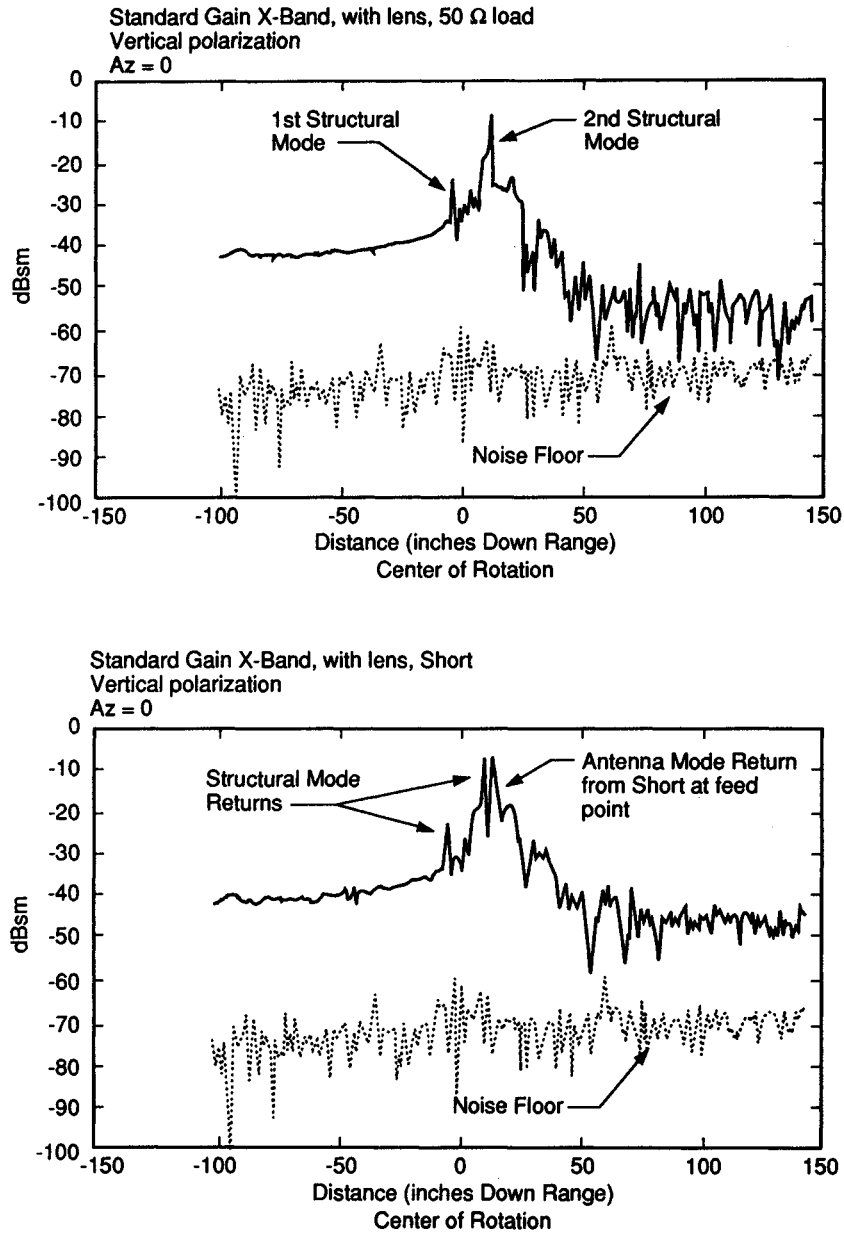

Figure 10.4. Horn RCS as a function of range over the frequency band 6.27–12.32 GHz for vertical polarization (a) with a 50 Ω load and (b) with a short circuit termination (from [14]).

Therefore, the antenna mode RCS is much less than might be expected from a narrowband measurement, likely because of the dispersive properties of the waveguide termination.

Horns make moderate to high gain antennas for which it is relatively easy to visualize the origins of the structural and antenna mode scattering. Structural scattering is dominated by edge diffraction and reflection of nonpropagating modes in the throat and transmission line. Antenna mode scattering is dependent on the mismatch between the antenna and its termination. Although the analysis of detailed scattering for large horns is difficult, numerical methods such as finite difference time domain are becoming capable of providing useful results. In addition, for specific cases, wideband measurements provide a method for diagnosing horn scatter, and recognizing the origin of the scatter is the first step toward reducing it.

10.3.2 Reflector Antennas

Reflector antennas are used in a wide variety of military applications where high gain is desired. A typical reflector antenna consists of a main reflector, a feed structure, and a support structure for both the main reflector and the feed. The feed structure might be simply a horn with its transmission line, or it might consist of a feed antenna and one or more subreflectors that illuminate the main reflector. In any event, reflector antennas are typically complicated structures that have complicated scattering patterns.

In [10], Williams also provides an analysis of a typical reflector antenna system. Figure 10.5 shows a Cassegrain antenna with a four-horn monopulse feed. Four different scattering components are analyzed for this antenna. The first is the scatter from the main reflector, from which the second component, blockage caused by the subreflector, must be subtracted. The third component is the antenna mode return—that incoming energy reflected from the main reflector to the subreflector and into the feed which is not absorbed in the load, but is reradiated. The fourth component is the scatter from the back of the subreflector and the struts. Figure 10.6 provides the envelope of those returns for angles near the peak of the antenna pattern. As expected, the antenna mode return labeled *Feed horns* dominates the scattering. The peak level shown for this 70λ diameter reflector is about 63 $dB\lambda^2$. From (10.6), the maximum RCS might be expected to be about 83 $dB\lambda^2$ (52 dBsm for a 2.1 m diameter antenna at X band), so a reflection coefficient of 0.1, or a VSWR of 1.22 : 1 has been implicitly assumed. Note that the other components are much smaller than the reradiated component, even for this case of a relatively well-matched load.

Because reflector antennas are generally designed for high gain, they also generally have the potential for high RCS. Lambert, Rudduck, and Lee [16] provide

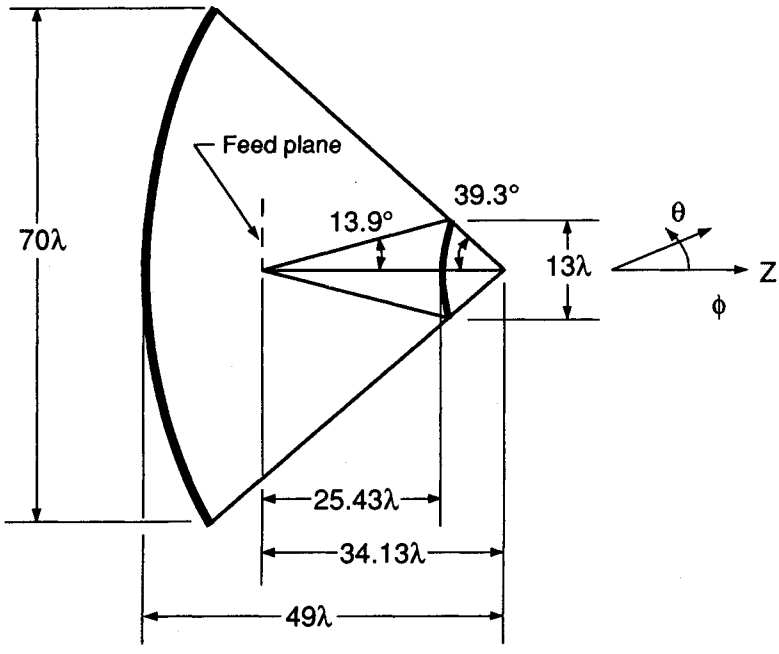

Figure 10.5. Cassegrain reflector antenna with a four-horn split static feed (from [10]).

measured data on a 0.6 m (2 ft) diameter Cassegrain antenna at K_a band that graphically illustrates the potential magnitude of the RCS problem for reflectors. The data provided in the paper were actually collected to calculate the gain of the antenna using the relationship derivable from (10.4) and (10.5) for the antenna component with a short-circuit termination such that

$$G = \sqrt{4\pi\sigma}/\lambda \tag{10.26}$$

Figure 10.7 shows the boresight RCS results for the antenna measured using the Ohio State compact range at frequencies between 33 and 37 GHz. Four scattering "modes" are indicated on the graph. The mode listed as $n = 0$ plots data taken with the feed terminated in a matched load and so corresponds to what we have called the *structural scatter*. That component of the return varies from around 20 dBsm to 30 dBsm over the band.

The remaining modes were obtained with the antenna feed terminated by a short circuit. For all of the curves, wideband data were inverse Fourier transformed to provide high range resolution. The $n = 1, 2, 3$ modes occur because a part of the energy reflected from the short circuit toward the subreflector is, in turn,

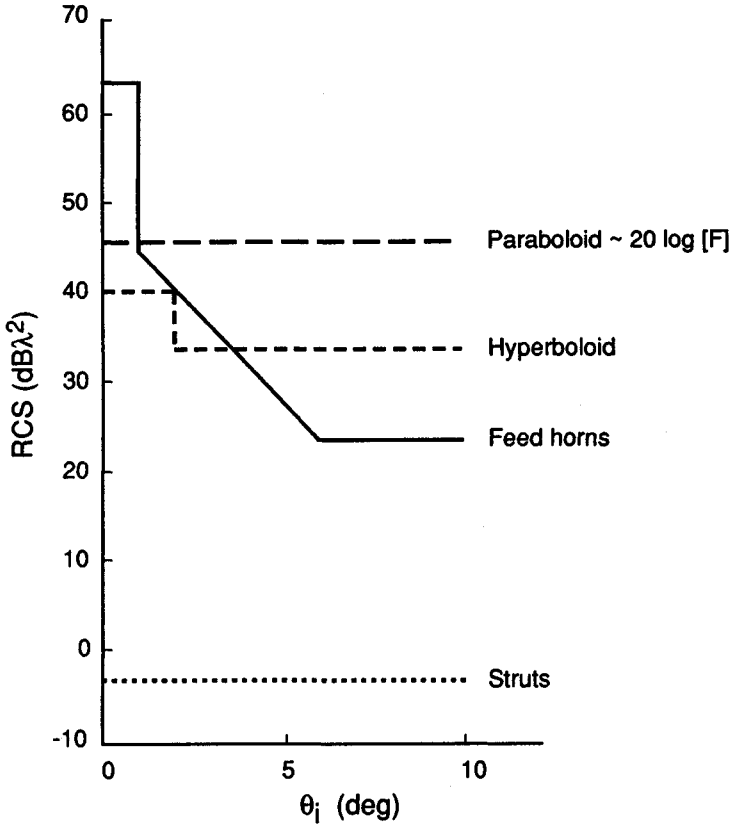

Figure 10.6. Envelope of RCS contributions as a function of angle off boresight for the antenna of Figure 10.5 (from [10]).

reflected back toward the feed by the subreflector. In a well-matched antenna most of this component would be absorbed by the load and never reflected, but with the short-circuit termination, the first three reflections are easily seen. As these individual reflections are separated in time due to their path length differences, they can be individually gated in the time domain and retransformed to the frequency domain to provide the curves shown.

Note that the $n = 1$ curve (what we have called the *antenna mode*) dominates the RCS of the antenna. From (10.6) this antenna could have an RCS as high as 41.6 dBsm at 35 GHz. However, in obtaining that result we have implicitly assumed that the actual antenna area and effective area are the same; an assumption that

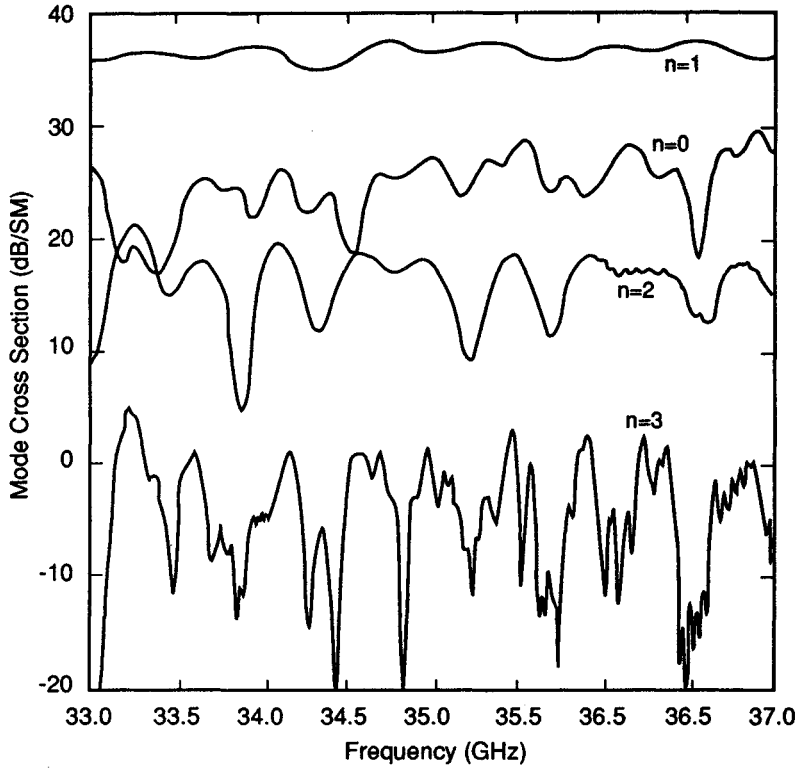

Figure 10.7. RCS for the first four scattering modes of a Cassegrain antenna (from [16]).

will rarely hold. Feed blockage, illumination taper, and losses will reduce the effective area relative to the physical area. The measured RCS at 35 GHz is about 38 dBsm. This corresponds to an effective area of about two-thirds the physical area, which is not an unreasonable value (remember, in Chapter 2 the rule of thumb for reflector antenna gain used a constant of 27,000 instead of the theoretically achievable value of 41,259, which corresponds to an effective area of about 65% of physical area).

In band, under normal operating conditions, antennas such as the ones just illustrated should have loads well matched to the antenna impedance. That will help minimize the scatter. However, for the antenna of Figure 10.7, the structural scatter is large (100–1000 m^2), even if the antenna mode scatter were completely eliminated. However, VSWR values over the antenna operating band of 1.2 : 1 would not be unusual, so antenna mode RCS values around 20 dBsm might be expected, even for a reasonably well-matched load. From the examples shown, it

is clear that reflector antennas present a potentially large problem, if they must be used on low RCS platforms.

10.3.3 Spiral Antennas

Spiral antennas find widespread use in military systems because they are wideband, can be made to conform to the platform, give wide angular coverage, and can provide monopulse direction finding capabilities. For multi-octave use, cavity-backed spirals with absorber loaded cavities are normally used, and the following discussion focuses on that type of spiral.

Figure 10.8 provides a drawing of a typical cavity-backed Archimedean spiral. Note that the cavity is loaded with absorber to provide wideband performance. Spiral antennas can also be backed with unloaded cavities, which will decrease the bandwidth to about an octave, but will increase the antenna gain over the usable bandwidth.

Spiral antennas normally can be conformally mounted into a surface of the vehicle with which they will operate. Thus, when specular to the surface of the

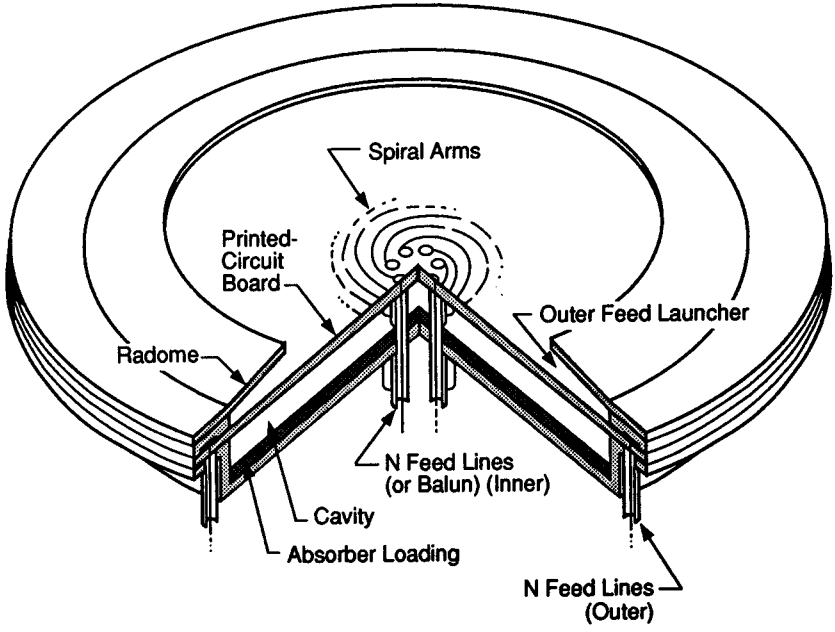

Figure 10.8. Cavity-backed Archimedean spiral (from [17]).

spiral, a radar will generally also be specular to the surface in which the spiral is mounted. For that reason, only on rare occasions does the normal incidence RCS of the spiral substantially affect the total RCS of the platform.

Therefore, the major concern for spiral RCS is for angles far off-normal to the spiral. One reason for the use of spiral antennas is that they provide broad angular coverage. However, a wide-angle gain pattern implies a wide-angle antenna mode RCS pattern. Figure 10.9 plots the gain as a function of aspect angle for a cavity-backed spiral designed to operate from 2–18 GHz. Spiral antennas are inherently circularly polarized, and their patterns are normally measured by using

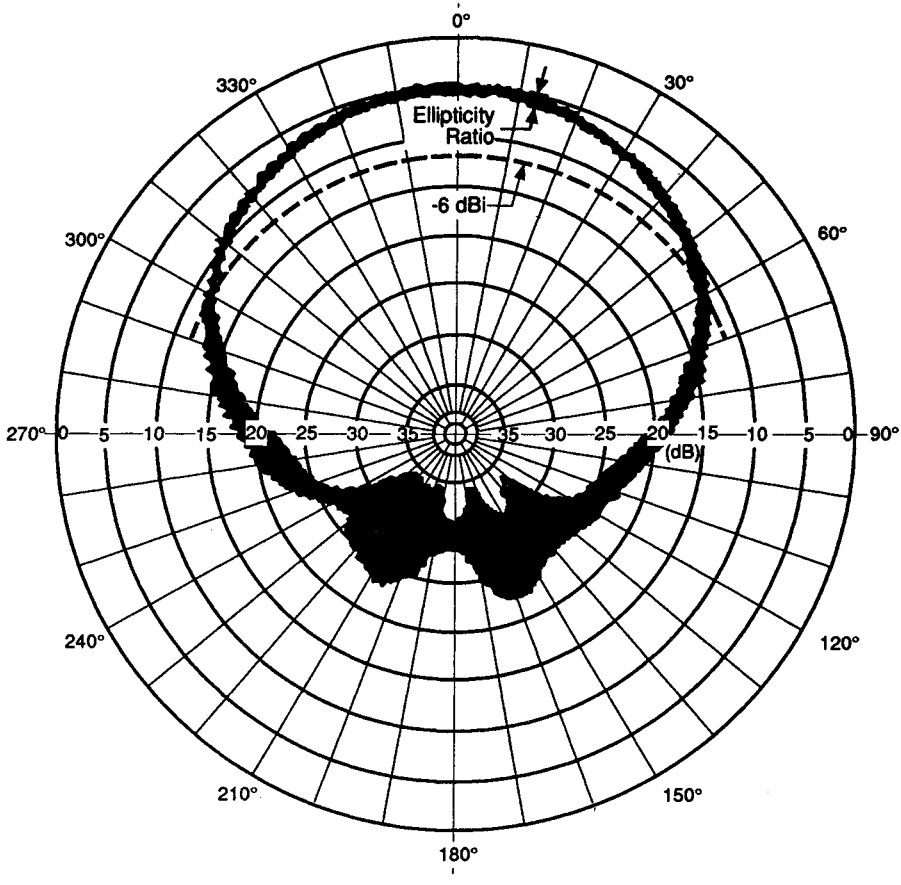

Figure 10.9 Typical pattern of an Archimedean spiral antenna designed to cover a 2–18 GHz bandwidth (from [17]).

a rotating linear source. For a perfect circularly polarized pattern, the response will be identical for any linear polarization, and so the response to the rotating linear source should be a thin line on the pattern plot. In practice, the spiral antenna will not be exactly circularly polarized. For that case, the width of the line on the pattern plot is a measure of the ellipticity of the antenna response, because an elliptically polarized antenna will be sensitive to the sense of the linear polarization.

Note that the peak gain of the example spiral is about +1 dBi (dB relative to an isotropic radiator) on axis, and drops to about −4 dBi at 45 degrees off-axis (which would generally be considered in the aircraft front sector for a fuselage mounted antenna). Because spirals are used for wideband reception or transmission, their feed networks are designed to provide wideband matching. VSWRs of 2:1 or 3:1 can be achieved over bands as large as the 2–18 GHz one covered by the spiral whose measured data are provided. Using (10.7), modified to be in terms of gain rather than effective area, gives an antenna mode RCS of −59 dBsm at 45° from grazing, a frequency of 10 GHz, and a VSWR of 2 : 1. That obviously does not represent a very large RCS. However, if the frequency drops to 2 GHz, and the VSWR rises to 3 : 1, the antenna mode RCS of the same spiral at 45° from grazing (assuming the same gain) is −38.5 dBsm, and, as the return from a single component, that level may be of concern.

Another concern with spirals is the structural scatter encountered at angles near grazing. The spiral antenna substrate will generally be a dielectric on which the conductor making up the antenna is bonded. Thus, there is a potential impedance discontinuity present that can serve to reflect incident waves. This discontinuity is typically more severe for the traveling wave polarization case than for the case where the electric field vector is parallel to the antenna surface.

10.3.4 Microstrip Antennas

The idea of conformal antennas and "smart skins" is attractive from an RCSR designer's point of view because it allows the shaping already accomplished to reduce a platform's RCS to be applied as well to the on-board sensors. Thus, antennas that naturally lend themselves to conformal configurations are of great interest, and microstrip antennas fall in that category. A microstrip antenna is defined as an antenna that consists of a thin metallic conductor bonded to a thin grounded dielectric substrate [18]. Generally the conductors are patches of some regular shape such as rectangles, circles, or ellipses. As the dielectric substrate thickness is typically very small (a few millimeters, at most), microstrip antennas can easily be implemented on the surface of a vehicle and would appear to be ideal for conformal antennas and arrays. Therefore, the RCS characteristics of microstrip antennas are of interest for possible application to low RCS vehicles.

One advantage of microstrip antennas from an analysis point of view is that typical dimensions of the patches are on the order of a half-wavelength at the first resonant frequency, so numerical methods such as method of moments can be used to study their scatter. Newman and Forrai [19] present an analysis of rectangular patch antennas that implicitly assumes an open circuit at the feed. Figure 10.10 provides a drawing of the geometry of a microstrip patch, and Figure 10.11 shows predictions for the RCS around the first resonance for a particular patch antenna. The data shown are for vertical polarization (θ pol.) with the patch horizontal. The incidence angle is 45° and the azimuth look angle is along the 2.5 cm length of the patch. Note that the RCS is generally less than the projected area of the patch at this viewing angle (−36.6 dBsm) and less than the normal incidence flat

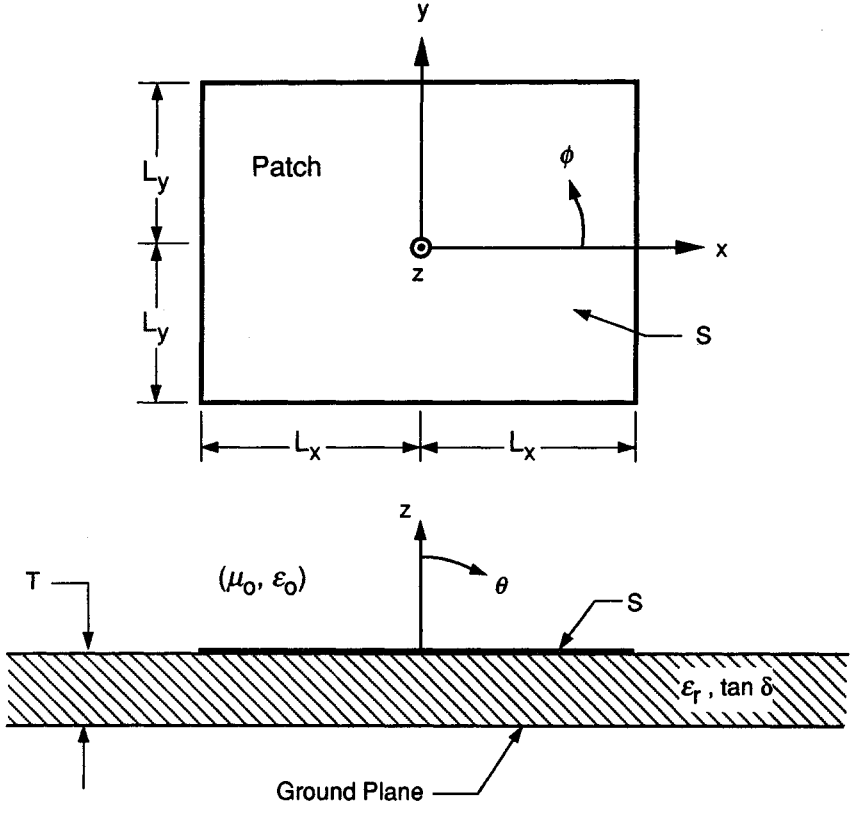

Figure 10.10. Geometry for a rectangular microstrip patch over a grounded dielectric substrate (from [19]).

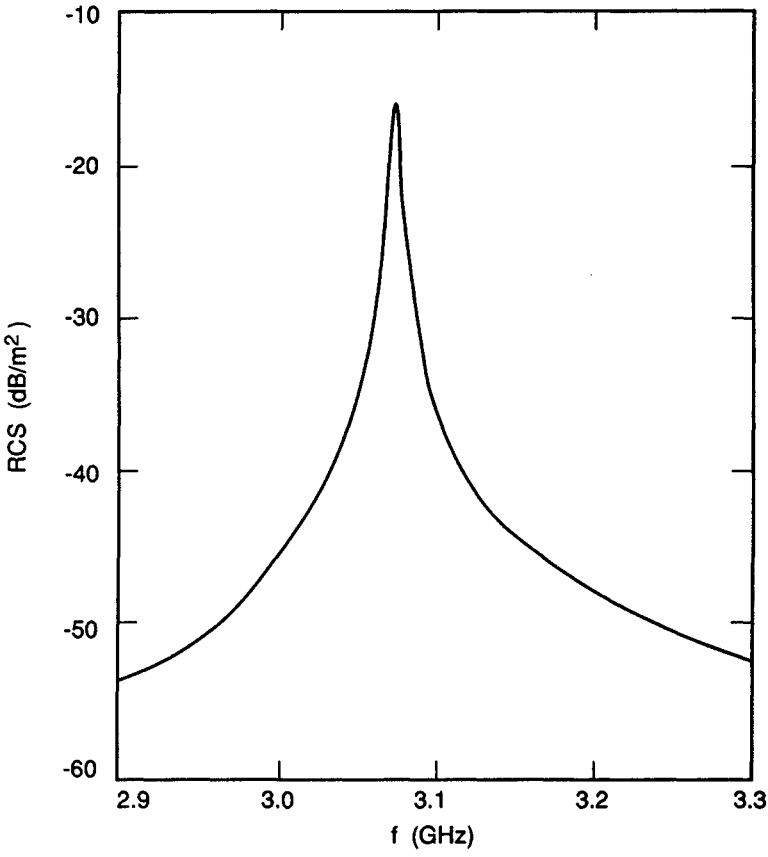

Figure 10.11. RCS of a microstrip patch with $2L_x = 2.5$ cm by $2L_y = 1.25$ cm on a substrate 0.03 cm thick with $\epsilon_r = 4.0$. The incident wave is from $\theta_i = 45°$, $\phi_i = 0°$, and is θ polarized (from [19]).

plate RCS (-38.8 dBsm at 3.1 GHz). However, at the patch resonance, the RCS is greater than -15 dBsm. Although the resonance peak is narrow, the magnitude of the RCS is certainly of concern. In addition, other resonances occur at higher frequencies. Those resonances are traced in [19] to two different effects. The first occurs when the patch self-impedance is a minimum (i.e., when the reactance is 0), which is referred to as an impedance resonance peak. The second type of resonance occurs for modes where the patch radiation pattern is a maximum in the backscatter direction, which is referred to as a pattern factor peak.

Pozar [20] extends the analysis of microstrip antenna scattering to include the effects of the feed and the terminating impedance. Figure 10.12 provides

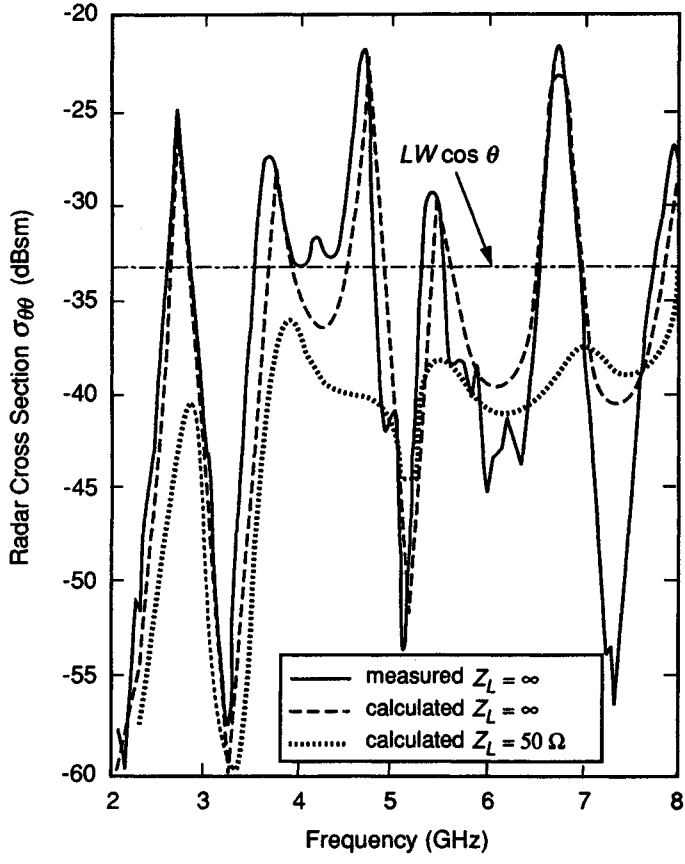

Figure 10.12. RCS versus frequency for a rectangular microstrip patch. Measured data for an open-circuited patch ($Z_L = \infty$); calculated data for $Z_L = \infty$ and $Z_L = 50\ \Omega$. $L = 3.66$ cm, $W = 2.6$ cm, $\epsilon_r = 2.17$, diectric thickness = 1.58 mm, feed position is $x = 0.163$ mm and $y = 0.11$ mm from patch corner, $\theta = 60°$ and $\phi = 45°$, θ pol. (from [20]).

measured data from [19] and compares results to an analysis from [20] including feed probe effects and with the feed probe matched and open circuited. Data are measured at an incidence angle of 60° and azimuth angle of 45°, so both x and y modes can be excited on the patch. Each of the peaks in Figure 10.12 can be related to a mode on the patch and is an impedance or pattern factor peak. The termination of the feed in a 50Ω load is seen to significantly reduce the predicted RCS at the peaks (10 to 20 dB). Note, however, that the feed point was chosen to be near a corner of the patch where it affects almost all of the resonant modes. Pozar notes that if the probe were connected at $y = 0$, as is typical for antennas

operating in a dominant x mode, it would not couple to many of the y modes and would not affect the peak RCS of those modes.

These examples illustrate the fact that scattering from microstrip patch antennas can be significant. The results shown were for single patches, but it would be more typical to find an array of patches. Obviously, for an array, the problems of obtaining low RCS will be multiplied. Nevertheless, Pozar's analysis indicates that there are ways to reduce the RCS, and consideration of how microstrip antennas are fed is part of the discussion of Section 10.4.

10.3.5 Array Antennas

The preceding subsections of 10.3 have considered individual antennas. However, modern antennas are often arrays of individual elements, which may employ dipoles, horns, microstrip patches, spirals, slotted waveguide, or other discrete sources as their radiators.

The RCS of an array antenna has the same two components as have been discussed for any antenna; an antenna component and a structural component. For the array, however, the antenna component is the phasor sum of the contributions from all of the elements in the array (taking into account mutual coupling between elements, if applicable). An additional complication with arrays is that they often have multiple feeds, and so the characteristics of the reradiation may be a strong function of the direction of the illuminating wave. For example, a scattering pattern feature that may be present although not typically seen in the transmitting or receiving antenna pattern is grating lobes. Normally, arrays are designed so that any grating lobes fall outside the visible region (nominally achieved by element separations of less than $\lambda/2$ for grating lobe suppression over all visible space for all possible antenna scan angles [21]). Figure 10.13 provides a predicted RCS pattern for the antenna mode component from an array of eight dipoles above a ground plane, with a separation of 0.65λ between dipoles. That separation would normally give a grating lobe out of visible space for a broadside directed array (which is shown). However, the two-way phase difference provided by the fact that the eight elements are not illuminated in phase gives a large grating lobe at about 50° from broadside.

Planar array antennas, whose elements often consist of slotted waveguide, are typical of one class of array antenna. The individual radiators (slots, in this case) are electrically small at the operating frequency, and so below the operating band the array simply looks like its flat front face (i.e., no energy propagates into the slots, because they are below cutoff). Therefore, at low frequencies, the array scattering pattern will resemble that of a flat plate the same size and shape as the array face. Above cutoff, energy will propagate into the slots, and the details of the pattern will depend on how the array is terminated and the interaction between the reradiated energy and that scattered from the front face.

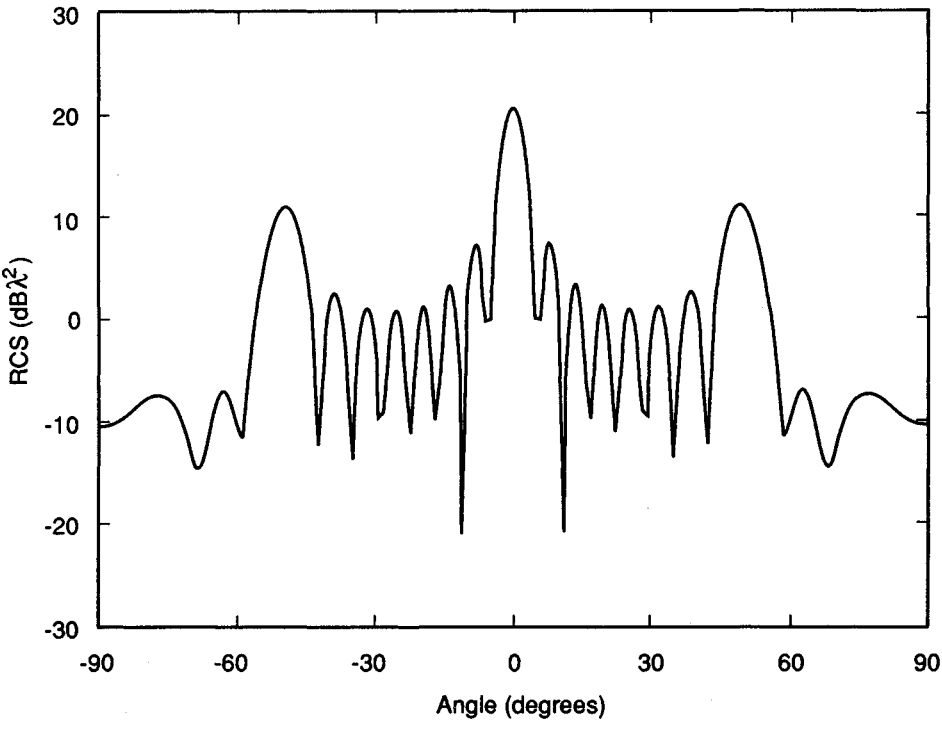

Figure 10.13. Predicted RCS for an eight-element X band dipole array (from [22]).

In calculating the RCS from an array for which energy is able to propagate through the transmission line structure that feeds the antenna, it is important to know what components are in the path of the incoming and outgoing waves. If, for example, all components in the lines are reciprocal and the signals reach a common termination point, then the reradiated signal pattern of the antenna mode component will match the transmitting pattern of the antenna. However, if there are nonreciprocal devices in the lines, or if each element has a separate termination point, then the reradiated pattern may be much different than what would normally be expected from the transmission pattern. Thus, arrays pose a particularly difficult problem in low RCS antenna synthesis because of the complexity of the feed structures often involved and because of the wide number of choices of how hardware might be implemented. Tittensor and Newton [22] provide an example of how various types of power dividers affect the RCS of a dipole array, which points out the importance of the details of the feed circuitry.

10.4 ANTENNA RCSR

Section 10.3 described the mechanisms that give rise to scattering for a number of antenna types in wide deployment. This section discusses some of the very fundamental considerations in providing low RCS antennas. The problem of RCSR for antennas breaks down neatly into the same two categories considered for antenna scattering analysis: reduction of structural scatter and reduction of antenna mode scatter. However, there is one additional technique for RCSR that does not precisely fall into either category: the use of frequency selective surfaces to control the energy that reaches the antenna. For example, the use of a shaped frequency-selective surface in front of an antenna, where feasible, reduces the RCSR task from a wideband to a narrowband problem. The requirement to implement only narrowband RCSR techniques can be particularly helpful in attempts to reduce both the structural and the antenna mode scattering. For antennas required to operate over wide bandwidths, the frequency-selective surface solution is not applicable, and wideband solutions to the RCSR problem must be considered.

10.4.1 Frequency-Selective Surfaces

Frequency-selective surfaces, which are discussed briefly in Section 8.5 in connection with circuit analog radar absorbing materials, depend on regular geometric patterns cut into a conducting screen to produce a bandpass or bandstop filter. Figure 8.22 provides a drawing of some typical FSS geometries. For cases where the basic geometric shape is implemented as a conducting patch, a bandstop filter is generally formed. For apertures in a conducting screen, a bandpass filter is formed [23]. Ideally, an FSS would be implemented by using a perfect conductor and a lossless dielectric substrate (and possible superstrate) to provide a lossless structure. In practice, frequency-selective surfaces are generally made of copper deposited on kapton, kevlar, or other low-loss dielectrics. Therefore, there is some amount of loss in both the conductor and dielectric, a fact of particular concern if the FSS is to be used in connection with a transmitting antenna.

Although Section 8.5 provides some basics on FSS design, it is worthwhile in this context to focus specifically on the implementation requirements of frequency selective surfaces for antenna RCSR and illustrate performance with some examples. For a review of appropriate analytical methods, Mittra, Chan, and Cwik [23] provide an excellent overview of design techniques applicable to FSS structures.

Figure 10.14 illustrates several of the ways that a frequency selective surface might be employed to reduce the RCSR of an antenna. In the first instance, a shaped bandpass radome is used to reflect all out-of-band signals away from the antenna (and the threat direction) while allowing in-band signals to reach the radar

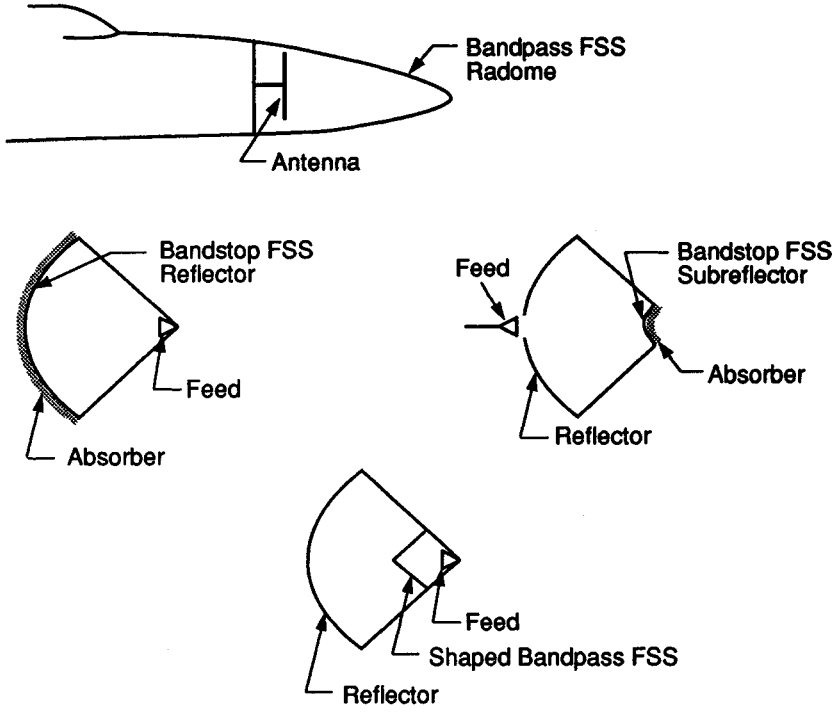

Figure 10.14. Frequency-selective surfaces concepts for RCS control.

antenna. In the second case, a bandstop reflector surface transmits all signals not in the operating band. The reflector is backed by a layer of RAM that absorbs those signals, while signals within the operating band of the antenna are reflected into the feed. In the third case, a bandstop FSS is used as a subreflector. Again, the FSS is backed by absorber to attenuate out-of-band signals, with in-band signals being reflected into the feed. Finally a shaped bandpass FSS is used in front of the feed so that all out-of-band signals are reflected away and only in-band signals reach the feed.

For systems required to handle high powers, significant engineering challenges are associated with implementing any of the illustrated FSS designs. First, for those designs that utilize absorber, the power handling capability of the absorber must be sufficient to handle the in-band leakage through the FSS. The frequency-selective surfaces also have to meet stringent requirements. The ohmic losses in both the conductor and the supporting dielectric must be minimized, and the structure must be able to handle the heating from whatever losses remain. In addition, the

conducting parts of the FSS must be able to handle extremely high field strengths without arcing or corona discharge (a problem akin to what you will see if you put a fork in a microwave oven). For systems that have only a receiving function or for low power applications, the design requirements are certainly easier, although rarely insignificant even for those cases.

The ability to create a bandpass or bandstop filter allows the RCSR designer to control the radar energy reaching an antenna. However, the application of FSS radomes to RCSR depends on the ability to shape the radome so that it reflects the incoming out-of-band radar energy away from the threat sectors. For in-band energy, the radome should be transparent and not affect the direction of arrival or the polarization of the incoming (or, in the transmitting case, outgoing) waves. For FSS radomes along a fuselage, a conformal design might be desired. For nose mounted antennas (e.g., airborne intercept radars), an ogival radome might be preferred. In either case, the angles of incidence of the incoming or outgoing waves relative to the radome surface may vary significantly, and so the FSS must retain its transmission and reflection properties over all expected angles.

Figure 10.15 provides a drawing of two single-layer bandstop FSS designs and predictions for the normal incidence reflection coefficient as a function of frequency. The normal incidence behavior of the two structures is similar, but would be expected to diverge as incidence moved away from normal. Note that the Jerusalem cross size is on the order of $\lambda/2$ at the resonant frequency. Figure 10.16 shows the effect of incidence angle on the performance of a bandpass FSS. Note that, as the incidence angle increases from 1° (very near normal) toward grazing, the bandpass null broadens and moves up in frequency. At 80° incidence, the FSS shows poor out-of-band performance, as indicated by the relatively low reflection coefficient values, particularly at frequencies above 15 GHz.

Additional layers of dielectric and FSS can be used to tailor the properties of a composite bandstop or bandpass structure to meet requirements. Pous and Pozar [24] demonstrate a design for a two-layer aperture-coupled microstrip patch FSS shown in Figure 10.17. Figure 10.18 shows the transmission coefficient (this is a bandpass FSS, as the patches couple the incident field through the slots in the ground-plane only over a narrow range of frequencies) for several ground-plane slot widths. Of perhaps more interest is the behavior as a function of angle, shown in Figure 10.19 for two polarizations. Note that the performance is relatively insensitive to incidence angle, although because of the narrow slot in the ground plane beneath each patch there is significant ϕ (i.e., azimuth angle) dependence. The ϕ dependence can be reduced through the use of crossed slots. Reference [24] provides measured data on the FSS design shown, which provides an 8% 3 dB passband, very close to the predicted value.

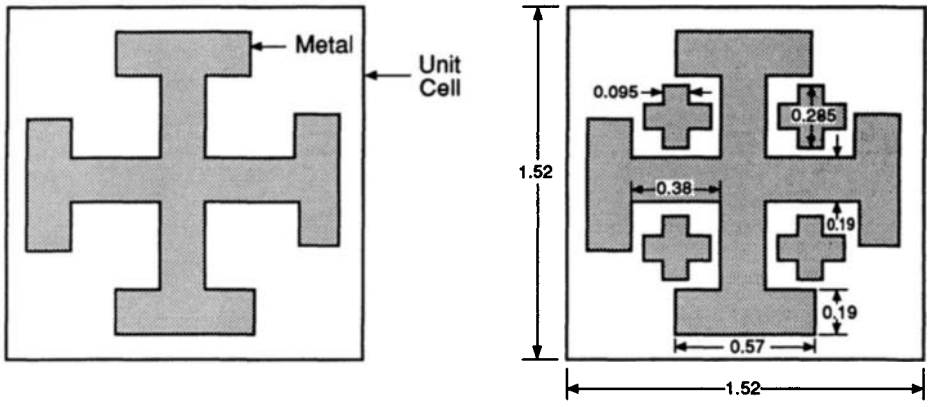

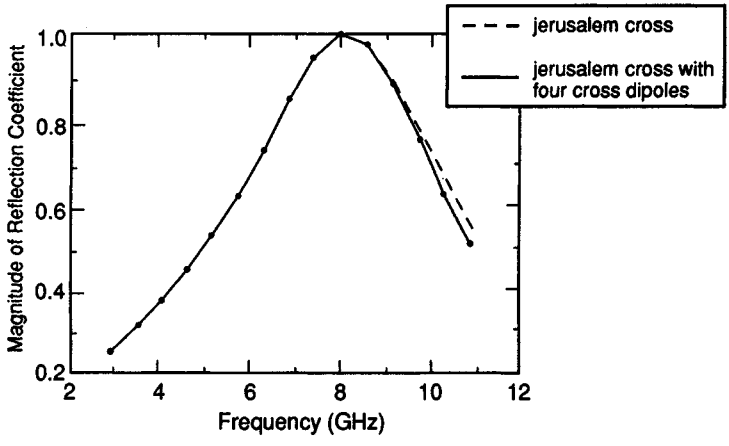

Figure 10.15. Magnitude of the normal incidence reflection coefficient versus frequency for infinite arrays of two free-standing FSS designs (from 23]).

10.4.2 Antenna Mode RCSR

Antenna mode RCS is the phenomenon that distinguishes antennas from other structures. As we have defined it, antenna mode RCS is due to energy that has traveled down the transmission line and is reflected from the termination. The

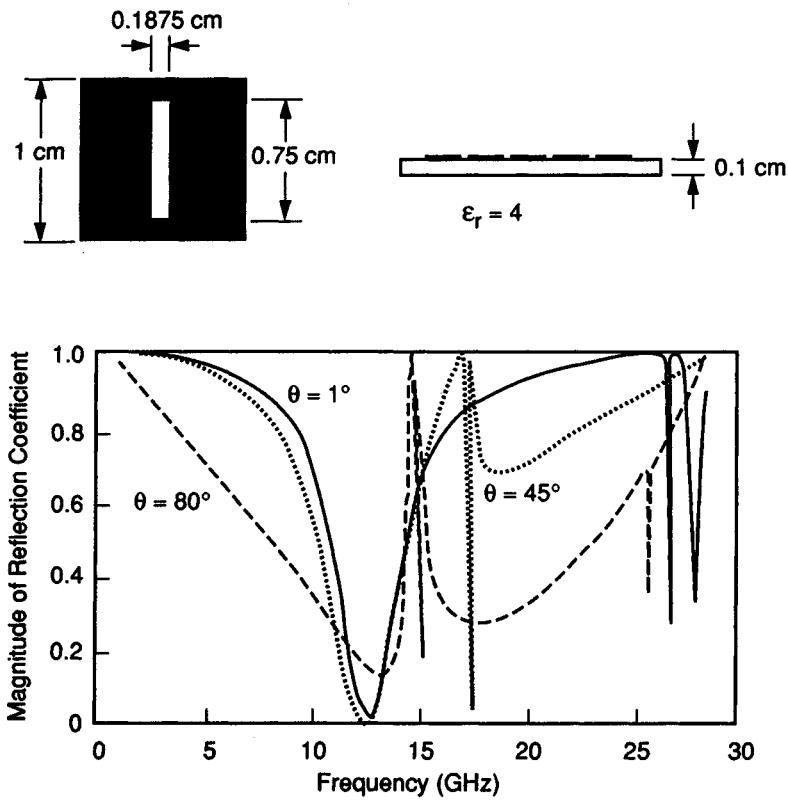

Figure 10.16. Magnitude of the reflection coefficient versus frequency for an infinite array of the FSS shown, for three incidence angles and TM polarization (from [23]).

parameter typically used to define the mismatch on transmission lines is the voltage standing wave ratio, S, which is simply the ratio of the maximum to the minimum voltage on a transmission line. The VSWR is related to the magnitude of the reflection coefficient by [25]

$$|\Gamma| = (S - 1)/(S + 1) \tag{10.27}$$

A load perfectly matched to its transmission line has a VSWR of 1 and a reflection coefficient of 0. Progressively larger values of S denote larger mismatches and larger reflection coefficients. Figure 10.20 provides a plot of the reflection coefficient as a function of VSWR. Remember that the power reflection coefficient in dB is 20 log(Γ), so $\Gamma = 0.1$ corresponds to a reflected wave that is 20 dB down

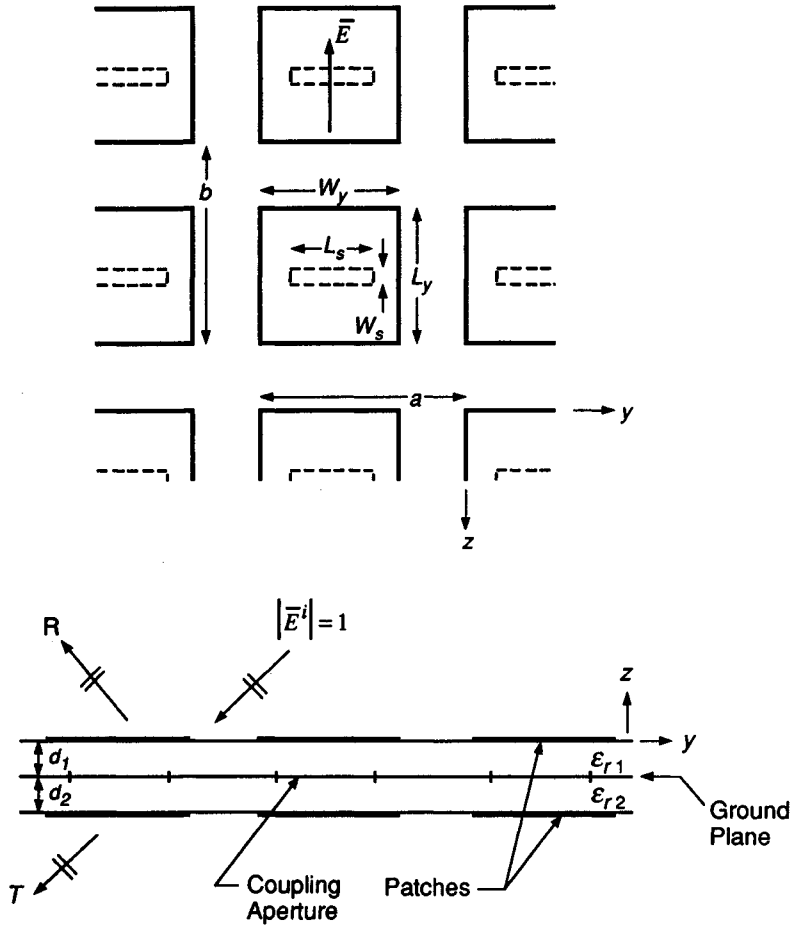

Figure 10.17. Top view and cross section of a FSS using aperture coupled patches (from [24]).

from the incident wave and a VSWR of 1.22 : 1. Reduction of the reflected wave by 40 dB requires that the VSWR be reduced to 1.02. Going in the other direction, a VSWR of 2 : 1 provides a reflection only 9.5 dB down from a short circuit, and a 5 : 1 VSWR is only 3.5 dB down. Although a VSWR of 5 : 1 would be considered a poor match for an antenna in band, VSWR values out of band may often be expected to far exceed that value.

Reduction of the antenna mode RCS through load matching requires that low VSWR values be achieved. Typically a number of components are between

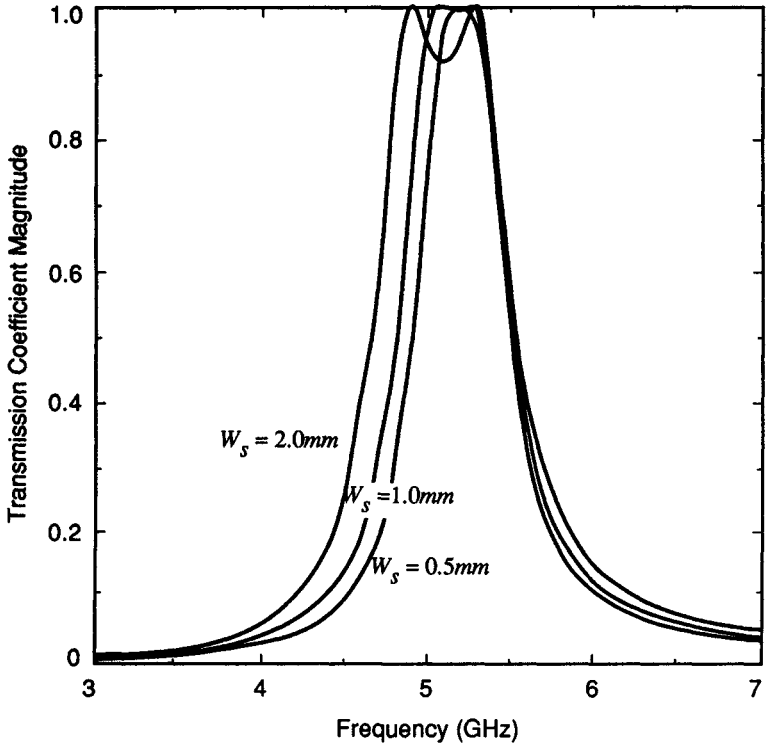

Figure 10.18. Variation of the transmission coefficient of the FSS of Figure 10.17 as a function of frequency with slot width as a parameter: $L_p = W_p = 17.1$ mm, $L_s = 7$ mm, $\epsilon_r = 2.33$, $d_1 = d_2 = 1.6$ mm, and $a = b = 28.3$ mm (from [24]).

the antenna and the termination to the transmission line (e.g., rotary joints, couplers, isolators, phase shifters, duplexers, switches), and each of them can provide mismatch. Kefalas and Wiltse [26] provide a description of a large number of typical microwave components, with associated nominal characteristics listed for many. For most of the devices listed, maximum VSWR values in band are noted to be in the 1.1–1.3 range. If those values represented overall VSWR, rather than individual component VSWR, they would correspond to reductions in the antenna mode component of the RCS of 17.7 dB to 26.4 dB below the value seen with a short-circuit termination.

Obviously, if very low antenna mode RCS is to be achieved, careful consideration must be given to component choice and load matching. Even then, it is difficult to provide very low VSWR values over very wide bandwidths. Antennas are normally designed to have transmission lines matched to the antenna impedance

(a)

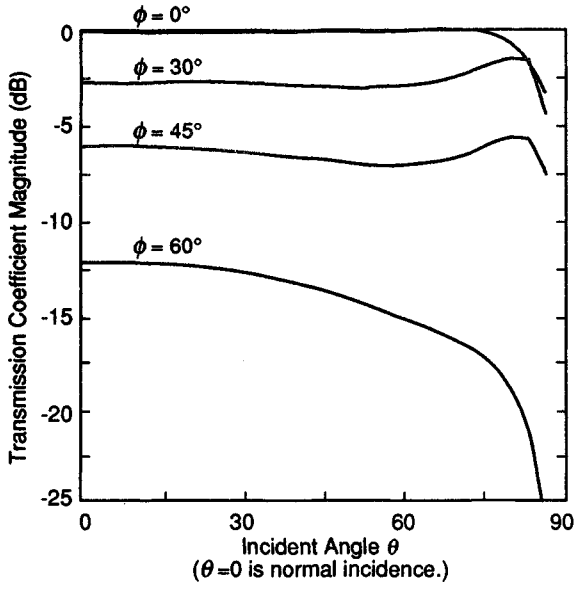

(b)

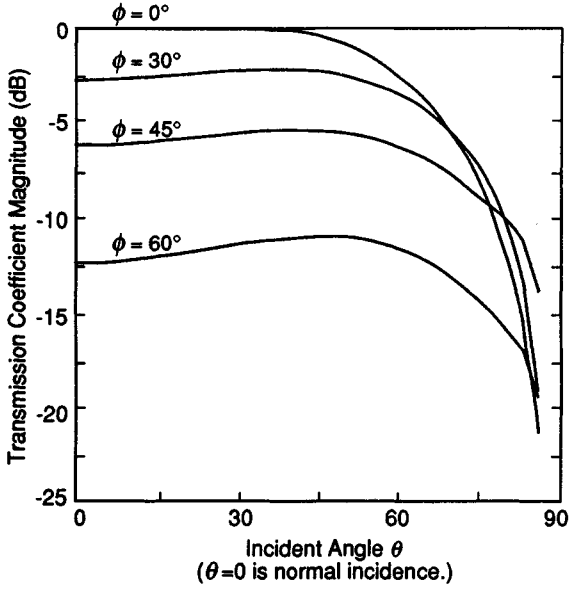

Figure 10.19. Scan performance of the FSS of Figure 10.18 with ϕ as a parameter, W_s = 1 mm, f = 5.15 GHz, for (a) TM incidence and (b) TE incidence (from [24]).

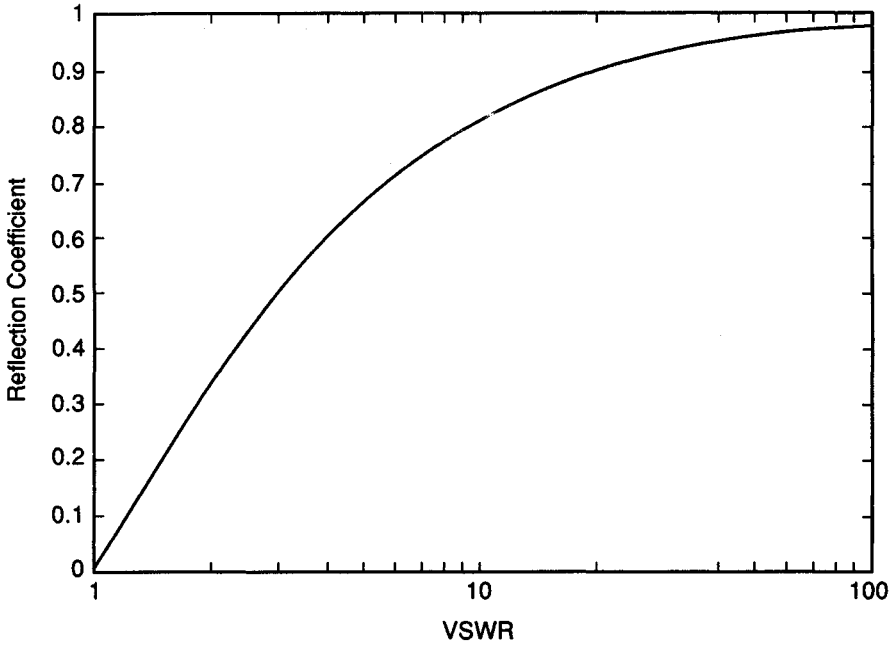

Figure 10.20. Reflection coefficient as a function of voltage standing wave ratio.

and load in their operating band. However, one of the problems of designing wideband antennas is the difficulty of providing a match over a wide bandwidth. So if a FSS can be used to reduce the problem to an in-band match problem, it makes the job of providing antenna mode RCSR much easier.

Insofar as mismatches in the transmission line and load can be reduced over all incidence angles, the antenna mode RCS can be reduced over all angles. However, for angles far off the direction of the mainbeam, sidelobe control can also be used to reduce the RCS. For example, if a conformal antenna in the side of the fuselage is used, then the normal incidence RCS of the antenna will generally be dominated by the structure around it. In that case, the far off-normal RCS is of concern (as was noted for the spiral), and that RCS is controlled by the sidelobes of the antenna. Reducing the sidelobes through illumination taper or element taper (in an array) will also reduce the antenna mode RCS. However, the difficult RCS control problems may be seen out of the antenna operating band, as the illumination achieved in that case may be very different from that in-band.

For microstrip antennas Figure 10.12 showed that termination of a patch can markedly reduce the RCS. However, [20] also explores other avenues to reduce

the RCS of microstrip patches. One technique applicable for a narrowband patch antenna is to place a row of shorting pins where they do not affect the dominant mode on the patch, but short out higher order modes. This technique can markedly help off-axis and out-of-band RCS performance. Also, placing the feed point off the symmetry plane will allow the load to reduce the effect of some of the higher order modes. A final suggestion from [20] is to insert a bandpass filter between the patch and the load to pass the desired frequency signals but show a very low impedance to out-of-band signals.

Jackson [27] explores the effect of lossy substrates or superstrates on the RCS and efficiency of rectangular patch microstrip antennas. Figure 10.21 shows the normal incidence RCS and antenna efficiency for such a system as a function of superstrate thickness normalized by the free-space wavelength. The substrate has a dielectric constant of 2.1, the superstrate has a dielectric constant of 2.0, and the parameter l is the loss tangent of the superstrate. Note that the RCS is significantly reduced for the higher loss tangents and thicker layers, but that the antenna efficiency is likewise significantly reduced. Therefore, only moderate RCSR results appear practical using this method, although reduction of higher order mode RCS might be feasible, as the superstrate becomes electrically thicker with increasing frequency.

Pozar [28] examines the effect of a biasing magnetic field on a patch antenna mounted on a ferrite substrate. He finds that a variable magnetic-field bias effect can be used to reduce the RCS of the microstrip at selected frequencies. Obviously, if threat frequency were available from another source, the biasing magnetic field could be adjusted to minimize RCS at the threat frequency.

10.4.3 Structural Mode RCSR

Consideration of reducing the structural mode RCS of an antenna simply returns us to the RCSR concepts applied for any body. That is, first do shaping to prevent scatter into the threat regions, then apply RAM selectively to take care of trouble spots. However, a few differences must be kept in mind for antenna RCSR. If the antenna is narrowband, attempts to shield it from out-of-band signals by using frequency-selective surfaces may be worthwhile. Also, absorber use and shaping must be such that the radiating properties of the antenna are not compromised. Finally, mode control can sometimes be used to reduce scatter from modes other than the primary antenna mode.

For example, with horn antennas and transmission-line structures where a single propagation mode is desired, septums or resistive cards can sometimes be used to prevent the formation or propagation of higher order modes (this technique is identical in intent to the shorting pin recommendation of Pozar [20] for reducing microstrip patch scatter). These devices must be placed in a position where the

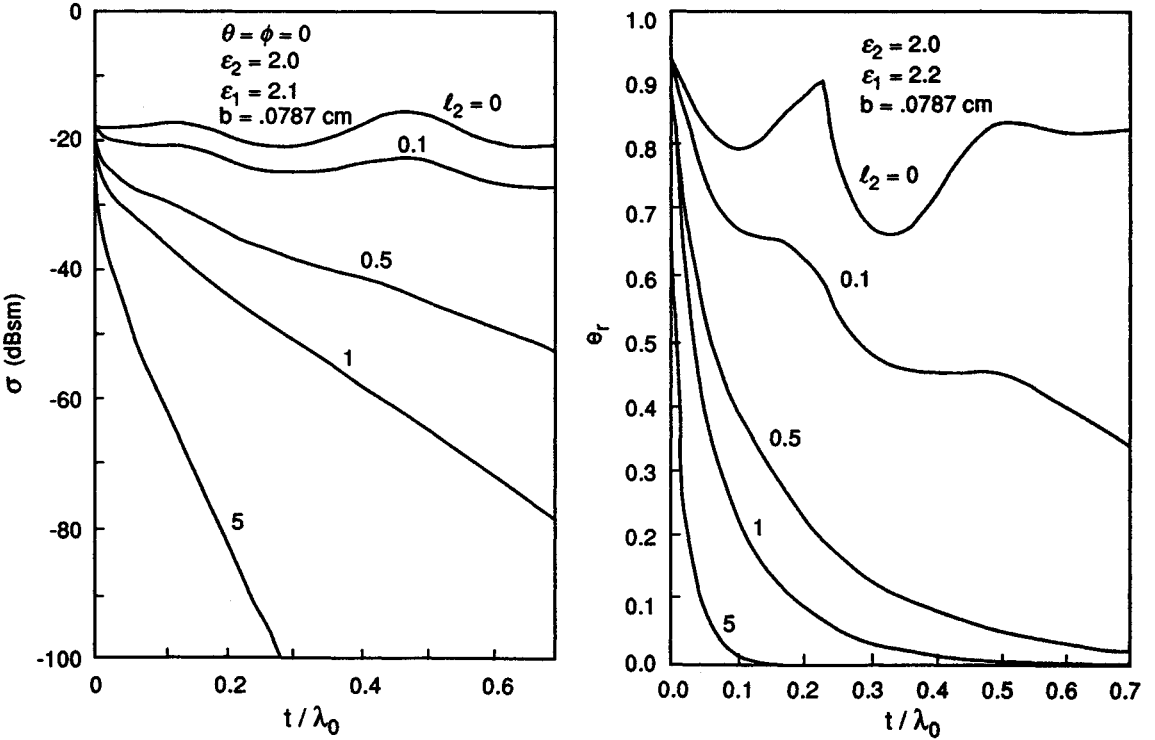

Figure 10.21. Normal incidence RCS and efficiency as a function of superstrate thickness for a resonant patch on a lossless substrate with superstrate loss tangent as a parameter (from [27]).

electric field of the desired mode is 0, but where higher order modes would normally have high field values.

Some antennas have a very large structural return, which falls nicely within the guidelines put forth earlier for shaping. For example, a waveguide array often looks like a large, flat plate with a regular pattern of slots cut into it. Clearly, for such an antenna, the orientation of the antenna face should be controlled so that the antenna surface is never seen specularly in the threat zone (that may well require the beam to be squinted away from the normal to the array surface). For an antenna that scans horizontally or vertically, a diamond shape, rather than a square or circle, might be considered, with the scan direction along the diagonal to minimize sidelobes in that plane. If possible, the edge of the array should be terminated in a tapered resistive strip or a tapered bulk edge to reduce diffraction and traveling wave effects.

For other antenna types it is not so obvious how shaping may be implemented or what improvement it might bring. With reflector antennas, the struts, pedestal, feed structure, and subreflectors may all be significant contributors to the RCS. Again, the basic shaping rules should be applied to eliminate specular returns from the threat sector. Diffraction from the edge of the reflector (or from the edges of horns) can be controlled by using edge treatments, but, for transmitting antennas, the power handling capabilities of edge treatments must be considered. Struts should be angled well out of the threat sector, and their shape should be such as to further minimize RCS.

For conformally mounted antennas, the structural return of most interest is often far off antenna boresight. In the near-grazing region, traveling wave effects become of concern, and RCSR efforts must deal with presenting as small a geometric and electrical discontinuity as possible to the surface wave. Local magnetic RAM treatments can be used to help attenuate the surface wave. It may also be possible to provide a tapered resistive transition into and out of the antenna area. Shaping can be employed to minimize the reflection coefficient back in the direction of the radar (e.g., mount a square conformal antenna with a diagonal along the length of the fuselage, rather than in an orientation providing a station line). In every case, stack lines where possible.

10.5 SUMMARY

The purpose of this chapter has been to present an overview of antenna RCS and its control. All investigators who deal with antenna RCS separate the signature into two components. One, the structural component, is that scattering which is independent of the fact that the object investigated is designed to be an antenna. The second component is the antenna mode scatter, whose character is directly related to the antenna pattern. However, there are a number of different definitions

of what portion of the total return constitutes structural versus antenna mode scatter. Hansen [6] has shown that the definitions are arbitrary, and because of its intuitive appeal, we have chosen to use one that defines the structural scatter as that seen when the antenna is terminated in a matched load.

The amplitude of the antenna mode scatter depends on the mismatch between the antenna and its load, but the maximum value can be equal to the RCS of a flat plate with the same area as the effective aperture of the antenna. Reducing the antenna mode scatter is accomplished mostly by ensuring that the antenna and its load are well matched, so that energy is absorbed in the load rather than reradiated. Out of the band in which the antenna is to operate, frequency-selective surfaces can sometimes be used to ensure that only in-band energy reaches the load, making the job of keeping the antenna and load well matched more manageable.

Structural scatter must be handled the same way that RCSR is handled for any platform: through shaping and selective application of RAM. The goal is to eliminate specular returns in the threat sector. Nonspecular RAM may be applied where necessary to reduce diffraction and traveling wave returns. However, if the treatment is being applied to a transmitting antenna, the power handling capabilities of the RAM used must be sufficient to withstand the effects of the expected incident field.

Although the relationship between antenna scattering and gain has been known for a long time, only recently have significant analytical and experimental efforts been focused on antenna RCS and RCSR. For that reason the area is rapidly evolving. This chapter provides only a snapshot of a technology that will likely change significantly over the next few years. Nevertheless, the fundamental principles of antenna RCS presented will continue to hold, even as the applications technology evolves.

REFERENCES

[1] Sinclair, G., E. C. Jordan, and E. W. Vaughn, "Measurement of Aircraft Antenna Patterns Using Models," *Proc. IRE,* Vol. 35, December 1947, pp. 1451–1467.

[2] King, D. D., "Measurement and Interpretation of Antenna Scattering," *Proc. IRE,* Vol. 37, July 1949, pp. 770–777.

[3] Appel-Hansen, J., "Accurate Determination of Gain and Radiation Patterns by Radar Cross-Section Measurements," *IEEE Trans. on Antennas and Propagation,* Vol. AP-27, September 1979, pp. 640–646.

[4] Collin, R. E., "The Receiving Antenna," *Antenna Theory,* Part 1, R. E. Collin and F. J. Zucker (eds.), McGraw-Hill, New York, 1969, pp. 123–133.

[5] Carpenter, D. D., and D. R. Anderson, "Antenna Scattering Theory Study Final Technical Report," Document No. DO-0164, TRW Military Electronics and Avionics Division, April 29, 1988.

[6] Hansen, R. C., "Relationships Between Antennas as Scatterers and as Radiators," *Proc. IEEE,* Vol. 77, May 1989, pp. 659–662.

[7] Green, R. B., "The General Theory of Antenna Scattering," Report 1223-17, Antenna Laboratory, Ohio State University, November 30, 1963.
[8] Montgomery, C. G., R. H. Dicke, and E. M. Purcell, *Principles of Microwave Circuits,* McGraw-Hill, New York, 1948.
[9] Kahn, W. K., and H. Kurss, "Minimum Scattering Antennas," *IEEE Trans. on Antennas and Propagation,* Vol. AP-13, September 1965, pp. 671–675.
[10] Williams, N., "The Radar Cross-Section of Antennas— An Appraisal," Military Microwaves Conf. Proc., Brighton Metropole Convention Center, June 1986, pp. 502–508.
[11] Green, R. B., "The Effect of Antenna Installations on the Echo Area of an Object," Report 1109-3, Antenna Laboratory, Ohio State University, September 1961.
[12] Garbacz, R. J., "The Determination of Antenna Parameters by Scattering Cross Section," Report 1223-10, Antenna Laboratory, Ohio State University, November 1962.
[13] Amitay, N., and M. J. Gans, "Design of Rectangular Horn Arrays with Oversized Aperture Elements," *IEEE Trans. on Antennas and Propagation,* Vol. AP-29, November 1981, pp. 871–884.
[14] Lindsey, J. F., "Radar Cross-Section Effects Relating to a Horn Antenna," *IEEE Trans. on Antennas and Propagation,* Vol. 37, February 1989, pp. 257–260.
[15] Feinstein, J., et al., "UHF and Microwave Devices," *Electronic Engineer's Handbook,* D. G. Fink (ed.), McGraw-Hill, New York, 1975, p. 9–10.
[16] Lambert, K. M., R. C. Rudduck, and T. H. Lee, "A New Method for Obtaining Antenna Gain from Backscatter Measurements," *IEEE Trans. on Antennas and Propagation,* Vol. 38, June 1990, pp. 896–902.
[17] King, H. E., and J. L. Wong, "Helical Antennas," *Antenna Engineering Handbook,* 2nd ed., R. C. Johnson and H. Jasik (eds.), McGraw-Hill, New York, 1984.
[18] *IEEE Standard Dictionary of Electrical and Electronics Terms,* 3rd ed., ANSI/IEEE Std 100-1984, IEEE, New York, 1984, p. 547.
[19] Newman, E. H., and D. Forrai, "Scattering from a Microstrip Patch," *IEEE Trans. on Antennas and Propagation,* Vol. AP-35, March 1987, pp. 245–251.
[20] Pozar, D. M., "Radiation and Scattering from a Microstrip Patch on a Uniaxial Substrate," *IEEE Trans. on Antennas and Propagation,* Vol. AP-35, June 1987, pp. 613–621.
[21] Ajioka, J. S., "Frequency-Scan Antennas," *Antenna Engineering Handbook,* 2nd ed., R. C. Johnson and H. Jasik (eds.), McGraw-Hill, New York, 1984, p. 19-7.
[22] Tittensor, P. J., and M. L. Newton, "Prediction of the Radar Cross-Section of an Array Antenna," *Sixth Int. Conf. Antennas and Propagation,* London, April 1989, pp. 258–262.
[23] Mittra, R., C. H. Chan, and T. Cwik, "Techniques for Analyzing Frequency Selective Surfaces— A Review," *Proc. IEEE,* Vol. 76, December 1988, pp. 1593–1615.
[24] Pous, R., and D. M. Pozar, "A Frequency-Selective Surface Using Aperture-Coupled Microstrip Patches," *IEEE Trans. on Antennas and Propagation,* Vol. 39, December 1991, pp. 1763–1769.
[25] Paris, D. T., and F. K. Hurd, *Basic Electromagnetic Theory,* McGraw-Hill, New York, 1969, pp. 414–418.
[26] Kefalas, G. P., and J. C. Wiltse, "Transmission Lines, Components, and Devices," *Radar Handbook,* M. I. Skolnik (ed.), McGraw-Hill, New York, 1970.
[27] Jackson, D. R., "The RCS of a Rectangular Microstrip Patch in a Substrate-Superstrate Geometry," *IEEE Trans. on Antennas and Propagation,* Vol. 38, January 1990, pp. 2–8.
[28] Pozar, D. M., "Radar Cross-Section of Microstrip Antenna on Normally Biased Ferrite Substrate," *Electronics Letters,* Vol. 25, August 3, 1989, pp. 1079–1080.

Chapter 11
RCS Measurement Requirements

E. F. Knott

11.1 MEASUREMENT OBJECTIVES

There are five basic reasons for conducting RCS measurements, and each has a different influence on the way the measurements are carried out. The five reasons are

- Acquire understanding of basic scattering phenomena;
- Acquire diagnostic data;
- Verify system performance;
- Build a database;
- Satisfy a contractual requirement.

Some of these may seem to overlap, but the overlapping depends on the particular objective of the measurement program. This will become more clear in a moment.

The most basic of the five reasons is the pursuit of an understanding of fundamental scattering phenomena. Despite the completeness of electromagnetic theory, some phenomena remain incompletely described, such as the scattering from the base of a cone. In the early 1960s, for example, Keller applied his new geometric theory of diffraction to the scattering from a cone [1,2]. Remarkable for its "cookbook" simplicity, this theory accurately predicted the radar return from a cone, except over certain angular sectors.

Bechtel noted errors in Keller's 1961 paper and gave the corrected results in 1965 [3]. Nevertheless, comparisons between measurements and predictions made with the correction formula still showed disagreement, a problem reiterated by Bechtel in 1969 [4]. Blore conducted an experimental study of blunted cones [5]

and noted the failure of the theory, but offered no explanation of the failure nor of a correction that might be applied.

Using an equivalent current approach, Burnside and Peters sought to improve the predictions by accounting for multiple diffraction across the base of the cone [6]. This was done for axial incidence only, and Knott and Senior extended the analysis to additional aspect angles [7]. Although this resulted in an improvement, it appears that even higher order terms must be included. Knott and Senior conducted a careful series of measurements of right circular cones, measured with and without a pad of absorber cemented to the base, demonstrating the importance of the multiple cross-base diffraction effects [8].

Not all these researchers carried out measurements, but the evaluation of the theory depended on comparisons between measurements and predictions, and during the 12-year span between Keller's comparisons and the measurements by Knott and Senior, the pursuit of a single idea motivated the measurements: *a better way to explain diffraction by the base of a cone.* This is merely one example of measurements conducted to understand a basic scattering phenomena.

A second reason for making RCS measurements is to acquire diagnostic data. Although many of the cone measurements were used to gauge the validity of a theory being applied, it is doubtful that any of the data were used to assess the elusive cross-base interaction terms. For that purpose, it would have been necessary to isolate only those interactions, a difficult task considering the physical sizes of the targets being tested.

However, more often than not, diagnostic testing currently means the isolation of "flare spots" on major weapons systems. One way to accomplish this is to somehow conceal or cover up a suspected flare spot and compare measurements made with and without such treatment. The difference in the two patterns is an indication of the intensity of the flare spot, provided its contribution to the total return is not masked by contributions from the remainder of the target. Typically, all suspected flare spots must be treated and measurements made selectively, with each flare spot exposed one at a time.

The identification of flare spots can be made considerably easier with the use of specialized instrumentation, as mentioned in Chapter 13. Certain radars are designed to emit chirped pulses, and when the data are processed, a radar "image" of the target can be produced. The image is a plot of the intensity of the scattering as a function of range and cross range, and the resolution of some instrumentation systems is as good as 6 in. or better. Images can be produced for virtually any aspect angle, and their diagnostic value lies in identifying the major scattering centers as functions of aspect angle.

The third reason for RCS measurements is to verify that the RCS performance of a system, a new aircraft, for example, meets specified levels. Although, as we have seen, several computer programs may be capable of predicting that performance, no prediction technique is all-encompassing and all codes have limitations.

Therefore, it is often necessary to test the final, integrated weapons system, although portions of the system already may have been treated or investigated individually.

Verification of system performance must often be carried out at several threat frequencies, and the measured performance must be compared with specifications. This can be done informally at a contractor's facility, but the government may demand that the measurements be performed at a national facility, such as RATSCAT.

The fourth reason for conducting RCS measurements is to build a database. Although this is an admirable objective, the database seldom satisfies the needs of a *true* database. This is because the users of the data often reduce an entire pattern to a single number used to develop evaluation criteria or to assess a sensor's target response. Moreover, the comparison of patterns from one target with those of another often becomes an excruciating task because of the sheer human effort required to sift through a multitude of patterns. As a result, the patterns are often reduced to a handful of numbers compared by computer algorithms, and the very necessary injection of human judgment is bypassed. The patterns making up a large and significant database are usually examined but once, if that, and then collect dust in a repository until the documentation itself crumbles to dust.

The fifth and final reason for RCS measurements is for contractual purposes. Although this may be necessary to ensure compliance with specifications, for example, some program managers order the measurements simply as insurance against criticism. RCS measurements are time consuming and costly, and they should never be ordered offhandedly.

Thus, the five basic reasons for conducting RCS measurements range from a purely academic endeavor to a purely contractual requirement. Whatever the reason, it influences (or should influence) the design of the experiment and the way in which the experiment is carried out. Measurements made for scientific purposes are best conducted when a single parameter is carefully varied from one test to another. The next test in the sequence is often based on a running analysis of previous tests, hence, the direction taken by experimental work often cannot be predicted in advance. By contrast, database measurements usually follow a rigid test plan, and as such, there is little opportunity to explore unusual or inexplicable results. Therefore, the purpose of the measurements should always govern the design of the experiments and thereby precisely determine what information is to be collected.

11.2 TYPES OF RCS MEASUREMENTS

The purpose of a radar cross section measurement range is to collect radar target scattering data. Usually — but not always — the range user requires farfield data, corresponding to the case where the target is located far enough from the instru-

mentation radar that the incident phase fronts are acceptably flat. Many times this requirement can be satisfied only on an outdoor range. On the other hand, many research and development programs can and should be conducted indoors in anechoic chambers.

Whether indoors or outdoors, an RCS measurement facility must have at least five features:

1. An instrumentation radar capable of launching and receiving a microwave signal of sufficient intensity;
2. Recording instruments, either analog or digital or both, for saving the information;
3. A controllable target rotator or turntable;
4. A low background signal environment, including "invisible" target support structures, to minimize contamination of the desired signals;
5. A test target suitable for the measurements.

These five basic elements can, of course, be embellished and augmented by other equipment and instrumentation. The instrumentation used indoors may be different from that used for outdoor measurements, as shown later in this chapter.

Once the decision has been made to pursue a measurement program, a suitable facility must be found. As we shall see, several large corporations have their own facilities, and the selection of a test range is automatically bypassed. Sometimes, however, corporate facilities may not be suitable, and negotiations will have to be conducted with outside agencies. Occasionally, a contractor must use the RATSCAT range in New Mexico as a contractual requirement.

Negotiations usually involve the specification of a set of test conditions and a test matrix, and the prospective range will submit a bid. Unfortunately, some customers are not sure of their own test requirements, and they may ask for more test conditions than they actually need. In many cases, the prospective range offering its services can suggest alternate conditions that satisfy the customer's needs at lower cost.

There are four basic kinds of RCS measurements, classified according to pulse width (long or short) and coherence (coherent or noncoherent). In long-pulse measurements, the transmitted pulse is wide enough to bracket the target by a comfortable margin. As such, the measured RCS characteristics are identical to those that might be measured using a CW radar. In fact, many measurements made in indoor chambers are CW measurements because chamber reflections complicate the design of pulsed radar receivers.

The pulse width for short-pulse measurements is usually narrow enough that range resolutions on the order of 10 to 20 cm can be achieved, which is typically a fraction of the total target length. Narrow pulses are useful for diagnostic measurements, but they impose system bandwidth requirements that are not always easy to meet. The sensitivities of short-pulse systems are less than those of long-pulse systems because of the additional bandwidth required for the system.

Long- and short-pulse measurements are easiest to make if the radar system is noncoherent. Noncoherent systems sense only the amplitude of the return signal, whereas coherent systems sense the in-phase and quadrature components (I and Q) of the received signal. The phase angle of the return signal can be computed from the I and Q components. However, coherent radar instrumentation is more costly than noncoherent instrumentation.

Most RCS measurements of interest are for the monostatic case, for which the radar transmitter and receiver are sensibly at the same point in space. For the bistatic case, the transmitter and receiver are separated, sometimes at angles as high as 180° (see Fig. 11.1). In fact, some radars employ separate transmitter and receiver antennas, even for monostatic measurements, hence a nonzero bistatic angle is subtended at the target. However, the antennas are usually so close to each other that the measurement is indistinguishable from the monostatic case.

Modern radio frequency generation technology makes it possible to synthesize high-resolution measurements using frequency-stepping techniques. The RF source is typically a low power, voltage-controlled oscillator phase-locked to a highly stable quartz crystal oscillator. Thus, a controller or computer can step the radar frequency across a specified band at specified intervals. The output of the low power source usually must be amplified (with a traveling wave tube amplifier, for example) to achieve the necessary transmitted signal level. The received data are typically recorded on magnetic tape or hard disk for subsequent processing. Software processing is then used to create radar imagery.

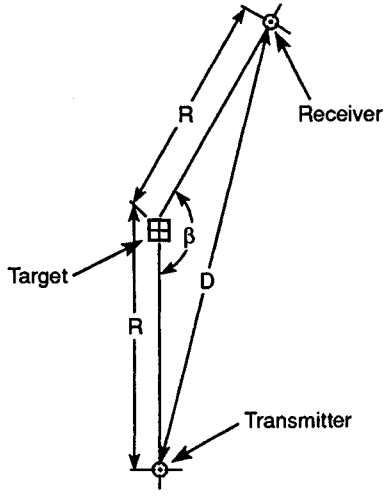

Figure 11.1. Bistatic measurement layout.

The following list includes almost all the types of radar signature measurements of interest:

- Conventional (amplitude only)
  - monostatic
  - bistatic
- High resolution
- Coherent (amplitude and phase)
  - glint
  - doppler
- Frequency stepped, coherent
  - radar imagery
  - high resolution

Examples are shown in Figures 11.2 through 11.7.

Figure 6.22, discussed earlier, is an example of a conventional long-pulse, amplitude-only measurement. The ordinate is the radar cross section of the model in dB relative to a square meter, and the abscissa is the yaw angle as measured between the longitudinal aircraft axis and the radar line of sight. The rectangular plot is a very common form of displaying measured patterns.

No bistatic patterns are available for display here. In practice, the transmitter and receiver are set up at the appropriate bistatic angle, and their positions relative to the target are held fixed. The target is rotated for this fixed transmitter-receiver orientation, generating a pattern similar to the monostatic RCS pattern. However, the greater is the bistatic angle, the fewer the pattern scintillations.

Figure 11.2 is an example of high-resolution RCS measurements and how they may be displayed. This particular form of presentation is often called a *waterfall plot,* and the information could easily be displayed as a contour chart. It shows the amplitude of the return as a function of range and target aspect angle, and as judged from the plot, the range resolution for this particular chart was of the order of 15 cm. The target itself appears to have been about 10 ft long. If the chart is examined very carefully, it can be seen that the returns from the near end of the body moved away from the radar, and those from the far end moved toward the radar, as the aspect angle increased. At the higher aspect angles, the returns become larger. This form of display helps isolate the scattering centers on the target, but the display itself cannot be generated unless the instrumentation radar is designed for short-pulse generation and reception.

A coherent radar system allows the measurement of the relative phase of the signal return in addition to the amplitude. Figure 11.3 is a typical phase plot, showing the phase of the return as a function of target aspect angle [9]. Because the phase angle is constrained to lie between 0 and 2π (or between $-\pi$ and $+\pi$ rad), the recorded phase variation has a "sawtooth" behavior, as shown in the upper diagram. Under many circumstances, the phase plot can be "unwound" to account for the number of complete 2π cycles undertaken by the total phase excursion. This is shown in the lower diagram of Figure 11.3. Interestingly enough,

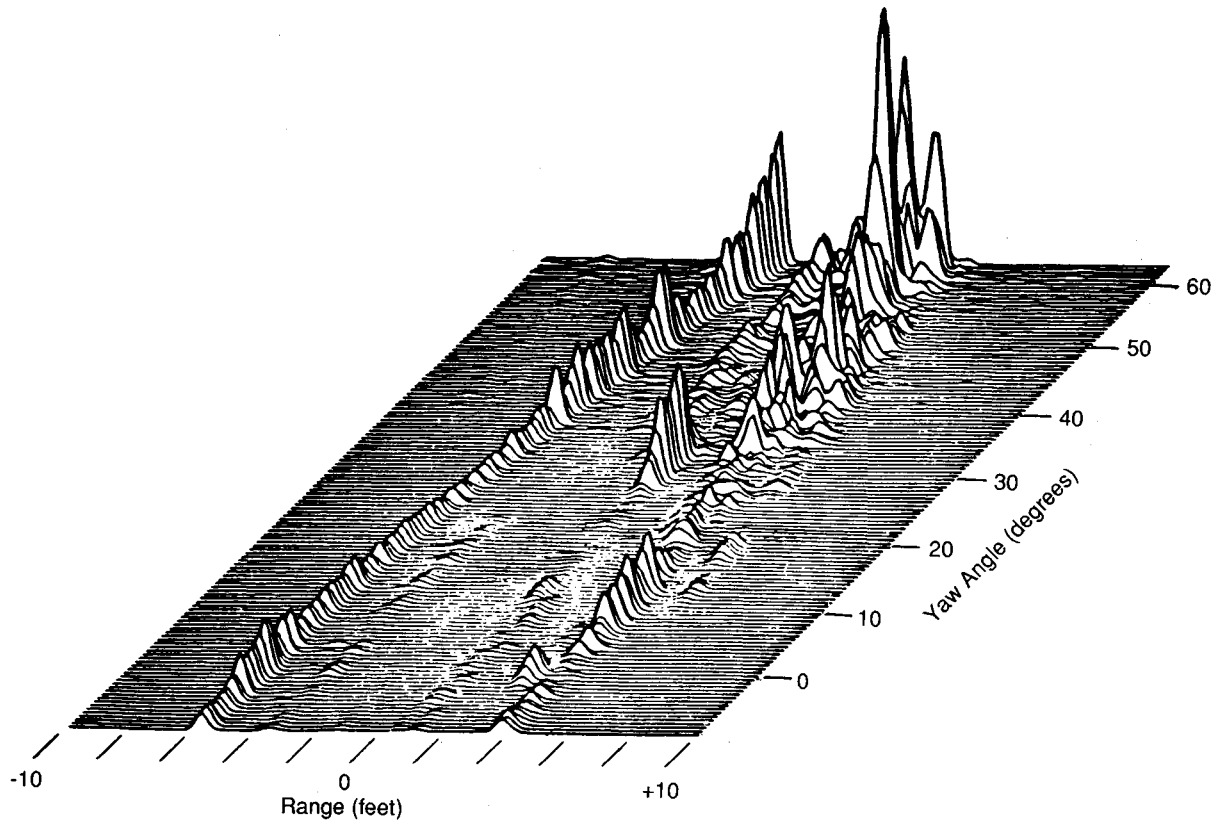

Figure 11.2. High-resolution RCS data.

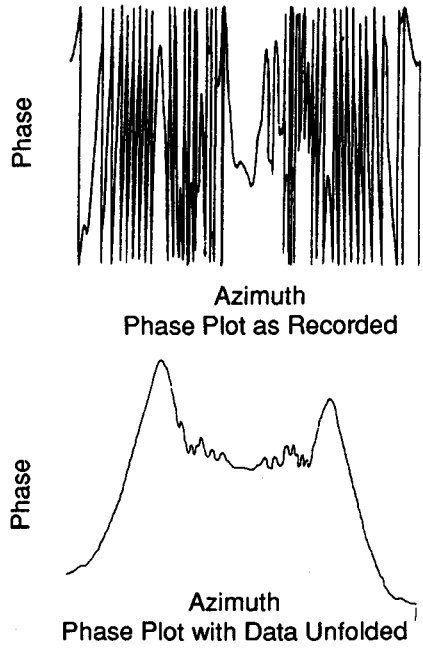

Figure 11.3. Phase plots (from [9]).

the lower diagram is skewed, suggesting that this particular target had not been placed symmetrically on the axis of rotation or that the phase behavior has not been adequately "unwound." In many cases, especially over aspect angles where the phase changes rapidly, it cannot be established whether the change in the phase angle from one aspect to the next was positive or negative. The pattern of Figure 11.3 suggests that the target apparently had a pair of echo sources, one of which was dominant over two-thirds of the pattern.

Phase information, as plotted in Figure 11.3, is useful only for diagnostic, interpretive reasons. By processing the coherent data collected by a suitably designed radar, we can calculate the target glint. Glint is the cross-range location of the effective center of target scattering and is due to the way the individual contributions of all the scatterers add together. It is possible for the apparent center of scattering to lie beyond the physical constraints of the target.

A glint pattern can be generated by plotting a quantity proportional to the rate of phase charge with respect to the angle of rotation. Such a pattern is shown in Figure 11.4, and the data can be collected by using a single antenna. However, it is not essential that a coherent radar be used. Glint patterns can also be generated

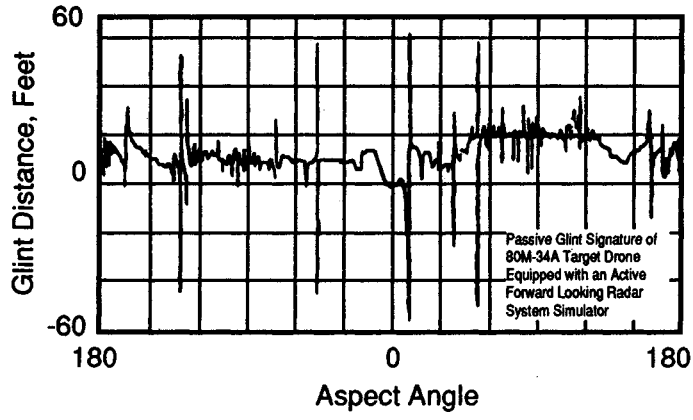

Figure 11.4. Target glint pattern (from [9]).

by measuring the phase difference between the signals received by a pair of antennas stationed at some known distance apart.

A coherent radar system is essential for recording the doppler characteristics of targets that have exposed moving parts. After coherent detection in the receiver, the received IF signal must be compared with a coherent reference IF signal so as to separate the negative doppler shifts from the positive ones. The process generates data such as shown in Figure 11.5, recorded for a two-engine, propeller-driven aircraft [10]. Note that the dominant doppler frequency changes with aspect angle, and the spectral lines are not symmetrical with respect to the dominant frequency.

It also requires a coherent radar system to generate radar imagery, an example of which is shown in Figure 11.6. The radar must transmit a chirped pulse in which the radar frequency is swept linearly across an interval in the radar band, preferably at least 1 GHz wide. A sample of the transmitted signal is mixed with the received signal, and the spectral content of the detected output serves to locate the individual scatterers in range.

The received data must be recorded and processed to generate the plot shown in Figure 11.6. This involves a two-dimensional Fourier transformation, as was accomplished in the early days with optical processing techniques. However, the availability of frequency stepping technology makes it possible to accomplish the same effect by using digital processing techniques. The resolution in range depends on the frequency intervals used, and the resolution in cross-range depends on the angular width of the aspect angle sector over which the data are processed.

As suggested by the display of Figure 11.6, the engine of the drone is a large scatterer. Other important scatterers are the pods on the wing tips and the empennage at the rear of the fuselage. This plot was generated by using data collected

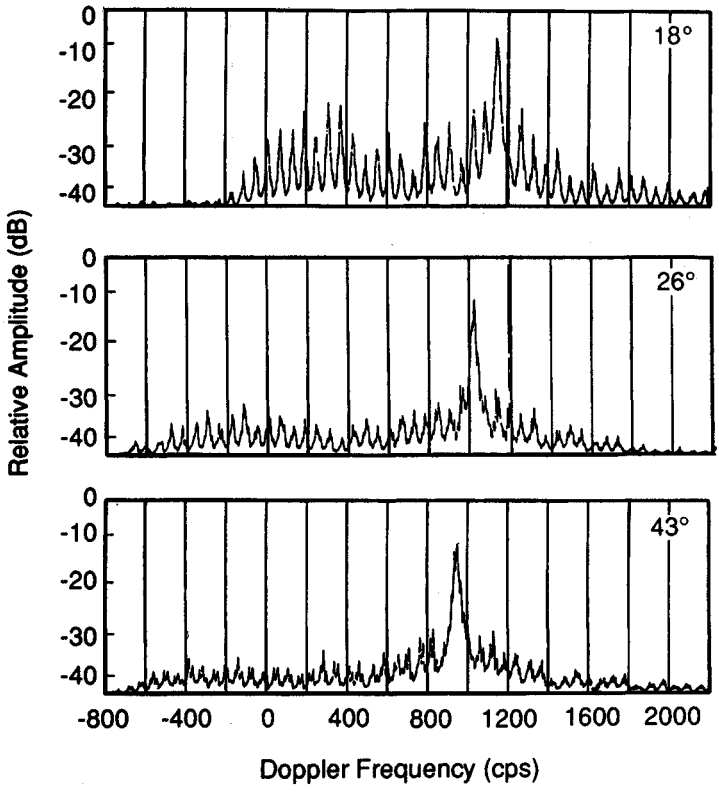

Figure 11.5. Measured doppler spectrum of a propeller-driven aircraft (from [10]).

for a narrow angular sector centered on the nose-on aspect angle. Images can be created for any other aspect angle, of course, but the relative strengths of the scatterers will be different.

11.3 THE FARFIELD REQUIREMENT

Equation (1.11), the formal definition of radar cross section, states that the distance r between the radar and target must become infinite. The reason for this is to eliminate any distance dependence in the RCS characteristics. The limiting process essentially requires that the target be illuminated by a plane wave, yet the wave incident on a target in practical measurement situations is nearly always a spherical wave, due to the finite separation between the target and the instrumentation radar. As a matter of practical interest, we may wonder how "spherical" the

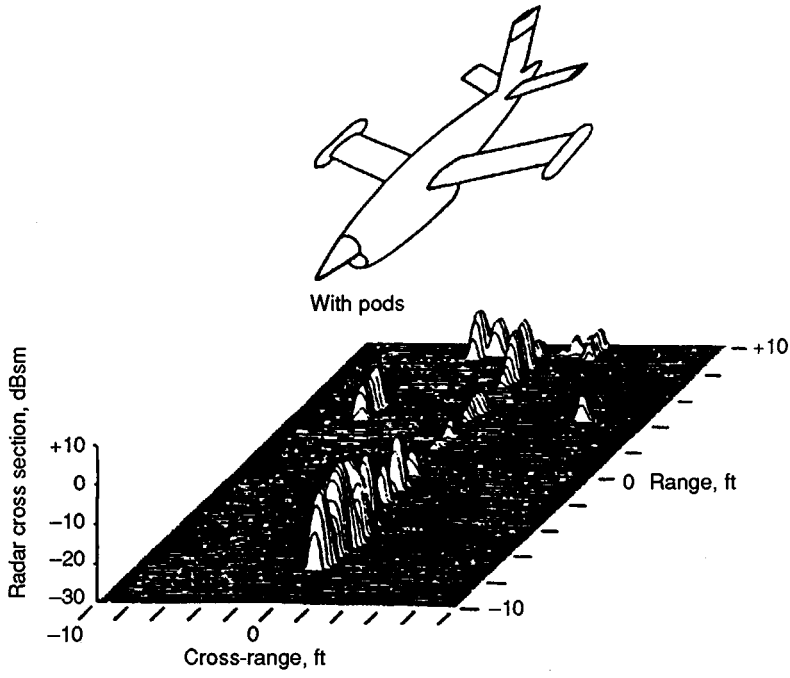

Figure 11.6. Radar imagery in range and cross range.

incident wavefronts can be while still being reasonably good approximations of a plane wave.

One way to resolve the question is to assume the radar to be a point source and examine the deviation of the incident phase fronts from perfect uniformity over an aperture having the same width as the target. From the geometry of Figure 11.7, we can find the distance h in terms of the range r and the transverse width d:

$$h = r\left\{1 - \left[1 - \frac{d}{2r}\right]^2\right\}^{1/2} \tag{11.1}$$

which, assuming $d \ll 2r$,

$$h \simeq \frac{d^2}{8r} \tag{11.2}$$

Therefore, the phase of the incident wave at the center of the target is different from the phase at the extremes of the target by the amount kh. If we arbitrarily

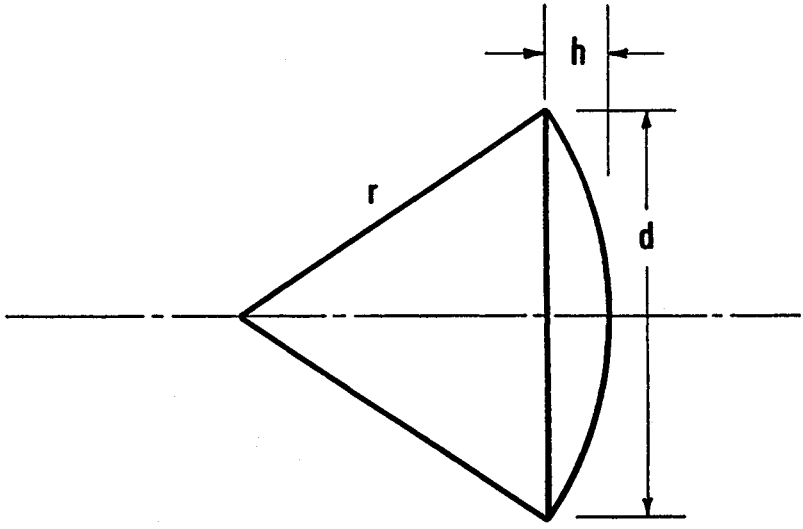

Figure 11.7. Phase deviation over a transverse aperture due to spherical incident wavefronts.

require that this phase deviation be less than $\pi/8$ rad (22.5°), then the familiar farfield condition is obtained:

$$r \geq 2\frac{d^2}{\lambda} \tag{11.3}$$

Note that the requirement $kh \leq \pi/8$ is quite arbitrary and does not consider any accuracy statements about the measurement of the far scattered field. Despite its arbitrary nature, (11.3) has become a widely used yardstick for "ensuring" the accuracy of farfield RCS measurements.

Kouyoumjian and Peters considered the range requirement in far greater detail [11], including the axial decay in incident field strength as well as the transverse phase deviation. They concluded that a measurement can "be optimized with respect to minimum range and maximum sensitivity by a proper choice of antenna size," although no general statements could be made on the accuracy of the measurements. Knott and Senior later conducted a numerical study of errors on very simple targets [12] and assigned values to the errors; and they concluded that even the standard farfield criterion of (11.3) might not be sufficient for certain classes of targets. Some of the large errors noted were due to nearfield cancellation of the returns from various scattering centers on the targets that would not, in fact,

occur for true plane wave incidence. Nevertheless, (11.3) remains a good rule of thumb for establishing the minimum range at which targets should be measured.

A plot of the farfield distance prescribed by (11.3) is given in Figure 11.8 for a variety of frequencies and target size. The farfield requirement is not too hard to meet at low frequencies, but typical radar sensitivities make it hard to meet at high frequencies. For example, a 10 ft target should be measured at a range of not less than 200 ft at 1 GHz, but not less than 2000 ft at 10 GHz.

In some cases, the radar sensitivity is not good enough for the target to be measured at the farfield distance, and a considerably smaller range may have to be selected to ensure adequate received signal strengths. For very simple targets, such as cylinders and flat plates, the first symptom of nearfield effects is the filling in of nulls and the reduction of the amplitudes of the sidelobes [13]. As the range is further shortened, the nulls become entirely filled in, the sidelobes become shoulders in the pattern, and the main lobe amplitude decreases significantly.

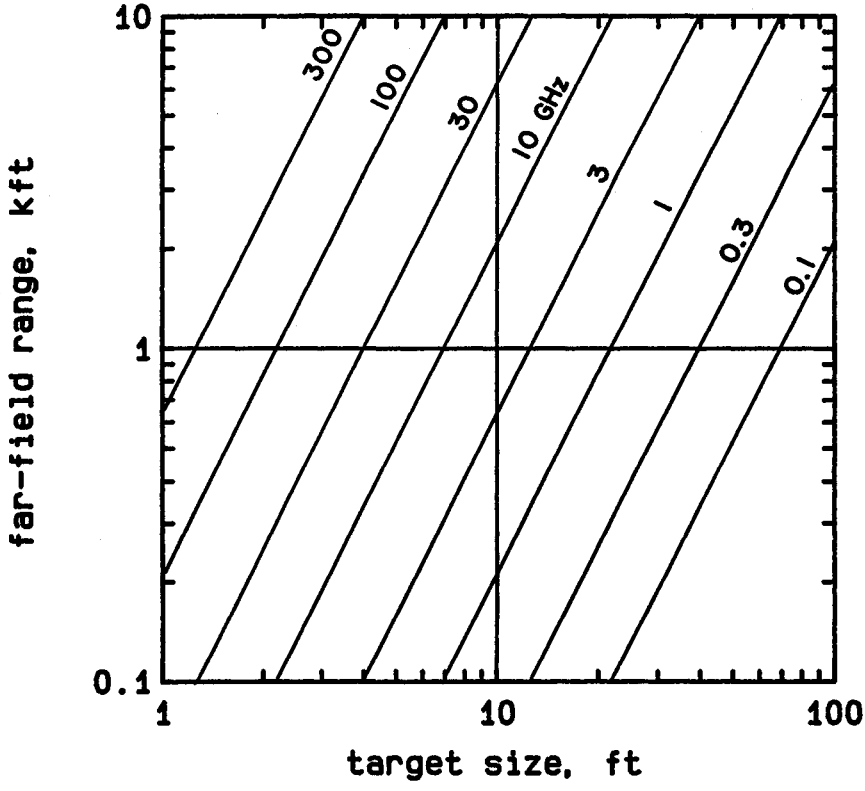

Figure 11.8. The farfield distance.

The effects of measuring more complex targets at less than the standard farfield distance are less obvious. At high frequencies, each feature of the target scatters energy more or less independent of other target features, and each feature is usually significantly smaller than the overall target. Such features, which could be tail fins, engine intakes, nose tips, or other target surfaces, could each be in the far field with respect to its own characteristic size, although the composite target may not be. Therefore, the amplitude of the scattering from each feature, as well as the locations of peaks and nulls in its own pattern, are less sensitive to the measurement range. The primary effect of a nearfield measurement in this case is the slight shifting of the lobes and nulls of the composite pattern as compared with the true farfield pattern. Therefore, measurements performed at less than the standard farfield distance can often be defended.

Moreover, high accuracy in RCS measurements is often unnecessary unless the data are to be used as the basis for detailed analytical work or the development of scattering predictions. Often, users of test data require only median values, which are statistical representations of the return over an aspect angle window that is moved across the RCS pattern. Many other approximations of physical processes are made that could be worse than the error in the RCS data. Therefore, when determining how important the nearfield effects may be, the end use of the data should be considered.

Finally, it should be pointed out that the transverse target dimension figures predominately in calculating the farfield range. In the nose-on or end-on aspect angle region, the transverse target dimension of missiles and slender bodies allows the target to be brought much closer to the radar. Because the end-on returns are usually much smaller than the broadside return, this helps to improve the RCS sensitivity of the system. RCS patterns in the broadside aspect angle region can usually be measured comfortably at a greater range. Although it requires two separate measurements and "splicing together" separate RCS patterns valid over separate aspect angle regions, this is often the price that must be paid for high-quality data.

11.4 GREAT CIRCLE VERSUS CONICAL CUTS

One of the decisions faced by a program manager is whether to specify great circle or conical "cuts." A *cut* refers to an RCS pattern recorded for a complete revolution of the target in azimuth. Whether or not that cut is a great circle trajectory or a cone trajectory depends on the tilt angle of the axis of rotation, as shown in Figure 11.9.

In Figure 11.9, the radar is off to the left, out of view of the diagram, and the target axis of symmetry lies in the plane of the figure. The left-most diagram shows the target mounted on a support column in a level flight attitude and in the

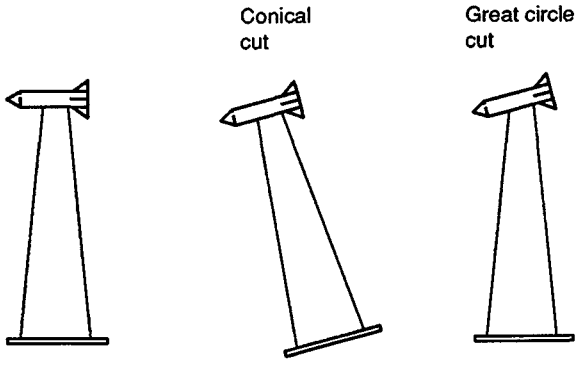

Figure 11.9. Axis of rotation is tilted for conical cuts.

nose-on viewing position. As the target turntable is rotated through 360°, the radar line of sight remains in the yaw plane of the target.

If the axis of rotation is now tilted toward the radar, as shown in the center diagram, the radar line of sight maintains a constant angle with respect to the axis of rotation. Consequently, the line of sight sweeps out a cone centered on the yaw axis (which is perpendicular to the yaw plane) as the target is rotated. This generates the conical cut referred to previously, and is indicated schematically in Figure 11.10. In Figure 11.10, α is the angle by which the axis of rotation is tilted toward the radar.

If the axis of rotation is brought back to perpendicular to the line of sight, as shown in the left-most diagram of Figure 11.9, the cone angle flares out to a

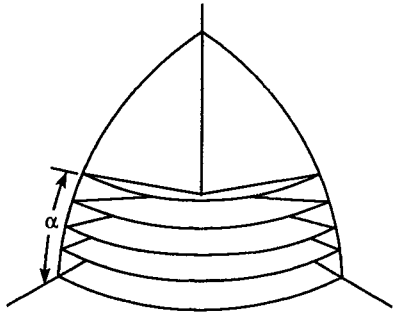

Figure 11.10. Conical cuts; α is the angle by which the rotator is tilted toward the radar.

disk, which is a special case of the conical cut. This represents a great circle cut, and it remains a great circle cut, even if the target is pitched atop its support column. As shown in the right-most diagram of Figure 11.9, the axis of rotation remains at right angles to the line of sight, even if the target is pitched.

However, the plane of the great circle cut is inclined to the yaw plane, as suggested in Figure 11.11. The angle of inclination is the pitch angle α, not to be confused with the tilt angle used for conical cuts. The difference between a collection of conical cuts and a collection of great circle cuts can be grasped from a comparison of Figure 11.10 and 11.11. Whereas all the great circle cuts intersect at the broadside aspect in the yaw plane, conical cuts never intersect. Thus, conical cuts provide more coverage of the spatial pattern of a target than great circle cuts.

Great circle cuts can provide the same kind of coverage, however, if combinations of pitch and roll are used. If the target is rolled instead of pitched, the great circle cuts intersect along the roll axis (longitudinal target axis), instead of along the pitch axis. Clearly, the line of intersection between the yaw plane and a great circle cut can be "walked" around the yaw plane using a sequential selection of roll and pitch angles.

However, there are more practical considerations in the selection of great circle or conical cuts. The top of the foam support column must be custom-built to fit the surface contour of the target. This distributes the target weight over the contact area between the target and the support column, and it minimizes distortion of the column at the load-bearing surfaces. The fabrication of these support "saddles" represents a considerable cost investment in an RCS test program and so should be minimized.

The use of conical cuts helps to do this. Using a single support saddle, all that needs to be done to index from one conical cut to another is to change the tilt angle of the axis of rotation. The use of great circle cuts, on the other hand,

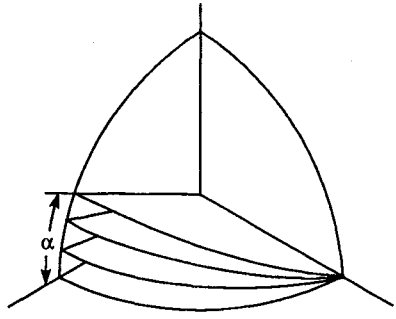

Figure 11.11. Great circle cuts; α is the pitch angle of the target as mounted on the support column.

requires that the target be dismounted from the column, the support saddle exchanged for one designed for a different pitch and roll angle, and the target remounted on the new saddle. In addition to the fabrication of a costly collection of support saddles, great circle cuts entail a great deal of target handling. This represents a significant portion of the test program cost, especially for large targets.

Nonetheless, there are limitations to the otherwise advantageous use of the conical cut measurement configuration. Target support columns cannot support large bending movements required when the rotation axis is tilted, although they can support considerable vertical loads in the upright position, and there is the risk of the target sliding off the support column. Therefore, the cone angle is limited in practice to about 30° at best.

Despite the disadvantages of the great circle cuts, it is possible to make measurements at much higher angles above the yaw plane than with conical cuts. Indeed, a target can be mounted on its nose or tail with its axis along the vertical, whereupon a great circle cut includes viewing angles to look directly down on, and directly up to, the target. This is impossible with conical cuts.

Therefore, the conical cut is the favored method of target rotation for RCS measurements because much more data can be collected in much less time at less cost than a great circle cut can provide. Nevertheless, the great circle cut can provide high-elevation viewing angles not possible with the conical cut. In the end, the test objectives, test requirements, and cost dictate whether great circle or conical cuts are used or whether combinations of the two are necessary.

11.5 TARGET SUPPORT STRUCTURES

Several target support techniques are available. These include

- Low-density plastic foam columns;
- High-strength nonmetallic support lines;
- Absorber-covered metal pylons;
- Hollow solid plastic support columns.

Of these four, the first has been the most widely and successfully used, and the last has been the least used. Each has its advantages and limitations. Plastic foam columns offer relatively low background return when properly designed and used, but have limited weight-handling qualities. Suspending targets from filamentary lines is attractive because support lines can have smaller returns than foam plastic columns, but target attitude is hard to control. Metal pylons have excellent load-bearing properties, but require special attachments to mate with the target, and the target may have to be disfigured at the mounting point. Moreover, an absorber-covered metal pylon increases the electromagnetic target-to-support coupling and is very expensive. Hollow plastic columns are probably useful over only a narrow frequency range, where the front and rear column returns can be "tuned" to cancel

each other; but, outside these narrow limits, the returns can be nearly as high as those of a bare metal column.

Freeney [14] discusses the four methods, but offers no data by which to assess the echo properties of metal or solid plastic support columns. He presents data for dielectric support lines and some data for foamed plastic columns. However, more detailed information on foamed plastic support is available in other references.

As pointed out by Plonus [15], and Senior, Plonus, and Knott [16], the radar echo of a plastic foam column can be ascribed to two mechanisms. One is a reflection from the surface of the column, and the other is a "noncoherent" volume return due to millions of tiny internal scatterers (i.e., the cell structure). The volume contribution is conceptually independent of the shape of the column, and therefore is irreducible; that is, column tuning can have no effect. Plonus's result for the noncoherent return is

$$\sigma = \frac{\pi}{2} t^2 k^4 a |\epsilon_r - 1|^2 V \tag{11.4}$$

where t is the mean cell wall thickness, a is the mean cell radius, V is the volume of the column, and ϵ_r is the dielectric constant of the base polymer from which the foam is made. Note that the theoretical noncoherent return rises with the fourth power of the radar frequency.

Extensive experiments conducted at the University of Michigan [17] did not confirm this prediction. Because of the very small returns from test blocks and ogives, the measured data showed large deviations. Nevertheless, a value of about -58 dBsm per cubic foot seems typical of the averaged data for several classes of plastic foams, as suggested in Table 11.1. This table summarizes the properties of five foam materials examined in [17]. It should be appreciated that the properties listed in Table 11.1 were obtained by measurement of a few small samples. The densities of foams are controllable, hence foams can be made with properties different from those listed in the table.

The expandable bead foam and the three types of styrofoam are made of a polystyrene polymer. The expandable bead foam is easily molded to complex shapes and is found in ice chests and as a packaging cushion for fragile products of all kinds. The effective dielectric constant of the material depends on the material density: the lower the density, the lower the dielectric constant.

The styrofoams listed in Table 11.1 are used in the construction industry as insulation materials. They are heavier and much stronger than the expandable bead foams, and one of the materials (styrofoam FR) has a very small cell structure. Were it not for the fact that foams are unavailable in large monolithic blocks, they would be candidates for target support structures.

The polyurethane foam is nearly twice as heavy as the expandable bead foam, but has about the same strength. The polyurethanes are useful because of their

Table 11.1
Properties of Some Plastic Foams [17]

	Material	*Expandable bead foam*	*Styrofoam* FB*	*Styrofoam* DB*	*Styrofoam* FR*	*Polyurethane*
Base polymer	Type	Polystyrene	Polystyrene	Polystyrene	Polystyrene	Polyurethane
	Density, lb/cu ft	66.50	66.50	66.50	66.70	70.00
	Dielectric constant	2.55	2.55	2.55	2.55	2.06
Foamed product	Cell size, in	0.125	0.025	0.057	0.011	0.019
	Density, lb/cu ft	1.150	1.760	1.800	1.970	2.040
	Elastic modulus, psi	733	2061	1692	3000	710
Noncoherent returns, dBsm/cu ft	Theoretical	−25.8	−47.5	−35.8	−54.6	−50.4
	measured	−58.0	−56.7	−57.4	−60.1	−60.2

*Registered trade name, Dow Chemical Company, Midland, Michigan.

fine cell structure—despite their reduced strength—pound-for-pound, compared with styrofoam. Polyurethane columns are attractive because they can be molded in one piece, eliminating the need to bond several smaller pieces together to build a single column.

Figure 11.12 is a theoretical prediction of the radar return from a conical support column 12 ft tall having a dielectric constant of 1.04, which is typical of a styrofoam or polyurethane foam. The column diameter at the top was taken to be 1 ft and the base diameter was assumed to be 2 ft, hence the sides of the column were slanted at 2.4° with respect to the column axis.

To obtain the plot of Figure 11.12, the radar was assumed to be in a horizontal plane intersecting the column at its midpoint, and the column was tilted away from the vertical either toward or away from the radar by the amount shown on the abscissa. The two large peaks of the pattern are due to specular reflections from the front and rear slanted column surfaces, which occur when those surfaces are perpendicular to the radar line of sight. The rear surface is visible through the front surface because the foam is nearly — but not perfectly — transparent. The return from the rear surface attains its peak value when the column is tilted away from the radar. These peaks have amplitudes of about −12 dBsm, an objectionable value for some targets.

Figure 11.13 is a measured pattern for a polyurethane column of the same size used to generate Figure 11.12. This pattern was recorded at the McDonnell-Douglas Microwave Test Facility near Palmdale, California. Differences between the measured and predicted patterns are due to the fact that the actual column was slightly bent and its base was shielded from the incident radar wave because it was mounted on a turntable below ground level.

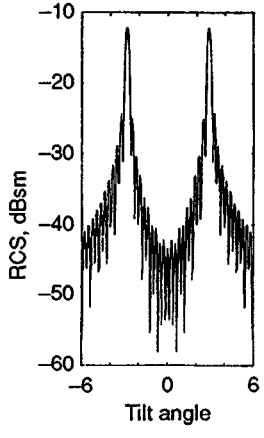

Figure 11.12. Theoretical return from a 12 ft conical support column at a radar frequency of 10 GHz.

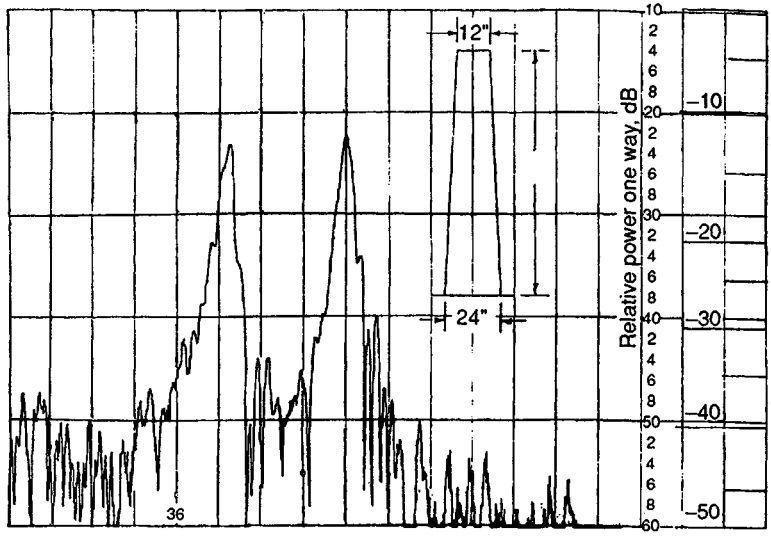

Figure 11.13. Measured pattern of a 12 ft polyurethane support column.

The specular reflections from the sides of the column occur for any azimuth angle because the conical column is circularly symmetric. However, if the column is fabricated with a diamond cross section, as shown in Figure 11.14, the specular reflections can be confined to four narrow azimuth regions. This is particularly

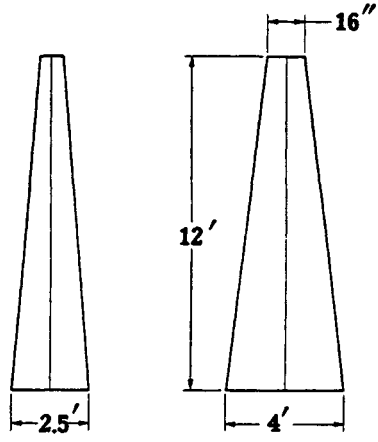

Figure 11.14. Support column with diamond cross section.

useful when measurements are to be made of targets whose returns are very small in the nose-on region. If the support column of Figure 11.14 were to be oriented with an edge facing the radar, and tilted either toward or away from the radar, only the noncoherent return would be recorded. The two peaks shown in Figure 11.12 and 11.13 for the conical column would be absent. The diamond-shaped design is used routinely by the Boeing Company.

An effect in reflectivity measurements that is not always appreciated is the amount of contact area between the target and its support column. As shown by Knott and Senior [17], this area should be minimized to reduce distortion in the incident field in the vicinity of the target. The wave propagates slower within the foam material than it does in the surrounding air, but the electromagnetic boundary conditions require that the phase fronts be continuous across the boundary. After propagating over a considerable length of the interface, the phase fronts just inside the surface will lag behind those just outside, and they will become distorted to maintain continuity. Although the distortion is due to the phase front lag, the amplitude of the wave will also become distorted because energy must propagate in a direction normal to the phase fronts.

Minimizing the contact area is not always possible because of conflicting strength and safety requirements, but experimenters should be aware of the effects of extended target-to-support interfaces. It is possible to design "finger cradles" that will support light objects, much as an experienced waiter or waitress carries a large tray with one hand. Unfortunately, such fragile support cradles can seldom be used by heavy targets or for guyed targets.

A modern improvement (mid-1970s) in target support technology is the absorber covered metal pylon. The pylon is shaped much like the wing of a commercial jet liner, as shown in Figure 11.15, and is mounted on a heavy base fixture embedded in the ground. The pylon has sharp leading and trailing edges and is inclined toward the radar. The return from an inclined edge is very small (theoretically zero), and the inclination angle is selected to minimize interactions between the pylon and the ground.

The pylon is stationary to preserve the favorable edge-on orientation toward the radar, and the target rotator is mounted at the top of the pylon. In practice, the target must be modified so that the rotator fits inside the target. Thus, the rotator and the top of the pylon are concealed by the target itself. Unfortunately, this means that the target now has a hole in it that would not exist except for this mounting requirement.

The hole itself can alter the radar signature of the target, hence some means must be devised for concealing the hole or suppressing the effect. Absorbers and special shields can be designed for this purpose. The metal pylon cannot be used to support operational missiles and aircraft, unless a military agency can be found that is willing to sacrifice a production vehicle.

RATSCAT has installed a 75 ft pylon (at pit 7), and an even taller one (95–120 ft) has been used an advanced measurement site (see Chap. 12). The load-bearing

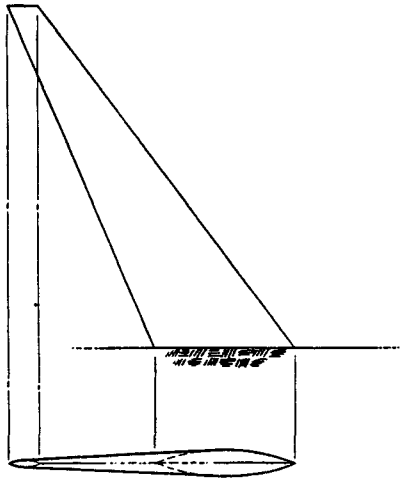

Figure 11.15. Absorber-covered metal support pylon.

capabilities of these structures are not known, but they are probably limited to a few thousand pounds. Light developmental model targets will probably be used almost exclusively, and operational vehicles will continue to be measured with conventional foam support column technology.

The relatively large returns from foam support columns can also be circumvented by suspending the target from overhead with strong nonmetallic lines. When implemented outdoors, this requires the erection or availability of a pair of towers straddling the target region. The towers should be placed outside the range gate and well outside the main lobe of the radar antennas, as in Figure 11.16. A sling or harness must be made to support the target, which must be guyed to a rotator to control the aspect angle of the target (see Fig. 11.17). The support lines must be strong enough to bear the tension of these guy lines in addition to the weight of the target. The line tension is usually such that the target will oscillate in aspect angle even with the rotator moving at constant speed. It requires calm conditions, very careful attention to target alignment, and a great deal of patience to obtain RCS patterns by using this suspension technique, but the effort may often be well worth it. The experimenter should be aware that all the guy lines to the rotator will be normal to the incident wave at two points in a 360° azimuth cut, and their returns, although small, will likely be visible in the recorded data.

The suspension line support technique has been considerably refined by the Boeing Military Airplane Company in the fabrication of its millimeter wave modeling facility [18]. The model is suspended in a harness of fine lines between a pair of turntables, one in the floor and one in the ceiling of an indoor anechoic chamber. The turntables are "slaved" together, and the support lines are wound on small

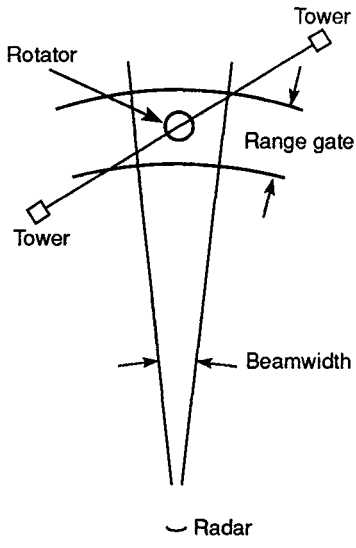

Figure 11.16. Tower placement for target suspension over the target rotator.

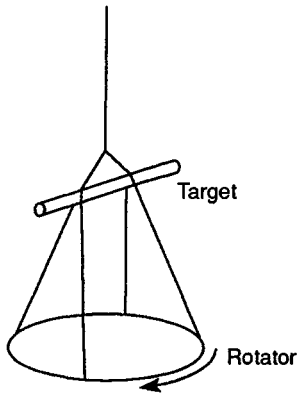

Figure 11.17. A method of target suspension.

reels driven by stepping motors. Under computer control, the turntables can be rotated and the stepping motors activated to simulate dynamic target motion. A television monitor in the control room gives the range operator a continuous view of the target motion.

11.6 TARGET-GROUND INTERACTIONS

No matter where we install our test target for measurement — in an indoor anechoic chamber or an outdoor range — the ground, floor, or walls of the facility may be close enough to the target for undesired interactions. As shown in Figure 11.18, they involve bistatic scattering from the target to the ground or floor, a reflection back to the target, and then a second bistatic scattering from the target back to the instrumentation radar. If the test range is adequately instrumented, some of these interactions may be purged from the test data; in other cases it may be impossible to reduce them. Whether or not we can suppress them, it is prudent that we be aware of them and therefore alert to possible data contamination (errors due to the interaction).

One way to reduce data contamination due to interactions under long-pulse operation is to shorten the range gate to the minimum possible width. By *long* we mean pulses of sufficient duration that the contributions from all the target scatterers are contained in the received echo signal. When that is the case, the measured target scattering characteristics will be the same as those measured with CW instrumentation operated at the same frequency. The use of the minimum possible pulse width is counter to long-pulse operation, however, and in some cases the two requirements cannot be simultaneously satisfied.

If we represent the downrange target length by L, the time required for energy to travel the length of the target and back again is $2L/c$, where c is the speed of light. If the target were, say, 20 ft long, the range gate would therefore have to be at least 40 ns wide to allow all target echoes to be bracketed within the

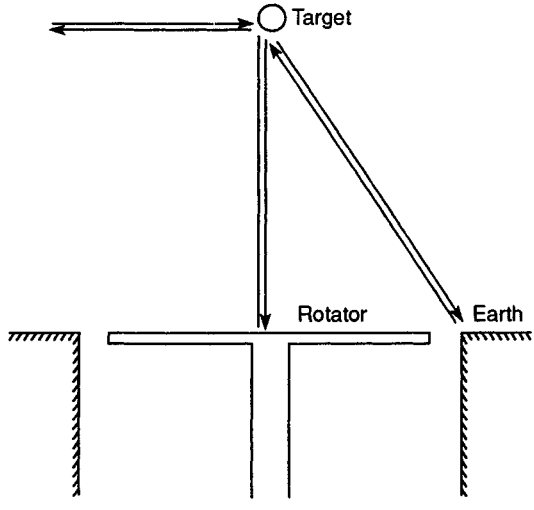

Figure 11.18. Target-rotator interactions.

measured echo. The range gate would have to be somewhat wider than this, however, if for no other reason than to avert errors due to inadequate signal sampling at the very leading and trailing edges of the pulse. It would be difficult, moreover, to accomplish the fine adjustment demanded in the timing of the pulse, as its leading and trailing edges would have to be precisely synchronized (timed) to coincide with the echoes from nearest and farthest target extremes.

Therefore, we typically use a range gate 50 to 100% wider than the absolute minimum dictated by the maximum length of the target. In the case of our 20 ft target, the width would range from 60 to 80 ns. But even then there is no guarantee that measured target echo would correspond to truly long-pulse conditions, especially for those targets that support multiple scattering interactions. An example is the traveling waves that rattle back and forth along a thin wire, as discussed in Chapter 6. Although this may represent an extreme case, the attempt to include in the echo pulse multiple interactions between scattering centers on the target itself might demand pulses as much as 10 times wider than might be suggested by the physical length of the target.

Indeed, our instrumentation radar cannot discern multiple interactions between target scattering centers from interactions between the target and the ground. It merely responds to whatever echoes are present in the return pulse, and we, as designers and operators of the test range, must decide which to include and which to exclude from the receiver. If we choose a range gate width that is 10 times the length of the target, for example, our pulse would be 400 ns wide and would not exclude contributions from the floor or ground due to the bistatic interactions mentioned earlier. To do so would demand that we physically separate the target from the ground by five times the target length, implying that we must install our 20 ft target atop a 100 ft tall support fixture. This is clearly out of the question for almost all test ranges.

However, the interaction may not be as strong as we might suspect. Although the scattering from real-world test objects may be very complex, as we saw in Chapter 6, it is possible to estimate the strength of the interaction between the target and the ground for a few simple cases. Using some of the analytic prescriptions discussed in Chapter 5, for example, Knott developed estimates of the strength of the interaction for flat plates, cylinders, and spheres [19].

The orientation of these objects with respect to the incident wave and the ground is shown in Figure 11.19. The vertical flat plate in the upper diagram is a rectangular one presented broadside to the radar, with one edge parallel to the ground at some height h above it. The vertical dimension of the plate is w, and the interaction mechanism investigated is the bistatic diffraction from the lower edge. The same diffraction mechanism is also investigated for the plate in the center diagram, except that the plate there lies in a horizontal plane (parallel to the ground). The lower diagram shows the interaction mechanism for a cylinder or sphere. For all but the sphere, the length of these objects is L, measured perpendicular to the plane of the figure.

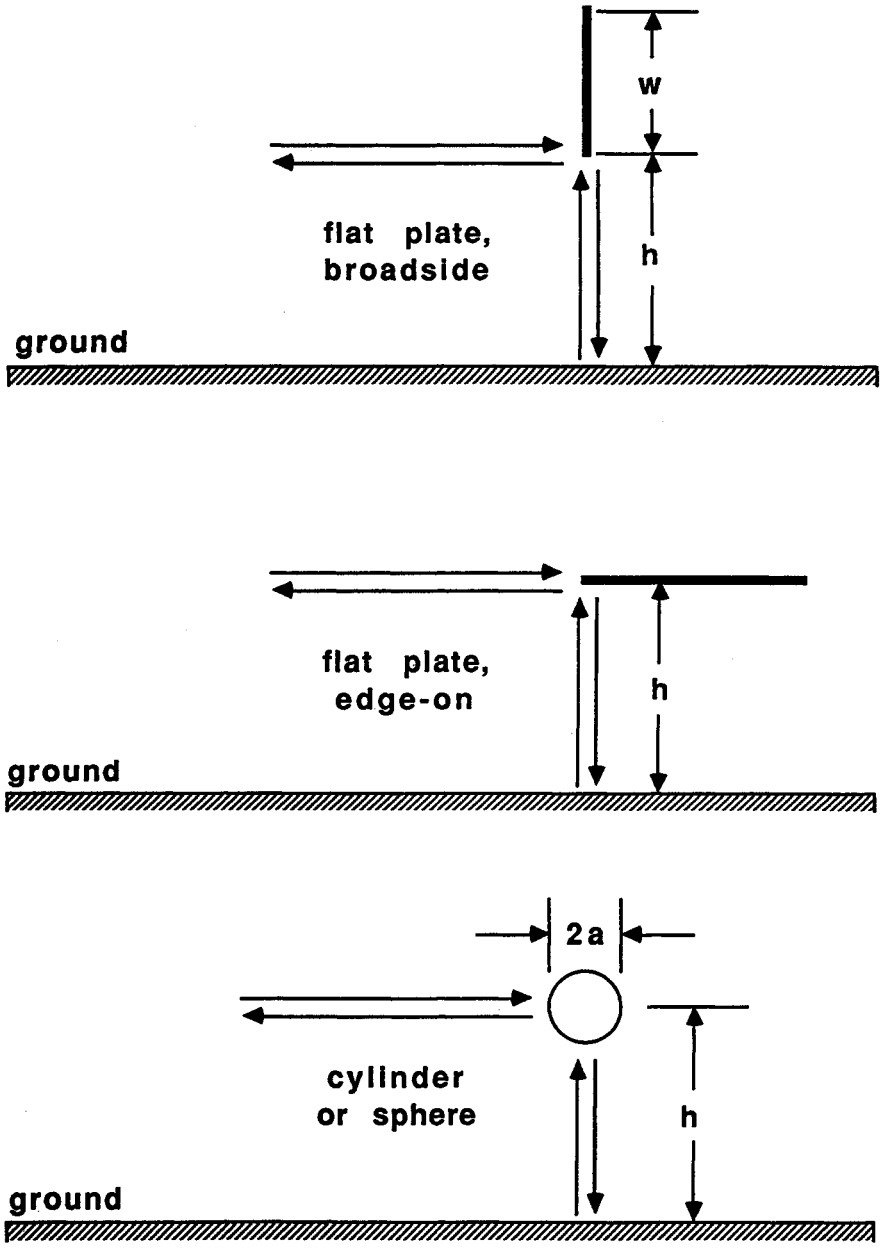

Figure 11.19. Three simple ground interaction mechanisms (from [19]. Copyright 1993 Van Nostrand Reinhold; reprinted with permission).

Table 11.2 lists the analytical results of Knott's calculations. Shown there are the strengths of the direct backscattered fields of the objects and the strength of the bistatic contribution due to the ground interaction, both measured at the radar when the objects are illuminated by a plane wave. The fourth column lists the ratio between the two returns for the four cases, which is probably a more useful characterization of the interaction effect. Note that the height, h, of the object appears in the denominators of the four bistatic formulas.

Figure 11.20 is a graphical display of the behavior listed in Table 11.2. The abscissa for all except the sphere is the ratio of the target height above ground normalized with respect to the length of the object perpendicular to the line of sight to the radar. The sphere's height is normalized with respect to the radius of the sphere. In all four cases, the relative power decays inversely with the square of the height of the object above the ground.

Because the normal-incidence echo from a flat plate rises with the square of the frequency, whereas the bistatic interaction echo is independent of frequency, the interaction effect drops rapidly with increasing electrical size, as indicated by a comparison of the three traces in the upper left diagram. The relative strength of the interaction decreases directly with frequency (not inversely with the square), for a cylinder, on the other hand. Therefore, the relative interaction effect increases as the cylinder becomes electrically larger, as seen from a comparison of the three traces in the diagram at upper right.

This is not the case for the horizontal plate in the chart at lower left nor for the sphere in the chart at lower right. The bistatic interaction scattering and the direct backscattering in both cases are independent of frequency, and a single trace serves to characterize the relative strength for each. Note that the interaction for

Table 11.2
Comparison of Direct and Interference Terms (from [19])

Target	*Backscattered field strength*	*Bistatic field strength*	*Power ratio, (bistatic/backscatter)*
Flat plate, normal incidence	$\frac{wL}{\lambda R_o}$	$\frac{L^2}{4\pi^2 h R_o}$	$\frac{L^2}{(2\pi k w h)^2}$
Flat plate, edge-on (hor. pol.)	$\frac{L}{2\pi R_o}$	$\frac{L^2}{4\pi^2 h R_o}$	$\frac{L^2}{(2\pi h)^2}$
Cylinder, broadside incidence	$\sqrt{\frac{a}{2\lambda}} \cdot \frac{L}{R_o}$	$\frac{aL^2}{4\lambda h R_o}$	$\frac{kaL^2}{\pi(4h)^2}$
Sphere	$\frac{a}{2R_o}$	$\frac{a^2}{8hR_o}$	$\frac{a^2}{(4h)^2}$

L = length of cylinder or plate perpendicular to line of sight
h = height of test object above ground
w = width of plate
a = radius of cylinder or sphere
k = $2\pi/\lambda$, the wavenumber
R_o = distance from the radar to the test object

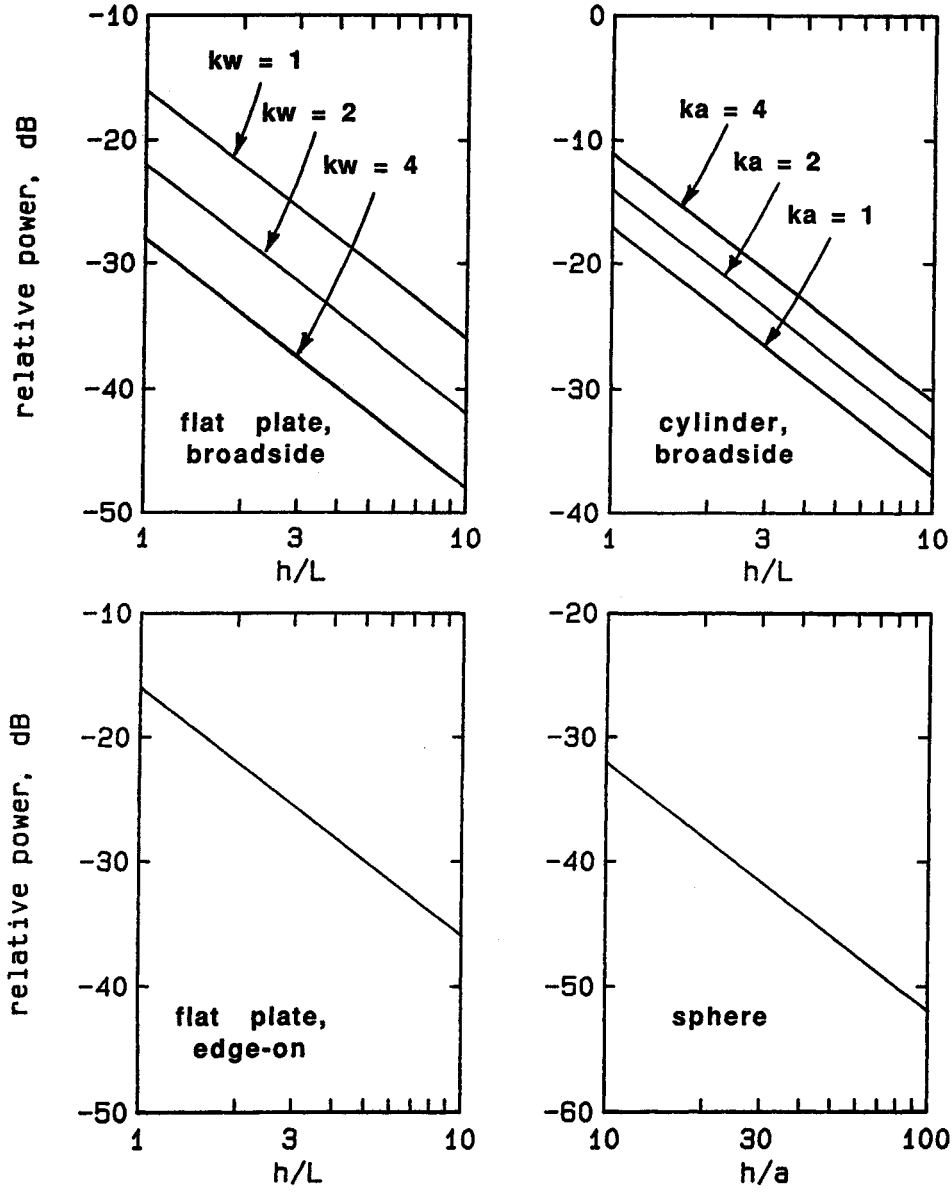

Figure 11.20. Target-ground interaction estimates. Ordinate is the magnitude of the interaction echo normalized to that of the backscattering echo to be measured. Charts for the horizontal flat plate hold only for horizontal polarization (parallel to the ground), and those for the cylinder and sphere are for optically large bodies (independent of polarization). For all except the sphere, L is the target length parallel to the ground and perpendicular to the direction of incidence (from [19]. Copyright 1993 Van Nostrand Reinhold; reprinted with permission).

the sphere is charted for a normalized height variation 10 times greater than for the cylinder and flat plate cases.

The charts show that the interaction becomes small (less than −30 dB) for all but the smallest plates when they are mounted on test fixtures at least four plate lengths above the ground. The interaction for the sphere is less than −30 dB if the sphere is mounted at least five sphere diameters (10 radii) above the ground. Depending on its electrical diameter, however, we may have to install a cylinder considerably more than 10 cylinder lengths above the ground if we are to keep the relative interaction return below −30 dB.

These comparisons give us some guidelines for possible data contamination due to ground interactions, even if devised for relatively simple objects for special orientations. We must bear in mind, however, that all four test objects were assumed to be metallic, and that no allowance has been made for any stealth features that may be present. It is altogether possible that, although stealthy target features may reduce the backscattered echo, they may not have much influence on the bistatic scattering. If this is the case, it may be far more challenging to choose the appropriate target height (if, indeed, that height is selectable) for stealthy targets than for the simple bodies listed in Table 11.2. Consider, for example, the leading edge of the B-2 stealth bomber, which we may model at low frequencies as the edge of a plate.

If this edge is a reasonably good conductor, if we demand a measurement accuracy of not less than 1 dB when the edge is presented perpendicular to the line of sight, and if the ground interference mechanism were the only source of possible error, that mechanism would have to be at least 20 dB weaker than direct return from the edge. The lower left chart of Figure 11.20 suggests that the wing leading edge should be held nearly two wing lengths above the ground for such accuracy. Because the leading edge of the B-2 bomber is about 100 ft long, this amounts to a target height of more than 200 ft.

Even if the edge were metal, which it is not, the indicated height outstrips the capability of any known static test range. If the edge is not metal, but instead shielded by some kind of radar absorber, and if the bistatic scattering from the edge is not reduced by the same amount that the backscattering is reduced, the problem is even worse. In this event we would have to install the wing on a support fixture some five times the length of the wing (500 ft), a device we feel safe in predicting will never be built.

This absurd example illustrates the skepticism that must be exercised in the appraisal of estimates like those charted in Figure 11.20. Although the estimates may be close to the truth, we are not obliged to take the course they indicate. Indeed, it can be argued with reasonable conviction that this particular ground interaction mechanism disappears when the leading edge is slightly skewed with respect to the line of sight to the radar. If we are content to assess the leading edge echo at perpendicular incidence by other means, we may very likely collect

quite accurate test data (uncontaminated by ground interaction effects) for nearly all other aspect angles of incidence. This being the case, we may well choose more practical target heights for our tests.

There is no practical height for the B-2, however. The only way we can measure large, operational targets is on a dynamic test range, where the target supports itself. Although dynamic RCS measurements are much more costly than static measurements, some test ranges have been designed and instrumented for this very purpose. Although not much has been published about them, Knott discusses some of the design requirements of dynamic test ranges [19, Chapter 11].

11.7 CALIBRATION

It is possible to solve the radar range equation developed in Chapter 2 for the radar cross section σ, measure all the remaining parameters appearing in the equation, and then process the measured test data to produce patterns of the RCS as a function of aspect angle. Indeed, with little modification, this is the procedure that must be used in the measurement of RCS on almost all dynamic test ranges. When we measure the RCS on a static range, however, we usually take advantage of the stationary nature of the range.

For example, the range to the target never varies, and the target always remains in the main lobe of our instrumentation antennas. And even though the ground plane of the static RCS test range may have some influence on the details of the incident wave illuminating the target (see Chapter 12), we may account for these factors in our calibration procedure. This is because the static test range allows us to use a *substitution* procedure.

The calibration of the radar system demands that the system output, even if nothing more than a stream of digital bits (0s and 1s), be rigidly related to the echo signals received from the target. Most of the time we produce two streams of bits, one stream being those collected with the test target in place and the other those from a reference target measured at a different time. The two data sets need not contain the same number of entries, but the latter set must contain, as a minimum, the information we need to convert the target bit-stream to absolute RCS, usually in dBsm.

To do so we must account for the relationship between the input and output of the instrumentation system, and for the relationship between the input (or output) and the absolute RCS the input signal represents. The first relationship is called the *transfer function* of the radar, and it may be established by the measurement of its output when known signals are fed into it. Although the transfer function is, in general, a complex function having real and imaginary parts (gain and phase shift), we need only the real part for noncoherent (amplitude only) instrumentation radars. (Indeed, this is the only part of the transfer function the

noncoherent radar is capable of furnishing us.) By virtue of the linearity of Maxwell's equations, we need only one point in the second relationship to relate the strength of the received signal to the RCS of the target. Thus, a complete calibration of the tests demands a measurement of the transfer function and measurement of some quantity, ideally a constant, that can be used to convert the output stream of bits to an absolute RCS.

The transfer function of a simple, monochromatic radar is a list of one or two sets of numbers (one if noncoherent, two if coherent) by which we relate the output to the input. We typically measure it by varying the amplitude of a known input signal over a discrete range of levels, sometimes only 1 dB apart, but sometimes as coarse as 5 or 10 dB, and recording the radar output indication, whether analog or digital, at each step. If the radar is a coherent one, we measure, in addition, the shift in the phase of the output signal compared to that of the input signal. The result of such a measurement is indicated schematically in Figure 11.21.

Both input and output are measured at discrete intervals, and the two curves sometimes contain no more than a dozen or so data points. The amplitude relationship is monotonic and nearly linear, making it very easy to interpolate between measured data points. And even if the phase shift through the system is not linear, it too varies relatively slowly, making interpolation reasonably accurate. Therefore, output can be related to input relatively simply.

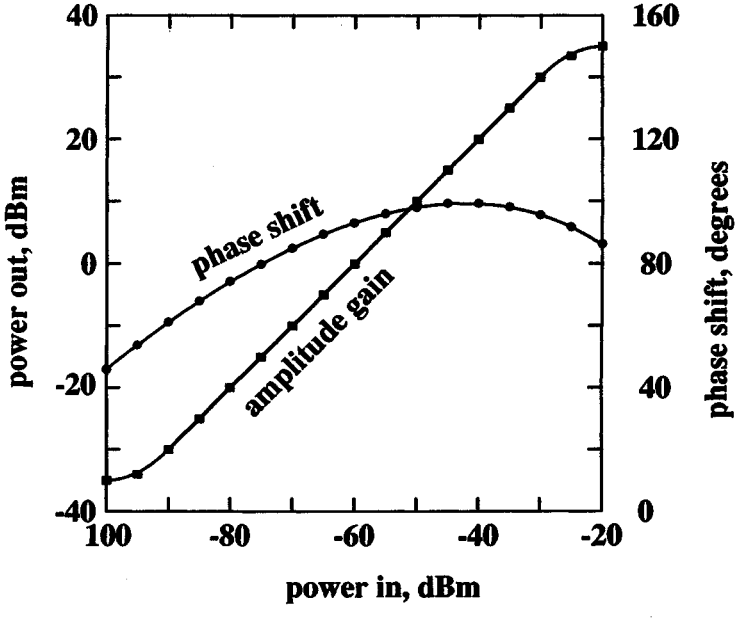

Figure 11.21. Schematic representation of instrumentation system transfer function.

Although most instrumentation radars are *not* monochromatic, the receiver IF is, and a single transfer function measured at some mid-band RF serves to characterize the system response for all. When digital processing is not easily implementable, as is the case of some vintage analog radars still in operation, we simply examine the gain curve to determine if the linearity is acceptable, deviating by, say, not more than 0.5 dB from a straight line drawn between the knees of the curve near saturation and near the receiver noise level. Depending on the cost and the accuracy demanded of our tests, we may elect to continue with measurements even if the deviation is greater than this. If we are awash with resources and time, on the other hand, we may elect to replace the IF amplifiers, if not the entire receiver.

Those of us with the resources and foresight to implement a digital data collection system need not worry about replacing the receiver or tolerating a departure from linearity. We can easily interpolate between measured values on the transfer curve, and if we are particularly resourceful, we can even manage, by means of software and hardware interfaces, to have the data collection system record its own transfer function. Because we typically operate the radar at several frequencies over the band, particularly those radars devoted to the collection of radar imagery, we often demand that our automatic calibration software measure and record the transfer function at each frequency we plan to use in testing. It is therefore not atypical to collect and store several kilobytes of instrumentation calibration data in the form of measured transfer functions.

Establishing the relationship between the output bit stream and the actual target RCS demands more than software. Having the relationship between input and output at hand, we are obliged to relate at least one point on the input/output curves to the signals scattered by the object atop our support fixture. To do this we typically remove the unknown target from the support structure and substitute one whose echo is known or can be calculated with confidence. We almost always select one of the simple targets listed in Table 6.1.

We use this substitution method because at any single frequency, the only quantity that varies in the radar range equation is the RCS of the target. At that frequency the wavelength is fixed, as are the gains of our antennas and the range to the target. This combination of parameters can be represented by a single constant. When we install a calibration target whose RCS is known with reasonable accuracy, and when we note the output signal generated by that echo (or the bit combination representing it), we have, in effect, measured the constant of proportionality. Because this constant is actually a function that depends directly on frequency, and indirectly on frequency via the frequency dependence of the gains of our transmitting and receiving antennas, we must measure it for each of the frequencies in our emitted waveform.

This task may be routinely performed by a few lines of code embedded in our calibration software. Indeed, if we have adequately anticipated the varying demands of the typical user, we will have provided that user the option of specifying

the type, size, and orientation of his calibration device, and we will compute in our software its theoretical RCS and thereby establish for the duration of the test the value of the calibration constant. Moreover, we will do this for all the frequencies to be used in the test program. What we cannot do in software is install the target, a task we delegate to the user alone.

Calibration on an outdoor test range is not a simple task, primarily because of the time and equipment required. When performed by substitution of a known test object for the target to be measured, it usually takes not less than an hour, and often more. If the test range is equipped with a mobile target shelter, it must be powered up and positioned over the target support fixture, often a 15 min process. Lifting slings must then be looped under or attached to the target, the target lifted off the support structure, and the calibration scatterer installed in its place. The range must be cleared of the shelter and all other ancillary equipment before the calibration can be completed.

If the range is equipped with mobile cranes instead of a self-propelled servicing structure, lifts must be driven to the support structure along with the cranes, and the target must be lowered onto a dolly that can be trundled off the range along with all the other equipment in this array of service vehicles. Once the calibration data have been collected, the deployment of this array of heavy equipment is repeated in reverse. Vehicles or gantries are driven back to the support structure, the calibration target is removed, the test target is reinstalled, and the test sequence is continued, usually for a different set of frequencies or for a new target configuration.

Because of the time required for this target substitution, we do it only when we think it necessary — but rarely less than once per eight hr shift. And when we do, we schedule it, when possible, to coincide with those occasions when the target must be removed or reconfigured for the next set of measurements called out in the test plan, thereby making the most efficient use of active range time.

11.8 SUMMARY

Although several kinds of RCS measurements were discussed in this chapter, no known test facility is equipped to conduct all of them. The most common test requirement is the collection of backscattering patterns, and, in the few instances when bistatic data are needed, they must usually be collected on an outdoor range. The most common backscattering requirement is for amplitude-only patterns, but the collection of coherent data (phase as well as amplitude) for the generation of radar imagery is rapidly becoming routine. Long-pulse (low-resolution) data were once the most common kinds of patterns recorded, but the versatility of the chirped (stepped-frequency) waveform now makes it possible to electronically synthesize quite narrow pulses. A coherent radar is demanded for the measurement of target glint and doppler characteristics.

Whatever the radar and the kinds of data to be collected, we demand that the target be illuminated by a wave whose phase varies across the target zone by

22.5° or less. Although this particular value may seem arbitrary, it seems to yield data accuracies of 1 dB or better when the phase variation does not exceed it. When we invoke this minimum phase-taper requirement, we find that the range to the target must exceed a value known as the farfield distance. Despite the usefulness of the farfield criterion, there are times when we must violate it in the interest of achieving adequate system sensitivity, such as when we must measure particularly stealthy test objects.

We discussed foam columns, strings, and the steel pylon used as target support structures. Although a plastic foam support structure is generally regarded to be invisible, it is not. The return from such a column rises with the frequency and the volume of the structure, due to the random scattering by the cells in the foam. Strings offer a lower residual echo than foam columns, but only if the string is never perpendicular to the line of sight. String support systems are very difficult and clumsy to work with, but one large airframe manufacturer uses them routinely in one of its test facilities. The steel pylon offers much greater strength and can therefore support the target at much greater heights than the foam column, and its echo is surprisingly small, given the amount of metal exposed to the radar.

No matter where we conduct our tests, there is a possibility that the target will interact with the ground or floor via a bistatic scattering mechanism. Its effect, when it occurs, can be minimized by optimizing the width of the range gate or by installing the target at least two target lengths above the ground. We listed the strength of the interaction for a few simple cases, which showed that the effect becomes stronger with increasing size for cylinders, but weaker for flat plates and edges. We did not examine target-ground interactions for oblique angles of incidence, but ventured the guess that it would be much weaker than for normal incidence.

We concluded the chapter with a short discussion of the calibration of the system. Two calibrations are required: one to characterize the transfer function of the radar; the other to relate the system output indication, in whatever form it may take, to the RCS of the test object. The latter amounts to a substitution method, in which the test target is replaced by an object whose RCS is known with a high degree of confidence. Although the calibration scatterer is usually one of the four bodies listed in Table 6.1 (corner reflector, flat plate, right circular cylinder, sphere), this is not essential. What is essential is that the RCS of the body be well known at the frequency and for the orientation used.

REFERENCES

[1] Keller, J. B., "Backscattering from a Finite Cone," *IRE Trans. on Antennas and Propagation,* Vol. AP-8, March 1960, pp. 175–182.

[2] Keller, J. B., "Backscattering from a Finite Cone—Comparison of Theory and Experiment," *IRE Trans. on Antennas and Propagation,* Vol. AP-9, July 1961, pp. 411–412.

[3] Bechtel, M. E., "Application of Geometric Diffraction Theory to Scattering from Cones and Disks," *Proc. IEEE,* Vol. 53, August 1965, pp. 877–882.

[4] Bechtel, M. E., "Vertically Polarized Radar Backscattering from the Rear of a Cone or Cylinder," *IEEE Trans. on Antennas and Propagation,* Vol. AP-17, March 1969, pp. 244–246.
[5] Blore, W. E., "The Radar Cross Section of Spherically Blunted 8° Right Circular Cones," *IEEE Proc. Antennas Propag.,* Vol. AP-12, March 1973, pp. 252–253.
[6] Burnside, W. D., and L. Peters, Jr., "Radar Cross Section of Finite Cones by the Equivalent Current Concept with Higher Order Diffraction," *Radio Science,* Vol. 7, No. 10, October 1972, pp. 943–948.
[7] Knott, E. F., and T. B. A. Senior, "Comparison of Three High Frequency Diffraction Techniques," *Proc. IEEE,* Vol. 62, November 1974, pp. 1468–1474.
[8] Knott, E. F., and T. B. A. Senior, "Second Order Diffraction by a Ring Discontinuity," Report No. AFOSR-TR-73-1237, University of Michigan, Radiation Laboratory, July 1973.
[9] "RATSCAT Facilities and Capabilities," brochure published by the 6585th Test Group, Air Force Systems Command, Holloman AFB, NM. (*Note:* Brochure is not dated, but was probably issued in 1977 or 1978.)
[10] Gardner, R. E., "Doppler Spectral Characteristics of Aircraft Radar Targets at S-Band," NRL Report 5656, US Naval Research Laboratory, 3 August 1961, p. 17.
[11] Kouyoumjian, R. G., and L. Peters, Jr., "Range Requirements in Radar Cross Section Measurements," *Proc. IEEE,* Vol. 53, August 1965, pp. 920–928.
[12] Knott, E. F., and T. B. A. Senior, "How Far Is Far?" *IEEE Trans. on Antennas Propagation,* Vol. AP-22, September 1974, pp. 732–734.
[13] Mack, Richard B., "Basic Design Principles of Electromagnetic Scattering Measurement Facilities," Report RADC-TR-81-40, Rome Air Development Center, Griffiss AFB, NY, March 1981.
[14] Freeny, C. C., "Target Support Parameters Associated with Radar Reflectivity Measurements," *Proc. IEEE,* Vol. 53, August 1965, pp. 929–936.
[15] Plonus, M. A., "Theoretical Investigation of Scattering from Plastic Foams," *IEEE Trans. on Antennas and Propagation,* Vol. AP-13, January 1965, pp. 88–93.
[16] Senior, T. B. A., M. A. Plonus, and E. F. Knott, "Designing Foamed-Plastic Materials," *Microwaves,* December 1964, pp. 38–43.
[17] Knott, E. F., and T. B. A. Senior, "Studies of Scattering by Cellular Plastic Materials," Report No. 5849-1-F, University of Michigan, Radiation Laboratory, April 1964.
[18] Burke, H. S., T. G. Dalby, W. P. Hansen, Jr., and M. C. Vincent, "A Millimeter-Wave Scattering Facility," presented at the 1980 Radar Camouflage Symposium, Orlando, FL, November 18–20, 1980, Report No. AFWAL-TR-81-1015, Air Force Wright Aeronautical Laboratories, Wright-Patterson AFB, March 1981, pp. 327–336.
[19] Knott, E. F., *Radar Cross Section Measurements,* Van Nostrand Reinhold, New York, 1993.

Chapter 12
Outdoor RCS Test Ranges

Eugene F. Knott

12.1 OVERVIEW

Having examined some general considerations attending the measurement of radar scattering characteristics, we now consider outdoor test ranges in particular. Although we would prefer the convenience, economy, and security of measuring test objects indoors, most targets are simply too big for us to do so. For example, a target as small as 5 ft should be measured at a range of not less than 500 ft for a test frequency of 10 GHz if we are to satisfy the farfield criterion. Because such distances outstrip the capabilities of even the largest indoor chamber, we are often forced to measure even relatively small test bodies outdoors.

The single most pervasive electromagnetic feature of the outdoor range is the ground itself. We may manage to eliminate or sharply reduce unwanted reflections from the walls of indoor test chambers, but there is little we can do about the reflections from the ground on outdoor ranges. Although the operators of some outdoor ranges have attempted to overcome the effects of this *ground plane,* the most effective course of action appears to be to accommodate it. The ground-plane effect forces us to maintain a rather rigorous relationship between target height, antenna height, operating wavelength, and range to the target; and in many cases we deliberately pave the range to render its behavior more predictable.

When we manage to accommodate the operating requirements of the ground-plane range, we will discover an enhancement of the sensitivity of our instrumentation system. The theoretical sensitivity can be as much as 12 dB greater than that of a comparable free-space test facility and is directly attributable to the mirroring of the antenna in the ground plane. In effect, the target is illuminated

by two antennas, one the image in the ground plane of the real one above it. Paradoxically, we lose some of this enhancement when we increase the gain of our antennas.

The enhancement is also degraded by the roughness of the ground plane, but this is not why we pave the ground. The signal reduction due to roughness seldom exceeds 1 dB, a tolerable loss. More important is the quality of the images of the target and the antennas in the ground plane and therefore the uniformity of the fields to which both are exposed. Although it might be thought that we should attempt to metallize the ground plane to improve the reflection from it, if not to make it smoother, this is unnecessary for all but the lowest test frequencies. The dielectric constant of asphalt and most soils is high enough, and the grazing angle of incidence low enough, that the reflection coefficient of the ground plane is greater that 90%.

Almost all the world's large outdoor ranges are owned and operated by the U.S. government or large U.S. airframe manufacturers. Most are found west of the 105th meridian in the United States, three of them in southern California alone. Two of them rely on massive retractable support structures to expose the target to the instrumentation radar, and at least two of them use huge mobile barns to protect and service the target. The oldest of the large outdoor facilities is probably the U.S. Air Force RATSCAT test range, built by the Ft. Worth Division of General Dynamics in the early 1960s, and the newest is the Boeing test range in Oregon, completed in 1990.

All are *static* RCS ranges, in which the test target is exposed to the instrumentation radar on a controllable support fixture. Although the target may be rotated in aspect during the measurements, or even caused to rock, tilt, or dip during that rotation by a string support system, the tests are, nevertheless, static tests because the target never leaves the ground and the radar is trained in a fixed direction. In sharp contrast, the target measured on a *dynamic* test range operates under its own power and may fly courses several miles long. This demands that the instrumentation radars track the target in both angle and range, a function often accomplished by a separate tracking radar. The design and operation of the two kinds of test range are quite different, and in this chapter we focus attention exclusively on the static RCS test range.

12.2 INSTRUMENTATION

The quality, quantity, and complexity of test range instrumentation varies considerably from one installation to another, and we cannot hope to cover this broad topic in detail here. We describe instead the general features of a pair of common pulsed systems, one of them having the coherence demanded for the generation of *radar imagery* (see Chapter 14). Whether coherent or not, the features sketched in Figure 12.1 are common to both, and all are essential.

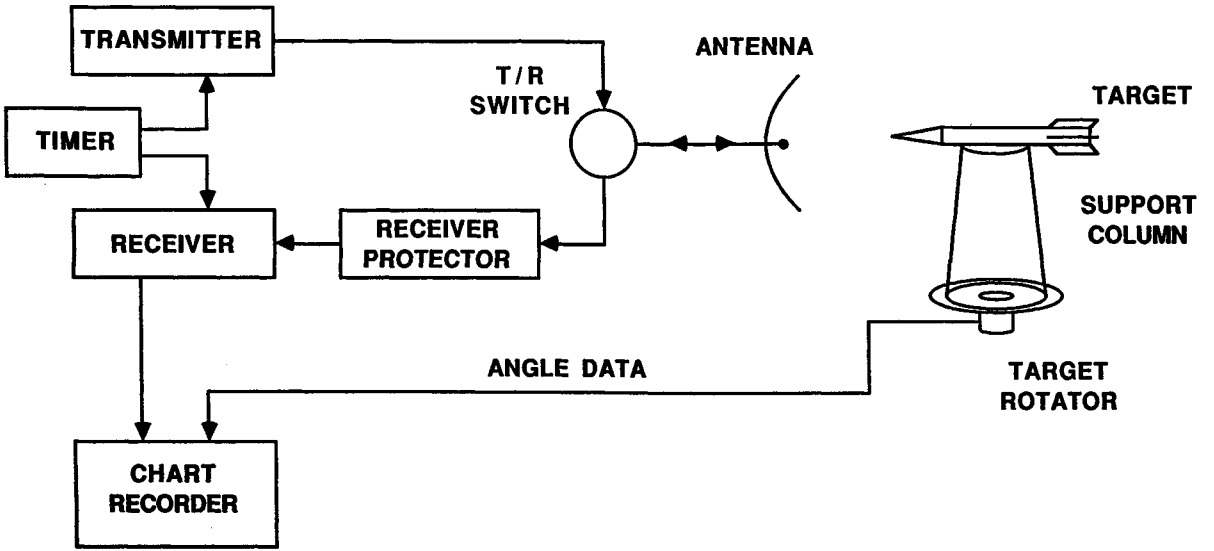

Figure 12.1. Elements of the single-antenna pulsed instrumentation radar.

The transmitter at upper left generates the RF signal to be radiated, and the receiver below it detects echo signals and converts them to other signals that can be recorded as a permanent record. The recording device shown in the diagram is a chart recorder, but this may be replaced with or augmented by a digital system (computer or microprocessor). Some systems are fitted with a video monitor on which samples of the measured data stream may be displayed in real time.

Although not shown in the diagram, the signal out of the transmitter is a train of rectangular pulses of RF energy. The generation of each pulse is controlled by a system timer that delivers a trigger signal to the transmitter at uniform time intervals. The timer also supplies that receiver with a delayed pulse command that alerts the receiver to the arrival of an echo pulse. Depending on the quality of the test environment, the radar operating frequency, and the range to the target, these pulses may be repeated at rates as high as 100,000 pulses per second or as low as 2000 or 3000 per second. Although some transmitters have been built that develop 100 kW of peak power, 1 kW or less is now more common. This results in a reduction in system sensitivity that is typically recovered by the use of digital signal integration.

The purpose of the pulsed waveform is to exclude, as much as possible, all signals except those reflected by the target. If we were not to do this, the receiver would respond continuously to all echo returns, and we would have to devise other schemes to extract the desired target echo from the signal stream. The receiver sensitizing command is a pulse called the *range gate*, and it must lag the transmitter trigger by approximately the time it takes a signal to propagate out to the target and back to the receiver. This delay obviously depends on the range to the target, and amounts to about 2 μs per 1000 ft of target range.

To minimize background echoes from all other sources except the test target, the range gate pulse should be as narrow as possible, but not so narrow that it excludes the echo from some parts of the target. The maximization of receiver sensitivity, on the other hand, demands the use of long pulses. Therefore, the overall system design is essentially a reconciliation of design conflicts. Recognizing that no single pulse width may serve all users or all test conditions, the designers of some instrumentation systems allow the radar operator to make the optimization decision by providing the option to select the pulse width or system bandwidth. Common options are pulse widths of 30, 100, and 300 ns.

In the particular configuration shown in Figure 12.1, a single antenna services the target illumination requirements of the transmitter and the echo collection requirements of the receiver. The T/R (transmit-receive) switch automatically routes the proper signal to the proper device for this dual service, but cannot isolate the receiver completely from the transmitter. Because the receiver can be destroyed by signals only a tiny fraction as strong as those developed in the transmitter, a protection device is provided between the T/R switch and the receiver.

Indeed, a receiver protector may be needed even if the transmitter and receiver are serviced by separate antennas (not shown). In that event the T/R

switch is not needed, but the direct leakage of signals from the transmitting antenna to the receiving antenna sometimes dictates the inclusion of receiver protection in two-antenna installations.

An important data link in the RCS instrumentation system is the aspect angle of the target. This information is extracted from a device installed on or geared to the rotation axis of the target turntable or rotator. Analog three-phase *selsyns* are still in use in some facilities, but the modern trend is toward digital shaft encoders. Because almost all test ranges now rely on digital computers for data collection as well as data processing, the use of digital shaft encoders is particularly compatible with an integrated data collection requirement.

The typical instrumentation radar receiver has the components sketched in Figure 12.2. Its function is to produce a stream of bits that, when later decoded, provide a record of the RF input signal. That output signal is usually boosted by a low-noise RF amplifier and then converted in a mixer to a more convenient intermediate frequency for further amplification. This function is accomplished in the superheterodyne receiver by combining the RF signal to be measured with the signal from a local oscillator. The local oscillator frequency is chosen so that the difference between it, or any harmonic of it, and that of the RF signal is equal to the desired IF. The intermediate frequency itself is chosen with due regard for the capabilities (gain and bandwidth) of IF amplifiers available for the design. Many receiver designers choose an IF center frequency of 60 MHz.

The result of the conversion process is a spectrum rich in harmonics, most of which are greatly attenuated by the IF amplifier fed by the mixer output, while the desired IF is typically amplified by 60 dB or more. An IF filter may be used to further suppress all but the desired frequency, possibly followed by an IF limiter if excessively strong signals are anticipated. The slowly varying amplitude of the signal is extracted by a video detector, which may be followed by a stage of video amplification. Governed by a command from the system timer, a sample-and-hold device holds the video output of each pulse at a nearly constant level for a short time, and this voltage is then digitized by an analog-to-digital converter, also commanded by the system timer. The result is a string of bits—one string per pulse—delivered to a microprocessor (not shown) with the task of storing the data, processing them, or distributing them to other digital devices.

Although it shares some of the components of the simple receiver just discussed, the coherent receiver is more complex. As shown in Figure 12.3, it contains two oscillators instead of one (a STALO and a COHO), and it develops a signal that is routed to the transmitter. This stems from the requirement that to extract the phase of a signal as well as its amplitude, we must compare the unknown signal with a *reference* signal of the same identical frequency. The comparison is performed at IF by the synchronous detector near the lower right of the diagram, which replaces the video detector in Figure 12.2. Note that, in contrast to the video detector, the synchronous converter generates two outputs—in-phase and quadrature (I and Q)—instead of one.

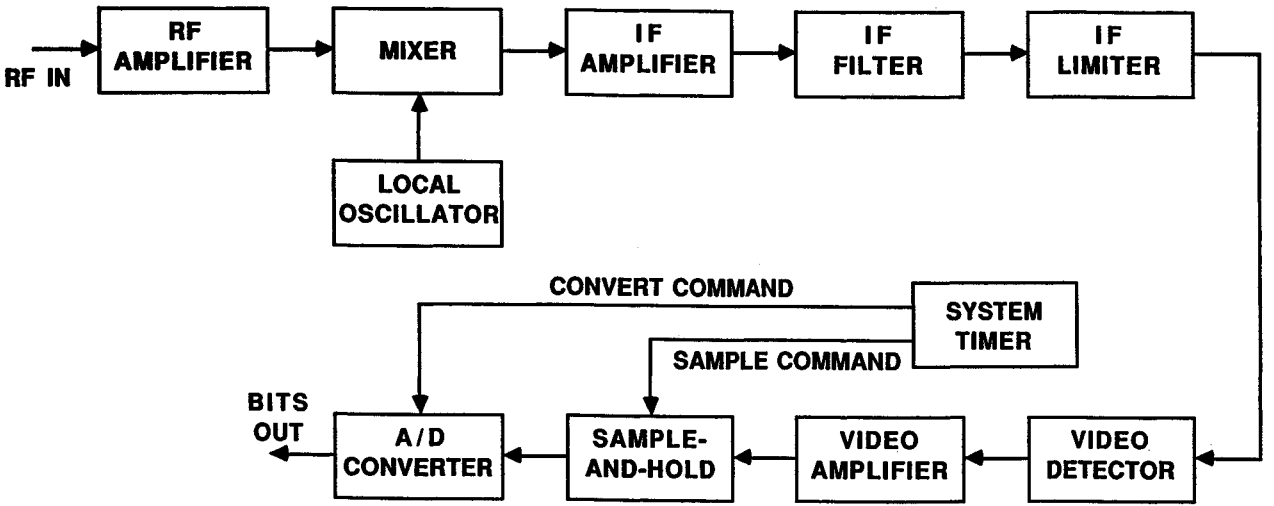

Figure 12.2. Generic instrumentation radar superheterodyne receiver (from [1]) (Copyright 1993 Van Nostrand Reinhold; reprinted with permission.)

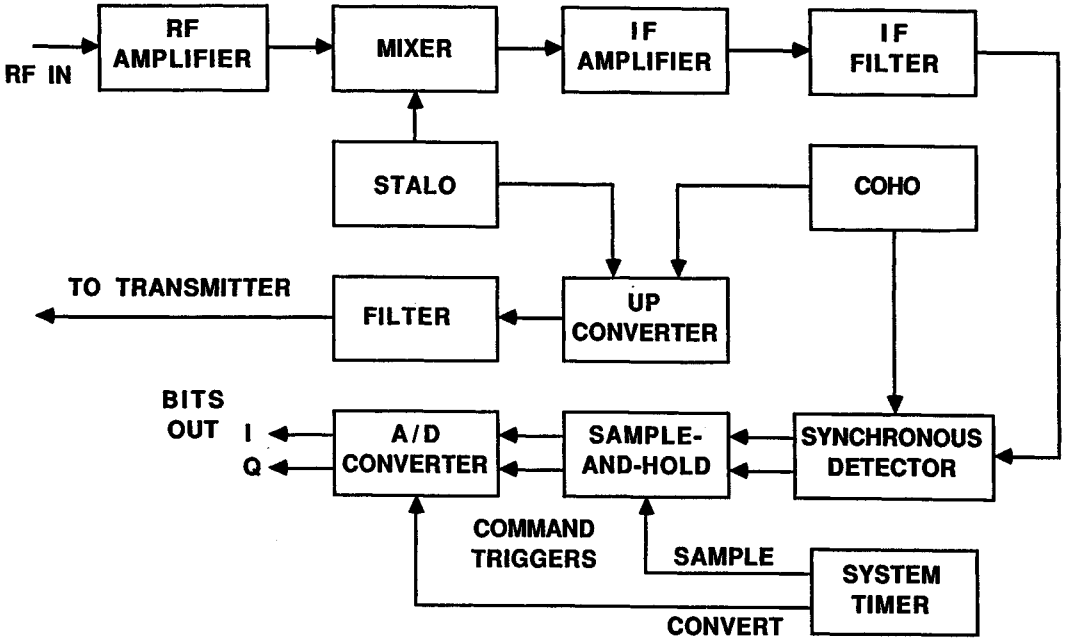

Figure 12.3. Coherent radar receiver (from [1]) (Copyright 1993 Van Nostrand Reinhold; reprinted with permission.)

Therefore, the major difference between the amplitude-only receiver and the coherent receiver is the *coherent oscillator* (COHO), near the upper right of the diagram, and the *stabilized local oscillator* (STALO) feeding the mixer. In the design of contemporary instrumentation systems, both are typically very stable *frequency synthesizers* phase-locked to a common (shared) crystal oscillator. The COHO generates the reference signal, which is also the IF of the system. This being the case, the frequency of the incoming RF signal and that of the STALO must differ by precisely this frequency. Hence, the RF signal to be developed in the transmitter must be derived from sum of the COHO and STALO outputs. This is accomplished in the up-converter in the center of the diagram.

The up-converter is simply a mixer called by a different name. Like the mixer, it is a nonlinear device that generates a rich spectrum of harmonics of the two frequencies delivered to it, as well as harmonics of the sums and differences of those frequencies. All but the desired RF (the sum of the COHO and STALO frequencies) are suppressed by bandpass filters installed in the converter itself or provided separately, as shown in the figure. After amplification and radiation by the transmitter, the RF signal is bounced off the target, captured by the antenna and fed to the RF amplifier at the upper right of the diagram. Therefore, the frequency of the signal out of mixer is the same as that of the COHO, and the signals compared in the synchronous detector have identically the same frequency, as intended.

This generic receiver is essential for the generation of radar imagery because phase information is vital in such processing. As we shall see in Chapter 14, the formation of the downrange profile of a target demands a wideband signal typically derived in a deliberate sweep of the frequency over the required bandwidth. Although that sweep may be accomplished continuously in the analog FM/CW radar, modern equipment allows us to step the frequency over the band in discrete steps. Hence, the waveform emitted in most RCS test installations is a stepped one, in which the frequency may vary from one pulse to the next. The generic coherent receiver in Figure 12.3 is the one used to generate and receive these waveforms.

This stepped-frequency sweep is possible when the STALO is a programmable frequency synthesizer addressed by the system controller (computer). We need not disturb any of the components shown in the figure except the STALO, and even then we need add only a slender cable by which to deliver our commands to the STALO to index to the next frequency. Because the best of available frequency synthesizers can change frequency in a few microseconds or less, we can step the frequency at rates approaching 50 kHz. If we choose to integrate a string of received pulses in the interest of improving sensitivity, however, this very high stepping rate is seldom necessary.

The designers of instrumentation radars have found it convenient and economical to increase the signal-to-noise ratio of their system, and therefore systems sensitivity, by exploiting digital integration instead of boosting the raw power emitted by the transmitter. This being the case, we typically integrate a string of pulses and record (store) the accumulated result before issuing a command to index

to the next frequency. If we choose to integrate 1000 pulses to achieve an integration gain of 30 dB, for example, and if the PRF is, say, 50 kHz, we need change the STALO output frequency at a mere 50 Hz rate (once every 2 ms). Thus, very high frequency-switching rates are a necessity only when we choose not to implement coherent signal integration.

We must always bear in mind, however, that improvements are seldom brought about without a price. In the case of improving the signal-to-noise ratio by digital integration, the price is more time (more pulses). In some cases the additional time investment reduces the effectiveness of the test range, and on occasion it becomes downright annoying.

The generation of radar imagery demands a transformation of data sets from the angle domain to the cross-range domain, and from the frequency domain to the range domain. These transformations inevitably exploit the discrete fast Fourier transform, which demands only discrete samples of continuous signal variations. Even if continuous data were to be available, such as might be collected with an analog FM/CW radar, we would digitize them for input fodder for the voracious FFT. As such, the discretely stepped signals we get from the STALO frequency synthesizer are no less adequate for the radar imagery task than the continuous signals developed by the FM/CW radar.

12.3 THE GROUND-PLANE EFFECT

Because it is nearly impossible to avoid illuminating the ground with our antennas on an outdoor range, it is essential that we understand how the ground reflection influences the incident field in the target zone and the scattered fields at the radar antenna. As shown in Figure 12.4, energy reaches the target via a direct path D and an indirect reflection path whose length is $S_1 + S_2$. Energy scattered by the

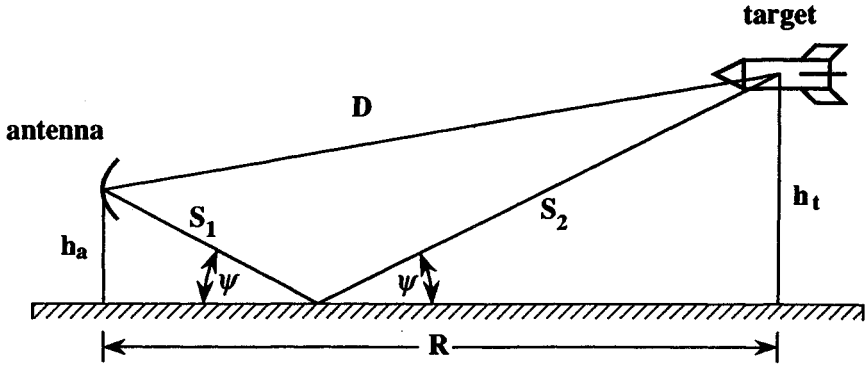

Figure 12.4. Ground-plane range geometry showing the direct path D and the indirect path $S_1 + S_2$ due to the ground reflection.

target travels back to the radar along the same paths but in the opposite direction. Therefore, the ground-plane effect involves no fewer than four distinct roundtrip propagation paths, two of which involve a monostatic geometry and two a bistatic geometry.

Note that the direct path D and the second leg S_2 of the indirect path converge on the target from slightly different directions in the vertical plane. However, the bistatic angle in that plane is so small (typically less than 1°) that the target echo we measure on the ground-plane range is indistinguishable from the monostatic echo. Of the four possible roundtrip propagation paths, there are only three distinct path lengths:

- Roundtrip distance along the direct path; $2D$
- Roundtrip distance along the indirect path: $2I$
- Roundtrip distance along direct and indirect paths: $D + I$

where $I = S_1 + S_2$ is the indirect path length. If we vary the target height h_t, the antenna height h_a, or the range R, the phase changes due to the variation in the three path lengths will generate an interference pattern. We will focus attention on the interference pattern in the vertical plane due to a variation in the target height.

Because the phase of the echo contributions received via the four paths is the most influential factor in determining that pattern, we use eq. (1.12) to represent the received echoes. Because the angles of the direct and indirect paths nearly coincide at the target, the amplitudes of the four contributions will be the same as that measured in a free-space environment, which we denote by σ_0. Coherently summing the four contributions, we may write

$$(\sigma)^{1/2} = (\sigma_0)^{1/2}\{\exp[\mathrm{i}2kD] + 2\rho \exp[\mathrm{i}k(D + I)] + \rho^2 \exp[\mathrm{i}2kI]\} \quad (12.1)$$

in which the second term is the sum of the two bistatic contributions. In this expression we have represented the reflection coefficient of the ground with the symbol ρ.

The first term in (12.1) is the free-space echo of the target, as would be measured in the absence of the ground plane. The third term is the echo of the image of the target in the ground plane, with the factor ρ^2 accounting for a double reflection from the ground, the first in the path from antenna to target and the second from the target back to the antenna. The second term is a ground-plane contribution involving a single reflection off the ground. Note the factor 2, accounting for a pair of identical contributions along the same total path but in opposite directions.

We may reference the phase of the second and third terms with respect to that of the first by suppressing the exponential term $\exp[\mathrm{i}2kD]$ from all three. We

may do this without penalty, because only the relative phase between terms concerns us here. The amplitude of the interference pattern may thus be expressed as

$$\sigma/\sigma_0 = |1 + \rho \exp[ik(I - D)]|^4 \tag{12.2}$$

If the ground plane is perfectly conducting, the reflection coefficient $\rho = -1$, and (12.2) becomes

$$\sigma/\sigma_0 = 16 \sin^4[(k/2)(I - D)] \tag{12.3}$$

Although the ground planes of few outdoor test ranges are perfectly conducting, the interference pattern given by this expression is a good representation of observed behavior.

A plot of this simple function is shown in Figure 12.5. Note that the apparent echo signal is 16 times the free-space echo of the target at the peaks of the pattern and, perhaps equally important, that it also drops to zero at regular intervals. We may maximize the sensitivity of our system, therefore, by choosing the range geometry so that the path-length difference is an odd multiple, m, of a half-wavelength. For reasons to be given in a moment, we always choose the first peak in the pattern ($m = 1$).

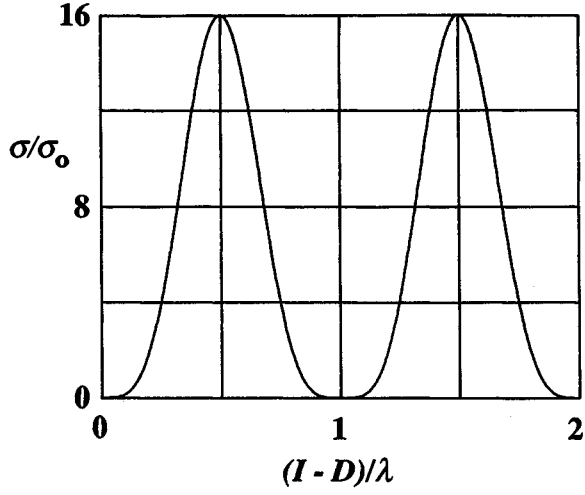

Figure 12.5 Plot of eq. (12.3).

We may establish how this peak is influenced by the four influential range parameters—target height, antenna height, range, and wavelength—from the geometry of Figure 12.1. The path lengths I and D are

$$I = [(h_t + h_a)^2 + R^2]^{1/2} \approx R + (h_t + h_a)^2/2R \tag{12.4}$$

$$D = [(h_t - h_a)^2 + R^2]^{1/2} \approx R + (h_t - h_a)^2/2R \tag{12.5}$$

in which the approximations are very good ones because the antenna and target heights are almost always but a small fraction of the range. On forming the difference between the two path lengths and setting it equal to a half-wavelength, we obtain

$$h_a h_t = R\lambda/4 \tag{12.6}$$

Equation (12.6) is a rule of thumb widely used in the design and operation of outdoor test ranges.

It may be a bit bewildering to decide how to choose the four parameters to optimize the test range, but practical considerations make the selection for us. First, by virtue of the test plan and its requirements, the operating wavelength is seldom negotiable. Second, we usually select the distance R to the target so as to satisfy, if possible, the farfield criterion. This distance depends on the target size as well as the wavelength, and sometimes we must even violate it to obtain sufficient sensitivity for our measurements. Because we cannot afford to shuffle our support structure back and forth along the range to accommodate each change in frequency or target size, we typically establish two or three permanent locations on the range (sometimes call *pits*) where we will plant our target support structure. Therefore, the range R will take on two or three fixed values at most.

Third, because we can no more afford to raise and lower our target than to shuffle it back and forth in range, we equip the range with a small set of, say, three, more or less permanent target support fixtures. Hence, like the range to the target, target height will be restricted to a few standardized values. The single parameter we *can* control relatively easily is the antenna height. Indeed, the antennas on many outdoor test ranges are installed on sliding carriages that may be winched up and down, either manually or by remote control. In preparing for a test program, therefore, we typically choose the range from one of perhaps three fixed distances, choose one of our standardized support fixtures that will safely support and rotate the target, and then adjust our antenna heights, if necessary, to center the first lobe of the ground plane interference pattern on the target.

There are at least three reasons why we always use the first lobe in this pattern. First, the product $h_a h_t$ is the smallest it can ever be at the first lobe, which keeps one height, if not both, reasonably close to the ground. Second, the physical

width of the lobe decreases with increasing m, thereby reducing the vertical distance over which the echo response remains acceptably flat. This is demonstrated by the relative pattern compressions shown in Figure 12.6 for $m = 3$ and 5, as compared with $m = 1$. Note that the target lobes for $m = 3$ and 5 are one-third and one-fifth the width of the lobe for $m = 1$. Third, the lobe fans up and down through the target zone when we employ swept-frequency waveforms.

Although we may satisfy the requirements of (12.6) at any single frequency, we cannot possibly satisfy it for all the frequencies in such a waveform. To do so implies the capability of indexing either the antenna height or the target height along with the frequency change, a rate impossible to match by mere mechanical means. However, the microwave spectrum is composed of a collection of abutting frequency bands whose widths seldom exceed an octave (2 : 1 frequency variation), and each band is serviced by its own antenna system. Given fixed range and target height, we typically choose the midband wavelength to insert in (12.6) for calculating our optimum antenna height, and accept less-than-ideal target illumination at the upper and lower band edges. Over the duration of a stepped-frequency pulse train, therefore, the desired peak in the interference pattern fans up or down

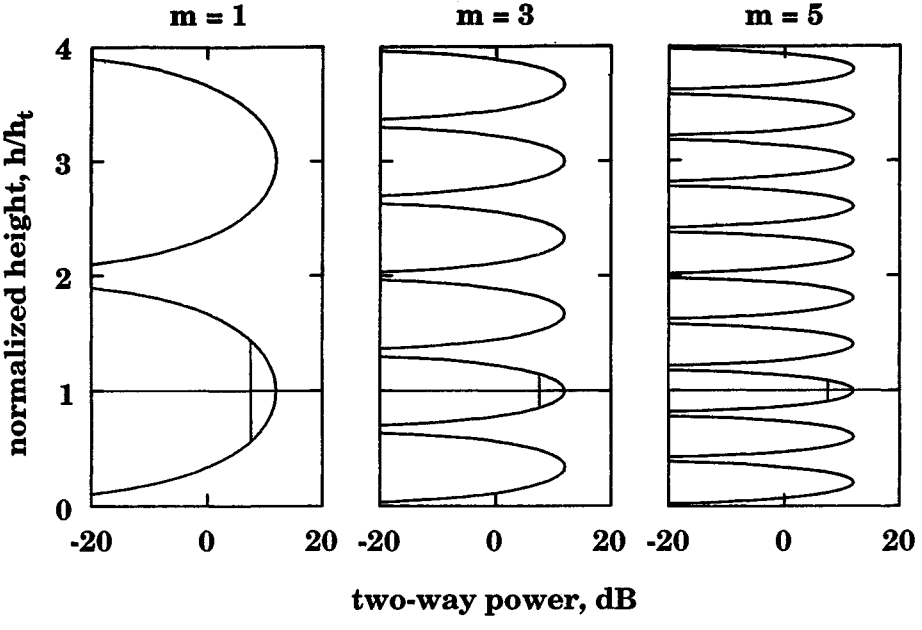

Figure 12.6. We use $m = 1$ when we use the ground plane because this maximizes the vertical width of the target lobe.

through the target zone. At the lower edge of an octavewide band, this peak is some 33% lower than the desired height, and at the upper edge is some 33% higher.

If we were to use the second peak of the vertical interference pattern, these displacements would become 100%, resulting in a significant taper in the incident field intensity over the vertical target profile. Indeed, the illumination of the target at the upper and lower band edges might even be weak enough to compromise system sensitivity at those frequencies. Therefore, we always attempt to place the target at none other than the first peak of the vertical ground plane interference pattern.

We have assumed that ground plane to be a perfect reflector thus far, for which $\rho = -1$, but it is legitimate to establish the validity of the assumption. Because the reflection from the ground of an outdoor range may be less than unity, and because the phase shift may not be exactly 180°, it is of interest to examine the impact of these less-than-ideal conditions. The effect of a reduction in the amplitude of the reflection coefficient, but still with a 180° phase shift, is charted in Figure 12.7. Note that a 10% reduction reduces the peak of the interference pattern by about 0.9 dB. The effect of a phase shift other than 180° is plotted in Figure 12.8, where it can be seen that, although the amplitude of the lobe remains unchanged, a reduction in the phase angle raises the peak higher above the ground plane.

This shift from the assumed 180° phase shift influences the accuracy of our ground-plane rule of thumb in (12.6). Unless we are very confident of the ground-plane behavior, perhaps from years of experience in the operation of a specific facility, it is good practice to probe (measure) the incident field structure in the

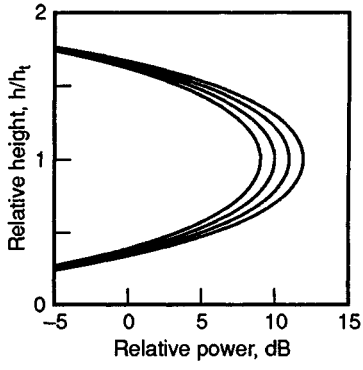

Figure 12.7. Effect of imperfect reflection by the ground plane. The four traces are for reflection coefficients ranging from −0.7 to −1.0 in 0.1 intervals.

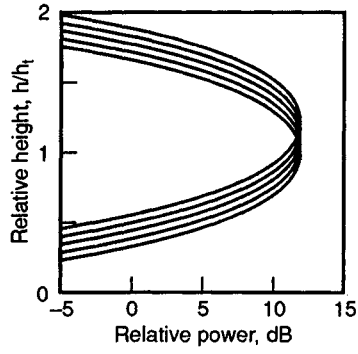

Figure 12.8. Effect of the phase angle of the ground reflection coefficient with the amplitude fixed at unity. The five traces are for phase angles from 140° to 180° at 10° intervals. The pattern shifts upward as the phase angle decreases.

target zone to verify that the peak of the pattern is where we expect it to be. This should be done *before* the onset of a test program, not after its completion, particularly on unpaved test ranges whose soil moisture may vary with the season, and perhaps even from week to week.

12.4 EFFECT OF THE ANTENNA PATTERN

We have assumed the instrumentation antennas to be omnidirectional thus far, which made it easy to characterize the ground plane and assess the effects of imperfections in it. To maximize system sensitivity and reduce the influence of unwanted echoes on our measurement, however, we attempt to concentrate energy in the target zone, hence the antennas are no longer omnidirectional radiators. Although this is necessary, the ground plane has the effect of slightly reducing the apparent antenna gain.

Even in the absence of the ground plane, one of the decisions facing the test range designer is the optimization (selection) of the radar antennas. Although we would like to choose large antennas and thereby maximize system sensitivity, the primary consideration is the uniformity of the incident field in the target zone. That uniformity (flatness) depends on the beamwidth of the antenna and the distance to the target, neither of which remains fixed for the entire test program.

Any of several methods may be used to size the antenna for this estimate, but we will assume one with a cosinusoidal field excitation across a rectangular aperture. We will further assume that the resulting pattern is a figure of revolution about the boresight axis, independent of polarization. The angular field pattern of such an antenna is given by the pattern function

$$f(\phi) = \frac{\cos(\pi w/2)}{1 - w^2} \tag{12.7}$$

where

$$w = (2d/\lambda) \sin \phi \tag{12.8}$$

and d is the antenna diameter and ϕ is the off-boresight angle. The radiated power pattern is the square of (12.8), and the gain of the antenna is given approximately by

$$G = \eta(\pi d/\lambda)^2 \tag{12.9}$$

where η is the antenna efficiency, usually no more that 50%. The first sidelobes of this pattern are 23.5 dB below the main lobe.

A rule of thumb for accurate RCS measurements is that the amplitude of the incident field not taper by more than 0.5 dB from the center of the target to its lateral extremes. Selecting the antenna size that satisfies the requirement demands that we establish the maximum target width that will be presented to the radar, determine the angle ϕ at the lateral extremes, insert this value in (12.7), and then solve the equation for the antenna diameter d when (12.7) is forced to take on the value $f = 0.944$ (-0.5 dB).

Finding d/λ given f demands the solution of a transcendental equation, which we may effect graphically or by numerical methods, such as the Newton-Rafson method of successive approximations. Omitting the details of such methods, we list a few useful values in Table 12.1. A numeric example serves to illustrate the antenna selection procedure.

Table 12.1
Argument w in (12.7) as a Function of Field Taper

Field taper, dB	w
0.1	0.22178
0.2	0.44253
0.5	0.49438
1.0	0.69642
2.0	0.97709
3.0	1.18703
∞	3.00000
Half-power	1.18896

Assume that a target of length L is to be measured at a range R, that L is much less than R, and that we must allow the amplitude to taper by less than our rule of thumb, 0.5 dB. The function sin ϕ is approximately

$$\sin \phi \approx L/2R \tag{12.10}$$

which we may insert in (12.8). Solving for d, we find that the antenna diameter should be no larger than

$$d \approx w\lambda R/L \tag{12.11}$$

By way of example, assume that we have designed the test range to accommodate a 40 ft target at a test range of 5000 ft. For a maximum amplitude taper of 0.5 dB, we find that the antenna should be no more than 62λ in diameter. We usually make this calculation at the upper edge of the frequency band to ensure that the requirement is met for the remaining (lower) frequencies serviced by the antenna. The resulting sizes are listed in Table 12.2 for a few commonly used bands in the microwave spectrum. Because most of the antenna diameters range from 31λ at the lower edge to 62λ at the upper edge of each band, the antennas would all have similar patterns and comparable gains. Their midband gains would be 40 or 41 dB and would be some 3 dB lower and 3 dB higher at the lower and upper edges of the band, respectively. The sizes listed in the table are representative of those actually selected for outdoor test range service.

We devised (12.1) early in our discussion of the ground-plane effect so that we could explore that impact of the ground reflection on our RCS measurements. Although we assumed the antennas to be omnidirectional sources to simplify our exploration, the optimization of sensitivity of the data collection system demands a considerable concentration of energy in the target zone. We therefore return to

Table 12.2
Example of Antenna Selection for 40 ft Target Measured at a Range of 5000 ft

Frequency band, GHz	*Antenna diameter sized for upper band edge, ft*	*Diameter likely to be chosen, ft*	*Typical gain at midband, dB*
1–2	30.5	30	40
2–4	15.2	15	40
4–8	7.6	8	41
8–12	5.1	5	41
12–18	3.4	3.5	41

(12.1) to assess how the ground plane influences the antenna pattern in the target zone.

It is apparent that the antenna pattern governs the intensities of the fields radiated and received along the directions of the direct and indirect paths to the target. If that is the case, should we point the antenna up to the target, down toward the target image, or perhaps along the bisector of the two directions? To answer the question, we will modify (12.1) by accounting for the antenna pattern, assuming the boresight axis to be tilted up from the local horizontal by the angle ϕ indicated in Figure 12.9. The upward angle ϕ_d indicates the direction to the target and the downward angle ϕ_i indicates the direction to the image of the target in the ground plane.

The appropriate modification of (12.1) is

$$\sqrt{\sigma} = \sqrt{\sigma_0}\{f^2(\phi_d - \phi) \exp[\mathrm{i}2kD] + 2\rho f(\phi_d - \phi)f(\phi_i + \phi) \exp[\mathrm{i}k(D + I)] + \rho^2 f^2(\phi_i + \phi) \exp[\mathrm{i}2kI]\} \tag{12.12}$$

Note that the antenna field pattern function f is raised to the second power in each term. This is because it governs the intensity of both the field radiated toward the target and the field scattered back to the antenna. Although the transmitted and received directions are identical for the first and third terms, they are different for the second term.

As before, we may suppress the exponential term $\exp[\mathrm{i}2kD]$ from all three terms in (12.12), with the result

$$\sigma = \sigma_0 |f(\phi_d - \phi) + \rho f(\phi_i + \phi) \exp[\mathrm{i}k(I - D)]|^4 \tag{12.13}$$

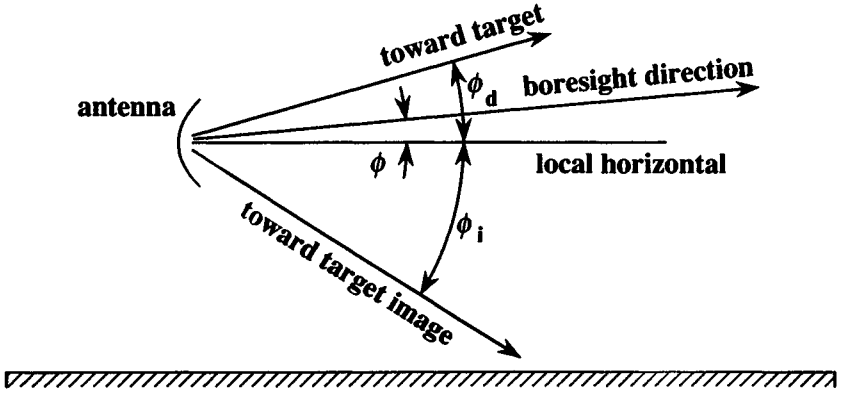

Figure 12.9. Definition of angles for exploring the effect of the pointing direction of the antenna.

The first term in this expression represents that total signal received via the direct path and the second represents the signal received via the indirect path. As before, the two terms alternately reinforce and cancel each other as the target height is varied.

We may illustrate the effect of the antenna pattern on the ground-plane interference pattern by considering a specific, but typical, example. Assume for this purpose that we have selected a 4.5 ft antenna to illuminate a target at a range of 5000 ft at a wavelength of 0.1 ft (frequency of about 10 GHz). This antenna is slightly smaller than the one shown in Table 12.2 for the 8 to 12 GHz band. The target will be installed 25 ft above the ground plane, forcing us to set the antenna height at 5 ft in accordance with (12.6). As seen from the antenna, the angle to the target will be 0.23° above the local horizontal and the angle to the target image will be 0.34° below it.

If we sweep the antenna beam from 1° below the horizontal to 1° above it, we will observe the behavior charted in Figure 12.10. The five traces there are for different ground reflection coefficients, ranging from -1 for the trace at the right

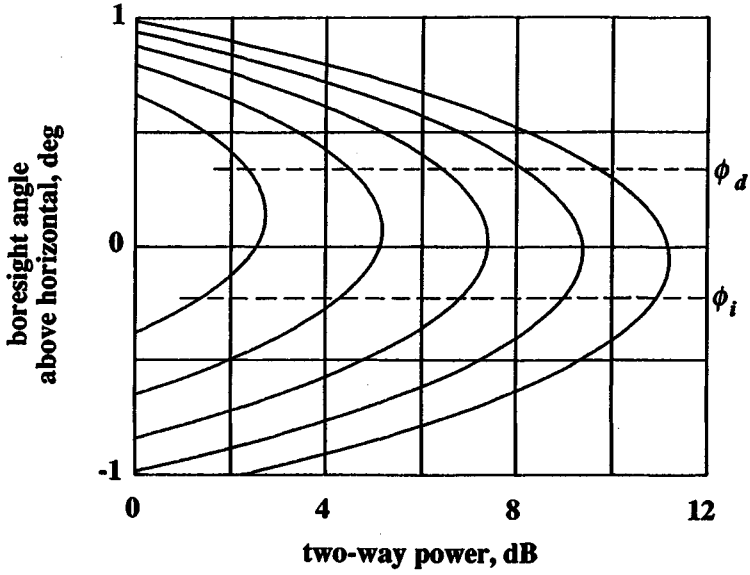

Figure 12.10. Received signal variation as the antenna boresight is swept vertically through the target zone. Reflection coefficient of the ground plane varies from -0.2 for the inner trace to -1 for the outer trace at intervals of 0.2. Upper and lower dashed lines represent the angles to the target and the target image, respectively. Other parameters are wavelength = 0.1 ft, antenna diameter = 4.5 ft, range = 5000 ft, antenna height = 5 ft, and target height = 25 ft.

to -0.2 for the one at the left. The angles to the target and its image are indicated by the dashed lines. As we should have expected, the peak of the interference pattern decreases in intensity as the ground becomes less reflective. Note, however, that even when the ground is perfectly reflecting, the peak amplitude is about 11.2 dB, somewhat less than the 12 dB noted earlier for omnidirectional sources.

This reduction in the pattern peak is brought about by a slightly reduced illumination of the ground. By concentrating energy along the boresight direction, we cannot help but reduce the energy directed toward the ground. However, the 0.8 dB reduction in the peak of the ground-plane interference pattern is insignificant in comparison to the 80 dB improvement in the two-way sensitivity of the system we gained by increasing the directivity of our antenna.

A more subtle effect of the antenna pattern is the shift in the angular location of the peak, which becomes more pronounced the smaller is the reflection from the ground. Indeed, when the ground is perfectly reflecting, we find that the received signal achieves its peak value when we point the antenna very slightly (about 0.06°) below the local horizontal. This is along the bisector of the angle subtended at the antenna by the directions to the target and to its image in the ground. When the ground reflection coefficient decreases to 20%, the received signal peaks when we align the boresight slightly above the horizontal (about 0.13°). Therefore, the optimum pointing angle is toward neither the target nor its image, but somewhere between the two extremes. This angle moves closer to the direction to the target as the reflection from the ground becomes weaker and moves closer to the bisector as the reflection becomes stronger. It never moves past the bisector.

Because the range to the target is much greater than the antenna and target heights, all these angles are small, even when the reflection to the ground is poor. When the ground reflection is strong, the optimum antenna pointing angle is along the angle bisecting the directions to the target and its image, but this is close enough to the horizontal to be barely measurable, even with a good bubble inclinometer. Therefore, unless the beam of the antenna is much narrower than considered here and unless the ground reflection is very low, there is not much point in trying to find the elevation angle that optimizes the system sensitivity. For typical outdoor test range geometries, the best course of action is to align the boresight parallel to the ground plane and clamp it there.

12.5 GROUND REFLECTION COEFFICIENT

The reflection from the ground depends on the type of soil, its dampness, and its roughness. The surface roughness diffuses energy in all directions, with the diffusion being greater for greater roughness. The diffused energy reduces the amount of energy reflected in the specular direction, therefore the ground plane enhancement becomes less significant the rougher the ground. Vegetation can increase the apparent roughness and absorb some of the incident energy.

The two effects can be accommodated by an effective reflection coefficient that contains two factors independent of each other. It may be written as

$$\rho = \Gamma \rho_s \tag{12.14}$$

where Γ is the classical Fresnel reflection coefficient associated with a perfectly flat dielectric interface and where ρ_s accounts for the reduction in reflection due to surface roughness.

We have seen that the Fresnel reflection coefficients in Chapter 3 were derived by invoking the boundary conditions at a dielectric interface. These conditions require that the total tangential electric and magnetic fields be continuous at the boundary. For typical soils, the magnetic permeability is essentially the same as that of free space, hence, the Fresnel reflection coefficients can be expressed entirely in terms of the permittivity of the two media on either side of the interface. One of the media is air, whose permittivity is essentially that of free space, ϵ_0.

For the geometry of Figure 12.4, the Fresnel reflection coefficients can be written as

$$\Gamma_h = \frac{\sin \psi - (\epsilon_r - \cos^2 \psi)^{1/2}}{\sin \psi + (\epsilon_r - \cos^2 \psi)^{1/2}} \tag{12.15}$$

$$\Gamma_v = \frac{\epsilon_r \sin \psi - (\epsilon_r - \cos^2 \psi)^{1/2}}{\epsilon_r \sin \psi + (\epsilon_r - \cos^2 \psi)^{1/2}} \tag{12.16}$$

where ϵ_r is the relative permeability of the soil, the subscripts h and v refer to horizontal and vertical incident polarizations, respectively, and ψ is the grazing angle. If we know what the dielectric constant is, we can calculate the reflection coefficients for a variety of incidence angles ψ.

Not many soils on outdoor ranges have been measured, but we do have some values for the soil at RATSCAT. The measurements were carried out by the Physical Science Laboratory (PSL) of New Mexico State University [2] at a frequency of 1.5 GHz. It should be noted that the soil at RATSCAT is primarily gypsum, a form of calcium sulfate whose properties are different from those of most soils. PSL fitted a fourth-order polynomial through the measured data, and the results are shown in Figure 12.11.

For the RATSCAT soil, a dielectric constant of $\epsilon_r = 5.5 + i2$ might be typical for a soil moisture content of 12%. Using this value in (12.15) and (12.16), we can plot the amplitude and phase of the Fresnel reflection coefficients, as in Figure 12.12. Note that the amplitude and phase for vertical polarization drop much faster with increasing grazing angle than for horizontal polarization. Nevertheless, the grazing angle seldom exceeds 1° for measurements made on an outdoor range,

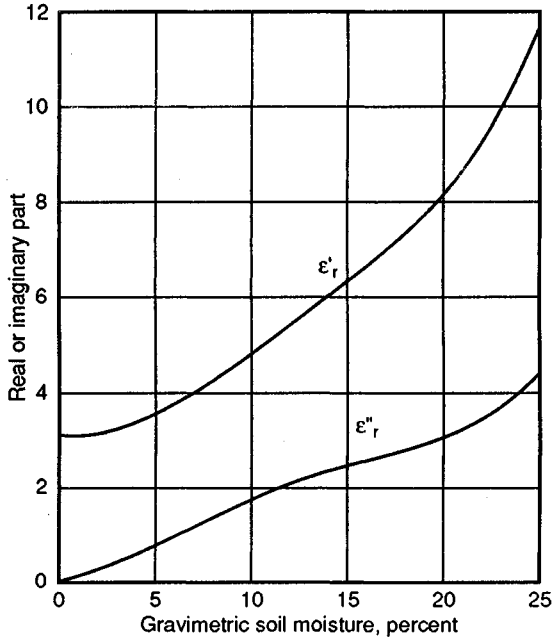

Figure 12.11. PSL's fitted polynomial to measurements of the complex dielectric constant of RATSCAT soil at 1.5 GHz.

hence, the reflection coefficients remain above 0.95 in amplitude and 179° in phase. At least for these conditions, the ground plane is not far from ideal.

Because the reflection coefficients differ for horizontal and vertical polarization, ground-plan measurements made for circular polarization are subject to error. The net incident wave at the target is, in general, elliptically polarized, and the ellipticity can be accentuated by the second ground reflection back to the instrumentation radar. There is no easy way to avoid this. The effect becomes more pronounced as the frequency decreases and can be particularly troublesome for frequencies in the UHF and VHF bands.

It is possible for the refection coefficient to be precisely zero for certain combinations for grazing angle and dielectric constant. This occurs for vertical polarization and all of the energy is propagated into the ground. It corresponds to the case when the numerator of (12.16) vanishes, and the angle at which it occurs is called the *Brewster angle*. The geometry and dielectric constants of ground-plane ranges are such that this rarely occurs, however.

The surface roughness of the ground plays an important role because it reduces the effective reflection coefficient. The effect of surface roughness can be estimated by use of the factor ρ_s.

$$\rho_s = \exp[-2(k\ \sigma_h \sin\ \psi)^2] \tag{12.17}$$

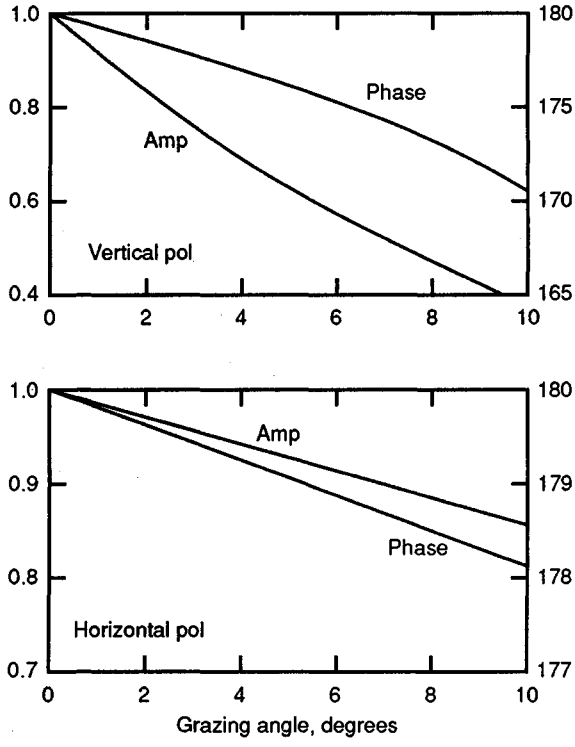

Figure 12.12. Plots of the amplitude and phase of the Fresnel reflection coefficients for small grazing angles; $\epsilon_r = 5.5 + i2$. Note the difference in the scales of the two plots.

where σ_h is the RMS surface height variation. the roughness factor ρ_s which should be used in (12.14) accounts for the dispersion of energy in directions other than the specular direction, thereby decreasing the energy along the specular. Ground vegetation will modulate the ground-plane reflection because brush and grass blades are moved by the wind, and there is hardly ever a perfectly calm day. Vegetation will also reduce the reflected signal, and hence, a good ground plane should be barren.

The properties of ρ_s are illustrated in Figure 12.13 for small grazing angles. The grazing angle for typical outdoor operation seldom exceeds 5°, and 1° or less is quite common. If $\sigma_h = 2\lambda$ is established as an upper limit on the tolerable RMS surface roughness (which corresponds to $\rho_s = 0.91$ at $\psi = 1°$), the ground plane can be quite rough and still give good performance at low frequencies. For example, this translates to 16 in, at 1.5 GHz, which is quite rough. On the other hand, the requirement becomes a fraction of an inch at millimeter wavelengths and, unless the ground plane is a concrete or asphalt runway, maintaining such smoothness

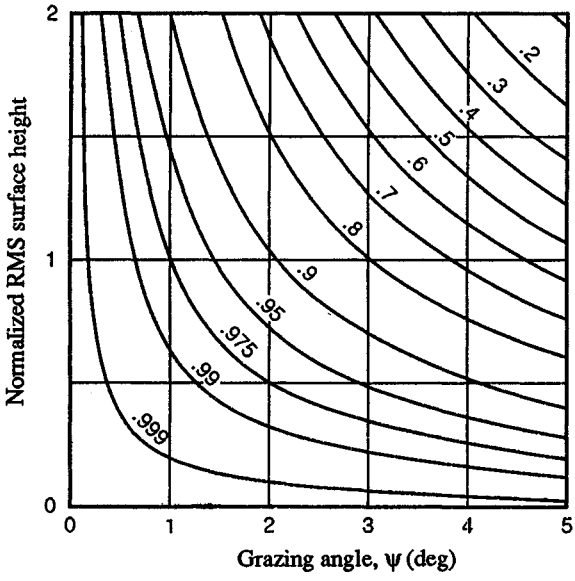

Figure 12.13. The surface roughness factor ρ_s for small grazing angles. The contours are for constant values of ρ_s.

would be difficult. So for millimeter wavelengths it may be necessary to suppress ground reflections using such techniques as high-gain antennas (to minimize ground illumination), large antenna and target heights, and perhaps radar fences erected between the radar and the target.

12.6 PASSIVE CLUTTER AND MULTIPATH REDUCTION

Clutter and multipath can introduce measurement errors unless they can be suppressed or exploited. As mentioned earlier, a ground-plane range actually exploits the multipath effect by providing a smooth surface between the radar and target. However, other multipath effects are undesirable; for example, nearby buildings, trees, and shrubbery. Multipath returns differ from clutter returns in that clutter or background signals arise from scatterers located at, or near, the target distance. The target positioner is a clutter source unless adequately shielded, and of course, a finite contribution comes from the target support column, even though it may be made from "invisible" plastic foam, which, as we have seen, is not invisible. Multipath contributions may arise from obstacles considerably farther away, as may be seen from the following analysis.

Surfaces of equal time delay are ellipsoids of revolution, as suggested by Figure 12.14, which shows a slice of the ellipsoid along its major axis. The radar

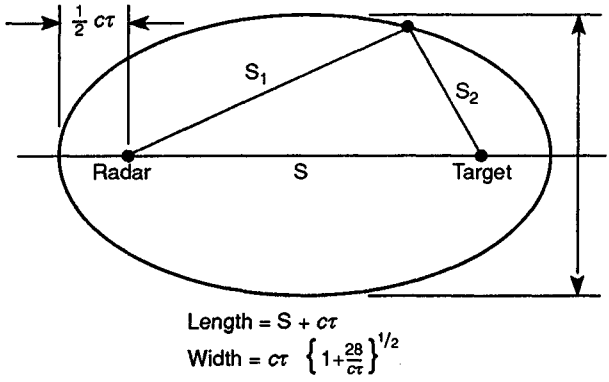

Figure 12.14. Ellipsoid of constant delay.

and test target lie at the foci, and the axis of revolution coincides with the line of sight. The indirect path $S_1 + S_2$ is constant for any point on this surface, hence the path length difference δ is constant. The maximum path length difference must be greater than $c\tau$, where c is the speed of light and τ is the transmitted pulse width. If the path length difference exceeds this value, the multipath return will not be detected. In fact, depending on the type of pulse detection system used, the path length difference should be a little greater than $c\tau$.

If S is the distance between the radar and the target, the total length of the ellipsoid is

$$l = S + c\tau \tag{12.18}$$

and its width is

$$w = c\tau\left(1 + 2\frac{S}{c\tau}\right)^{1/2} \tag{12.19}$$

By way of example, if $\tau = 0.2\ \mu s$, then $c\tau = 197$ ft; if the target range is $S = 1400$ ft, then

$$l = 1400 + 197 = 1577 \text{ ft}$$

$$w = 197\left(1 + \frac{2800}{197}\right)^{1/2} = 768 \text{ ft}$$

Hence, the clear (obstacle-free) width of this test range should be about half its length. Multipath returns can be generated by obstacles or scatterers that share the range gate with the target.

Clutter can be reduced by illuminating as little ground area as possible in the vicinity of the target. The ground itself should be smooth and bare. Target support structures should be carefully designed for minimal return, and target rotators should be well shielded. If necessary, the rotator and the surrounding ground should be covered with radar absorbing material to minimize interactions between the target and the ground.

The use of radar clutter fences can reduce the specular return from the ground in the event the ground-plane effect is undesired, as might be the case at millimeter wavelengths. However, PSL concluded in its study of the RATSCAT ground plane range [2] that clutter fences offer no distinct advantages. This is because the top edge of the fence diffracts incident energy toward the target as well as back toward the radar, and edge diffraction is very hard to suppress. One way to reduce the diffraction is to tighten up the transmitted beam and increase the target height to minimize the illumination of the edge—but this is precisely what would be done to eliminate the specular reflection from the ground. Consequently, the cost and effort of deploying radar clutter fences seem hard to justify. However, if the ground has vegetation that cannot be eliminated or controlled, the use of fences should not necessarily be ruled out.

12.7 DEFEATING THE GROUND PLANE

There are instances when it is more advantageous to defeat the ground-plane effect than to try to exploit it. There may be several reasons, one of which is to avoid vertical antenna height adjustments. As we saw earlier in this chapter, the antenna height, target height, range, and wavelength all influence the height of the first lobe in the vertical interference pattern. To exploit the ground-plane effect, the target must be centered in this lobe.

In most measurement situations, the range and target height remain fixed throughout a measurement program. If the frequency were also fixed, the antenna height could be adjusted and left at that optimum for the duration of the test program. However, this is not always typical. In many programs, measurements must be made at several frequencies within a given band, requiring that the antenna height be adjusted and set for each frequency. This can be avoided if the ground-plane effect is defeated.

The effect can be worse for short-pulse (wideband) measurements. The height of the first lobe of the incident field profile varies directly with the radar frequency. Therefore, if the bandwidth of the transmitted pulse is, let us say, 15% of the center frequency, the lobe jiggles up and down as much as 15% from the intended height over the frequencies in the pulse. If the target subtends a significant fraction of this first lobe, the target illumination will be seriously degraded.

Moreover, at millimeter wavelengths, particularly at 95 GHz, it may be difficult to create a ground plane smooth enough to support the forward ground

reflection. For example, if a surface roughness height of 2λ is imposed, corresponding to $\rho_s = 0.91$ at $\psi = 1°$, the ground-plane roughness cannot exceed 0.25 in. It is doubtful that a ground plane could be maintained to this degree of smoothness and, hence, at millimeter wavelengths, ground reflections may have to be suppressed rather than exploited.

One way to suppress the ground reflection has already been mentioned, radar fences, and a typical arrangement is shown in Figure 12.15. The purpose of the fences is to eliminate the reflection from the specular point on the ground, and a single fence is hardly ever sufficient; multiple fences are often installed to suppress diffuse scattering toward the target from the ground. The fence must be made of metallic sheets or screens and may be covered on their front sides with absorber to reduce backscattering to the radar. The upper edges may be serrated to suppress diffraction off the edge toward the target, but the effectiveness of serrations is questionable. The Boeing Company in Seattle once installed radar fences on its 4000 ft outdoor range to suppress the ground reflection, but later removed them.

Another technique is to construct a berm running between the radar and the target. The berm should be in the shape of an inverted *vee*, as shown in Figure 12.16. The berm can be a mound of earth, but it should be covered with asphalt or cement to retard erosion. The apex of the berm should be sharp, rather than rounded, to minimize reflection off the edge toward the target. The slanted sides should be reasonably flat to deflect energy well out of the target zone.

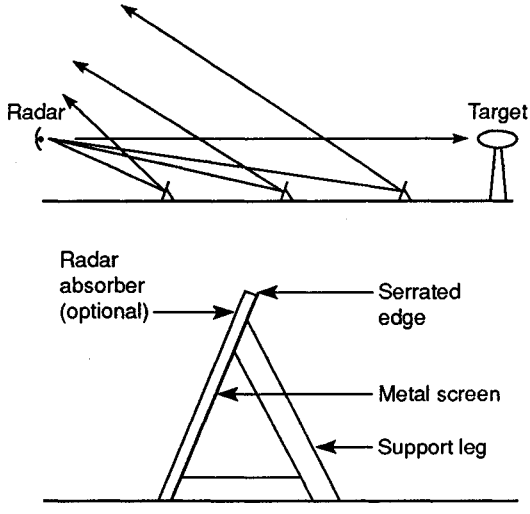

Figure 12.15. Radar fences.

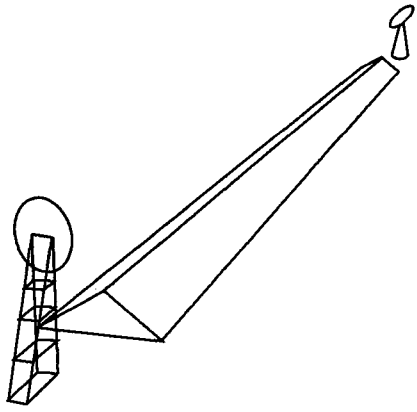

Figure 12.16. A berm constructed between the radar and the target suppresses the ground reflection.

There seem to be no established design values for this kind of berm. The Teledyne Micronetics Company in San Diego operated an outdoor measurement range for a number of years with an asphalt berm about 4 ft tall and 20 ft wide. The apex of this berm did not have a sharp edge.

12.8 EXAMPLES OF PAST AND EXISTING RANGES

Several large airframe manufacturers operate their own RCS test ranges in support of internal development programs or government contracts for weapons research and development. Whether internal or not, these developmental programs ultimately target military customers, as there are no RCS requirements in the civilian market. The U.S. Department of Defense does not necessarily constitute the sole military market of U.S. airframe manufacturers.

Examples of large, privately owned outdoor test ranges are those of Boeing, McDonnell Aircraft, Lockheed, and Northrop. Private capital has also built the world's two largest *compact ranges*, about which we will have more to say in Chapter 13. The U.S. Air Force operates two large national ranges in New Mexico, one of them since 1964.

It is interesting to note the similarities and differences between large outdoor ranges in the late 1960s. In a 33-month study of ranges conducted by the University of Michigan at the time [3,4], five ranges were selected to participate in an assessment of large-target measurement capabilities. Of the five, two were later dismantled, and one has changed hands at least twice. (The five are listed in Table 12.3.) Conductron Corporation and Radiation Services were the two companies

Table 12.3
Reflectivity Ranges Evaluated in the Late 1960s

Site	*Transmitter*	*Max. range used, ft*	*Geometry*	*Type*	*Data Recorded Dynamic range*	*Digital equipment*
Conductron Corp.	CW	200	Ground plane	Amplitude	40 dB	Paper tape
Radiation Services	Pulse	1000	Ground plane	Amplitude	40 dB	Punch cards
General Dynamics	Pulse	1800	Ground plane	Amplitude phase	50 dB	Paper tape
RATSCAT	Pulse	1200	Ground plane	Amplitude phase (L-band)	50 dB	Paper tape
Micronetics	Pulse	600	Berm	Amplitude	40 dB	Magnetic tape

that failed to survive the competitive RCS measurement business. Micronetics Corporation became a Teledyne company after the range comparison and now conducts business as Mission Gorge Research Company.

Of the five ranges listed in Table 12.3 all except Micronetics used the ground plane in their measurements. The Micronetics range is unusual, as we have seen, in that an asphalted berm in the shape of an inverted *vee* runs from the transmitter to the target turntable. The purpose of this berm is to deflect ground reflected waves away from the target and away from the receiver, and it is therefore intended to provide free-space target illumination conditions. Micronetics was in the forefront of data recording in those days, being the only range to take advantage of the high-speed features of magnetic tape as a recording medium. The other four recorded data on paper tape and punched cards, which was a very slow process. Very few modern ranges, if any, record data on these media now.

Conductron and Micronetics both made measurements at much less than the farfield range for the largest target and highest frequencies in the test program. The remaining three ranges also used less than the farfield range, although not as foreshortened as the ranges used by Conductron and Micronetics. The data collected by Conductron suffered severe nearfield distortion, with the broadside lobe of a metal cylinder being split into a pair of lobes with a shallow null between them, and with the measured amplitude being several dB below the true farfield value. This was a consequence of using a CW instrumentation system that radiated very low power, probably much less than a watt. The other ranges used more conventional pulsed systems, with pulse widths ranging from 0.1 to 1 μs.

Only two ranges (RATSCAT and General Dynamics) were able to measure the phase of the backscattered signal. General Dynamics, it might be noted, had the prime contract to build and instrument the RATSCAT range. Hence, it is not unexpected that both ranges had the same capability for coherence. General Dynamics used the longest range in the measurement of the test objects, which was a collection of precision cylinders, the largest being 32 ft long and 5 ft in diameter. Of particular interest is that the now-defunct Radiation Services range turned in the most accurate results for the lowest cost in the least time, a tribute to the company and its range crew. Unfortunately, not all of these virtues are apparent in Table 12.4, which is a summary of how the five ranges were rated on their measurements of the precision cylinders.

Present-Day Outdoor Ranges

In its attempt to take advantage of the capabilities of outdoor test ranges, the U.S. government has conducted or contracted other surveys since the Michigan evaluation was published in 1969. Although the details of those surveys are not available, we list in Table 12.5 the salient features of most of the outdoor RCS test

Table 12.4
Range Ratings

Range	*Facilities, techniques, procedures*	*Cylinder Data Accuracy*		*Relative cost*
		Direct polarization	*Cross polarization*	
Conductron Corp.	B−	D	C	1.12
Radiation Services	B	B	C	0.47
General Dynamics, Ft. Worth	B+	C	D	1.32
RATSCAT	B	C	C	GFE
Micronetics	B−	D	D	1.09

ranges in the United States. The first six are federal-government facilities and the remainder are privately owned.

As indicated in the third column of the table, not all of the ranges rely on the ground-plane effect, and at least one is instrumented for dynamic RCS measurements. The distance listed in the third column is the maximum distance available or used for testing, as many of the test ranges are equipped with several permanent target pits (turntables) at shorter distances. Note that the two listed look-down facilities are operated in support of U.S. Navy testing.

The fourth column shows that the majority of the ranges rely on commercial instrumentation radars. All of these systems are coherent, one of the requirements for generating ISAR imagery. Most of the radars can cover a decade of continuous-frequency bandwidths, and some of the facilities have implemented spot-frequency coverage at millimeter wavelengths.

Although much of the data listed in the table represent maximum capabilities, not all combinations are possible. The 100 Klb target capability listed for RATSCAT, for example, is available only on a special, heavy-duty turntable at ground level. This results in very strong interactions between the target and the ground that do not appear in more conventional free-space or ground-plane testing. Similarly, the 800 ft maximum range listed for the Mission Gorge facility precludes farfield testing for all but small targets (a few feet in size at best) for most of the listed instrumentation frequencies.

When the Air Force accepted the RATSCAT site from the contractor in 1964, it was the most advanced outdoor test range in the world [5]. Located on several square miles of alkali flats on the White Sands Missile Range in south-central New Mexico, the facility sported the latest technology. Its radars featured the *sigma servo*, an accurate device for measuring the amplitude of the received target echo, and the range was equipped with three target rotators embedded in concrete bunkers known as *pits*. Each pit was encircled by a *bistatic road*, anywhere along which could be stationed a van housing the receiver of a bistatic radar. All three

Table 12.5
Summary of Range Capabilities

Range	*Location*	*Range type**	*Radar type***	*Freq. coverage (GHz)*	*Comments*
Naval Air Warfare Center	Patuxent River, MD	F/D	Pulsed		
RAMS	White Sands, NM	*G* 8500 ft	SPC MKIII	0.145–18	ISAR
RATSCAT	White Sands, NM	*G* 7500 ft	Pulsed, Coherent	0.15–18, 35, 95	100Klb targets
Naval Air Warfare Center	China Lake, CA	*L* 17000 ft	SPC MKI	2–4, 8–12, 36	ISAR
Naval Air Warfare Center	China Lake, CA	*G* 4000 ft	SPC MKII	0.75–18, 35–37	ISAR
Naval Surface Warfare Center	Santa Cruz Island, CA	*L*	SPC MKIII	0.15–35	lookdown area is ocean, ISAR
Lockheed	Helendale, CA	*G*	SPC MKIII	0.15–18	ISAR
Martin Marietta	Orlando, FL	*G* to 6000 ft	SPC MKIII	0.7–18, 35	1kW EIA at 35 GHz
Northrop	Tejon, CA	*G*	SPC MKIII	0.15–18	ISAR
McDonnell Douglas	Palmdale, CA	*G* 3385 ft	SPC MKIII	0.15–18	20Klb targets, ISAR
McDonnell Douglas	Palmdale, CA	*G* 3750 ft	Pulsed	0.15–35	fixed PRF, very high power, magnetron
Rockwell	Tulsa, OK	*G*			Noncoherent
Pratt & Whitney	West Palm Bch, FL	*G*	SA/CW, SPC MKIV	1–18, 8–12	ISAR
General Dynamics	Meridian, TX	*G* 6500 ft	SPC MKIV	1–18	ISAR
General Dynamics	Meridian, TX	*G* 2000 ft	SPC MKIV	0.1–2	ISAR
Mission Gorge	San Diego, CA	*G* 800 ft	Pulsed, Coherent	0.125–40, 56, 78, 94	ISAR
Boeing	Boardman, OR	*G* 7500 ft	SA Pulsed, Coherent	0.1–18, 33–40	5Klb targets, ISAR
Boeing	Kent, WA	*G* 2000 ft		2–18	
General Dynamics	San Diego, CA	*G* 2000 ft	SA/CW	1–18	

*G = ground bounce, F = free space, L = lookdown, D = dynamic
**SA = Scientific Atlanta, SPC = System Planning Corporation

pits were illuminated by transmitting antennas installed at a central operations building.

The target pits ranged from 458 to 2358 ft from the transmitters, and each contained a 17 ft turntable that could be raised or lowered a few feet by means of a hydraulic ram. The rotation axis could also be tilted away from the vertical. Styrofoam columns up to 24 ft tall were mounted on the turntables to support test objects, and large mobile target shelters were used to protect, service, install, or remove targets from these columns. Resembling small metal barns on wheels, these shelters were rolled away from the pit during RCS measurements. The site was therefore equipped for efficient, state-of-the-art measurements of both the monostatic and bistatic RCS of large targets. Its designers regarded it as an important tool not only for routine RCS testing, but for research purposes as well.

The original configuration of RATSCAT changed as measurement requirements changed and technology advanced. Although the sigma servo was an accurate signal measurement device, it relied on the operation of an electromechanical servo system and was therefore very slow by today's standards. It was replaced in the mid-1970s by much faster, if not more accurate, signal measurement and encoding devices. Extruded styrofoam logs for the fabrication of target support columns became unavailable and were replaced by beaded-foam billets. Pit 1, at a range of only 458 ft, was dismantled and filled because it failed to satisfy projected as well as then-current test requirements. A large, heavy-duty turntable was installed at Pit 6, but was abandoned in the mid-1970s. A state-of-the-art 75 ft steel pylon was installed at about the same time at an unprecedented range of 7500 ft, permitting farfield measurements that could be conducted previously only at less than farfield distances. (Even though no bunker there qualifies it for the appellation, the 7500 ft range is nevertheless called *Pit 7*.)

RATSCAT was upgraded in 1981 with the installation of ARMS, an acronym for advanced radar measurement system. ARMS was a collection for four separate radars, all operating simultaneously, that reduced target exposure and range time. Each radar was equipped with its own chart recorder, and although it was sometimes doubtful that all four could remain "on the air" for the duration of a test program, the system quartered the time it took to collect RCS data for four radar bands. ARMS is now obsolete, however, due to the advances in coherent, stepped-frequency instrumentation discussed in Section 12.2: the RATSCAT version of it is called *IRMS* (integrated radar measurement system).

Despite these improvements, RATSCAT did not satisfy one of the most important requirements of outdoor testing: security. Although the site did have, and still does have, the capability to measure large targets at distances near, if not beyond, the far field, it demanded not less than an hour, and often more than an hour, to remove the target from the 75 ft pylon at Pit 7. The same amount of time must also be invested when the target is installed on the pylon, severely restricting available measurement time between transits of spy satellites over the site. Because we must deny unfriendly powers the opportunity to assess U.S. weapons development, we must deny them visual access to the target, and this limits test time on the range.

Although this can be accomplished by testing under starlight between dusk and dawn, it still severely restricts available range time. A significant improvement was the construction of the RAMS (radar advanced measurement site) test facility some 25 miles north and west of RATSCAT. Completed in the early 1980s, RAMS is equipped with a huge retractable pylon some 95 ft tall. Patterned after the concept implemented at Lockheed's outdoor range near Helendale, California, the pylon and its test target can be lowered in a matter of minutes into a deep silo bored into the desert floor. Rumored to have cost $30 million, this impressive installation makes it possible to secure a target from satellite observation in a fraction of the time formerly required for pylon testing.

We now know that Lockheed had developed the faceted configuration of the predecessor of the F-117A stealth fighter by 1978 [6]. Although this aircraft and other prototypes were flown against some tactical radars of the day on dynamic test ranges, no static RCS test range was capable of measuring their RCS characteristics under more rigidly controlled test conditions. We suspect, therefore, that RAMS and Lockheed's Helendale ranges were built in direct response to the need to support the development and testing of stealth aircraft like the F-117A and the B-2.

The lower portion of the retractable RAMS pylon is shielded from the instrumentation radars by the *shadow-plane range* sketched in Figure 12.17. Although it might seem that the purpose of this configuration is to reduce the influence of residual echoes from the pylon, a necessity in the measurement of targets with small radar cross sections, another objective was probably to shield the building at the base of the pylon. Because this structure covers the retracted pylon and the target on it, it is the center of great activity. All target-related work must be done here, including the unloading and storage of models trucked to the site, initial preparation of a target for measurement, its attachment to the retracted pylon, and configuration changes that must be accomplished from time to time during a test program.

Although these activities could be accomplished just as well in a huge, covered bunker embedded in the ground at the level of the ground plane itself, people who work there need access to it, by means of either an underground tunnel or an

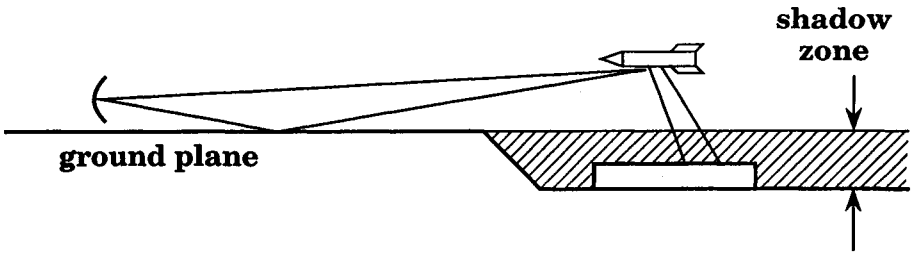

Figure 12.17. The shadow-plane range concept implemented at RAMS.

access road on the ground plane, but probably by both. When we consider the potential loss of range time due the need for people and vehicles just to get to and from the target support structure, the cost of housing their activities in a huge, underground bunker, the cost of building an alternative access route (a tunnel), and the frequency with which people arrive at and depart the site, the shadow-plane concept becomes very attractive. Because they are shielded in the shadow of the range, vehicles and people may come and go at will with virtually no impact on tests underway. Thus, the logistics of operating and servicing the range were probably just as important in its design as the minimization of unwanted background returns from the lower part of the pylon.

The underground silo is not the only solution to rapid target deployment and retrieval, however. When Boeing constructed the most recent of North America's large outdoor test ranges in 1990, the company elected to use a huge, self-propelled barn to protect, secure, and service the test target. Called the TAG (test article gantry) and ballasted with 400 tons of concrete in its base, this big, steel barn is designed to withstand 100 mph winds against its 95 ft tall sides. Although the upper half of the structure is sheathed in protective steel siding, the lower half is not. Therefore, when seen from the operations building some 8000 ft uprange, the TAG looms on the horizon like mechanical monster from a *Star Wars* film.

When not in use for servicing or protecting the target, the TAG is parked some 500 ft to the side and downrange from a 55 ft pylon installed 7500 ft from the instrumentation antennas. It propels itself to and from the pylon over a pair of steel rails by electric traction motors located at the four corners of its base. Traction power is derived from one of two on-board, diesel-powered generators, which also supplies power to operate the hydraulic systems of lifts installed along the inner sides of the structure. In addition to lifts for servicing the target, the TAG is equipped with a crane for installing and retrieving the target from the pylon.

The second of the two generator units is held in reserve against possible failure of the first. This is to ensure that a target need never be compromised (exposed) for the lack of motive power. Boeing's TAG can probably be rolled over its target in about the same time the RAMS pylon can be retracted and its target covered.

The large, mobile target-handling concept is also used on the Martin-Marietta Aerospace Company outdoor test range constructed near Orlando, Florida, in the early 1980s. Like RAMS and the newer Boeing test range, the Martin-Marietta ground plane is paved, and the facility is equipped with coherent, frequency-stepped radars. Indeed, the only large outdoor range that has not been paved is the one at RATSCAT, and for good reason. The alkali flats are frequently scoured by high winds, particularly in late winter and spring, that can pile the gypsum in drifts as tall as 5 ft. The unpaved ground must be periodically smoothed with road-grading equipment, and because this would have to be done even if the range were paved, paving it would be fruitless.

Northrop's Tejon range is in California's Antelope Valley some 100 miles north of Los Angeles. Like RAMS, it is nestled in the foothills of a low mountain range. The paved ground plane at Tejon slopes slightly downward away from the transmitters, resulting in a slight bias that must be accounted for when the target is installed and aligned on the target pylon. The Tejon site has two RCS ranges nearly side by side, angled a few degrees apart to form a vee. Two sets of instrumentation radars are housed in equipment buildings at the apex of the vee. Although comparative data are not available, the Tejon range seems to be plagued by windy conditions as often as RATSCAT. The site has a third, shorter range that seems to be used mostly for antenna testing.

Also in the Antelope Valley is the McDonnell test range, some 25 miles east of Palmdale. It is among oldest of the outdoor ranges, predating the Martin-Marietta, Boeing, Northrop, and Lockheed ranges. At a time when fewer test ranges competed for the business of outside customers, the McDonnell range enjoyed high utility and high visibility, and it was staffed by experienced engineers and equipment operators. The construction of more and newer test ranges in the last decade has led to heightened marketing activity among range owners, however. Indeed, the McDonnell-Douglas Technical Institute (MDTI), the current owner of one of the two largest compact ranges ever built, has aggressively advertised the availability of its facility to outside customers.

In much the way the RAMS and Helendale ranges were built with specific weapons in mind, the General Dynamics Corporation built its test range near Ft. Worth to support development of the TFX fighter, which eventually became the swing-wing F-111 fighter-bomber. The GD/FW range is one of the earliest of the outdoor ranges, and RATSCAT, also built by General Dynamics, was patterned after it. The GD/FW radars were initially housed in vans that could be parked nearly anywhere on the test range, but more permanent structures have since replaced most of the vans. One of the more interesting features of the range is a temporary shelter erected over the target pit.

The shelter is a large air bag more than 100 ft long kept inflated at low pressure by a high-volume air pump. The incident radar wave and the returned echo pulse from the target both pass through the walls of the air bag with little distortion. Although the incident wave suffers partial reflection at the near and far sides of the bag, they are displaced in time far enough from the target echo that their effects are sensibly eliminated from the desired signal by range gating. In addition to this advantageous displacement in time, the inclination of the surface of the bag to the direction of arrival of the incident wave further reduces interference by deflecting the reflection away from the radar. The operators of the GD/FW range report that the inflatable shelter does not seriously degrade the uniformity of the incident wave over the target. Being opaque, the shelter makes it possible to measure classified targets during daylight hours as well as at night.

The Mission Gorge (formerly Micronetics) test range in suburban San Diego is one of the shortest of the outdoor test ranges (1000 ft), and its very location makes the measurement of classified targets nearly impossible. It is unusual in two

respects, however: the range was once fitted with the ground-defeating berm discussed in Chapter 11, and it once had a shallow, water-filled "test pond" for the measurement of submarine periscope models and other fixtures associated with marine targets. The over-water range was equipped with a hydraulic support system to adjust the above-water exposure of the test object, rotate it in azimuth, and even tilt it away from the vertical. The berm has been removed, with the consequence the range must be operated in accordance with the rules of the ground-plane range. The test pond was drained in the autumn of 1982, a testimony to the continuing change in RCS test requirements.

12.9 SUMMARY

The measurement of target echoes on the static outdoor RCS test range must take into account reflections from the ground. Unlike reflections from the walls of indoor test chambers, the suppression of ground reflections is very difficult.

Energy reaches the target via a direct path and reflection off the ground, and target echoes return to the radar via the same two paths. The result is an interference between the signals received via the two paths, and we must be careful to minimize any degradation due to the interference. We developed a simple rule-of-thumb relationship between wavelength, antenna height, target height, and range to the target governing the operation of the outdoor test range. We emphasized that, although we can rely on this relationship in the design and operation of the range, the incident field structure should be probed periodically to verify that the ground plane effect has been properly accounted for.

We discussed the instrumentation typically used on contemporary outdoor test ranges, pointing out that the current demand for radar imagery relies, in turn, on the use of stepped- or swept-frequency waveforms and the coherent detection of received signals. The changing frequency of such waveforms causes the interference pattern in the target zone to expand or compress like an accordion, thereby sweeping the desired lobe of the pattern through the target zone. Because this sweep occurs once on the emission of each swept pulse or frequency-stepped pulse train, we cannot compensate for its effect by any mechanical means. The effect is not detrimental for bandwidths of a few dozen percent, however.

A serendipidous benefit of the ground-plane reflection is that it can increase the available signal by 12 dB over that of a comparable free-space test range when the reflection is perfect and the radar antennas are omnidirectional. This may drop by only a decibel or two when the reflection is imperfect, and paradoxically enough, we may even have to give up another decibel when we use practical antennas with substantial gain to concentrate power on the target. The small loss of sensitivity in that latter case is insignificant when compared to the increased sensitivity brought about by higher antenna gain, however. We explored the question of where to point the antenna on the ground-plane range and concluded that, for all practical purposes, the antenna should be aimed parallel to the ground plane, pointed neither up to the target nor down to its image.

There are times when it is more difficult to accommodate the ground plane interference phenomenon than to suppress it, and we cited radar fences and berms as devices used in the past to defeat the ground plane. Radar fences have never been proven effective, however, and we are aware of no instance in which they are now used outdoors. It appears that the berm running between the radar and the target has suffered a similar lack of demonstrated utility.

We showed that, along with the pulse width, bistatic interactions between the target and objects on the test range govern the clear area that must be maintained on the outdoor range. This area is an ellipse whose major axis is aligned along the range centerline, and this major axis must often be significantly greater than the distance between the radar and the target.

We concluded our discussion of outdoor test ranges with a brief summary of the capabilities and characteristics of the six largest and best known facilities. Two are operated by the U.S. Department of Defense, two have retractable target support fixtures, and no fewer than two rely on gigantic mobile barns for target protection, installation, removal, and servicing. Aside from the two DoD ranges, all are owned and operated by large U.S. airframe manufacturers. All rely on swept- or stepped-frequency radar systems, all have demanded the investment of great capital, and all are costly to maintain and operate. All are testimonials of the importance of radar as a tool of war.

REFERENCES

[1] Knott, E. F., *Radar Cross Section Measurements*, Van Nostrand Reinhold, New York, 1993.

[2] Bush, T. F., (ed.). "Evaluation of the RATSCAT Ground Plane Range," Report No. PE00911, Physical Science Laboratory, New Mexico State University, Las Cruces, August 1978.

[3] Hiatt, R. E., E. F. Knott, and T. M. Smith, "Evaluation of Selected Radar Cross Section Measurement Ranges, Part I," University of Michigan Radiation Laboratory, Report No. 7462-1-F(I), March 1969.

[4] Hiatt, R. E., E. F. Knott, and T. M. Smith, "Evaluation of Selected Radar Cross Section Measurement Ranges, Part II: Cylinder Tests and Range Evaluation Procedures," University of Michigan Radiation Laboratory, Report No. 7462-1-F(IIA), March 1969.

[5] Marlow, H. C., D. C. Watson, C. H. Van Hoozer, and C. C. Freeny, "The RATSCAT Cross Section Facility," *Proceedings IEEE*, Vol. 53, August 1965, pp. 946–954.

[6] Sweetman, Bill, and James Goodall, *Lockheed F-117A*, Motorbooks International, Osceola, WI., 1990, p. 23.

Chapter 13
Indoor RCS Ranges

M. T. Tuley and E. F. Knott

13.1 INTRODUCTION

Indoor RCS measurement ranges offer advantages not possible on outdoor ranges. Probably the single most important disadvantage of outdoor measurements is the necessity of dealing with both the vagaries and the long-term effects of weather. Measurements cannot be made in the rain because of moisture collection on targets and target support columns and the backscatter from the raindrops in the measurement zone. Although many of the outdoor ranges listed in Table 12.5 are in the desert, where rain is rarely a problem, wind is a major concern. All outdoor ranges have requirements that limit operation in even moderate winds. If foam support columns are employed, light guy lines are almost always used to secure the target and prevent it from blowing off its support. Those guy lines contribute to the RCS, and even with lines providing additional support, measurements must often be halted when wind speeds approach 10 m/s. The weather encountered on outdoor ranges is also hard on range equipment exposed to the elements (support columns or pylons, turntables, RAM, antennas). For example, at RATSCAT over a period of time hygroscopic gypsum dust coats and penetrates the surface of support columns and the RAM used to shield turntables. The dust adversely affects scattering characteristics, particularly in wet or humid weather, requiring more frequent replacement of those components than on indoor ranges.

Moreover, outdoor measurements are subject to overhead observation by aircraft or satellites, a significant problem with sensitive targets. Although many ranges are in controlled airspace areas and satellite schedules are known, having to dismount or shield the target during potential observation times can significantly

reduce measurement throughput. Night operations are often used to prevent observations within the visible spectrum, but they increase target-handling problems and do not prevent observation within the infrared or radar bands. The desire for unobserved measurement of sensitive targets often forces the location of ranges at remote sites, making range access time consuming and inefficient.

An indoor facility eliminates the hazards of weather and unauthorized viewing that collectively account for an estimated 35% loss of range time at outdoor installations such as RATSCAT. The target is completely shielded from the weather and unauthorized observation, and personnel (and equipment) can work in a comfortable environment. The chamber ceiling can be fitted with hoists to facilitate target installation and removal, and the enclosure itself prevents radar energy from escaping into the environment and allows protection of the target from unauthorized viewing. Although a large building is required to house the range, much less real estate is required than for outdoor ranges.

Nevertheless, the indoor range is not without its disadvantages. Target sizes are limited, although indoor compact ranges exist that feature 12 m diameter or larger measurement zones. A great deal of care must be taken to reduce the effects of reflections from the chamber walls. Such reflections provide both forward scatter (multipath), which causes phase and amplitude variations in the field illuminating the target, and backscatter (clutter), which raises the background level of the measurements. However, significant efforts over the past decade or so in characterizing and improving indoor range performance and producing wideband coherent instrumentation systems have resulted in indoor ranges with excellent capabilities to measure even relatively large targets to very low RCS levels.

The remainder of this chapter discusses some of the fundamentals of chamber design, describes compact range techniques, and presents an overview of range instrumentation with a focus on wideband coherent operation and its employment to enhance indoor range operation. Much of the material on range design and compact range fundamentals is drawn from chapters by L. Pellett [1] and M. Tuley [2] in *Radar Reflectivity Measurement: Techniques and Applications*. The interested reader is directed to those references for more detail.

13.2 CHAMBER DESIGN

The design of chambers for modern RCS measurements is strongly influenced by the physical size of the targets to be measured, the RCS levels that must be achieved, the frequency bands to be covered, and the type of instrumentation to be used for the measurements. Early indoor ranges were mostly implemented using continuous wave radars, and so reflections from any part of the range could interfere with the target return. Along with the use of absorbers, a simple analog nulling loop was generally the only means available to reduce the effect of background

returns. Modern measurements are typically made by using wideband coherent instrumentation radars. When wideband data are processed (i.e., transformed to the time domain) to provide high-range resolution, much of the undesired reflected energy from other parts of the chamber can be gated out of the return, leaving a "cleaner" target signal. On systems that store data digitally, the background can be recorded and subtracted from the target-plus-background return to increase sensitivity and accuracy. In addition, coherent integration can be used to reduce the receiver noise floor. These processing steps provide the opportunity to accurately measure much lower RCS levels than those achievable with the older techniques and also significantly modify the requirements on chamber scattering characteristics. Nevertheless, even with modern processing techniques, intelligent chamber design can reduce the processing burden and can result in better range sensitivity and accuracy.

On outdoor ranges, the clutter that competes with the target return can be controlled by making the surface of the range smooth in the target resolution cell so that very small amounts of the incident power are backscattered toward the radar. Similarly, the only possible multipath surface on an outdoor range is generally the ground plane, which has been specifically designed to provide an in-phase component to the incident field, thereby increasing range sensitivity (see the discussion of ground plane ranges in Chapter 12). On indoor ranges, however, the walls, floor, and the ceiling of the chamber provide ample opportunity for forward and backscattered signals to interfere with accurate measurements. One of the major thrusts in indoor chamber design has been to control chamber reflections so that high-quality RCS measurements can be obtained.

At least three methods are available to reduce the problem of undesired reflected signals on indoor ranges. Two of the methods, careful design of the chamber size and shape and use of RAM, are discussed in the following subsections. Use of high-range resolution processing to discriminate against unwanted returns is mentioned in the next subsection and discussed in more detail in Section 13.4.

13.2.1 Chamber Geometry

Although compact ranges have recently become very popular for RCS measurements, a majority of the existing indoor ranges are conventional farfield ranges. Much of the work done in designing chamber geometries is based on the farfield setup, with an antenna located at one end of a chamber to illuminate a target at the other end, as illustrated in Figure 13.1. As with ground-plane ranges, a chamber is subject to multipath effects, even though its walls may be covered with absorbing materials. In a chamber there are four possible specular bounce paths like those shown in Figure 13.1 (floor, ceiling, and two walls), and thus the multipath problem is potentially much worse than on an outdoor ground-plane range.

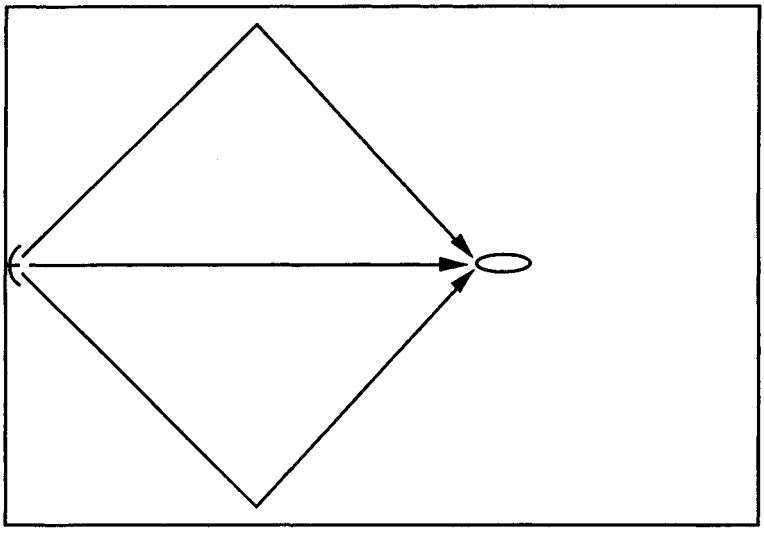

Figure 13.1. A rectangular anechoic chamber suffers multipath illumination due to wall reflections.

If a software or hardware range gate can be placed around the target, then one method to reduce multipath is to simply ensure that signals forward scattered from the enclosure toward the target are delayed for a long enough time that they lie outside the range gate. As the range gate must encompass the entire target in the downrange direction, gating is effective only if multipath components reaching the target area have a time delay relative to the direct signal in excess of $2D/c$, where D is the target downrange extent, and c is the speed of light. For a rectangular chamber, ensuring that the field forward scattered from the specular point to the target can be discriminated from the direct path return requires

$$\sqrt{R^2 + (2W)^2} - R > 2D \tag{13.1}$$

where R is the distance between the antenna and target, and W is the length of the normal drawn from the antenna or target to the nearest sidewall, ceiling, or floor. Another possible multipath problem arises from interaction of the target and the enclosure areas adjacent to it. To ensure that such interaction returns fall outside the target extent requires that the chamber width and height be at least three times the largest target dimension [1].

At low frequencies, where absolute bandwidth is generally limited so that narrow range gates are difficult to provide, possibly the best geometry for an anechoic chamber is the tapered design illustrated in Figure 13.2. The taper region

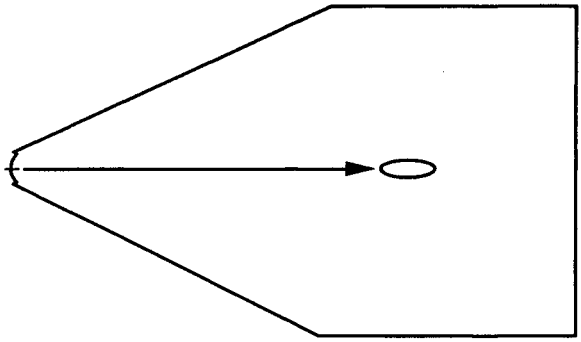

Figure 13.2. Tapered anechoic chamber has little sidewall reflections.

effectively removes the sidewall, floor, and ceiling regions where specular reflections can occur; hence, chambers with this design are superior to the conventional rectangular chamber. The tapered concept was first described by Emerson and Sefton [3]. King, Shimabukuro, and Wong [4] built small models of rectangular and tapered rooms and probed the internal fields using a small horn as a transmitter. They found that the multipath fields were apparently almost eliminated, although they also discovered that the decay in field strength with propagation distance deviated from the normal free-space fall-off rate. Later, it was discovered that the improper decay in field strength with distance was due to multipath reflections from near the apex of the tapered chamber. These reflections arise because the illuminating antenna is not a point source that can be placed at the very apex of the chamber. Because image sources created by the wall reflections lie very close to the antenna, an interference pattern is created along the chamber axis. For sufficiently low frequencies the period of this pattern is so long that it cannot be measured in the chamber, yet its influence is sufficient to alter the apparent rate of decay of the radiated field. A reference target is always used to calibrate RCS, so this multipath effect can be calibrated out, making tapered chambers superior to rectangular chambers for conventional indoor farfield RCS measurements, especially at low frequencies.

To meet *radio frequency interference* (RFI) and security requirements, indoor ranges often must be in shielded enclosures, or "screen rooms." Security requirements may dictate isolation values of as much as -120 dB over a frequency range from 1 kHz to 40 GHz [5]. Such rigid specifications for RF isolation require continuous soldered seams between metal sheets or screens, the shielding of power lines, cables, and communications lines entering the chamber, and the use of RF gaskets on doors. Screen room design is complicated by requirements for lighting, heating, cooling, ventilation, and adherence to fire safety codes. Enclosures meet-

ing approved isolation specifications are available from several manufacturers, so we will not further concern ourselves with those requirements here.

13.2.2 RAM for Anechoic Chamber Applications

Although it would be ideal to always employ a chamber geometry that completely eliminates the problems of clutter and multipath, this is rarely practical because of the large chamber size required for a given target size. Hence, indoor ranges are typically implemented in anechoic chambers, where RAM is used to reduce the effects of chamber reflections to a manageable level. As the requirements on range absorbers are much different than those described in Chapter 8 for operational RAM, a special set of absorber designs has evolved for use in chambers. In general, anechoic chamber absorber has much less stringent thickness and mechanical performance requirements than absorbers for use on aircraft or other platforms. However, the relaxation of those requirements is offset by significantly higher absorption and bandwidth requirements than would generally be seen in other applications.

Currently, almost all of the absorber seen in chambers is made of carbon-impregnated polyurethane foam. Pyramidal and wedge-shaped absorber are most often used, although twisted-wedge and convoluted absorbers are also available. The pyramidal concept appears to have been originated by Tiley [6], who suggested that the absorber be cast in molds into which a "high-loss mixture" is poured. The mixture, Tiley went on to say, "may include a finely divided carbon in the form of lamp black, graphite, deflocculated graphite in water, or other resistant materials retained in position by a suitable binder, such as plaster of paris, a synthetic resin, or other dielectric material." Although the pyramidal shape was recommended by Tiley, the binders he recommended were too heavy for practical applications.

Modern foam absorbers are made of an open cell foam that is compressed and immersed in a latex solution containing carbon particles (and, generally, fire retardant salts). The block is allowed to expand, drawing the solution into the cells of the foam. The foam is then compressed, driving out most of the liquid, but leaving the conductive particles trapped in the foam structure. After drying, an oscillating hot wire or numerically controlled saw can be used to cut a sawtooth wedge design. If pyramidal rather than wedge absorber is desired, the block is rotated 90° and fed through the cutting mechanism a second time to form pyramids. Finally, a layer of low radar reflectivity paint is applied to provide protection and to improve the visual lighting in the anechoic chamber.

The performance of the absorber is dependent on its thickness in wavelengths (see Figure 8.19, for example), so the thickness chosen for a chamber is dependent on the lowest frequency of expected operation and the amount of absorption required. The pyramidal block absorbers manufactured in the United States typ-

ically have square bases 24 in. on a side. High-frequency pyramidal absorbers can be as thin as 3 or 4 in., and very low-frequency pyramids as tall as 12 ft have been produced (see Figure 13.3). Blocks of absorber can be fastened to the walls of the chamber with special adhesives (a permanent installation) or by means of mating fasteners (e.g., velcro strips) glued to the wall and the rear of the absorber panel.

The pyramidal design is a geometrical way of matching the impedance "experienced" by the incident wave just outside the tips of the absorber to the short-circuit (zero impedance) value of the metal bulkhead at the base of the absorber. A heuristic way to visualize the macroscopic effect is to examine the impedance of a very thin transverse layer through the pyramid as a function of the depth inward from the tip. Assuming that the net admittance associated with a particular

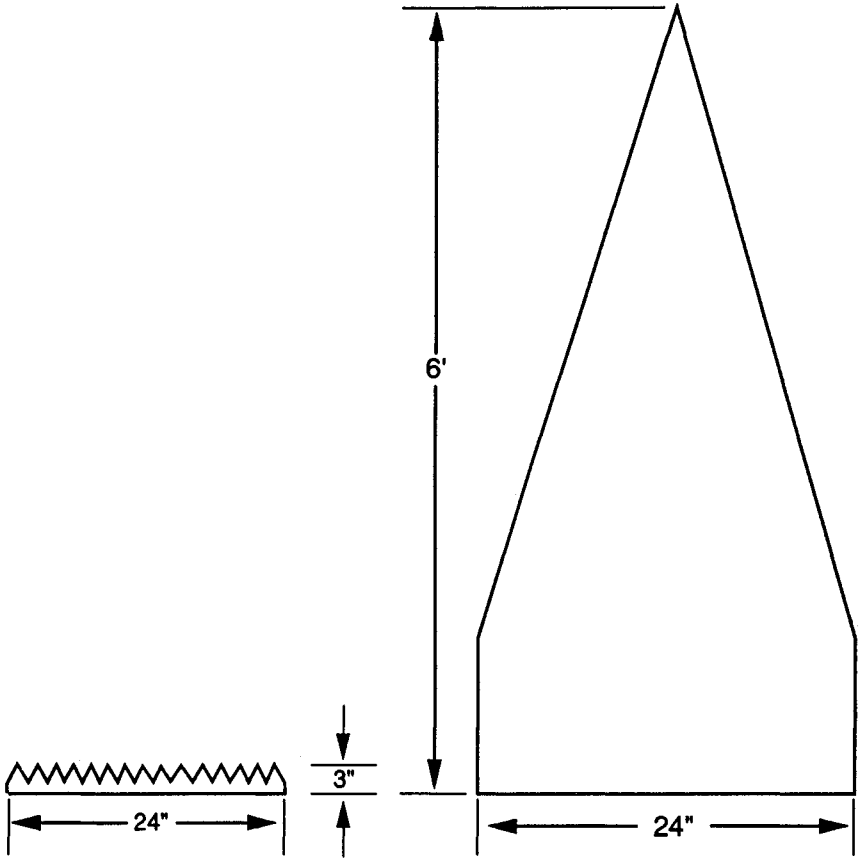

Figure 13.3. Some extremes in pyramidal absorbers.

location is proportional to the area of the absorber times its conductance relative to the remaining area not covered by the absorber, the net admittance is given by

$$Y = (1 - z/h)^2 Y_0 + (z/h)^2 G \qquad 0 \leq z \leq h \tag{13.2}$$

where z is the distance into the absorber from the plane of the tips, h is the total absorber thickness, Y_0 is the admittance of free space, and G is the conductance of the absorber material. Outside the absorber and beyond the tips, the admittance takes on the free-space value. As the wave propagates inward, the admittance rises with the square of the distance. Finally, at the base of the pyramid ($z = h$) the admittance is simply G, the value of the material conductance.

Whatever the actual variation in impedance, the measured incident field appears to decay exponentially once inside the tips. Figure 13.4 shows the results

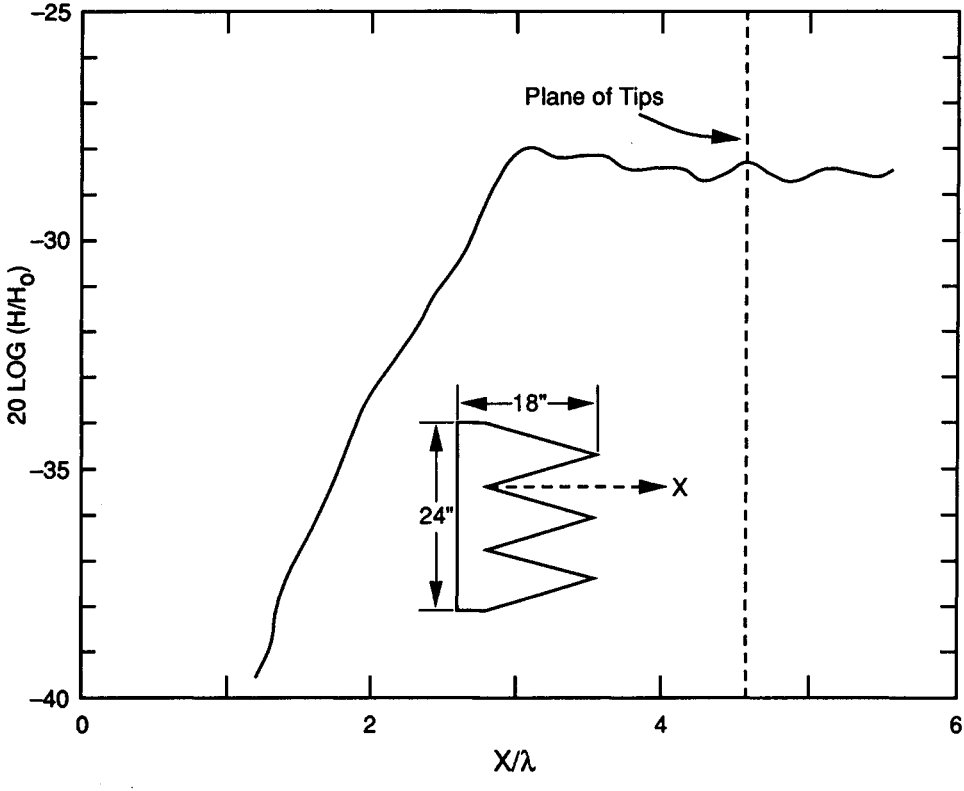

Figure 13.4. Measured field intensity between the pyramids of a pyramidal absorber.

of fields probed between the pyramids of a block of absorber, where the abscissa is the distance x/λ measured *outward* from the trough at the bottom of the pyramids. The field strength remains essentially at the incident field strength level for a distance of approximately 1.5λ inside the tips. Then it decays at a rate of about 6 dB per wavelength for this particular sample.

It is tempting to ascribe the performance of geometric transition absorber solely to a quadratically tapered matching impedance, but the mechanisms involved are much more complex than that. In fact, several recent theses have been concerned with chamber absorber performance analysis and modeling [7, 8]. Two distinct mechanisms come into play in the performance of anechoic chamber absorber. The first involves the scattering properties of the RAM. If energy reflected from the absorber toward the receiver or target is not all in phase, there will be an apparent reduction in the signal strength with respect to that provided by a coherently scattering surface. Energy may also be scattered coherently, but away from the directions of interest (the premise on which a tapered chamber operates). For example, measurements made by Emerson and Cuming at normal incidence on a metallized pyramidal absorber showed an apparent 13 dB of RCSR compared to a flat metal plate [9]. For that case, the apparent loss was due to scattering of energy away from the receiver, rather than absorption.

The amount of scattering is dependent on the surface impedance mismatch between the absorber and free space and the shape of the surface. There will also be internal volume reflections within the absorber due to inhomogeneities. These reflections tend to increase with increasing frequency. Fire-retardant salts add to the internal reflections, sometimes resulting in as much as a 10 dB performance degradation [8].

The second, and desired mechanism, is absorption. Once the electromagnetic wave has entered the absorber, the dielectric loss mechanisms described in Chapter 8 cause the EM energy to be converted to heat. If a geometric optics (ray trace) view of absorber performance is taken, it becomes obvious that the pyramids must be designed so that the angles between adjacent pyramids are small. This will force multiple reflections of rays within the absorber structure. At each ray bounce, some amount of the energy will be transmitted into the absorber to be dissipated. Obviously, the worst design would have adjacent pyramid sides forming right angles. In that case, a ray would suffer only two bounces before being reflected back toward the transmitter.

Figure 13.5 provides average measured backscatter as a function of angle from grazing for pyramidal and wedge absorbers about 15λ thick. The look angle relative to the absorber block geometry is a parameter, with $\phi = 90$ being perpendicular to the axis of the wedges or into the flat side of a pyramid. Therefore, $\phi = 0$ is looking along the trough for the wedge, and $\phi = 45$ is looking into a corner of the pyramids or diagonally across the wedges. The worst performance at low grazing angles is looking across the troughs for the wedge absorber. This

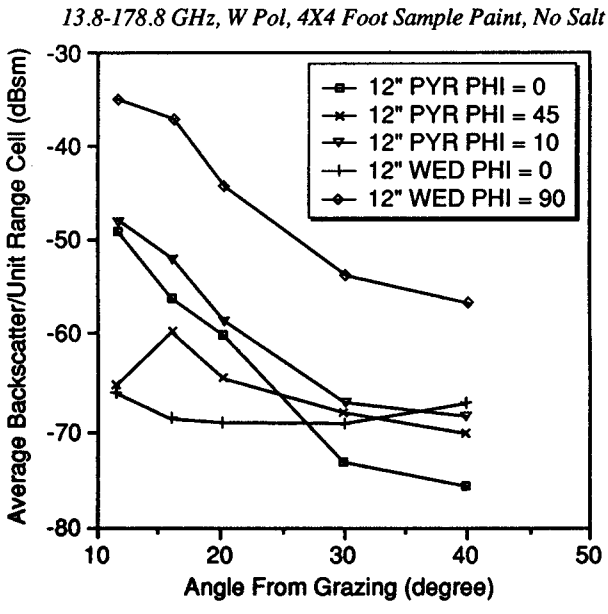

Figure 13.5. Average backscatter of wedge and pyramidal absorber at various grazing angles (from [8]).

is intuitively satisfying, as the absorber appears to be a series of specular knife edges for backscatter at these angles.

The best performance near grazing is given by the wedge absorber at $\phi = 0$ (looking down the troughs). For that reason, wedge absorber is often used in the target zone, where grazing angles are shallow and backscatter is a concern because it raises the background level in the target range cells [1]. Pyramidal absorber is typically used where grazing angles are large (e.g., on backwalls and around collimators on compact ranges) because of its superior absorption performance in those areas. In any event, through use of appropriate absorber and through modern signal processing techniques (hardware and software gating, coherent digital background subtraction, and coherent integration), the target zone background level on modern RCS ranges can often be reduced to much less than -60 dBsm.

13.3 COMPACT RANGES

With limited indoor distances and conventional range concepts, it is difficult to obtain acceptably flat incident phase fronts on targets of useful size, particularly at the higher frequencies. If the $2d^2/\lambda$ farfield criterion is to be met, measurement

of even a 2 m target at X-band requires a range nearly 300 m long. A 4 m target increases the farfield distance to 1100 m. As such chamber sizes are clearly impractical, some alternative technique is necessary if large targets are to be measured indoors.

The compact range represents a successful attempt to significantly increase the size of the targets that can be measured in a given chamber. In fact, compact ranges can now provide some farfield equivalent measurements that even the largest outdoor ranges cannot. The largest current compact ranges have a quiet zone (i.e., the area of near-constant amplitude and phase into which the target must fit) in excess of 10 m in diameter at frequencies up to 35 GHz. A conventional range able to make farfield measurements on a 10 m wide target at K_a band would have to be over 23 km long. There are certainly no fixed outdoor ranges nearly that length, nor any K_a band radars with enough power to make the measurements, even if a range were available.

The compact range concept is based on the premise that devices can be constructed which will collimate a spherical or cylindrical wave to produce a plane wave. Two different collimator implementations are available: lenses and reflectors. Within certain limitations, these devices straighten out the incident phase fronts, making it possible to conduct measurements indoors within a fraction of the distance normally required to satisfy the farfield range requirement. In one case, energy passes through the device and in the other it is reflected. Therefore, the lens must be stationed between the source antenna and the target, while the source antenna and target must be placed on the same side of a reflector device.

Because of the problems in manufacturing large blocks of very homogeneous low-density foam, lens compact ranges have not enjoyed commercial popularity. Design guidelines for lenses are provided in [2], and that chapter should be consulted for more details. The remainder of this section concentrates on the reflector-based compact range.

13.3.1 Theory of Operation

The compact range concept, as developed by R. C. Johnson [10, 11], recognizes that the spherical wavefront from a point source can be converted by a paraboloidal reflector into a quasi-plane wave (at least for a few reflector diameters from the reflector surface). The principle is illustrated in Figure 13.6, where a point source feed at the focus is shown illuminating the surface of a paraboloid. If an imaginary plane, commonly called the *aperture plane*, is erected perpendicular to the axis of the paraboloid, the distance traveled by a ray from the focal point, f, to a reflection point, R, on the paraboloidal surface and then to the corresponding point, P, on the plane is independent of the position of the reflection point. Therefore, the distance from f to R_1 to P_1 in Figure 13.6 is equal to the distance from f to R_2 to P_2. Because the two rays start from f in phase, they reach points P_1 and P_2 with the same phase, making the plane of P_1 and P_2 a plane of constant phase.

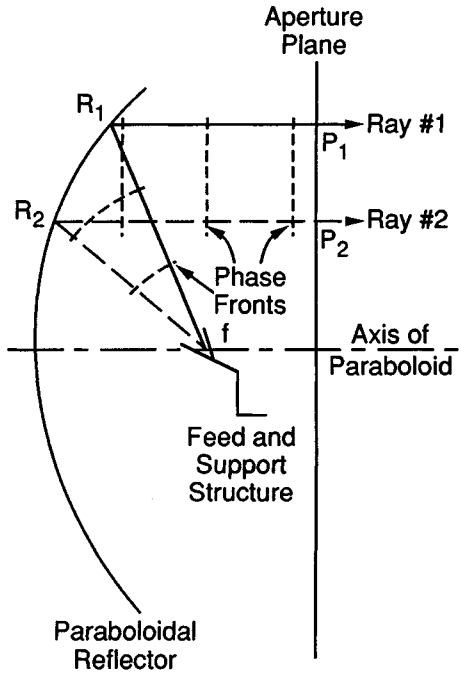

Figure 13.6. Principle of plane wave generation (adapted from [12]).

For RCS measurements, the wave illuminating the target must be both planar and uniform. Once a plane wave is generated, the amplitude profile is independent of position along the direction of propagation. That is to say, if the measurement plane is moved along the axis of the paraboloid to some other position, the amplitude of each ray is the same as if it were in the original position. However, as the wave propagates from the feed to the reflector surface, it diverges as a spherical wave. Therefore, if rays 1 and 2 are emitted from f with equal amplitudes, the ray at R_1 has a smaller amplitude than the ray at R_2, simply because it has traveled a greater distance. Also, the ray at P_1 has a smaller amplitude than the ray at P_2 because the amplitude profile does not vary after the wave becomes a plane wave. For rays 1 and 2 to have equal amplitudes at points P_1 and P_2, ray 1 must be initiated with a larger amplitude than ray 2.

Any microwave feed placed at the focal point will have an amplitude pattern with some taper. Through proper design of the feed (or the feed and a subreflector, in some implementations), the shape of the pattern can be used to compensate for the fact that different rays must travel different distances to reach the reflector

surface. Achieving a desirable illumination pattern over the entire surface of a dish would be difficult. Furthermore, if the lower half of the reflector were illuminated, the wave propagating from the lower portion would be incident on the feed support structure. Diffraction from this structure would provide stray radiation, degrading the uniform and planar characteristic of the wave in the target area. For these reasons, unless an offset feed design is used, only a section of a dish is employed.

A compact range can use the same feed to transmit and receive energy. By reciprocity, if uniform plane wave illumination of the target is produced on transmission, the receiving pattern is equivalent to that of a receiving antenna in the far zone of the target. This becomes evident if we consider a target in the vicinity of points P_1 and P_2 in Figure 13.6. The field scattered from any target can be thought of as a superposition of plane waves propagating in different directions. The plane wave that propagates back in the direction parallel to the axis of the paraboloid will be reflected to the focal point and thus will be received by the feed. However, plane waves propagating back toward the reflector in directions not parallel to the axis will be focused at points other than f, and the energy in these waves will not be received by the feed. Thus, the compact range operates as a plane wave transformer on transmission, converting the spherical wave at the feed to a plane wave, and as a plane wave filter on reception, collecting into the feed only the plane wave scattered back parallel to the axis of the paraboloid. This is exactly the effect achieved on a farfield range by ensuring that the distance is sufficient that a tolerably small phase taper exists across the target.

13.3.2 Reflector Options

The foregoing discussion has assumed a directly fed paraboloidal reflector, one of the three techniques commercially exploited for compact range designs. The Scientific Atlanta line of compact ranges has historically utilized directly fed paraboloidal reflectors, such as that shown in Figure 13.7. The reflector pictured is specified to have a 4 ft high $\times$ 6 ft wide quiet zone over a 2 GHz to 94 GHz frequency range. Much larger reflectors (and, hence, quiet zones) are available from all of the compact range manufacturers. In the range shown, note the use of wedge absorber on the sidewalls, floor, and ceiling of the chamber, and pyramidal absorber around the feed support and the reflector.

Another reflector alternative, employed by March Microwaves, uses two parabolic cylinders to collimate the feed energy [13]. As shown in Figure 13.8, the spherical wave from the feed strikes the first reflector and is collimated in either elevation (as shown in the figure) or azimuth. The partially collimated wave then travels to the second reflector, where it is collimated in the other dimension, and the resulting plane wave travels to the target area. One advantage of this design

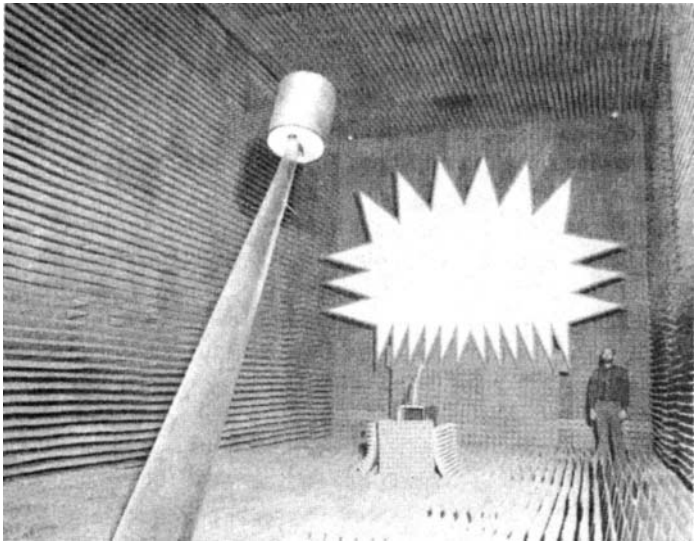

Figure 13.7. Scientific Atlanta Model 5704 compact range with support pylon and "top hat" rotator (courtesy of Scientific Atlanta).

lies in the relative ease of machining precise singly curved surfaces compared to the doubly curved reflector of the conventional design. Another advantage is the relative polarization purity provided by the long effective focal length (the amplitude of the cross-polarized component of the scatter from a reflector is directly related to its curvature and so inversely related to its focal length). Disadvantages include the requirement for two large reflectors instead of one, increased accuracy requirements on surface tolerances, and possible feed spillover into the target zone.

The third type of range design, developed and marketed by Harris Corporation, places a subreflector between the feed and the main reflector, as illustrated in Figure 13.9. One major factor determining the size of the compact range's quiet zone at low frequencies is the amount of energy diffracted into the target area from the edges of the reflector (hence the serrations at the edge of the reflector in Figure 13.7). A shaped subreflector can be used to provide a sharper field taper on the main reflector than can be obtained with a feed horn alone, leaving less energy to be diffracted by the reflector edges. In addition, main reflector shaping can also be used for further control of field purity [14].

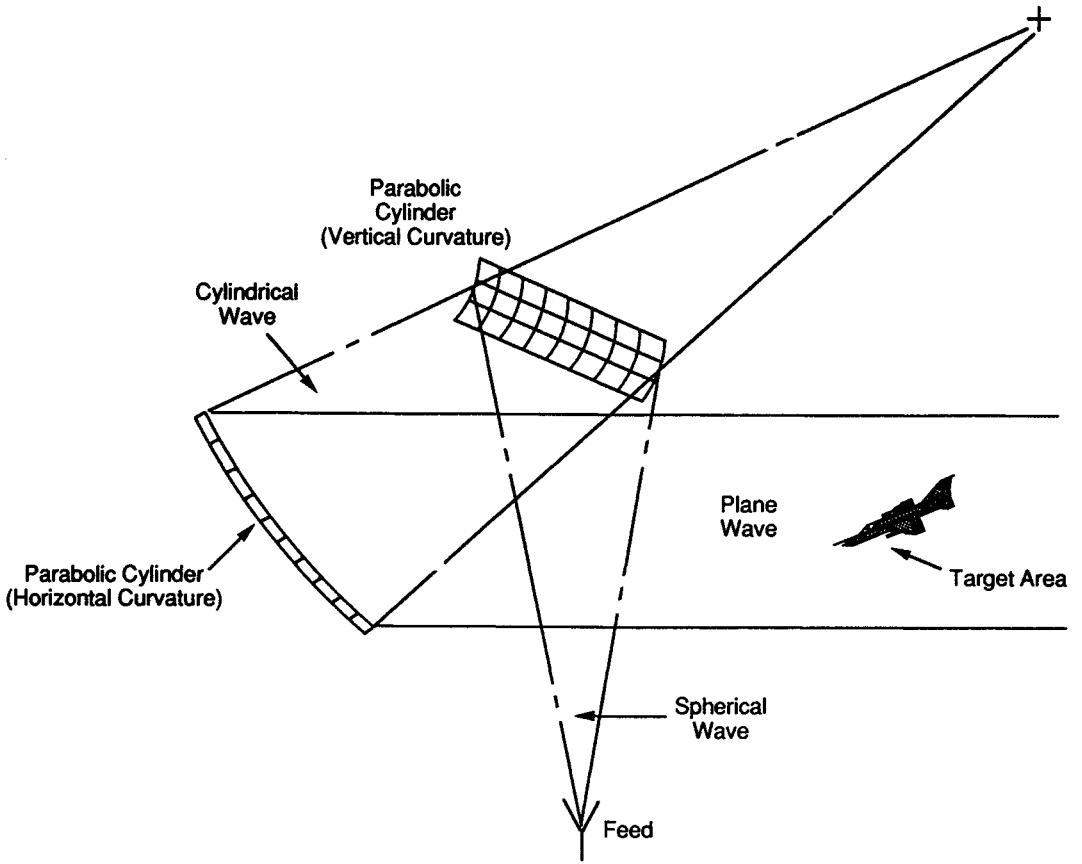

Figure 13.8. Dual crossed parabolic cylinder compact range design.

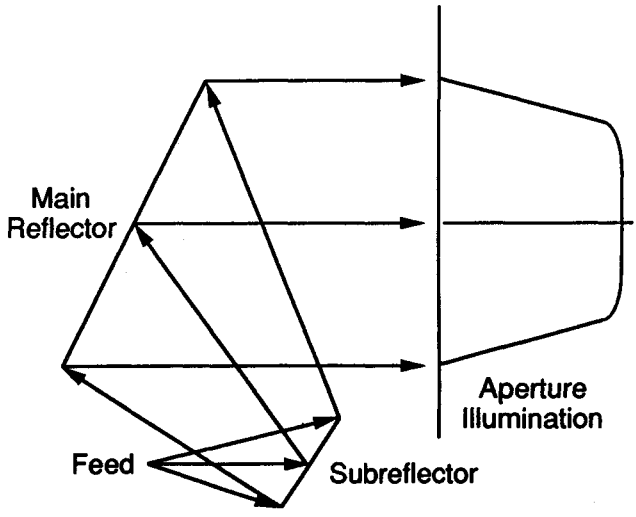

Figure 13.9. Subreflector-fed shaped reflector compact range antenna (from [14]).

13.3.3 Operating Limitations

The compact range is a device designed using optics principles, and its operation is limited to those frequency regions where the conventional optics assumptions hold. At the high-frequency end of the operating envelope, surface tolerance limits the ability to provide a smooth field. At the low-frequency end, diffraction of energy from the edge of the reflector causes ripples in the quiet-zone field.

Random perturbations in the surface of a compact range reflector generally have a more severe effect on the field purity of a compact range system than would the same perturbations on the farfield pattern of the antenna. In the farfield case, the field intensity at any point is given by an integral of the surface currents across the entire reflector. At large distances, all parts of the reflector contribute nearly equally to the integral. Thus, random perturbations in the surface of the reflector tend to integrate out, so that a smooth (albeit, perhaps somewhat lower gain) pattern results. For the compact range case, the field at any point in the quiet zone is dominated by the scattered field from a small part of the reflector in front of that area. Deviations from the desired reflector profile will produce the greatest field degradation when they are comparable to a Fresnel zone in size. Deviations less than a square wavelength in area tend to average out, and deviations from the ideal shape that are on the order of the reflector size tend to produce a slight amount of defocusing, although still leaving a smooth field taper.

An analysis by R. C. Johnson [12] indicates that the fractional amplitude change caused by Fresnel zone sized deviations is given by $8\Delta/\lambda$, where Δ is the rms deviation from the ideal reflector shape, and the associated phase change is given by $4\pi\Delta/\lambda$. This implies that the reflector tolerance must be held to 0.007λ, if less than 0.5 dB of amplitude ripple is desired (assuming peak-to-peak ripple is twice the ripple standard deviation). Therefore, at 94 GHz, an rms surface deviation of less than 22 μm would be required if less than 0.5 dB ripple were a specification.

At the low-frequency end of the operating range, diffraction tends to dominate field perturbations. Aperture diffraction generally becomes an important mechanism when the principal dimensions of the reflector are only a few wavelengths. So the diameter of the reflector must be at least a few tens of wavelengths before those effects can be ignored. Edge diffraction occurs due to the discontinuity of illumination produced by the edges of the reflector. Users always desire a quiet zone as large as possible relative to the reflector size, but full illumination of the reflector surface to reduce amplitude taper inevitably leads to field discontinuities at the reflector edge. Those discontinuities often result in fields being diffracted into the quiet zone. Several approaches have been taken in an attempt to provide maximum quiet-zone area for a given reflector size, while minimizing the effects of diffraction.

The basic method used to ameliorate diffraction effects is to provide a taper to the field (either geometrically or electromagnetically) that reduces the level of diffracted field seen in the quiet zone. Four different methods are currently being used to achieve that result. Serrated reflector edges provide a geometric transition designed to diffract energy away from the quiet zone [15]. Rolled edges also provide a geometric transition that minimizes diffraction into the target area [16]. A shaped subreflector may be used to provide a feed pattern that tapers off sharply but smoothly close to the reflector edge [14]. Finally tapered resistive cards may be used around the edge to slowly transition the currents to zero. The design of such cards follows closely that for edge treatments discussed in Chapter 8. Questions of effectiveness and cost are both important in deciding which of the techniques to employ, and, at this moment, none of the techniques can be considered a clear-cut winner.

13.4 INSTRUMENTATION

Arguably, the one device that has done most to make indoor ranges practical for measuring very low-RCS targets is the stable, computer-controlled, digital frequency synthesizer. Twenty years ago, indoor ranges typically relied on a phase-locked klystron source. A pure CW signal was transmitted, and an analog nulling loop was used to reduce the background return to an acceptable level (see, e.g., [11]). The major fault with such systems lay in the requirement to null the return

from the entire chamber. In a compact range, major background sources include mismatch reflections at the feed horn (due to nonunity VSWR for the feed), circulator leakage (or transmitter feed to receiver feed coupling in a bistatic system), scattering from the reflector (or subreflector) back into the feed, backscattering from the sidewalls, ceiling, and floor, scattering from the target support, and scattering from the backwall.

Note that most of the background sources named do not lie at the same range as the target. Therefore, discrimination in range allows much of the background to be suppressed without the necessity for nulling it out. However, because of limited receiver recovery times, it is not generally practical to use conventional short pulse systems as indoor range instrumentation radars. The alternative, employed on all modern indoor ranges (and on many modern outdoor ranges also) is to collect coherent data over a wide bandwidth, transform the data from the frequency domain to the time domain by using an inverse Fourier transform, gate out returns that fall outside the target zone, and transform the gated data back to the frequency domain to provide total RCS as a function of frequency. In addition, such instrumentation is capable of providing high-range resolution RCS profiles and ISAR images of the target.

Figure 13.10 is a block diagram of a vector network analyzer based compact range instrumentation system. One noticeable feature of the instrumentation is the presence of the transmitter and receiver gates. Although software gating is used to remove signals at different ranges than the target as a part of post-data collection signal processing, processing sidelobes remain. In addition, the presence of high-amplitude background signals increases receiving system dynamic range and resolution requirements. Hence, hardware gates can be used to remove large signals that are well separated in time from the target return (e.g., feed coupling or backwall returns), thereby easing receiver design and processing requirements.

Systems such as that shown in Figure 13.10 typically operate by transmitting one or more pulses at a given frequency within the operating band, stepping to the next frequency, transmitting a block of pulses at that frequency and continuing until data have been transmitted and received at each of the frequencies over the band. This method of operation is often called *step-chirp*, in contrast with a conventional "chirped" pulse compression system, which provides wideband operation through intrapulse frequency modulation (see, for example, Figure 2.3). The number of pulses transmitted at each frequency is determined by the amount of integration required to achieve a given receiver noise floor. For perfectly efficient coherent integration, the gain with respect to the single pulse signal-to-noise ratio is given by the product of the number of pulses at each frequency and the number of frequencies. All of the pulses at a given frequency are coherently averaged (i.e., in-phase and quadrature-phase components considered), and the resulting complex numbers form the one-dimensional complex matrix transformed to obtain time-domain data. To produce ISAR images, sets of stepped-frequency data are recorded

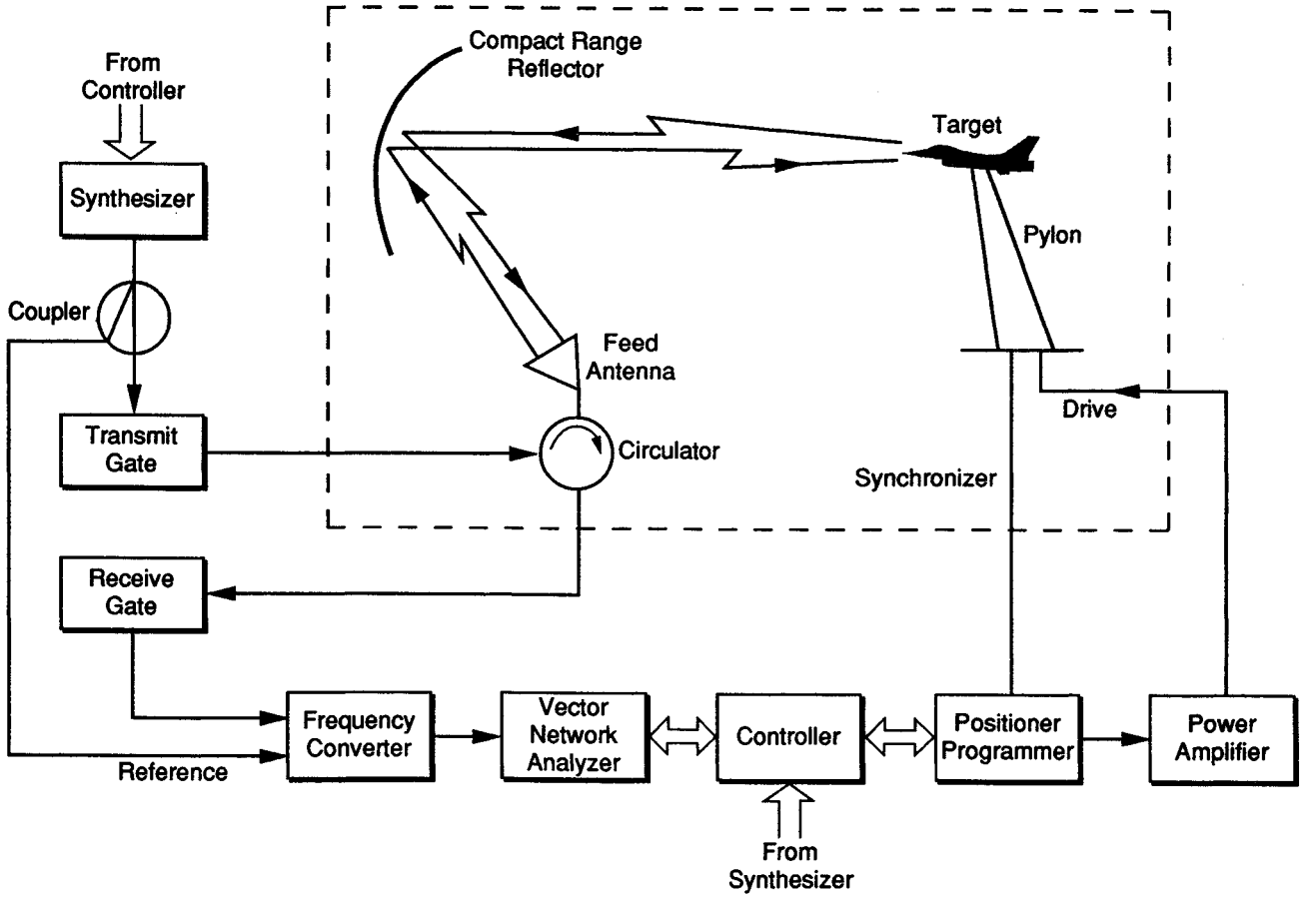

Figure 13.10. Block diagram of a step-frequency RCS system using a vector network analyzer and hardware gating.

as a function of target rotation angle, and the two-dimensional matrix of frequency versus angle is passed through a two-dimensional transform to produce range versus cross-range data. Equations (2.7) and (2.12) can be used to compute the bandwidth and angular rotation required to achieve given range and cross-range resolutions.

To successfully use a software gate to remove all extraneous signals not at the target range, the frequency step size must be such that other parts of the chamber (of most concern is the backwall) do not *alias* into the target zone. The unambiguous range provided in the transformed signal is simply the range resolution times the number of frequency steps, N, or

$$R_{\text{unambig.}} = Nc/2B \tag{13.3}$$

where c is the speed of light and B is the total bandwidth over which the frequency is stepped. For a given chamber length, L, the maximum frequency step size for unambiguous operation is given by

$$\Delta f_{\max} = c/2L \tag{13.4}$$

so that for a 30 m chamber length, a step no larger than 5 MHz could be used. If hardware gating can be used to remove signals that might alias into the target zone, the unambiguous range can be limited to the gate length, with an attendant increase in step size. It is important to note that the step size, the number of frequency steps, the number of pulses integrated at each frequency, and the rotation rate must all be coordinated to achieve the desired sensitivity and resolution without aliasing in range or cross range. Kurtz and Scheer [17] provide an excellent presentation of the set of equations that relate the conditions to be satisfied in making ISAR measurements using a step-chirp system.

13.5 RANGE OPERATION

Most of the operating procedures that apply to indoor ranges also apply to outdoor ranges and are discussed in Chapter 12. This section highlights some of the differences. In describing range operation, use of a wideband system, such as that in Figure 13.10, is assumed.

One measurement procedure generally performed on outdoor ranges but even more critical on indoor ranges is probing of the field in the quiet zone. On outdoor ground-plane ranges, a vertical field probe establishes that the target is at the peak of a multipath lobe. On the compact range, a two-dimensional field probe is used to diagnose the structure of the incident field in the target zone. Three techniques are available for probing the field. A one-way probe can be conducted by using a small receiving antenna (e.g., open-ended waveguide or small

horn) scanned over the quiet zone. The amplitude and phase of the field received by the probe correspond to the field incident on the target at that point (as modified by the probe pattern).

A two-way probe can be used, where the raster-scanned receiving antenna is replaced by a reflector (e.g., sphere, plate, trihedral). The scattered field received back from the reflector will exhibit twice the amplitude and phase fluctuations as would be seen in the one-way probe. As with the probe antenna, the pattern of the reflector used will modify the actual field to give an apparent field structure. That effect can be illustrated by assuming that a flat plate is used as the probe reflector. Incident field components arriving from directions far off the normal of the plate would not be reflected back toward the receiving horn, and so fewer perturbations would be seen in the field than if a sphere were used as the reflector, where every incident direction could provide a specular reflection back toward the receiver.

A third field probe technique is to use a long thin rod as a target and rotate it in azimuth [18]. Doppler processing can be used to separate the returns from different cross-range segments, providing amplitude and phase as a function of cross-range position. The test can be repeated at different scatterer heights to provide a two-dimensional map of the field.

A technique often used on indoor ranges (but often not needed on outdoor ranges) to reduce the background level relative to the target is coherent background subtraction, and it is the purpose of the analog nulling loop used on CW systems. On modern systems, the amplitude and phase of the background return are recorded at each of the frequencies of interest with the target support structure in place but no target, or as is more common, with a very low-RCS target in place of the actual target. An assumption is made that the background return does not change with the target in place, and so the background vector can be digitally subtracted from the target-plus-background return vector, in theory cancelling the effect of the background on the measurement. In fact, by virtue of the fact that the target has a different shape and scattering pattern than the pylon termination target or the support with no target in place, the background will be different, and the cancellation will not be perfect.

The remaining data collection procedures on an indoor range are identical to those on outdoor ranges. A calibration target is required to provide absolute RCS. Secondary calibration targets are not used because of the difficulty in ensuring that they do not corrupt the target return. On wideband systems, the calibration target also provides a method to correct for unequal amplitudes or nonlinear phase effects in stepping across the frequency band. The magnitude of the return from the calibration target provides an RCS reference. In addition, for a given calibration target type, the relationship of the return (both amplitude and phase) from one frequency step to the next is known, and that information can be used to correct the "transfer function" of the system. If such a correction is not made, and if the

amplitude is not flat or the phase not linear from one frequency step to the next, then the target may "smear" in range and high range sidelobes will generally result. An excellent diagnostic for overall system calibration is to image a target with very little range extent (e.g., a small flat plate at normal incidence) and then look at the range and cross-range images. A good system calibration will result in an image with a sharp peak and regular sidelobes matching the pattern expected for the windowing function used. A smeared image or irregular or higher than expected sidelobes indicate system calibration problems.

13.6 SUMMARY

In this chapter we have discussed the salient features of indoor RCS ranges. Those features include the absorbing material used to line the interior of the chamber, the chamber geometry, the instrumentation needed to make the measurements, and some of the measurement procedures unique to indoor ranges. The pyramidal and wedge absorbers used to provide an anechoic measurement environment must be chosen with regard to the desired performance at the lowest expected measurement frequency. The lower this frequency, the thicker and more expensive the material will be.

The shape of the chamber can be optimized to reduce multipath; the conventional rectangular shape is not as good as a taper provided at the transmitting end of the chamber (obviously impractical for a large reflector compact range). A number of sources contribute to the background on a range, but the largest source is generally the backwall. Although analog nulling of the background or digital background substraction can be used to reduce interference effects, errors will remain, because the background changes with the target in place, due to target forward scatter and shielding of the backwall of the chamber.

Wideband measurement systems can be used to suppress much of the background through range gating of the return signal. This is most commonly done by using a stepped or chirped transmitted waveform and an inverse fast Fourier transform to produce temporal data from the recorded spectral data. Hardware gates can be used to reduce the dynamic range with which the system must contend and can further reduce the noise floor on the range.

REFERENCES

[1] Pellett, L. F., "Indoor RCS Facility Design," *Radar Reflectivity Measurement: Techniques and Applications,* N. C. Currie, (ed.), Artech House, Norwood, MA, 1989.

[2] Tuley, M. T., "Compact Ranges," *Radar Reflectivity Measurement: Techniques and Applications,* N. C. Currie (ed.), Artech House, Norwood, MA, 1989.

[3] Emerson, W. H. and H. B. Sefton, Jr., "An Improved Design for Indoor Ranges," *Proc. IEEE,* Vol. 53, August 1965, pp. 1079–1081.

[4] King, H. E., F. I. Shimabukuro, and J. L. Wong, "Characteristics of a Tapered Anechoic Chamber," *IEEE Trans. on Antennas and Propagation,* Vol. AP-15, May 1967, pp. 488–490.
[5] Lawrence, B. F., "RF Anechoic Chamber Test Facilities," 2nd ESTEC Spacecraft EMC Seminar, May 1982.
[6] Tiley, J. W., "Radar Wave Absorption Devices," U.S. Patent 2,464,006, granted March 8, 1949 (filed April 28, 1944).
[7] DeWitt, B. T., "Analysis and Measurement of Electromagnetic Scattering by Pyramidal and Wedge Absorbers," Ph.D. dissertation, Ohio State University, 1986.
[8] Brumley, S. A., "Evaluation of Microwave Anechoic Chamber Absorbing Materials," M.S. thesis, Arizona State University, May 1988.
[9] Cuming, W. R., personal communication.
[10] Johnson, R. C., "Antenna Range for Providing a Plane Wave for Antenna Measurements," U.S. Patent 3,302,205; granted January 31, 1967.
[11] Johnson, R. C., H. A. Ecker, and R. A. Moore, "Compact Range Techniques and Measurements," *IEEE Trans. on Antennas and Propagation,* Vol. AP-17, September 1969, pp. 568–586.
[12] Bodnar, D. G., et al., "Compact Range Study for RATSCAT," Final Technical Report on Contract F29601-77-C-0051, Georgia Institute of Technology, Atlanta, January 1978.
[13] Vokurka, V. J., "Seeing Double Improves Indoor Range," *Microwaves and RF,* February 1985, p. 71.
[14] Phelan, H. R., "Model 1640—The Harris Large Compact Range," *Antenna Measurements Techniques Assoc. Symp. Proc.,* 1987, pp. 33–38.
[15] Hess, D. W., and K. Miller, "A Serrated-Edge Virtual Vertex Compact Range Reflector," *Antenna Measurements Techniques Assoc. Symp. Proc.,* 1988, pp. 6–16 to 6–24.
[16] Gupta, I. J., K. P. Erickson, and W. D. Burnside, "A Method to Design Blended Rolled Edges for Compact Range Reflectors," *IEEE Trans. on Antennas and Propagation,* Vol. 38, June 1990, pp. 853–861.
[17] Kurtz, J. L. and J. A. Scheer, "High Resolution RCS Measurements," *Radar Reflectivity Measurement: Techniques and Applications,* N. C. Currie (ed.), Artech House, Norwood, MA, 1989.
[18] Yuan, H. C. M., "A Comparison of Three Field Probing Techniques," *Antenna Measurements Techniques Assoc. Symp. Proc.,* 1987, pp. 249–254.

Chapter 14
Hip-Pocket RCS Estimation, Data Presentation, and Reduction

J. F. Shaeffer

14.1 INTRODUCTION

The objective of this chapter is to present the considerations required in estimating the RCS of a complex target, data presentation formats, and data reduction. Topics to be covered are

- High-frequency scattering by a complex target—this is a discussion of the scattering mechanisms and phasor addition from multiple scattering centers;
- Simple hip-pocket formulas for estimating scattering;
- RCS data requirements and presentation formats;
- RCS sector statistical characterizations, including examples of geometric and arithmetic averages.

14.2 HIGH-FREQUENCY SCATTERING BY A COMPLEX TARGET

High-frequency scattering occurs when the wavelength of the incident radiation is much smaller than the scattering body and the various scattering center components constituting the body. This condition is usually met for most targets of interest in the microwave region. The following scattering mechanisms usually make up the net scattering from a target. They are listed in rough order of importance:

1. Specular scattering from planar, singly curved, and doubly curved surfaces when their surface normals point back toward the radar (for backscatter); the specular mechanism is the bright flash return;

2. Multiple bounce dihedral or trihedral corner reflectors with only a few bounces or cavity-like returns with many bounces;
3. End-region returns from planar and singly curved surfaces that create the sidelobe envelope;
4. Diffraction from edges when normal to the edge for leading edge with E parallel and for trailing edges with E perpendicular;
5. Surface wave scattering; traveling wave reflections from aft discontinuities from planar or singly curved surfaces or wires; edge wave reflections from aft vertices; creeping wave scattering from uninterrupted paths around curved surfaces;
6. Tip diffraction;
7. Scattering from surface discontinuities such as gaps, cracks, and construction joints.

Specular Scattering

Specular backscatter occurs when the surface normal points back toward the radar. The magnitude is due to that region or area of the surface for which the surface currents add in phase to create the scattered E field:

$$\sigma_{\text{specular}} = 4\pi \frac{(A_{\text{effective}})^2}{\lambda^2} \tag{14.1}$$

where for flat plates the effective area A is just the physical area.

For curved surfaces the effective area is considered that area at the specular point where the phase varies by no more than 22.5° or $\lambda/16$. Consider a curved surface cross section of whose radius is a, Figure 14.1. The width L of the constant phase region can be obtained from the triangle shown:

$$\frac{L}{2} = \sqrt{a^2 - \left(a - \frac{\lambda}{16}\right)^2} \tag{14.2}$$

which has the approximate solution for L, when $a \gg \lambda$, of

$$L \approx \sqrt{\frac{a\lambda}{2}} \tag{14.3}$$

which shows that the constant phase dimension increases with the square root of curvature and wavelength. For a fixed curvature, the constant phase region becomes smaller at higher frequencies.

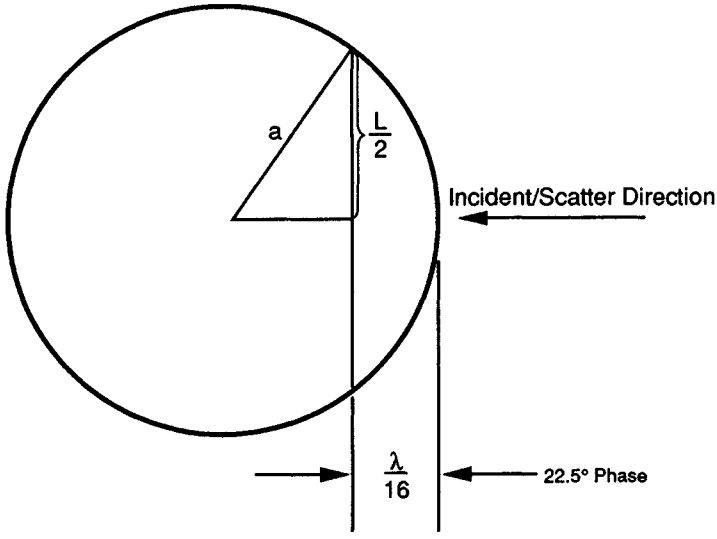

Figure 14.1. Region of width L of relatively constant phase; that is, less than $\lambda/16$ variation, on a curved surface.

The specular return from a single curved surface is determined by the effective area at the specular point, which is the product of physical length l and constant phase width L, Figure 14.2, giving the cylinder specular flash as

$$\sigma_{cyl} = \frac{4\pi\left(\sqrt{\frac{a\lambda}{2}}\, l\right)^2}{\lambda^2} = \frac{2\pi a}{\lambda} l^2 = kal^2 \tag{14.4}$$

which is the cylinder circumference measured in wavelengths times length squared. This expression can be used with singly curved surfaces that are not exactly cylinder-like by simply using effective values for radius and length.

The specular return from a doubly curved surface has an approximate constant phase area at the specular point given by the product of two constant phase dimensions; that is, one for each principal curvature, Figure 14.2. If we neglect the fact that the constant phase area is actually a zonal disk and simply use a rectangular area of side L given by (14.3), we obtain, in spite of our approximations, the geometric optics specular backscatter formula for a doubly curved surface:

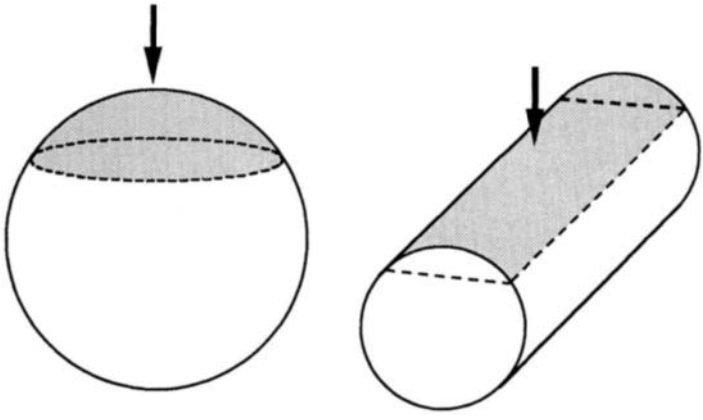

Figure 14.2. Constant phase areas for sphere and cylinder responsible for backscatter specular return when perpendicular to surface.

$$\sigma_{go} = \frac{4\pi \left(\sqrt{\frac{a_1\lambda}{2}}\sqrt{\frac{a_2\lambda}{2}}\right)^2}{\lambda^2} = \pi a_1 a_2 \tag{14.5}$$

where a_1 and a_2 are the radii of curvature at the specular point (where the surface normal points back toward the radar). This result is independent of frequency and may be used for all doubly curved surfaces whose curvature is large compared to a wavelength.

Specular scattering for linear polarization is independent of polarization.

The null-to-null beamwidth for planar surfaces is a function of plate dimension as measured in wavelengths and is approximately given by (in degrees)

$$\theta_{\text{null-to-null beamwidth}} = 57\frac{\lambda}{L} \tag{14.6}$$

For unequal planar dimensions, the spike flash has unequal beamwidths. For single curved surfaces such as a cylinder, the specular flash is disklike, constant in the "roll direction" and spikelike in the cross-roll direction with spike width given by (14.6) and cylinder length used for L. For doubly curved surfaces there is no spike phenomena.

Multiple-Bounce Scattering

Multiple-bounce dihedredals and trihedrals have specular returns over extended viewing angles (which is why these devices are often used to enhance RCS). The RCS is given by (14.1) where the effective area is that over which various ray paths have equal path lengths; that is, constant phase.

Cavity returns are difficult to estimate, however, we can derive a rough estimate provided we assume (1) all the energy that goes into the cavity eventually is reflected out (no absorption) and (2) there are sufficient randomizing bounces inside the cavity that the reflected energy is reradiated uniformly back into the half-space toward the radar. If we define the incident EM wave power flux as P_i W/m^2 then the power captured by the cavity is (Area $\times$ P_i) watts where Area is the cavity projected area. This energy is assumed to be reradiated uniformly into half-space, therefore the radiated power intensity is approximated as P_r = (Area $\times$ P_i) / ($2\pi R^2$) W/m^2. Using the definition of cross section as the ratio of reflected power density to incident power density, we obtain our cavity high-frequency RCS estimate as

$$\sigma_{\text{cavity}} = 4\pi R^2 \frac{P_r}{P_i} = 2 \times \text{Area} \tag{14.7}$$

which we take as just twice the projected physical capture area of the cavity opening.

End-Region Returns

End-region scattering is due to physical optics like currents at surface discontinuities. These end regions contribute to sidelobe scattering. Scattering is due to the finite discontinuity in current magnitude. If currents could smoothly taper to zero over several wavelengths, little end-region scattering would occur. For a flat plate viewed perpendicular to its edges, the end regions are adjacent to the two edges. The return from these phases add and subtract to form the sidelobe envelope. Figure 14.3 shows the scattering from a physical optics current distribution (edge diffraction not included) when viewed perpendicular to the edges. An analytical image, using the method described in [1] coupled to a physical optics code prediction, of the scattered radiation is shown in Figure 14.4. For this viewing angle, the area of the end region is proportional to the edge length of the plate. When the plate is viewed in a plane along its diagonals, the sidelobe levels are shown in Figure 14.3, where they are seen to be much less than when viewed perpendicular to the edges because the physical optics current taper has smaller discontinuities. An analytical image along the diagonal of the plate, Figure 14.5, shows the scat-

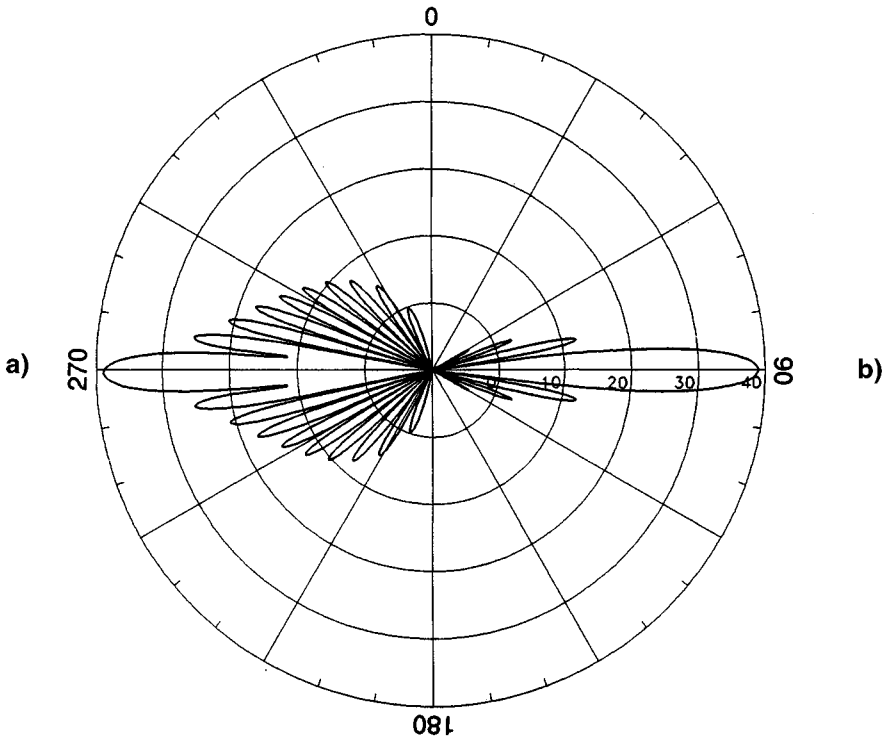

Figure 14.3. Physical optics computed return from a 5λ plate when perpendicular to edges, left side, and along the diagonal, right side. Edge diffraction is *not* included in this computation. λ = 1 m.

tering as due to the four corners of the plate; that is, the four end region discontinuities. These four end regions, determined by plate-included angle, are much less than when viewing the plate perpendicular to its edges; hence, plate diagonal sidelobe levels are much less. End-region sidelobe envelope scattering from a flat plate, when viewed perpendicular to a pair of edges of length L, is

$$\sigma_{\text{end region}} = \frac{L^2}{\pi} \frac{1}{\tan^2 \theta} \tag{14.8}$$

where $\tan^2 \theta$ is the viewing angle factor. For this case the sidelobe levels are proportional to L^2. When the square plate is viewed along the diagonal the end-region sidelobe envelope is

$$\sigma_{\text{end region}} = \frac{\lambda^2 \cos^2 \theta}{\pi^3 \sin^4 \theta} \tag{14.9}$$

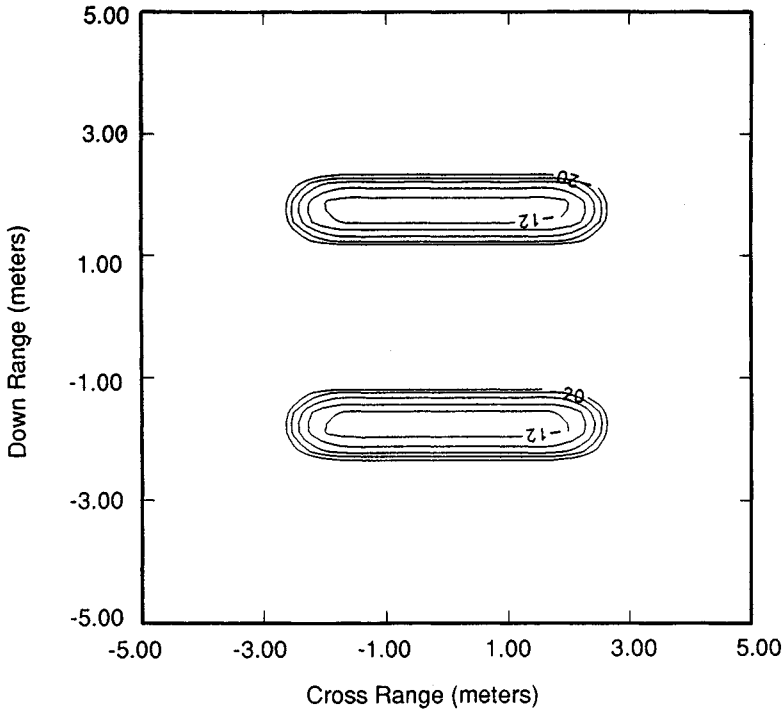

Figure 14.4. Flat-plate physical optics end-region return for oblique 45° backscatter looking perpendicular to edge of plate. These end regions produce the sidelobe envelope as they phase add or subtract. Image analytically computed using physical optics currents; that is, edge diffraction is not included, which at this angle, 45°, is not yet significant. Plate size 5λ.

which is independent of plate size. In this case, scattering is proportional to λ^2 and consequently falls off at high frequencies. This equation follows directly from the physical optics solution for a flat plate.

End-region returns can also occur on singly curved surfaces such as cylinders viewed off specular. In this case the end regions are as suggested in Figure 14.6. The level of scattering can be estimated by using the constant phase dimension (14.3) in the end-region expression for a flat plate, (14.8), to obtain

$$\sigma_{\text{end region, cyl}} = \frac{a\lambda}{2\pi} \frac{1}{\tan^2 \theta} \tag{14.10}$$

which shows the cylinder end-region RCS becomes smaller at higher frequencies or for smaller radius cylinders.

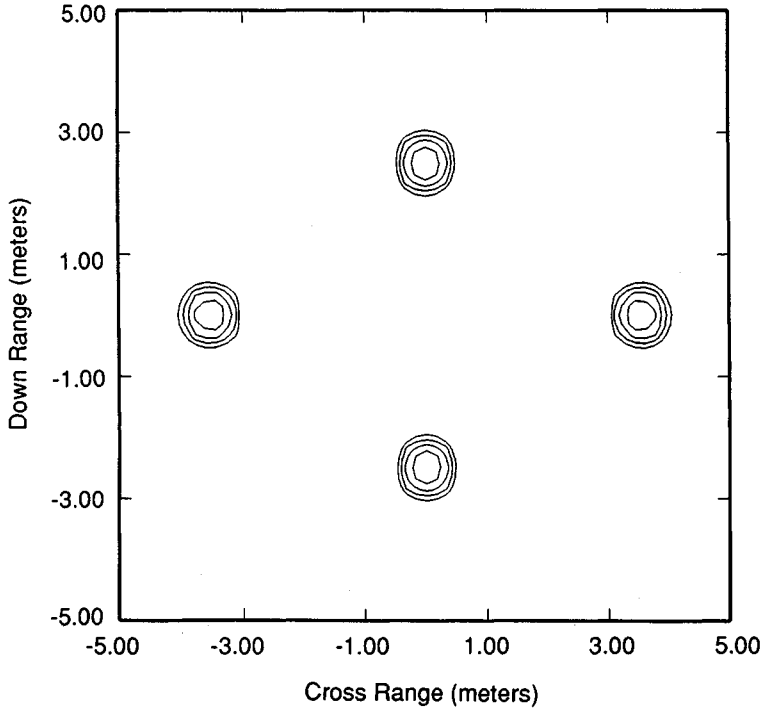

Figure 14.5. Flat-plate physical optics end-region return for oblique 45° backscatter looking into corners of plate. These four end regions produce the sidelobe envelope as they phase add or subtract. Image analytically computed using physical optics currents; that is, edge diffraction is not included, which at this angle, 45°, is not yet significant. Plate size 5λ.

End-region returns do not occur from doubly curved surfaces because there is no sudden discontinuity in currents. For these surfaces, currents taper smoothly toward 0 in shadow regions thus producing little contribution to scattering.

Edge Diffraction

Edge scattering is diffraction in the specular direction, which for backscatter occurs when the radar is perpendicular to the edge. Two cases are required because edge diffraction depends on polarization. Leading edge (in an EM sense!) is defined when E incident is parallel to an edge, and trailing edge diffraction occurs when E incident is perpendicular to the edge. The nominal edge return (it does not vary much with included wedge angle) is

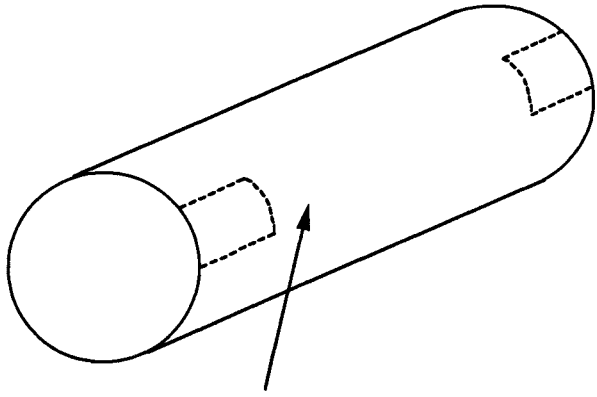

Figure 14.6. Cylinder end regions that create off-specular sidelobe envelope as they phase add or subtract.

$$\sigma_{\text{edge}} = \frac{(L_{\text{effective}})^2}{\pi} \tag{14.11}$$

where for straight edges the effective constant phase length is the physical length and for curved edges we use (14.3) for the effective length to obtain

$$\sigma_{\text{curved edge}} = \frac{a\lambda}{2\pi} \tag{14.12}$$

where a is radius of curvature at the specular point. For leading edge parallel polarization returns these formulas give very adequate estimates. However, the formulas were originally derived by using an infinite half-plane model, which is not a good physical model for viewing a trailing edges because the radiation source, receiver, and leading edge are all collated at infinity. The theory results for trailing edges suggest the return given by (14.11); however, for finite sized bodies, the perpendicular polarization trailing edge return falls to much smaller values at small grazing angles. As we move up from grazing, the return grows to a peak value given by (14.11). The angular location of this peak depends on the length of the surface measured in wavelengths in front of the edge. A flat-plate return computed by using physical optics plus edge diffraction modeled by using equivalent currents from a 5λ plate is shown in Figure 14.7, where for parallel polarization the leading

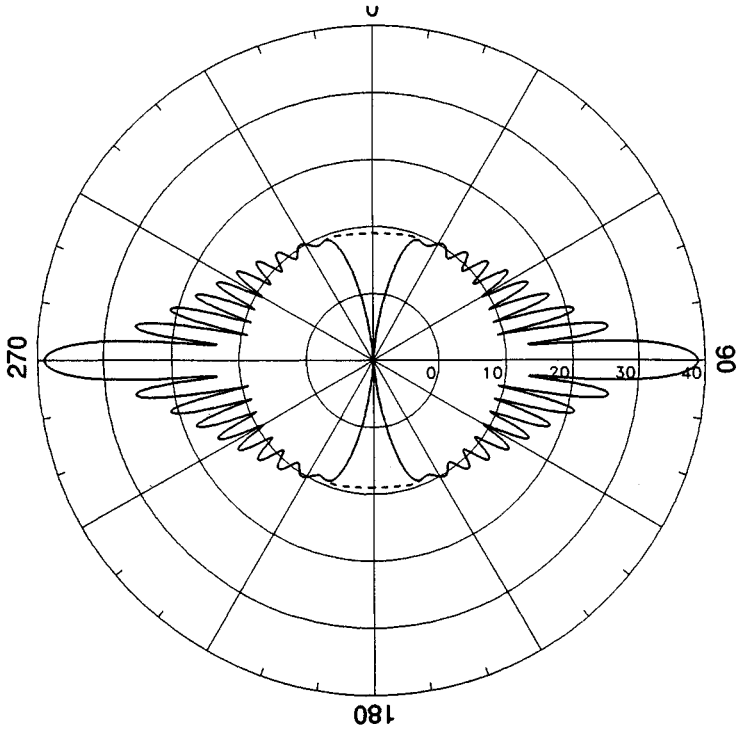

Figure 14.7. Flat-plate (physical optics plus edge diffraction modeled by using equivalent currents) computed backscatter showing leading and trailing edge diffraction. Perpendicular and parallel polarization shown as solid and dashed lines. Diffraction dominates pattern near grazing. Plate size 5λ with $\lambda = 1$ m.

edge RCS is (14.11) and the trailing edge RCS does not peak to (14.11) until $22°$. This angle is not unlike that for the traveling wave return that peaks at $49\sqrt{\lambda/L}$. Trailing edge returns can be expected to peak closer toward grazing at higher frequencies and larger surfaces. The reader may compare the PO-only flat-plate RCS to that with edge diffraction (modeled with equivalent currents) by comparing Figures 14.6 and 14.7. Edge diffraction dominates the flat plate RCS near grazing angles away from the specular directions.

Straight edges also have a beamwidth null to null given by (14.6).

A rim is a special type of edge that conceptually can be thought of as an edge wrapped back on itself. Rim RCS returns can be considered edgelike. The specular direction for a rim is perpendicular to the plane of the rim. The specular rim RCS can be estimated from (14.11) by using one-half the rim circumference as the

effective length because only one-half of the rim is perpendicular to the incident E field. For a circular rim, the approximate RCS is given by

$$\sigma_{\text{rim}} = \frac{(L_{\text{effective}})^2}{\pi} \approx \frac{\left(\frac{1}{2} 2\pi a\right)^2}{\pi} = \pi a^2 \tag{14.13}$$

Again, although edge diffraction does depend on wedge angle, it does so only weakly, hence we do not include those effects in our hip-pocket estimates.

Surface Wave Scattering

Surface traveling wave returns are lower level nonspecular mechanisms whose scattering amplitude is proportional to λ^2. This mechanism is usually important only when high level specular scattering is not present, such as for low observable targets when viewed in the low cross-section angular sector. The surface wave mechanism occurs when the E field polarization is in the plane of incidence. The induced surface wave gains energy from the incident field. Backscatter occurs when this energy is reflected from some aft discontinuity such as a wing tip, or aft body termination. The peak return occurs near grazing angles given by

$$\theta_{\text{traveling wave peak}} \approx 49 \sqrt{\frac{\lambda}{L}} \tag{14.14}$$

The amplitude was discussed in Chapter 5 and depends on the aft reflection coefficient and how much of the surface wave actually reaches the aft discontinuity without absorption. A rule of thumb is that the surface traveling wave return is usually less than $3\lambda^2$.

Tip Diffraction

Tip diffraction, like surface wave scattering, is a low-frequency dominant scattering mechanism because it is proportional λ^2:

$$\sigma_{\text{tip}} \approx \frac{\lambda^2}{16\pi} \tan^4 \alpha \tag{14.15}$$

where α is the tip included half-angle. Blunt tips thus scatter more than sharp tips. At X-band we seldom see tip scattering because it is easily masked by other much larger scattering centers.

Surface Discontinuities

Surface discontinuity scattering occurs when induced surface currents suffer a path deviation due to a discontinuity. The path deviation then causes backscatter radiation. This scattering is predominant for perpendicular polarization where there may be surface wave propagation. This type of scattering can become important contributors to low cross-section fuzz ball RCS levels at higher frequencies where surface discontinuities no longer are Rayleigh region scattering centers.

14.3 PHASOR ADDITION

The RCS of a collection of scattering centers is the coherent sum of the contributions of the individual scattering centers. We shall examine the effects of phasor addition on the peak values of the RCS as well as on the average.

For our purposes, multiple scattering is the net return from a collection of scattering centers, each of which acts independent of all others. We assume that there are no mutual interactive reflections. We further assume that the incident field on each scatterer is the field impinging on the collection, thereby ignoring multiple bounces and shadowing effects. The objective of this exercise is to illustrate what happens when the returns from N scatterers are added in and out of phase.

As discussed previously, the net return from a collection of N scatterers is given by

$$\sigma = \left[\sum_{i=1}^{N} \sqrt{\sigma_i}\, e^{j2\mathbf{k}\cdot\mathbf{R}_i} \right]^2 \tag{14.16}$$

where σ_i is the complex RCS (magnitude and phase) of each scatterer and usually depends on the viewing angle, relative position, polarization, and frequency. Here, $(2\mathbf{k}\cdot\mathbf{R}_i)$ is the roundtrip phase distance from the radar to the ith scattering center, and the summation is a complex addition of electric field phasors. The square of this sum is the net power scattered back to the radar. Peaks occur when the phase difference between scattering centers, that is, delta path length as measured in wavelengths, is a multiple of 2π, and nulls occur when the phasors subtract, that is, when phase differences are odd multiples of π.

To illustrate phasor addition, consider the RCS of a 1 m^2 (0 dBsm) point target, that is, a target that backscatters uniformly in all directions, Figure 14.8. Now consider the RCS from two equal point targets located on the X-axis with a spacing of 5λ. The RCS from these two scatterers now exhibits phase addition and subtraction, Figure 14.8. The peak return is four times or 6 dB higher than the return from one point scatterer and the null depths are infinitely deep because equal returns subtract identically. The RCS pattern goes in and out of phase most

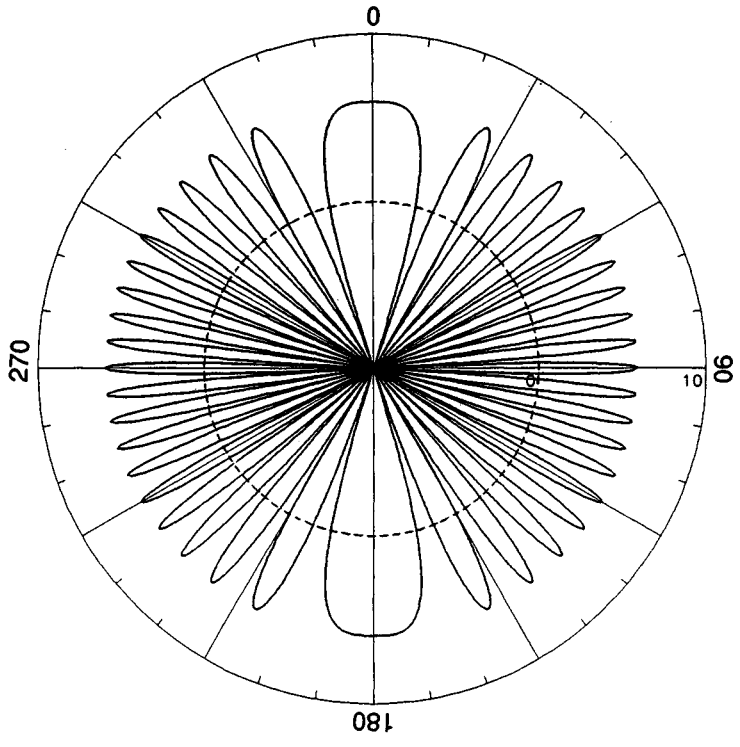

Figure 14.8. RCS in dBsm showing phase addition from one and two 0 dBsm (1 m^2) point targets, dashed and solid lines, respectively. The two point targets located 5λ apart along 0–180° line.

rapidly when viewing broadside to the scatterers because at this aspect large changes in phase can be caused by small rotation. The RCS pattern scintillates the least when viewing along the line connecting the two point targets, where there is little change of phase or path length with rotation angle.

The RCS from these two scatterers is given by (14.16),

$$\begin{aligned}\sigma &= [\sqrt{\sigma_1}\, e^{j2\mathbf{k}\cdot\mathbf{R}_1} + \sqrt{\sigma_2}\, e^{j2\mathbf{k}\cdot\mathbf{R}_2}]^2 \\ &= \sigma_1 + \sigma_2 + 2\sqrt{\sigma_1\sigma_2}\cos[2\mathbf{k}\cdot(\mathbf{R}_1 - \mathbf{R}_2)]\end{aligned} \tag{14.17}$$

For the case of equal scatterers, the peak RCS is four times or 6 dB higher than only one scatterer. This value is the coherent maximum, given by

$$\sigma_{max} = [\sqrt{\sigma_1} + \sqrt{\sigma_2}]^2 \tag{14.18}$$

which when generalized for N scattering centers becomes

$$\sigma_{\max} = \left[\sum_{i=1}^{N} \sqrt{\sigma_i}\right]^2 \tag{14.19}$$

The minimum or null value RCS is the coherent minimum that for our point target example is zero because each scattering center has the same magnitude. For unequal magnitudes, the minimum would have the value

$$\sigma_{\min} = [\sqrt{\sigma_1} - \sqrt{\sigma_2}]^2 \tag{14.20}$$

The average value over a large sector in aspect angle (say 10 lobe widths or more) for these two equal scatters is just twice that of one. This is simply the sum of the individual RCS values of the pair. This value is called the *noncoherent sum:*

$$\sigma_{\text{noncoherent}} = \sigma_1 + \sigma_2 \tag{14.21}$$

which generalizes for N scattering centers to

$$\sigma_{\text{noncoherent}} = \sum_{i=1}^{N} \sigma_i \tag{14.22}$$

Note that if the two scattering centers have the same value, the coherent sum is just twice or 3 dB higher than the noncoherent sum.

The phasor summation described by (14.17) to (14.20) must be performed with voltages (not power or square meters of RCS), because we are adding scattered electric fields, not scattered power. Averaging over sectors, as in (14.21) and (14.22), is performed using noncoherent power or RCS.

14.4 HIP-POCKET RADAR CROSS-SECTION ESTIMATION

Estimation of RCS can be a very useful exercise to (1) confirm that a set of experimental measurements or analytical computer results are within reasonable bounds; (2) establish and understand major scattering mechanisms; and (3) provide estimates when no other data are available. Estimation is used for specular scattering for which we have simple backscatter formulas. Estimation, therefore, is best applied to "specular" types of targets. Estimation of reduced cross-section targets where there are few if any specular returns is difficult because the residual scattering is now due to second-order mechanisms that do not lend themselves to simple predictive formulas.

The goal of estimation is to arrive at some sort of "average" or noncoherent cross section as a function of look angle. We usually do not try to estimate peaks and nulls (i.e., coherent RCS) unless a given spatial region is dominated by one scattering mechanism.

Estimation works well because we typically desire dBsm logarithmic-type results, which are not sensitive to errors. Usually we are satisfied with estimation for complicated targets if we are within 3 dB, which is a factor of 2 in linear square meter space. For simple targets we should probably be able to do better.

The approach for RCS estimation is straightforward. We start by specifying the frequency or wavelength, the polarization, and the viewing "cut" for the desired RCS estimated pattern. In the "cut" plane we then identify the specular scattering mechanisms, those surfaces and edges whose normals point back toward the illumination radar. At each specular direction we use the simple formulas discussed earlier to compute RCS in square meters. If more than one scattering mechanism exists in a given view direction, then we add their square meter values noncoherently. We then continue this process around the "cut" plane. Finally we convert the square meter values to dBsm. Table 14.1 is a condensed list of formulas that may be used for estimation.

We do not need to be critical in the estimation process. For example, the specular flash from a cone frustrum, Figure 14.9, can be estimated by using the cylinder singly curved surface formula by using the average radius of the frustrum. If the frustrum degenerates into a cone with 0 tip radius, then the average radius is one-half the base radius. For a torus, which is a cylinder wrapped back on itself, the broadside specular flash is from the cylinderlike singly curved surface. For estimation we may simply use the circumference as the cylinder length, Figure 14.9.

14.4.1 Cylinder Ogive Geometry RCS Estimation

As an example of this process, we can estimate the RCS for several view directions for a missilelike cylinder ogive geometry, Figure 14.10, and compare to measured and predicted results from [2].

This geometry is a cylinder 36 in. long with an ogival nose 15.75 in. long, for a total length of 51.75 in. The diameter is 5.75 in. The RCS was measured at 2.93, 5.4, and 9.5 GHz, and the incident and received polarizations were horizontal (i.e., in the plane perpendicular to the axis of rotation).

The broadside peak at 90° is due to the specular broadside return from the cylinder and is well approximated by the theoretical values of

$$\sigma = kal^2 \begin{cases} 5.7 \text{ dBsm at } 2.93 \text{ GHz} \\ 8.4 \text{ dBsm at } 5.4 \text{ GHz} \\ 10.9 \text{ dBsm at } 9.5 \text{ GHz} \end{cases} \tag{14.23}$$

Table 14.1
Hip-Pocket RCS Formula Summary

Constant phase characteristic dimension:	$L = \sqrt{\frac{a\lambda}{2}}$
Specular:	$\sigma = 4\pi\frac{(A_{\text{effective}})^2}{\lambda^2}$
Flat surface:	$A_{\text{effective}} = A_{\text{physical}}$
Singly curved surface (cylinder):	$\sigma = \frac{2\pi a}{\lambda}\ell^2$
Doubly curved surface:	$\sigma = \pi a_1 a_2$; a_1 and a_2 at specular point
Beam width in degrees:	$\theta_{\text{null to null}} = 57\frac{\lambda}{L}$degrees
Reentrant geometries	
Dihedral:	$\sigma = 8\pi\frac{(ab)^2}{\lambda^2}$
Trihedral:	$\sigma = 12\pi\frac{b^4}{\lambda^2}$
Cavity, $E_{\text{in}} = E_{\text{out}}$, random bounces:	$\sigma \approx 2$ Area
Edge diffraction in specular direction:	$\sigma = \frac{L^2_{\text{effective}}}{\pi}$
Straight edges:	$L_{\text{effective}} = L_{\text{physical}}$
Curved edges:	$\sigma = \frac{a\lambda}{2\pi}$
Rim edge:	$\sigma = \pi a^2$
End-region sidelobe peak envelope	
Flat-plate perpendicular edges:	$\sigma = \frac{L^2}{\pi}\frac{1}{\tan^2\theta}$
Curved edge (cylinder):	$\sigma = \frac{a\lambda}{2\pi}\frac{1}{\tan^2\theta}$
Flat plate looking along diagonal:	$\sigma = \frac{\lambda^2}{\pi^3}\frac{\cos^2\theta}{\sin^4\theta}$
Tips:	$\sigma = \frac{\lambda^2}{16\pi}\tan^4\alpha$
Surface traveling wave	
Peak grazing angle:	$\theta \approx 49\sqrt{\frac{\lambda}{L}}$
Magnitude usually less than	$3\lambda^2$

The broadside region echo from about 70° to near 90° is due to the specular return from the ogival nose. The specular point first pops up onto the ogive tip at an aspect near 70° and then moves aft along the ogive to the point where the ogive joins the cylinder. The geometric optics formula for doubly curved surfaces can

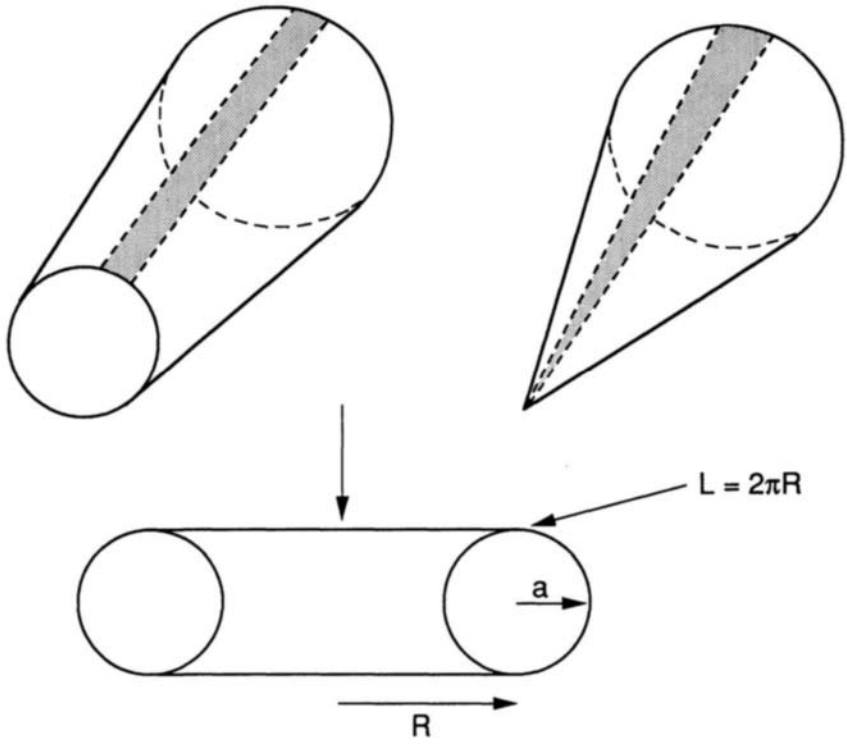

Figure 14.9. Constant phase areas producing backscatter specular RCS can be adequately estimated by using "average" or approximate dimensions for singly or doubly curved surfaces.

be used to estimate the contribution due to the ogive. The principal radii of curvature at the join are estimated to be $R_1 = 2.87$ in. and $R_2 = 36$ in., so that

$$\sigma = \pi R_1 R_2 = -6.8 \text{ dBsm} \tag{14.24}$$

Note that R_2 is large and unchanging whereas R_1 ranges from zero at the tip to the body radius at the join as the specular point moves from the tip toward the join. The estimate based on these radii agree with the measured data, provided we realize that the ogive and the cylinder sidelobe returns add in and out of phase with changing aspect angle.

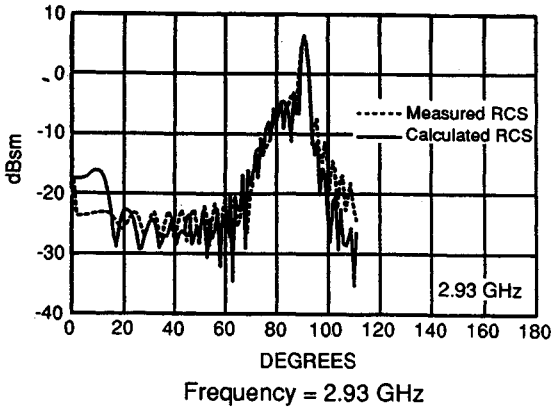

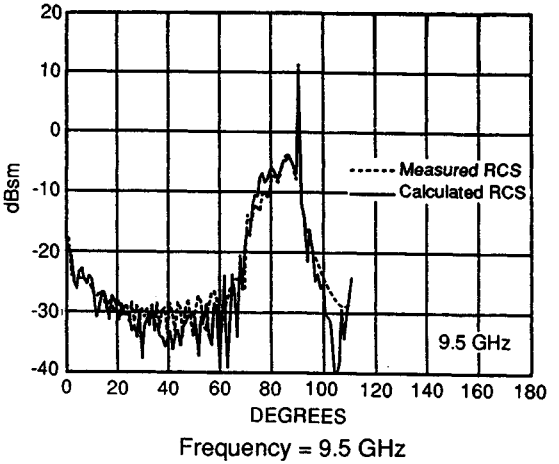

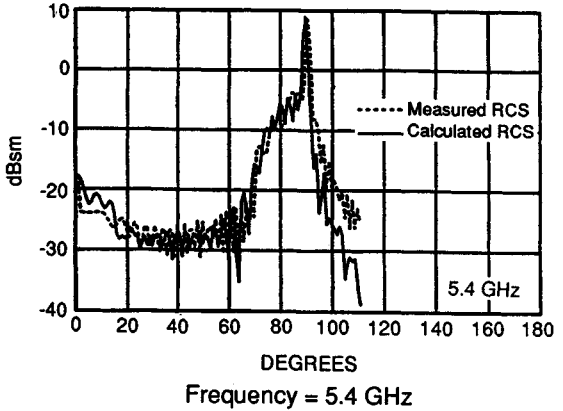

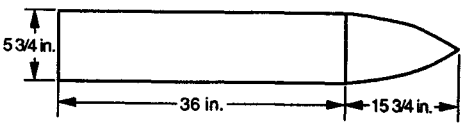

Figure 14.10. Comparison of measured and predicted results for a cylinder with an ogive nose, horizontal polarization (from [2]).

The nose-on value is due to the circular rim at the rear of the body and may be estimated as

$$\sigma = \pi R_1^2 = -17.8 \text{ dBsm} \tag{14.25}$$

We note that the measured nose-on values are very close to this estimate and that they indeed are independent of frequency. Off nose-on, the RCS decreases because the rear edge discontinuity is no longer illuminated in phase, and only one contributing specular point remains on the rear corner. The scattering from the rear circular edge decreases with increasing azimuth angle until a specular flash point first appears on the ogive tip.

An indication of the presence of a traveling wave is given at the lowest measurement frequency, 2.93 GHz. The angular location of the first peak of that pattern is predicted to be

$$\theta = 49\sqrt{\lambda/l} = 14° \tag{14.26}$$

The magnitude upperbound of $3\lambda^2 = -15$ dBsm agrees reasonably well. At the higher frequencies, there is no indication of a *traveling wave* (TW) return, supporting the notion that the TW return decreases with frequency.

Figure 14.10 shows that the predictions of the MISCAT II code, except for the possible TW lobe, give a reasonable prediction.

14.4.2 Hypothetical Target Estimation

For purposes of additional illustration, we will demonstrate the elementary prediction techniques using the hypothetical missile geometry shown in Figure 14.11 with the indicated dimensions and frequencies.

The scattering in the broadside region will be dominated by specular scattering from the body. For a singly curved cylindrical body, the peak RCS is given by

$$\sigma = kal^2 = 53 \text{ m}^2 = 17.3 \text{ dBsm} \tag{14.27}$$

where a is the cylinder radius and l the length. This RCS value increases by 3 dB for each doubling of the frequency.

For a doubly curved surface missile body, such as shown in Figure 14.11, the specular cross section is given by the geometric optics formula

$$\sigma_{\max} = \pi a_1 a_2 = 2.2 \text{ m}^2 = 3.4 \text{ dBsm} \tag{14.28}$$

where a_1 and a_2 are the principal radii of curvature at the specular point. The specular point typically first appears on a body like that in Figure 14.11 in the

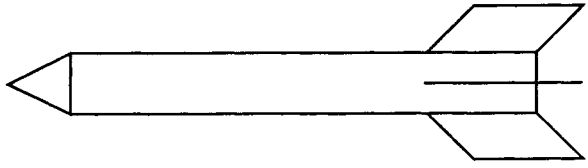

Cylinder radius = 3" (0.076 m)
Cylinder length = 6' (1.83 m)

A. A Cylindrical Body

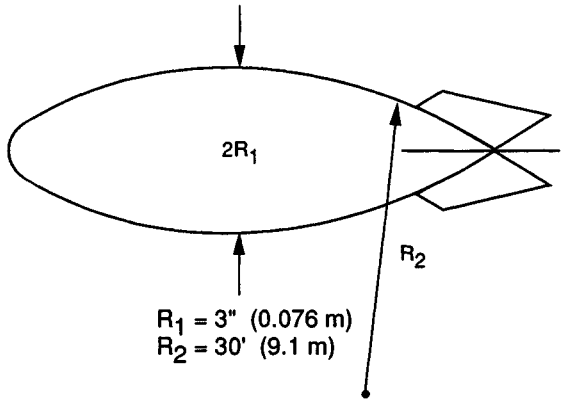

B. Revolved Doubly Curved Surface

Figure 14.11. Hypothetical missile geometries: calculations in text assume a frequency of 10 GHz, for which the wavelength is 0.03 m.

60–70° region. The RCS increases more or less uniformly as the specular point slides aft along the body, along which the radius of curvature increases.

The specular scattering from doubly curved surfaces varies smoothly (without rapid oscillations) because the variation in the principal radii of curvature is a smoothly varying function of the aspect angle. This is different from the specular scattering from a cylinder or flat plate, for which the specular peak may be so narrow that, when we move slightly off the specular direction, the RCS contains rapid oscillations due to the sidelobes.

In addition to body scattering, the return from fins presented normal to the radar can also contribute. For a 0° roll, this requires the fins to be oriented perpendicular to the line of sight. Because this is not the usual missile fin orientation, this scattering mechanism is not applicable.

Scattering mechanisms contributing to the echo in the nose-on sector are more difficult to estimate. This is because the nose-on sector is usually dominated by nonspecular scattering. The nose-on sector is usually taken to be that angular region within 60° to either side of nose-on. The nonspecular RCS pattern in this region has been described by some as the "fuzz ball region," indicating the difficulty they experience in understanding the RCS mechanisms contributing to the RCS for these aspect angles. The RCS in the nose-on sector is very sensitive to frontal geometry. For example, if a seeker radome is present, the nose structure is similar to a reentrant duct for which the return is controlled by internal geometric structures behind the radome. If there is no radome, and if the nose has a sharp tip with a very low return, the nose-on sector can be dominated by other mechanisms, such as rear corner curved edge diffraction, straight edge diffraction from fins, and traveling wave contributions. In the absence of a radome and in the presence of a blunt nose, specular scattering is possible in the nose-on region. An example is a hemispherical nose configuration.

When a radome is present the return is extremely difficult to predict. This is true even if the geometric structure behind the radome is known, because the internal geometry behind the radome may not be simple. However, an upper bound can be obtained by modeling the radome as a trihedral corner reflector. For this purpose, assume a reflector length of 4 in. and an incident frequency of 10 GHz. The equation for the maximum return from a trihedral suggests

$$\sigma = \frac{12\pi a^4}{\lambda^2} = 4.5 \text{ m}^2 = 6.5 \text{ dBsm} \tag{14.29}$$

This large return, of course, is to be expected because the trihedral reflects incident EM energy back to the radar over a rather wide angle, although the actual radome geometries backscatter less incident energy.

The diffraction from rear edges viewed in the nose-on region can be estimated from the maximum return from a straight edge. We use half the perimeter as the edge length l, accounting for the fact that only half the perimeter is illuminated by an incident electrical field perpendicular to the edge:

$$\sigma \simeq \frac{l^2}{\pi} = \frac{(0.5 \times 2\pi a)^2}{\pi} = \pi a^2 = 0.018 \text{ m}^2 = -17.4 \text{ dBsm} \tag{14.30}$$

where a is the radius of the rear edge discontinuity.

Two important features of this result should be noted: it is independent of frequency and depends only on the radius of the discontinuity at the rear. Although

this formula is similar to that for the RCS of a sphere, the underlying scattering mechanisms are fundamentally different. In one case, we have diffraction from an edge at normal incidence, and in the other we have a surface specular geometric optics return. At angles well away from nose-on incidence for which none of the rear edge contributions are no longer in phase, the rear edge return will fall off as suggested by $[(\sin x)/x)]^2$. Off axis, only one flash point on the rear edge will be visible to the radar.

Diffraction due to the straight leading and trailing edges of control surfaces has a maximum value given by (14.11). As stated earlier, this result does not depend on frequency, and it occurs only when the edge is viewed in the specular direction. As suggested earlier, an edge 1 ft long has a maximum specular return of -15.7 dBsm. When straight edges are viewed in nonspecular directions, the return can be expected to vary as $[(\sin x)/x]^2$. Edge scattering is polarization dependent: front edges have maximum return when the incident electric field is parallel to the edge; and rear edges have maximum return when the electric field is perpendicular to the edge. Because the edges of most fins are presented obliquely to the radar in the nose-on sector, fin edge scattering in the nose-on sector is not usually a dominant mechanism.

The traveling wave return is polarization dependent. It occurs only when there is a component of the incident electric field along the body surface and in the plane of incidence. The TW return is due to a reflection of the induced forward surface wave at the rear termination of the body. This reflected current wave radiates back toward the radar like an end-fed long-wire antenna. The peak of the traveling wave return, if present at all, occurs in the nose-on region at an angle given by (14.14). Therefore, as the body becomes electrically longer, the TW peak moves closer to nose-on incidence.

Specular scattering may be an important mechanism if a radome is not present and the nose geometry is not a sharp tip. For example, a spherical metallic nose cap with a 3 in. radius would have an RCS of

$$\sigma = \pi a^2 = 0.018 \text{ m}^2 = -17.4 \text{ dBsm} \tag{14.31}$$

The echo areas of other frontal geometries can be estimated using formulas related to those in Table 14.1.

The returns in the broadside aspect sectors are due to specular scattering mechanisms and, hence, can be estimated fairly accurately. The forward sector returns, however, are generally due to nonspecular mechanisms: hence, it is much more difficult to identify the scattering mechanisms or to estimate the RCS. Forward sector mechanisms include returns due to the seeker or radome, rear edges, straight edges, surface traveling waves, and specular contributions from the nose.

14.5 DATA REDUCTION

An important element of RCS analysis is what to do with raw measured data, and how to reduce and present the data. Although there are no standards for doing this, a possible approach is outlined in this section.

For typical test programs, raw data are obtained for several targets or configurations for multiple pitch angles, roll angles, frequencies, and polarizations. Typical data sets can number over 700 individual runs, with perhaps 50 or more runs over the test matrix for just one target or configuration. Each raw data set is in the form of (angle, RCS) data pairs, typically obtained every 0.5° to 0.1° for either a partial or complete azimuthal cut. Data reduction includes not only each raw data set, but also summaries for each target in the test matrix.

Data reduction can take many forms, and although we cannot possibly cover them all, it is worthwhile mentioning how data are smoothed. Most targets of interest have dozens or even hundreds of scattering elements, and we have seen that the RCS pattern with even a handful of scatterers scintillates rapidly with changing aspect angle. At the higher frequencies, the individual lobes in the pattern may be spaced less than 0.1° apart, and a measured pattern can often consist of a band of ink across the chart paper. Even though the RCS specialist may be interested in the details of such lobe structures, managers and radar system designers need characterizations of the data in a much broader sense. Averages, medians, and standard deviations of individual test runs are more meaningful, as well as the statistics formed over the parameters in the test matrix.

In forming an average or median, we must decide how many contiguous data points will be used. Because the RCS pattern is usually sampled at a fixed angular rate, often at intervals of 0.1°, the decision amounts to selecting an angular "window" over which the averaging will be performed. Typically, the window ranges in width from 1° to 10°, depending on the characteristics of the RCS fluctuations. A scientific criterion may be used in the selection, such as ensuring that at least three or four lobes be included in the window, or we may select the width on the basis of previous experience with similar data sets. In one case, the selection is based on a scientific objective, but in the other it is simply because "that's the way we've always done it."

Once the angular window width has been selected, we must choose the "slide," or the amount by which the window will be indexed across the RCS pattern. The slide should never be greater than the width of the window, for this will create gaps in the pattern over which no averaging is performed. The slide can be as small as one datum, for which one new datum is added to the collection to be averaged while the oldest datum is dropped from the list, or it can be as large as the window itself, for which a complete set of new data points are fetched and

averaged. Obviously, smaller slides generate finer patterns, but require more processing time. Slides of 1° and 2° are common, and slides are often set to the window width to generate preliminary "quick-look" RCS plots. These plots are usually only for the purpose of preliminary assessment of a test run just completed during measurements, with the expectation that finer processing will be performed later.

The raw (but calibrated) data are invariably stored on the recording medium in decibel values, and depending on the kind of processing to be performed, we may need to take the antilog of each datum prior to further processing. This is particularly true of the square meter mean (average), because the logarithm of the square meter average of a collection of numbers is not the same as the average of their logarithms. On the other hand, the logarithm of the median value of a collection of numbers is the same as the median of their logarithms; hence the antilog need not be taken prior to subsequent processing. In the discussion that follows, *linear space* refers to the antilogs of the data values, and *log space* refers to the decibel (logarithmic) form of the recorded data.

Each reduced data run may take several forms: smoothed data over a specified window and slide for three percentile levels; sector data over three specified angular regions for median, mean, and standard deviation in dB (log) space; mean and standard deviation in square meter (linear) space; and *probability density function* (PDF) and *cumulative distribution function* (CDF) for each of the sectors. The test matrix summary may have the following forms:

- A matrix "roadmap" showing run number, pitch, roll, frequency, polarization, and operator comments and the front sector median, mean, and standard deviation;
- A data file for use in plotting a target response as a function of the test matrix variables such as RCS versus pitch angle, frequency, polarization, and roll angle.

An example of a matrix roadmap is shown in Figure 14.12. Test matrix summary plots, as might be obtained from the summary data, are shown in Figure 14.13.

14.5.1 RCS Data Requirements

The raw data typically are in the form of the cross section in dBsm for every 0.1°, or 3600 data points per 360° run. The objective of data reduction is to present this data in a format more meaningful to its various users. Therefore, the display format and reduction technique must be selected with the user in mind. A data base objective, for example, could have a variety of purposes:

- Modeling threat effectiveness;
- Determining the impact of component signatures on total vehicle signatures;
- Reducing the radar cross section;

System: *Example*

Pitch (degrees)	Roll	Freq. (MHz)	Pol.	Run #	Median RCS(dBsm)	Mean RCS(dBsm)	STD (dBsm)
-20	0	3200	V	1000	0.00	0.00	0.00
-20	0	3200	H	1000	0.00	0.00	0.00
-20	0	6500	V	1000	0.00	0.00	0.00
-20	0	6500	H	1000	0.00	0.00	0.00
-20	0	9700	V	1000	0.00	0.00	0.00
-20	0	9700	H	1000	0.00	0.00	0.00
-20	0	16000	V	1000	0.00	0.00	0.00
-20	0	16000	H	1000	0.00	0.00	0.00
-10	0	3200	V	1000	0.00	0.00	0.00
-10	0	3200	H	1000	0.00	0.00	0.00
-10	0	6500	V	1000	0.00	0.00	0.00
-10	0	6500	H	1000	0.00	0.00	0.00
-10	0	9700	V	1000	0.00	0.00	0.00
-10	0	9700	H	1000	0.00	0.00	0.00
-10	0	16000	V	1000	0.00	0.00	0.00
-10	0	16000	H	1000	0.00	0.00	0.00
0	0	3200	V	1000	0.00	0.00	0.00
0	0	3200	H	1000	0.00	0.00	0.00
0	0	6500	V	1000	0.00	0.00	0.00
0	0	6500	H	1000	0.00	0.00	0.00
0	0	9700	V	1000	0.00	0.00	0.00
0	0	9700	H	1000	0.00	0.00	0.00
0	0	16000	V	1000	0.00	0.00	0.00
0	0	16000	H	1000	0.00	0.00	0.00
10	0	3200	V	1000	0.00	0.00	0.00
10	0	3200	H	1000	0.00	0.00	0.00
10	0	6500	V	1000	0.00	0.00	0.00
10	0	6500	H	1000	0.00	0.00	0.00
10	0	9700	V	1000	0.00	0.00	0.00
10	0	9700	H	1000	0.00	0.00	0.00
10	0	16000	V	1000	0.00	0.00	0.00
10	0	16000	H	1000	0.00	0.00	0.00
20	0	3200	V	1000	0.00	0.00	0.00
20	0	3200	H	1000	0.00	0.00	0.00
20	0	6500	V	1000	0.00	0.00	0.00
20	0	6500	H	1000	0.00	0.00	0.00
20	0	9700	V	1000	0.00	0.00	0.00
20	0	9700	H	1000	0.00	0.00	0.00
20	0	16000	V	1000	0.00	0.00	0.00
20	0	16000	H	1000	0.00	0.00	0.00

PROJ #0000 15-MAR-84

Figure 14.12. Test matrix "roadmap" example.

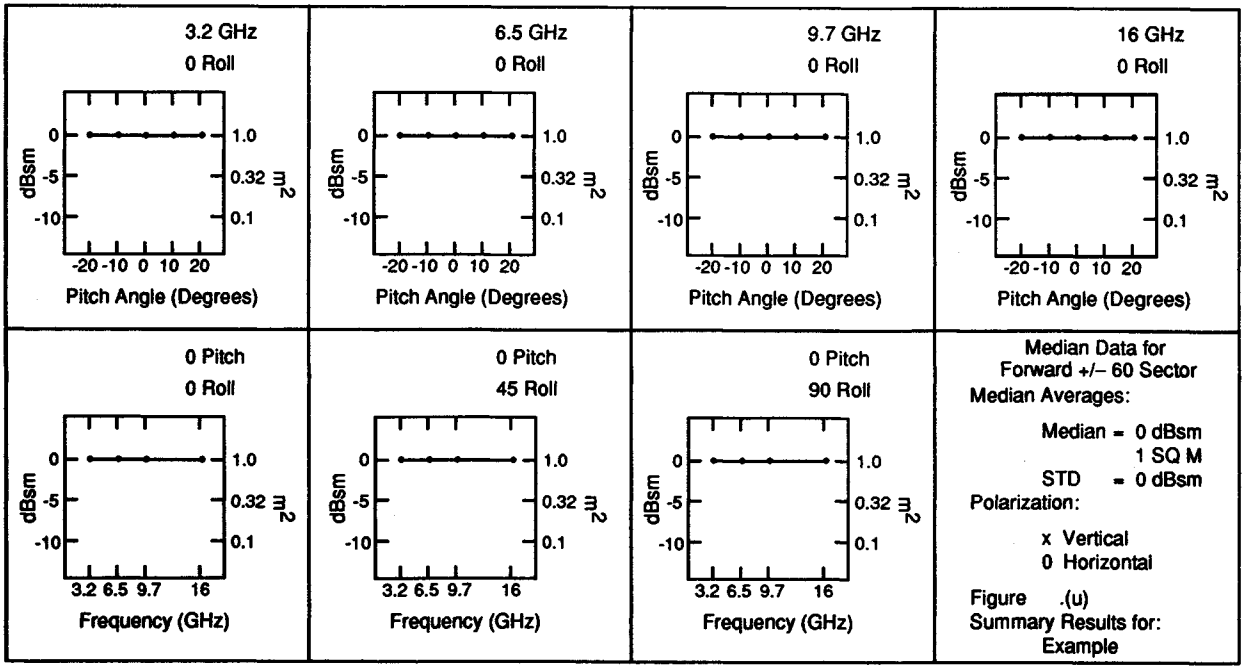

Figure 14.13. Summary results format example.

- Developing design requirements;
- Specifying requirements.

The following discussion presents the rationale for the various reduction formats along with examples.

One purpose for measuring RCS is to determine the target detectability by a given radar. Detection, however, is a statistical process that involves the signal level at the radar receiver. Most detection analyses use a statistical model for target fluctuations and a statistical description for unwanted contaminating signals such as clutter, multipath, and noise. The typical track radar antenna has high gain (a narrow pencil beam, typically 1° to 2° wide) in one or both angular directions.

The RCS of airborne targets is typically of interest over a limited sector or cone in space for which a threat is present. For aircraft, this threat sector is a forward cone in both the yaw and pitch planes of the target. Targets can be characterized over given threat sectors by median data or RCS distribution functions, which include medians, averages, and standard deviations. The average median is defined as the average over the test matrix (frequency, polarization, pitch, and roll) of each sector median.

RCSR analysts are usually interested in raw or nearly raw RCS data. This is because they are concerned with the scattering mechanisms responsible for the return in some localized sector for which they may be able to suggest methods for reduction. Data of interest to project managers and operations analysts, on the other hand, are for encounter scenarios or engagement computer codes. Generally, they seek only one or two numbers, rather than dozens or hundreds of numbers, characterizing a given target over a sector in space. These are the mean and standard deviation or median.

From this discussion, it is evident that the types of RCS data required by various members of the user community are

- Raw data;
- Smoothed data;
- Statistical data;
- Single number, median, mean, and standard deviation characterizations.

A final consideration in any data reduction exercise is the large volume of data to be processed. For example, over 700 runs, if one page were devoted to presenting each reduced RCS pattern, would require 700 pages to display the raw data patterns. For two pages per run, 1400 pages would result, and so on. It is clear that data reduction should be limited to one page per run, and it should place as much information as possible onto this single-page format.

14.6 RCS DATA PRESENTATION FORMATS

Presentation of RCS data has evolved considerably now that significant computational and presentation graphics capability has become increasingly available.

Index

S